Numerical analysis of light-round ignition in annular spray-flame combustors with realistic thermal wall conditions

Karl Töpperwien

université PARIS-SACLAY

Numerical analysis of light-round ignition in annular spray-flame combustors with realistic thermal wall conditions

Analyse numérique de l'allumage circulaire dans les foyers annulaires diphasiques avec conditions thermiques de paroi réalistes

Thèse de doctorat de l'Université Paris-Saclay

École doctorale n° 579, Sciences mécaniques et énergétiques, matériaux et géosciences (SMEMaG)
Spécialité de doctorat: Combustion
Graduate School: Sciences de l'ingénierie et des systèmes
Référent: CentraleSupélec

Thèse préparée dans l'unité de recherche **EM2C (Université Paris-Saclay, CNRS)**, sous la direction de **Ronan VICQUELIN**, Professeur des Universités

Thèse soutenue à Paris-Saclay, le 29 juin 2022, par

Karl TÖPPERWIEN

Composition du jury:

Christine Rousselle Professeur, Université d'Orléans (PRISME)	Présidente
Laurent Gicquel Chercheur senior, CERFACS	Rapporteur
Epaminondas Mastorakos Professeur, University of Cambridge	Rapporteur
Sébastien Candel Professeur, CentraleSupélec (EM2C), Université Paris-Saclay	Examinateur
James Dawson Professeur, Norwegian University of Science and Technology (NTNU)	Examinateur
Denis Veynante Directeur de recherche, CNRS (EM2C)	Examinateur
Stéphane Richard Chef du Service DT/MD/CC, Safran Helicopter Engines	Invité
Ronan Vicquelin Professeur, CentraleSupélec (EM2C), Université Paris-Saclay	Directeur de thèse

THESE DE DOCTORAT
NNT: 2022UPAST093

To my parents

Acknowledgments

The preparation of this PhD thesis involved not only excellent supervision, but also multi-national collaborations and funding from the European Commission without which this work wouldn't have been possible.

First, I would like to thank the members of my jury for having accepted to review my manuscript on a quite short notice, in particular Laurent Gicquel and Epaminondas Mastorakos. I thoroughly enjoyed our discussion on the day of my defense, and I was overwhelmed by the detailed reports and the critical acclaim of my work. It's a pity that we haven't met very often (if at all) during the ANNULIGhT project (mostly due to the pandemic), but I hope my defense did not mark our last encounter and I look forward to many more discussions yet to come.

The same holds true for Christine Rousselle, president of the jury, whom I would also like to thank for her enthusiastic appreciation of my slide deck. It was a pleasure meeting and discussing with you and I am thankful that you had managed to keep me calm despite all issues with room audio in the Rousseau Theater we were facing that day (honorable mention of Preethi and Maxime who were managing the livestream and had also helped testing the equipment).

I am also honored to have had the opportunity to collaborate with Sébastien Candel. I have fond memories of our conversations and discussions related to my first paper for the ASME Turbo Expo 2020 (and numerous ones thereafter), never short of helpful suggestions and feedback, an unparalleled knowledge of the scientific literature and fundamental theories, always kind and patient, and never hesitant to reexplain his arguments when I struggled to follow along.

Special thanks to James Dawson, not only for his role as a jury member, but also for managing the ANNULIGhT project as well as our biannual meetings and training sessions. Besides, I am very grateful for the opportunity of a virtual secondment at NTNU (again due to the pandemic) and the exchanges and collaboration with you and Yi-Hao Kwah.

The jury list goes on with Denis Veynante whom I would like to thank particularly for the helpful discussions on dynamic combustion modeling. This subject seemed to me quite daunting at first (some would even argue you must have a French passport to do research in that field), but Denis' comprehensive explanations have left no question unanswered and made me recognize the ingenuity of dynamic closure approaches.

I also wish to thank Stéphane Richard for his first-hand feedback from an industry viewpoint (or, as Laurent had put it, from an "AVBP customer viewpoint"), highlighting the much appreciated cooperation between academia and industry.

Lastly, I couldn't be happier with my supervisor Ronan "Roro" Vicquelin who I look up to for being a great scientist, a great mentor, teacher and an absolutely great character. Even when I hit a seemingly insurmountable roadblock, I always left our meetings and discussions with renewed enthusiasm and more clever ideas to work around a problem. Most memorable are our countless rehearsals to give my presentations the finishing touch, hands-on code debugging

sessions, overnight shifts (Vancouver!), bad puns and even nerdier jokes (some of which may actually have resonated with him), lighthearted comments on the quirks of German and French nationals, the purported superiority of Macbooks, or the infamous RV-compile-test™! His thorough understanding of fundamentals and complex theories paired with efficient problem solving and a good sense of humor had clearly struck a chord with me, and has been a vital source of my motivation and passion about scientific research. I can wholeheartedly say that it has always been a pleasure working with you!

Beyond my jury, it was my privilege to work with a few more renowned researchers at our lab, notably Daniel Durox who has been a treasure trove of knowledge about every little aspect related to annular combustion chambers (and beyond). Whether I needed experimental data, old lab records, or detailed information of experimental setups, he could always provide great help while leaving me wondering how he could possibly manage to remember all of that even after years.

When it comes to two-phase flow problems, I could reliably get answers from Aymeric Vié while improving my French language skills in conversations with a high WPM count (the same positive "side effects" actually hold true for conversations with Christopher Betrancourt, though with more casual topics).

I should also mention two venerable researchers who were chiefly concerned with taming my immensurate hunger (due to riding my bike uphill the steep road from Lozère Station to the campus of Paris Télécom, next to Polytechnique, every day): Morgan Chabanon and Christophe Laux. My campaigning for an adequate "*croissant*-payment" aside (*e.g.,* for PhD students putting extra work in presentations for lab visits and open days that Morgan organized), I always appreciated those days where I could have an extra snack of fine French pastry.

Of course, the lab wouldn't be the same without the support from Brigitte Llobel, Noï Lavaud and Nathalie Rodrigues. Their help and efficiency with handling the administrative paperwork (*e.g.,* for travels) is second to none, and on top of that they even assisted in getting my rental agreement signed (which involved Brigitte having a serious word with the real estate agent) and making my arrival in France as smooth as possible.

Similarly, Jean-Michel Dupays and Sébastien Turgis had me covered whenever I had issues with HPC clusters, compiler packages, data hoarding, slow iMacs, or extras (second screen, more storage space, travel Macbooks). Most often they could help me out in no time, at day and at night. I can't thank Jean-Michel enough for signing me up for the beta tester program on the Mésocentre's new HPC cluster RUCHE (or as I like to call it: "Ruru"). Having had 2k cores essentially for my own during several weeks has certainly helped accelerating my calibration simulations for fuel injection.

Special thanks to the big bosses Sébastien Ducruix and Gabi Stancu for their commitment and support of all PhD students even in the most complicated situations that came with the pandemic.

Next, I am convinced that the entire "PhD experience" including life in and around the lab would be quite dull without my fellow colleagues (PhDs and post-docs) and friends: Théa who was about to graduate when I arrived at the lab, and whose work on light-round simulations has instigated further research works not only at our laboratory, but also at CERFACS.

Preethi, a painstaking researcher, has been such a great pleasure to work with, offering experimental insights and any sort of help whenever needed. We had a fun time together during coffee breaks with Guillaume, ANNULIGhT travels and workshops, and I will most

definitely miss the awesome Indian food!

Speaking of Guillaume, I look up to his expertise and ingenuity in analyzing and interpreting data, and I am grateful for sharing his unparalleled knowledge on dynamic combustion phenomena in annular combustors. Thanks to him I could improve the calibration and fidelity of the fuel injection model in my numerical simulations using data from a fully-fledged and meticulous experimental measurement campaign he had carried out for me. Beyond research, we have shared a passion for exquisite food, resulting in countless cooking sessions with tons of fun.

Also, one cannot spell MICCA simulations without Stephano (DisplayMixture!) whose meticulous work has paved the way for my later light-round simulations. Stefano has been a great mentor, and our countless discussions and our collaboration have definitely helped me to pursue my work with confidence. I also look back to the days where we could still hang out together (before the pandemic), and of course the trip to Aachen for ICNC '19. A huge thanks to all of you!

Then there is Pedro (when in doubt: `grep 500`) and Lorella whom I would like to thank for the crash course in OpenPALM right before their PhD defenses. Kevin and I have picked up development later and we were having a great time during our coding sessions (`bidouille.py`) where I could simultaneously spice up my French slang vocabulary to increase my street cred'! Not to forget the emoji-filled Wiki entries on Gitlab (which we wrote with the same diligence as the code itself), or our famed Zoom call with the Prince of Wales (ok, technically it was a prerecorded address for ASME Turbo Expo 2020, but we were in the same Zoom room, so I'm sure it counts)! Most of the time however we hung out with the rest of the Roro-crew: Guilhem (aka G^2, commit hash `41ce2aa` & `agath_table_clean`), Luc (screw PowerPoint, imma usin' Outlook[1] for my presentations) and Matteo. You guys were absolutely killing it!!! Special thanks to G^2 for his expertise in COMMCOMB that had helped me pulling off the table magic for the tabulated wall model!

It is obviously no secret that the PhD student's life elixir is coffee and there is no way I could not toast to my Team Nespresso (#notsponsored): Hernando (*attention – atención – atenção*), Constantin (or Constantiiiiiiiiin), Junghwa, and our recent newcomers Tan Phong, Yanis and Sam, as well as our "oldies", Yacine and Livia (though strict opponents of coffee pods). Cin Cin guys!

I also spent a great two weeks of ~~vacation~~ conference in Vancouver with Valentin (aka Michael) and Hernando, and probably had the best road trip through Canada so far!

Victorien (*Je bois (systématiquement*); *Il s'appelle Just Leblanc*; *(Il n'a pas dit) Bonjour*) and Pierre (*présent !*) deserve an honorable mention as well for being the ambassadors of French culture (music, theater and cinema). Thank you for sharing all the references and anecdotes I didn't quite understand at first, leaving me wondering why you were having a great lough while I didn't get the joke *at all* (now I do though!).

I will also miss the private jokes about the peculiarities of the university canteen we made with Nicolas, Arthur, Erwan, Moises and Roxane (*C'est 6 points !! — J'enlève le pain ?!?*) which had become our ritual at lunch.

As already foreshadowed previously, another infamous "ritual" involved Morgan searching for volunteers presenting some of the activities of our lab. I am convinced it had to be a

[1] Sometimes also a terminal

coincidence that I always found myself with the same "usual suspects": Marie, Olivier, Axel, Maxime, Junghwa, Gaël, Victorien, Jean and Corentin. Thank you guys for your commitment! I truly believe that it is an important task to share our passion for scientific research with future generations, as much as it is important to *always* remember to ask for croissants as a compensation!!!

And of course I would like to take a minute to appreciate the great community of ANNULIGhT fellows: Yi Hao, Thomas(z), Sylvain, Ermanno, Abhijeet, Javier, Carlos, Guillaume, Naman, Abel, Francesco, Roberto, Stephano, and Preethi. I absolutely enjoyed every time we could meet during our trainings and workshops, including checking out restaurants and bars in European cities. (Also, James, if you're still reading, it wasn't me who ordered the expensive bottle of Pomerol in Toulouse that somehow found it's way on the bill — I had just ordered the more reasonably priced Pouilly fumé for it's better pairing with the fish. Anyway, thanks European Commission!)

Speaking of Toulouse, I am very grateful for CERFACS that had hosted two extended secondments in 2019. It has been an excellent opportunity to collaborate with Bénédicte Cuenot, Eleonore Riber and Felix Collin-Bastiani, and has resulted in my very first paper. Getting support from the developers of AVBP has jumpstarted my own development work and proved to be a valuable experience, not to mention the "ARC-bootcamp" with Quentin, Simon and Davide, as well as the support from Florent "Big Flo" Duchaine for AVTP and OpenPALM.

On that note, I wish to thank Thierry Poinsot who had closely followed my work and shown great interest in our results, leading to "sticky situations" where he was simultaneously probing me on the implementation of evaporation models while having four *éclairs* in a row (that I had brought for my birthday among other pastry of course (I can recommend *Au poussin bleu*, it's Thierry-approved!)), which was then concluded with a thirty minute presentation I had to prepare on short notice. Joking aside, Thierry has an incredible ability of getting a grasp on *any* scientific subject in virtually no time and articulates his honest opinion quite bluntly — which I strongly endorse, always leaving me with enough food for thought (no pun intended). I genuinely believe that this kind of feedback is vital for young researchers and so far I have always looked forward to every single encounter we had.

Before this chapter gets too long I (finally) wish to address my office mates in ED.202, the bestest office ever to exist (no, dear freshmen, we're *not* the SGAE, they're in the *opposite* block): David, my first-year French teacher and probably the only person who could discuss the appropriateness of certain colormaps as enthusiastically as me; Thomas (*Pourquoi est-ce que c'est drôle ?!*) who was never short of punchlines from *Les Guignols*; Mathieu, Claire, Suzanne (Wakanda forever!!!), and of course Alexandre, my biggest supporter helping to enforce lunch breaks at 11:30 am (honk twice!) and member of the 9:30 am coffee club with Valentin and me; Jean who had the ingenious idea to show me videos by David Castello-Lopes (*Bonjour-in*, also known as *e prépausal*), involuntarily causing me to adopt the Parisian accent; Gaël (*n'est-il pas ?!*) and Junghwa (Team Expats), the only person I could initially understand (in English...) and who made me feel less alone in a foreign country. Thank you all of you for all the highs and lows, the fun, the silly jokes (on repeat) and the unforgettable time we spent together every day! The same holds for the "oldies" (David, Ulysse, Arnaud, Maxime, Arthur) and all the recent newcomers: Yuri, Julie, Guillaume, Véranika, Cyrine, Jean-Baptiste (2x), Geoffrey, Fred, Nicolas, Renaud, Lorenn and Stéphane.

On a separate note it shouldn't go unmentioned that Jean and Victorien are also distinguished members of the SSAVE® (*Société Savante des Amateurs de Viennoiseries de l'EM2C*,

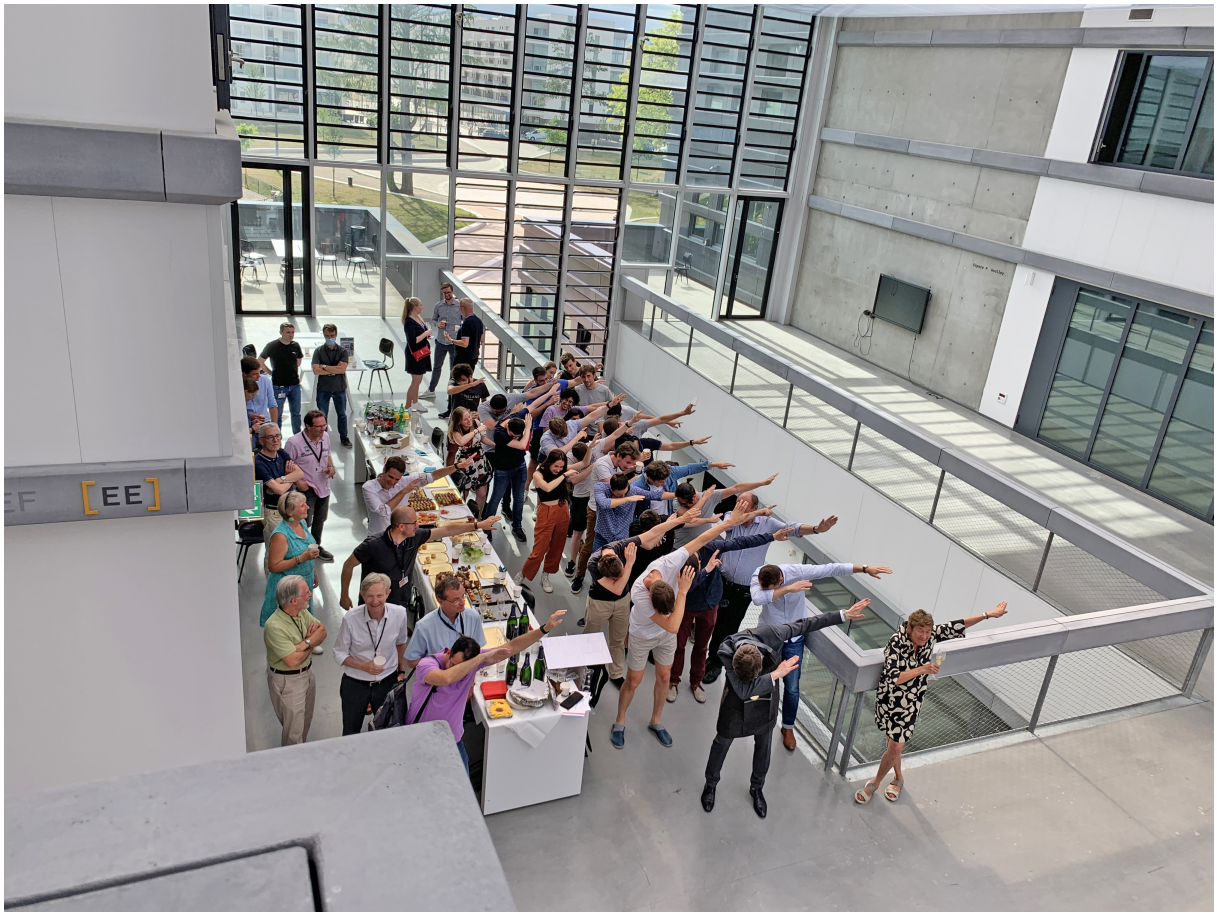

Figure 1: Mission accomplished: official dab (aka PhDab) after my PhD defense at CentraleSupélec on June 29, 2022.

"Academy of Pastry Enthusiasts at the EM2C lab") which I had the honor to preside. Our principal goal has always been to ensure an abundance of croissants which involved each and every employee bringing a selection of pastry on various occasions (*e.g.*, birthdays, poster awards, onboarding, farewell ceremonies). Thank you Jean and Victorien for helping to enforce our Academy's rules, and thank you all of you for the fulfillment of your duties.

And lastly, I wish to express my most sincere gratitude and appreciation to my family and friends from Germany who joined via Teams (from Aachen, Berlin, Düsseldorf or Hamburg) or even made the extra effort to travel to France (family, "die Beises", Uli & Doris). I can't thank my parents enough for the continuous support, not only during my time in France, but also long before and throughout my entire life, prioritizing my well-being over everything else, even with a $428\,\mathrm{km}$ distance between Düsseldorf and Orsay. You have managed to pull off an amazing feat at the day of my defense which involved a sophisticated plan made behind the scenes, and complex logistical challenges. Thank you for such a memorable day! I would also like to thank my brother who has been not only a great help when moving to a new apartment, but also encouraged me to take the next step in the right direction when I was undecided. Thank you once again to all of you!

Abstract

The forthcoming transition in aviation burner technology towards renewable energy sources and reduced emissions requires aero-engine combustors to operate on increasingly cleaner fuels and new designs without compromising on safety. Engine restart in particular is of paramount importance, as its success must be ensured under a variety of operating conditions, which are specified by certification authorities. Restart scenarios involve (among others) quick relight in climb, or restart from windmilling at high altitude, equivalent to a large range of inflow temperatures, restart delay periods, and combustor wall temperatures. In quick relight, engine parts will remain at an elevated temperature as there is not enough time for the air flow to cause a noticeable cooling effect. Conversely, restart from windmilling at high altitude after extended delay periods is likely to be performed with substantially cooled combustor walls, impeding fuel evaporation and successful ignition. Academic test facilities which can emulate real engine conditions in terms of both temperature and pressure are extremely scarce due to their complexity and cost. However, the study of wall temperature effects on ignition in simplified lab-scale annular combustors has recently received more attention. In particular, the impact on flame propagation during light-round — the final phase in a complex four-step process of forced ignition in annular combustors — has been revealed experimentally, indicating faster flame propagation and shorter light-round durations at increased wall temperatures over ambient temperature walls. Despite its first order impact, the role of heat transfer was not fully clarified in a comprehensive analysis. Therefore, we study light-round ignition numerically and theoretically in the annular spray-flame combustor MICCA-Spray in a lab-scale setting in two configurations to enhance the effect of heat transfer: (i) ambient temperature walls, approximating restart from windmilling, and (ii) preheated combustor walls, approximating quick relight. Large-Eddy Simulations are performed in a unique setup including Lagrangian particle tracking for the polydisperse liquid fuel spray, a dynamic combustion model, and a novel tabulated wall model with a detailed description of thermophysical properties in the boundary layer. Predicted light-round durations agree remarkably well with experimental data. It is shown that the volumetric expansion of burnt gases induces a flow acceleration in azimuthal direction which constitutes the main driving mechanism of flame propagation in the first case. Droplet accumulations in the wake of swirling jets are generated ahead of the propagating flame fronts, which in turn cause a characteristic sawtooth propagation mode of the leading point. A cooling effect of the combustor walls on burnt gases is particularly pronounced downstream, diminishing the resulting flame propagation speed. For the second case, precursor Conjugate Heat Transfer simulations are carried out to obtain realistic wall temperature profiles in stationary operating conditions, which are not readily available from the experiment. These temperature profiles are subsequently imposed as boundary conditions for prefueling and final light-round simulations in preheated conditions. Results suggest that preheating diminishes the effect of the liquid phase, and enhances the azimuthal flow acceleration. Fresh gas preheating in the second case causes a substantial increase of the laminar flame speed over the first case, outweighing the observed decrease of the density ratio. These observations are supported

by a theoretical analysis by means of a low-order model, capable of predicting average flame propagation speeds from LES data. It is also used to emphasize the importance of detailed modeling, and proves that all governing mechanisms must be accurately modeled in LES, which would otherwise be impaired by compensating errors. The comprehensive analysis also clarifies the role of heat transfers during light-round. Finally, a dynamic flame stabilization process is examined, initially observed during light-round and studied in detail in a single-injector combustor. Two distinct phases are observed, starting with a flame anchoring inside the injector unit during a characteristic time, before transitioning into the final position detached from the injector.

Résumé

La transition vers des technologies à faibles émissions nécessite que les chambres de combustion des moteurs aéronautiques fonctionnent avec des carburants de plus en plus propres. Le redémarrage du moteur doit se produire de manière fiable et sûr et doit être assuré pour différentes points de fonctionnement, qui sont spécifiés par les autorités de certification. Les scénarios de redémarrage impliquent (entre autres) un rallumage rapide en montée, ou un redémarrage à haute altitude en auto-rotation, ce qui entraine une large gamme de températures d'air, de délais de redémarrage et de températures pariétales de chambre de combustion. L'étude des effets de la température pariétale sur l'allumage dans des foyers annulaires simplifiés à l'échelle du laboratoire a récemment reçu plus d'attention. En particulier, l'impact sur la propagation de la flamme pendant l'allumage circulaire (*light-round* en anglais) — la phase finale du processus en quatre étapes d'allumage forcé dans les chambres de combustion annulaires — a été révélé expérimentalement, indiquant une propagation plus rapide de la flamme et des durées d'allumage plus courtes à des températures de paroi élevées par rapport aux parois à température ambiante. Malgré son impact de premier ordre, le rôle des transferts de chaleur n'a pas été entièrement clarifié. Par conséquent, l'allumage circulaire est étudié numériquement et théoriquement dans la chambre de combustion annulaire diphasique MICCA-Spray en deux configurations :(i) parois à température ambiante, représentant un cas de redémarrage à haute altitude, et (ii) parois de la chambre de combustion préchauffées, ce qui correspond à un rallumage rapide. Des simulations aux grandes échelles (*LES* en anglais) sont effectuées dans une configuration unique comprenant une description lagrangienne polydispersé des gouttes du spray de combustible, un modèle de combustion dynamique et un nouveau modèle de paroi tabulé avec une description détaillée des propriétés thermophysiques dans la couche limite. Les durées prédites d'allumage retrouvent remarquablement bien les données expérimentales. Il est démontré que l'expansion volumétrique des gaz brûlés induit une accélération azimutale de l'écoulement qui constitue un mécanisme clé de la propagation de flamme dans le premier cas. Des accumulations de gouttes dans le sillage des jets swirlés sont générées en avant des fronts de flamme, ce qui provoque un mode de propagation caractéristique en dents de scie de la pointe avant de la flamme. Un effet de refroidissement des parois de la chambre de combustion sur les gaz brûlés est particulièrement prononcé en aval, diminuant la vitesse de propagation résultante. Pour le deuxième cas, des simulations de transfert conjugué de chaleur sont effectuées pour obtenir des profils de température de paroi réalistes dans des conditions de fonctionnement stationnaires, qui ne sont pas disponibles expérimentalement. Ces profils de température sont ensuite imposés comme conditions aux limites pour les simulations de carburation ainsi que d'allumage. Les résultats montrent que le préchauffage diminue l'effet de la phase liquide, et augmente l'accélération azimutale de l'écoulement. Le préchauffage des gaz frais dans le second cas provoque une augmentation importante de la vitesse de la flamme laminaire, qui compense la diminution observée du rapport de densité. Ces observations sont ensuite analysées théoriquement à l'aide d'un modèle d'ordre réduit, capable de prédire les vitesses moyennes de propagation de la flamme à partir des données LES. Ce modèle souligne

également l'importance d'une modélisation détaillée, et prouve que tous les mécanismes pilotant la propagation de flamme doivent être modélisés avec précision dans les simulations, afin d'éviter de possibles compensations d'erreur. L'analyse complète clarifie également le rôle des transferts de chaleur pendant l'allumage circulaire. Enfin, un processus dynamique de stabilisation de la flamme est examiné, initialement observé pendant la phase d'allumage et étudié en détail dans une chambre de combustion mono-brûleur. Deux phases distinctes sont observées, commençant par une flamme attachée à l'intérieur de l'injecteur pendant un temps caractéristique, avant la transition vers la position finale détachée de l'injecteur.

Contents

List of Figures

List of Tables

Chapter 1

Introduction

The global transition to renewable energy sources to get the world on track with climate targets requires concerted effort in terms of technological development, regulatory measures and economic incentives. This transition over several decades would not only require multiple steps in different sectors but might also see different paces of advancement (*e.g.,* light duty vehicles vs aviation) (Masri, 2021). Decarbonizing the power generation and aviation sector will strongly depend on the cost of conversion. Therefore, developing clean combustion technologies and advanced renewable fuels, while relying on existing hardware and supply infrastructure are both reasonable and economically viable options, at least in the early stages of the transition process. Thus, making the net-zero emission targets and the energy transition a reality certainly requires intensified research and scientific progress.

Such ambitious endeavors are never achieved in siloed positions but rather in ecosystems of teamwork and international collaboration. The present thesis for example is part of the Innovative Training Network (ITN) "ANNULIGhT" on instabilities, ignition and blow-off in annular combustors. It is funded by the European Commission under the Marie Skłodowska-Curie Actions as part of the Horizon 2020 research and innovation program, hosting a group of Early-Stage Researchers across multiple countries and institutions. Acknowledging the power generation and transportation sector's vital role to play in the energy transition, ANNULIGhT aims at the development of next generation low emission combustors. This task has seen some pitfalls in the past for the following reasons: (i) engine development and improvement can only be performed within the limits of safe and stable operation which itself is limited by the occurrence of unsteady combustion phenomena. Yet, these phenomena are often discovered late into the development process due to the lack of accurate prediction tools. (ii) From an experimental perspective, unsteady combustion problems have been studied in isolated single flames for reasons of cost or simplicity, even though real engines typically feature annular combustor designs with multiple flames. Apart from the fact that certain phenomena can only be studied in those annular designs, their stability characteristics are also known to vastly differ from single-flame combustors. Therefore, the research program seeks to improve and advance our understanding of unsteady and dynamic combustion phenomena by studying them in annular geometries. Three main challenges are specifically addressed:

1. the occurrence of self-excited combustion instabilities associated with large pressure fluctuations threatening the engine's structural integrity,

2. the increased probability of lean blow-off, and

3. ignition and light-round, considered to be safety critical for engine certification.

An in-depth understanding and good control over these aspects is a key enabling step for designing clean combustors.

This thesis is concerned with the numerical investigation and modeling of ignition and light-round in annular combustors and has been carried out at the EM2C laboratory in France. The work faces several challenges actively investigated in the combustion community:

- **Mixture formation:** clean combustion is greatly aided by homogeneous mixture generation, which itself is the subject of intensified research. For today's, as well as for future liquid fuels — commonly used in aero-engines — evaporation rates determine the mixing process and require good knowledge of spray generation, droplet size distributions and droplet number densities. Hence, a first step towards reduced emissions can be made by studying spray generation processes in appropriate injector designs and improving models for multiphase flows in realistic configurations.

- **Chemistry modeling:** reaction mechanisms for hydrocarbon fuels typically involve several hundreds of species and reactions, exacerbating the problem of multi-dimensionality and varying time scales. Therefore, detailed kinetic schemes would render a simulation of complex industrial engines computationally stiff and more difficult to solve with efficient algorithms on computational resources available today. Instead, these cases rely on reduction techniques trading accuracy and generality for more reasonable solution speeds. The resulting simplified reaction schemes are designed for a small set of specific requirements, for example accurate pollutant predictions, study of chemistry/turbulence interactions, or auto-ignition, and are less accurate *beyond* their specifications (*e.g.,* different pressure or fresh gas temperature ranges). Additional research may be needed for future fuels or fuel blends to determine their reaction paths. While promising approaches have been developed claiming to overcome the problem of dimensionality versus accuracy, advances have also to be made in terms of leveraging the power of new and potentially heterogeneous computational hardware, where certain calculations are handed over from traditional CPUs to GPUs.

- **Combustion modeling:** the prediction capability of numerical simulations also depends largely on the employed combustion model and its accuracy. Realistic combustion processes often involve more than one of the asymptotic combustion regimes (premixed, non-premixed or homogeneous auto-ignition), which is particularly challenging to model due to increasing complexity or limitations of the computational resources (*e.g.,* in terms of available memory). Hence, developing and improving combustion models is crucial for accurate predictions of pollutant formation or spray flame combustion for example, and extremely useful to design cleaner combustion engines in general.

- **Multiphysics approaches:** apart from the research fields mentioned above, real combustion devices involve multiple physical processes of equal importance that occur simultaneously. Due to their complexity, they are often neglected, or deliberately simplified at best. Among these processes are heat transfer problems between the internal fluid flow and structural parts of an engine, thermal radiation, or interactions of the combustor with other components of an engine which can all interact with the combustion process under consideration. The study of such interaction demands for true multiphysics approaches to improve our understanding of the coupling between multiple concurrent phenomena, enhance the fidelity of our modeling tools, and ultimately aid clean engine development without compromising on safety. Moreover, research is required to describe each process accurately and efficiently to optimize the utilization of computational resources.

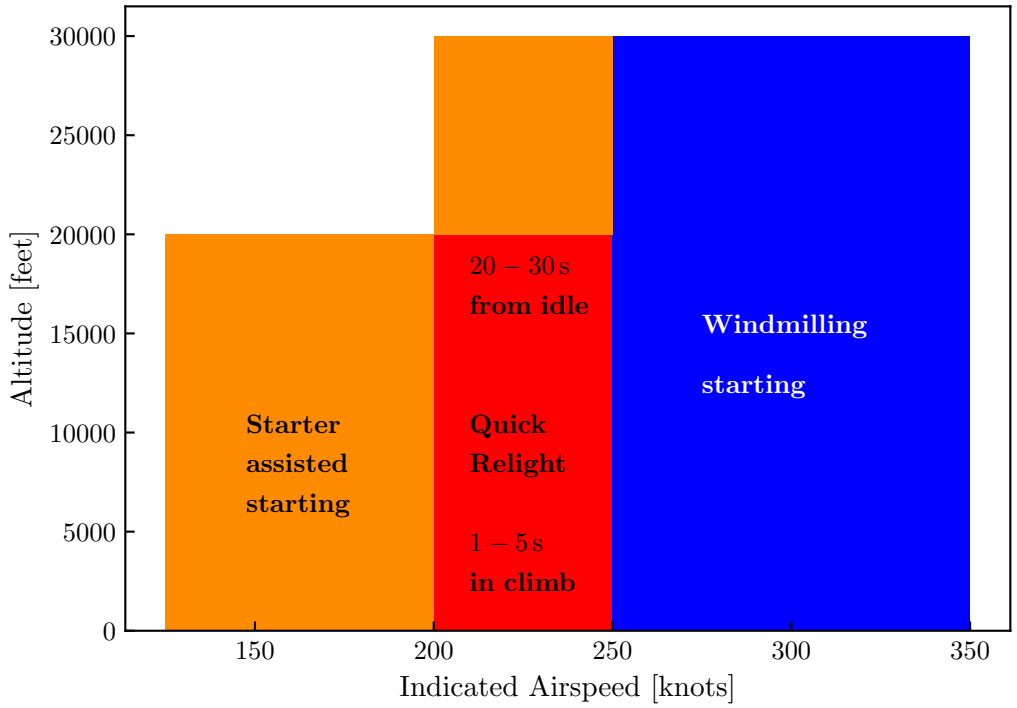

Figure 1.1: Engine certification relight requirements (adopted from Klinger et al. (2011)).

The challenges mentioned above are intricately linked to the ignition process in aero-engines and give a taste of the subjects addressed throughout this manuscript. More specifically, realistic thermal conditions of the combustor walls are of central interest here, and mechanisms by which they affect the ignition process in aero-engine combustors. The need for a detailed characterization and examination originates from engine certification requirements on one hand, and experimental observation on the other hand, which are discussed in the following sections.

Engine certification requirements

According to the EASA's engine certification requirements, restarting capabilities must be proven from

> *"[...] sea-level to the maximum declared restarting altitude in all appropriate configurations likely to affect restarting, including the emergency descent configuration"* (EASA Certification Memorandum CM-PIFS-010, (p. 5), see also EASA CS-E 910).

Thus, the absolute requirement of successful engine restart implies large variations of engine conditions determined by a given restart scenario. An engine's restart capabilities are often assessed in terms of air speeds and altitude, as illustrated in Fig. 1.1. Multiple restart modes can be identified which involve (Klinger et al., 2011):

- **Starter assisted starting:** the engine must restart in-flight with starter assistance within a set time after a commanded or uncommanded in-flight shutdown.

- **Quick Relight:** the engine must immediately relight in-flight while spooling down after a flame-out caused *e.g.,* by pilot error, an interruption of the fuel supply or compressor surge.

- **Windmilling starting:** the engine must restart in-flight within a set time after a commanded or uncommanded in-flight shutdown.

Except for quick relight which is performed within $5\,\mathrm{s}$ after engine shutdown during climb or within $30\,\mathrm{s}$ from idle, additional "delay tests" must be passed during which the delay period between shutdown and restart is intentionally extended. Two delay periods are specified in the Certification Memorandum: (i) up to two minutes, and (ii) at least $15\,\mathrm{min}$ or until the engine oil temperatures are stabilized at their cold soak value.

The following scenarios are thus chosen for their vastly different thermal state at the combustor walls: during quick relight in climb, walls remain at elevated temperatures and the pressure drop is comparably moderate. Due to the short time delays of $5\,\mathrm{s}$ between shutdown and restart, the combustor walls do not have sufficient time to cool, and the compressor has not yet spooled down entirely, still maintaining an elevated pressure level. Conversely, relight at high altitude after extended delays defines another worst-case scenario worth investigating: at $30\,000\,\mathrm{ft}$ of altitude ($9144\,\mathrm{m}$), air temperatures and pressures can be as low as $228\,\mathrm{K}$ and $0.3\,\mathrm{bar}$, respectively. Due to the ram pressure from the momentum of the aircraft, the compressor is windmilling, causing a continued airflow through the engine without elevating the pressure level. Hence, the longer the delay period, the more intense the cooling effect of the air flow. Ensuring successful ignition under these conditions is certainly the most challenging task to achieve, particularly with poor atomization at low pressures and cold environments.

The vastly different conditions in both scenarios promise a noticeably different ignition behavior, which is not fully understood. Therefore, they are considered here in a simplified manner, as specified later.

Investigation of light-round ignition in a lab-scale annular multi-burner setup

Forced ignition in annular multi-burner combustors is a complex process involving four phases (Lefebvre and Ballal, 2010; Mastorakos, 2017): after a spark is generated in phase I, and the initial flame kernel has grown (phase II) to establish a full-scale ignition of the first burner (phase III), a burner-to-burner flame propagation can finally be observed (phase IV) referred to as light-round (Mastorakos, 2017). In aero-engines and gas turbines, a spark is usually generated by an external ignition unit, feeding a high voltage into a discharge igniter plug (also called spark plug) and providing sufficient energy for the onset of the combustion process. Conversely, auto-ignition does not require external forcing to ignite a flammable mixture and can thus start spontaneously if certain conditions in terms of local temperature, pressure or other mixture properties are met. Forced ignition in turn offers full control not only over the discharge rate, but also over the position of the initial flame kernel, and is therefore predominantly used in many types of combustors.

In order to study the full light-round process including flame front merging, an annular multi-burner configuration is required. However, first studies of multi-burner ignition were initially performed in simpler linear burner arrays, neglecting some of the mechanisms that can only be found in annular configurations: Cordier et al. (2013); Barré et al. (2014) have investigated the linear five-burner array KIAI (see Fig. 1.2), observing distinct patterns of

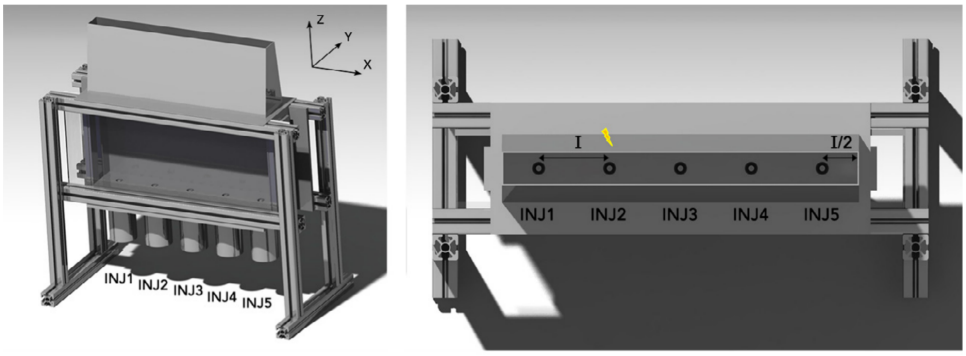

Figure 1.2: Experimental setup of the KIAI multi-burner equipped with 5 injectors (left: side view, right: top view). Image taken from Barré et al. (2014).

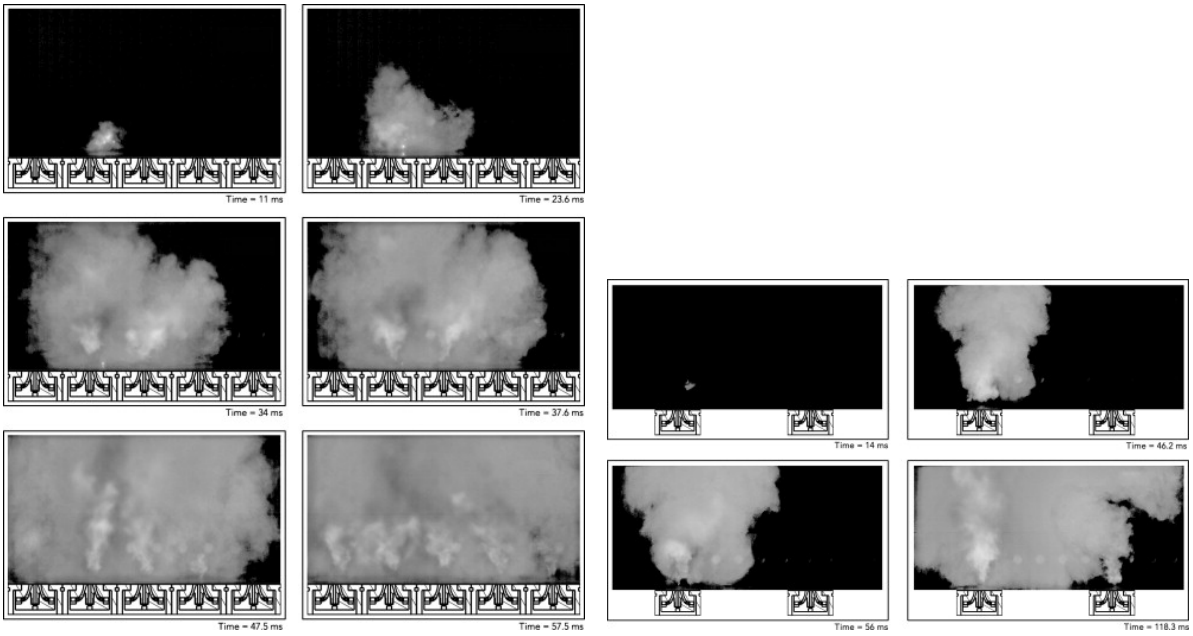

(a) Spanwise flame propagation case (b) Axial flame propagation case

Figure 1.3: Experimental high-speed imaging of flame propagation in the linear premixed five-burner array KIAI. Images taken from Barré et al. (2014).

flame propagation (spanwise, axial and hybrid) in premixed configurations (see experimental imaging in Fig. 1.3). In turn, propagation along flammable bridges is found in a non-premixed configuration of a linear array with five swirled bluff-body burners (Machover and Mastorakos, 2017b).

These are different from patterns with liquid fuel injection systems which exhibit a branch propagation across neighboring spray branches or an arch-like propagation (Marrero-Santiago et al., 2017, 2019). The arch propagation mode is primarily attributed to flow aerodynamics isolating adjacent spray branches between two injectors and leading to an overall lean inter-injector region which the flame cannot cross. Marrero-Santiago et al. (2019) also note that the arch propagation mode substantially increases the ignition delay time. All works cite injector spacing as an influential parameter controlling the resulting pattern or causing the pattern to switch.

Kao et al. (2015) have proposed an empirical model for the flame spreading time in a linear, five-injector setup with radial swirler stages. The governing parameters were identified to be the inter-injector spacing, the air/fuel ratio, the flow Reynolds-number and a normalized

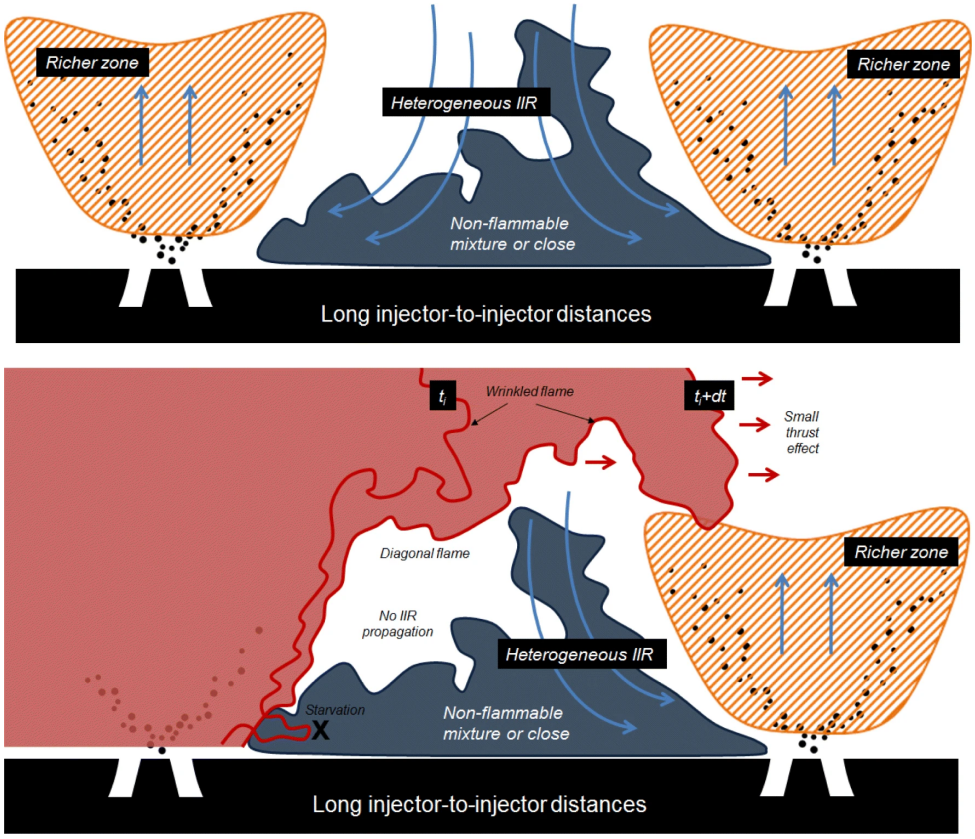

Figure 1.4: Illustration of the flame propagation behavior in the linear five-burner array KIAI fueled with liquid n-heptane. Flow aerodynamics generate non-flammable mixtures in the inter-injector recirculation zone (IIR, top image) for long injector-to-injector spacings, causing the flame to propagate along arches from injector to injector (bottom image). Images taken from Marrero-Santiago et al. (2019).

Figure 1.5: Annular combustor MICCA designed at the EM2C laboratory, equipped with 16 swirled fuel injectors and operated with propane/air mixtures. Image taken from Bourgouin et al. (2013).

air temperature. Ranking each parameter by its associated time scale revealed that the flame spreading time is most sensitive to the inter-swirler spacing, the air/fuel ratio and the Reynolds-number.

While linear burner arrays provide detailed insights into the flame spreading process, they lack key features of industrial annular combustors (*e.g.*, flame propagation as arch, flame front merging). Lab-scale representations of annular designs — the subject of the present work — have emerged with experimental studies by Bourgouin et al. (2013), examining light-round ignition in the premixed 16 burner combustor MICCA at the EM2C laboratory (see Fig. 1.5). High-speed imaging has revealed the flame's distinct shapes during different phases of light-round ignition (see Fig. 1.6): at early instants (*e.g.*, at $t = 10\,\mathrm{ms}$ to $t = 30\,\mathrm{ms}$), a characteristic arch-shape is observed. As the flame elements reach the outlet of the combustion chamber, two separate flame fronts are found propagating through each half of the chamber (between $t = 40\,\mathrm{ms}$ and $t = 80\,\mathrm{ms}$). Flame front merging occurs between $t = 80\,\mathrm{ms}$ and $t = 90\,\mathrm{ms}$, after which residual elements of the flame front disintegrate and exit the combustion chamber, while 16 individual flames are found anchoring at each injector in fully ignited conditions ($t = 110\,\mathrm{ms}$). These characteristic phases and flame shapes were also observed in different operating conditions.

In Cambridge, light-round investigations have been pursued in an annular combustor initially designed by Worth and Dawson (2013) (see Fig. 1.7). The combustor can be operated in various configurations with 12 or 18 bluff-body burners, with or without swirl, and in premixed or non-premixed conditions. Interestingly, Machover and Mastorakos (2017a) report a sawtooth movement from burner to burner in the 12-burner premixed bluff-body configuration with swirl, which was recorded through high-speed imaging of OH^* chemiluminescence (Fig. 1.8). The authors also note that removing swirl attenuated the observed sawtooth pattern.

More recent works also outline an effect of common ignition modes "Spark First, Fuel Later" (SFFL) and "Fuel First, Spark Later" (FFSL) (Xia et al., 2019), bulk flow velocity and equivalence ratio (Gao et al., 2021) on the observed propagation pattern. Experiments have been carried out in an annular design (dubbed "TurboCombo") derived from the MICCA combustor. In FFSL, an arch-like flame propagation is observed, while SFFL exhibits a sawtooth pattern. Furthermore, the SFFL mode is inherently less sensitive to varying equivalence ratios compared to FFSL since the local equivalence ratio may not have reached the target equivalence ratio yet. This behavior is attributed to the time delay imposed by the mass flow controller.

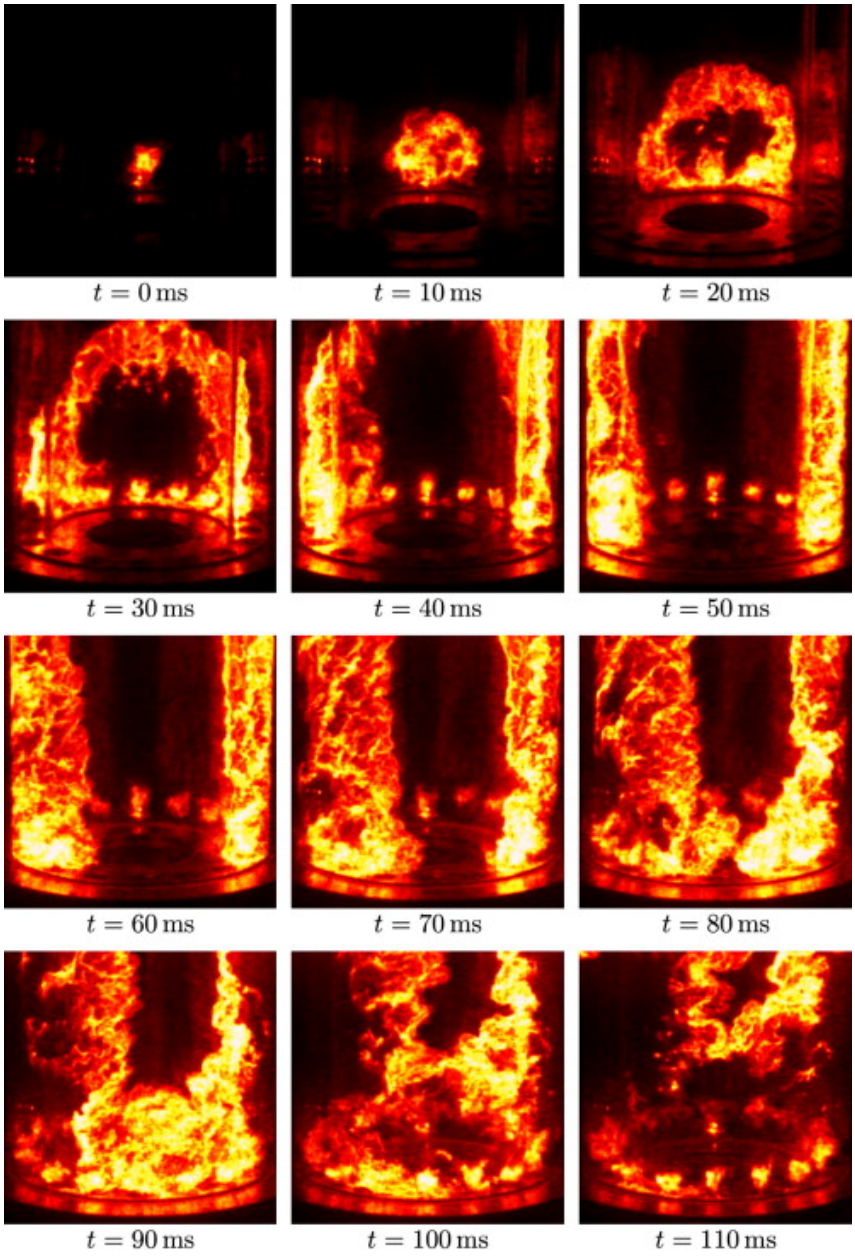

Figure 1.6: High-speed imaging of an ignition sequence in the annular MICCA combustor at the EM2C laboratory. The combustor is operated with a propane/air mixture at $\phi = 0.76$ and an injection velocity of $u_0 = 12.2\,\mathrm{m/s}$. Instantaneous snapshots are shown in false colors. Sequence taken from Bourgouin et al. (2013).

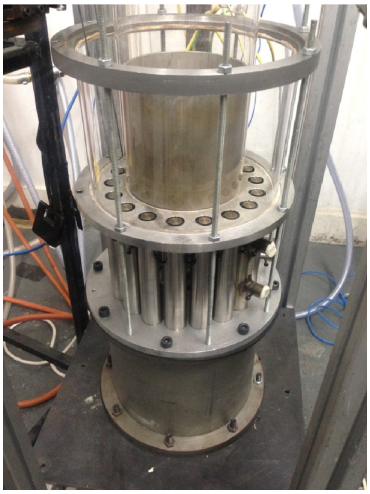

Figure 1.7: Annular premixed burner assembly in Cambridge. Image taken from Machover and Mastorakos (2017a).

Gao et al. (2021) in particular extend the analysis made in linear combustor arrays to a complex, staged annular spray combustor configuration. Depending on the bulk flow velocity and equivalence ratio, the observed flame propagation patterns vary between a spanwise-upstream, an arch-like entrainment and spanwise entrainment pattern.

Beyond propagation patterns, the propagation speed and the resulting light-round duration are subject to extensive research as well and are found to be controlled by (i) burnt gas expansion, (ii) the laminar flame speed and (iii) wall heat transfer (among others). The volumetric expansion of burnt gases in the chamber constitutes a key mechanism (Bourgouin et al., 2013; Machover and Mastorakos, 2017a) governing the flow acceleration in azimuthal direction, which is proportional to the density ratio of fresh and burnt gases (ρ_u/ρ_b). Supported by a theoretical analysis, Bourgouin et al. (2013) have put forth the argument that the flame front is convected by the azimuthal flow velocity component modulating the observed flame propagation speed. During the initial instants in particular, *i.e.* between $t = 20\,\mathrm{ms}$ and $t = 30\,\mathrm{ms}$ in the example of Fig. 1.6, the authors cite buoyancy to contribute to the vertical flame acceleration as well.

The injector velocity is yet another driving mechanism inversely proportional to the measured light-round duration (Bourgouin et al., 2013; Kao et al., 2015; Philip et al., 2015b; Ciardiello et al., 2020). This relation is investigated by Machover and Mastorakos (2017a) in the premixed annular combustor featuring 12 or 18 bluff-body burners. The authors note that adding swirl, or increasing the equivalence ratio, increases the flame propagation speed, leading to shorter light-round durations. Bourgouin et al. (2013) have approximated the light-round duration by a power-law function of the injector velocity matching experimental measurements remarkably well, which underscores the impact of flame/turbulence interactions. A similar relation can also be observed in the data published by Philip et al. (2015b). Only Bach et al. (2013) have measured longer light-round durations for increasing injector velocities.

Interestingly though, the impact of the flow velocity on light-round duration is less pronounced for non-premixed operating conditions (Machover and Mastorakos, 2016). In turn, the bulk flow velocity (precisely its circumferential component) becomes the main governing effect of flame propagation in the particular case of oblique injectors, eliminating the influence of the equivalence ratio (Ye et al., 2018). As for linear setups, the same behavior in terms of flame propagation speed is reproduced in annular chambers when the inter-burner spacing is varied (Machover and Mastorakos, 2016, 2017a).

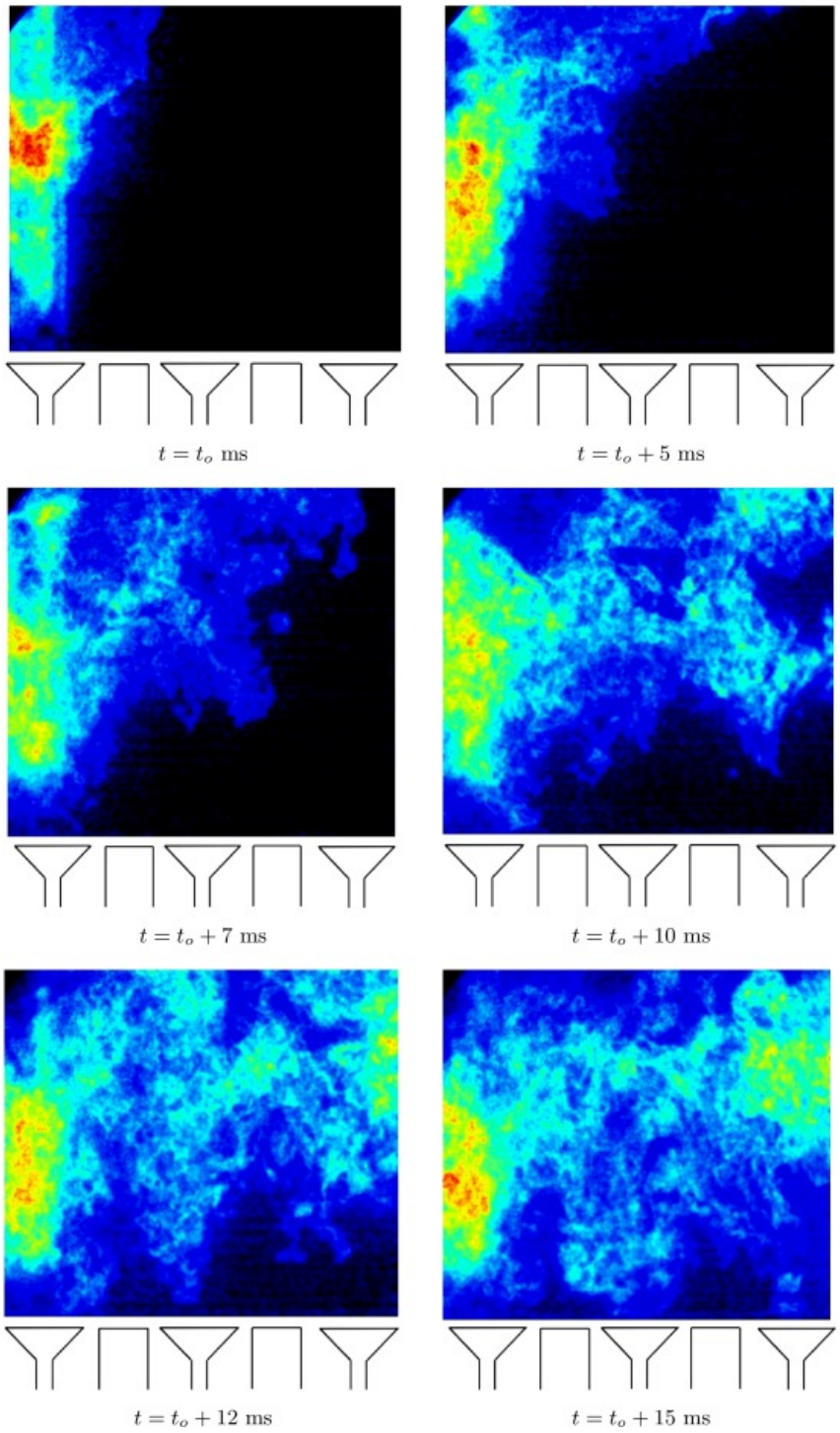

Figure 1.8: High-speed imaging of OH^* chemiluminescence in the 12-burner premixed bluff-body configuration with swirl. Image taken from Machover and Mastorakos (2017a).

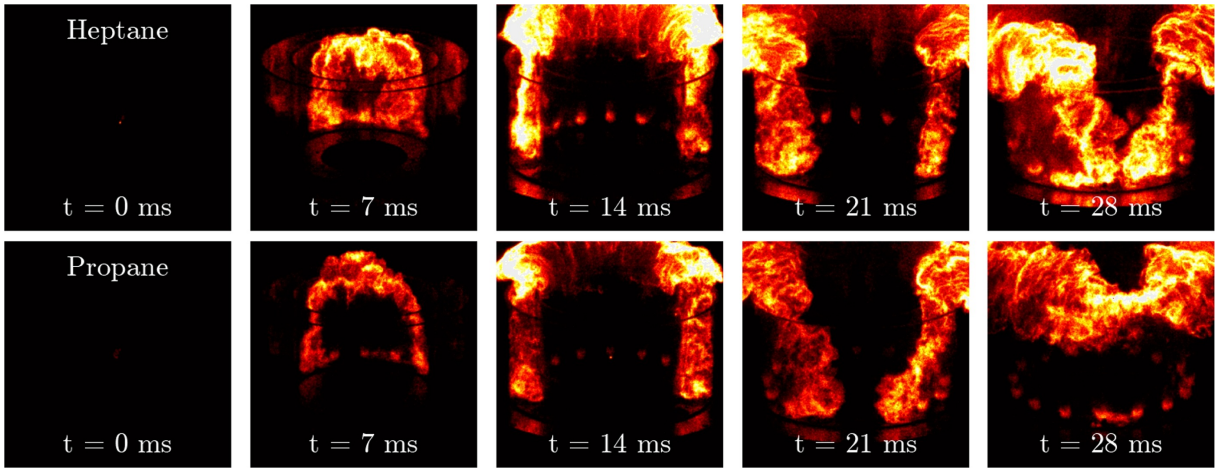

Figure 1.9: Light emission during the ignition sequence of n-heptane (top) and propane (bottom) fuels. Yellow corresponds to high light intensity while dark red represents low light emission. Each sequence features equivalent injection conditions: $u = 31.5\,\mathrm{m/s}$, $\phi = 0.90$ and $\mathcal{P} = 80\,\mathrm{kW}$. Images taken from Prieur et al. (2017).

The laminar flame speed should also be mentioned as an influential parameter for flame propagation. In the context of liquid fuels, detailed insights were initially gained from academic cases. Laminar flame speeds in droplet mists for overall lean conditions are generally lower than the gaseous laminar flame speed at the same equivalence ratio, suggesting that spray flames propagate at a leaner equivalence ratio than the overall equivalence ratio (Ballal and Lefebvre, 1981; Neophytou and Mastorakos, 2009; de Oliveira and Mastorakos, 2019). Such trends are confirmed by Prieur et al. (2017) who have carried out ignition experiments in the swirled annular combustor MICCA-Spray, with different liquid fuels and compared the data with premixed gaseous fuels (see Fig. 1.9). While the flame shapes remain comparable for all cases, liquid fuels generally tend to increase the light-round duration, depending on the fuel volatility. This implies that flame propagation speeds are lower than in the equivalent gaseous case.

More recently, similar studies were performed by Ciardiello et al. (2020) for different gaseous fuels. Given a matched laminar flame speed, fixed bulk velocity and spark location, but otherwise variable parameters (fuel type, equivalence ratio, thermal power), the light-round duration of two setups is essentially constant. The authors conclude that the laminar flame speed S_l has a first order impact on the resulting flame propagation speed during light-round: the higher S_l, the shorter the light-round duration (see Fig. 1.10).

Furthermore, the rate of burnt gas dilatation is characterized at a fundamental level for flame propagation in droplet mists and appears to be influenced by turbulence, initial droplet diameter and liquid equivalence ratio (Wacks et al., 2016; Wacks and Chakraborty, 2016) (*i.e.* the contribution of *liquid* fuel to the gaseous carrier phase).

Data on light-round durations for pre-heated and cold combustor walls have been reported in Philip et al. (2015b); Puggelli et al. (2020), which is compiled in Fig. 1.11. At constant bulk flow velocity, preheating the combustor walls drastically reduces the light-round duration by $50-70\%$, suggesting that combustor wall temperatures are crucial for the understanding of flame propagation. Reduced light-round durations through preheating are observed regardless of the fuel type (gaseous or liquid).

Few published studies exist to date which are concerned with ignition in realistic high-altitude scenarios in terms of both low pressure *and* low temperature (Read et al., 2008; Mosbach et al., 2010; Denton et al., 2018; Martinos et al., 2020) as experimental setups be-

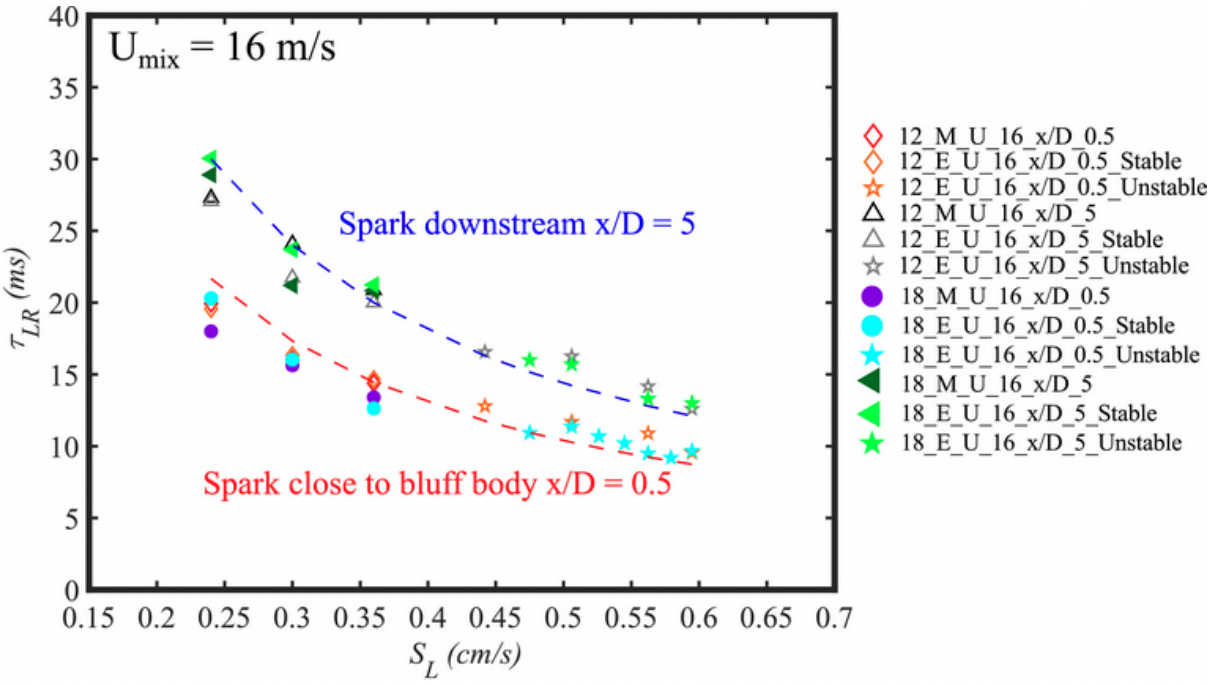

Figure 1.10: Plots of the light-round time as a function of the laminar flame speed S_l. For all cases $u_{mix} = 16\,\mathrm{m/s}$. The hollow markers and full markers represent the 12- and 18-burner configurations, respectively. Label is in the form of XX_F_U_V_x/D_L, where XX is the number of burners, F is the fuel (M for methane and E for ethylene), V is the bulk velocity and L the longitudinal spark location. For the tests with ethylene, the addition of unstable refers to mixtures that give rise to thermoacoustic instabilities. Image taken from Ciardiello et al. (2020).

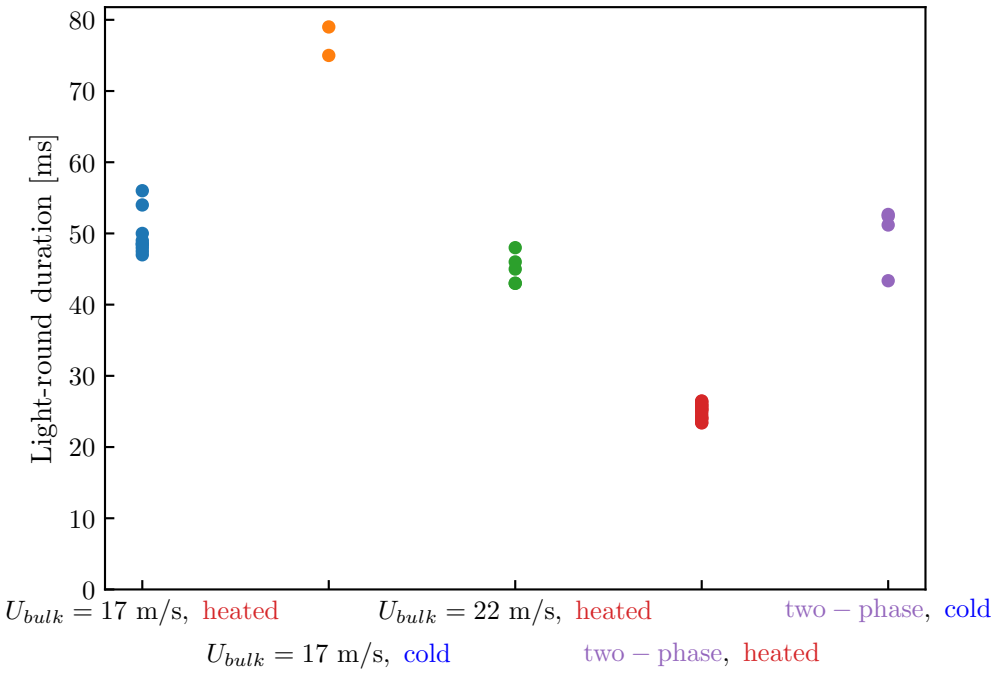

Figure 1.11: Experimentally measured light-round durations in EM2C's MICCA combustor for different operating conditions and fuels. Data taken from Philip et al. (2015b); Puggelli et al. (2020).

come increasingly complex and expensive. Single-sector combustors are therefore preferred, while full annular rigs are even more scarce (Klinger et al., 2011). Liquid fuels pose additional challenges for experimental diagnostics as fuel films may occur on walls and optical windows due to poor evaporation at low temperatures (Mosbach et al., 2010). Instead, gaseous multi-burner ignition experiments are usually carried out at a more elevated, constant wall temperature (around $500\,\mathrm{K}$) for the sake of repeatability of a certain phenomenon, without further investigation of wall temperature effects (Ye et al., 2018; Xia et al., 2019; Wang et al., 2021). Similarly, ignition studies in spray flame combustors have been carried out in Marrero-Santiago et al. (2020) at wall temperatures around $416\,\mathrm{K}$. The authors note that fuel evaporation is enhanced under non-reacting conditions, with full evaporation in most parts of the inner and outer recirculation zone.

Within the ANNULIGhT network, light-round experiments have also been carried out at the NTNU University in an annular chamber similar to the configuration of Worth and Dawson (2013). This work is pursued by Yi Hao Kwah and offers insights into flame propagation based on a large range of parameter variations. Efforts have also been made to control wall temperatures prior to relight (through infrared pyrometry) to establish consistent initial conditions between consecutive runs. An experimental characterization of the ignition process in a spinning combustor is also performed in Kwah et al. (2022).

Large-Eddy Simulations have proven to be a useful tool in order to study light-rounds numerically. In general, two pioneering works of the past two decades should be mentioned that can be regarded as beacons of engine simulation, foreshadowing the prediction capabilities of numerical tools for the upcoming years. In 2008, Boileau et al. (2008) have carried out the first ignition simulation in a full annular combustion chamber. While some of the modeling choices in the initial work would probably be considered as over-simplification by today's standards (*e.g.,* chemistry, liquid phase description or combustion modeling), the authors have still reached impressive results and have incentivized the development and improvement of more accurate models, leading to a better description and prediction of the ignition process. In 2020, Pérez Arroyo et al. (2020) have demonstrated the feasibility of multi-part fan-to-combustor simulations studying the interaction between different engine components. In the wake of these works, further research has emerged, focusing particularly on light-round with gaseous (Philip et al., 2015b,a; Zhao et al., 2019) and liquid fuels (Lancien et al., 2017; Collin-Bastiani, 2019b; Lancien et al., 2019). Most of these numerical studies still rely on a simplified combustion chemistry to limit the computational costs of LES, and the thickened flame model (TFLES, Colin et al. (2000); Legier et al. (2000)). A tabulated chemistry approach based on filtered flamelets (F-TACLES (Fiorina et al., 2010)) was shown to perform similarly to TFLES (Philip et al., 2015a). Detailed kinetics have been included directly in Zhao et al. (2019) considering each cell as a perfectly stirred reactor. In terms of the liquid phase description, both monodisperse Euler-Euler (EE) (Lancien et al., 2019) as well as polydisperse Euler-Lagrange (EL) (Collin-Bastiani, 2019b) simulations of light-round were performed.

It is noteworthy that all light-round simulations of the MICCA combustor cited above were performed with adiabatic walls. This modeling choice has initially been justified by the experimental operating and ignition procedure: in order to minimize wall heat losses and allow for a comparison with simulations, the experiment was operated for at least $10\,\mathrm{min}$ in fully ignited conditions, before performing an abrupt shutdown and immediate relight (Philip et al., 2015b). While this argument appears to be reasonable, it neglects the effect of fresh gas preheating shortly before relight, *i.e.* simulations were started from a converged solution with fresh gases at *ambient* temperature. Therefore, it is rather intriguing that a good agreement with experimental data was found in Philip et al. (2015b); Lancien et al. (2019); Collin-Bastiani (2019b).

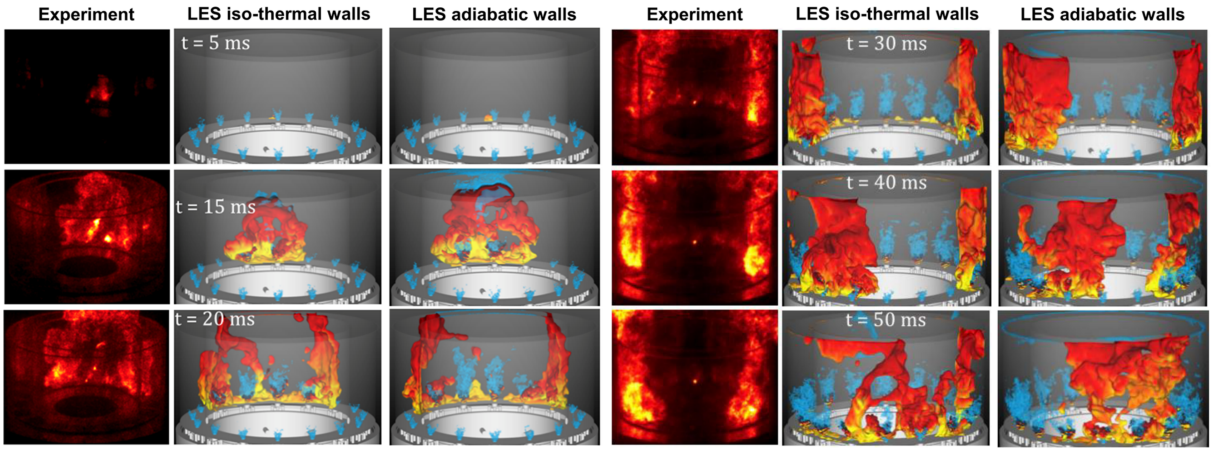

Figure 1.12: Comparison of instantaneous snapshots of flame propagation during light-round between experiment and simulations. The experimental combustor is operated with cold combustor walls and compared to LES with iso-thermal and adiabatic walls. The simulated flames are visualized as an iso-surface of the progress variable at $c = 0.9$ and are colored by the axial gaseous velocity (yellow: $u = -10\,\mathrm{m/s}$, black: $u = 25\,\mathrm{m/s}$). Images taken from Puggelli et al. (2020) compiling results from Lancien (2018).

The first study was published in Lancien (2018) addressing the impact of wall heat transfer modeling in light-round simulations more explicitly. Liquid n-heptane and air have been injected at ambient temperature, and an iso-thermal wall boundary condition of $T_w = 300\,\mathrm{K}$ was imposed. Surprisingly however, the predicted light-round duration was substantially *shorter* than the duration found in experiments, as seen in Fig. 1.12.

Follow-up works have mentioned concerns over the simplifications of wall heat transfers (Puggelli et al., 2020) and the combustion model (Puggelli et al., 2021). More specifically, wall modeling of light-round LES has relied on algebraic wall models with constant thermophysical properties of the boundary layer. *A priori* estimations have suggested however, that these simplified models tend to underpredict the wall heat fluxes compared to detailed models accounting for variable thermophysical properties, as illustrated in Fig. 1.13.

Apart from wall modeling, the suitability of a constant flame surface wrinkling parameter was assessed within the framework of the thickened flame model. Simulations with a dynamic modeling approach have underscored the inherent heterogeneity and unsteadiness of the flame surface wrinkling during light-round in MICCA (Puggelli et al. (2021), shown in Fig. 1.14), concluding that no "universal" value exists for the flame surface wrinkling parameter. Thus, imposing a constant value would inevitably result in an inaccurate prediction of the flame propagation speed. Given prior adiabatic simulations with seemingly matching light-round durations compared to experimental measurements, Puggelli et al. (2021) have put forth the following hypothesis: hidden error compensation is suspected to have concealed poor modeling choices, generating simulation results that give the impression of a good agreement with experimental data. This hypothesis will be thoroughly investigated in the present work.

It is worth mentioning that light-round studies have not been limited to investigations of propagating flames only. The final flame stabilization process at each injector in the wake of the propagating flame fronts has attracted some attention as well. Since flame stabilization can be a safety concern as well (*e.g.*, failure to stabilize a flame, or flashback), it must necessarily succeed to complete the ignition process. It is therefore important to understand the relevant stabilization mechanisms to ensure safe and reliable ignition, and prove the engine's restart

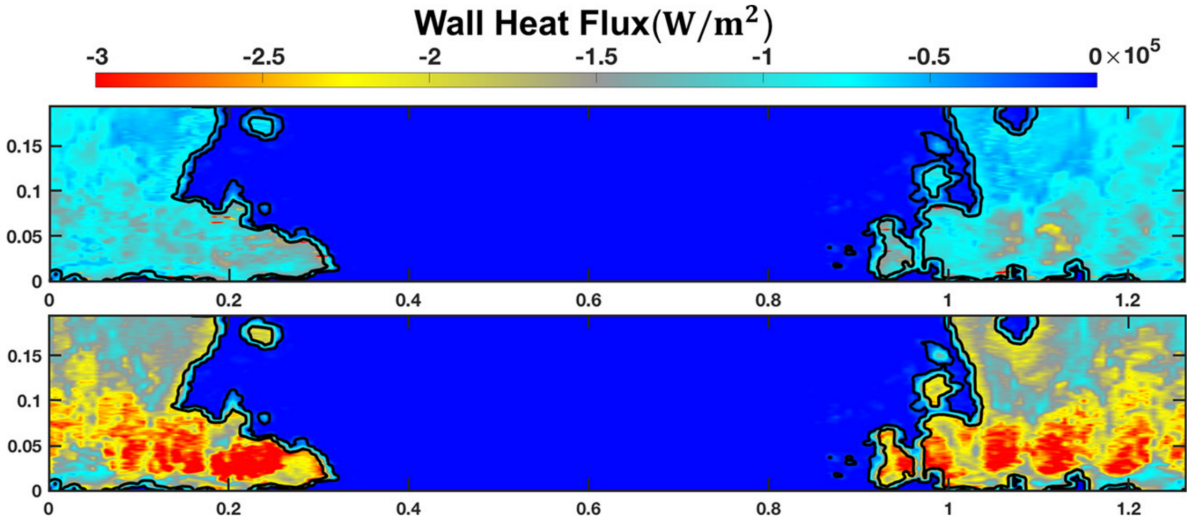

Figure 1.13: Comparison of LES wall heat fluxes at the external quartz wall of the MICCA combustor with different wall modeling approaches. Top: LES with a classical logarithmic wall law with constant thermophysical properties. Bottom: *a priori* estimation of wall heat fluxes if thermophysical properties were variable. Images taken from Puggelli et al. (2020).

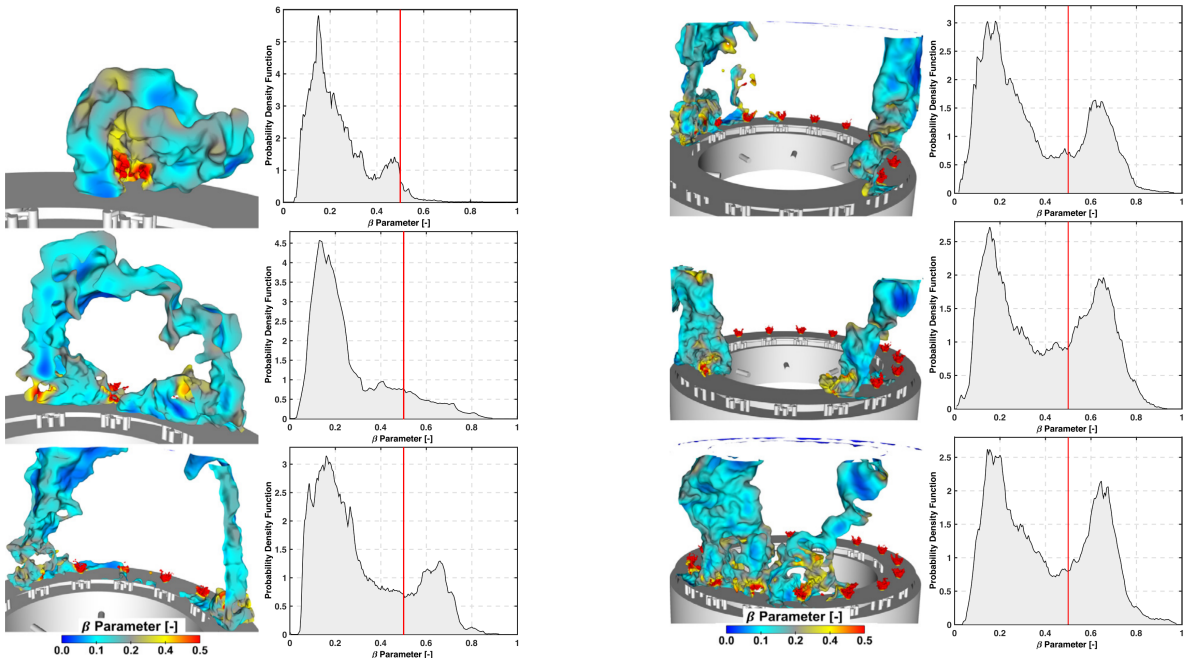

Figure 1.14: Light-round simulation in the MICCA combustor with the thickened flame model and a dynamic evaluation of the flame surface wrinkling parameter β. Instantaneous snapshots of the flame front are shown as iso-surface of the progress variable $c = 0.5$, which are colored by the local value of β. The probability density function (PDF) of β is shown for each instant, revealing its heterogeneous distribution. The PDFs underscore that the flame surface wrinkling parameter cannot be described by a constant value (*e.g.*, $\beta = 0.5$, red vertical line) as commonly assumed in previous works. Images taken from Puggelli et al. (2021).

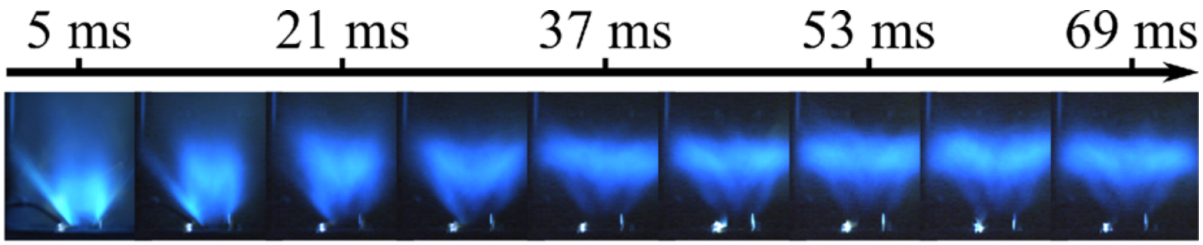

Figure 1.15: High-speed imaging of the transient flame stabilization processes during ignition in the single-injector combustor SICCA. The burner is ignited at $t = 0\,\mathrm{ms}$. A compact flame can be observed in the first two images anchoring attached to the injector, while a more open flame shape is observed in the later instants detached from the injector. Sequence taken from Prieur et al. (2019).

capabilities.

Such a transient flame anchoring and stabilization behavior was first revealed during light-round ignition in MICCA by Prieur et al. (2019). The authors have successfully reproduced the stabilization process in the single-injector combustor SICCA, allowing for a detailed investigation. Two distinct phases were observed experimentally by means of high-speed imaging as shown in Fig. 1.15: after the initial burnt gas expansion, a flame was found anchoring attached to the injection unit, with a lower flame brush penetrating the injector. This configuration persisted throughout a characteristic time, before the lower flame brush quenched and the flame stabilized at a certain distance in its final position, *i.e.* detached from the injector. Prieur et al. (2019) have noted that this process could be observed for liquid as well as for gaseous fuels.

Flame stabilization mechanisms were also reported in an annular combustor with a novel $90°$ bend fuel injector design, generating a distinct azimuthal flow in the combustion chamber (Agostinelli et al., 2020). This concept is also known as Spinning Combustion Technology (SCT). Due to the swirling motion exiting each fuel injector, characteristic flame shapes with six branches were observed, interacting with the combustor walls. The flames were found to stabilize in the low-velocity region immediately downstream of the injector. Local injector equivalence ratios and the global equivalence ratios are cited as the main influential parameters controlling the flame shapes and positions.

Objectives

Given the results of previous investigations, we define the following objectives for this work: first, we develop and implement enhancements for the evaporation model, and propose a tabulation approach to improve the description of wall heat transfers. A new baseline configuration is assembled for light-round simulations, consisting of our improvements along with a dynamic combustion model. Such a setup has not yet been considered in the previous literature, allowing for a comprehensive *a posteriori* analysis of each model's impact on flame propagation. It is also a significant departure from adiabatic simulations cited above.

Second, with the improved setup, we investigate flame propagation mechanisms during light-round in the annular MICCA-Spray combustor with realistic thermal wall conditions by means of Large-Eddy Simulations. Two configurations are intentionally chosen, which enhance the impact of wall heat transfers on flame propagation:

1. light-round ignition with cold combustor walls at $T_w = 300\,\mathrm{K}$,

2. light-round ignition with preheated combustor walls.

The first configuration attempts to mimic cold wall conditions as would be encountered in in-flight relight from windmilling. The second configuration in turn targets wall conditions that would be encountered in quick relight during climb. Fresh gas preheating is also accounted for in the latter case. Both configurations admittedly represent an idealization of real engine conditions; yet, they constitute a first step towards characterizing heat transfer during light-round in a lab-scale setting. Most importantly, they can safely and reliably be established in the MICCA combustor operated at ambient pressure.

Third, we derive a macroscopic model for flame propagation which accounts for all relevant governing mechanisms. It is applied to the main light-round configurations to examine and quantify how a change of the combustor walls' thermal state changes the relative importance of each governing mechanism.

Finally, we study a dynamic flame stabilization process observed during light-round in the wake of propagating flame fronts. A detailed numerical analysis is performed in a single-injector configuration to facilitate the observation and characterization of the flame's transient behavior.

Outline of the thesis

The structure of the manuscript follows from main objectives previously defined.

Chapter 2:

We start with a general presentation of the equation set required to perform Large-Eddy Simulations of reacting multiphase flows. We highlight modeling challenges arising from the simultaneous interaction of multiple reacting species with a turbulence spectrum of varying length and time scales, and a disperse droplet phase. Sub-grid scale closure strategies are introduced to suitably describe the behavior of scales and processes that are not resolved by the computational mesh. Given the distinct multiphase nature of the flow, we discuss appropriate (dynamic) combustion models, Lagrangian particle tracking, heat and mass transfer between the liquid and the gas phase, and injection handling. Classic algebraic wall models are also reviewed and assessed in terms of potential limitations in light-round simulations.

Chapter 3:

We proceed with an outline of the two main combustors investigated in this work: the annular multi-burner combustor MICCA-Spray, and the complementary single-injector combustor SICCA. The numerical domains are introduced that are required for fluid flow simulations, followed by an overview of the numerical setup and boundary conditions which are common to all simulations. Case-specific adjustments to the global setup are highlighted in the later chapters, where appropriate. After illustrating the numerical ignition procedure, we briefly discuss results of a grid convergence study.

Chapter 4:

This chapter is entirely dedicated to enhancements of the liquid phase description. Its first part consists of an improved implementation of the Abramzon-Sirignano evaporation model into AVBP. Given substantially varying gas phase properties along a droplet's trajectory, we

demonstrate that droplet evaporation can be more suitably described if variable properties of the droplet film are taken into account. These film properties follow from correlations with Prandtl and Schmidt numbers, which are no longer assumed constant, but computed from polynomial expressions fitted to generic mixtures with detailed transport properties. Such enhancement allows for a more accurate evaporation time retrieval.

The second part focuses on droplet injection with phenomenological injection models. A model calibration is performed to obtain an optimal parameter set which can best reproduce spray characteristics determined from experimental measurements.

Chapter 5:

In this chapter, we address wall heat transfer problems and suitable modeling approaches. Given the limitations of algebraic wall models, we develop and implement a tabulated wall model based on the solution of the Thin Boundary Layer Equations. This new model explicitly accounts for variable thermophysical properties of the boundary layer, which are known to critically affect the resulting wall heat fluxes and wall shear stresses.

We present a numerical approach allowing to determine wall temperatures from coupled fluid/solid simulations, referred to as Conjugate Heat Transfer simulations. Realistic wall temperature profiles in MICCA-Spray under preheated conditions are of paramount importance for quick relight simulations, which cannot be approximated by adiabatic boundary conditions. Given the lack of experimental data, we propose a coupled simulation strategy including a comprehensive description of wall heat transfers.

Chapter 6:

With the previous model enhancements, we perform light-round simulations with cold combustor walls in MICCA-Spray ($T_w = 300\,\mathrm{K}$), mimicking the thermal wall conditions encountered in windmilling restart. The initial conditions represent a fully converged two-phase flow field consisting of an n-heptane/air mixture, which is ignited with a flame kernel of burnt gases. For a global assessment of the simulation, we compare the light-round duration to experimental measurements. Moreover, we examine flame shapes and propagation mechanisms, and study their interaction with wall heat transfers, the liquid phase and turbulence. The importance of an appropriate description of heat transfers is substantiated by a complementary simulation with adiabatic boundary conditions.

Chapter 7:

This chapter's main subject is a quick relight simulation with preheated combustor walls which would be encountered during relight in climb. The first step consists in Conjugate Heat Transfer simulations of steady-state operating conditions, giving access to wall temperature profiles of the combustion chamber and the injector assembly. These stationary wall temperature profiles are subsequently imposed as static boundary conditions during prefueling and light-round simulations. Thus, initial conditions represent a converged flow solution with a *preheated* fresh gas mixture. The ignition procedure is identical to the previous case. After a comparison of the obtained light-round duration with experimental data, we examine flame propagation mechanisms and highlight differences with regard to windmilling restart.

Chapter 8:

Based on the previous light-round simulations, we derive a macroscopic model for a comprehensive analysis of flame propagation. The model is benchmarked against our simulation results and yields good approximations of average flame propagation speeds. It is further used to provide *a priori* estimations to quantify how the flame propagation speed would change if light-round simulations were carried out with different models for the main governing mechanisms. We finally quantify the impact of the thermal wall condition on flame propagation mechanisms.

Chapter 9:

This chapter is concerned with the investigation of transient flame stabilization during light-round. Unlike the previous chapters, we focus on fully ignited burners downstream of the propagating flame fronts. Large-Eddy Simulations are performed in the complementary single-injector combustor SICCA-Spray with preheated combustor walls. A fully converged initial flow solution is established during prefueling simulations until thermal equilibrium is reached between the fresh gas mixture and the combustor walls. Ignition is then performed through energy deposition in the outer recirculation zone. The transient flame stabilization process is investigated by studying the effect of an acoustic pressure excursion and burnt gas cooling in the vicinity of the combustor walls.

Publications

- K. Töpperwien, F. Collin-Bastiani, E. Riber, B. Cuenot, G. Vignat, K. Prieur, D. Durox, S. Candel, and R. Vicquelin. Large-Eddy Simulation of Flame Dynamics During the Ignition of a Swirling Injector Unit and Comparison With Experiments. *Journal of Engineering for Gas Turbines and Power*, 143(2):021015, 2021.
  Available at: DOI: 10.1115/1.4049297.

- K. Töpperwien, S. Puggelli, and R. Vicquelin. Analysis of flame propagation mechanisms during light-round in an annular spray flame combustor: the impact of wall heat transfer and two-phase flow. *Combustion and Flame*, 241:112105, 2022.
  Available at: DOI: 10.1016/j.combustflame.2022.112105.

- K. Töpperwien, R. Vicquelin. Numerical analysis of relight in an annular spray-flame combustor with preheated walls. Submitted to the *39th International Symposium on Combustion* (accepted for publication), 2022.

Conferences

- International Conference on Numerical Combustion (ICNC) 2019, Aachen, Germany
- European Combustion Meeting (ECM) 2019, Lisbon, Portugal
- ASME Turbo Expo 2020 Turbomachinery Technical Conference, London, UK (online)
- 73rd Annual Meeting of the APS Division of Fluid Dynamics (2020), Chicago, USA (online)

- Yearly conference of the French division of the Combustion Institute ("François Lacas Day") (2021), Toulouse, France (online)
- 5th Colloquium on the Initiative of Advanced Combustion ("INCA") (2021), Paris, France (online)

Acknowledgments

This project has received funding from the European Union's Horizon 2020 research and innovation program (grant number 765998) "ANNULIGhT". We gratefully acknowledge the support by the following institutions through HPC resources made available for conducting the research in this work:

- the National Computing Center for Higher Education (CINES), providing access to the supercomputer OCCIGEN,
- the Institute for Development and Resources in Intensive Scientific Computing (IDRIS), providing access to the supercomputers TURING and Jean-Zay,
- the French Alternative Energies and Atomic Energy Commission's (CEA) HPC center (TGCC), providing access to the Joliot Curie supercomputer,
- the Mésocentre's computing cluster of CentraleSupélec and École Normale Supérieure Paris-Saclay supported by CNRS and Région Île-de-France.

These resources are associated with the GENCI allocation grant numbers A0042B10118, A0062B10118, A0082B10118, A0082B10159 and A0102B10159.

Chapter 2

Fundamentals of turbulent two-phase reactive flow simulations

Numerical simulations of reacting two-phase flows require a mathematical framework of governing equations and efficient solvers adapted for parallel execution on high-performance computing clusters. Thus, we present the fundamental equation set for flow and droplet motion in an Euler-Lagrange approach, species transport and reaction, combustion, and heat and mass transfer (among others). We introduce the concept of Large-Eddy Simulations (LES), capable of resolving large-scale flow structures on a computational mesh, and address the problem of sub-grid closures for unresolved scales. Various sub-models are briefly outlined, along with the implementation of the governing equations into CERFACS' AVBP solver, which we employ throughout this work. This chapter is also relevant for model enhancements which we developed and implemented into AVBP, as outlined in chapters 4 and 5.

Contents

2.1 Introduction

Modeling reactive two-phase flows as found for example in aeroengine combustors requires the solution of the fundamental equations of fluid dynamics, as well as additional equations for heat and mass transfer, species transport and an appropriate combustion model. Light-round ignition in particular involves a simultaneous interaction of propagating flames with turbulent flows and liquid fuel, posing substantial modeling challenges: due to the large size of the combustors, model accuracy must be carefully balanced against computational costs. As we have already established in the general introduction, previous works have investigated the governing mechanisms of flame propagation and made suggestions how these mechanisms could be more accurately described. In light of possible hidden error cancellation depending on the employed models, three key aspects have been separately identified for improvement, which require fundamental knowledge of: (i) the description of the liquid phase including heat and mass transfer, (ii) the combustion model, and (iii) wall heat transfers. Thus, we wish to provide a general mathematical framework, upon which our simulations are based, before discussing avenues of model improvement in Chap. 4 and 5.

First, a mathematical description of the gaseous fluid flow is presented, followed by an overview of computational approaches to solve the corresponding equations. Subsequently, combustion models are covered that allow for simulations of complex combustion phenomena found in modern aeroengines. Liquid fuel droplets are tracked in a Lagrangian framework and require the solution of the fundamental equations of droplet motion, heat and mass transfer between the continuous gas phase and the polydisperse liquid phase, as well as a simplified approach for the injection of pre-atomized sprays. We also address the modeling challenges arising from the interaction between flames and two-phase flows. Finally, we discuss the description of wall heat transfers and briefly highlight strategies for an efficient numerical solution and implementation of physical models into solvers running on massively parallel high-performance computing clusters.

2.2 Governing equations for compressible gaseous flows

Fluid flow is governed by the Navier-Stokes Equations, which comprise the conservation of mass, species mass, momentum and energy:

$$\frac{\partial \rho}{\partial t} + \frac{\partial}{\partial x_i}\left(\rho u_i\right) = 0 \tag{2.1}$$

$$\frac{\partial \rho Y_k}{\partial t} + \frac{\partial}{\partial x_i}\left(\rho\left(u_i + V_{k,i}\right) Y_k\right) = \dot{\omega}_k \tag{2.2}$$

$$\frac{\partial}{\partial t}\left(\rho u_j\right) + \frac{\partial}{\partial x_i}\left(\rho u_i u_j\right) = -\frac{\partial p}{\partial x_j} + \frac{\partial \tau_{ij}}{\partial x_i} \tag{2.3}$$

$$\frac{\partial}{\partial t}\left(\rho E\right) + \frac{\partial}{\partial x_i}\left(\rho E u_i\right) = \frac{\partial}{\partial x_j}\left(\tau_{ij} u_i - p\delta_{ij}\right) + \frac{\partial q_i}{\partial x_i} + \dot{\omega}_T + \dot{\mathcal{Q}} \tag{2.4}$$

where ρ, u, p, τ_{ij} and Y_k denote the density, velocity field, pressure, stress tensor and species mass fraction of the kth species respectively (Poinsot and Veynante, 2005). In Eqs. 2.3 and 2.4 we have already omitted external volume forces including gravity.

For Newtonian fluids the stress tensor is defined as

$$\tau_{ij} = \mu\left[\left(\frac{\partial u_j}{\partial x_i} + \frac{\partial u_i}{\partial x_j}\right) - \frac{2}{3}\delta_{ij}\frac{\partial u_k}{\partial x_k}\right] \tag{2.5}$$

with μ denoting the dynamic viscosity and δ_{ij} the Kronecker-Delta.

Species transport by diffusion can be approximated in multi-species gases through the Hirschfelder and Curtiss law (Hirschfelder et al., 1964), providing an expression for the species diffusion velocity $V_{k,i}$ of species k in ith direction. This expression is given as

$$V_{k,i} = -\frac{D_k}{Y_k}\frac{W_k}{W}\frac{\partial X_k}{\partial x_i} + V_i^c \tag{2.6}$$

with the equivalent diffusion coefficient D_k of the kth species in a multicomponent gas (unlike binary diffusion coefficients of Fick's law (Kuo, 2005)). X_k is the mole fraction defined as $X_k = Y_k W / W_k$, and W and W_k denote the mixture's mean molar mass and the species molar mass respectively. A correction velocity V_i^c is added to ensure global mass conservation

$$V_i^c = \sum_{k=1}^{N} D_k \frac{W_k}{W}\frac{\partial X_k}{\partial x_i} \tag{2.7}$$

such that the condition $\sum_{k=1}^{N} Y_k V_{k,i} = 0$ is satisfied. Mass conservation also applies to the sum of all species source terms, which gives $\sum_{k=1}^{N} \dot{\omega}_k = 0$.

The energy equation (Eq. 2.4) introduces the total non-chemical energy E per unit mass, which is defined as

$$E = \int_{T_0}^{T} c_v(T')dT' + \frac{1}{2}u_i u_i \tag{2.8}$$

where c_v and T denote the specific heat capacity at constant volume, and temperature, respectively. We wish to clarify that the transport equation could also be written for the total *chemical* energy per unit mass $E_t = \int_{T_0}^{T} c_v(T')dT' + \frac{1}{2}u_i u_i + \sum_{k=1}^{N} \Delta h_{f,k}^0 Y_k$, which differs from the total non-chemical energy only in the added species formation enthalpy $\Delta h_{f,k}^0$.

q_j is associated with the heat flux given by

$$q_j = -\lambda \frac{\partial T}{\partial x_j} + \rho \sum_{k=1}^{N} h_k Y_k V_{k,i} \tag{2.9}$$

with λ representing the thermal conductivity. The heat release rate from chemical reactions, $\dot{\omega}_T$, and other volume sources, $\dot{\mathcal{Q}}$ (*e.g.,* from radiative sources), constitute the source terms in the energy equation. For the former we can write

$$\dot{\omega}_T = -\sum_{k=1}^{N} \dot{\omega}_k \Delta h^0_{f,k} \tag{2.10}$$

summing the products of each species source term times its formation enthalpy at reference conditions $\Delta h^0_{f,k}$ (which are defined as $T_{ref} = 0\,\mathrm{K}$ in the solver AVBP). If multiple reactions are involved, we can obtain $\dot{\omega}_k$ of the kth species by performing a summation of all source terms $\dot{\omega}_{k,j}$ in each reaction $j \in [1,\, M]$

$$\dot{\omega}_k = \sum_{j=1}^{M} \dot{\omega}_{k,j} = W_k \sum_{j=1}^{M} \nu_{k,j} \mathcal{Q}_j \tag{2.11}$$

which can be rewritten as the sum of the stoichiometric reaction coefficient $\nu_{k,j} = \nu''_{k,j} - \nu'_{k,j}$ times the reaction progress $\mathcal{Q}_j$. In reaction j, the reaction progress is given by

$$\mathcal{Q}_j = \mathrm{K}_{f,j} \prod_{k=1}^{N} \left(\frac{\rho Y_k}{W_k} \right)^{\nu'_{k,j}} - \mathrm{K}_{r,j} \prod_{k=1}^{N} \left(\frac{\rho Y_k}{W_k} \right)^{\nu''_{k,j}} \tag{2.12}$$

The forward reaction rates $\mathrm{K}_{f,j}$ are computed from the well-known Arrhenius law

$$\mathrm{K}_{f,j} = A_j T^{\beta,j} \exp\left(-\frac{E_{a,j}}{RT} \right) \tag{2.13}$$

with the pre-exponential factor A_j, the temperature exponent β and the activation energy $E_{a,j}$. The reverse reaction rates $\mathrm{K}_{r,j}$ are computed from the equilibrium constants K_{eq}.

In compressible flows, the coupling of pressure and density may be expressed by an equation of state, *e.g.,* the ideal gas equation

$$p = \rho r T \tag{2.14}$$

The specific gas constant is $r = c_p - c_v = R/W$ where c_p and c_v denote the specific heats at constant pressure and constant volume, respectively.

In general, the presented formulation of the Navier-Stokes Equations is valid for any type of Newtonian fluid, in particular for laminar as well as for turbulent flows. The existence of an universal solution to these equations in closed-form, however, is not known until today (Fefferman, 2000). As a consequence, iterative solution methods have been developed to numerically calculate the solution of the Navier-Stokes Equations up to arbitrary accuracy. Since we use the AVBP solver (Schönfeld and Rudgyard, 1999; Colin and Rudgyard, 2000) for the present work, we focus on solution methods implemented in this code.

2.3 Computational Fluid Dynamics (CFD)

Computational Fluid Dynamics (CFD) is the study of fluid flow by numerical simulation. Its fundamental idea is to use appropriate algorithms to approximate solutions to the governing equations presented in this chapter. As computers cannot parse differential equations, we must discretize any continuous domain of interest with finite volumes known as cells of a computational mesh. Discrete spatial integration schemes can then be employed, which operate on the cell vertices (or cell centers), where information about the flow are stored. Solving the fundamental equations implies that all spatial and temporal scales of the solution are taken into account to maintain maximum accuracy. As we shall see, this requirement can be a major hindrance for realistic turbulent flow applications with a wide range of length and time scales.

Let us first consider a generic flow problem of characteristic length and time scales L and T to illustrate the grid-cell requirements. We can infer the general flow regime from a very fundamental dimensionless quantity, the Reynolds number Re, defined as ratio of inertial and viscous forces

$$\mathrm{Re} = \frac{\rho u L}{\mu} \tag{2.15}$$

where ρ, u, L and μ denote the flow density, its velocity, the characteristic length scale and the flow viscosity. For sufficiently high Reynolds numbers, turbulent flow structures of initial size L will eventually break down into smaller structures, and repeatedly so, until energy can be dissipated by viscous forces at the smallest scales. This concept of energy transport from large to small scale structures is known as "energy cascade" (Richardson, 1922). Since energy dissipation occurs at the smallest scales, we can estimate their spatial and temporal size (η and τ) through

$$\eta = \left(\frac{\nu^3}{\epsilon}\right)^{1/4} \tag{2.16}$$

$$\tau = \left(\frac{\nu}{\epsilon}\right)^{1/2} \tag{2.17}$$

with ν denoting the kinematic viscosity and ϵ the kinetic energy dissipation rate. We refer to these scales as Kolmogorov scales (Kolmogorov, 1941).

If we attempt to resolve the full spectrum of length and time scales, we are clearly constrained by the smallest scales, *i.e.* the Kolmogorov scales. Thus, our discrete numerical domain must have cell sizes of the order of $\Delta x \sim \eta$, and the temporal integration scheme must be of the order of $\Delta t \sim \tau$. If these conditions are satisfied, we can faithfully resolve the entire turbulent spectrum without having to rely on any closure model for turbulence. This approach is therefore termed Direct Numerical Simulation (DNS). Yet it is possible to employ models for *other* properties of the flow, *e.g.,* the equation of state for ideal gases, the assumption of Newtonian fluids, or an incompressibility assumption.

Chapman (1979) has estimated in his hallmark paper the grid-cell requirement for a full resolution of all spatial scales to be $N \sim \mathrm{Re}^{9/4}$ cells, which was later amended by Choi and Moin (2012) as $N \sim \mathrm{Re}^{37/14}$ cells. Applying the revised Chapman criterion to flow simulations of the MICCA combustor (presented later in Sec. 3.2.1), where the Reynolds number is of the order of $\mathrm{Re} = 20\,000$ based on the hydraulic chamber diameter, we would obtain a scaling relation of $N \sim \mathrm{Re}^{37/14} = 2.32 \times 10^{11}$ cells in a computational mesh. It is clear that such high cell counts are still beyond reach today considering the available hardware, available computational hours, scalability and parallelization, or load balancing (to name only a few). Moreover, the above estimate disregards the large flow velocities in the injector near-field and,

most importantly, the thin reaction zones of turbulent flames requiring even finer resolutions. It should therefore be considered as a lower bound in terms of grid cell resolution, rather than a necessary criterion.

To overcome these issues, other solution techniques can be derived by explicitly considering the characteristics of turbulent motion and employing statistical modeling (Pope, 2013). A widely used approach consists in decomposing any quantity Ψ into a mean part $\bar{\Psi}$ and a fluctuation part Ψ' such that $\Psi = \bar{\Psi} + \Psi'$. The mean part is usually defined as an ensemble average, which can be interpreted as an average over a large number of flow realizations at the same time instant and the same flow. For steady mean flows, we can substitute this average by a temporal averaging operation over a sufficiently long period t

$$\bar{\Psi} = \frac{1}{t} \int_0^t \Psi(t')\, dt' \tag{2.18}$$

Performing this operation for the governing equations of fluid motion yields the Reynolds-Averaged Navier-Stokes (RANS) equations. This approach has been quite popular for complex applications as it solves for the mean quantities $\bar{\Psi}$, which require a much coarser spatial resolution compared to DNS. Numerical simulations based on this averaging procedure are therefore called RANS simulations. The principal challenge of RANS simulations remains in finding appropriate models for the fluctuation parts Ψ' of a given quantity, which are not resolved by design. These terms must be derived from correlations with available mean quantities of the flow and are known as turbulence models in the literature. Nevertheless, RANS simulations are much less demanding in terms of computational costs, contributing to their attractiveness for industrial applications.

An alternative approach to DNS and RANS simulations are Large-Eddy Simulations (LES). As the name implies, LES resolves the problem dependent large-scale structures, whereas small-scale structures are modeled, since they are assumed to have a universal behavior. Scale separation is achieved through a spatial filtering operation for which the cell size of the computational mesh can conveniently be used. Consequently, all structures can be resolved, which are at least of the order of the cell size, while those smaller than the cell size are modeled through so-called sub-grid scale (SGS) models. Unlike large anisotropic turbulent structures, small-scale structures exhibit a distinct isotropy regardless of the flow geometry, which can justify the development of sub-grid scale models. Yet there is no single universal SGS model and efforts have been made to account for certain features of the flow, which can have an impact on the small-scale behavior. For further insights into the ongoing discussion of sub-grid scale modeling, we wish to refer the reader to the review article by Meneveau and Katz (2000).

As with DNS, Choi and Moin (2012) have also estimated the grid-cell requirement for LES as $N \sim \mathrm{Re}^{13/7}$, if the near-wall flow should be resolved. We will address issues related to the resolution of wall boundary layers in Sec. 2.7, but we already wish to point out that the computational costs of LES can be greatly reduced to $N \sim \mathrm{Re}$ (Choi and Moin, 2012), if we employ wall models instead. This is the main reason why LES has been very attractive for academia (and lately for industry as well) to study complex, high-Reynolds number flows. We will therefore provide a brief overview of the LES simulation techniques in the following sections.

Despite its reduced computational costs and attractiveness, LES is far from being "perfect" and the conceptual questions raised by Pope (2004) certainly deserve some attention. Moreover, substantial computational resources are still required to achieve light-round simulations of increasing complexity, even on the fastest available computing cluster, the Joliot-Curie Rome Bull Sequana XH2000 cluster operated by the French Alternative Energies and Atomic

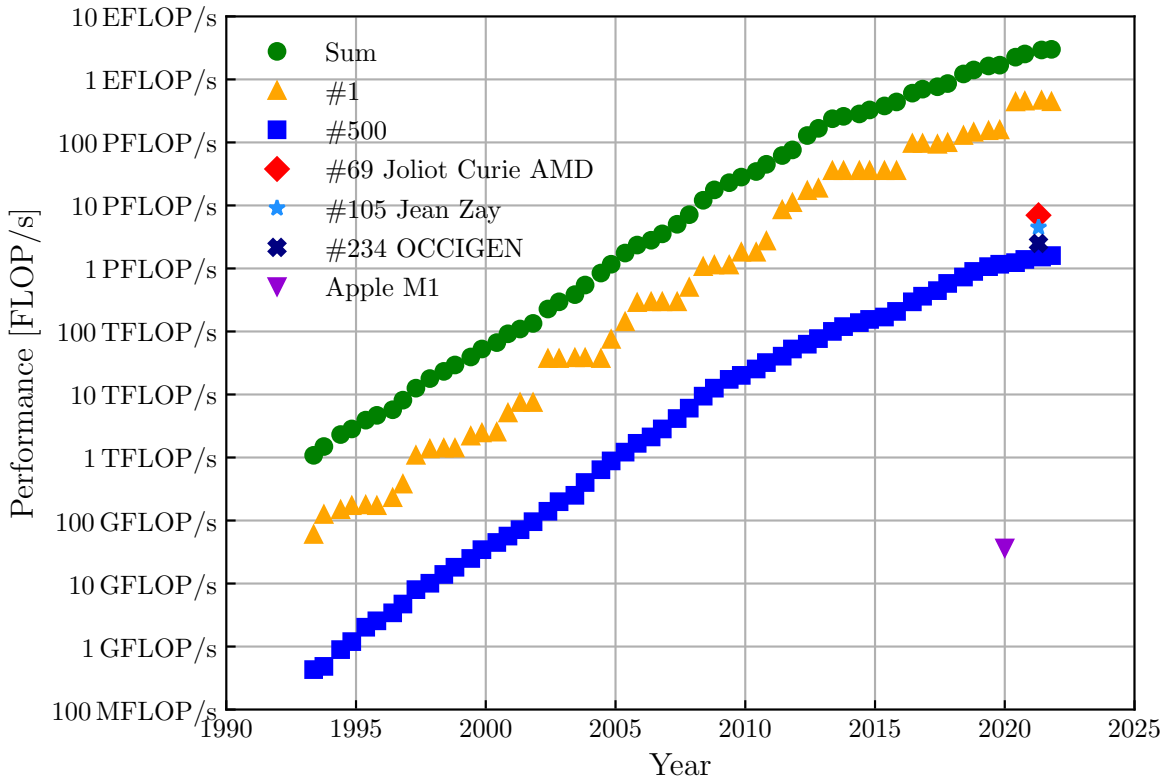

Figure 2.1: Evolution of the floating point performance of the world's fastest 500 supercomputers in floating point operations per second (FLOP/s) (Meuert et al., 2021). Results are based on the LINPACK benchmark (maximal performance achieved) (Petitet et al., 2018). The performance of the three French compute clusters used for this work and a M1 Macbook Pro are given for comparison.

Energy Commission (CEA). This cluster ranks 69th in the TOP500 list of the world's supercomputers (Meuert et al., 2021) and is more than one order of magnitude slower than the fastest supercomputer at the time of writing (see Fig. 2.1). Towards the end of light-round an average performance of $0.96\,\mathrm{iterations/s}$ can be reached with the solver AVBP on 4096 cores of AMD's EPYC™ 7002 Series processors running at a base clock speed of $2.6\,\mathrm{GHz}$ and allowing a boost clock up to $3.3\,\mathrm{GHz}$. Yet, a full light-round simulation takes more than one month to complete (depending on the boundary conditions), highlighting the principal challenge of carefully balancing modeling accuracy with computational costs.

2.3.1 Governing equations for LES

The governing equations for LES can be obtained from the general Navier-Stokes equations by performing a filtering operation to establish a separation of scales. The filter acts as a high-pass filter for scales, or a low-pass filter in wavenumber or frequency space (Garnier et al., 2009). It is represented as a convolution product in physical space yielding the resolved part $\bar{\Psi}$ of a spatially and temporally varying quantity Ψ as

$$\bar{\Psi} = \frac{1}{\Delta} \int_{-\infty}^{\infty} \int_{-\infty}^{\infty} G\left(\frac{\boldsymbol{x} - \boldsymbol{\xi}}{\Delta}, t - t'\right) \Psi\left(\xi, t'\right) dt' d^3\boldsymbol{\xi} \tag{2.19}$$

where the spatial filter size is denoted by Δ and the filter kernel by G (for example a box filter or a Gaussian filter) (Deardorff, 1970). We can obtain the sub-grid part through $\Psi' = \Psi - \bar{\Psi}$.

For varying density flows, a density-weighted notation is often employed using a tilde instead of an overbar

$$\bar{\rho}\tilde{\Psi} = \overline{\rho\Psi} = \frac{1}{\Delta}\int_{-\infty}^{\infty}\int_{-\infty}^{\infty}\rho(\xi,t)G\left(\frac{\boldsymbol{x}-\boldsymbol{\xi}}{\Delta}, t-t'\right)\Psi\left(\xi,t'\right)dt'd^3\boldsymbol{\xi} \tag{2.20}$$

Applying the filtering operation to Eqs. 2.1 - 2.4 yields the filtered Navier-Stokes equations, which constitute the mathematical framework for LES

$$\frac{\partial\bar{\rho}}{\partial t} + \frac{\partial\bar{\rho}\tilde{u}_i}{\partial x_i} = 0 \tag{2.21}$$

$$\frac{\partial\bar{\rho}\tilde{u}_i}{\partial t} + \frac{\partial\bar{\rho}\tilde{u}_i\tilde{u}_j}{dx_i} = -\frac{\partial\bar{p}}{\partial x_j} + \frac{\partial}{\partial x_i}\left[\bar{\tau}_{ij} + \tau_{ij}^{SGS}\right] \tag{2.22}$$

$$\frac{\partial\bar{\rho}\tilde{e}}{\partial t} + \frac{\partial}{\partial x_i}\left[\bar{\rho}\tilde{e} + \bar{p}\tilde{u}_j\delta_{ij} + \bar{q}_i - \tilde{u}_j\bar{\tau}_{ij} + q_i^{SGS}\right] = \bar{\dot{\omega}}_T + \bar{\dot{\mathcal{Q}}} \tag{2.23}$$

$$\frac{\partial\bar{\rho}\tilde{Y}_k}{\partial t} + \frac{\partial}{\partial x_i}\left[\bar{\rho}\tilde{Y}_k\tilde{u}_i + \bar{J}_{k,i} + J_{k,i}^{SGS}\right] = \bar{\dot{\omega}}_k \tag{2.24}$$

The expressions for the filtered parts are approximated as

$$\bar{\tau}_{ij} \simeq 2\bar{\mu}\left(\tilde{S}_{ij} - \frac{1}{3}\delta_{ij}\tilde{S}_{kk}\right) \quad \text{with} \quad \tilde{S}_{ij} = \frac{1}{2}\left(\frac{\partial\tilde{u}_j}{\partial x_i} + \frac{\partial\tilde{u}_i}{\partial x_j}\right) \tag{2.25}$$

$$\bar{q} \simeq -\bar{\lambda}\frac{\partial\tilde{T}}{\partial x_i} + \sum_{k=1}^{N}\bar{J}_{k,i}\tilde{h}_{s,k} \tag{2.26}$$

$$\bar{J}_{k,i} = \overline{\rho Y_k V_{k,i}} \simeq -\bar{\rho}\left(\bar{D}_k\frac{W_k}{\bar{W}}\frac{\partial\tilde{X}_k}{\partial x_i} - \tilde{Y}_k\tilde{V}_i^c\right) \quad \text{with} \quad \tilde{V}_i^c \simeq \sum_{k=1}^{N}\bar{D}_k\frac{W_k}{\bar{W}}\frac{\partial\tilde{X}_k}{\partial x_i} \tag{2.27}$$

where the viscosity, the species diffusion coefficients and the thermal conductivity can be written in terms of filtered quantities

$$\bar{\mu} \simeq \mu(\tilde{T}), \qquad \bar{\lambda} \simeq \frac{\bar{\mu}\bar{C}_p(\tilde{T})}{\mathrm{Pr}}, \qquad \bar{D}_k \simeq \frac{\bar{\mu}}{\bar{\rho}\,\mathrm{Sc}_k} \tag{2.28}$$

The unresolved quantities denoted with a superscripted "SGS" are unknown, and require closure models which we will explore in the following section.

2.3.2 LES closure models for unresolved fluxes

Closure models are used in LES to model the sub-grid scale fluxes, which are lost in the filtering approach. An inherent advantage of LES over RANS is the ability to resolve large-scale flow structures, which offers the possibility to infer the unresolved small-scale behavior from resolved quantities. In fact, Bardina et al. (1980) have first established the notion of scale similarity, stating that turbulent structures above a certain scale Δ are similar to those below Δ. This concept has been crucial for the development of closure models not only for sub-grid scale viscous fluxes (*e.g.*, the dynamic Smagorinsky model (Germano et al., 1991)), but also for combustion modeling as we shall see later.

The unresolved Reynolds stress tensor τ_{ij}^{SGS} can be approximated as

$$\tau_{ij}^{SGS} = -\bar{\rho}(\widetilde{u_iu_j} - \tilde{u}_i\tilde{u}_j) \approx \mu_t\left(\frac{\partial\tilde{u}_i}{\partial x_j} + \frac{\partial\tilde{u}_j}{\partial x_i}\right) - \frac{2}{3}\mu_t\frac{\partial\tilde{u}_k}{\partial x_k}\delta_{ij} + \frac{2}{3}\bar{\rho}k \tag{2.29}$$

where μ_t denotes the turbulent viscosity, and $k = \frac{1}{2}\sum_{k=1}^{3}\widetilde{u_k'' u_k''}$. Models which estimate μ_t have been proposed in the literature such as the Smagorinsky model (Smagorinsky, 1963), the WALE model (Ducros et al., 1998), or the SIGMA model (Nicoud et al., 2011) used in this work, which computes the turbulent viscosity from the singular values $\sigma_1 \geq \sigma_2 \geq \sigma_3$ of the velocity gradient tensor $\partial u_i / \partial x_j$

$$\mu_t = \rho (C_\sigma \Delta)^2 \frac{\sigma_3(\sigma_1 - \sigma_2)(\sigma_2 - \sigma_3)}{\sigma_1^2} \tag{2.30}$$

The model constant is set to $C_\sigma = 1.35$ and the characteristic cell size is approximated from its volume V as $\Delta = V^{1/3}$.

The unresolved heat flux q_i^{SGS} and unresolved species flux $J_{i,k}^{SGS}$ can be expressed similarly as

$$q_i^{SGS} = -\bar{\rho}\left(\widetilde{u_i e} - \tilde{u}_i \tilde{e}\right) = -\lambda_t \frac{\partial \tilde{T}}{\partial x_i} + \sum_{k=1}^{N} J_{i,k}^{SGS} \tilde{h}_{s,k} \tag{2.31}$$

$$J_{k,i}^{SGS} = \bar{\rho}\left(\widetilde{u_i Y_k} - \tilde{u}_i \tilde{Y}_k\right) = -\bar{\rho}\left(D_k^t \frac{W_k}{\bar{W}} \frac{\partial \tilde{X}_k}{\partial x_i} - \tilde{Y}_k \tilde{V}_i^{c,t}\right) \tag{2.32}$$

with a turbulent heat conduction coefficient λ_t and a turbulent species diffusivity D_k^t computed from the turbulent Prandtl number Pr^t and the turbulent Schmidt number Sc_k^t (both set to 0.6)

$$\lambda_t = \frac{\mu_t \bar{C}_p}{\mathrm{Pr}^t} \tag{2.33}$$

$$D_k^t = \frac{\mu_t}{\rho \mathrm{Sc}_k^t} \tag{2.34}$$

The turbulent correction velocity $\tilde{V}_i^{c,t}$ ensures mass conservation and is given as

$$\tilde{V}_i^{c,t} = \sum_{k=1}^{N} D_k^t \frac{W_k}{\bar{W}} \frac{\partial \tilde{X}_k}{\partial x_i} \tag{2.35}$$

These closure models are essential for Large-Eddy Simulations of turbulent flows, without (yet) addressing combustion processes, in particular the species source term ($\overline{\dot{\omega}}_k$, Eq. 2.24). Its modeling offers new challenges, mainly due to the following three reasons: first, chemical reaction pathways of hydrocarbon fuels can consist of several hundreds of species (Law, 2007) for which the species transport equation must be solved. Thus, the more species, the longer the solution time, and the more computational resources are required.

Second, due to the strong non-linearity of the Arrhenius reaction rates (see Eq. 2.13), small turbulent fluctuations can lead to intense fluctuations of the reaction rates. Therefore, we cannot develop closure approaches based on (statistical) mean values (Poinsot and Veynante, 2005; Pope, 2013), at least not easily for complex reaction mechanisms (Veynante and Vervisch, 2002), since

$$\overline{\dot{\omega}_k(T, Y)} \neq \dot{\omega}_k(\overline{T}, \overline{Y}) \tag{2.36}$$

Instead, closure models must be developed from physical analysis, involving a closer examination of the relevant scales and the combustion regime.

Third, interactions between the flame and turbulence arise due to the flame's exposure to turbulent structures on one hand, and local modifications of turbulence parameters in the vicinity of the flame front on the other hand (Hilbert et al., 2004). The flame/turbulence

coupling can thus affect the flame surface area, its consumption speed and thickness. Most importantly however, the different scales of chemistry and turbulence conflict with the notion of a single characteristic time (constructed *e.g.,* from a characteristic length scale and a fluctuation velocity) in order to describe these interactions.

Several strategies have been developed to address these challenges which we summarize in the following sections. The interested reader may find further information in the references cited therein and *e.g.,* in Poinsot and Veynante (2005).

2.4 Modeling of reaction kinetics

Beyond the vast amount of species, chemical reaction mechanisms in turbulent flows may also introduce a large range of length and time scales. The length scales may vary from a characteristic length of the combustion device to the thickness of the reaction zone, while the time scales may range from the residence time to the smallest chemical time scales of some intermediate species (Pope, 2013). In some cases, the smallest chemical scales can even be smaller than the smallest scales associated with turbulent motion (η and τ). Modeling approaches for reaction mechanisms therefore aim at reducing the computational costs to make numerical simulations more tractable.

In identifying the quantities of interest a simulation should reliably predict, complex reaction mechanisms can be simplified and reduced to a much smaller subset of species for computational expediency. Key quantities usually involve the laminar flame speed, the adiabatic combustion temperature, fuel conversion or (some) pollutants. In turn, minor species, fuel pyrolysis, autoignition, pollutant formation (*e.g.,* soot) or heat loss effects are less well predicted or even entirely omitted. Reduced mechanisms can therefore greatly lower the computational costs if the conditions they have been designed for are met, and different techniques have been proposed in the literature to achieve this goal. Classical techniques employ for example quasi-steady assumptions, partial equilibria or sensitivity analyses to eliminate elementary reactions and develop global reaction steps instead (see for example Smooke (1991); Peters and Rogg (1993); Warnatz et al. (2001)). These reduced mechanisms often consist of one or two global reactions and a few species as derived by *e.g.,* Jones and Lindstedt (1988) for hydrocarbon fuels. Other techniques can involve intrinsic low-dimensional manifolds (ILDM) (Maas and Pope, 1992), the flame prolongation of ILDM (known as "FPI", Gicquel et al. (2000)), flamelet-generated manifolds (FGM) (van Oijen and de Goey, 2000), the flame-progress variable model (FPV) (Pierce and Moin, 2004), in-situ adaptive tabulation (ISAT) (Pope, 1997), in-situ adaptive manifolds (ISAM) (Lacey et al., 2021), directed relation graph with error propagation methods (DRGEP) (Pepiot-Desjardins and Pitsch, 2008) or analytically reduced chemistries (ARC) (Felden et al., 2019). A recent review article with focus on approaches for LES can also be found in (Fiorina et al., 2015).

For the present work, we employ a global reaction mechanism for n-heptane (C_7H_{16}) developed by Paulhiac et al. (2020) consisting of two reactions and 6 species

$$2\,C_7H_{16} + 15\,O_2 \rightarrow 14\,CO + 16\,H_2O \tag{2.37}$$

$$CO + 1/2\,O_2 \leftrightarrow CO_2 \tag{2.38}$$

Without further treatment however, such mechanism would only provide satisfactory results within a very narrow range of conditions. By contrast, practical combustion devices may operate under partially premixed conditions as encountered with liquid fuels for example, causing large spatial and temporal variations in composition space, and thus in heat release rate or flame speeds (Lipatnikov, 2017). Therefore, fitting procedures of the pre-exponential factor

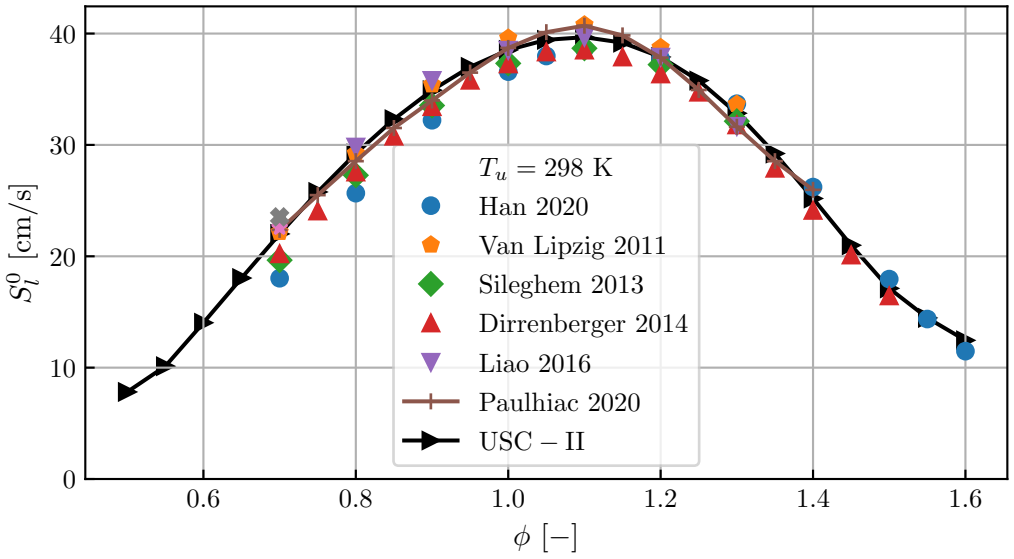

Figure 2.2: Experimental measurements of the laminar flame speed S_l^0 for gaseous n-heptane/air flames for variable equivalence ratios ϕ at a fresh gas mixture temperature of $T_u = 298\,\mathrm{K}$. Validations simulations with the two-step mechanism developed by Paulhiac et al. (2020) are represented by cross symbols. For comparison, we also include a detailed mechanism (USC-II, Smallbone et al. (2009)).

appearing in Eq. 2.13 (also referred to as pre-exponential adjustment (PEA, Franzelli et al. (2010)) can be employed to improve the prediction of key quantities (flame speeds, adiabatic temperatures or flame thicknesses) over a wider range of operating conditions. For the n-heptane reaction mechanism, this improvement has been performed in Paulhiac et al. (2020) and tested for a sufficiently wide range of equivalence ratios at atmospheric pressure and unstrained flames. Additional validation simulations of one-dimensional flames that we have carried out confirm an accurate prediction of S_l^0 using this mechanism, which lies within the spread of available experimental data (see Fig. 2.2).

We emphasize that the simplified mechanism relies on a unitary Lewis number assumption for all species ($\mathrm{Le}_k = \lambda/(\rho C_p D_k) = \mathrm{Le} \equiv 1$) and a constant Prandtl number $\mathrm{Pr} = \mu C_p/(\lambda\,\mathrm{Pr}_0)$. While the evaluation of the transport properties of the mixture is simplified under these assumptions, it essentially renders the flame insensitive to strain effects (Haworth and Poinsot, 1992). In reality, Lewis numbers of heavier hydrocarbon fuels such as n-heptane greatly exceed unity, leading to a decrease of key properties, notably the heat release rate and the flame speed S_l, when the flame is subjected to an increased strain rate (Law, 1989; Poinsot et al., 1991). Strain effects may be due to velocity gradients or flame curvature during the flame motion, and can even lead to local extinction (Law, 1989). With unitary Lewis numbers however, heat release and flame speed remain constant over a wide range of strain rates up to extinction, which can be observed in Fig. 2.3. Consistent with theoretical considerations, S_l of the two-step reaction mechanism remains virtually constant over the plotted strain rate range, whereas the detailed mechanism (USC-II, Smallbone et al. (2009)) exhibits an approximately linearly decreasing flame speed for increasing strain rate. At $a = 1000\,\mathrm{s}^{-1}$, the relative modeling error induced by the two-step mechanism can thus be 38%.

Although this may seem concerning at first, we will show that *mean* flame quantities averaged over the flame surface are of particular interest. Following the asymptotic flame theory (Matalon and Matkowsky, 1983; Williams, 1985; Clavin, 1985), we can express the

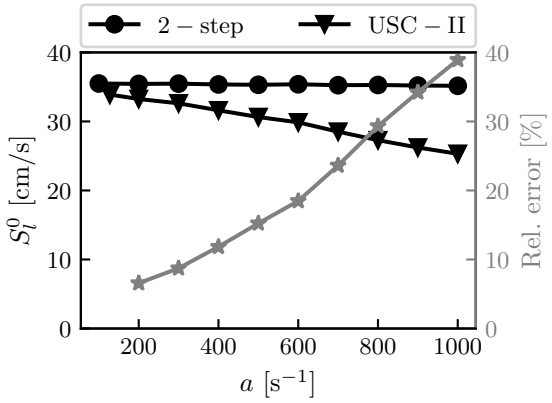

Figure 2.3: Laminar flame speed S_l^0 for variable strain rates a at $\phi = 0.89$ as predicted by a two-step reaction mechanism ("2-step") (Paulhiac et al., 2020) and a more detailed mechanism ("USC-II") (Smallbone et al., 2009) associated with the left axis. The relative error based on the reference values of the detailed mechanism is plotted as gray curve and is associated with the right axis.

laminar flame speed as

$$S_l = S_l^0 - \mathcal{L}a \tag{2.39}$$

where S_l and S_l^0 denote the strained laminar flame speed and the unstrained (fundamental) flame speed respectively, $\mathcal{L}$ the Markstein length and a the strain rate. Equation 2.39 thus states that the laminar flame speed of a strained flame decreases with increasing strain rate for $\mathrm{Le} > 1$. In order to ensure reasonable *mean* flame speeds under strained conditions with a reduced mechanism, the strain rate a (Eq. 2.39) must necessarily be zero on average, for strain effects to cancel out. We will further substantiate this hypothesis in Sec. 8.2.1.1.

Finally, note that validation simulations with the reduced mechanism exhibit a significant departure from the published reference in Paulhiac et al. (2020) for $\phi \geq 1.35$. We suspect an inconsistency in the parameters of Table 4 in Paulhiac et al. (2020) and chose to exclude these data points from Fig. 2.2.

2.5 Turbulent combustion modeling

Turbulent combustion commonly falls in one of the following two regimes: premixed and non-premixed combustion (Williams, 1971; Peters, 1986). These two regimes occupy a central role in the development of combustion models. If no *a priori* assumptions are made about the nature of the underlying combustion process, resulting models tend to be very general, but come with a high computational cost. Transported Probability Density Function (TPDF, Pope (1985)) models or the Linear Eddy Model (LEM, McMurthy et al. (1992)) fall into this class and can be applied for premixed and non-premixed combustion (Peters, 2000). Alternatively, the most appropriate combustion model can be assigned to the prevailing local combustion process based on a given metric to preserve the generality of such modeling approach while maximizing its efficiency (Wu et al., 2015). In turn, with certain *a priori* assumptions about the combustion process, models can be developed for a specific application and reduce the computational costs. Examples for this class of models are flamelet models (see Peters (1984, 1986) for non-premixed, and van Oijen et al. (2016) for premixed), or the Conditional Moment Closure (CMC, Klimenko and Bilger (1999), non-premixed). Other approaches for premixed

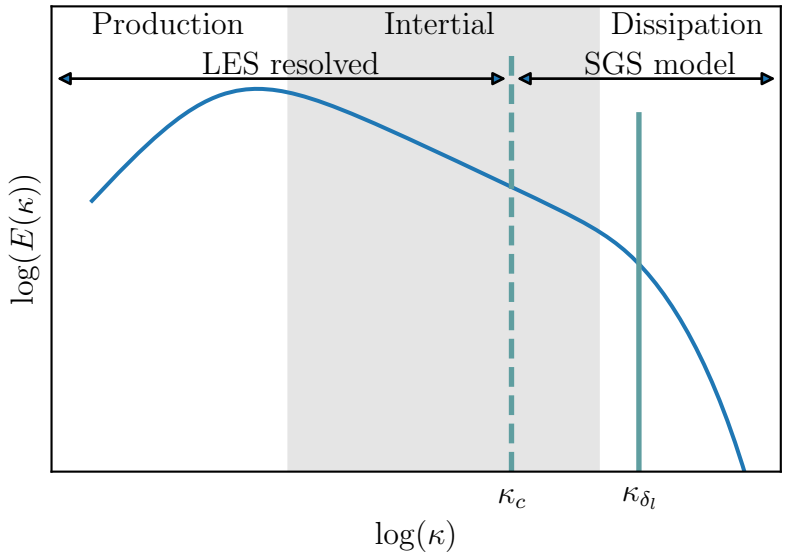

Figure 2.4: Model spectrum of the turbulent kinetic energy as a function of the wavenumber κ. The cell size is associated with a cutoff wavenumber κ_c and limits the range of length scales which can be directly resolved on the mesh. In turn, larger wavenumbers corresponding to smaller scales are unresolved and require closure models. The wavenumber associated with a typical flame thickness in realistic combustion devices is given as κ_{δ_l} and is usually found in the range of unresolved scales.

combustion involve the G-Equation (Kerstein et al., 1988), the Artificially Thickened Flame model (ATF, Butler and O'Rourke (1977)), or filtering approaches such as the Flame Surface Density concept (FSD, Boger et al. (1998)) and Filtered Tabulated Chemistry of LES model (F-TACLES, Vicquelin et al. (2009); Fiorina et al. (2010)). We limit our discussion of combustion models to the thickened flame model used in this work and refer the interested reader to reviews of Fiorina et al. (2015), Peters (2000) or Huang and Yang (2009) (specifically for premixed combustion) for further details.

As foreshadowed at the end of Sec. 2.3.2, the interaction between a flame and turbulence is a multi-scale problem in the most general case and complicates the combustion model development. Under the assumption of premixed combustion, however, a single length and time scale emerge, which can be related to the combustion process: the laminar flame thickness δ_l and the characteristic flame time $\tau_F = \delta_l / S_l$ constructed with the laminar flame speed S_l (Peters, 2009). This notion is of paramount importance for the development of combustion models for the premixed regime such as the thickened flame model, which we briefly outline in the following section.

2.5.1 Artificially Thickened Flame Model

Although the laminar flame thickness constitutes a characteristic length scale in premixed combustion simplifying the scale problem associated with flame/turbulence interactions, it is often too thin to be resolved on meshes commonly used for Large-Eddy Simulations. Figure 2.4 may serve as an illustration of that issue, showing a model energy spectrum of the turbulent kinetic energy E (Pope, 2000) as a function of the wavenumber κ (an inverse length scale). While the mesh size (associated with a cutoff wavenumber κ_c) is found in the inertial range, which is resolved in LES, δ_l (associated with a wavenumber κ_{δ_l}) clearly remains in the unresolved dis-

sipation range. To overcome this problem, Butler and O'Rourke (1977) proposed to multiply the diffusion term in the species transport equation by a factor $\mathcal{F}$, and to divide the source term by the same factor $\mathcal{F}$, ensuring a correct laminar flame speed retrieval of the *thickened* flame. This procedure has the desired effect of an artificially thickened flame, which can be resolved on the LES grid.

Invoking the fundamental theory of laminar premixed flames (Williams, 1985), O'Rourke and Bracco (1979) present the underlying mathematical framework for the thickening approach under the assumption of a stationary reaction regime, where

$$S_l \propto \sqrt{D\bar{\dot{\omega}}} \tag{2.40}$$

$$\delta_l \propto \frac{D}{S_l} \tag{2.41}$$

In the above equations, D denotes the thermal diffusivity, $\bar{\dot{\omega}}$ the mean reaction rate and S_l the laminar burning velocity. If we transform these equations by setting $D^1 = \mathcal{F}D^0$ and $\bar{\dot{\omega}}^1 = \bar{\dot{\omega}}^0/\mathcal{F}$ where a superscripted "1" denotes the respective quantities of the thickened flame and "0" the quantities of the unthickened flame, we find that S_l (Eq. 2.40) remains invariant to this transformation, while δ_l (Eq. 2.41) is increased by $\mathcal{F}$. For consistency, the transformation is also applied to the energy equation and remains valid as long as the thickened flame thickness ($\delta_l^1 = \mathcal{F}\delta_l^0$) is much smaller than a characteristic length scale of the geometry, which is generally satisfied in practical combustion devices.

There is no requirement in imposing a constant thickening factor $\mathcal{F}$ in the entire domain. The amount of thickening applied locally to the flame may vary in both space and time. Common techniques to determine the local amount of thickening are summarized in Sec. 2.5.3.

Since the Artificially Thickened Flame model is based on the Arrhenius reaction rates, it can inherently account for various phenomena without requiring *"ad hoc"* sub-models (Colin et al., 2000), for example: ignition, flame stabilization or flame/wall interactions. Moreover, it can also handle heat loss effects and yield acceptable results in partially premixed conditions induced by *e.g.,* liquid fuels (Cuenot et al., 2021), contributing to its popularity. Thus, the thickening approach overcomes the under-resolution problem for the species source term (Eq. 2.36), allowing to evaluate $\bar{\dot{\omega}}$ using the Arrhenius law.

Despite this, it comes with an undesired side effect of "artificially suppressed" interactions with small-scale turbulence (Peters, 2009). More specifically, the ratio between turbulence (τ_t) and the characteristic flame time scale (τ_F) expressed through the Damköhler number Da

$$\mathrm{Da} = \frac{\tau_t}{\tau_F} = \frac{l_t}{u'}\frac{S_l}{\delta_l} \tag{2.42}$$

is decreased by $\mathcal{F}$. Two major consequences result from this observation: (i) small-scale turbulent structures cannot wrinkle the artificially thickened flame to the same extent as the *unthickened* flame (Poinsot et al., 1991), and thus do not contribute to an increase of the flame surface. Turbulent flame speeds would therefore be underestimated. (ii) The flame's sensitivity to strain is increased by $\mathcal{F}$ (Veynante and Poinsot, 1997) such that the thickened flame is exposed to an "effective" (Popp et al., 2019) strain rate of $\mathcal{F}a$, whereas the unthickened flame would only experience a strain rate of a. High strain rates combined with the artificially thickened flame approach tend to be poor representations of the turbulent premixed flame structure, particularly at elevated thickening factors (Han et al., 2019).

An attempt to remedy the first effect ("Damköhler effect") is proposed by Colin et al. (2000). In defining an efficiency function E as the ratio of the flame surface wrinkling factors

of the unthickened and thickened flame

$$E = \frac{\Xi(\delta_l)}{\Xi(\mathcal{F}\delta_l)} \tag{2.43}$$

the correct flame surface wrinkling can be restored. We can then employ the efficiency function such that the thermal diffusivity of the thickened flame becomes $D^1 = E\mathcal{F}D^0$ and the reaction rate $\overline{\dot{\omega}}^1 = E/\mathcal{F}\overline{\dot{\omega}}^0$. Rewriting the species transport equation Eq. 2.24, we finally have

$$\begin{aligned}&\frac{\partial \overline{\rho}\tilde{Y}_k}{\partial t} + \frac{\partial \overline{\rho}\tilde{u}\tilde{Y}_k}{\partial x_i} = \\ &\frac{\partial}{\partial x_i}\bar{\rho}\left[(E\mathcal{F}D_k + D_k^t(1-\theta_F))\frac{W_k}{\bar{W}}\frac{\partial \tilde{X}_k}{\partial x_i} - \tilde{Y}_k(E\mathcal{F}\tilde{V}_i^c + \tilde{V}_i^{c,t}(1-\theta_F))\right] \\ &+ \frac{E}{\mathcal{F}}\bar{\dot{\omega}}_k\end{aligned} \tag{2.44}$$

Similarly, the laminar flame speed of the thickened flame becomes ES_l. Note that the flame zone of the thickened flame is now fully resolved by construction, requiring turbulent fluxes to be set to zero. Detecting the flame zone can be achieved through a flame sensor θ_F which is the subject of Sec. 2.5.3. The flame surface wrinkling factors are yet to be defined and discussed in Sec. 2.5.2.

Regarding the second aspect (elevated strain *and* elevated thickening), Popp et al. (2019) revealed through laminar flame investigations that the flame thickness may be underpredicted by the "classical" thickened flame approach of Butler and O'Rourke (1977) (or even Colin et al. (2000)). Although this effect clearly deserves further investigations in *turbulent* flames, we wish to reiterate that local strain effects cannot alter the laminar flame speed (over a wide range of strain rates) if the reaction mechanism is based on a *unitary* Lewis number ($\mathrm{Le} = 1$, see also Sec. 2.4). In our case, the reduced reaction mechanism (Paulhiac et al., 2020) necessarily yields a laminar flame speed of the unstrained flame (S_l^0), even at effective strain rates of $\mathcal{F}a$, as shown in Sec. 8.2.1.1. This behavior was already characterized by Haworth and Poinsot (1992). The expected impact on the simulations in this work is assessed in Sec. 8.2.1.1.

2.5.2 Models for flame surface wrinkling

Closure models for the subgrid scale flame surface wrinkling often invoke the theory of Damköhler (1940) who proposed a fundamental scaling relation for the turbulent flame speed S_T with respect to the laminar flame speed S_l^0, which reads (see also Peters (2000))

$$\frac{S_T}{S_l^0} = \frac{A_T}{A} = 1 + \alpha\left(\frac{u'_\Delta}{S_l^0}\right)^n \tag{2.45}$$

It states that an increase of the turbulent flame surface A_T caused by interaction with turbulence results in an increase of the turbulent flame speed over its value in laminar conditions (associated with the laminar flame surface A). Equation 2.45 uses the subgrid scale velocity fluctuations u'_Δ and two model parameters, α and n. Peters (2000) has compiled various studies providing suggested values for these parameters and further adjustments of Eq. 2.45.

As we mentioned in the previous section, Colin et al. (2000) attempt to compensate for the unresolved flame wrinkling at subgrid scale in their thickened flame approach to recover the correct S_T. Unlike large eddies, however, insights from DNS (Poinsot et al., 1991) and

experiments (Roberts et al., 1993) have suggested that low velocities or small eddy sizes relative to the laminar flame velocity and thickness only weakly affect the flame front wrinkling. This motivated the development of an improved scaling relation for the wrinkling factor Ξ_Δ with a spectral efficiency function Γ_Δ obtained from separate DNS, which reads

$$\frac{S_T}{S_l^0} = \Xi_\Delta \approx 1 + \alpha\Gamma_\Delta\left(\frac{\Delta}{\delta_l^0}, \frac{u'_\Delta}{S_l^0}\right)\frac{u'_\Delta}{S_l^0} \tag{2.46}$$

where α is a model constant and Δ a filter size (*e.g.,* the LES filter size). Colin et al. (2000) then use Ξ_Δ to evaluate the efficiency function E according to Eq. 2.43.

Charlette et al. (2002b) have instead proposed a power-law relation with additional improvements to correct some limit cases at low Δ/δ_l^0 where the linear model of Colin et al. (2000) tends to become insensitive (clipping of S_T/S_l^0, also referred to as "cutoff behavior")

$$\Xi_\Delta = \left(1 + \min\left[\frac{\Delta}{\delta_l^0} - 1, \Gamma_\Delta\left(\frac{\Delta}{\delta_l^0}, \frac{u'_\Delta}{S_l^0}, \mathrm{Re}_\Delta\right)\frac{u'_\Delta}{S_l^0}\right]\right)^\beta \tag{2.47}$$

In the above expression, Re_Δ denotes the subgrid scale Reynolds number defined as $\mathrm{Re} = u'_\Delta\Delta/\nu$, with ν being the fresh gas kinematic viscosity. Note that the term (-1) in the first expression of the minimum was later added by Wang et al. (2011) to maximize the wrinkling factor when it is dominated by the first expression, *i.e.,* $\Xi_\Delta^{\max} = (\Delta/\delta_l^0)^\beta$.

Charlette et al. (2002b) do not require the flame surface wrinkling parameter β to take a specific value. If however β is independent of the filter size and the cutoff scale, and satisfies $0 < \beta < 1$, their model resembles fractal approaches for the description of highly wrinkled (flame) surfaces — a theory put forth by Mandelbrot (1975). Those fractal-based closure models for premixed combustion have been successfully applied for example in Gouldin (1987); Gouldin et al. (1989); Gülder (1991). Initially however, Charlette et al. (2002b) (as well as Colin et al. (2000)) assumed a local equilibrium between the flame surface and turbulence at subgrid scale level, and set $\beta \equiv 0.5$ as an *ad hoc* solution. We refer to this version of the wrinkling factor model as *static* formulation.

While the equilibrium assumption can be justified for example in stationary conditions, it appears to be inappropriate for light-round simulations, as highlighted by Puggelli et al. (2021) as well as in Sec. 6.5.5.3. Instead, the authors recommend a more general model formulation with a *dynamic* closure approach for β (Charlette et al., 2002a) discussed in Sec. 2.5.2.2.

Independent of the β parameter, DNS data provides evidence that for high u'_Δ/S_l^0 ratios the minimum term in Eq. 2.47 is essentially governed by $\Delta/\delta_l^0 - 1$ (Veynante and Moureau, 2015). The flame surface wrinkling factor is then considered to be "saturated" and simplifies to

$$\Xi_\Delta = \left(\frac{\Delta}{\delta_l^0}\right)^\beta \tag{2.48}$$

For the remainder of this work we assume Eq. 2.48 to hold true.

2.5.2.1 Differences between the efficiency function in Colin et al. and Charlette et al.

Upon comparing the expressions of the efficiency functions between Colin et al. (2000) and Charlette et al. (2002b), we wish to emphasize that Charlette et al. (2002b), and subsequent works (Wang et al., 2011, 2012; Veynante and Moureau, 2015), do *not* employ the efficiency function definition in Eq. 2.43. Rather, (Charlette et al., 2002b, see p. 169) argue that $\Delta/(\mathcal{F}\delta_l) \approx 1$ in typical applications, yielding a spectral efficiency function $\Gamma_\Delta = 0$ (see

Eq. 2.47). To put it in another way, the thickened flame is locally supposed to be barely wrinkled by the smallest resolved scales, since its thickness $\mathcal{F}\delta_l$ is of the order of the mesh size Δ. Therefore, the wrinkling factor of the thickened flame becomes $\Xi_\Delta(\mathcal{F}\delta_l) \equiv 1$, which in turn results in a simplified Eq. 2.43, written as

$$E \equiv \Xi_\Delta(\delta_l) \tag{2.49}$$

This argument is consistent with the notion that turbulent structures smaller than $\mathcal{F}\delta_l$ cannot wrinkle the *thickened* flame. The following discussion of the flame surface wrinkling parameter β implicitly assumes that the conditions that lead to Eq. 2.49 are met.

2.5.2.2 Dynamic evaluation of the flame surface wrinkling parameter β

The dynamic closure approach proposed by Charlette et al. (2002a) specifically focuses on the evaluation of the flame surface wrinkling parameter β in Eq. 2.48 (or Eq. 2.47 in its general form), owing to the fact that there is no *universal* value for this parameter. Instead, β is inferred from information contained in the resolved scales in LES. Inspired by the so-called "Germano-identity" (Germano et al., 1991), the reaction rate is evaluated in two ways: (i) the resolved (i.e. LES) reaction rate is test-filtered at scale $\gamma\Delta$ with $\gamma > 1$; (ii) the resolved quantities *entering* the reaction rate expression are test-filtered at scale $\gamma\Delta$, which can be thought of as LES performed with an LES filter of $\gamma\Delta$.

Although the reaction rate can be expressed through an Arrhenius law (as initially done by Charlette et al. (2002a) for a one-step irreversible global reaction), it is more convenient to consider a geometrical description of the flame surface wrinkling. An expression in terms of a flame surface density based on the gradient of the progress variable c can be more advantageous in premixed combustion, as shown later. The progress variable is commonly based on a combination of reactive scalars, *e.g.,* species or temperature, such that $c = 0$ in purely fresh gases and $c = 1$ in purely burnt gases. Its construction with respect to species certainly depends on the employed reaction mechanism and is not unique. For this work, we follow the definition of Fiorina et al. (2003, 2005) given in its normalized form as

$$c = \frac{Y_{\mathrm{CO_2}} + Y_{\mathrm{CO}}}{(Y_{\mathrm{CO_2}} + Y_{\mathrm{CO}})|_{eq}} \tag{2.50}$$

Normalization is achieved by division of the local CO_2 and CO mass fractions by their equilibrium value (subscripted "eq"). A brief discussion of this definition may be found in Fiorina et al. (2015), and various other definitions are compiled in *e.g.,* Ihme et al. (2012).

We can thus write the progress variable source term as

$$\dot{\omega}_c = \rho_u S_l \Sigma \tag{2.51}$$

where ρ_u denotes the fresh gas density, S_l the flame speed and Σ the generalized flame surface density, i.e. the flame surface area per unit volume (Veynante and Vervisch, 2002), which is defined as the gradient of the progress variable

$$\Sigma = \overline{|\nabla c|} = \Xi_\Delta \, |\nabla \bar{c}| \tag{2.52}$$

Note that the overbar represents a filtering operation specified later. Invoking the "Germano-like identity" (Charlette et al., 2002a), *i.e.,* the conservation of the total flame surface computed at scales Δ and $\gamma\Delta$, we have

$$\widehat{\langle \Xi_\Delta \, |\nabla \bar{c}| \rangle} = \left\langle \Xi_{\gamma\Delta} \left| \nabla \hat{\bar{c}} \right| \right\rangle \tag{2.53}$$

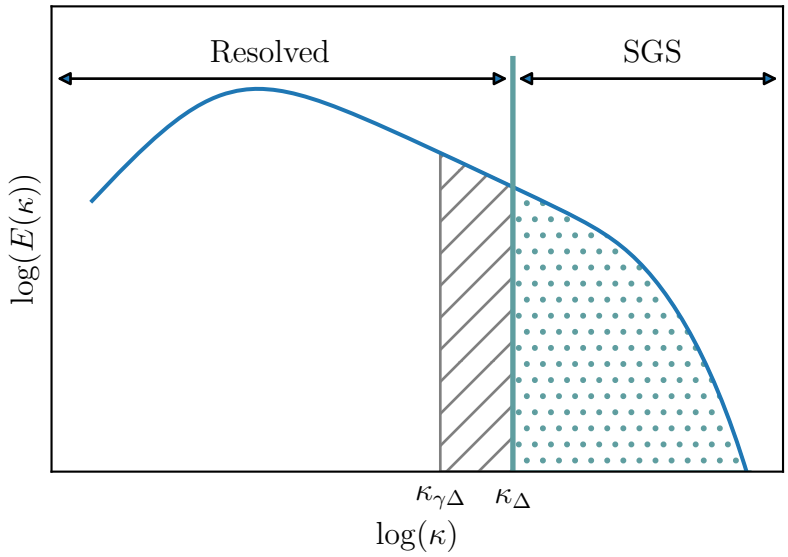

Figure 2.5: Visualization of the dynamic closure approach: the flame surface wrinkling at the smallest resolved scales ranging between Δ and $\gamma\Delta$ (or their respective wavenumbers) is test-filtered to infer the wrinkling of the unresolved ("SGS") scales.

and after substitution of the flame surface wrinkling factor with Eq. 2.48

$$\left\langle \widehat{\left(\frac{\Delta}{\delta_l}\right)^{\beta} |\nabla \bar{c}|} \right\rangle = \left\langle \left(\frac{\gamma\Delta}{\delta_l}\right)^{\beta} |\nabla \hat{\bar{c}}| \right\rangle \tag{2.54}$$

A hat operator represents the test-filtering operation (at scale $\gamma\Delta$), and angular brackets denote volume averaging, which was introduced by Charlette et al. (2002a) in order to avoid unphysical fluctuations upon computation of β (also referred to as "weak form"). Assuming that β is (i) uniform over the averaging volume and (ii) independent of the filtering scale, we can solve Eq. 2.54 for β

$$\beta = \frac{\log\left(\left\langle \widehat{|\nabla \bar{c}|} \right\rangle \Big/ \left\langle |\nabla \hat{\bar{c}}| \right\rangle\right)}{\log(\gamma)} \tag{2.55}$$

The scale invariance implies that β, and thus the flame surface, exhibit a fractal behavior similar to the description of Gouldin (1987) and Mandelbrot (1975), at least within some limits (as also discussed in Gouldin et al. (1989)). Put differently, the β value obtained between the scales Δ and $\gamma\Delta$ (hatched region in Fig. 2.5) is considered to be representative of the *unresolved* scales below the LES filter Δ, corresponding to the dotted region in Fig. 2.5 (Charlette et al., 2002a). In turn, such assumption clearly requires a sufficient amount of flame surface wrinkling to be resolved in order to obtain reasonable results from the dynamic modeling procedure.

In order to determine the effective test filter scale $\gamma\Delta$ for a combination of two Gaussian filters, we define

$$\gamma = \left[1 + \left(\frac{\hat{\Delta}}{\Delta}\right)^2\right]^{1/2} \tag{2.56}$$

where $\hat{\Delta}$ denotes the test filter size, and Δ is specified in the next section.

As demonstrated by Veynante and Moureau (2015), the advantage of expressing β in terms of flame surfaces rather than Arrhenius laws lies in the fact that Eq. 2.53 satisfies two key requirements by construction: (i) for fully resolved laminar flames, a unity wrinkling factor is obtained ($\Xi_\Delta = \Xi_{\gamma\Delta} = 1$), since $\widehat{|\nabla \bar{c}|} = |\nabla \hat{\tilde{c}}|$. (ii) Similarly, the identity $\left\langle \widehat{|\nabla \bar{c}|} \right\rangle = \left\langle |\nabla \hat{\tilde{c}}| \right\rangle$ is satisfied as well. Equation 2.53 also allows to perform the volume averaging (indicated by angular brackets) in the same manner as a Gaussian filtering operation, which is easier to implement on unstructured meshes.

2.5.2.3 Solution strategies for the flame surface wrinkling parameter

Four practical problems remain when implementing Eq. 2.55 in LES solvers: first, this equation contains *unweighted* filtered fields (denoted with an overbar) instead of Favre-averaged (*mass-weighted*) fields, which are solved in LES (Veynante and Moureau, 2015). Therefore, β must be approximated as (note the tilde operator)

$$\boxed{\beta \approx \frac{\log\left(\left\langle \widehat{|\nabla \tilde{c}|} \right\rangle \Big/ \left\langle \left|\nabla \hat{\tilde{c}}\right| \right\rangle\right)}{\log\left(\gamma\right)}} \tag{2.57}$$

which is only exact for infinitely thin flame fronts (see implementation in AVBP in Volpiani et al. (2016)).

Second, an artificially thickened flame is *not* equivalent to a filtered flame in an LES context. Although filtering a flame front has the same effect as the thickening factor $\mathcal{F}$, the thickened flame model by Colin et al. (2000) applies thickening only to the diffusion and source term of the species transport equation. Conversely, filtering in LES also effects the velocity field, which is unaffected by $\mathcal{F}$ in the artificially thickened flame approach (Duwig, 2007). Thus, an equivalent "combustion filter size" must be defined for the thickened flame, which can be written as

$$\Delta = \alpha \mathcal{F} \delta_l \tag{2.58}$$

with a parameter $\alpha \equiv 1$ (also referred to as "TFLES filter factor") used in this work (Veynante, 2021, private communication).

Third, the test filter must be sufficiently large to contain enough wrinkling of the resolved flame fronts. This condition may conflict with strongly wrinkled flames, which tend to develop cusps that can be smaller than the test filter size $\hat{\Delta}$. Filtering such a cusp will necessarily fail, since the evolution of the progress variable at test filter scale is no more strictly monotonic due to the presence of two flame front elements (instead of a single flame front with a monotonic evolution of c). Consequently, the dynamic closure approach will *locally* yield unphysical values for the flame surface wrinkling parameter β, as the Gaussian filtering operation fails to "detect" either flame front.

Mouriaux et al. (2017) propose a modified evaluation of the test-filtered flame surface density based on the orientation of the normal vectors of the resolved and test-filtered flame surfaces. The scalar product of both surface normal vectors is used as a criterion to locally correct the flame surface density expression if both vectors are not collinear. Results obtained by Mouriaux et al. (2017) for ignition in internal combustion engines and Puggelli et al. (2021) for light-round ignition in annular combustors show substantial improvements of the predicted flame surface wrinkling parameter over the uncorrected formulation, despite the fact that the correction was derived from one-dimensional flames. Most notable is the boundedness of β, which does not exceed unity with the correction applied, consistently with the fractal interpretation of the wrinkled flame surface.

Lastly, an algorithm is required to compute filtered fields on an unstructured mesh. Instead of discretizing the filter kernel (as in Wang et al. (2011)), we can express the convolution of a filter G with a quantity ϕ through a Taylor series expansion of ϕ and moments of the filter (Moureau et al., 2011). In a one-dimensional case we can write the filtered quantity $\bar{\phi}$

$$\bar{\phi}(x) = \sum_{k=0}^{\infty} \frac{1}{k!} \mathcal{M}_k \frac{\partial^k \phi}{\partial x^k}(x) \tag{2.59}$$

where the moment $\mathcal{M}_k$ of the filter is given as

$$\mathcal{M}_k = \int y^k G(y) dy \tag{2.60}$$

Considering only a finite number of moments, we eventually obtain for a one-dimensional Gaussian filter with a filter width of Δ

$$\bar{\phi}(x) = \phi(x) + \frac{\Delta^2}{24} \frac{\partial^2 \phi}{\partial x^2}(x) + \frac{\Delta^4}{1152} \frac{\partial^4 \phi}{\partial x^4}(x) \tag{2.61}$$

Equation 2.61 resembles a diffusion equation and is solved in AVBP with an explicit scheme.

Regarding the volume averaging operation in Eq. 2.57, we can define different averaging volumes: averaging β over the entire numerical domain results in a global value that only varies with time ("global formulation"). In turn, local averaging volumes — the preferred method for light-round simulations — allow for a spatial and temporal variation of β ("local formulation"), but are difficult to implement on unstructured meshes. Therefore, local averaging is performed like a filtering operation in AVBP, leveraging the same solution strategy as the test filter operation given in Eq. 2.61 with a separate "averaging filter width" Δ_{avg}.

2.5.3 Variable evaluation of the thickening factor ("Dynamic thickened flame model")

As we state in Sec. 2.5.1, a local adjustment of the thickening factor $\mathcal{F}$ can be desired for example with spatially varying mesh sizing or equivalence ratios. Moreover, imposing a thickening factor greater than unity over the entire numerical domain may conflict with pure (non-reacting) mixing far upstream of a flame. Legier et al. (2000) address both cases with a modified version of the artificially thickened flame model originally developed by Colin et al. (2000). In applying a flame sensor, the thickening is limited to the reaction zone only, as opposed to thickening in the entire domain. The sensor function θ_F is written as

$$\theta_F = \tanh\left(\beta \frac{\Omega}{\Omega_0}\right) \tag{2.62}$$

where Ω is an "Arrhenius-like expression", which reads

$$\Omega = Y_F^{\nu_F} Y_O^{\nu_O} \exp\left(-\Gamma \frac{T_a}{T}\right) \tag{2.63}$$

and Ω_0 is its maximum value tabulated as a function of the local equivalence ratio. The calibration parameter β in Eq. 2.62 is set to 50 (not to be confused with the flame wrinkling parameter), and the activation coefficient Γ in Eq. 2.63 is set to 0.5 consistently with Legier et al. (2000). Fuel and oxidizer mass fractions are denoted as Y_F and Y_O, respectively and ν_F and ν_O correspond to their stoichiometric reaction coefficients. The activation energy for

the first reaction of the two-step reaction mechanism (Paulhiac et al., 2020) is $T_a = 14\,593\,\mathrm{K}$ and T is the local temperature. This mathematical framework allows the detection of the reaction zone where $\theta_F = 1$, *i.e.* the sensor is active and thickening is applied, and $\theta_F = 0$ elsewhere in the domain, *i.e.* outside of the reaction zone. We note that the flame sensor may be defined differently for other use cases, for example for other combustion models or reaction mechanisms (Durand and Polifke, 2007; Rochette et al., 2020).

Furthermore, this thickening procedure (Colin et al., 2000; Legier et al., 2000) is *locally* adaptive to account for varying mesh sizes and mixture inhomogeneities within the domain. Perfect premixing — a key assumption of the thickened flame model — is particularly hard to achieve in realistic combustors (Masri, 2015), and even more so with liquid fuels. Mixtures of fuel and air tend to be inhomogeneous and combustion processes will necessarily take place over a *range* of equivalence ratios, which is generally referred to as stratified combustion (Masri, 2015).

Thus, rather than imposing a constant thickening factor $\mathcal{F}$, a number of grid nodes n is imposed to resolve the flame structure. The local amount of thickening can then be determined from

$$\mathcal{F} = 1 + (\mathcal{F}_{\max} - 1) \underbrace{\tanh\left(\beta \frac{\Omega}{\Omega_0}\right)}_{\theta_F} \tag{2.64}$$

where the maximum required thickening $\mathcal{F}_{\max}$ follows from the local laminar flame thickness δ_l (tabulated as a function of local the equivalence ratio), the local cell size Δ and the requested number of grid points n

$$\mathcal{F}_{\max} = \frac{n\,\Delta}{\delta_l} \tag{2.65}$$

We emphasize that this procedure should *not* be confused with the dynamic closure approach for the flame surface wrinkling parameter. The terminology introduced by Legier et al. (2000) ("Dynamic thickening") is misleading, and we prefer the term "local thickening" as Wang et al. (2011) to avoid confusion.

2.5.4 Treatment of non-premixed combustion induced by liquid fuels

Mixture stratification can be viewed as a special case of partial premixing (Masri, 2015) that is likely to occur in realistic combustors with liquid fuel injection. Tabulation approaches as described above (Sec. 2.5.3), or a recently developed extension of the thickened flame model (Kazmouz et al., 2022) are reasonable modeling strategies for stratified combustion from an engineering standpoint. Yet it is conceivable that mixing may be incomplete so that (partially) premixed regions coexist with non-premixed regions. This is substantially more challenging to model, since combustion now pivots towards a multi-regime (or multi-mode) combustion process, simultaneously involving premixed and non-premixed regions. The longstanding question of how to adequately model multi-regime combustion is discussed more fundamentally for example in Knudsen and Pitsch (2010) or Masri (2021), given that the thickened flame model is developed for pure premixed combustion. With insights gained from prior works (Lancien, 2018), however, flame propagation during light-round is predominantly found to occur in the premixed regime, which we substantiate in Sec. 7.5.5.

In turn, applying the same thickening procedure to non-premixed regions, which are far less observed during light-round (as shown later), is clearly inappropriate: unlike premixed

combustion, where one length scale stands out from the spectrum of scales relevant for turbulence/flame interactions (see Sec. 2.5.1), non-premixed combustion is instead controlled by the diffusion coefficient, at least at a given strain rate. Therefore, previous light-round simulations have resorted to imposing $\mathcal{F} \equiv 1$ (no thickening) in non-premixed regions, while preserving the thickening procedure (Colin et al., 2000; Legier et al., 2000) in the premixed region. This approach is also employed in the present work and relies on the Takeno flame index FI (Yamashita et al., 1996) to identify the local combustion regime. The flame index is defined for a planar flame as

$$\mathrm{FI} = \frac{\nabla Y_{C_7H_{16}} \cdot \nabla Y_{O_2}}{|\nabla Y_{C_7H_{16}} \cdot \nabla Y_{O_2}|} \tag{2.66}$$

By definition, it is $+1$ in the premixed regime, since fuel and oxidizer gradients (C_7H_{16} and O_2) have the same sign for planar one-dimensional flames, and -1 in non-premixed conditions.

Attempts have been made to correct the numerical diffusion errors and errors due to the unresolved subgrid strain rate by a multiplicative factor applied to the diffusion coefficient in the species transport equation. Different implementations have recently been proposed by Cuenot et al. (2021) or De Luca (2021) for non-premixed combustion.

2.6 Equations and models for the liquid phase

Modeling of reacting flows in aeroengine combustors often requires a multiphase flow approach when liquid fuels are used. Therefore, a mathematical framework must be developed to describe the relevant physical phenomena, e.g. fuel injection or heat and mass transfer between the individual phases. The theory underpinning the handling of the liquid phase is briefly described in the following.

2.6.1 Fuel sprays and general modeling approaches

Combustion of liquid fuels can usually be improved through an effective atomization process, a breakdown of bulk liquid into droplets, to achieve high rates of mixing and evaporation through increase of the specific surface area of the fuel (Lefebvre and Mcdonell, 2017). A small fuel droplet size is often beneficial for the operation of a combustor in general, and pollutant emission control in particular. Droplets, or other physical dispersions of small particles in an atmosphere, are referred to as sprays and usually comprise a wide range of droplet (or particle) sizes, which can be produced through atomization (Lefebvre and Mcdonell, 2017).

Sprays are commonly classified into three flow regimes based on the occupied volume fraction α_l (Jenny et al., 2012):

- Very dense sprays ($\alpha_l > 10^{-3}$) are characterized by droplet collision and coalescence, which dominate the dispersed phase dynamics.
- In the dilute regime ($10^{-6} < \alpha_l < 10^{-3}$), there is still a phase interaction, but droplet collisions are assumed to be negligible.
- If the volume fraction is below 10^{-6}, any effect of the liquid phase on the continuous gas phase can be neglected.

Despite arbitrarily set regime boundaries, which can be controversial, this definition simplifies the study of the respective flow types, especially in large-scale applications, which would otherwise be unfeasible (Masri, 2016): for example, the assumption of a dilute spray allows to

shift the focus on *other* phenomena of specific interest, such as droplet evaporation, mixing and interaction with the surrounding turbulence, essentially neglecting droplet collisions and coalescence. The phenomena of interest occur farther away from the injector where the dilute spray assumption can certainly be justified (Menon and Patel, 2006). The dilute regime is therefore addressed in a large amount of publications relevant for research in aeroengine combustors (Faeth, 1983; Reveillon and Vervisch, 2005; Neophytou et al., 2012; Kariuki and Mastorakos, 2017; Sacomano Filho et al., 2020) and constitutes a main assumption for the present work.

For a mathematical description of fuel droplets, a microscopic approach to (turbulent) multiphase flows is usually impractical for (large-scale) engineering applications. The wide range of length and timescales, often imposes prohibitive computational costs, or only allows for a very small number of droplets to be resolved (Masri, 2016). Nevertheless, the knowledge of microscopic phenomena and their corresponding governing equations is useful to derive models of reduced order, which are known as (i) Euler-Euler (EE) and (ii) Euler-Lagrange (EL) models (Faeth, 1987; Fox, 2011).

Euler-Euler models are obtained from volume/ensemble averaging of the microscopic governing equations, thus losing information about individual droplets. Conservation equations are solved for the liquid volume fraction occupying a given location, a liquid phase velocity, temperature and first and second order moments of the droplet size distribution. The similarity of these equations with the equations of the (continuous) gaseous phase allows for a straightforward implementation into numerical solvers. However, polydispersion or particle interactions are difficult to model.

Conversely, Euler-Lagrange models follow from a reduction of degrees of freedom of the microscopic governing equations through physical approximations (Fox, 2011). For example, the droplet phase is assumed to consist of rigid, spherical droplets with a diameter, velocity and temperature, whose evolution can be tracked for each droplet individually in space and time. Closure models are used to describe the interaction of the droplet phase with the carrier phase. In principle, information such as particle trajectories, particle interactions and polydispersion can readily be obtained from Euler-Lagrange approaches. In turn, including an Euler-Lagrange description into highly parallel solvers can be challenging. Yet it is the preferred approach for Large-Eddy Simulations of ignition in aeroengines, as will be discussed later. The mathematical framework for the description of lagrangian particles is covered in the following section.

2.6.2 Lagrangian particle tracking

The governing equations for individual droplet tracking in non-uniform, unsteady flows at low Reynolds numbers have first been rigorously derived by Maxey and Riley (1983). A simplified formulation which covers all relevant phenomena in this work can be obtained through a list of assumptions based on physical considerations:

- the fuel is already "pre-atomized" consisting of perfectly spherical, rigid droplets which are small in size compared to the turbulence integral length scale;
- droplets can be treated as point sources of momentum and energy: instead of resolving all forces *at* the scale of each droplet, a resulting force it modeled for a (corresponding) spherical particle using information of the surrounding fluid;
- similarly, the temperature field *inside* each droplet is not resolved, but assumed constant; however, the individual temperature can vary for different droplets;

- any droplet interactions including secondary breakup are negligible by invoking a dilute spray assumption;
- the effect of pressure gradients and shear on droplet motion is negligible;
- the droplets' density is assumed to be much larger than that of the fluid, allowing neglect the Basset force and the apparent mass term;
- finally, gravitational effects are omitted.

The equations can then be written as follows (Pope, 2000; Crowe et al., 2011):

$$\frac{d\boldsymbol{x}_p}{dt} = \boldsymbol{u}_p \tag{2.67}$$

$$m_p \frac{d\boldsymbol{u}_p}{dt} = F_p \tag{2.68}$$

with $\boldsymbol{x}_p$, $\boldsymbol{u}_p$ and m_p denoting the particle position, velocity and mass, respectively. The droplet mass is given by $m_p = 4/3(d_p/2)^3\pi\rho_{liq}$. Due to the previous assumptions, the only force F_p acting on the particle is a drag force. Other forces resulting from pressure gradients and shear, the virtual (or apparent) mass term and the Basset force are not considered as they are at least one order of magnitude smaller than the drag force (Faeth, 1987).

Stokes (1851) derived an expression for the drag force on spherical particles in a steady flow which is given as:

$$F_p = C_D \frac{\pi d_p^2}{8} \rho \left|\boldsymbol{u}_{@p} - \boldsymbol{u}_p\right| \left(\boldsymbol{u}_{@p} - \boldsymbol{u}_p\right) \tag{2.69}$$

where $\boldsymbol{u}_{@p}$, d_p, ρ, μ_g and C_d correspond to the gaseous velocity at the droplet position, the droplet diameter, the density and viscosity of the gas phase and the drag coefficient, respectively. The Stokes drag coefficient of $C_D = 24/\mathrm{Re}_p$ is valid for small droplet Reynolds numbers computed from the relative (or slip) velocity between the droplets and the carrier gas ($\mathrm{Re}_p < 1$):

$$\mathrm{Re}_p = \frac{\rho \left|\boldsymbol{u}_{@p} - \boldsymbol{u}_p\right| d_p}{\mu_g} \tag{2.70}$$

Here, μ_g refers to the viscosity of the gas phase. For higher droplet Reynolds numbers, corrections to the drag coefficient have been developed in order to account for the fact that inertial forces become gradually more important, increasing the drag force through the formation of a wake, detachment of vortices and generation of a boundary layer (Lefebvre and Mcdonell, 2017). Therefore, other empirical correlations have been proposed for example by Schiller and Naumann (1935):

$$C_d = \frac{24}{\mathrm{Re}_p}(1 + 0.15\mathrm{Re}_p^{0.687}) \tag{2.71}$$

Finally, the simplified Eq. 2.68 is often written in the form:

$$\frac{d\boldsymbol{u}_p}{dt} = \frac{1}{\tau_p}\left(\boldsymbol{u}_{@p} - \boldsymbol{u}_p\right) \tag{2.72}$$

where τ_p can be interpreted as a characteristic droplet relaxation time

$$\tau_p = \frac{\rho_p d_p^2}{18\mu_g C_d} \tag{2.73}$$

which can be used to make inferences about the droplet's general behavior. In fact, relating τ_p to a characteristic time scale of the fluid τ_k yields a time scaling ratio similar to a Stokes number St expressed as (Crowe et al., 1988):

$$\mathrm{St} = \frac{\tau_p}{\tau_k} \tag{2.74}$$

Defining a convective characteristic time scale of the (gaseous) flow $\tau_k = \eta_k / u'_k$ based on the Kolmogorov length scale η_k and the corresponding velocity fluctuations u'_k results in three possible cases: (i) for small values of the Stokes number ($\mathrm{St} \ll 1$), particle motion is essentially governed by the flow of the carrier fluid; (ii) large values ($\mathrm{St} \gg 1$) in turn indicate that flow structures of the gaseous flow have insufficient time to influence the particle trajectory; (iii) finally, for Stokes numbers of the order of unity, droplets may be entrained by vortical structures and preferential droplet concentration can be observed.

It is also worth noting that the correct estimation of $\boldsymbol{u}_{@p}$ constitutes a critical task for the calculation of the drag force: since droplets do not necessarily lie *on* a grid point of the Eulerian mesh where fluid velocities are readily available, $\boldsymbol{u}_{@p}$ must be interpolated at the droplet's location, *e.g.,* through weighted inverse-distance interpolation. Moreover, the undisturbed fluid velocity should be used for $\boldsymbol{u}_{@p}$ (Maxey and Riley, 1983), but is not available in two-way coupled LES (see Sec. 2.6.4), where fluid and droplet phase influence each other. Instead, the *disturbed* fluid velocity is commonly used, which is an acceptable approximation as long as the droplet diameter is much smaller than the mesh size ($d_p \ll \Delta$, Boivin et al. (1998)). This condition is clearly satisfied in this work, as Δ is at least one order of magnitude larger than d_p, but could require a correction in highly resolved DNS (see for example Horwitz and Mani (2016)).

2.6.3 Heat and mass transfer between phases

Droplet evaporation is characterized by simultaneous heat and mass transfer between the dispersed phase and the carrier fluid. When heat for evaporation is transferred to the droplet surface, fuel vapor is fed back into the surrounding gas through convection and diffusion (Lefebvre and Mcdonell, 2017). Evaporation is considered as a critical process in most liquid-fueled combustors controlling not only the combustion efficiency, but also pollutant emissions.

From a modeling point of view, the rate of heat and mass transfer are the key quantities of interest in order to describe the phase exchanges. A fundamental mathematical framework was initially developed by Spalding (1953) and deserves some closer inspection as it serves as a starting point for several more advanced models (see *e.g.,* (Sazhin, 2006; Sirignano, 2010)).

2.6.3.1 Spalding evaporation model

The Spalding evaporation model (Spalding, 1953) considers an isolated, spherical, single-component droplet with infinite thermal conductivity in a quiescent fluid. It is assumed that the evaporation rate is governed by molecular diffusion (Lefebvre and Mcdonell, 2017). As we shall see later, empirical correlations can be found to extend the Spalding model for more realistic spray evaporation cases, which would otherwise be incompatible with its initial set of assumptions.

First, we write the governing equations of the gaseous phase for the original problem of a

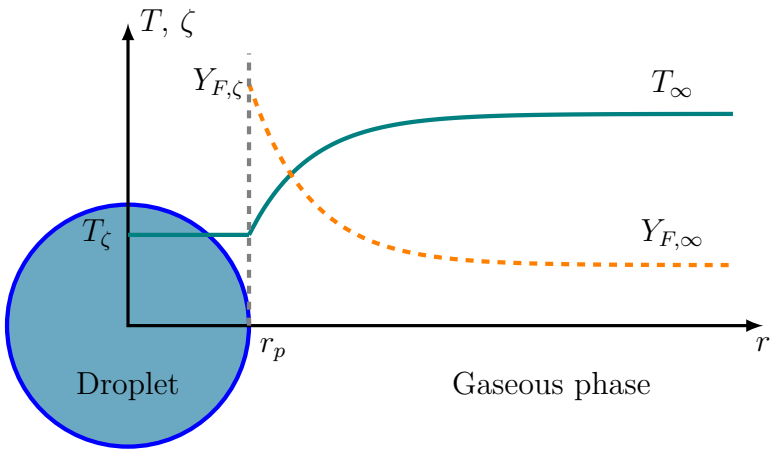

Figure 2.6: Sketch of an isolated evaporating mono-component droplet with infinite thermal conductivity. Temperature and fuel mass fraction profiles are plotted for a quasi-steady gas phase. Boundary conditions are labeled which are used for the integration of the conservation equations (Eqs. 2.75 - 2.77).

single evaporating droplet in the absence of convective effects (Faeth, 1983):

$$\text{Conservation of mass:} \qquad \frac{d}{dr}(r^2 \rho u) = 0 \tag{2.75}$$

$$\text{Conservation of species:} \qquad \frac{d}{dr}\left[r^2\left(\rho u Y_F - \rho D \frac{dY_F}{dr}\right)\right] = 0 \tag{2.76}$$

$$\text{Conservation of energy:} \qquad \frac{d}{dr}\left[r^2\left(\rho u h_s - \lambda \frac{dT}{dr}\right)\right] = 0 \tag{2.77}$$

In Eqs. 2.75 - 2.77, r denotes the radial coordinate, ρ the density of the gas phase, Y_F the fuel species mass fraction, D the fuel diffusivity in the gas phase, h_s the sensible enthalpy, T the gas temperature and λ the thermal diffusivity.

Since we aim at deriving an expression for the net mass transfer rate $\dot{m}$, we start with the integration of Eq. 2.75

$$r^2 \rho u = \frac{\dot{m}}{4\pi} \tag{2.78}$$

Next, u is eliminated in the species conservation equation (Eq. 2.76) through substitution of Eq. 2.78 and a set of boundary conditions is defined at the droplet surface ($r = r_p$) and in the farfield ($r = r_\infty$, see Fig. 2.6):

$$\begin{aligned} r = r_p: &\quad T = T_\zeta, \quad Y_F = Y_{F,\zeta} \\ r = r_\infty: &\quad T = T_\infty, \quad Y_F = Y_{F,\infty} = 0 \end{aligned} \tag{2.79}$$

Integrating Eq. 2.76 from the droplet surface r_p to infinity using the relations 2.79 yields

$$\dot{m} = 2\pi d_p \rho D \, \ln(1 - Y_{F,\zeta}) \tag{2.80}$$

Here, the droplet radius is already substituted by its diameter $d_p = 2r_p$. In order to obtain the final expression for the evaporation rate $\dot{m}$, we define

$$B_\mathrm{M} = \frac{Y_{F,\zeta} - Y_{F,\infty}}{1 - Y_{F,\zeta}} \tag{2.81}$$

and use the relation $\ln(1 - Y_{F,\zeta}) = -\ln(1 + B_{\mathrm{M}})$ which gives

$$\boxed{\dot{m} = 2\pi d_p \rho D \, \ln(1 + B_{\mathrm{M}})} \tag{2.82}$$

Equation 2.81 is famously known as the *Spalding number of mass transfer* and requires the solution of the Clausius-Clapeyron equation to compute the mass fraction of the fuel species at the droplet surface $Y_{F,\zeta}$. It should be noted that $Y_{F,\infty} = 0$ (*cf.* Eq. 2.79) is not a strict requirement and could also be non-zero. If the fuel species diffusion coefficient is not obtained by computing detailed transport properties, it may be derived from a correlation with the gas viscosity μ and the Schmidt number Sc.

$$\rho D = \frac{\mu}{\mathrm{Sc}} \tag{2.83}$$

We wish to emphasize that the computation of transport properties is of paramount importance throughout this work and has motivated the development of improvements of the AVBP solver presented in Sec. 4.2.

In order to examine the heat transfer during droplet evaporation we proceed as follows. In the absence of radiation, only diffusive heat fluxes are initially considered. Integrating the conservation equation of energy (Eq. 2.77)

$$r^2 \left(\rho u C_p T - \lambda \frac{dT}{dr} \right) = 0 \tag{2.84}$$

and performing another integration with respect to r, we have

$$r^2 \rho u C_p T = r^2 \lambda \frac{dT}{dr} + c_1 \tag{2.85}$$

The integration constant c_1 can be determined from the boundary conditions at the droplet surface, where $T(r = r_p) = T_\zeta$, while the temperature gradient follows from the latent heat of vaporization Δh_v

$$\lambda \left. \frac{dT}{dr} \right|_{r_p} = \rho u \Delta h_v \tag{2.86}$$

As noted by Faeth (1983), Eq. 2.86 implies that the droplet has reached its wet-bulb temperature, *i.e.* a steady ($(dT_p)/(dt) = 0$) and uniform droplet temperature, and thus all energy is exclusively used for evaporation.

We can now apply the boundary conditions and write

$$r_p^2 \rho u C_p (T - T_\zeta + \frac{\Delta h_v}{C_p}) = r^2 \lambda \frac{dT}{dr} \tag{2.87}$$

Separating the variables and integrating the above equation under the assumption that the local heat capacity of the gas phase is independent of temperature, we have

$$-\frac{r_p^2 \rho u C_p}{r \lambda} = \ln\left(T - T_\zeta + \frac{\Delta h_v}{C_p} \right) + c_2 \tag{2.88}$$

Here, we employ the boundary condition $T(r \to \infty) = T_\infty$ so that

$$\frac{r_p^2 \rho u C_p}{r \lambda} = \ln\left(\frac{T_\infty - T_\zeta + \Delta h_v / C_p}{T - T_\zeta + \Delta h_v / C_p} \right) \tag{2.89}$$

Now r is set to r_p at the droplet surface and the expression on the RHS is further simplified, giving

$$\frac{r_p \rho u C_p}{\lambda} = \ln\left(1 + \frac{C_p(T_\infty - T_\zeta)}{\Delta h_v}\right) \tag{2.90}$$

Using Eq. 2.78 and rearranging terms, we have

$$\boxed{\dot{m} = \frac{4\pi\lambda r_p}{C_p}\ln(1 + B_\mathrm{T})} \tag{2.91}$$

As for ρD in Eq. 2.82, the gas phase properties λ and C_p are computed according to the following simplified expression

$$\lambda = \frac{C_p \mu}{\mathrm{Pr}} \tag{2.92}$$

$$C_p = \sum_{k=1}^{N} Y_k C_{p,k} \tag{2.93}$$

The heat capacity C_p is obtained from the species heat capacity $C_{p,k}$ weighted by the species mass fraction Y_k. The conductivity λ however also requires a Prandtl number (Pr), which we discuss later in Sec. 4.2 together with the Schmidt number of Eq. 2.83.

Similar to Eq. 2.81, B_T is defined as the *Spalding number of heat transfer*

$$B_\mathrm{T} = \frac{C_p(T_\infty - T_\zeta)}{\Delta h_v} \tag{2.94}$$

If we compare Eqs. 2.82 and 2.91, we can establish a relation between B_M and B_T, and thus between the surface fuel mass fraction $Y_{F,\zeta}$ and the surface temperature T_ζ

$$2\pi d_p \rho D \ln(1 + B_\mathrm{M}) \equiv \frac{4\pi\lambda r_p}{C_p}\ln(1 + B_\mathrm{T}) \tag{2.95}$$

Rearranging terms and defining a Lewis number of the fuel species as $\mathrm{Le}_F = \mathrm{Sc}_F/\mathrm{Pr} = \mu/(\rho D)\cdot\lambda/(\mu C_p)$, we obtain

$$B_\mathrm{T} = (1 + B_\mathrm{M})^{1/\mathrm{Le}_F} - 1 \tag{2.96}$$

Equation 2.96 simplifies to $B_\mathrm{T} = B_\mathrm{M}$ in the limit of unitary Lewis numbers and for $C_p = C_{p,F}$ (heat capacities of the gas mixture and the fuel species). Since the surface fuel mass fraction $Y_{F,\zeta}$ is proportional to its partial pressure $p_{F,\zeta}$ at the surface

$$Y_{F,\zeta} = \frac{p_{F,\zeta}}{p}\frac{M_F}{M} \tag{2.97}$$

with the molar weights of fuel (M_F) and the gas (M), we can employ the Clausius-Clapeyron equation to solve for the surface temperature

$$\ln\left(\frac{p_{F,\zeta}}{p_{F,ref}}\right) = \frac{\Delta h_v}{R}\left(\frac{1}{T_{ref}} - \frac{1}{T_\zeta}\right) \tag{2.98}$$

Variables with subscripted "ref" denote reference values and R the universal gas constant. Equation 2.98 is not evaluated directly in the AVBP solver, but pre-tabulated instead.

When the evaporation rate is known, the droplet evaporation time t_v can be computed. This quantity is of specific interest for combustor design, since the evaporation time of the largest droplets determines (among other parameters) the minimum residence time a droplet is allowed to reside in the combustion chamber (Kuo, 2005). Moreover, full droplet vaporization is generally desired to achieve complete mixing of fuel and air as well as a high combustion efficiency (Lefebvre and Mcdonell, 2017). Incomplete vaporization in turn can lead to increased NO emissions.

Thus, we relate the rate change of the droplet volume ($\dot{V} = 4\pi r^2(dr/dt)$) to the evaporation rate (see Eq. 2.82)

$$\frac{dm}{dt} = 4\pi\rho_{liq}\frac{r^2 dr}{dt} \doteq -\dot{m} = -2\pi d_p \rho D \ln(1 + B_{\mathrm{M}}) \tag{2.99}$$

The above equation can be rearranged to yield

$$\frac{r dr}{dt} = -\frac{\rho D}{\rho_{liq}} \ln(1 + B_{\mathrm{T}}) \tag{2.100}$$

Finally, we can integrate this expression, substitute the droplet radius by its diameter and define an initial droplet diameter $d_0 = d(t = t_0)$ at the time t_0, which results in the so called D^2 ("D-squared") law of evaporation

$$\boxed{d^2 = d_0^2 - \frac{8\rho D}{\rho_{liq}} \ln(1 + B_{\mathrm{T}}) \cdot t} \tag{2.101}$$

It states that the square droplet diameter diminishes linearly in time after attaining steady-state conditions (Lefebvre and Mcdonell, 2017). An evaporation constant may be defined, which can be determined experimentally for a specific fuel and given conditions:

$$\lambda_{d^2} = \frac{8\rho D}{\rho_l} \ln(1 + B_{\mathrm{T}}) \tag{2.102}$$

Since Spalding considered evaporation of motionless particles, Eqs. 2.82 and 2.91 are poor approximations of spray evaporation with moving droplets. Therefore, a correction factor is commonly employed, which is formally written as a Sherwood number $\mathrm{Sh}^\star$ for mass transfer and a Nusselt number $\mathrm{Nu}^\star$ for heat transfer. Correlations with the droplet Reynolds number ensure correct retrieval of $\mathrm{Sh}^\star = \mathrm{Nu}^\star = 2$ in the limit of droplets at rest.

2.6.3.2 Analysis of convective effects

So far, heat and mass transfer rates have been developed for a motionless droplet neglecting any convective effect on heat and mass transfer. This assumption can not be justified for *moving* droplets such as in fuel sprays in practical combustors, where the relative motion between the droplet and the gas phase enhances the evaporation rate ($\mathrm{Re}_p > 0$, see Eq. 2.70), thus shortening the droplet's lifetime (Lefebvre and Mcdonell, 2017). The departure from the classic Spalding model therefore often involves one of the following methods to include convective effects (Faeth, 1983):

1. the equations for a motionless droplet (see previous section) are solved and empirical correction factors are employed to account for convection. For example, Sherwood and Nusselt numbers are introduced respectively in Eqs. 2.82 and 2.91 as

$$\dot{m} = \pi d_p \mathrm{Sh}_0 \rho D \ln(1 + B_{\mathrm{M}}) \tag{2.103}$$

$$\dot{m} = \pi d_p \mathrm{Nu}_0 (\lambda / C_p) \ln(1 + B_{\mathrm{T}}) \tag{2.104}$$

Frössling (1938) and Ranz and Marshall (1952) proposed correlations for Sh_0 and Nu_0 as functions of the droplet Reynolds number and the Schmidt (respectively Prandtl) number

$$\mathrm{Sh}_0 = 2 + 0.55\mathrm{Re}_p^{1/2}\mathrm{Sc}_F^{1/3} \tag{2.105}$$

$$\mathrm{Nu}_0 = 2 + 0.55\mathrm{Re}_p^{1/2}\mathrm{Pr}_F^{1/3} \tag{2.106}$$

In the limit of droplets at rest, *i.e.* $\mathrm{Re}_p \to 0$, a value of 2 is retained for both expressions, which corresponds to the value initially proposed by Spalding (see Eqs. 2.82 and 2.91).

However, Sirignano (2010) discusses some pitfalls associated with these formulations and does not recommend their usage to describe droplet evaporation in combustors, at least not in their initial form without further modifications.

2. A different approach widely used in the literature exploits the so-called "film theory" (Bird et al., 2002). As stated by Abramzon and Sirignano (1989, p. 1607) "[...] the resistance to heat or mass exchange between a surface and a gas flow may be modeled by introducing the concept of gas films of constant thicknesses: δ_T and δ_M" (*i.e.* for heat and mass transfer). Similar to the first concept, these values are expressed through empirical correlations involving convection parameters (Faeth, 1983), which consist of *modified* Sherwood and Nusselt numbers.

   A well-known example for this approach is the model developed by Abramzon and Sirignano (1989), which is referred to as "Abramzon-Sirignano evaporation model" in their honor. Since it is one of the core models in the present work, we present more details in the following section.

We wish to clarify that neither of the Sherwood and Nusselt numbers mentioned above should be confused with the *actual* Sherwood and Nusselt numbers, which instead are defined as (see *e.g.*, (Sazhin, 2017))

$$\mathrm{Nu} = \frac{h d_p}{\lambda(T_\infty - T_\zeta)} \tag{2.107}$$

$$\mathrm{Sh} = \frac{h_m d_p}{D} \tag{2.108}$$

The heat transfer coefficient for a droplet per unit surface area, h, is written for wet-bulb conditions as

$$h = \frac{\dot{m}\Delta h_v}{\pi d_p^2} \tag{2.109}$$

Substituting for h in Eqs. 2.107 and 2.108 then yields

$$\mathrm{Nu} = \mathrm{Nu}^\star \frac{\ln(1+B_\mathrm{T})}{B_\mathrm{T}} \tag{2.110}$$

$$\mathrm{Sh} = \mathrm{Sh}^\star \frac{\ln(1+B_\mathrm{M})}{B_\mathrm{M}} \tag{2.111}$$

These more general expressions are often found in the literature (Faeth, 1979, 1983; Kuo, 2005; Lefebvre and Mcdonell, 2017), with $\mathrm{Nu}^\star$ and $\mathrm{Sh}^\star$ termed as *modified* Nusselt and Sherwood numbers. In the limit of vanishing heat or mass transfer, *i.e.* for $B_\mathrm{T} \to 0$ and $B_\mathrm{M} \to 0$, the classic value of 2 is found, and thus $\mathrm{Nu}^\star \to \mathrm{Nu}_0$ and $\mathrm{Sh}^\star \to \mathrm{Sh}_0$.

2.6.3.3 Abramzon-Sirignano evaporation model

The Abramzon-Sirignano model extends the classic Spalding model to account for convective transport due to relative motion between the droplet and the surrounding gas. As foreshadowed in the previous section, moving droplets are assumed to develop a film layer of finite thickness, which can be computed from the following relations

$$\delta_{\mathrm{T0}} = \frac{2r_d}{\mathrm{Nu}_0 - 2} \tag{2.112}$$

$$\delta_{\mathrm{M0}} = \frac{2r_d}{\mathrm{Sh}_0 - 2} \tag{2.113}$$

Moreover, the effect of the Stefan flow is included through additional correction factors F_{T} and F_{M} expressed as

$$F_{\mathrm{T}} = \frac{\delta_{\mathrm{T}}}{\delta_{\mathrm{T0}}} = (1 + B_{\mathrm{T}})^{0.7} \frac{\ln(1 + B_{\mathrm{T}})}{B_{\mathrm{T}}} \tag{2.114}$$

$$F_{\mathrm{M}} = \frac{\delta_{\mathrm{M}}}{\delta_{\mathrm{M0}}} = (1 + B_{\mathrm{M}})^{0.7} \frac{\ln(1 + B_{\mathrm{M}})}{B_{\mathrm{M}}} \tag{2.115}$$

The modified Sherwood and Nusselt numbers then write

$$\mathrm{Nu}^\star = 2 + \frac{\mathrm{Nu}_0 - 2}{F_{\mathrm{T}}} \tag{2.116}$$

$$\mathrm{Sh}^\star = 2 + \frac{\mathrm{Sh}_0 - 2}{F_{\mathrm{M}}} \tag{2.117}$$

Again, for vanishing film thicknesses, the correction factors F_{T} and F_{M} approach unity ensuring correct retrieval of $\mathrm{Nu}^\star \to \mathrm{Nu}_0$ and $\mathrm{Sh}^\star \to \mathrm{Sh}_0$. Finally, the modified Sherwood and Nusselt numbers ($\mathrm{Sh}^\star$ and $\mathrm{Nu}^\star$) are substituted for the expressions Sh_0 and Nu_0 respectively in Eqs. 2.103 and 2.104 to solve for the evaporation rate. The exponent in Eq. 2.96 is replaced by a more general formulation where the heat capacities of the fuel species and the gas are not equivalent

$$B_{\mathrm{T}} = (1 + B_{\mathrm{M}})^{\beta} - 1, \quad \text{with } \beta = \left(\frac{C_{p,F}}{C_p}\right)\left(\frac{\mathrm{Sh}^\star}{\mathrm{Nu}^\star}\right)\frac{1}{\mathrm{Le}_F} \tag{2.118}$$

2.6.3.4 Droplet film properties

Beyond the discussion of dimensionless quantities, care must also be taken with regard to the evaluation of transport properties in the gas, specifically λ, C_p, D and μ. Throughout the mathematical description in the previous sections, we assumed these properties to be constant along the radial coordinate r (see Fig. 2.6), since the original Spalding model does not consider the notion of a droplet film resulting from droplet motion. Despite this, such simplification cannot be justified from a physical standpoint, and it is therefore more appropriate to account for variable transport properties due to finite film thicknesses. Hubbard et al. (1975) showed that best results can be obtained, if we define a reference state T_{ref} and $Y_{F,ref}$, from which we compute the transport properties

$$T_{ref} = T_\zeta + \frac{1}{3}(T_\infty - T_\zeta) \tag{2.119}$$

$$Y_{F,ref} = Y_{F,\zeta} + \frac{1}{3}(Y_{F,\infty} - Y_{F,\zeta}) \tag{2.120}$$

The above equations are known as "third-rule" (or rule of thirds) in the literature and serve as reference values for the computation of λ, C_p, D and μ

$$\lambda_{ref} = \frac{\mu_{ref} C_{p,ref}}{\mathrm{Pr}} \tag{2.121}$$

$$C_{p,ref} = \sum_k Y_{k,ref} C_{p,k} \tag{2.122}$$

$$\rho D_{ref} = \frac{\mu_{ref}}{\mathrm{Sc}_F} \tag{2.123}$$

$$\mu_{ref} = \sum_{i=1}^{N} \frac{X_{i,ref}\mu_{i,ref}}{\sum_{j=1}^{N} X_{i,ref}\phi_{i,j}} \tag{2.124}$$

$$\text{where } \phi_{i,j} = \frac{1}{\sqrt{8}}\left(1+\frac{W_i}{W_j}\right)^{-1/2}\left[1+\left(\frac{\mu_{i,ref}}{\mu_{j,ref}}\right)^{1/2}\left(\frac{W_j}{W_i}\right)^{1/4}\right]^2 \tag{2.125}$$

The reference viscosity for a multi-component gas is expressed through a semi-empirical formula proposed by Wilke (1950). The species mole fraction in a mixture of N species is denoted as X_i, μ_i is the corresponding viscosity of the pure species i and W_i its molar weight. For consistency, μ_i is also evaluated at the reference state (*i.e.* at T_{ref}), thus yielding $\mu_{i,ref}$.

2.6.3.5 Default implementation of the Abramzon-Sirignano model in AVBP

Sacomano Filho et al. (2019) have recently outlined the importance of an accurate description of the carrier gas properties for evaporating droplets. In particular, the authors mention that simplifications of the mixture composition can lead to wrong evaporation rates, and, at worst, wrong flame propagation speeds in spray-flame simulations. Yet, simplifying assumptions are often made to strike a reasonable balance between accuracy and computational costs of more demanding complex evaluations of transport properties (see *e.g.*, Hirschfelder et al. (1964)). For example, the set of Eqs. 2.121 - 2.124 represents a simplified (*i.e.* species averaged) approach to emulate complex transport properties at acceptable costs in the AVBP solver. Moreover, the Prandtl and (fuel species) Schmidt numbers required for the modeling of droplet films are replaced by corrected values termed Pr_{evap} and Sc_{evap}, which result from complex film simulations as described in Hannebique et al. (2013) (initially developed by Sanjosé (2009) and extended by Sierra Sanchez (2012)). For the remainder of this work, we refer to this approach as "default implementation" in AVBP. We propose an enhancement for the treatment of Pr_{evap} and Sc_{evap} in Sec. 4.2.

2.6.3.6 Influence of droplet heat-up

Recalling the assumption that led to Eq. 2.86 (and later to Eq. 2.109), we assumed that the wet-bulb condition is satisfied and the droplet's temperature has reached a steady state. Such is the case for the classic D^2 law, however we emphasize that this condition is not necessarily met in general. Since droplet heat-up is accounted for by the Abramzon-Sirignano evaporation model, we briefly present the derivation of the relevant heat transfer equations.

Our entry point is the conservation equation of the droplet's sensible enthalpy $h_{s,p}(T_p) = C_{p,liq}dT_p$ (Faeth, 1983)

$$\frac{d}{dt}(m_p h_{s,p}(T_p)) = h\pi d_p^2(T_\infty - T_\zeta) - \dot{m}\Delta h_v \tag{2.126}$$

It states that the enthalpy flux required to raise the droplet's *internal* temperature is equivalent to the difference between the total enthalpy flux that reaches the droplet surface (first term on the RHS) and the enthalpy flux required for evaporation (second term on RHS). h denotes the total heat transfer coefficient which is substituted by Eq. 2.107. A final substitution for the Nusselt number using Eq. 2.110 yields

$$\boxed{m_p C_{p,liq} \frac{dT_p}{dt} = \pi d_p \lambda \mathrm{Nu}^\star (T_\infty - T_\zeta) \frac{\ln(1+B_\mathrm{T})}{B_\mathrm{T}} - \dot{m} h_{s,p}} \tag{2.127}$$

The first term on the RHS is equivalent to the conductive gaseous heat flux (from the farfield to the droplet surface), which follows from an enthalpy balance at the droplet surface assuming an equilibrium between the liquid and the gaseous phase

$$\dot{Q}_g^c \equiv \pi d_p \lambda \mathrm{Nu}^\star (T_\infty - T_\zeta) \frac{\ln(1+B_\mathrm{T})}{B_\mathrm{T}} \tag{2.128}$$

2.6.4 Phase coupling

Exchanges of mass, momentum and energy between droplets and the gas phase necessarily involve additional source terms (Faeth, 1983, 1987) in the Navier-Stokes equations. For example, the evaporating fuel species mass must be accommodated in the transport equation of the gaseous phase, while the energy to evaporate liquid fuel is usually provided by the gas phase. In case of mutual exchanges between both phase, the coupling relation is often referred to as "two-way" coupling (or "retro-coupling"). The modified equations thus read (in Einstein notation):

$$\frac{\partial \bar{\rho}}{\partial t} + \frac{\partial \bar{\rho} \tilde{u}_i}{\partial x_i} = \dot{\rho}_s \tag{2.129}$$

$$\frac{\partial \bar{\rho} \tilde{u}_i}{\partial t} + \frac{\partial}{dx_j} \left[\bar{\rho} \tilde{u}_i \tilde{u}_j + \bar{p} \delta_{ij} - \bar{\tau}_{ij} + \tau_{ij}^{sgs} \right] = \dot{F}_{s,i} \tag{2.130}$$

$$\frac{\partial \bar{\rho} \tilde{E}}{\partial t} + \frac{\partial}{\partial x_i} \left[(\bar{\rho} \tilde{E} + \bar{p}) \tilde{u}_i + \bar{q}_i - \tilde{u}_j \bar{\tau}_{ji} + H_i^{sgs} + \sigma_i^{sgs} \right] = \dot{Q}_s \tag{2.131}$$

$$\frac{\partial \bar{\rho} \tilde{Y}_k}{\partial t} + \frac{\partial}{\partial x_i} \left[\bar{\rho} \tilde{Y}_k \tilde{u}_i - \bar{\rho} \tilde{Y}_k \tilde{V}_{i,k} + Y_{i,k}^{sgs} + \theta_{i,k}^{sgs} \right] = \bar{\dot{\omega}}_k + \dot{S}_{s,k} \tag{2.132}$$

The source terms on the RHS can then be written as

$$\begin{pmatrix} \dot{\rho}_s \\ \dot{F}_{s,i} \\ \dot{Q}_s \\ \dot{S}_{s,k} \end{pmatrix} = \begin{pmatrix} \frac{1}{\Delta V} \sum_m \psi_p \dot{m} \\ \frac{1}{\Delta V} \sum_m \psi_p (\dot{m} u_{i,p} - \frac{4\pi}{3} \rho_{liq} r_p^2 \frac{du_{i,p}}{dt}) \\ \frac{1}{\Delta V} \sum_m \psi_p (\dot{m} \Delta h_v - 4\pi r_p^2 h (T_\infty - T_\zeta)) \\ \frac{1}{\Delta V} \sum_m \psi_p \dot{m} \end{pmatrix} \tag{2.133}$$

Since multiple droplets can be present in a numerical cell at a given time, a summation (index m) over their corresponding source terms must be performed, which is then weighted by the cell volume ΔV. Furthermore, all source terms must be interpolated at the locations of the grid nodes, where information about the (continuous) gas phase is available. The interpolation function ψ used in this work is a simple inverse distance interpolation (shown in Fig. 2.7 for one droplet in an arbitrary cell), where the weight of the ith droplet with respect to node j of N_c total nodes per cell is computed from

$$\psi_{i,j} = \frac{1/d_j}{\sum_{k=1}^{N_c} 1/d_k} \tag{2.134}$$

$1/d_j$ corresponds to the inverse distance between droplet and a grid node.

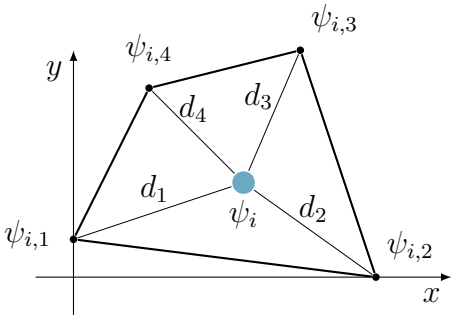

Figure 2.7: Illustration of droplet source term projection onto grid nodes of a quadrilateral cell in an Eulerian grid. Interpolation weights $\psi_{i,1}$ to $\psi_{i,4}$ for the ith droplet are proportional to the inverse distances d_1 to d_4 between a node and a droplet.

2.6.5 Interaction with the Artificially Thickened Flame approach

Apart from its impact on the combustion regime, the liquid phase itself may be affected by the artificially thickened flame model (see Sec. 2.5.3 and 2.5.4) as a consequence of the thickened flame front. Droplets crossing a thickened flame evaporate over a greater portion of their trajectory compared to crossing an unthickened ("real") flame. This undesired behavior is corrected in the simulations by dividing the heat and mass transfer source terms as well as the momentum source term (RHS in Eqs. 2.130, 2.131 and 2.132, see Paulhiac (2015) for reference) by the same factor $\mathcal{F}$, by which the flame is thickened.

Dressler et al. (2021) argue that such correction is appropriate as long as droplet trajectories are mostly orthogonal with respect to the flame front, but would require further modification if droplets propagation is instead parallel to the flame front. For light-round simulations in the present work, the former condition (orthogonal crossing) is assumed to be reasonable.

2.6.6 Liquid fuel injection

Fuel injection systems in gas turbines and aero-engines commonly employ atomizers to generate a spray with desired characteristics in terms of its shape, droplet size distribution and spray angle (Faeth, 1979). The underlying atomization process however is extremely complex, involving the break-up of liquid sheets due to aerodynamic instabilities, primary and secondary atomization, droplet collisions, coalescence and droplet/wall interaction. Following the general discussion of Sec. 2.6.1, we thus use pre-atomized sprays for the simulations in this work, rather than attempting to include models for fuel atomization at prohibitive computational cost. Essentially, spray parameters are imposed such that they best match experimentally measured spray characteristics in the injector far-field, where the dilute spray assumption is justified. For hollow-cone sprays of the present work, we use a modified version of the phenomenological FIM-UR model (Sanjosé et al., 2011; Vignat et al., 2021) (*Fuel Injection Model by Upstream Reconstruction*) to reproduce the desired spray characteristics.

2.6.6.1 Phenomenological approach for the injection of pre-atomized droplets: FIM-UR

The original FIM-UR model (Sanjosé et al., 2011) has been developed for pressure-swirl atomizers, where liquid fuel enters a swirl-chamber tangentially before reaching the discharge orifice (see Fig. 2.8). Due to high rotational velocities, an air core is formed in the discharge channel so that the liquid outflow occurs through a boundary layer around it (Lefebvre and

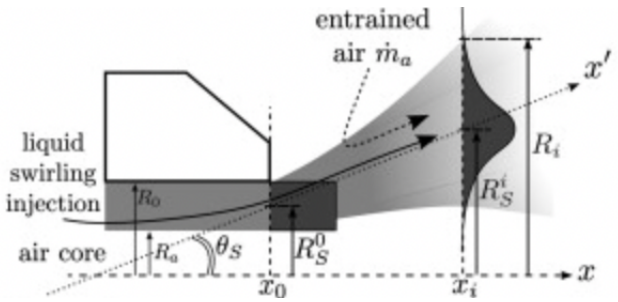

Figure 2.8: Illustration of the FIM-UR model and corresponding parameters as initially developed by Sanjosé et al. (2011). Image adapted from Sanjosé et al. (2011).

Mcdonell, 2017). The effective outflow cross section of the liquid is therefore a disk defined by the nominal radius of discharge orifice R_0 and the radius of the air core R_a. The ratio between these radii can be derived from the half-angle of the resulting spray cone θ

$$X = \frac{R_a^2}{R_0^2} = \frac{\sin^2(\theta)}{1 + \cos^2(\theta)} \tag{2.135}$$

The velocity at the moment of injection is then given in a cylindrical coordinate system as

$$u_{p,x}^0(\theta, r_0) = \frac{\dot{m}_{liq}}{\rho_{liq}\pi R_0^2(1 - X)} \tag{2.136}$$

$$u_{p,r}^0(\theta, r_0) = 0 \tag{2.137}$$

$$u_{p,\theta}^0(\theta, r_0) = \tan(\theta) u_{p,x}^0(\theta, r_0) \tag{2.138}$$

Droplets are randomly seeded on the injection disk (defined by $r \in [R_a, R_0]$) and assigned a normal ($u_{p,x}^0$), a radial ($u_{p,r}^0$) and a tangential ($u_{p,\theta}^0$) velocity component. The droplet diameter at injection is sampled from an experimentally measured droplet distribution (see Sec. 4.3) or alternatively from a parameterized distribution. After injection, the droplet's trajectory and diameter can evolve freely and entirely depend on the flow conditions.

2.6.6.2 Modified FIM-UR model

A modified version of the original FIM-UR model has been developed by Vignat et al. (2021) to facilitate the model calibration with respect to available experimental data. In particular, it provides more control over the injection half-angle by defining a fixed (mean) injection half-angle $\bar{\theta}$ and a randomized spread $\delta\theta$ (or deviation angle) such that the effective injection half-angle is sampled within $\theta = \bar{\theta} \pm \delta\theta$. Moreover, a Box-Muller transform (Box and Muller, 1958) is performed to obtain pairs of normally distributed deviation angles and seed locations on the injection surface for each droplet. The normal component of the initial injection velocity is imposed (which is also possible with the original FIM-UR model), from which the injection surface follows through Eqs. 2.135 to 2.136. Equations 2.137 and 2.138 remain unchanged. A value of $X \equiv 0.5$ was empirically found from measurements, which is deemed more appropriate for atomizers with small orifice diameters (as used in this work) compared to much larger atomizers discussed *e.g.* in Lefebvre and Mcdonell (2017).

An extensive calibration procedure of the modified FIM-UR model based on detailed experimental data kindly provided by Dr. G. Vignat is presented in Sec. 4.3.

2.6.7 Wall film model

The interaction between fuel droplets and walls is modeled in a simplified manner in this work. Essentially, droplets may either rebound from walls or form a wall film, depending on the imposed wall boundary condition. For wall films, we employ a model developed by Chaussonnet et al. (2013) which is based on the thin film hypothesis: it states that the film thickness is small by comparison to relevant length scales of the gaseous phase. Consequently, the film does not affect the near-wall gas phase velocity profile. Rather, it is assumed to instantaneously adapt to the shear stress imposed by the gas phase, which is set equal to the (gaseous) wall shear stress. In addition, all streamwise gradients are assumed to be negligible except for the streamwise pressure gradient. Under these conditions, an averaged film velocity can be computed as

$$\bar{u}_f = \frac{h_f}{2\mu_l}\tau_w - \frac{h_f^2}{3\mu_l}\frac{dp}{dx} \tag{2.139}$$

where h_f is the film height, μ_l the liquid viscosity, τ_w the tangential component of the wall shear stress, and dp/dx the streamwise pressure gradient. Since the latter affects the squared film height, it is also assumed to be negligible. This average film velocity is then assigned to particles flagged as "film particles" at a given time step.

2.7 Wall-bounded flows

So far, we have presented concepts to study complex flow problems by means of LES, where the size of the governing flow phenomena corresponded to the size of large-scale structures, which are directly resolved. Free shear flows are suitable candidates for LES for example, since the shear layer thickness is of the order of the resolved structures. In wall-bounded flows, however, the near-wall flow structures become very small relative to the boundary layer thickness (Menter et al., 2021) and would require exceedingly high computational costs, if resolved directly. This problem of conflicting interests (flow resolution versus costs) is known as near-wall problem and must be addressed in scale-resolving simulations such as LES: the transport of momentum and energy in the boundary layer would be severely impacted, if the near-wall flow was not sufficiently resolved. In turn, an appropriate boundary layer resolution is mostly not practical for more complex applications such as industrial or even lab-scale combustors, since the boundary layer decreases with increasing Reynolds number (Schlichting and Gersten, 2017). Thus, from the plethora of solutions to overcome this problem, as reviewed *e.g.* by Spalart (2009), we chose to use the Wall-Modeled LES (WMLES) and present its core concepts in the following.

Essentially, the strategy of WMLES is to replace the no-slip wall boundary condition by phenomenological relations for the wall shear stress (and wall heat flux for non-adiabatic walls) to restore the flux of momentum (and energy) at the wall, which the coarse grid cannot resolve (Piomelli and Balaras, 2002). Since the wall-normal grid-spacing is much larger than the viscous sublayer, a no-slip boundary condition cannot be imposed to compute the wall shear stress from the reconstructed wall-normal velocity gradient as done in wall-*resolved* simulations (Deardorff, 1970). Instead, we take advantage of the coarseness of the grid in the near-wall region to treat turbulent structures in a statistical sense, *i.e.* with a RANS approach (see Sec. 2.3): we consider a *collection* of eddies in a given grid cell and assume that only their average behavior must be represented by a model, which can be achieved by the Reynolds-averaged Navier-Stokes equations (Piomelli and Balaras, 2002). In any case, the solution of these models yields the desired the wall shear stress and wall heat flux based on off-wall flow

conditions and are subsequently fed back to the simulation of the outer (or far-field) flow.

Possible implementations into numerical codes range from full three-dimensional, compressible Navier-Stokes equations to "simple" algebraic functions. While the former can take multiple physical phenomena into account such as the three-dimensionality of the flow, compressibility effects, or inhomogeneous pressure gradients, it is also the most demanding and complex approach in terms of its implementation and the computational costs. Therefore, much simpler algebraic functions are still widely used in the literature, in particular if the near-wall flow is expected to have only a negligible effect on the problem under consideration. Unfortunately, such strong assumption would be in violation of recent insights by Puggelli et al. (2020), highlighting the importance of the boundary layer flow for light-round ignition. Thus, with our custom wall-model in mind (see Sec. 5.3), it is useful to first recall the general (one-dimensional) boundary layer equations, followed by a brief discussion of algebraic wall functions and their limitations in the context of the present work.

2.7.1 Boundary layer equations

As stated in the previous section, we can model the near-wall flow in a statistical sense using the Reynolds-averaged conservation equations of mass, momentum and energy, which we recall here as

$$\frac{\partial \bar{\rho}}{\partial t} + \frac{\partial \bar{\rho}\tilde{u}_i}{\partial x_i} = 0 \tag{2.140}$$

$$\frac{\partial \bar{\rho}\tilde{u}_i}{\partial t} + \frac{\partial \bar{\rho}\tilde{u}_i\tilde{u}_j}{\partial x_j} = -\frac{\partial \bar{p}}{\partial x_i} + \frac{\partial \bar{\tau}_{ij}}{\partial x_j} - \frac{\partial \widetilde{\bar{\rho}u_i''u_j''}}{\partial x_j} \tag{2.141}$$

$$\frac{\partial \bar{\rho}\tilde{h}}{\partial t} + \frac{\partial \bar{\rho}\tilde{u}_j\tilde{h}}{\partial x_j} = \frac{D\bar{p}}{Dt} - \frac{\partial \bar{q}_j}{\partial x_j} + \overline{\tau_{ij}\frac{\partial u_i}{\partial u_j}} - \frac{\partial \widetilde{\bar{\rho}u_j''h''}}{\partial x_j} \tag{2.142}$$

As we shall see, we can obtain the so-called boundary layer equations through simplification of the above set of equations to provide expressions for the quantities of interest: the wall shear stress $\bar{\tau}_w$ and the wall heat flux $\bar{q}_w$.

We consider a developed, steady-state ($\partial/\partial t = 0$), one dimensional ($\partial/\partial x = 0$, $\partial/\partial z = 0$) and incompressible boundary layer flow over a flat plate. For these conditions, we obtain

$$\frac{\partial \widetilde{\bar{\rho}u''v''}}{\partial y} = -\frac{\partial \bar{p}}{\partial x} + \frac{\partial \bar{\tau}_{xy}}{\partial y} \tag{2.143}$$

$$\frac{\partial}{\partial y}\left(\bar{\lambda}\frac{\partial \bar{T}}{\partial y} - \bar{\rho}\widetilde{v''h''}\right) = 0 \tag{2.144}$$

We write the stress tensor $\bar{\tau}_{xy}$ for a Newtonian fluid as

$$\bar{\tau}_{xy} = \bar{\mu}\frac{\partial \bar{u}}{\partial y} \tag{2.145}$$

and assumed Fourier's law for heat conduction

$$\bar{q} = -\lambda\frac{\partial \bar{T}}{\partial y} \tag{2.146}$$

We can now define the total stresses and the total heat flux as the sum of their respective

laminar and turbulent contributions

$$\bar{\tau}_{tot} = \bar{\mu}\frac{\partial \bar{u}}{\partial y} - \bar{\rho}\widetilde{u''v''} = \overline{\tau}_w \tag{2.147}$$

$$\bar{q}_{tot} = \bar{\lambda}\frac{\partial \bar{T}}{\partial y} - \bar{\rho}\widetilde{v''h''} = \overline{q}_w \tag{2.148}$$

The unclosed term in the momentum equation can be expressed through a classic eddy viscosity model (Boussinesq, 1872) and, by analogy, a similar term can be found for the unclosed turbulent heat flux

$$\frac{\partial}{\partial y}\left[\left(\bar{\mu} + \mu_t\right)\frac{\partial \bar{u}}{\partial y}\right] = 0 \tag{2.149}$$

$$\frac{\partial}{\partial y}\left[\left(\bar{\lambda} + \lambda_t\right)\frac{\partial \bar{T}}{\partial y}\right] = 0 \tag{2.150}$$

Equations 2.149 and 2.150 represent a general form of the boundary layer equations for a steady, one-dimensional and turbulent boundary layer flow, also referred to as Thin Boundary Layer Equations (TBLE). The streamwise pressure gradient $\partial\bar{p}/(\partial x)$ is neglected. They provide continuous velocity and temperature profiles, from which the wall shear stress and wall heat flux can be computed. μ_t denotes the turbulent viscosity and may be expressed through the Prandtl mixing-length approach

$$\mu_t = \bar{\rho} l_m^2 \left(\frac{\partial \bar{u}}{\partial y}\right) = \bar{\rho}(\kappa y)^2 \frac{\partial \bar{u}}{\partial y} \tag{2.151}$$

where the mixing length $l_m = \kappa y$ is a function of the wall distance and the von Kármán constant κ (Pope, 2000). A similar expression is found for the turbulent heat conductivity, which is a function of the turbulent Prandtl number

$$\lambda_t = \mu_t \frac{\overline{C}_p}{\mathrm{Pr}_t} = \overline{\rho}\overline{C}_p \frac{(\kappa y)^2}{\mathrm{Pr}_t}\frac{\partial \overline{u}}{\partial y} \tag{2.152}$$

With Eqs. 2.151 and 2.152 we can finally write after integration

$$\overline{\tau}_w = \overline{\mu}\frac{\partial \overline{u}}{\partial y} + \overline{\rho}(\kappa y)^2 \left(\frac{\partial \overline{u}}{\partial y}\right)^2 \tag{2.153}$$

$$\overline{q}_w = -\overline{\lambda}\frac{\partial \overline{T}}{\partial y} - \overline{\rho}\overline{C}_p \frac{(\kappa y)^2}{\mathrm{Pr}_t}\frac{\partial \overline{u}}{\partial y}\frac{\partial \overline{T}}{\partial y} \tag{2.154}$$

2.7.2 Algebraic wall models

Although Eqs. 2.149 and 2.150 can be implemented into LES codes to provide values for $\overline{\tau}_w$ and $\overline{q}_w$, simpler, yet less general algebraic relations can be derived for these quantities. Taking advantage of the internal structure of turbulent boundary layers, which consist of a thin viscous sub-layer and a much larger log-layer, we can approximate velocity and temperature profiles for each sub-layer. Boundary layer analysis is then performed in non-dimensional (or stretched) coordinates defined as

$$y^+ = \frac{\rho_w u_\tau y}{\mu_w} \tag{2.155}$$

$$u^+ = \frac{\bar{u}}{u_\tau} \tag{2.156}$$

Quantities with a subscripted "w" represent fluid properties evaluated *at* the wall. The friction velocity u_τ is derived from dimensional analysis and can be interpreted as a characteristic velocity for turbulent flows at a given wall shear stress (Schlichting and Gersten, 2017)

$$u_\tau = \sqrt{\frac{\overline{\tau}_w}{\rho}} \tag{2.157}$$

For non-adiabatic flows, we must also include the non-dimensional temperature profile, which is given as

$$T^+ = \frac{|\overline{T} - T_w|}{T_\tau} \tag{2.158}$$

In the above equation, T_w denotes the wall temperature, whereas T_τ is a friction temperature written as

$$T_\tau = \frac{|\overline{q}_w|}{\overline{C}_{p,w}\overline{\rho}_w u_\tau} \tag{2.159}$$

Thus, the non-dimensional forms of the wall shear stress (Eq. 2.153) and wall heat flux (Eq. 2.154) are obtained through normalization by wall properties

$$\frac{\bar{\mu}}{\bar{\mu}_w}\frac{\partial \bar{u}^+}{\partial y^+} + \frac{\bar{\rho}}{\bar{\rho}_w}(\kappa y^+)^2\left(\frac{\partial \bar{u}^+}{\partial y^+}\right)^2 = 1 \tag{2.160}$$

$$\frac{\overline{\lambda}}{\overline{C}_{p,w}\overline{\rho}_w\overline{\nu}_w}\frac{\partial \overline{T}^+}{\partial y^+} + \frac{\overline{\rho}\overline{C}_p}{\overline{\rho}_w\overline{C}_{p,w}}\frac{(\kappa y^+)^2}{\mathrm{Pr}_t}\frac{\partial \overline{u}^+}{\partial y^+}\frac{\partial \overline{T}^+}{\partial y^+} = 1 \tag{2.161}$$

In the viscous sub-layer, momentum transport is governed by molecular transport. Turbulent velocity fluctuations vanish *at* the wall, resulting in

$$\frac{\bar{\mu}}{\bar{\mu}_w}\frac{\partial \bar{u}^+}{\partial y^+} = 1 \tag{2.162}$$

By analogy, we obtain the following expression for the wall heat flux

$$\frac{\overline{\lambda}}{\overline{C}_{p,w}\overline{\rho}_w\overline{\nu}_w}\frac{\partial \overline{T}^+}{\partial y^+} = 1 \tag{2.163}$$

Implicitly assuming constant fluid properties, in particular no variation of the viscosity and heat conductivity, we can finally write the non-dimensional velocity profile, and similarly the non-dimensional temperature profile as

$$\boxed{u^+ = y^+} \tag{2.164}$$

$$\boxed{T^+ = \mathrm{Pr}\cdot y^+} \tag{2.165}$$

where $\mathrm{Pr} = \overline{C}_{p,w}\overline{\mu}_w/\overline{\lambda}$. By definition, these equations are valid in the viscous sub-layer only, *i.e.* for $y^+ \leq 5$ (Schlichting and Gersten, 2017). Conversely, turbulent transport of momentum and energy is dominant in the log-layer and we can find the corresponding non-dimensional profiles of velocity and temperature through integration of Eqs. 2.149 and 2.150 with the relations in Eqs. 2.155 and 2.156:

$$\boxed{u^+ = \frac{1}{\kappa}\ln y^+ + C} \tag{2.166}$$

$$\boxed{T^+ = \frac{\mathrm{Pr}_t}{\kappa}\ln y^+ + C'} \tag{2.167}$$

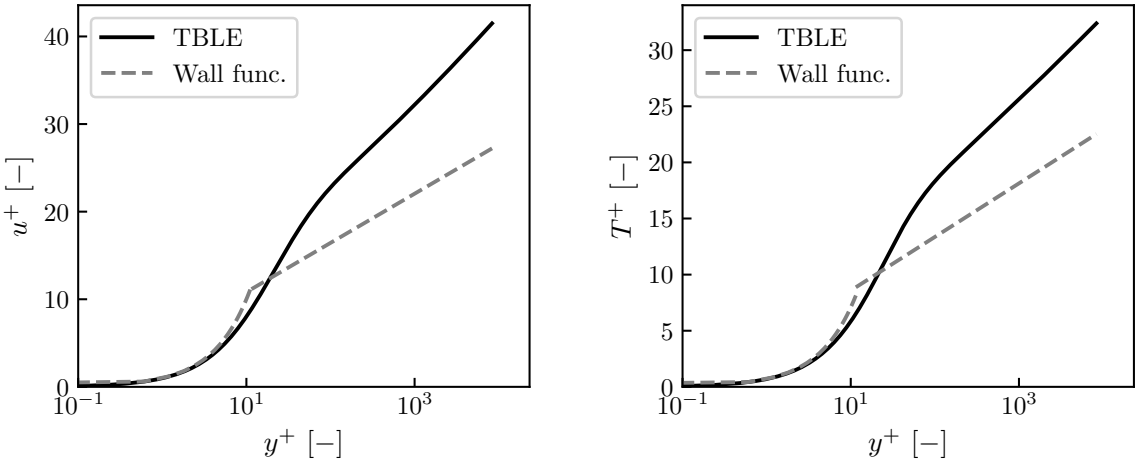

(a) Non-dimensional velocity profile

(b) Non-dimensional temperature profile

Figure 2.9: Non-dimensional velocity and temperature profiles of a generic turbulent and stationary boundary layer. Solid lines: general boundary layer equations (Eqs. 2.149 and 2.150); dashed lines: wall functions (Eqs. 2.164 - 2.167).

The integration constant for the dimensionless velocity is found to be $C = 5$ for smooth walls (Schlichting and Gersten, 2017), while C' is expressed as a function of the Prandtl number as proposed by Kader (1981)

$$C' = (3.85\mathrm{Pr}^{1/3} - 1.3)^2 + 2.12 \ln \mathrm{Pr} \tag{2.168}$$

Depending on the non-dimensional wall distance of the *matching point* (MP), at which the velocity and temperature profile of the outer flow and the boundary layer should match, we either solve Eqs. 2.164 and 2.165 if $y^+ \leq 5$, or Eqs. 2.166 and 2.167 if $y^+ \geq 30$. In this work, we use the first off-wall node of the computational mesh as matching point. Note, that the AVBP solver assumes Eqs. 2.164 and 2.165 to be valid within $y^+ \leq 11.445$, and Eqs. 2.166 and 2.167 otherwise. With these non-dimensional velocity and temperature profiles, we can solve for the friction velocity and friction temperature through Eqs. 2.156 and 2.158, and eventually for the wall shear stress (Eq. 2.157) and the wall heat flux (Eq. 2.159).

Compared to more sophisticated approaches, the implementation of these equations into numerical solvers is straightforward and computational efforts are very moderate. Specifically, constant fluid properties are traded for mathematical simplicity, hence the reduced numerical cost. In turn, large temperature gradients can exist in the boundary layer in practical engineering problems such as heat exchangers, reacting flows in combustion chambers, turbomachinery flows, or rocket propulsion systems, causing large variations of thermophysical properties (λ, C_p, μ, ρ). These variations alter the conventional behavior of turbulence due to a strong coupling between energy and momentum transport (Patel et al., 2015). Therefore, scaling laws derived for constant property flows do no longer hold, rendering wall functions a particularly inappropriate modeling choice. The discrepancies with respect to *e.g.*, the solution of the general boundary layer equations with variable fluid properties can become quite substantial and strongly deteriorate the accuracy of the predicted wall shear stress and wall heat flux. To illustrate such a problem we plot the boundary layer profiles for the non-dimensional velocity and temperature in Fig. 2.9 based on a generic turbulent boundary layer in stationary conditions. In this example, we consider a fluid flow of burnt gases at their adiabatic combustion temperature (n-heptane/air mixture at $\phi = 0.89$) over a flat plate with a constant temperature

of $T_w = 300\,\mathrm{K}$. The friction Reynolds number is $\mathrm{Re}_\tau = \rho\delta u_\tau/\mu \approx 1000$. The solution of the Eqs. 2.149 and 2.150 is plotted as solid lines in Fig. 2.9(a) and (b), whereas profiles estimated from the wall functions (Eqs. 2.164 - 2.167) are plotted as dashed lines. The discrepancies in both profiles are particularly striking in the log-layer, resulting from an (invalid) assumption of constant fluid properties. Furthermore, we can also observe the inherent discontinuity originating from an artificially sharp distinction between the viscous sublayer and the log-layer based on an arbitrary value of y^+ (here: $y^+ = 11.445$). Such discontinuity is not visible in the solution of the general boundary layer equations, exhibiting a smooth transition between the viscous sublayer and the log-layer. This transition region at $8 \leq y^+ \leq 20$ is also referred to as buffer layer, where neither asymptotic wall function is suitable.

Attempting to overcome the limitations induced by the assumption of constant fluid properties, one may resort to semi-local scaling (Huang et al., 1995; Patel et al., 2015) defined as

$$y^\star = \frac{\rho u_\tau^\star y}{\mu} \tag{2.169}$$

$$u_\tau^\star = \left(\frac{\tau_w}{\rho}\right)^{0.5} \tag{2.170}$$

Unlike Eq. 2.155, density and viscosity may evolve as a function of the wall distance, rather than being evaluated at the wall. While this approach improves the accuracy of the predicted boundary layer profiles using simple wall functions, it does not overcome the discontinuity in the buffer layer. With regard to available wall functions in AVBP (all of which are algebraic), only density is currently allowed to vary in the boundary layer, which was shown to yield unsatisfactory results in light-round simulations (Puggelli et al., 2020). Therefore, we propose a different approach to wall modeling based on the Thin Boundary Layer Equations in Sec. 5.3, which aims at addressing the problems related to wall functions while maintaining acceptable computational costs and, more importantly, variable boundary layer properties. We discuss and justify the equilibrium assumption separately in Sec. 6.5.5.3.

2.8 Numerical solution schemes and their implementation in AVBP

Due to the Euler-Lagrangian description of the multi-phase flow, separate solution schemes are used for each phase. The AVBP solver (Schönfeld and Rudgyard, 1999; Colin and Rudgyard, 2000) is based on the finite volume method (Hirsch, 2007) to discretize the compressible conservation equations in physical space. The discretization of the gas phase is implemented as cell-vertex approach (Rudgyard, 1993), where conserved variables are stored at the cell vertices (or grid nodes), while conservation relations are applied to the grid cells. Convective fluxes are discretized based on the explicit Two-step Taylor Galerkin (TTGC) scheme (Colin and Rudgyard, 2000), reaching a third order accuracy in time and space on arbitrary meshes. For stability reasons, the time step Δt is limited by imposing a constant Courant-Friedrichs-Lewy (CFL) number of 0.7. Since AVBP is a fully compressible code, the CFL number is defined as

$$\mathrm{CFL} = \Delta t \frac{\max|u| + c}{\Delta x} \tag{2.171}$$

where u is the propagation speed of a perturbation in the flow, c the speed of sound, and Δx the mesh size. In turn, droplets are advanced according to the explicit algorithm developed by Haselbacher et al. (2007), which is coupled at each iteration to the solver of the gas phase.

The AVBP code is developed by CERFACS and written in FORTRAN90, with only a few mesh-related routines written in C/C++. It is designed for massively parallel simulations on HPC (High-Performance Computing) clusters, allowing to distribute the pre-partitioned computational domain across multiple compute nodes, which can each run multiple processes. Inter-node communication is handled by the Message Passing Interface (MPI) library. Solution data is stored under the HDF5 file format separately for each phase. Domain partitioning relies on the Parmetis library and uses static, unweighted partitioning. Due to issues with the MPI communicator (Infiniband), the individual partition size is neither weighted by the local number of droplets, nor are the partitions dynamically rearranged between consecutive runs of light-round simulations. As illustrated in Sec. 6.5.4, the spatial droplet distribution in MICCA-Spray changes substantially during light-round as a consequence of flame propagation, causing a strong droplet imbalance between partitions, and thus considerable performance penalties. Future works could therefore greatly benefit from performance gains if these issues were resolved.

2.9 Description of the flamelet solver AGATH

In addition to AVBP, we also employ the EM2C in-house code AGATH, which is a flamelet solver library similar to CHEMKIN (Kee et al., 1996) or Cantera (Goodwin et al., 2022). AGATH is a one-dimensional solver used to evaluate thermodynamic and transport properties, as well as chemical sources terms appearing in the Navier Stokes equations, implementing various kinetics and transport descriptions.

Given a set of conservative quantities such as a density, mixture composition or internal energy, AGATH can compute thermodynamic properties such as pressures or temperatures based on different thermodynamic models. In this work, we rely on polynomial fit functions for the evaluation of temperature-dependent quantities (*e.g.,* C_p, μ). AGATH also provides chemical source terms thanks to algorithms solving non-linear systems, *e.g.,* Radau5 or LSODE. Beyond flamelet simulations, we perform evaporation simulations serving as reference results for our model development.

2.10 Summary

Turbulent combustion in aeroengines offers a plethora of modeling challenges which can only be resolved by employing statistical modeling approaches, at least in practical applications. We specifically highlight three key modeling aspects relevant for this work: (i) dynamic combustion modeling for turbulent premixed flames, (ii) a Lagrangian description of polydisperse fuel sprays, and (iii) wall heat transfers.

In general, turbulent combustion involves, among others, a wide range of length and time scales, multiple species, and non-linear interactions of turbulence and chemical kinetics on multiple scales. We have introduced Large-Eddy Simulations (LES) as an attractive solution approach due to its scale-resolving capabilities and its successful application to "classic" turbulent flow problems. In filtering the governing equations of fluid flow, a scale separation is achieved, where the (flow) problem-relevant large-scale structures are resolved, while the unresolved small-scale structures are modeled through so-called subgrid-scale models, since their behavior is assumed to be universal.

Furthermore, we have discussed the concept of perfectly premixed combustion — an idealized view of real combustion processes — which greatly simplifies the multi-scale problem of

flame/turbulence interactions: essentially, premixed combustion is characterized by a single length scale, δ_l, and time scale, δ_l/S_l^0, constituting the foundation of premixed combustion model development. Even with today's LES meshes, however, the laminar flame thickness is too small to be fully resolved, at least in larger models of annular combustion chambers. A widely used solution to overcome this problem is the Artificially Thickened Flame model (or Thickened Flame for LES, TFLES), which was initially developed for laminar premixed combustion. Its application to turbulent combustion offers new challenges in terms of flame/turbulence interactions and requires a correction of the flame-surface wrinkling by means of an appropriate flame surface wrinkling model. Central to our work are dynamic modeling approaches which we have discussed in this chapter. We conclude the combustion modeling section with practical means to incorporate multi-regime combustion, employing regime indicators such as the Takeno flame index.

Beyond that, we have presented the fundamental equations for Lagrangian particle tracking for the description of droplet motion. Most importantly, we invoke the dilute spray assumption, allowing to focus the modeling efforts on phenomena of interest such as dispersion, evaporation, mixing or combustion, without accounting for atomization, droplet collisions or coalescence. We discuss the momentum exchange between the gas phase and the polydisperse droplet phase, specifically the Schiller-Naumann drag force model, as well as heat and mass transfer following the Abramzon-Sirignano evaporation model, constituting yet another central aspect of this work. Fuel injection is handled by the phenomenological FIM-UR model aiming at reproducing a pre-atomized fuel spray at a distance from the injector, where the dilute spray regime can usually be justified. We have highlighted specific improvements that have recently been developed and refer to Chap. 4 for detailed insights into the calibration procedure.

Finally, we have addressed the near-wall problem relevant for wall-bounded LES: thin boundary layers usually require very fine meshes to be accurately resolved and to ensure correct momentum and energy transport. In simulations of large annular combustion chambers, these restrictive mesh requirements cannot be met with a reasonable amount of computational resources. Instead, wall models can be used, or even simpler algebraic wall functions. We have subsequently outlined the limitations of those wall functions, which stem from additional assumptions shown to be particularly unsuitable for light-round simulations. Therefore, we propose a custom wall model in Chap. 5 based on the Thin Boundary Layer Equations (TBLE) previously introduced.

Chapter 3

Experimental configurations, numerical domains and setup

Academic research of combustion related phenomena in aero-engines is commonly performed in lab-scale combustion devices. Although representing idealized versions of their industrial counterparts, they share characteristic design features and often provide good optical access. Of particular interest for this work is the annular multi-burner combustor MICCA-Spray, and its complementary single-injector design SICCA, which are both presented in this chapter. In order to perform Large-Eddy Simulations in these geometries, computational domains and meshes are required. These are discussed in this chapter, along with the simulation setup and boundary conditions that are common to the following ignition simulations. We also provide evidence for a sufficient mesh resolution by presenting results of a grid convergence study.

Contents

3.1 Introduction

Industrial combustor designs commonly feature an annular combustion chamber containing multiple fuel injectors typically optimized for homogeneous mixture formation, clean and stable combustion, and low emissions. Studying such complex configurations in a laboratory environment however is mostly impractical: from an experimental perspective, real combustion devices offer (at best) limited capabilities for experimental diagnostics and are neither designed for detailed investigations of dynamic combustion phenomena. From a numerical perspective, their dimensions and complexity would demand for unreasonably high computational costs if a full combustion chamber, or even an entire engine were to be simulated. Therefore, lab-scale design concepts have emerged for single-injector, and later for multi-injector combustors to facilitate academic research. These are simplified, or idealized versions of realistic combustion chambers which are purpose-built to study dynamic combustion phenomena in great detail. Yet, they share important characteristics with industrial designs, for example in terms of the injector design, or an annular shape, while still offering optical access.

Of particular interest are two configurations, the annular multi-injector combustor MICCA-Spray and the complementary single-injector combustor SICCA at the EM2C laboratory in France, introduced in this chapter along with their numerical counterparts. We summarize the meshing strategy, the ignition methods, the simulation setups and boundary conditions common to all cases, and refer to case-specific details in the following chapters. Finally, we validate the computational meshes for air flow simulations by comparing the obtained velocity profiles to experimental data.

3.2 Experimental rigs

Two combustor setups at the EM2C laboratory are extensively studied in this work and presented in the following sections: (i) the annular spray-flame combustor MICCA-Spray (Prieur et al., 2017, 2019), and (ii) the single-injector combustor SICCA (Prieur et al., 2019). MICCA-Spray has been the first combustor allowing for a characterization of flame propagation during light-round with liquid fuels in a lab-scale configuration. SICCA is a complementary combustor designed for in-depth studies of phenomena observed during ignition and for detailed measurements of spray characteristics.

3.2.1 Annular spray-flame combustor MICCA-Spray

The MICCA-Spray combustor (Fig. 3.1) is a test rig at the EM2C laboratory (Prieur et al., 2017, 2019). Its design reflects key features of a combustor typical of small helicopter engines while being simple enough to safely operate under lab-scale conditions. Various fuels and swirler geometries can be accommodated relatively easily thanks to its modularity. The combustion chamber is confined by two concentric quartz tubes with dimensions $R_{in} = 0.15\,\mathrm{m}$, $R_{out} = 0.20\,\mathrm{m}$ and $h = 0.195\,\mathrm{m}$, which allow for optical access (Fig. 3.2(a)). Since its initial conceptualization, the MICCA combustor has been EM2C's workhorse in terms experimental

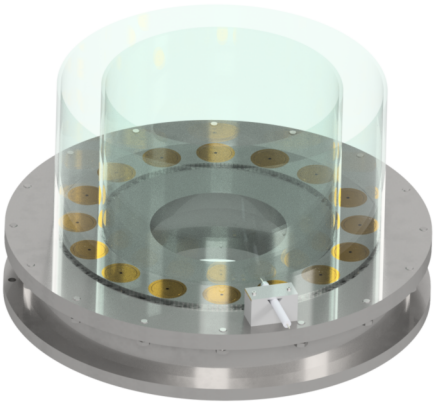

Figure 3.1: 3D model of the MICCA-spray combustor (Prieur et al., 2017, 2019) featuring 16 swirled spray injectors.

(Bourgouin et al., 2013; Prieur et al., 2017, 2019; Rajendram Soundararajan et al., 2021; Vignat et al., 2020b) and numerical (Philip et al., 2015b,a; Lancien et al., 2017, 2019; Puggelli et al., 2021) investigations of dynamic combustion phenomena in annular combustors. A recent review can also be found in Vignat et al. (2020a).

The configuration relevant for this work features sixteen swirled spray injectors arranged in an annular fashion at a radius of $R = 0.175\,\mathrm{m}$ (Fig. 3.2(a)). Each injector assembly (see Fig. 3.2(b)) consists of a swirler (measured swirl number $S = 0.68$), a concentrically mounted atomizer and a terminal plate with an integrated nozzle of $d_{inj} = 8\,\mathrm{mm}$ outlet diameter. All swirlers are fed with air from their corresponding injector block through six radially arranged ports and create a rotational flow in clockwise direction, exiting the swirlers in axial direction from their respective centers of rotation. The pressurized simplex atomizers (Faeth, 1979; Lefebvre and Ballal, 2010; Lefebvre and Mcdonell, 2017) (fuel pressure: $6\,\mathrm{bar}$) are recessed by $x_A = 5.9\,\mathrm{mm}$ relative to the nozzle outlets, allowing the hollow-cone fuel spray to partially interact with the nozzle walls and improve the atomization process (see Fig. 3.3). Liquid n-heptane (C_7H_{16}) is supplied from a pump controlled by a mass flow controller (Bronkhorst® mini CORI-FLOW™ M14), which has a precision of $\pm 0.2\%$ of the liquid flow rate (set in $\mathrm{kg/h}$). Sixteen hollow-cone fuel sprays are thus released into the combustion chamber.

The chamber is operated at ambient pressure and a global equivalence ratio of $\phi_{glob} = 0.89$, corresponding to a nominal thermal power output $\mathcal{P}_{th} = 79.3\,\mathrm{kW}$ under steady-state operating conditions. Ignition is triggered by an electrical spark plug in sector $S0$, serving as a reference to divide the chamber into a positive (H+) and negative (H-) half (Fig. 3.2(c)). Sectors in the negative half are labeled S-1 to S-7 in flame propagation direction (indicated by thick arrows in Fig. 3.2(c)), and S+1 to S+7 in the positive half. The clockwise swirl orientation is the same for each injector (thin arrows in Fig. 3.2(c)). A watercooling circuit is integrated in the combustor backplane and the air plenum.

3.2.2 Complementary single injector combustor SICCA

The SICCA-combustor (Prieur et al., 2019) in Fig. 3.4 is a swirled, single-injector spray-combustor operated at ambient pressure. It is designed to facilitate the investigation of flame dynamics occurring for example during ignition or thermoacoustic combustion instabilities. More specifically, SICCA allows to characterize the flow aerodynamics, spray structure and flame geometry, which would otherwise be difficult to measure in MICCA-Spray. From a simulation view point, SICCA allows to validate numerical model at a reduced computational

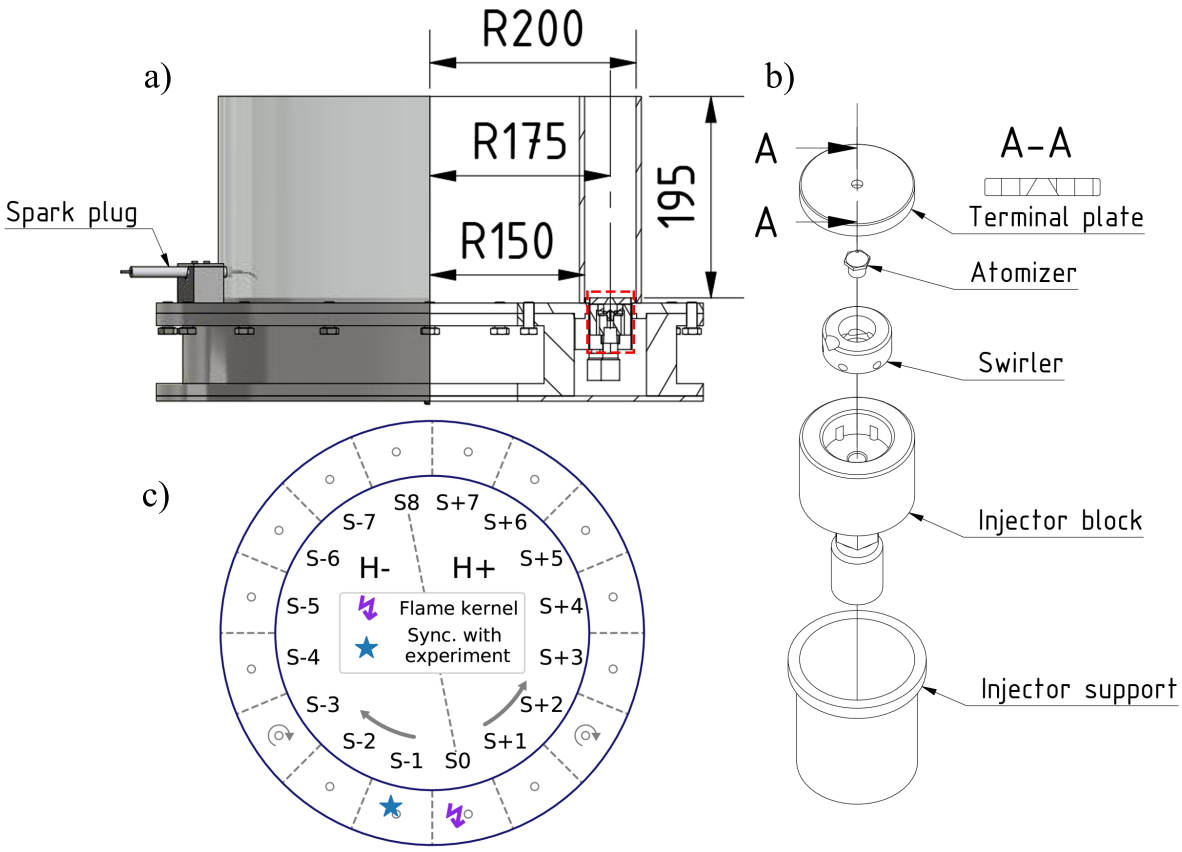

Figure 3.2: Main combustor features of MICCA-Spray: a) dimensions (in millimeter) of the combustion chamber and injector position; b) exploded view of an injector assembly (corresponding to the dashed rectangle in (a)) with concentrically mounted swirler and fuel atomizer; c) sector layout and labeling used in this work.

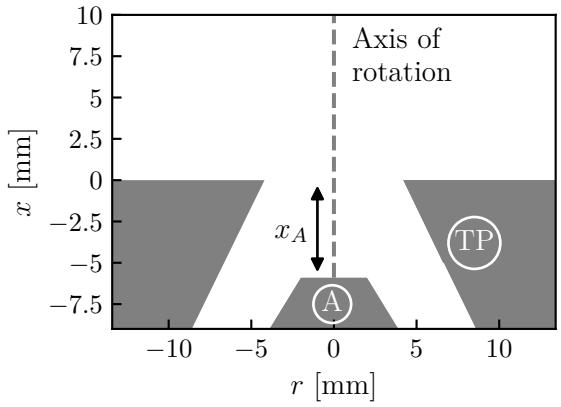

Figure 3.3: Sketch of an atomizer (“A”) and a terminal plate (“TP”) of one injection assembly. The atomizer is recessed by $x_A = 5.9\,\mathrm{mm}$ relative to the nozzle outlet.

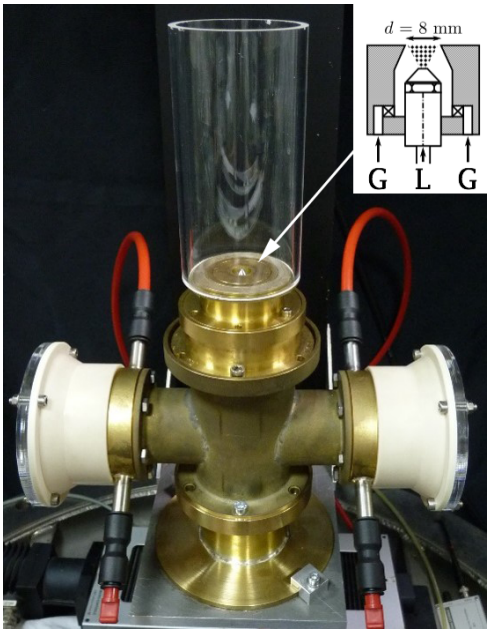

Figure 3.4: Experimental setup of the swirled single-injector combustor SICCA. The sketch in the top right corner visualizes a cut through the injection unit.

cost compared to MICCA-Spray. Consequently, it shares the exact same injector assembly as MICCA-Spray (see Fig. 3.2(b)) and thus represents 1/16th of the MICCA-Spray combustor. In this configuration, a hollow-cone spray is released into the combustion chamber, which is confined by a cylindrical quartz tube of $70\,\mathrm{mm}$ inner diameter, $150\,\mathrm{mm}$ height and $5\,\mathrm{mm}$ thickness. The quartz cross-sectional area has been chosen such to be equivalent to 1/16th of the MICCA chamber cross-sectional area. Under stationary conditions, a flame stabilizes at a distance from the swirler outlet. For ignition, a conventional spark plug is used as in MICCA-Spray, mounted close to the combustor back-plane.

We point out that a direct comparison of the flow field and flame shapes between SICCA and MICCA-Spray has certainly some limitations, which are the subject of ongoing research (see *e.g.,* Vignat (2020)). Despite this, SICCA offers valuable insights which cannot be (easily) obtained from a full annular combustor like MICCA-Spray.

3.2.3 Experimental diagnostics

Most of the detailed flow and spray characteristics are measured in SICCA such as air flow velocities, fuel droplet diameter distributions and droplet velocities. Thanks to an extensive dataset kindly provided by Dr. G. Vignat, we have recalibrated the injection model used in the simulations. The data as well as the calibration procedure is the subject of Sec. 4.3. Wall temperature measurements for the SICCA combustor were carried out for previous works and are exclusively utilized and shown in Chap. 9. External wall temperature profiles were measured in steady-state operation with a thermocouple, although with a longer quartz tube of $200\,\mathrm{mm}$ height. Wall temperature profiles of MICCA-Spray are extremely limited to a single-point thermocouple measurement at the outer quartz wall during steady-state operation. The lack of wall temperature data has been the main motivation for coupled simulations presented later in Sec. 7.2, allowing to determine the temperature profiles in reacting conditions.

Air mass flow rates in the plenum are measured through a hotwire during ignition in SICCA. Ignition sequences are recorded in SICCA and MICCA-Spray with a high-speed camera (Phantom V2512, frame rate: $6000\,\mathrm{FPS}$, shutter speed: $166\,\mu\mathrm{s}$, see Prieur et al. (2019)) to

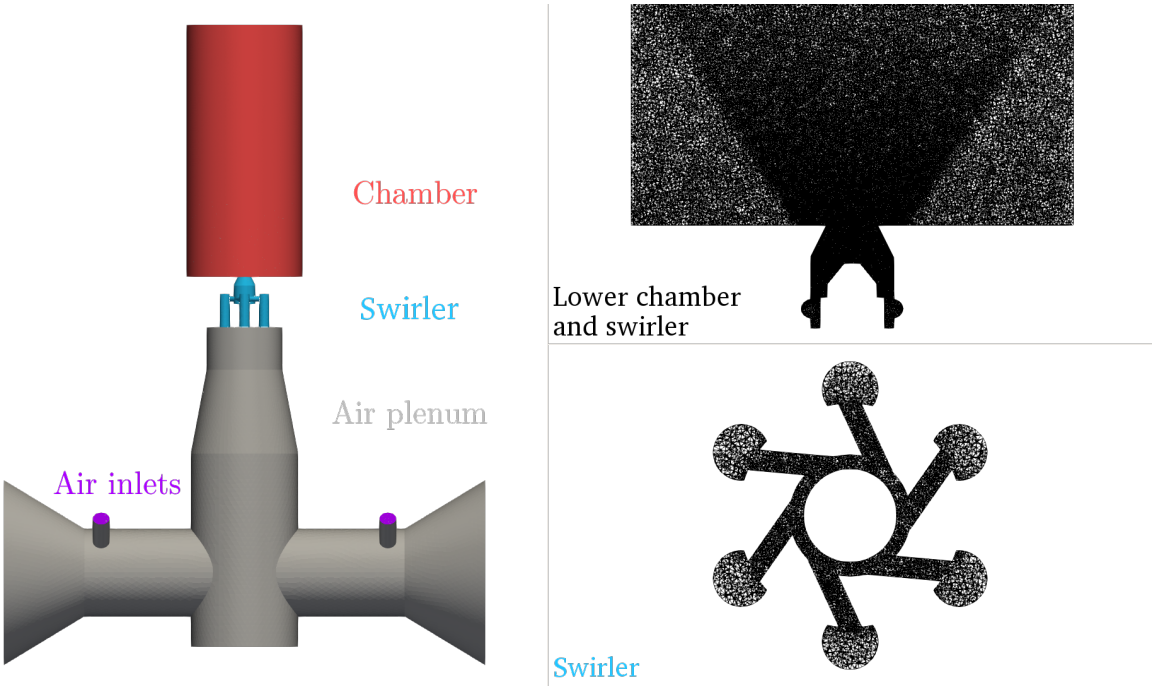

Figure 3.5: Left: fluid domain of the SICCA combustor (without ambient atmosphere). Top right: central mesh-cut of the injector and lower part of the chamber. Bottom right: mesh-cut of the swirler.

investigate flame shapes, flame propagation and flame dynamics. Moreover, light-round durations are measured in MICCA-Spray for two wall temperature conditions: (i) cold combustor walls at $T_w = 300\,\mathrm{K}$, and (ii) preheated combustor walls after reaching thermal equilibrium during prior steady-state operation. In the interest of brevity, we refer the reader to Prieur et al. (2019) and Vignat (2020) for more details on the employed experimental diagnostics.

3.3 Numerical domains and meshes

As in previous works, CAD geometries of both combustors were generated and subsequently meshed with tetrahedral cells. For all ignition simulations (SICCA and MICCA-Spray), we only use the fluid domain meshes. The solid domain mesh is added later for Conjugate Heat Transfer Simulations (CHT) of steady-state operation presented in Sec. 5.2.

3.3.1 Single injector geometry SICCA

The numerical domain of the SICCA combustor is shown in Fig. 3.5 (left image), consisting of an air plenum (in gray), the injector assembly including the swirler and atomizer (in cyan) and the combustion chamber (in red). For numerical reasons, the combustion chamber is immersed into a larger cylinder with a radius of $40\,\mathrm{cm}$ (referred to as "atmosphere", not shown here, see Appendix F for full domain views), extending $50\,\mathrm{cm}$ beyond the chamber outlet. This allows to impose an atmospheric pressure boundary condition far away at the atmosphere outlet, where $p = 1\,\mathrm{bar}$ can be safely assumed, rather than at the *chamber* outlet, which can potentially influence the solution. Since the computational mesh is unstructured and tetrahedral, we can use gradually larger cell sizes towards the end of the numerical domain (*i.e.* the atmosphere outlet) without incurring unreasonable penalties in terms of computational cost. Neither burnt gases nor flame elements can thus reach the atmosphere outlet during ignition simulations.

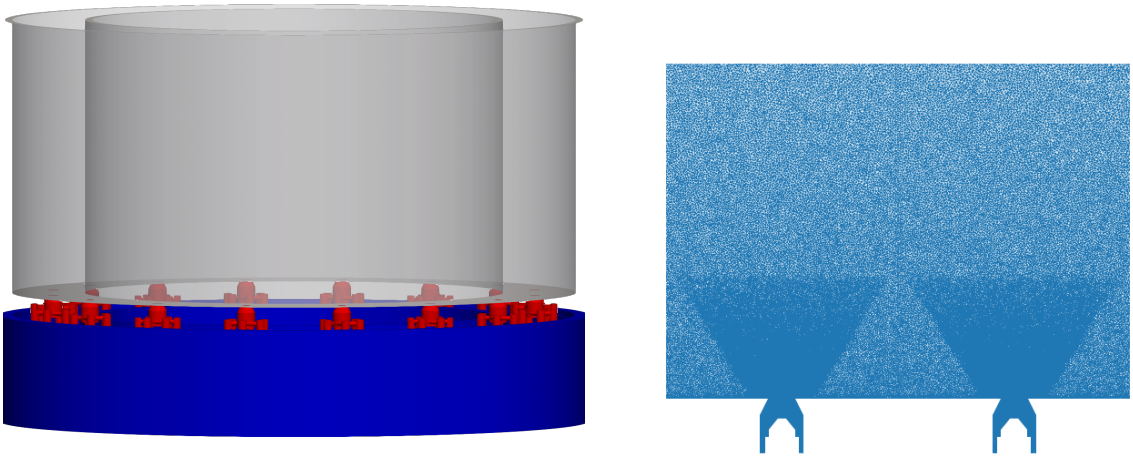

(a) Fluid domain comprising the air plenum (blue), injector assembly (red) and the combustion chamber (gray).

(b) Zoom on the mesh of two adjacent sectors including parts of the injector. Image clipped to lower half of the combustion chamber.

Figure 3.6: Fluid domain of the MICCA-Spray combustor (without atmosphere) and zoom on mesh in lower half of the combustion chamber (showing two sectors only).

The right half of Fig. 3.5 shows mesh cuts of the lower part of the combustion chamber including parts of the injector (top) as well as a flow-normal cutplane through the center of the swirler. Mesh refinement is applied to the flame region with cell sizes ranging between $0.2\,\mathrm{mm}$ and $0.5\,\mathrm{mm}$ (see Fig. 3.5 upper right image). The entire domain contains 3.4 million grid nodes, corresponding to roughly 19.1 million tetrahedral cells.

3.3.2 Annular geometries

For light-round simulations in MICCA-Spray, the full annular combustor geometry is meshed. Conversely, precursor non-reacting simulations (*e.g.,* to establish steady state conditions prior to ignition) and reacting Conjugate Heat Transfer Simulations are performed in 1/8th of the full combustor, referred to as "bisector".

3.3.2.1 Full annular combustor geometry

Figure 3.6(a) shows the fluid domain of the full annular geometry of MICCA-Spray including the air plenum, all sixteen injectors and the combustion chamber. As for SICCA, the surrounding atmosphere is taken into account by a larger cylinder extending $60\,\mathrm{cm}$ beyond the outlet of the combustion chamber (not shown, see Appendix F for a full domain view). Cell sizes and mesh refinement zones were adopted from SICCA and can be inspected in Fig. 3.6(b) for the lower part of the combustion chamber. Note that Fig. 3.6(b) represents a cylindrical mesh cut clipped to two adjacent sectors and subsequently transformed into a rectangular system. The full domain contains 56.6 million grid nodes, corresponding to roughly 323.9 million tetrahedral cells.

3.3.2.2 Bisector as intermediate geometry

To reduce the staggering computational costs associated with simulations of MICCA-Spray, we have taken advantage of the rotational symmetry of the annular chamber, where appropriate. More specifically, non-reacting simulations of fuel injection are carried out in 1/8th of the full

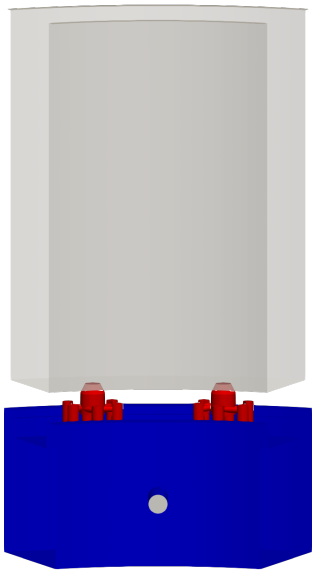

Figure 3.7: Fluid domain of the bisector representing 1/8th of MICCA-Spray. The atmosphere is included as well, but not shown.

chamber, referred to as "bisector". Similarly, coupled simulations in fully ignited stationary conditions also rely on the bisector, which consists of two injectors, 1/8th of the air plenum, the combustion chamber walls, and the atmosphere, as visualized in Fig. 3.7. Rotational periodicity (or axi-periodicity) is assumed at the circumferrential boundaries of the numerical domain.

In theory, even a single-sector domain with axi-periodic boundary conditions would be sufficient for such simulations and would further reduce the computational costs. However, MICCA-Spray is designed such that each pair of injectors shares a common air supply with a short feed pipe mounted to the air plenum in-between neighboring injectors (see gray dot in Fig. 3.7). Using only a single-sector numerical domain would necessarily create a symmetry plane through the feed pipe, which is undesired from a numerical standpoint, or otherwise modify the geometry, which is undesired from a modeling perspective. Hence we account for two injectors (*i.e.* bisector) to avoid those problems.

3.4 Numerical setup: employed schemes and models

Throughout this work, we mostly rely on a set of common models and numerical schemes for all our simulations, summarized in the following sections. Essentially, chapters 6 and 7 share the same models, which have progressively been developed and tested throughout this work. In turn, simulations in Chap. 9 (SICCA) were carried out prior to light-round simulations in MICCA-Spray and differ with respect to the injection model and the wall model. Since the mesh resolution is sufficiently fine in SICCA, we can directly resolve the near-wall flow as in Collin-Bastiani (2019b) without requiring a wall model. The fuel injection model and new experimental data however were available *after* the simulations in Chap. 9 were carried out and thus rely on a different calibration approach.

For the sake of clarity, we present the common models and numerical schemes in the following sections, and highlight case-specific changes were appropriate. For convenience, all models are also compiled in Tab. 3.2.

3.4.1 Treatment of the gas phase

The filtered governing equations of the gas phase presented in the previous chapter are solved on unstructured tetrahedral grids using the Two-step Taylor-Galerkin Centered scheme (TTGC) Colin and Rudgyard (2000) with third-order accuracy in space and time. Subgrid-scale contributions are computed following the classical eddy viscosity assumption. The turbulent eddy viscosity is evaluated according to the SIGMA model Nicoud et al. (2011). The turbulent species diffusivity and the turbulent heat conduction coefficient are determined from the turbulent Schmidt (Sc_t) and Prandtl (Pr_t) numbers (both equal to 0.6).

3.4.2 Reaction kinetics and combustion model

Reaction kinetics are based on a global two-step scheme for n-heptane/air mixtures (see Eqs. 2.37 and 2.38) containing 6 species (C_7H_{16}, CO_2, CO, H_2O, O_2, N_2, Paulhiac et al. (2020)). Reaction rates are computed from the Arrhenius law with adjusted pre-exponential factors depending on the local equivalence ratio (Franzelli et al., 2010), requiring a unitary Lewis number assumption (Le = 1). A validation against detailed schemes (Smallbone et al., 2009) performed in Paulhiac et al. (2020) shows a reasonably good prediction of the unstrained laminar burning velocity at ambient pressure and over a wide range of equivalence ratios. We recall that the unity Lewis number assumption renders the two-step reaction mechanism virtually insensitive to strain. As discussed later (see also Sec. 8.2.1.1), such simplification is acceptable for the description of flame front propagation during light-round.

It should also be emphasized that auto-ignition or pyrolysis effects are very unlikely to occur with cold combustor walls ($T_w = 300\,\mathrm{K}$) and fresh gases injected at $T_u = 300\,\mathrm{K}$, justifying the use of reduced chemical reaction schemes. In turn, preheated combustor walls may generate favorable conditions for these effects which are beyond the modeling scope of the two-step reaction mechanism employed in this work. Due to its limited accuracy with regard to auto-ignition, we chose to neglect this effect by clipping the species source terms below a certain cutoff value. This modification is only applied in the *fresh gas region*, identified via an unnormalized species progress variable $Y_c = Y_{\mathrm{CO_2}} + Y_{\mathrm{CO}}$ based on the species mass fractions of CO_2 and CO. Subsequently, we run 1D laminar premixed flame simulations with varying values of $Y_{c,\mathrm{cutoff}}$ at a given equivalence ratio ϕ and fresh gas temperature T_u. An optimal cutoff value is then selected such that it does not affect the predicted laminar flame speed value compared to the *reference* flame speed reported *e.g.,* in the literature. This procedure is illustrated in Fig. 3.8 for $\phi = 0.9$ and $T_u = 300\,\mathrm{K}$. For values of $Y_{c,\mathrm{cutoff}} > 0.03$ (hatched region), S_l^0 is found to gradually deviate from its reference value. For smaller values in turn, S_l^0 is correctly predicted. Thus, any value beneath the hatched region is an acceptable choice for $Y_{c,\mathrm{cutoff}}$, allowing to suppress auto-ignition in the fresh gas mixture *regardless* of its temperature. For this work, we arbitrarily retained $Y_{c,\mathrm{cutoff}} > 0.001$ (marked with a star in Fig. 3.8).

Despite such a pragmatic choice, we emphasize that ignition of the experiment always required external forcing (*e.g.,* a spark plug) for the considered preheated operating conditions. We thus conclude that light-round ignition involves a freely propagating, (dominantly) premixed flame generated through external forcing, rather than auto-ignition at hot combustor walls.

Note that the intentionally suppressed auto-ignition does *not* remedy the two-step reaction mechanism's poorer flame speed predictions with increasing fresh gas temperature. This aspect is discussed and corrected in a different manner, which is detailed in Sec. 7.4.

Fuel pyrolysis was independently investigated in an *a priori* study, which is included in Appendix C. Essentially, this effect would occur *beyond* a fresh gas temperature of $T_u =$

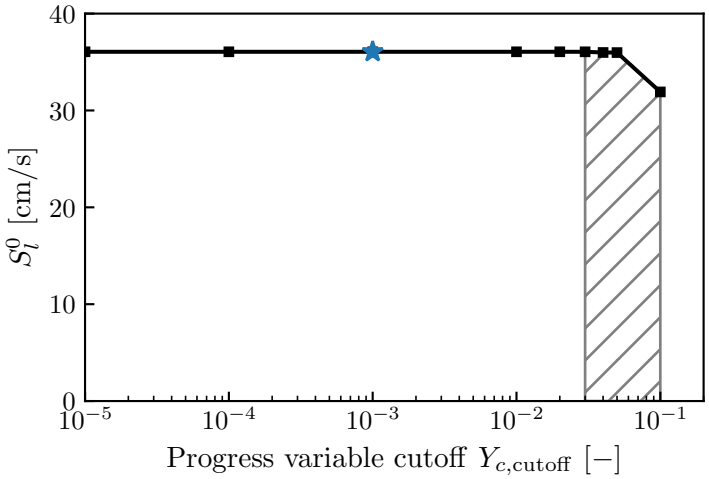

Figure 3.8: Laminar flame speeds predicted by the two-step reaction mechanism of Paulhiac et al. (2020) for varying values of $Y_{c,\mathrm{cutoff}}$. In this figure, we show data of 1D laminar flame simulations at $\phi = 0.9$ and $T_u = 300\,\mathrm{K}$. The hatched region marks unsuitable values of $Y_{c,\mathrm{cutoff}}$, as S_l^0 deviates from its reference value. The retained value is marked with a star.

$1000\,\mathrm{K}$, which is not reached in neither light-round setup. Moreover, we acknowledge that the two-step reaction mechanism is a simplification of a much more complex structure of the inner reaction zone of a realistic flame which we do not seek to resolve. Consequently we cannot capture said effect either. It is therefore neglected in the present modeling setup.

Since cell sizes are not sufficiently small to fully resolve the flame on the numerical grid, artificial thickening (TFLES) is applied (Colin et al., 2000; Legier et al., 2000), ensuring correct laminar flame burning velocity retrieval. The amount of local thickening by a factor $\mathcal{F}$ depends on the local cell size, the laminar flame thickness, and the number of prescribed grid points to resolve the flame profile (5 points in SICCA, 7 points in MICCA). A flame sensor (Legier et al., 2000) combined with the evaluation of the local Takeno flame index (Yamashita et al., 1996) limits the thickening procedure to the premixed reaction zone only. As a consequence of the two-phase flow configuration, thickening is also applied to drag and evaporation (Paulhiac et al., 2020). We will return to the discussion of the thickened flame model in two-phase flows in Sec. 7.5.5.

Interactions between strain effects and a thickened flame may result in a modified Damköhler number (Colin et al., 2000). Strain-correction models exist for *laminar* flames developed by Popp et al. (2019) which correct the laminar flame speed at elevated thickening factors. For the present investigations of turbulent flame propagation, no specific treatment is currently employed, but would be worth developing in future works. The two-step reaction mechanism thus predicts laminar flame speed values close to S_l^0 of unstrained flames for a given equivalence ratio, even at elevated thickening values.

Furthermore, we recall that the thickened flame approach involves a flame surface wrinkling factor accounting for unresolved sub-grid scale wrinkling effects, which is expressed as

$$\Xi_\Delta = \left(\frac{\Delta}{\delta_l}\right)^\beta \qquad \text{(2.48 (revisited))}$$

In the above equation, Δ corresponds to the local mesh size, δ_l to the laminar flame thickness and β to the flame surface wrinkling parameter. While all simulations in the present work apply the saturated form according to Eq. 2.48, they differ in the evaluation of β: for light-round

	Symbol	Expression
Combustion filter size	Δ	$\alpha\mathcal{F}\delta_l$
Test filter size	$\hat{\Delta}$	$c_1\Delta$
Effective test filter size	$\check{\Delta}$	$\gamma\Delta$
Averaging filter size	Δ_{avg}	$c_2\Delta$

Table 3.1: Model parameters for the dynamic evaluation of the flame surface wrinkling parameter β relevant for Chap. 6 and 7.

simulations in Chap. 6 and 7, β is dynamically evaluated as in Volpiani et al. (2016), also including a correction for flame front merging and flame/wall interactions (Mouriaux et al., 2017), whereas it is set to $\beta \equiv 0.5$ in Chap. 9 following the work of Charlette et al. (2002b). Additional model parameters required for a dynamic evaluation of the flame surface wrinkling parameter are summarized in Tab. 3.1. The TFLES filter factor is set to $\alpha = 1$, the test filter factor is $c_1 = 2$, the averaging filter factor is $c_2 = 2.7$, and the update frequency is set to every 250 iterations.

3.4.3 Treatment of the liquid phase

The fundamental equations of droplet motion (Eqs. 2.67 and 2.68) are solved in a Lagrangian framework with an explicit two-step Runge-Kutta scheme, which is coupled at every iteration to the gas phase solver. Each numerical droplet represents one physical droplet, *i.e.* $n_{\text{parcel}} = 1$. We assume that the injected fuel spray is dilute (liquid volume fraction in the range of $10^{-6} \leq \alpha_l \leq 10^{-3}$ as defined *e.g.,* in Jenny et al. (2012)), which can be justified further away from the injector where droplet interactions become less relevant (Masri, 2016). They are neglected here in favor of modeling the processes of interest such as dispersion, evaporation, fuel/air mixing or combustion whilst keeping the computational efforts affordable.

External forces acting upon the droplets are limited to drag force within this work, following the Schiller-Naumann drag force model (Schiller and Naumann, 1935). Heat and mass transfer between the gas and liquid phase is described according to the Abramzon-Sirignano evaporation model (Abramzon and Sirignano, 1989). Due to its paramount importance for light-round simulations, we have developed an extension for its implementation into AVBP, considered as a cornerstone of our work. It is therefore the subject of Chap. 4, where further details are provided.

Moreover, droplets are assumed to be spherical based on an estimation of the dimensionless Weber number, We, relating inertial (or deformation) forces acting upon droplets to cohesion forces (*i.e.* surface tension). It is defined as

$$\mathrm{We} = \rho_l u_R^2 D/\sigma \tag{3.1}$$

where ρ_l denotes the droplet density ($\rho_l = 688\,\mathrm{kg/m^3}$), u_R the relative velocity between a droplet and the gas phase, D the droplet's diameter and σ its surface tension. Weber numbers below unity indicate that cohesion forces outweigh deformation forces and droplets thus keep their spherical shape. For the present configuration, $\mathrm{We} < 1$ is a reasonable assumption at a certain distance from the injector (where the dilute spray assumption is valid), justifying spherical droplets.

Lastly, we note that subgrid-scale velocity fluctuations of the gas phase are not yet accounted for in the (simplified) governing equations of droplet motion. For convenience, we have compiled an overview of all employed models in Tab. 3.2.

	Chapter 6	Chapter 7	Chapter 9
SGS model	SIGMA	SIGMA	SIGMA
Kinetic scheme	two-step	two-step	two-step
Combustion model	TFLES	TFLES	TFLES
Wrinkling parameter evaluation	dynamic	dynamic	static
Flame sensor	Classic with flame index	Classic with flame index	Classic with flame index
Source term clipping	no	yes	yes
Evaporation model	AS (as in Chap. 4)	AS (as in Chap. 4)	AS (as in Chap. 4)
Drag force model	Schiller-Naumann	Schiller-Naumann	Schiller-Naumann
Injection model	modified FIM-UR	modified FIM-UR	FIM-UR
Droplet PDF	experimental, evap. corrected	experimental, evap. corrected	Rosin-Rammler distribution
Thickening on drag & evaporation	yes	yes	yes
Wall model	TABWM	TABWM	Wall-resolved
Wall temperature	$T_w = 300\,\mathrm{K}$	CHT profiles	Experimental data
Ignition	burnt gas deposition	burnt gas deposition	energy deposition

Table 3.2: Employed models for Euler-Lagrange simulations. TFLES designates the Thickened Flame model for LES (see Sec. 2.5.1), AS the Abramzon-Sirignano evaporation model as implemented in Chap. 4, FIM-UR the fuel injection models (see Chap. 4), and TABWM the tabulated wall model presented in Chap. 5.

3.5 Boundary conditions

Boundary conditions for Euler-Lagrange simulations are imposed separately for each phase. In Chap. 6 and 9, these are fully known *a priori* and set according to the corresponding experimental cases. Light-round simulations with preheated combustor walls in MICCA-Spray (see Chap. 7) use identical boundary conditions as in Chap. 6, except for wall temperature profiles determined from separate Conjugate Heat Transfer simulations instead.

In the following two sections, we briefly summarize the strategy of how the individual boundary conditions are imposed, and provide explicit values within the chapters mentioned above.

3.5.1 Boundary conditions for the gaseous phase

Since AVBP is a compressible solver, all inlet and outlet boundary conditions are based on the NSCBC formalism (Poinsot and Lele, 1992) for the gas phase. At the inlets of each combustor, mass flow rates and fluid temperatures are specified, which also applies to the inlets of the cylinders representing the atmosphere. As repeatedly mentioned in this chapter, outlet boundary conditions are imposed at the "outlet" of the atmosphere, where we assume ambient pressure.

3.5.2 Boundary conditions for the liquid phase

Liquid fuel is injected as a pre-atomized polydisperse hollow-cone spray at each atomizer. The calibration of the modified FIM-UR injection model (Sanjosé et al., 2011; Vignat et al., 2021) constitutes a key enhancement of the liquid phase description in Chap. 6 and 7 over a more simplified version used in Chap. 9 (similar to Collin-Bastiani (2019b)). Droplet/wall interactions are handled through simplified boundary conditions, involving either elastic rebound or a film boundary condition (Chaussonnet et al., 2013) where appropriate. Secondary atomization is not yet taken into account.

3.6 Experimental and numerical ignition procedure

Ignition is triggered by a spark plug delivering an electrical energy of $25\,\mathrm{mJ}$ at a repetition rate of $100\,\mathrm{Hz}$. The spark plug itself is mounted such that an initial flame kernel develops in the outer recirculation zone of sector $S0$ (marked by a bolt in Fig. 3.2(c)). These early stages of flame kernel initiation, however, involve high-temperature chemistry effects which are not covered by the selected modeling approach in LES. Rather, we wish to reiterate that our work explicitly focuses on flame propagation during light-round as defined in Lefebvre and Ballal (2010); Mastorakos (2017). Hence, we do not attempt to model any phenomena *prior* to flame propagation. Instead, the numerical ignition procedure involves either a deposition of burnt gases as in Chap. 6 and 7, or the energy deposition model (Lacaze et al., 2009) in Chap. 9. The former is illustrated in MICCA-Spray in Fig. 3.9, where the yellow volume corresponds to burnt gases delivered in the outer recirculation zone of sector $S0$. We acknowledge that the resulting initial flame development is a very simplified approximation of reality, but allows for a robust and reliable ignition in the simulations. We address the limitations of this method in the discussion of the synchronization point between experiment and simulation in Sec. 6.5.2.

It is worth mentioning that all simulations are ignited from a fully converged initial solution in this work. Specifically, a prefueling step is performed first during which air and fuel are

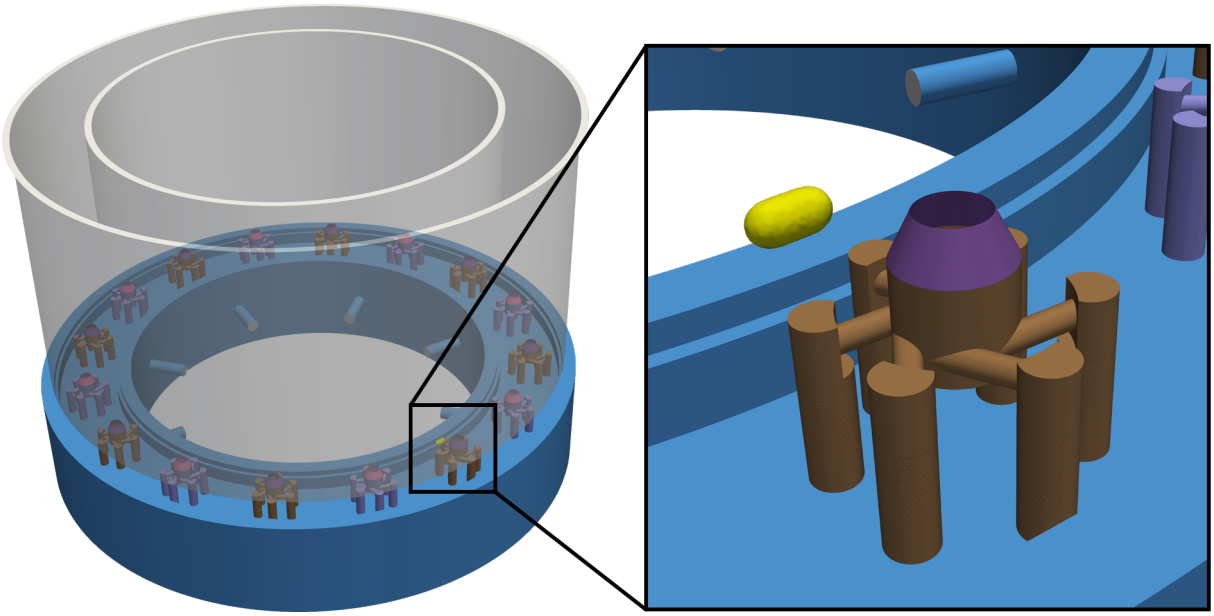

Figure 3.9: Initial flame kernel deposition (marked in yellow) in the outer recirculation zone of sector So of MICCA-Spray.

continuously injected. Equivalence ratios are monitored across the entire combustion chamber until stationary values are reached. Thus, the initial solution prior to ignition always involves a fully developed flow field and a stationary fresh gas mixture. Such procedure is also known as "Fuel First, Spark Later" (FFSL) in the literature (Ye et al., 2018). Most importantly, it ensures comparable and well-defined initial conditions between simulations and experiments. Further case-specific details are addressed later within the relevant chapters.

3.7 Grid convergence study

In order to ensure an appropriate mesh resolution, we first perform a grid convergence study of the pure air flow. Specifically, we seek to provide evidence that our baseline configuration strikes a reasonable compromise between accuracy and computational costs. We present the numerical domain and three meshes in the following section, and examine the resulting velocity profiles afterwards.

3.7.1 Numerical Domain and meshes

Figure 3.10 illustrates the numerical domain used for the grid independence study. It represents the unconfined SICCA combustor with the same injector configuration as used in all other simulations, including the atomizer. Air supplied through the air inlets (marked in red in Fig. 4.9) flows through the air plenum up to the injector, before being released into the atmosphere without any fuel injection at the atomizer. The flow is thus of pure single-phase nature. The ambient air (or atmosphere) is modeled as a large cylinder (not shown) of $h = 60\,\mathrm{cm}$ height and $R = 30\,\mathrm{cm}$ radius.

Three meshes are generated for the purpose of the mesh independence study: (i) a baseline mesh, (ii) a refined mesh, abbreviated as "MESH-FINE", and (iii) a coarsened mesh, also referred to as "MESH-COARSE". Meshes (ii) and (iii) are derived from the baseline mesh by imposing a global scale factor (0.75 and 1.5, respectively) in the meshing software, by which

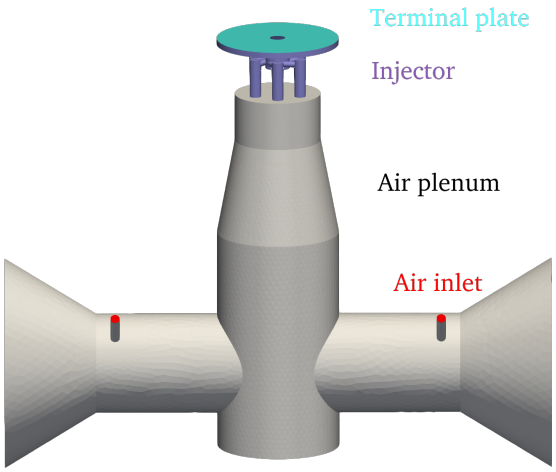

Figure 3.10: Numerical domain of the unconfined SICCA combustor used for the grid independence study. The ambient air is represented by a large cylinder (not shown) into which the injected air is released.

all cell length scales are multiplied. The total number of nodes and cells is thus different for each mesh and is not proportional to the scaling factor.

The baseline mesh adopts the cell sizing of the confined SICCA combustor setup already presented in Sec. 3.3.1. Since no combustion chamber must be accounted for, it has a slightly lower node count (approximately 3.07 million), corresponding to 17.6 million tetrahedral cells. In turn, MESH-FINE features 4.9 million nodes and 28 million cells, MESH-COARSE only 0.9 million nodes and 5.3 million cells.

We impose the same boundary conditions for all simulations of the present grid independence study: all injector walls have a uniform temperature of $T_w = 300\,\mathrm{K}$, atmospheric pressure is imposed at the outlet of the cylinder representing the atmosphere, and air is injected at ambient temperature with a mass flow rate of $\dot{m} = 1.94\,\mathrm{g/s}$.

3.7.2 Results

Figure 3.11 illustrates the axial velocity (instantaneous and time-averaged) on the central cutplane through the injector and the atmosphere. These images were obtained from the baseline mesh configuration with pure air and no fuel injection. The swirling flow (swirl number $S = 0.68$) is accelerated while passing through the injector nozzle, exhibiting peak axial velocities of $u \approx +50\,\mathrm{m/s}$. In its core, it features a distinct inner recirculation zone (IRZ) emerging from the injector into the atmosphere ($u \approx -20\,\mathrm{m/s}$) which is prone to substantially affect fuel injection, as we shall see in Sec. 4.3.4. By contrast, the outer recirculation zone (ORZ) exhibits close to zero axial velocities.

In comparing the numerical velocity profiles of all meshes to experimental data, we can examine the impact of the grid resolution on the flow. Mean and root mean square (RMS) profiles are sampled at $x = [2.5,\ 5,\ 10]\,\mathrm{mm}$ above the injector, which are plotted in Fig. 3.12 and Fig. 3.13, respectively. The averaging duration $t_{avg} = 60\,\mathrm{ms}$ is identical for all simulations. Experimental measurements were performed by seeding oil droplets in the air flow to serve as tracers, since no fuel is injected.

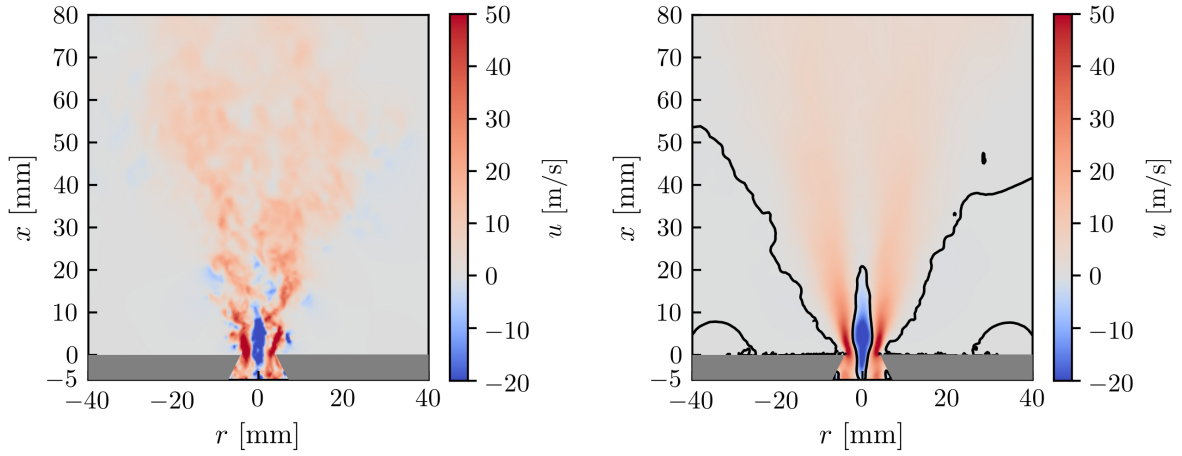

(a) Instantaneous axial velocity

(b) Time-averaged ($t_{avg} = 60\,\mathrm{ms}$) axial velocity and iso-contour of $u = 0\,\mathrm{m/s}$

Figure 3.11: Axial air flow velocity on the central cutplane through the injector and atmosphere (baseline mesh). A central recirculation zone is seen to emerge from the injector into the atmosphere. No fuel is injected at the atomizer in this configuration.

In general, we can observe a good agreement between the mean axial velocity profiles at all three axial distances above the injector. Similarly, mean azimuthal velocity profiles are also retrieved by the simulations with good accuracy. Although the mesh resolution appears to have an almost negligible impact on the prediction of mean velocity profiles, it is more pronounced when comparing RMS profiles between experiment and simulations. Peak RMS velocities are moderately overestimated by all meshes and at all axial distances, though MESH-COARSE appears to be the least accurate of all. Conversely, all profiles of the baseline mesh are essentially identical to those of MESH-FINE. We thus conclude that the baseline mesh is already capable of a sufficient flow resolution at reasonable computational costs. It is therefore preferred over the computationally more expensive MESH-FINE (due to no significant improvement), and also over the less accurate MESH-COARSE. Hence, we employ the mesh sizing of the baseline mesh for the remainder of this work.

3.8 Summary

Lab-scale combustion devices constitute a crucial enabling step for academic research of dynamic combustion phenomena. MICCA-Spray and SICCA — the main combustor configurations introduced in this chapter — represent idealized versions of industrial designs, sharing some of their characteristic features while still allowing for optical access.

In this chapter, we have presented the numerical domain considered for light-round simulations in MICCA-Spray, along with the corresponding domain of the SICCA combustor. The numerical setup, boundary conditions and solution schemes were specified, which are common to all simulations in this work. Case-specific differences are detailed later. For light-round ignition in MICCA-Spray, two individual cases are considered: (i) light-round ignition with cold combustor walls ($T_w = 300\,\mathrm{K}$), and (ii) light-round ignition with preheated combustor walls, with wall temperatures determined from Conjugate Heat Transfer simulations during steady state operation.

Furthermore, we have highlighted the simplified numerical ignition procedure, involving

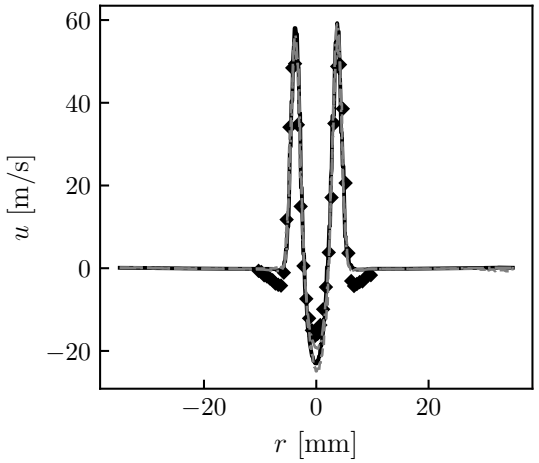

(a) Axial velocity at $x = 2.5\,\mathrm{mm}$

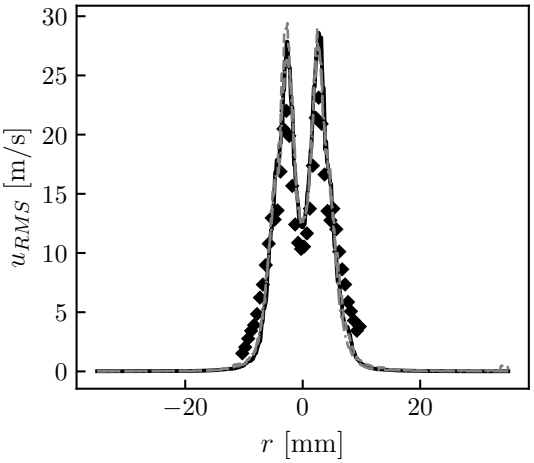

(b) Axial RMS velocity at $x = 2.5\,\mathrm{mm}$

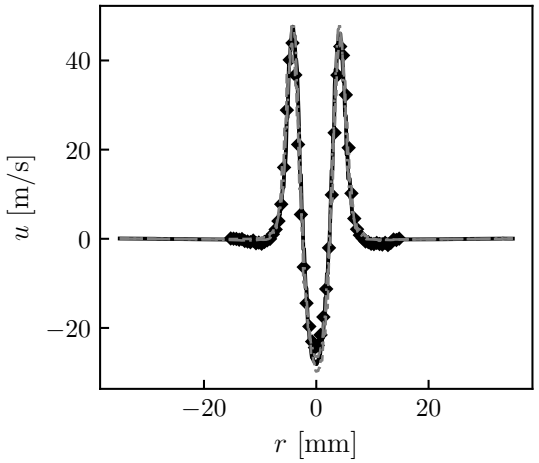

(c) Axial velocity at $x = 5\,\mathrm{mm}$

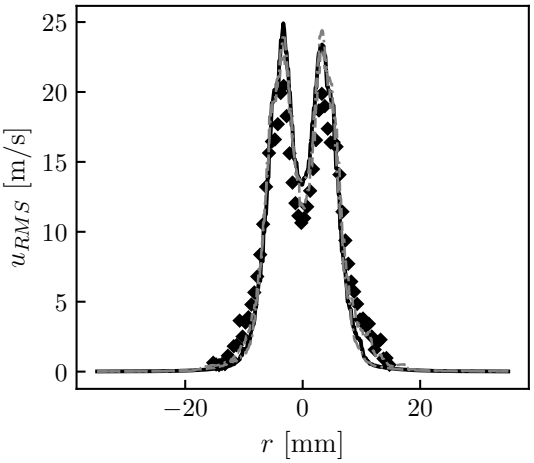

(d) Axial RMS velocity at $x = 5\,\mathrm{mm}$

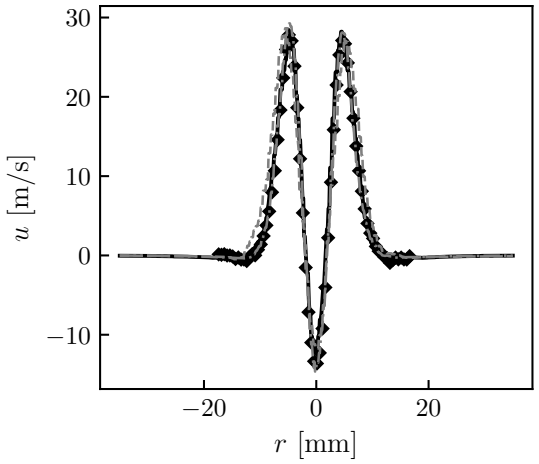

(e) Axial velocity at $x = 10\,\mathrm{mm}$

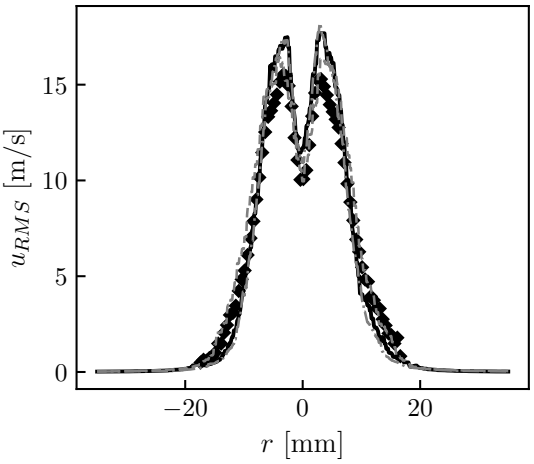

(f) Axial RMS velocity at $x = 10\,\mathrm{mm}$

Figure 3.12: Mean and RMS axial velocity profiles sampled at $x = 2.5\,\mathrm{mm}$ ((a), (b)), $x = 2.5\,\mathrm{mm}$ ((c), (d)) and $x = 2.5\,\mathrm{mm}$ ((e), (f)) above the injector. Symbols: experimental measurements; solid black lines: baseline mesh; dashed gray lines: MESH-COARSE; dash-dotted gray lines: MESH-FINE.

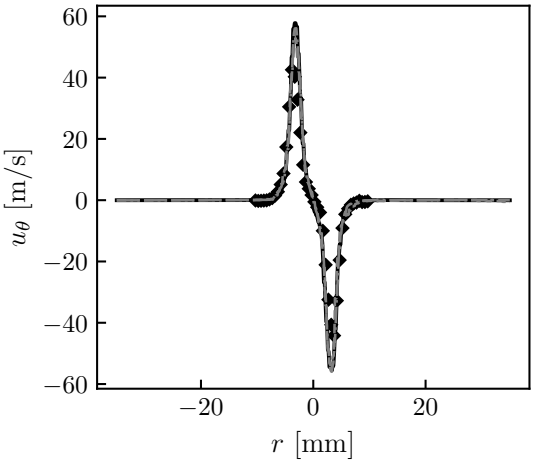

(a) Azimuthal velocity at $x = 2.5\,\mathrm{mm}$

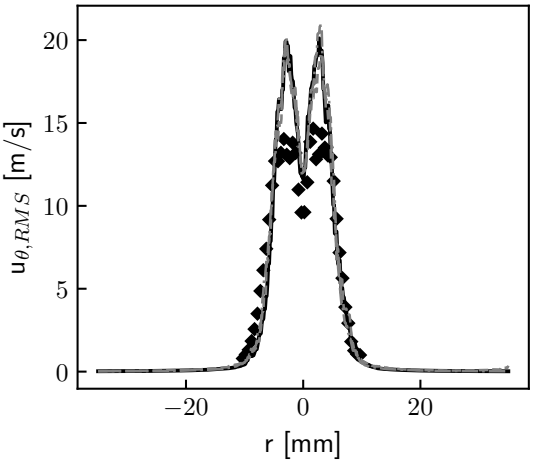

(b) Azimuthal RMS velocity at $x = 2.5\,\mathrm{mm}$

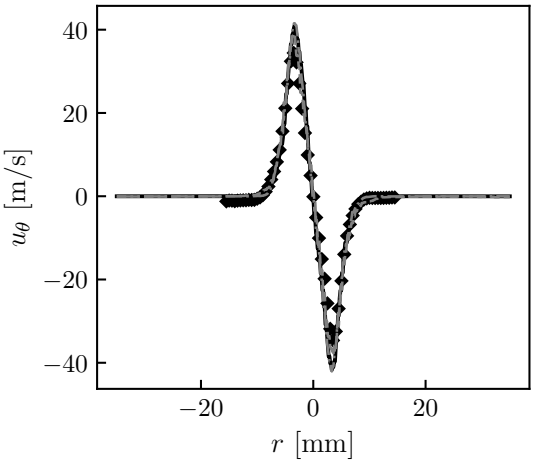

(c) Azimuthal velocity at $x = 5\,\mathrm{mm}$

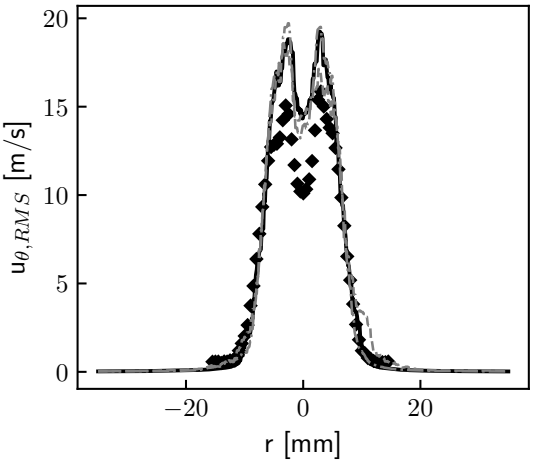

(d) Azimuthal RMS velocity at $x = 5\,\mathrm{mm}$

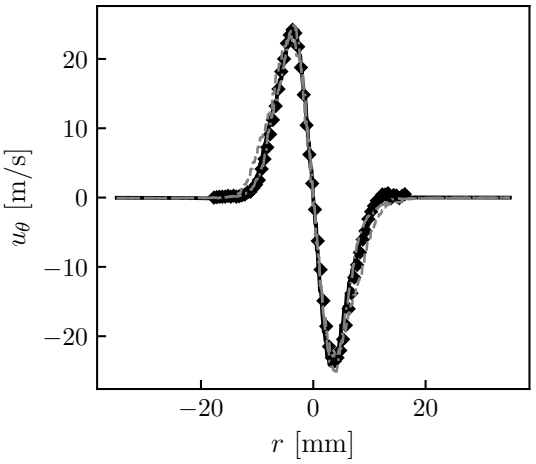

(e) Azimuthal velocity at $x = 10\,\mathrm{mm}$

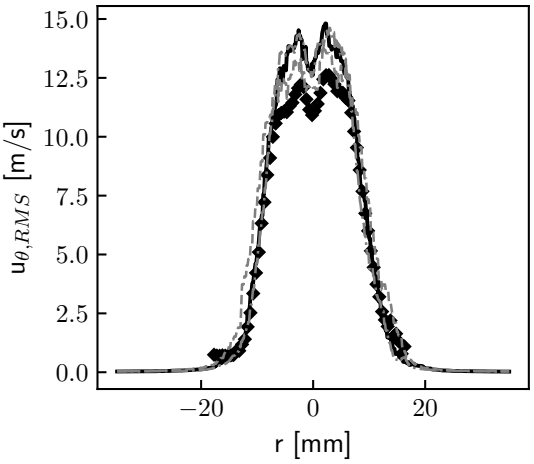

(f) Azimuthal RMS velocity at $x = 10\,\mathrm{mm}$

Figure 3.13: Mean and RMS azimuthal velocity profiles sampled at $x = 2.5\,\mathrm{mm}$ ((a), (b)), $x = 2.5\,\mathrm{mm}$ ((c), (d)) and $x = 2.5\,\mathrm{mm}$ ((e), (f)) above the injector. Symbols: experimental measurements; solid black lines: baseline mesh; dashed gray lines: MESH-COARSE; dash-dotted gray lines: MESH-FINE.

either a deposition of hot burnt gases (as in MICCA-Spray), or an energy deposition model (in SICCA). Although different from the experimental ignition method (electric spark plug), they serve the purpose of providing robust and reliable means for ignition in our simulations. We have clarified that the early stages of flame kernel development are intentionally neglected, since they are beyond the scope of this work and would certainly require different modeling approaches (*e.g.*, in terms of the selected kinetic scheme).

Finally, we have validated the computational meshes for air flow simulations by comparing simulated velocity profiles to experimental data.

Chapter 4

Enhancements for liquid phase models for fuel injection and evaporation

In most commercial aero-engines, liquid fuel is typically injected as a spray. Modeling spray generation however involves complex physical processes with high demands for computational resources, which would render their simulation unfeasible. For light-round simulations, some of these processes are less important and are often omitted by invoking the dilute spray assumption. It allows to focus the modeling efforts on processes relevant in the injector far-field such as evaporation or dispersion. Droplet evaporation is expressed through the Abramzon-Sirignano evaporation model in this work. However, its implementation into the AVBP solver cannot account for variable gas phase properties encountered along a droplet's trajectory upon injection into an igniting combustor. To avoid large errors in the predicted evaporation times, we propose an improved implementation where variable Schmidt and Prandtl numbers of droplet films are evaluated from polynomial functions, rather than defined as constants. In this manner, we can conveniently include variable carrier gas properties at reasonable computational costs. Further enhancements of the liquid phase description are achieved through calibration of the fuel injection model. Given the dilute spray assumption, we inject a pre-atomized spray which must reproduce select spray characteristics in the injector far-field as best as possible. This is achieved by a phenomenological fuel injection model, which is calibrated with experimental data.

Contents

4.1 Introduction

Our focus in this chapter is an accurate description of the two-phase flow in SICCA, which is also extremely relevant for light-round simulations in MICCA-Spray. With previous works in mind (Collin-Bastiani, 2019b), we adopt a polydisperse Euler-Lagrange setup, along with the Abramzon-Sirignano evaporation model (Abramzon and Sirignano, 1989) and a phenomenological fuel injection model (FIM-UR). Given the importance of droplet characteristics for flame propagation during ignition, we address the variability of carrier gas properties along a droplet's trajectory, which in turn can critically affect the evaporation rates. Therefore, we present an improved implementation of the evaporation model in Sec. 4.2, which is a cornerstone of this work.

Similarly, we perform a calibration of the fuel injection model based on experimental data, in order to replicate the droplet spray as best as possible. A detailed presentation of the calibration procedure in SICCA and the selection of optimal injection parameters is the subject of Sec. 4.3. Simulations rely on the baseline mesh validated in Sec. 3.7.2.

4.2 Extension of the evaporation model to variable droplet film properties

One question we have intentionally left open in Sec. 2.6.3 is the determining of transport properties of the gas phase during evaporation of liquid fuel. We have noted that the carrier gas properties critically affect heat and mass transfer rates, and along with that, the fuel droplets' evaporation time. These properties are known to influence the flame speed in multiphase combustion (Sacomano Filho et al., 2019), and most importantly, the light-round duration, as discussed later in Sec. 6.5.4.

We recall the equations for heat and mass transfer of evaporating droplets (Abramzon and Sirignano, 1989)

$$\dot{m} = 2\pi d_p \rho D \, \ln(1 + B_\mathrm{M}) \qquad \text{(2.82 (revisited))}$$

$$m_p C_{p,liq} \frac{dT_p}{dt} = \pi d_p \lambda \mathrm{Nu}^\star (T_\infty - T_\zeta) \frac{\ln(1 + B_\mathrm{T})}{B_\mathrm{T}} - \dot{m} \Delta h_v \qquad \text{(2.127 (revisited))}$$

which depend on the diffusion coefficient of the gas phase ρD, and the corresponding thermal conductivity λ. These properties are expressed through correlations with Schmidt and Prandtl numbers in AVBP (as mentioned in Sec. 2.6.3) to avoid a more complex evaluation of detailed

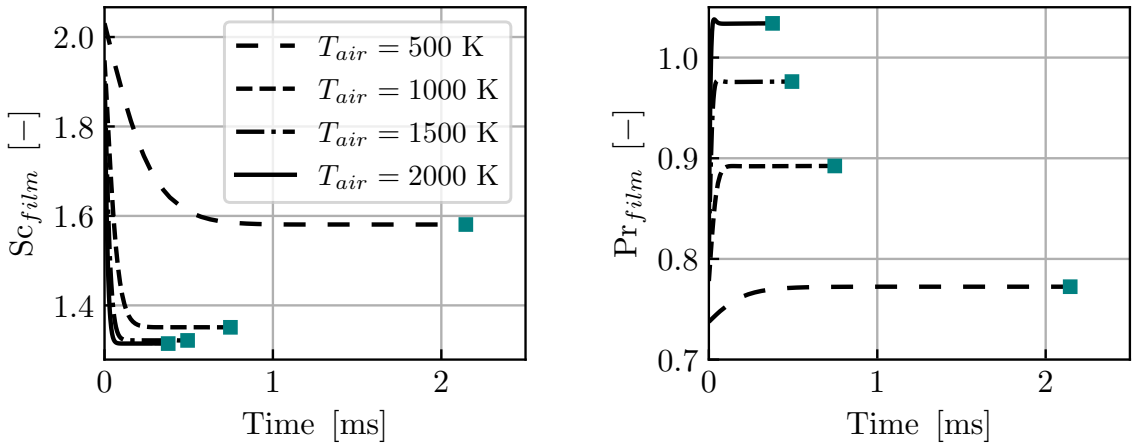

(a) Temporal evolution of the vapor film Schmidt number.

(b) Temporal evolution of the vapor film Prandtl number (line styles as in (a)).

Figure 4.1: Evolution of Schmidt and Prandtl numbers of a vapor film around an evaporating droplet of n-heptane at initial temperature $T_{d,0} = 300\,\mathrm{K}$ and droplet diameter $d_0 = 15\,\mu\mathrm{m}$. The droplet is exposed to pure air at four different temperatures. Square markers correspond to the respective evaporation time.

transport properties (as derived by Bird et al. (2002)). Thus, we use the following definitions

$$\rho D = \frac{\mu(T_{ref})}{\mathrm{Sc}} \qquad \text{(2.83 (revisited))}$$

$$\lambda = \frac{C_p \mu(T_{ref})}{\mathrm{Pr}} \qquad \text{(2.92 (revisited))}$$

where the viscosity is evaluated at the reference temperature according to the third-rule (see Eq. 2.119). Remaining unknowns are the Sc and Pr numbers; determining these quantities is the subject of the following discussion.

Running evaporation simulations with the EM2C in-house solver AGATH with detailed transport properties allows to assess the variation of the Schmidt and Prandtl numbers of a vapor film around an evaporating droplet. Figure 4.1 shows their temporal evolution for a quiescent droplet of n-heptane with an initial temperature and diameter set to $T_{d,0} = 300\,\mathrm{K}$ and $d_0 = 15\,\mu\mathrm{m}$ respectively, and four different air temperatures T_{air}, which remain constant with time. The instant of full evaporation is marked with a square for each case. As expected, the higher the air temperature, the shorter the evaporation time. Moreover, Sc_{film} decreases with increasing air temperature from an initial value of $\mathrm{Sc}_{film} = 2.1$ (see Fig. 4.1(a)), whereas we observe the opposite trend for Pr_{film} with an initial value of $\mathrm{Pr}_{film} = 0.73$ in Fig. 4.1(b). Constant Sc_{film} and Pr_{film} are found upon reaching the wet-bulb state after a transient time, which depends on the air temperature.

Hannebique et al. (2013) have proposed to use the final Schmidt and Prandtl numbers *at wet-bulb state* obtained from precursor detailed evaporation simulations as constants in Eqs. 2.83 and 2.92. For example, if a droplet of n-heptane is evaporating in pure air at $T_{air} = 500\,\mathrm{K}$, the imposed values should be $\mathrm{Sc}_{film} = 1.58$ and $\mathrm{Pr}_{film} = 0.77$, corresponding to the square markers of the sparsely dashed curves in Fig. 4.1(a) and (b). However, this strategy implicitly assumes an approximately constant carrier gas temperature or composition to justify *constant* values for Sc_{film} and Pr_{film} in the LES code. Avoiding the evaluation of detailed transport properties in this manner is certainly a reasonable compromise for simulations

of spray injection into a stationary carrier gas (either pure air or burnt gases). In turn, droplets may encounter fresh *and* burnt gases during light-round ignition, which conflicts with the assumption of constant carrier gas properties. More specifically, due to the presence of a *propagating* flame, droplets are likely to undergo more substantial changes of carrier gas properties along their trajectory, which necessarily affect their vapor film properties as well. For example, droplets trapped in the recirculation zone between adjacent injectors *upstream* of the propagating flame front may evaporate in an air/fuel mixture, while droplets injected *downstream* of the flame front evaporate in burnt gas conditions. Therefore, we propose computing variable Sc_{film} and Pr_{film} values from polynomial functions as outlined in the following section.

4.2.1 Evaluation of Sc_{film} and Pr_{film} based on polynomial functions

Essentially, we assume that Sc_{film} and Pr_{film} can be uniquely parameterized by the normalized film temperature Θ and the fuel mass fraction $Y_{\mathrm{C_7H_{16}}}$ in the droplet film, which are already computed by the LES solver. Independent of the droplet state, which can be in its heat-up phase or wet-bulb state, we define two polynomial functions

$$\mathrm{Sc}_{film}^{poly}(\Theta, Y_{\mathrm{C_7H_{16}}}) = \sum_{i,j}^{N} c_{i,j}^{\mathrm{Sc}} \cdot \Theta^i \cdot Y_{\mathrm{C_7H_{16}}}^j \tag{4.1}$$

$$\mathrm{Pr}_{film}^{poly}(\Theta, Y_{\mathrm{C_7H_{16}}}) = \sum_{i,j}^{N} c_{i,j}^{\mathrm{Pr}} \cdot \Theta^i \cdot Y_{\mathrm{C_7H_{16}}}^j \tag{4.2}$$

In the above equations $c_{i,j}^{\mathrm{Sc}}$ and $c_{i,j}^{\mathrm{Pr}}$ denote the respective fit coefficients for $\mathrm{Sc}_{film}^{poly}$ and $\mathrm{Pr}_{film}^{poly}$. The order N is deliberately chosen to be identical for both monomials (Θ and $Y_{\mathrm{C_7H_{16}}}$) and is discussed later. Normalization of Θ is introduced to remap its value range to [0, 1] using $T_{min} = 280\,\mathrm{K}$ and $T_{max} = 2300\,\mathrm{K}$

$$\Theta = \frac{T_{film} - T_{min}}{T_{max} - T_{min}} \tag{4.3}$$

In this manner, both Θ and $Y_{\mathrm{C_7H_{16}}}$ have the same value range, yielding more accurate fit functions. We recall that the film temperature T_{film} is evaluated according to the third-rule. The following preprocessing steps are then required to obtain the fit coefficients, and eventually the polynomial functions for $\mathrm{Sc}_{film}^{poly}$ and $\mathrm{Pr}_{film}^{poly}$:

1. We compute Sc_{film}^{ref} and Pr_{film}^{ref} for *generic* droplet films parameterized by Θ and $Y_{\mathrm{C_7H_{16}}}$ with detailed transport properties in AGATH. This step only requires the evaluation of purely gaseous mixture properties for a given n-heptane/air mixture and does *not* involve simulations of evaporating droplets. Tuples of Θ and $Y_{\mathrm{C_7H_{16}}}$ are generated between zero and unity: Θ is varied through variation of T_{film} in steps of $20\,\mathrm{K}$, and $Y_{\mathrm{C_7H_{16}}}$ is varied in steps of 0.01. We implicitly assume that linear mixing rules apply to the droplet film.

2. The generic Sc_{film}^{ref} and Pr_{film}^{ref} data obtained from step (1) is used to determine the fit coefficients $c_{i,j}^{\mathrm{Sc}}$ and $c_{i,j}^{\mathrm{Pr}}$ in Eqs. 4.1 and 4.2 by means of polynomial regression. We compute the least-squares solution to the linear matrix equation $Ax = b$ by minimizing its Euclidean 2-norm $\|b - Ax\|$. Each row in A contains all products of $\Theta^i \cdot Y_{\mathrm{C_7H_{16}}}^j$ up to the highest monomial order, x contains the fit coefficients, and b all Schmidt (or Prandtl) numbers of step (1). The equation system is given explicitly in Appendix A.

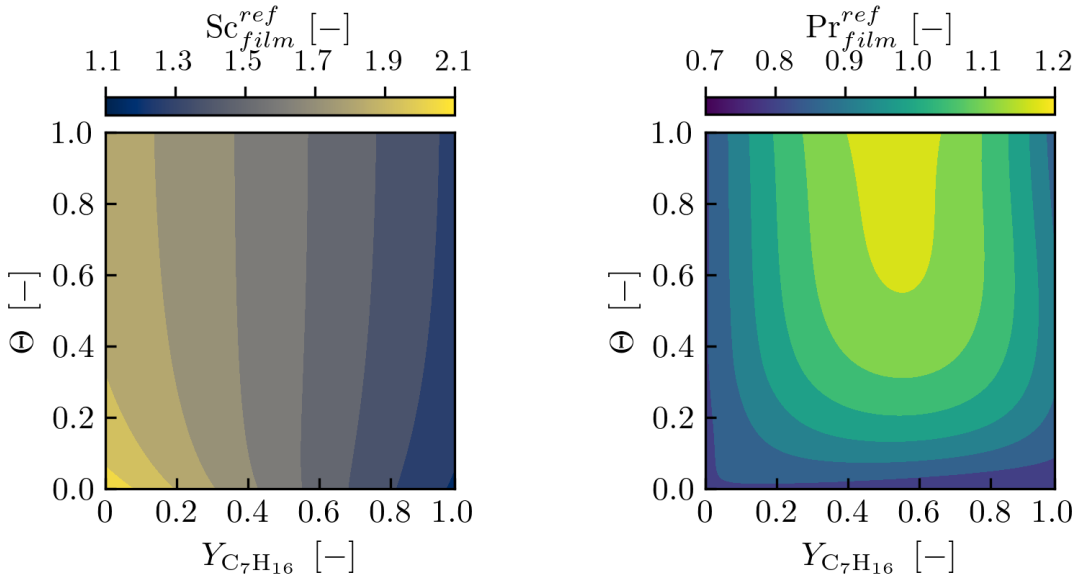

(a) Schmidt number as a function of the fuel mass fraction $Y_{\mathrm{C_7H_{16}}}$ and dimensionless temperature Θ. (b) Prandtl number as a function of the fuel mass fraction $Y_{\mathrm{C_7H_{16}}}$ and dimensionless temperature Θ.

Figure 4.2: Sc_{film}^{ref} and Pr_{film}^{ref} of generic n-heptane/air mixtures (purely gaseous) with detailed transport properties according to step (1).

3. The fit coefficients $c_{i,j}^{\mathrm{Sc}}$ and $c_{i,j}^{\mathrm{Pr}}$ from step (2) are implemented in AVBP and a routine is added to compute $\mathrm{Sc}_{film}^{poly}$ and $\mathrm{Pr}_{film}^{poly}$ according to Horner's rule (Horner, 1819), before proceeding with the evaluation of the heat and mass transfer equations (Eqs. 2.82 and 2.127). For higher order polynomials, Horner's rule outperforms a "naive" implementation of a polynomial function. Henceforth, we will refer to this approach as polynomial evaporation model.

Figure 4.2 visualizes Sc_{film}^{ref} and Pr_{film}^{ref} of generic n-heptane/air mixtures with detailed transport properties according to step (1). While the Schmidt number varies mostly with the fuel mass fraction $Y_{\mathrm{C_7H_{16}}}$ and barely with temperature (see Fig. 4.2(a)), the Prandtl number exhibits a distinct ridge at $Y_{\mathrm{C_7H_{16}}} \approx 0.55$ and $\Theta \gtrsim 0.6$ (see Fig. 4.2(b)).

These Schmidt and Prandtl numbers are subsequently approximated with bivariate polynomials according to step (2). In the present work, the monomial order is set to $N = 3$ (*i.e.* in Θ and $Y_{\mathrm{C_7H_{16}}}$) to avoid undesired oscillations of the polynomial functions (Burnham and Anderson, 2002) while still predicting Sc_{film} and Pr_{film} with reasonable accuracy. The relative error of each polynomial fit function (Eqs. 4.1 and 4.2) compared to the reference data of step (1) can be evaluated with different error metrics. For example, we can define a global metric based on the 2-norm as

$$\epsilon_{N=3}^{\mathrm{Sc}} = \frac{\left\| \mathrm{Sc}_{film}^{poly} - \mathrm{Sc}_{film}^{ref} \right\|_2}{\left\| \mathrm{Sc}_{film}^{ref} \right\|_2} = 0.0021897 \tag{4.4}$$

where $\mathrm{Sc}_{film}^{poly}$ are the Schmidt numbers computed according to Eq. 4.1, and Sc_{film}^{ref} the reference values from step (1). Similarly, we find $\epsilon_{N=3}^{\mathrm{Pr}} = 0.0031338$ for the Prandtl number. Note that the error is worse for a monomial order of $N = 2$ ($\epsilon_{N=2}^{\mathrm{Sc}} = 0.005273$ and $\epsilon_{N=2}^{\mathrm{Pr}} = 0.021873$, not shown). Apart from a global metric, we can also compute a relative fit error as $(\mathrm{Sc}_{film}^{poly} - \mathrm{Sc}_{film}^{ref})/\mathrm{Sc}_{film}^{ref}$ (and analogously for the Prandtl number) for given tuples of

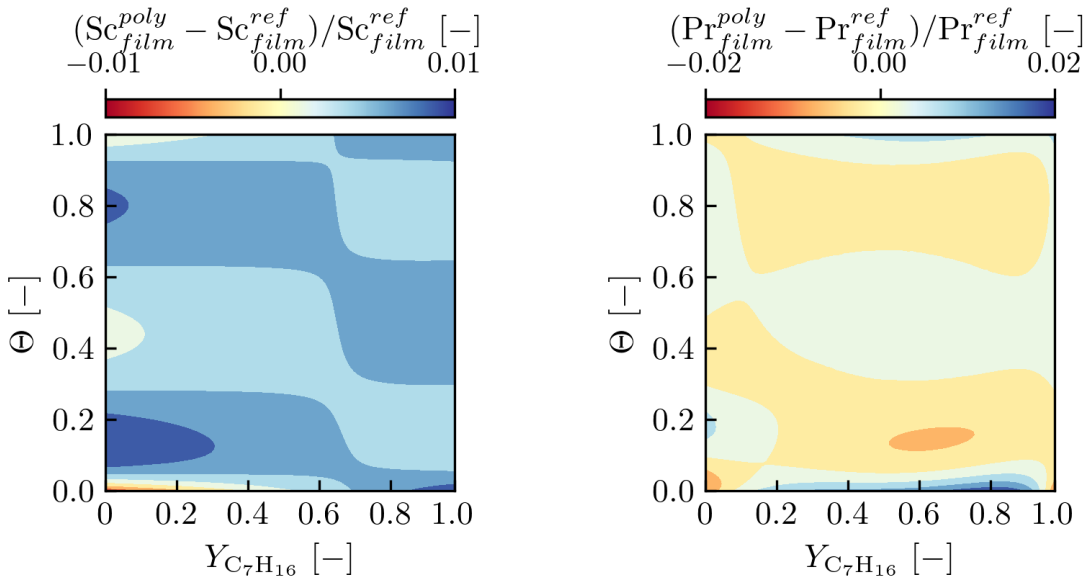

(a) Fit error of the predicted Schmidt number.

(b) Fit error of the predicted Prandtl number.

Figure 4.3: Relative fit error of the bivariate polynomial functions ($N = 3$) with respect to the reference data.

$Y_{C_7H_{16}}$ and Θ, which is illustrated in Fig. 4.3. For both dimensionless quantities, we find a relative error below 2% across the parameter range under consideration. This is a noticeable improvement over a monomial order of $N = 2$ with relative errors of up to 13% in the predicted Prandtl number (not shown). We attribute this behavior to the distinct peak in the evolution of Pr^{ref}_{film} (see Fig. 4.2(b)), which can be more accurately approximated with $N = 3$, rather than $N = 2$.

In spite of a fairly good match, we have so far only assessed the accuracy of the *fit procedure* for the *same* data points Θ and $Y_{C_7H_{16}}$ that we used to compute the reference data of step (1). Of main interest, however, is the polynomial model's accuracy in terms of the predicted droplet evaporation time t_{evap} for an *arbitrary* set of film parameters (Θ and $Y_{C_7H_{16}}$). Therefore, precursor evaporation simulations are performed in AGATH to benchmark the polynomial evaporation model as detailed in the following section.

4.2.2 Validation of the polynomial evaporation model

Published experimental data on evaporating n-heptane droplets is mostly available for very specific conditions, which are not representative of the operating conditions of the SICCA and MICCA-Spray combustor. Consequently, we have to proceed in two steps to assess the accuracy of the polynomial evaporation model in terms of t_{evap}, as summarized in Tab. 4.1: the first step involves a validation of the simulation case "SIM1" against experimental data (labeled as "EXP") by Chauveau et al. (2019) for same conditions. Second, evaporation simulations with the polynomial evaporation model ("POLY1" and "POLY2") are carried out for conditions relevant for this work and compared to reference simulations ("REF1" and "REF2") relying on detailed transport properties. While all simulations (carried out in AGATH) employ the Abramzon-Sirignano evaporation model (Abramzon and Sirignano, 1989), they differ in the computation of the carrier gas properties. We provide an overview of the employed models and the solved equations in each simulation in Tab. 4.2. Note that the same fit coefficients and additional routines for the polynomial evaporation model used in AVBP have also been

Case	$T_{d,0}$ [K]	d_0 [µm]	ϕ_∞ [−]	T_∞ [K]	Carrier gas
EXP	300	500	-	[473, 548, 623, 748]	nitrogen
SIM1	300	500	-	[473, 548, 623, 748]	nitrogen
REF1	300	15	$0.5 - 1.2$	$300 - 2000$	n-heptane/air
REF2	300	15	$0.5 - 1.2$	$400 - 2400$	burnt gases
POLY1	300	15	$0.5 - 1.2$	$300 - 2000$	n-heptane/air
POLY2	300	15	$0.5 - 1.2$	$400 - 2400$	burnt gases

Table 4.1: Initial conditions for experimental and numerical evaporation of n-heptane under atmospheric pressure. SIM1 replicates the conditions found in published experimental data, while the remaining cases emulate typical conditions found in SICCA and MICCA-Spray. $T_{d,0}$ denotes the initial droplet temperature, d_0 the initial droplet diameter, and ϕ_∞ and T_∞ the far-field equivalence ratio and temperature of the gas phase. The carrier gas composition is given in the last column.

Case	Heat and mass transfer	Transport properties
SIM1	Eqs. 2.82 and 2.127	detailed
REF1	Eqs. 2.82 and 2.127	detailed
REF2	Eqs. 2.82 and 2.127	detailed
POLY1	Eqs. 2.82 and 2.127	Eqs. 2.83, 2.92, 4.1, 4.2
POLY2	Eqs. 2.82 and 2.127	Eqs. 2.83, 2.92, 4.1, 4.2

Table 4.2: Overview of evaporation models for validation and error assessment.

implemented in AGATH for the sake of this validation.

Starting with the comparison of SIM1 and EXP, we plot the dimensionless droplet diameter $(d/d_0)^2$ during its evaporation time in Fig. 4.4. Filled symbols correspond to simulations in AGATH, while open symbols correspond to experimental data by Chauveau et al. (2019) in pure nitrogen and atmospheric pressure. After an initial droplet heat-up time, we observe a linear decrease of $(d/d_0)^2$ consistently with the D^2 law (see Eq. 2.101). Full evaporation is thus reached when $(d/d_0)^2 = 0$. Upon comparing filled and open symbols, we note that the simulations underestimate the droplet evaporation time at lower nitrogen temperatures, but become fairly accurate at higher temperatures. Given such discrepancies, it is worth emphasizing that the variation in the experimental data is quite substantial depending on the source. For example, data published by Nomura et al. (1996) indicates an almost two times faster evaporation at nitrogen temperatures of $T = 471\,\mathrm{K}$ (see dash-dotted line in Fig. 4.4) compared to the (approximately) identical case ($T = 473\,\mathrm{K}$) in Chauveau et al. (2019). While both studies were carried out under microgravity, discrepancies have also been found under normal gravity, likely due to heat conduction through the droplet support fiber (Chauveau et al., 2019). In light of a considerable spread in the experimental data set, the accuracy of the predicted evaporation time from simulations is acceptable.

Next, we evaluate the accuracy of the predicted evaporation time for conditions relevant for SICCA and MICCA-Spray. Simulations are carried out according to the parameter range specified in the second part of Tab. 4.1. Droplets of n-heptane are exposed to a mixture of pre-vaporized n-heptane and air of varying mixture equivalence ratios ϕ_∞ and temperatures T_∞, which are not to be confused with the properties of a droplet's vapor film. Computing a relative error between the predicted evaporation times of cases POLY1 and REF1 for each tuple of (T_∞, ϕ_∞), we obtain the error map in Fig. 4.5(a). As expected, evaporation times are

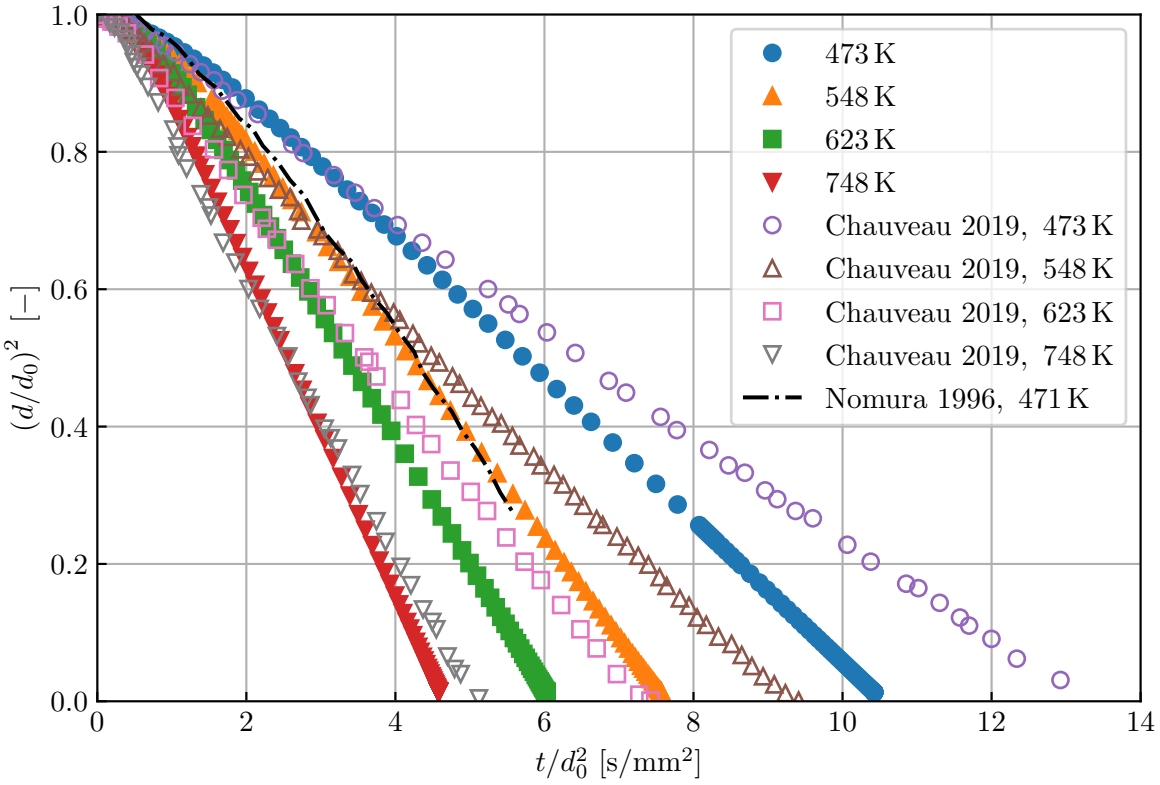

Figure 4.4: Comparison of normalized droplet diameter during evaporation in nitrogen at different temperatures: filled symbols: simulations carried out with AGATH according to conditions in Tab. 4.1 (SIM1). Open symbols: experimental data by Chauveau et al. (2019) according to conditions in Tab. 4.1 (EXP). Dash-dotted line: experimental data by Nomura et al. (1996).

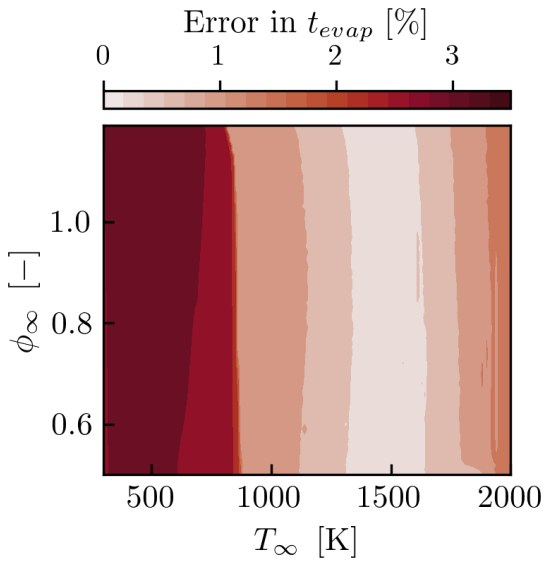

(a) Relative error in t_{evap} for droplet evaporation in an air/heptane mixture based on simulations POLY1 and REF1.

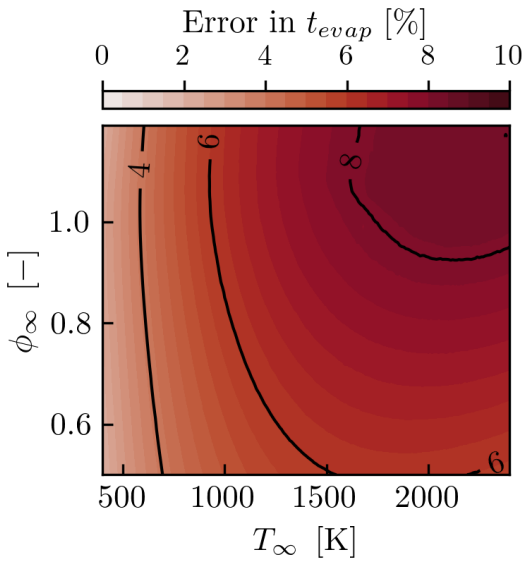

(b) Relative error in t_{evap} for droplet evaporation in burnt gases based on simulations POLY2 and REF2.

Figure 4.5: Error assessment of the evaporation time t_{evap} of a n-heptane droplet (initial diameter $d_0 = 15\,\mu\text{m}$, initial temperature $T_{d,0} = 300\,\text{K}$) predicted by the polynomial evaporation model compared to reference data: (a) evaporation in an air/heptane mixture for varying mixture temperatures T_∞ and equivalence ratios ϕ_∞. (b) Evaporation in a burnt gas mixture resulting from adiabatic combustion of n-heptane and air at mixture temperatures T_∞ and equivalence ratios ϕ_∞.

found to be in good agreement between the polynomial evaporation model and the reference data computed with detailed transport properties. The relative error is approximately 3% at worst and appears to decrease with increasing mixture temperature.

Of particular interest is the polynomial model's accuracy in burnt gas mixtures, since it is constructed from film properties sampled from n-heptane/air mixtures (see Sec. 4.2.1, step (1)). Proceeding in a similar fashion as in the previous comparison, we compute the relative error of evaporation times predicted by the cases POLY2 and REF2 in burnt gas conditions. The corresponding error map is plotted in Fig. 4.5(b). Interestingly, we observe only moderately higher relative errors of up to 8%, which are found at rich burnt gas mixtures ($\phi_\infty \geq 1$) and high burnt gas temperatures ($T_\infty \geq 1800\,\text{K}$). Given a moderately increased computational overhead due to the evaluation of polynomial functions instead of using constant values for Sc_{film} and Pr_{film} as in Hannebique et al. (2013), the agreement between the polynomial evaporation model and the reference data is fairly good.

For the sake of completeness, evaporation simulations based on the polynomial evaporation model have also been performed in AVBP and compared to the same reference data (REF1 and REF2) we used above. The existing tool "`EVOL_EVAPOD`" was forked to account for variable Schmidt and Prandtl numbers of the droplet film as done in AGATH. Evaporation simulations were carried out (in "`EVOL_EVAPOD_POLY`") for select tuples of ϕ_∞ and T_∞ to ensure a correct evaporation time retrieval as with AGATH.

4.2.3 Discussion

For a thorough evaluation of the polynomial evaporation model, it is worth discussing alternative formulations, which have not been considered or implemented here. In particular, the following choices for the parametrization of Sc_{film} and Pr_{film} have been tested along with a variation of the monomial order N, but discarded eventually due to poorer accuracy or performance:

- **No interaction terms:** for the approximation of the reference data with bivariate polynomials (see Sec. 4.2.1, step (2)), a separate set of fit coefficients has been computed. The polynomial functions are still based on Θ and $Y_{\mathrm{C_7H_{16}}}$, however all interaction terms are neglected in the polynomial regression procedure. The resulting polynomials consist of only $(N+1)(N+2)/2$ terms (instead of $(N+1)^2$ for bivariate polynomials with all interaction terms), but the accuracy of such approximation was found to deteriorate considerably. The highest relative error of the Prandtl number increases up to 16% for $N=3$ (not shown), compared to 2% with interaction terms (as shown in Fig. 4.3(b)).

- **Trivariate polynomial in Θ, Z and c:** in order to represent the state of the droplet vapor film more adequately regardless of its composition (n-heptane/air mixture or burnt gases), $Y_{\mathrm{C_7H_{16}}}$ has been replaced by the film mixture fraction Z and the film progress variable c for the parametrization of the Schmidt and Prandtl numbers. Unfortunately, their evolution in this three-dimensional parameter space is less smooth and particularly difficult to approximate with a trivariate polynomial, resulting in a relative fit error of the Prandtl number of 6% with $N=3$. The increase of polynomial terms over a bivariate polynomial function with a better accuracy renders this approach less attractive.

- **Trivariate polynomial in Θ, Y_{N2} and Y_{CO2}:** similar to the previous attempt, parametrization has been tested with the nitrogen (Y_{N2}) and carbon dioxide (Y_{CO2}) mass fraction in the vapor film instead of the fuel mass fraction. However, the relative fit error of the Prandtl number was found to increase to 12% with a trivariate polynomial and $N=3$.

Beyond polynomial functions, different strategies could certainly be devised to compute the carrier gas properties without solving complex equations for detailed transport. A comparably inexpensive approach in terms of numerical costs has been pursued in Collin-Bastiani (2019b), acknowledging the strong variability of carrier gas properties during light-round ignition. First, precursor evaporation simulations of a n-heptane droplet evaporating in air at different air temperatures T_∞ are carried out using the Abramzon-Sirignano model with detailed transport properties. Second, the evaporation simulations are repeated with constant Sc_{film} and Pr_{film} values used in Eqs. 2.83 and 2.92. These values are chosen such that they minimize the error in the evaporation time at two arbitrary target temperatures compared to the previous simulations with detailed transport properties. Although Sc_{film} and Pr_{film} are still taken at wet-bulb conditions (as in Hannebique et al. (2013)), they are no longer sampled at the same air temperature T_∞. Instead, the imposed Schmidt number is $\mathrm{Sc}_{film}(T_\infty = 1100\,\mathrm{K}) = 1.3431$, and the Prandtl number is $\mathrm{Pr}_{film}(T_\infty = 1500\,\mathrm{K}) = 0.97648$. In this manner, the predicted evaporation time is found to best match the evaporation times obtained with detailed transport properties for target temperatures $T_{\infty,1} = 300\,\mathrm{K}$ and $T_{\infty,2} = 1500\,\mathrm{K}$. These two target temperatures reflect to some extent the variable air temperatures a droplet may be exposed to along its trajectory.

Nevertheless, the accuracy of the predicted evaporation times deteriorates in burnt gas conditions, even more severely than the polynomial evaporation model. In an intermediate temperature range of $T_\infty \approx 500\,\mathrm{K}$ to $T_\infty \approx 1300\,\mathrm{K}$, an error of up to 22% can be found (see

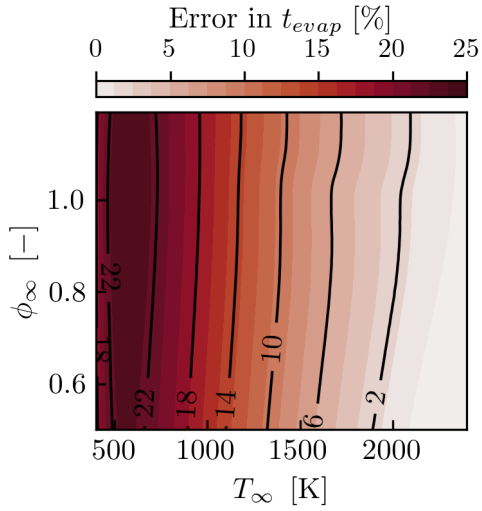

Figure 4.6: Relative error in the predicted evaporation time for evaporation of a n-heptane droplet in burnt gases of variable burnt gas temperature T_∞ and ϕ_∞. Constant Schmidt and Prandtl numbers ($\mathrm{Sc}_{film}(T_\infty = 1100\,\mathrm{K}) = 1.3431$ and $\mathrm{Pr}_{film}(T_\infty = 1500\,\mathrm{K}) = 0.97648$) are imposed as in Collin-Bastiani (2019b).

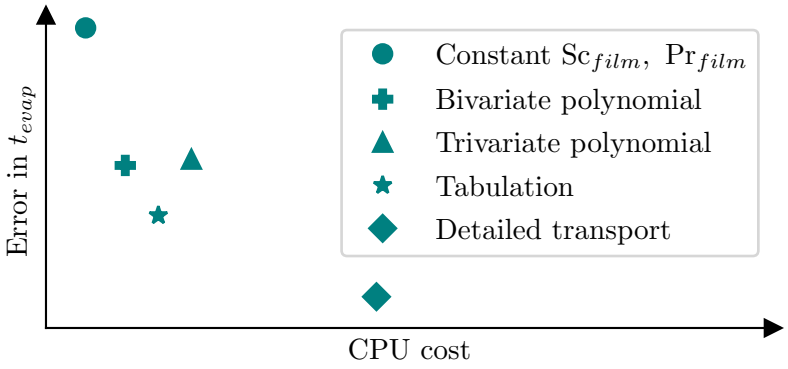

Figure 4.7: Ranking of model approaches for the computation of carrier gas properties in terms of error in evaporation time t_{evap} and CPU cost.

Fig. 4.6). Therefore, we consider the polynomial evaporation model as an improvement over imposing constant Schmidt and Prandtl numbers.

Finally, we note that tabulation of Sc_{film} and Pr_{film} as functions of *e.g.*, Θ, Z and c would also be an inexpensive option with good accuracy. However, such an approach would have required even more code development for multi-dimensional table interpolation and I/O routines, which are not natively available in AVBP. Alternatively, the EM2C in-house library COMMCOMB could have been used, which provides generic interpolation routines, but was not considered at that stage yet, mainly due to the fairly good results of the polynomial evaporation model.

We conclude from the previous discussion that the polynomial evaporation model presented in Sec. 4.2.1 strikes a reasonable balance between accuracy and computational cost, as visualized in Fig. 4.7. Bivariate polynomials rank considerably better than approaches relying on constant Schmidt and Prandtl numbers, or trivariate polynomials, both in terms of accuracy *and* cost. For future implementations, tabulation of Sc_{film} and Pr_{film} would certainly offer further improvements without unreasonably increasing the computational costs.

4.3 Calibration of the fuel injection model

Throughout the previous section, we have specifically addressed an improved description of droplet evaporation, owing to its importance for spray flame ignition. Although certainly not decoupled from evaporation, mixing and dispersion can be greatly affected by the spray generation process as well, which we have briefly discussed in Sec. 2.6.6. However, modeling all physics involved in the generation of the final droplet spray exceeds our computational resources due to the complexity of the combustor. Instead, we invoke the dilute spray assumption, as it simplifies the research problem (Masri, 2016): in dilute sprays, it is reasonable to neglect atomization, breakup or coalescence in favor of accurately modeling evaporation or mixing, which constitute the main phenomena of interest in this work. Nevertheless, key spray characteristics of real sprays must still be reproduced in an adequate manner, such as droplet diameter distributions or spray shapes, often requiring *ad-hoc* models. In order to achieve this goal, a parameter calibration of the modified FIM-UR model (Vignat et al. (2021), see Sec. 2.6.6.2) is necessary, which is the subject of the following sections. This step is certainly not universal and only valid for the present injection system and operating conditions. Yet it has revealed interesting aspects related to droplet/flow interactions and droplet/flame interactions that are worth discussing.

4.3.1 Experimental configuration and available data

The experimental configuration considered for data acquisition and numerical simulations is the SICCA-Spray combustor operated with n-heptane and air under atmospheric pressure. Contrary to reacting cases, no confinement is used to allow for unobstructed optical access to the flow. Thus, the fuel/air mixture is directly released into the ambient air at rest. Mass flow rates are set to represent the operating conditions encountered during light-round ignition in MICCA-Spray ($\dot{m}_{fuel} = 0.1111\,\mathrm{g/s}$, $\dot{m}_{air} = 1.94\,\mathrm{g/s}$). The same simplex pressure-swirl atomizer is used as in all other cases in this work, along with the terminal plate with an integrated nozzle (see Fig. 3.2(b)).

The principal challenge of the present calibration procedure arises from the spray's extreme sensitivity to the atomizer's axial position: on one hand, light-round experiments are carried out with a recessed atomizer ($x_A = 5.9\,\mathrm{mm}$, see Fig. 3.3), allowing for additional droplet/wall interactions (with the nozzle wall), before droplets enter the combustion chamber. On the other hand, the original FIM-UR model (Sanjosé et al., 2011) approximates hollow-cone sprays generated by simplex atomizers *without* any droplet/wall interactions, and would mandate a flush mounted atomizer for calibration purposes as in (Lancien, 2018; Collin-Bastiani, 2019a), *i.e.* $x_A \equiv 0\,\mathrm{mm}$ in Fig. 3.3. However, such a calibration would yield a poor representation of the droplet spray in the combustion chamber, once the parameters are applied to the desired recessed atomizer configuration. Two major reasons can be cited: first, we have no information about the additional droplet/wall interactions, which would occur with a recessed atomizer. Neither are these physics accounted for by the FIM-UR model. Second, the flow *inside* the injector critically depends on the axial position x_A of the atomizer and is prone to affect the spray characteristics as well. Since we prioritize an accurate representation of the spray in the combustion chamber, experiments and calibration simulations are both carried out with a recessed atomizer ($x_A = 5.9\,\mathrm{mm}$), despite the FIM-UR model being used in an "off-design" point. In this manner, we attempt to reproduce the experimental droplet spray as best as possible, without having to impose arbitrary injection parameters as in *e.g.,* Paulhiac et al. (2020). We also assume that the unconfined spray is a reasonable representation of the spray that we would encounter with a confinement, *i.e.* a quartz tube.

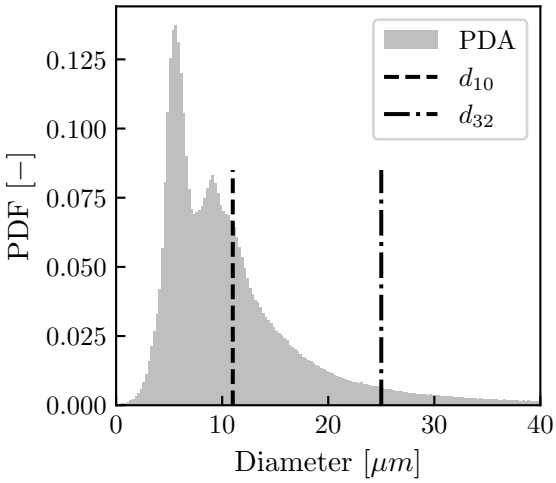

Figure 4.8: Experimentally measured droplet size distribution at $x = 5\,\mathrm{mm}$ above the combustor backplane and $r = 5\,\mathrm{mm}$ from the axis of rotation.

Detailed PDA measurements have been performed by Dr. G. Vignat, giving access to droplet size and velocity distributions at three different heights above the terminal plate and multiple radial positions. The probe volume has approximate dimensions of $0.14\,\mathrm{mm} \times 0.14\,\mathrm{mm} \times 0.23\,\mathrm{mm}$. In the simulations, we use a sphere of $R = 0.1\,\mathrm{mm}$ radius (yielding approximately the same volume), and apply azimuthal averaging for more homogeneous statistics.

A probability density function (PDF) of the experimental droplet size distribution measured at $x = 5\,\mathrm{mm}$ above the combustor backplane and $r = 5\,\mathrm{mm}$ from the axis of rotation is plotted in Fig. 4.8. The distribution exhibits a primary peak at $d = 5.5\,\mu\mathrm{m}$, and a much less pronounced peak at $d = 9.1\,\mu\mathrm{m}$. The mean diameter is $d_{10} = 11\,\mu\mathrm{m}$, and the Sauter Mean Diameter (SMD) is $d_{32} = 25\,\mu\mathrm{m}$.

4.3.2 Numerical domain and mesh

Figure 4.9 illustrates the numerical domain used for calibration simulations. As mentioned in the previous section, the numerical domain represents the unconfined SICCA combustor with the same injector configuration as used in all other simulations. Unlike the setup presented in Sec. 3.7.1, liquid n-heptane is now injected through the atomizer. Similar to reacting simulations, mesh refinement is performed above the terminal plate, with cell sizes ranging between $0.2\,\mathrm{mm}$ (right at the terminal plate) to $0.7\,\mathrm{mm}$ (at $5\,\mathrm{cm}$ above the terminal plate). The mesh around the atomizer is even further refined, with cell sizes set to $0.13\,\mathrm{mm}$. The entire mesh contains approximately 3.07 million nodes, corresponding to 17.6 million tetrahedral cells. Note that each numerical droplet represents one physical droplet throughout the entire simulations, consistent with all other simulations in this work.

4.3.3 Outline of the calibration strategy

We recall the four main parameters of the modified FIM-UR model (see Sec. 2.6.6.2), which have to be determined: the main injection half-angle θ, the deviation angle $\delta\theta$, the injection velocity u_{inj} and the time delay τ for evaporation correction of the measured droplet PDF. While we do not present the full test matrix that has led to the final parameter set, we highlight

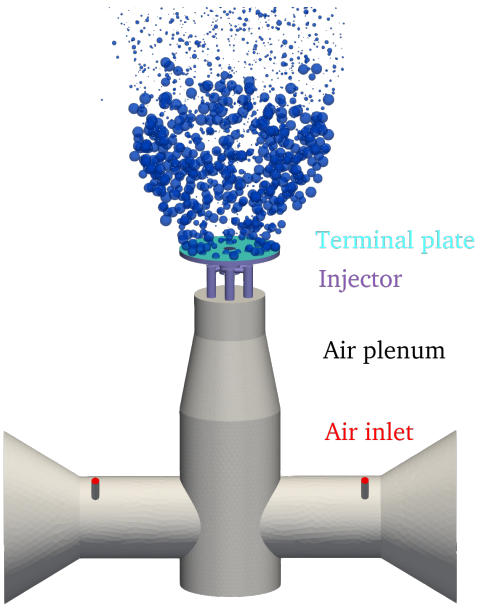

Figure 4.9: Numerical domain used for the calibration of the injection model. The ambient air is represented by a large cylinder (not shown) into which the fuel/air mixture is released. Some droplets are added for visualization purposes only (not to scale).

two specific cases, which can be assigned to two different regimes, as we shall see.

Multiple iterations were necessary to establish an optimal setup, following a four-step procedure. First, the half-angle θ and the deviation angle $\delta\theta$ are fixed. This sets the nominal injection angle for a given droplet at the time of its injection ("droplet birth") through random sampling from a Gaussian distribution with a θ-mean and a standard deviation of $\pm\delta\theta$.

Second, the injected diameter distribution must be imposed, which is derived from experimental measurements. As a starting point, we use the probability density function of droplet sizes (also referred to as "droplet PDF") measured at $x = 5\,\mathrm{mm}$ relative to the combustor backplane and $R = 5\,\mathrm{mm}$ from the axis of rotation. Most importantly, this measured droplet PDF is evaporation-corrected, owing to droplets having started to evaporate along their trajectory from the atomizer to the measurement position, thus decreasing in size. A droplet size correction is performed for each bin of the measured droplet PDF by solving the D^2-law (see Eq. 2.101) for the initial injection diameter d_0. The evaporation constant $\lambda_{d^2} = 0.0165\,\mathrm{mm}^2/\mathrm{s}$ (see Eq. 2.102) is taken from Chauveau et al. (2019) for n-heptane at $T = 300\,\mathrm{K}$. An initial guess must be made for the time delay τ appearing in the D^2-law, which is refined later. The evaporation correction can thus be understood as a PDF shift of the measured droplet PDF towards *larger* droplet diameters. Eventually, the size of each injected droplet in the simulation is sampled from the evaporation-corrected droplet size distribution.

Third, an initial guess is made for the droplet injection velocity (at droplet birth), which is assigned to each newly injected droplet regardless of its size. The injection velocity is chosen as the last parameter to be varied.

Fourth, Large-Eddy Simulations of fuel injection (without combustion) are carried out for a given parameter set for at least $100\,\mathrm{ms}$. Finally, droplet statistics are sampled from the simulation and compared to experimental data in order to evaluate the appropriateness of the chosen parameter set and make changes to the setup if required.

At this point, it is also important to mention that the parameter choices and their iterative refinement have been guided by a complementary air flow analysis and a study of specific droplet characteristics, rather than a scattershot approach. These are addressed in

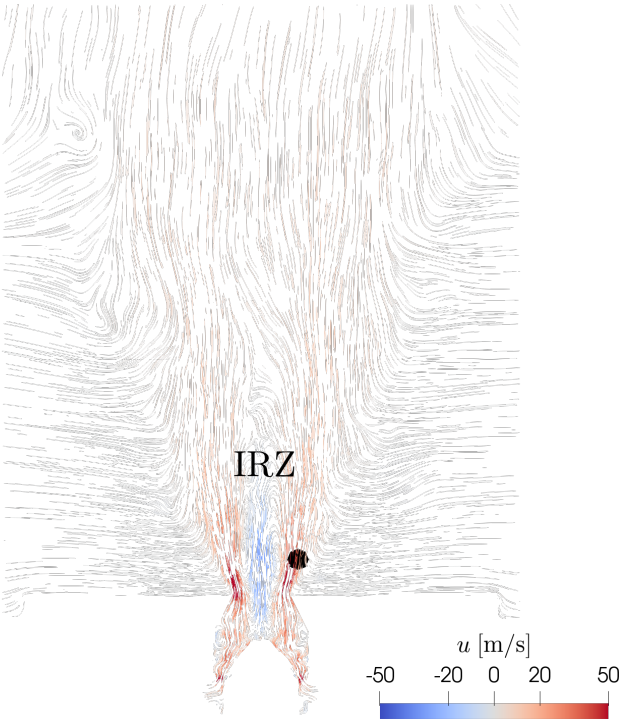

Figure 4.10: Averaged velocity streamlines colored by the axial velocity component u. A black dot marks the sampling position of the droplet PDF. The internal recirculation zone is marked as IRZ.

the following sections.

4.3.4 Air flow and droplet trajectory analysis

A closer examination of Fig. 4.10, showing surface streamlines of the time-averaged gas velocity (averaging duration $t_{avg} = 15\,\mathrm{ms}$), aids a better understanding of the mean flow direction. The streamlines are colored by the axial velocity component u, which takes negative values for a downward directed flow, and positive values in the opposite case. Similar to pure air flow simulations *without* fuel injection (see Sec. 3.7.2), we can observe a strong internal recirculation zone (IRZ) in Fig. 4.10, emerging from the atomizer tip into the atmosphere and reaching $u \approx -30\,\mathrm{m/s}$. Conversely, the air flow exiting the injector is found to have larger positive velocities of up to $u \approx +50\,\mathrm{m/s}$ in the vicinity of the nozzle edge. Moreover, the exiting air flow also entrains the quiescent ambient air, which follows the upward flow direction. Since the general flow features resemble the configuration observed in Sec. 3.7.2, we assert that the dispersed phase leaves the macroscopic air flow virtually undisturbed.

The presence of a strong internal recirculation zone however suggests that droplets injected at the atomizer tip are likely to be immediately subjected to negative axial velocities and thus deviate from their initial injection direction determined by θ. In order to infer the general droplet behavior, we define droplet *classes* and evaluate their respective Stokes numbers. We recall that droplets with $\mathrm{St} > 1$ tend to have a ballistic trajectory, which is barely influenced by the air flow, whereas for $\mathrm{St} < 1$, droplets behave as tracers, essentially following the air flow. The Stokes number can be expressed as the ratio between a characteristic droplet relaxation time τ_p (see Eq. 2.73), and a convective time τ_{TOF} (Vignat et al., 2021)

$$\mathrm{St} = \frac{\tau_p}{\tau_{\mathrm{TOF}}} \tag{4.5}$$

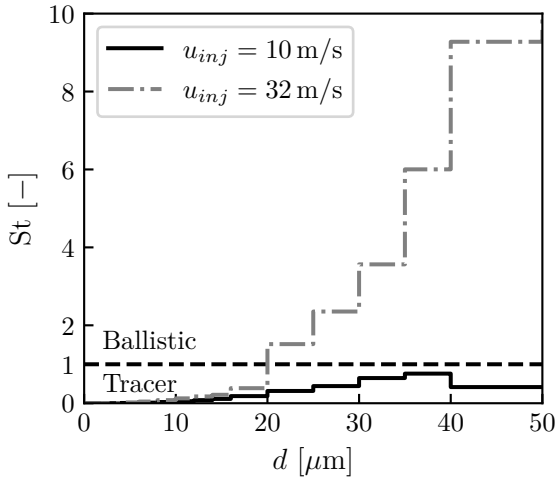

Figure 4.11: Averaged droplet Stokes number per droplet class for two different droplet injection velocities. The dashed lines classifies droplets into tracers, if $\mathrm{St} < 1$, or ballistic droplets, if $\mathrm{St} > 1$.

For this post-processing step, we evaluate τ_p at the instant of injection, where the relative velocity difference between a droplet and the local flow is largest. τ_TOF corresponds to the time-of-flight (TOF) from the atomizer tip to an arbitrary location, *e.g.,* the measurement position of the droplet PDF (black dot in Fig. 4.10). This time is computed for each droplet by means of Lagrangian particle tracking. Plotting an averaged Stokes number per droplet class in Fig. 4.11, where each class consists of droplets of similar sizes, reveals valuable information about the general droplet behavior: for injection velocities of $u_{inj} = 10\,\mathrm{m/s}$ (solid curve), all droplet classes exhibit $\mathrm{St} < 1$. We can therefore expect all droplets to behave as tracers and follow the air flow, rather than keeping their initially assigned direction θ and injection velocity. However, if we increase the injection velocities ($u_{inj} = 32\,\mathrm{m/s}$, dash-dotted curve), larger droplets will fall into the ballistic regime ($\mathrm{St} > 1$), specifically droplet classes with $d > 20\,\mu\mathrm{m}$ diameter.

In order to further substantiate this argument, we plot droplet trajectories for two injection half-angles, which have been studied here (see Fig. 4.12). In the first case, we impose $\theta = 26°$ such that the initial droplet direction is targeting the experimental measurement position of the droplet PDF (corresponding to the diamond marker). In the second case, we use $\theta = 40°$, targeting the nozzle edge of the terminal plate.

Figure 4.13 shows simulated trajectories of individual droplets as circle markers colored by the instantaneous and local axial droplet velocity. A spatial succession of circles represents the position of a given droplet at *different* time steps. We have deliberately selected only those droplets that cross the measurement position $x = 5\,\mathrm{mm}$ and $R = 5\,\mathrm{mm}$ at any given time after injection. The circle sizes are proportional to the instantaneous droplet sizes, but do not represent the droplets to scale. The left column of Fig. 4.13 shows droplet classes with initial diameters of $d_0 \leq 6\,\mu\mathrm{m}$ ((a), (c), (e)), and $d_0 > 20\,\mu\mathrm{m}$ in the right column ((b), (d), (f)).

Comparing the trajectories of the small droplets to the straight dash-dotted line given by θ (left column of Fig. 4.13) reveals that virtually all droplets deviate from their initial trajectory. More specifically, the droplets inside the injector are displaced in radial direction following the swirling air motion, until they have fully left the internal recirculation zone (see *e.g.,* the red arrow labeled as (1) in Fig. 4.13(a)). They are subsequently entrained by the exiting air flow and necessarily collide with the nozzle wall, where they start to form a thin liquid wall film (as

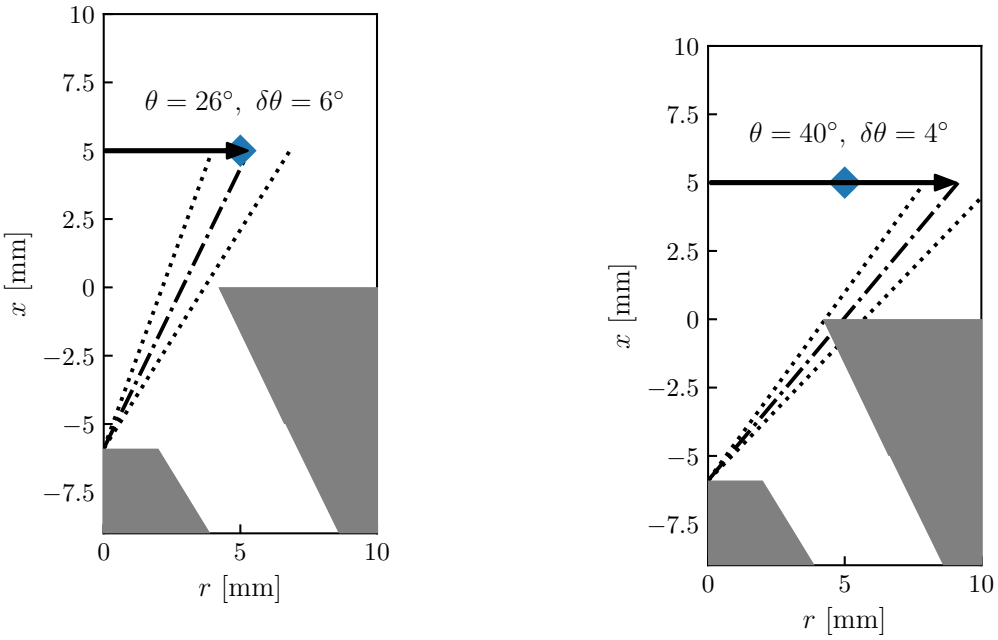

(a) Injection half-angle targeting the measurement position.

(b) Injection half-angle targeting the nozzle edge.

Figure 4.12: Sketch of nominal injection half-angle θ (dash-dotted line) and deviation angle $\delta\theta$ (dotted lines) in two different configurations. The vertical axis doubles as axis of rotation. The smaller trapezoid (lower left corner) represents half of the atomizer tip, the larger trapezoid (right corner) represents the nozzle integrated into the terminal plate. The sampling position used for the main droplet PDF is marked with a diamond.

defined by the local boundary condition). The air flow continuously transports the droplets to the nozzle edge (arrow labeled as (2)), where they detach from the nozzle wall and follow the general air flow direction (arrow labeled as (3)). Similar trajectories can be observed in Fig. 4.13(c) and (e) as well.

These images confirm that smaller droplets behave as tracers, regardless of their injection half-angle. Raising the injection velocity from $u_{inj} = 10\,\mathrm{m/s}$ (Fig. 4.13(a)) to $u_{inj} = 32\,\mathrm{m/s}$ (Fig. 4.13(e)) does not change their behavior either, consistently with our conclusion drawn from Fig. 4.11. Furthermore, larger droplets also behave as tracers if $u_{inj} = 10\,\mathrm{m/s}$, independently of θ (see Fig. 4.13(b) and (d)), as postulated earlier. Conversely, we clearly observe a ballistic behavior for $u_{inj} = 32\,\mathrm{m/s}$ (Fig. 4.13(f)), consistently with $\mathrm{St} > 1$ found in Fig. 4.11.

This analysis might suggest that the imposed injection parameters have little to no effect, as long as all droplets fall into the tracer regime. In that case, their trajectory is entirely governed by the air flow rather than the model parameters, which is most prominently visible once the droplets detach from the wall film and enter the atmosphere. Although it might appear that the calibration procedure is meaningless or unimportant under these circumstances, such conclusion would clearly be misguided.

Firstly, the full parameter matrix investigated for this work has revealed that similar results in terms of spray characteristics can be obtained through radically different model parameters. This is because, with phenomenological models, their parameters are not strictly determined by physical considerations, but instead by the user's choice to match *e.g.,* certain predefined metrics such as droplet size distributions. Similar results notwithstanding, these parameter sets will certainly differ in terms of their physical *fidelity*: for example, it is unlikely that all droplets exit the injector without interacting with the nozzle wall. Yet, a parameter combination can be

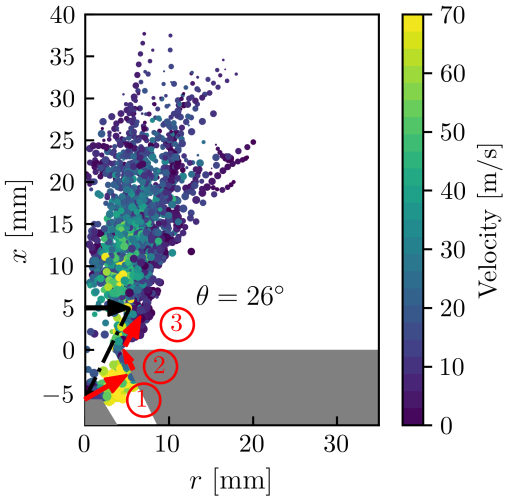

(a) $\theta = 26°$, $d_0 \leq 6\,\mu m$, $u_{inj} = 10\,m/s$

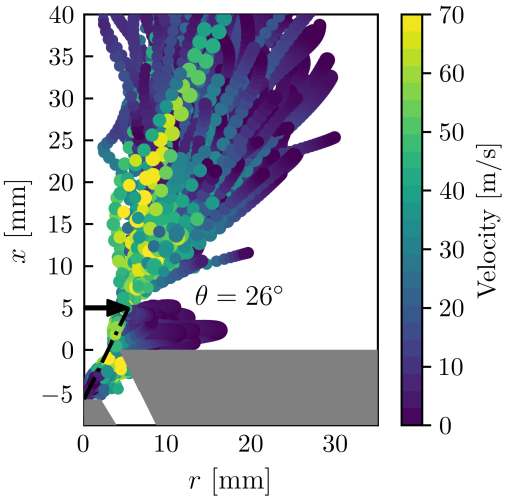

(b) $\theta = 26°$, $d_0 > 20\,\mu m$, $u_{inj} = 10\,m/s$

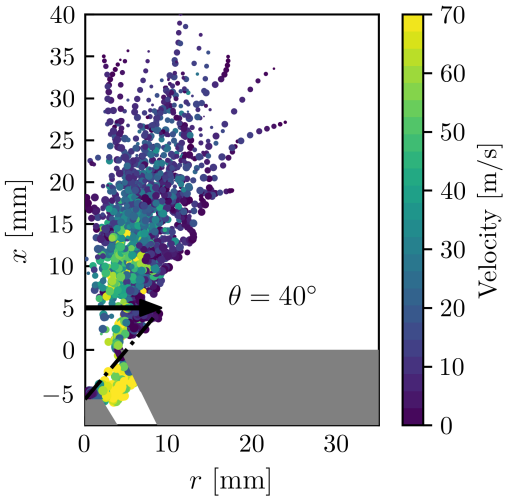

(c) $\theta = 40°$, $d_0 \leq 6\,\mu m$, $u_{inj} = 10\,m/s$

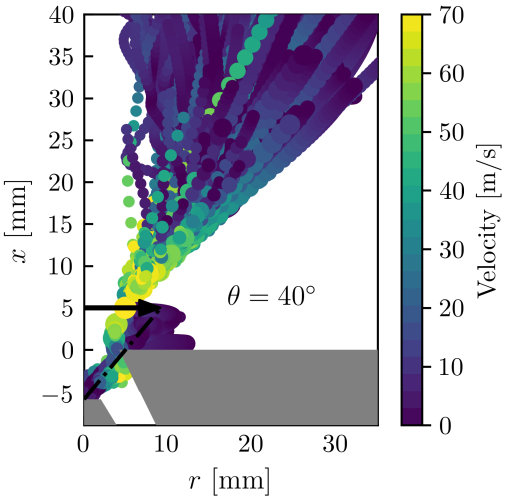

(d) $\theta = 40°$, $d_0 > 20\,\mu m$, $u_{inj} = 10\,m/s$

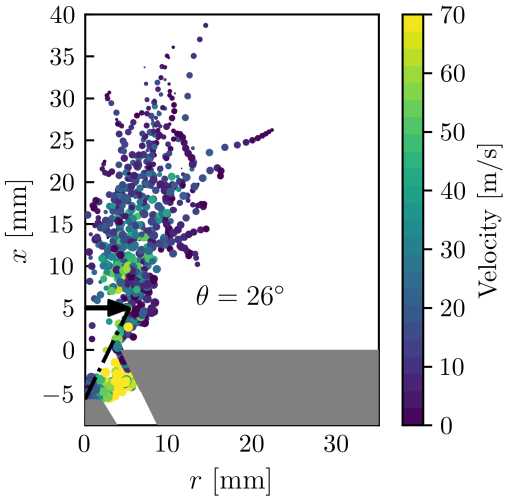

(e) $\theta = 26°$, $d_0 \leq 6\,\mu m$, $u_{inj} = 32\,m/s$

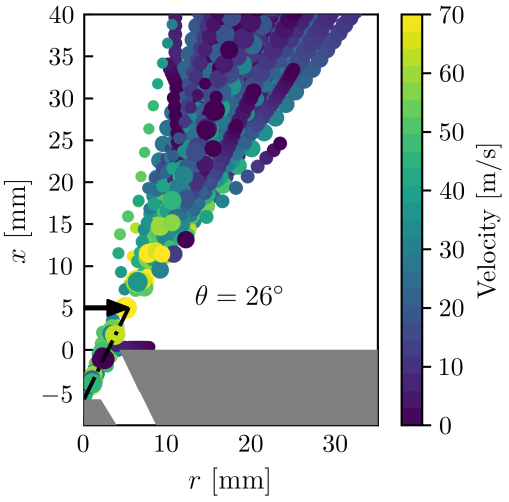

(f) $\theta = 26°$, $d_0 > 20\,\mu m$, $u_{inj} = 32\,m/s$

Figure 4.13: Droplet trajectories for different injection parameters (droplets not to scale).

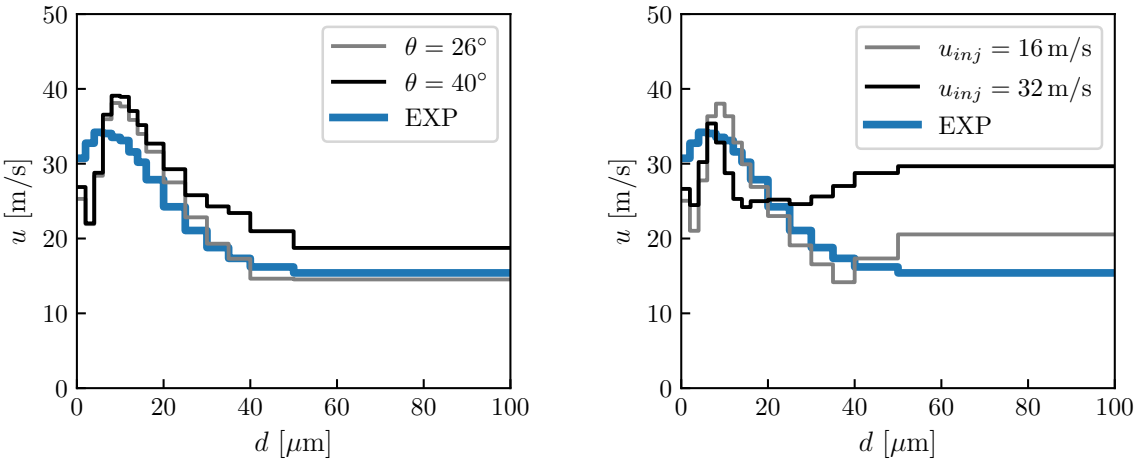

(a) Constant injection velocity.

(b) Constant injection angle.

Figure 4.14: Bin-averaged axial droplet velocities per droplet class compared to experimental data measured at $x = 5\,\mathrm{mm}$ and $R = 5\,\mathrm{mm}$: (a) impact of the injection angle at constant injection velocity $u_{inj} = 10\,\mathrm{m/s}$; (b) impact of the injection velocity at constant injection angle $\theta = 26°$.

imposed such that no wall interaction is taking place, while still matching droplet statistics at the measurement position, primarily through small injection half-angles, high injection velocities, and a more substantial evaporation-correction. Thus, identifying an optimal parameter set, which can also be justified from a physical standpoint, remains an important goal of the calibration procedure. Further discussion of this aspect can be found in Sec. 4.3.10.

Secondly, the injection model's accuracy in reproducing a spray should not be evaluated from droplet trajectories *alone*. Rather, additional metrics have to be taken into consideration, such as droplet velocities per class, local droplet size distributions or the radial droplet granulometry. These far-field properties, which are of principal interest, are addressed separately in the following sections. The impact on flame shapes is only briefly discussed, as their sensitivity to parameter variations is found to be weak.

4.3.5 Evaluation of droplet velocities per class

We start with a comparison of the droplet velocities in Fig. 4.14, sampled at the same location experimentally and numerically: $x = 5\,\mathrm{mm}$ above the combustor backplane and $R = 5\,\mathrm{mm}$ from the axis of rotation (see also black dot in Fig. 4.10). We sample all droplets which cross the specified location and plot their bin-averaged axial velocity component u for each bin (or droplet class). The experimental values are added in both images as thick line and serve as a reference. Smaller droplets exhibit the highest axial velocities, which are of the order of the air flow velocity ($u \approx 35\,\mathrm{m/s}$). Conversely, the impact of the gaseous flow motion gradually decreases with increasing droplet size, exhibiting $u \approx 15\,\mathrm{m/s}$ for the largest droplets.

This velocity distribution is a useful metric, which we attempt to match in the simulation as best as possible. In comparing the resulting droplet class velocities obtained from two injection half-angles in Fig. 4.14(a), we can observe a better agreement for $\theta = 26°$ (gray curve), rather than $\theta = 40°$ (black curve), particularly for larger droplets. The bin-averaged velocity of smaller droplets is moderately overestimated, regardless of the selected angle. Note that the injection velocity is intentionally kept constant ($u_{inj} = 10\,\mathrm{m/s}$) in both simulations. After repeating the same comparison at six more radial positions ($R = 2 - 8\,\mathrm{mm}$), we have

consistently found a better agreement between experiment and simulation with $\theta = 26°$.

As a next step, an appropriate injection velocity at *constant* injection half-angle must be determined. In Fig. 4.14(b), droplet class velocities of two additional simulations with $u_{inj} = 16\,\mathrm{m/s}$ and $u_{inj} = 32\,\mathrm{m/s}$ are shown, represented as thin gray and black curves, respectively. The experimental reference data is added as thick line. While the first simulation slightly improves the agreement at intermediate diameters ($d = 15 - 20\,\mu\mathrm{m}$), it overpredicts the axial velocity component for very large droplets. This undesired behavior is even more pronounced for $u_{inj} = 32\,\mathrm{m/s}$, since larger droplets now fall into the ballistic regime, as already illustrated in Fig. 4.13(f). Repeating the same comparison at other radial positions does not change the general conclusion either.

These results suggest that $\theta = 26°$ and $u_{inj} = 10\,\mathrm{m/s}$ constitute reasonable model parameters, at least in terms of the axial droplet velocity u. As we shall see in the following sections, a good agreement with experimental data is also achieved for *other* metrics using the same parameter set. Although we have not carried out a sensitivity analysis for the deviation angle $\delta\theta$ for all cases considered here, its influence was found to be very moderate. Therefore, we implicitly assume that a variation of $\delta\theta$ within reasonable bounds (as defined in Fig. 4.12) would not significantly change our conclusions. Thus, the retained value is $\delta\theta = 6°$.

4.3.6 Comparison of local droplet size distributions

Apart from droplet velocities, the local droplet size distribution constitutes yet another useful metric to facilitate an appropriate selection of injection model parameters. Reproducing an experimentally measured size distribution is arguably the most challenging task to achieve though: in reality, such distribution results from complex physical processes such as atomization, breakup, collisions or coalescence, which are deliberately ignored in phenomenological injection models for the sake of reducing computational costs. In turn, with the modified FIMUR model all of the aforementioned processes must be absorbed by the model parameters, notably a carefully chosen initial droplet size distribution, which we discuss later. We reiterate that such approach is generally acknowledged to be a reasonable compromise, allowing to focus the modeling efforts on processes relevant for combustor ignition, *i.e.* mixing, evaporation, dispersion or combustion (Masri, 2016).

In Fig. 4.15(a) we can examine if the previously identified injection parameters yielding good results in terms of droplet class velocities can *also* reproduce local droplet size distributions. We have included the experimental probability density function (PDF) of droplet sizes sampled at $x = 5\,\mathrm{mm}$ and $R = 5\,\mathrm{mm}$ (filled PDF, see also Fig. 4.8), which we first compare to the PDF obtained from the simulation (black curve). Interestingly, the PDF from LES is found to be in a remarkably good agreement with the experimental PDF, suggesting that the injection parameters ($\theta = 26°$ and $u_{inj} = 10\,\mathrm{m/s}$) constitute a suitable choice. Most noteworthy is a moderate overestimation at $d = 5.5\,\mu\mathrm{m}$, which is deemed to be acceptable in light of the present modeling approach.

However, it should be clarified that this result is expected: the initial droplet diameter at the moment of injection in LES is randomly sampled from the so-called evaporation-corrected PDF (labeled "Evap. corr." in the lower inset plot in Fig. 4.16). This size distribution is generated by taking the experimental measurement at $x = 5\,\mathrm{mm}$ and $R = 5\,\mathrm{mm}$ (filled PDF in Fig. 4.16), and subsequently shifting it towards *larger* droplet diameters (see red arrow in the lower inset plot in Fig. 4.16). Thus, the evaporation-corrected PDF and the experimental PDF have already a similar *shape*. We recall that droplet evaporation is the only physical process in LES, which affects the individual droplet sizes, as we do not account for droplet breakup or coalescence. Consequently, the injection model must ensure that droplets can undergo the

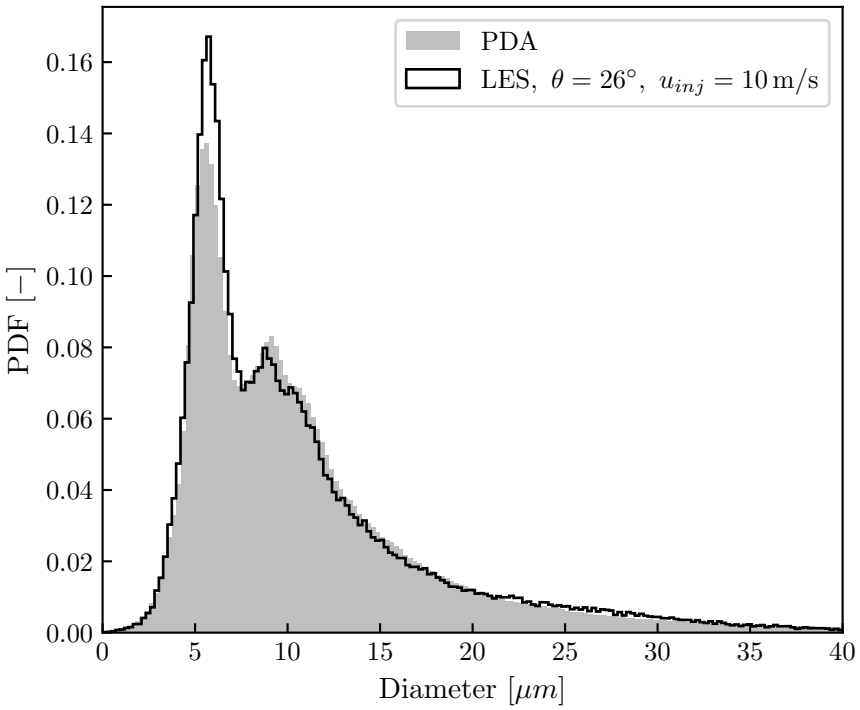

(a) Comparison between experimental measurement (filled PDF) and simulation (black curve) for an injection half-angle of $\theta = 26°$ and an injection velocity of $u_{inj} = 10\,\mathrm{m/s}$.

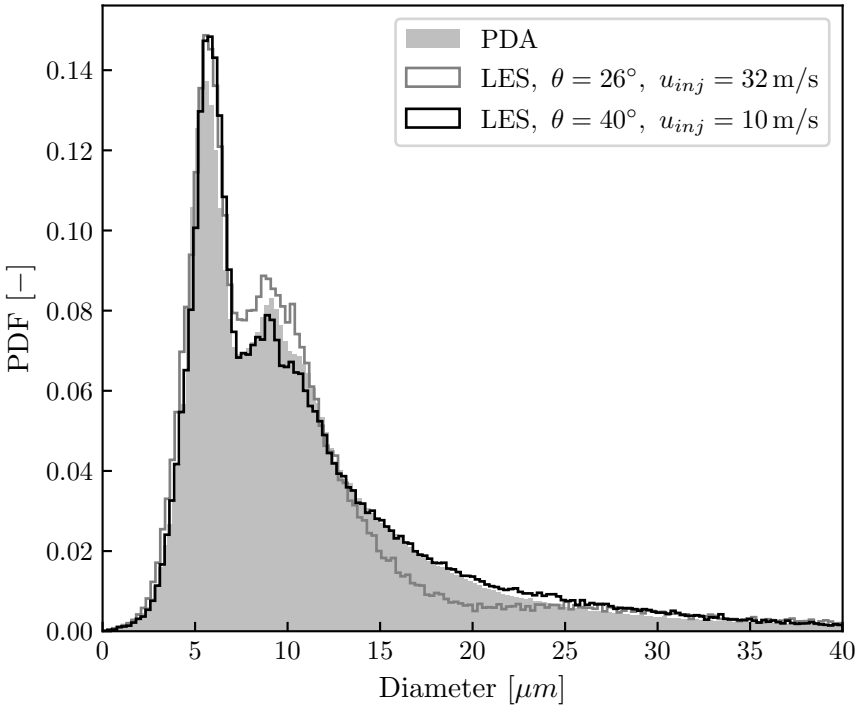

(b) Visualization of the impact of θ (black curve) and u_{inj} (gray curve) on the resulting PDF with respect to both the measured PDF *and* the parameter setup in Fig. (a).

Figure 4.15: Comparison of local probability density functions (PDF) of droplet sizes sampled at $x = 5\,\mathrm{mm}$ and $R = 5\,\mathrm{mm}$ (see black dot in Fig. 4.10) for different injection parameters. Filled PDF in both images: experimental measurement using PDA, included for reference (same as in Fig. 4.8).

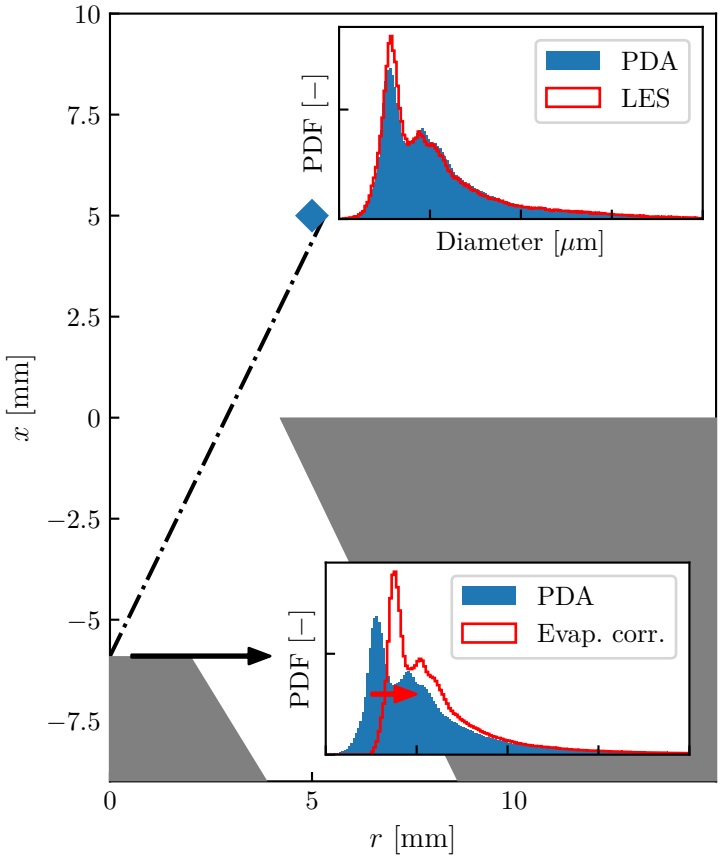

Figure 4.16: Qualitative visualization of the relation between the evaporation-corrected droplet size PDF used for injection, and the PDF sampled at $x = 5\,\mathrm{mm}$ and $R = 5\,\mathrm{mm}$.

right amount of evaporation along their trajectory to the measurement position (diamond marker in Fig. 4.16) in order to *"undo"* the deliberately imposed PDF shift at injection. If this condition is satisfied, we can expect the experimental and simulated PDF to match at the measurement position. Put differently, we have to select the injection model parameters such that they ensure a sufficiently long droplet path, since the evaporation time is directly related to the length of a droplet's trajectory.

We have repeatedly mentioned that said trajectory is chiefly controlled by the droplet's Stokes number. Therefore, it is worthwhile examining two additional parameter combinations in Fig. 4.15(b) to investigate if they can favorably influence the resulting droplet size PDF (at the measurement position). Note that the injection PDF is intentionally kept constant. In this manner, we can observe how the resulting droplet size PDF changes its shape depending on the imposed value of θ and u_{inj}.

Starting with an increased injection velocity ($u_{inj} = 32\,\mathrm{m/s}$, gray curve) for an otherwise unchanged injection half-angle θ (compared to Fig. 4.15(a)), we observe that varying u_{inj} appears to affect the *skewness* of the resulting PDF. In an intermediate droplet size range of $d = 13 - 25\,\mu\mathrm{m}$, the PDF decreases more steeply compared to the experimental data. A lower injection velocity (*i.e.* $u_{inj} = 10\,\mathrm{m/s}$) is therefore preferred. We attribute this behavior to the fact that convective effects enhance the evaporation rate, since the Sherwood and Nusselt numbers scale with the droplet Reynolds number Re_p (see Eqs. 2.105 and 2.106), and thus enhance heat and mass transfer rates. Consequently, stronger evaporation rates cause smaller droplets and an undesired increase of the secondary peak around $9.1\,\mu\mathrm{m}$.

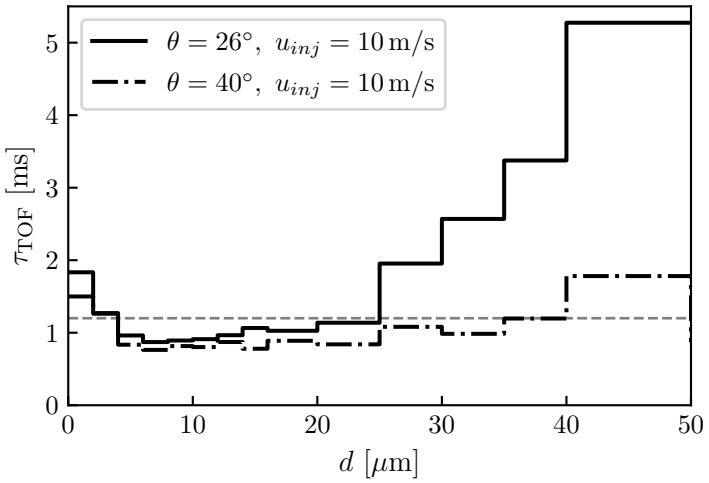

Figure 4.17: Time-of-flight τ_{TOF} per droplet class (computed from LES) corresponding to the elapsed time between injection and crossing of the measurement position at $x = 5\,\mathrm{mm}$ and $R = 5\,\mathrm{mm}$. The dashed gray horizontal line corresponds to the empirically found value ($\tau_{\mathrm{TOF}} = 1.2\,\mathrm{ms}$), which is used in the final setup.

Conversely, raising the injection half-angle to $\theta = 40°$ while keeping $u_{inj} = 10\,\mathrm{m/s}$ (black curve in Fig. 4.15(b)) appears to have only a moderate effect on the resulting PDF. It is most pronounced in a diameter range of $d = 20 - 25\,\mu\mathrm{m}$, where droplet sizes tend to be overestimated. We attribute this behavior to a limitation of the wall film model, which at present cannot account for film evaporation. With large injection half-angles, virtually all droplets will temporarily be part of the wall film at the injector nozzle (integrated into the terminal plate), where their diameter does not change (droplet type changed from freely moving droplet to non-evaporating "film-type" droplet). Evaporation resumes once a droplet detaches from the wall film, although without further diameter correction. We thus conclude that the previously identified parameter set ($\theta = 26°$ and $u_{inj} = 10\,\mathrm{m/s}$) should be preferred in light of a good prediction of the local droplet diameter distribution.

This leaves the question of how to select an appropriate evaporation correction (or PDF shift) in order to define the droplet size PDF used at the moment of injection. We recall that the evaporation correction is computed from the D^2-law (Eq. 2.101) with a *constant* time delay τ. A natural choice for τ is the droplet time-of-flight τ_{TOF} defined as the elapsed time between injection and crossing of the measurement position at $x = 5\,\mathrm{mm}$ and $R = 5\,\mathrm{mm}$. In Fig. 4.17, we plot τ_{TOF} extracted from LES as average for each droplet class. These values are computed by means of Lagrangian particle tracking using the injection time stored with each droplet and the physical time in the simulation, at which the droplet is crossing the measurement position.

Due to different track lengths per droplet class, τ_{TOF} necessarily depends on the droplet size as well, although to a varying degree, depending on the injection half-angle. For $\theta = 40°$ (dash-dotted line in Fig. 4.17), the time-of-flight remains close to $\tau_{\mathrm{TOF}} = 1\,\mathrm{ms}$ in a size range of $d = 5 - 40\,\mu\mathrm{m}$. In turn, for $\theta = 26°$ (solid line in Fig. 4.17), this is only true in the range of $d = 5 - 25\,\mu\mathrm{m}$, with larger droplets exhibiting increasing values of τ_{TOF}. Thus, using a simple averaged time-of-flight for the evaporation correction does not yield satisfying results in terms of the local droplet size distribution. A weighted average by the probability of each droplet class is considered as a better starting point, but may still need some iterative refinement. For the case of $\theta = 26°$, the weighted average is $\tau_{\mathrm{TOF}}^{avg} = 1.06\,\mathrm{ms}$, but optimal results were

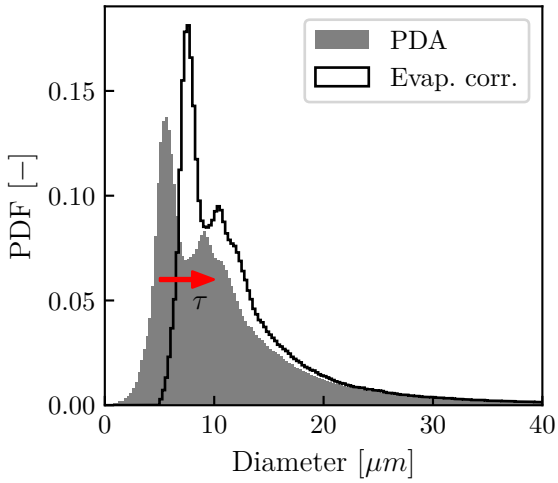

Figure 4.18: Experimentally measured droplet size distribution (filled) at $x = 5\,\mathrm{mm}$ and $R = 5\,\mathrm{mm}$ and evaporation-corrected distribution used for injection in LES (black curve) with $\tau \equiv 1.2\,\mathrm{ms}$.

obtained with an empirically found value of $\tau_{\mathrm{TOF}} \equiv 1.2\,\mathrm{ms}$ (gray dashed line in Fig. 4.17). The final evaporation-corrected PDF is plotted in Fig. 4.18 with the experimental PDF as reference.

So far, we have analyzed only one specific location in the injector far-field, at which we attempted to match the droplet statistics as best as possible. However, it is conceivable that the droplet size distribution is different at *other* locations in the flow and is not guaranteed to resemble the PDF obtained *e.g.*, at $x = 5\,\mathrm{mm}$ and $R = 5\,\mathrm{mm}$. Therefore, it is useful to collect droplet statistics at more than one location and compare them to data from LES in order to determine an optimal set of injection parameters.

4.3.7 Radial droplet granulometry

Rather than plotting multiple probability density functions, it is more convenient to compute moments of local droplet size distributions sampled across a pre-defined grid of discrete locations in the flow. In this manner, we obtain spatial information about the droplet size distribution, also referred to as *granulometry*. We limit the comparison to two commonly employed moments relevant for droplet sprays: the mean diameter d_{10} and the Sauter-Mean-Diameter (SMD) d_{32}. A general mean diameter for a finite number of droplet size classes is defined as

$$d_{pq} = \left(\frac{\sum_i n_i d_i^p}{\sum_i n_i d_i^q} \right)^{1/(p-q)} \tag{4.6}$$

For example, the SMD follows through $p = 3$ and $q = 2$ in the above equation. Samples are taken experimentally (using PDA) at three different heights ($x = [5,\ 10,\ 20]\,\mathrm{mm}$) and multiple radial positions. Due to the spray's hollow-cone shape, the radial resolution is adapted to cover the region of interest where a sufficient amount of droplets can be expected.

As in the previous sections, we present the data from two different injection half-angles ($\theta = 26°$ and $\theta = 40°$), although a larger amount of parameter combinations was investigated. Each column in Fig. 4.19 corresponds to a constant injection angle, and each row to a constant height above the combustor backplane. For the sake of this comparison, only the injection half-angle is varied in LES, while all other injection parameters are kept constant in both

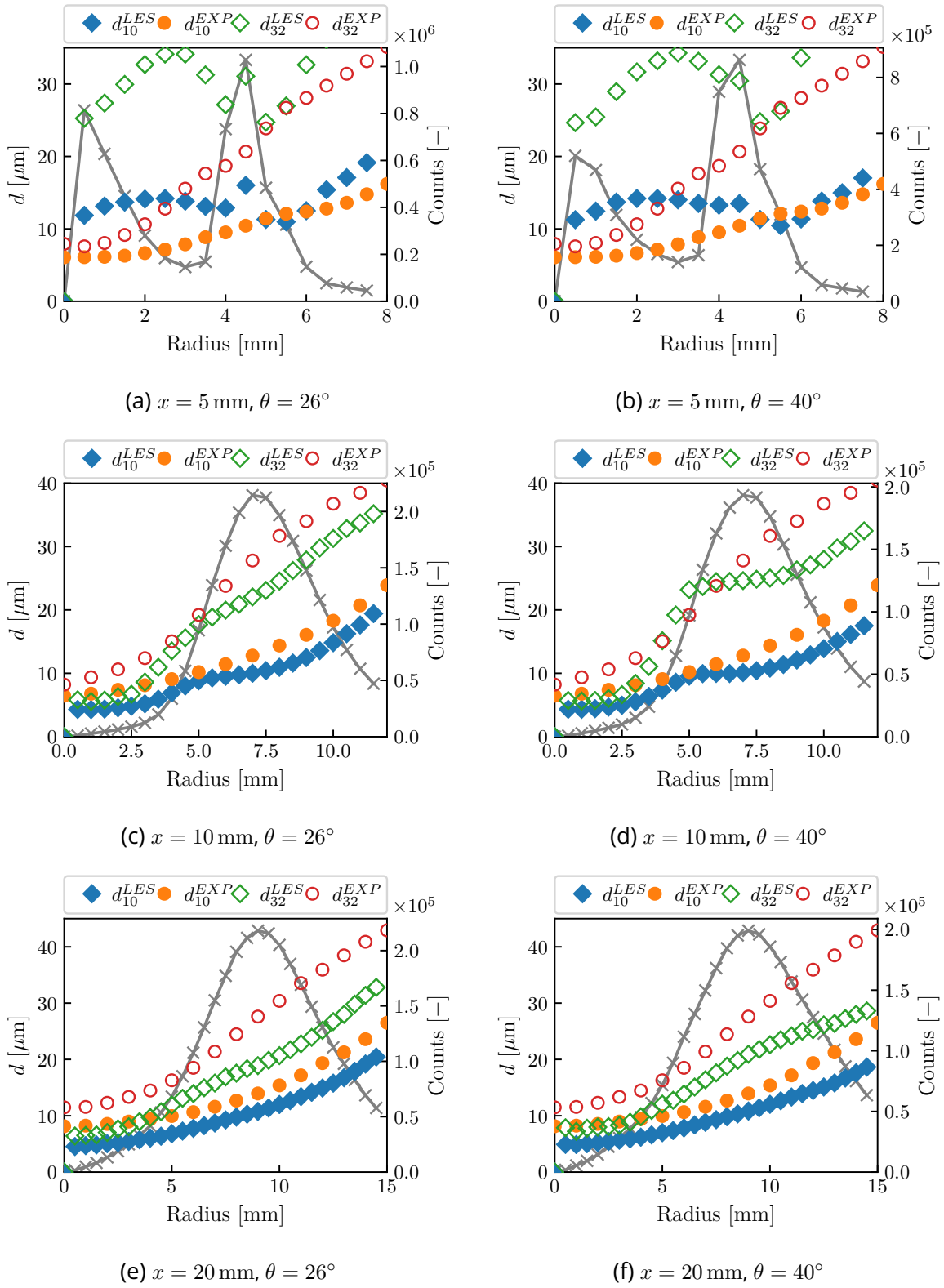

(a) $x = 5\,\mathrm{mm}$, $\theta = 26°$

(b) $x = 5\,\mathrm{mm}$, $\theta = 40°$

(c) $x = 10\,\mathrm{mm}$, $\theta = 26°$

(d) $x = 10\,\mathrm{mm}$, $\theta = 40°$

(e) $x = 20\,\mathrm{mm}$, $\theta = 26°$

(f) $x = 20\,\mathrm{mm}$, $\theta = 40°$

Figure 4.19: Spatial evolution of droplet moments d_{10} (filled symbols) and d_{32} (open symbols) at three different heights and two different injection half-angles (left column: $\theta = 26°$, right column: $\theta = 40°$). Diamond markers: LES cases; circle markers: experimental data, both associated with the left axis. Gray curve: droplet counts in LES at each radial position (associated with the right axis). For all simulations, $u_{inj} = 10\,\mathrm{m/s}$ and $\tau = 1.2\,\mathrm{ms}$ are used.

simulations, notably the injection velocity $u_{inj} = 10\,\mathrm{m/s}$ and the time delay for evaporation correction $\tau = 1.2\,\mathrm{ms}$. To facilitate the interpretation of the plots, we have added the local droplet count (gray line, associated with the right axis of each plot) in order to mark the spatial range, in which the majority of the droplets is expected. Note that azimuthal averaging is performed in LES for each radial position at each height.

Starting with $x = 5\,\mathrm{mm}$ (Fig. 4.19(a) and (b)), both the mean and Sauter-Mean-Diameter are overestimated in the simulation, regardless of the injection angle. This is particularly true for the internal recirculation zone ($r < 1.5\,\mathrm{mm}$), although the agreement between LES and experiment is slightly better for larger radii. As all droplets are known to behave as tracers in the present configurations, it is most likely that the droplets found in the IRZ have been entrained by the recirculating flow motion immediately after detaching from the nozzle wall film. Recalling that droplets in the wall film do not evaporate, we assume the film model to be the principal cause for the overestimated droplet diameter in the internal recirculation zone.

Interestingly, the agreement between experiment and LES is much better farther away from the combustor backplane (Fig. 4.19(c) - (f)) for both d_{10} and d_{32}, notably at $x = 10\,\mathrm{mm}$ and $\theta = 26°$ (Fig. 4.19(c)). With increasing height, the majority of droplets is also found outside of the IRZ, confirming the hollow-cone shape of the spray (peak droplet count shifted towards larger radii). At $x = 20\,\mathrm{mm}$, however, the Sauter-Mean-Diameter is generally underestimated, which is most pronounced towards larger radii (Fig. 4.19(e) and (f), $r > 10\,\mathrm{mm}$).

Despite this, the simulated droplet granulometry is certainly acceptable considering that it is achieved *without* modeling primary and secondary atomization processes, breakup, coalescence or other droplet interactions. Although the impact of the injection half-angle appears to be moderate, results are consistently better with $\theta = 26°$, which is the preferred value. Furthermore, the parameter combination of $\theta = 26°$, $u_{inj} = 10\,\mathrm{m/s}$ and $\tau = 1.2\,\mathrm{ms}$ has already been proven to yield satisfying results in terms of other metrics, which we use to facilitate the selection of an optimal injection setup.

4.3.8 Flame shape sensitivity to injection parameters

For an overall assessment of the injection parameters, we have also examined their impact on the flame shape. Large-Eddy Simulations of the fully ignited SICCA combustor were carried out in stationary conditions, and time-averaged flame shapes were compared for various injection parameter setups. Operating conditions are identical to those discussed in Chap. 9. As for all reacting simulations and experiments, the confined geometry presented in Sec. 3.3.1 must be used here instead of the unconfined geometry used for *non-reacting* cases in Sec. 4.3.1 - 4.3.7. Experimental evidence has shown that a confinement is mandatory in SICCA to stabilize a flame, *e.g.,* by adding a quartz glass tube as in Fig. 3.5. This implies, however, that the flow field downstream of the injector assembly is not necessarily identical between the confined and unconfined combustor configuration, which in turn could moderately influence the choice of injection parameters. The following comparison should therefore be considered as an additional verification or consistency check, rather than a strict evaluation criterion.

In Fig. 4.20((a) and (b)) we present the time-averaged line-of-sight integrated heat release rate (averaging period over $t_{avg} = 15\,\mathrm{ms}$) for two injection half-angles. Both configurations are very similar in terms of their respective flame shape, and also resemble other cases not shown here in the interest of brevity. The principal reason for the flame's relative insensitivity to the choice of injection parameters is clearly related to strongly enhanced evaporation rates in reacting conditions. Examining the liquid volume fraction α_l on the central cutplane through the combustion chamber (see Fig. 4.20(c)) proves that the liquid fuel contribution to the reaction zone — limited by the orange contour of the heat release rate — is markedly low. The

(a) $\theta = 26°$, $u_{inj} = 10\,\mathrm{m/s}$, line-of-sight integrated heat release rate

(b) $\theta = 40°$, $u_{inj} = 10\,\mathrm{m/s}$, line-of-sight integrated heat release rate

(c) Liquid volume fraction α_l for case (a) on the central cutplane

Figure 4.20: Line-of-sight integrated heat release rate of time-averaged solutions for two different injection setups ((a) and (b)). Time-averaged liquid volume fraction α_l (image (c)) for configuration (a). Orange contour line: time-averaged heat release rate for a value of $5 \times 10^7\,\mathrm{W/m^3}$.

Parameter	Unit	Optimal value
Injection half-angle θ	-	$26°$
Deviation angle $\delta\theta$	-	$6°$
Injection velocity u_{inj}	$\mathrm{m/s}$	10
Evaporation correction τ	ms	1.2

Table 4.3: Optimal injection parameter set used with the modified FIM-UR model. For all simulations, the ration of physical to numerical droplets is set to $n_{\mathrm{parcel}} = 1$.

reaction zone is essentially fed by a gaseous fuel/air mixture, since droplets barely penetrate the combustion chamber due to fast evaporation and a high volatility of n-heptane already under ambient conditions. We thus conclude that the overall flame shape is only of minor importance for an appropriate selection of injection parameters, at least in the present configuration.

Apart from Fig. 4.20(c), the interested reader may also find further evidence for a dominant premixed combustion mode in Appendix B, where we perform a regime identification for the present case based on the Takeno flame index.

4.3.9 Final injection parameter set

The final parameter set that was found to yield optimal results in terms of all metrics examined in the previous sections is compiled in Tab. 4.3. The evaporation-corrected PDF, from which the initial droplet diameter is sampled in LES, is given in Fig. 4.18. In all simulations, each numerical droplet represents one physical droplet, *i.e.* $n_{\mathrm{parcel}} = 1$. For the remainder of this work, we will only use the setup presented here.

4.3.10 Discussion

While the previously found injection parameters cannot be universally applied to other configurations, more general conclusions can still be drawn from the calibration procedure, notably with regard to the interaction between a phenomenological model and a physically determined flow. We recall that the FIM-UR model may produce similar results in terms of droplet statistics from very different parameter sets. Unlike the air flow, which is physically determined

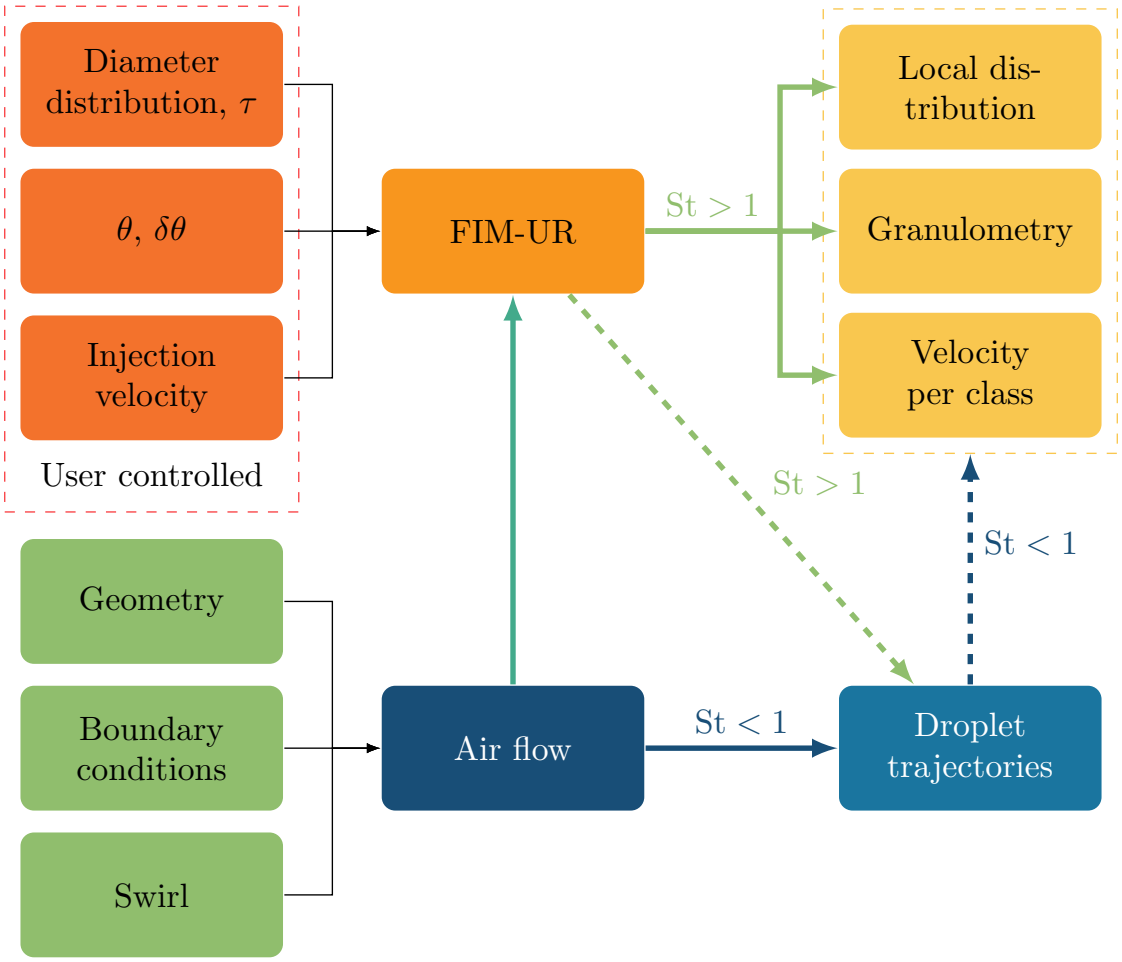

Figure 4.21: Flowchart for an assessment of FIM-UR model parameters.

by (among others) a given combustor geometry, boundary conditions or the swirl number, the FIM-UR parameters are entirely "user controlled". This allows us to emulate a droplet spray with available computational resources without modeling computationally intensive processes such as atomization, breakup or coalescence. However, not all parameter combinations are necessarily reasonable from a physical standpoint, which is an inherent ambiguity of phenomenological models. Therefore, the assessment of model parameters may be complemented by the flowchart in Fig. 4.21, visualizing the interaction between the air flow and the FIM-UR model.

Essentially, the imposed parameters control the extent to which the droplet motion is governed by the air flow, or a combination of the air flow and the FIM-UR model. As repeatedly stated in the previous sections, we can make inferences about the droplet behavior based on the Stokes number. If the FIM-UR parameters are chosen such that the resulting Stokes number is below unity, the air flow will most likely outweigh the effect of the model parameters, and dictate the droplet motion. Consequently, it will also influence other spray characteristics such as the local droplet size and velocity distributions, or the granulometry. In turn, if the parameters cause the Stokes number to be above unity, the air flow's impact will gradually decrease, at least for droplet classes with $\mathrm{St} > 1$.

The addition of other models in the simulation can unfortunately blur this simplified pic-

ture and render the selection of appropriate injection parameters even more complex. For example, the wall film model lacking any mechanism for film evaporation essentially excludes specific value ranges for the FIM-UR parameters, in particular larger injection half-angles θ (see Sec. 4.3.6 and 4.3.7). Furthermore, interactions between droplets and sub-grid scale fluctuations of the (gaseous) velocity are entirely neglected at present, but would certainly deserve a thorough characterization in a future study. Additional model improvement may also involve a more granular control over the injection velocity and the evaporation correction, which could be adjusted individually for each droplet class instead of setting constant values for *all* classes. A more physics motivated enhancement should also address the secondary atomization process at the nozzle edge of the terminal plate, which could be introduced in a similar fashion as in Chaussonnet et al. (2016).

With light-round simulations in mind, it is worth emphasizing that a properly calibrated injection model is crucial to ensure a correct flame propagation. Unlike stationary flames in a fully ignited combustor (see Sec. 4.3.8), propagating flames and liquid fuel droplets will be shown to mutually affect one another. As we shall see, the flame's trajectory critically depends on the *upstream* liquid volume fraction α_l, which itself results from interactions between the air flow and fuel droplets. In addition, droplet motion inside the combustion chamber is found to be modulated by burnt gas expansion, creating droplet accumulations ahead of the propagating flame fronts. Therefore, it is of principal interest to reproduce the experimentally observed spray as best as possible, in spite of the aforementioned limitations of the injection model.

4.4 Conclusions

Within the framework of the dilute spray assumption, we have presented enhancements for evaporation and dispersion, occurring in the injector far-field. With regard to evaporation, Abramzon and Sirignano (1989) have promoted the concept of gaseous droplet films to suitably describe the heat and mass transfer processes between a gaseous carrier phase and liquid droplets. The properties of these droplet films — precisely the diffusion coefficient ρD and the thermal conductivity λ — may be subjected to a strong variability along a droplet's trajectory, which was shown to critically affect the evaporation rates. In AVBP's default implementation, ρD and λ were evaluated from simplified expressions based on *constant* Schmidt and Prandtl numbers. This avoids the computationally more expensive evaluation of detailed transport properties, implicitly assuming constant film properties. Such an assumption is considered to be less appropriate for light-round ignition where large variations are expected, justifying the development of an improved implementation, termed "polynomial evaporation model". Essentially, we have replaced the constant Schmidt and Prandtl numbers by polynomial expressions, parameterized by the droplet film's non-dimensional temperature and fuel mass fraction, allowing to account for variations of the droplet film properties. The polynomial functions were obtained from a fit procedure based on generic droplet films with detailed transport properties. An error assessment of the polynomial evaporation model revealed a very good prediction of evaporation times in pure air compared to detailed approaches (error below 3%), and a still acceptable error in burnt gases (8% at worst). Moreover, the polynomial evaporation model performed significantly better within the temperature range of interest compared to an approach with constant Schmidt and Prandtl numbers. Lastly, possible avenues of improvement were discussed and benchmarked in terms of their accuracy and computational costs.

Apart from evaporation, we have also addressed fuel injection as an influential factor affecting mixing and dispersion. Attempting to reproduce experimentally measured spray charac-

teristics at a certain distance from the fuel injector, we rely on the phenomenological FIM-UR model to generate a pre-atomized hollow-cone spray without accounting for complex physical processes such as primary and secondary atomization, break-up, collision or coalescence. For optimal results, the model has been calibrated with available experimental data obtained from the SICCA combustor. The four main model parameters were determined from a simultaneous analysis of the air flow, the droplet class regime inferred from the individual Stokes number, traced droplet trajectories, droplet class velocities, droplet size distributions, and the overall granulometry. The injection diameter was sampled from an evaporation-corrected droplet size PDF measured at a distance of $5\,\mathrm{mm}$ from the injector. The amount of evaporation correction followed from the droplet time-of-flight obtained from the simulations. Interestingly, flame shapes were found to be almost insensitive to the choice of model parameters due to strongly enhanced evaporation rates (compared to pure air flows) and n-heptane's high volatility. The optimal parameter set was eventually compiled in Sec. 4.3.9.

Although the modified FIM-UR model was able to reproduce the experimental droplet spray in a satisfying manner, we have noted its inherent ambiguity in terms of the model parameters: since all complex processes that lead to the generation of a fuel spray must be absorbed by said parameters, similar results in terms of an arbitrary metric can be achieved with very different parameter sets. Therefore, we have put forth the argument that the optimal model parameters should not only be assessed in terms of their ability to reproduce certain spray characteristics, but also also be evaluated from a physical standpoint. Finally, we have proposed potential model improvements, which may be considered in future works.

Chapter 5

Modeling of heat transfers

Heat transfer problems impose substantial design constraints on aero-engine combustors, in addition to engine certification specifications. Safe and reliable ignition is one of these constraints, which itself is influenced by the thermal state of the combustor walls. Despite its importance, heat transfer between the internal combustor flow and the combustor walls is often overlooked or largely oversimplified, rendering investigations of flame propagation during ignition less accurate. On one hand, good control of wall temperatures is difficult to achieve experimentally. On the other hand, adiabatic numerical simulations have ignored the effect of preheating during prefueling entirely, while isothermal simulations (of cold combustor walls) have neglected the variability of thermophysical properties in the boundary layer. Modeling of heat transfer has therefore been prone to hidden error cancellation, as emphasized in previous works. These issues are addressed in this chapter: Conjugate Heat Transfer (CHT) simulations are presented as a useful tool to obtain more realistic predictions of combustor wall temperatures and heat fluxes. We introduce a coupled setup of a fluid and a solid domain solver, which are executed in parallel and exchange information at the domain interfaces via the OpenPALM coupling library. In addition, we develop and implement a wall model for numerical simulations which is based on the Thin Boundary Layer Equations (TBLE) and is able to account for variable thermophysical properties in the boundary layer.

Contents

Heat transfer is a central problem of combustor design as it determines the limits of stable and safe operation of combustion devices (among other parameters). On one hand, wall temperatures must not be exceeded when walls are exposed to hot burnt gases, imposing a major design constraint. On the other hand, heat transfer can enhance or weaken certain physical phenomena such as combustion instabilities or the ignition behavior, which may limit the operating range of a given combustor. For these reasons, tools that can make accurate predictions of heat transfer processes have become of utmost importance.

Of particular interest for the present work is the question of how non-adiabatic walls affect ignition and flame propagation in MICCA-Spray. Experimental measurements of light-round durations have suggested a strong sensitivity of the flame propagation speed to wall temperature conditions (Prieur et al., 2019). However, first simulation results obtained from precursor works with combustor walls at $T_w = 300\,\mathrm{K}$ (Lancien, 2018) were not conclusive, citing concerns over the suitability of the employed wall functions. Their deficiencies were later substantiated by Puggelli et al. (2020). Furthermore, light-round simulations with preheated combustor walls were approximated by adiabatic wall boundary conditions (Lancien, 2018; Collin-Bastiani, 2019b) for the lack of detailed experimental temperature measurements, disregarding potential effects on the liquid phase due to preheating.

Both cases (cold and preheated) have highlighted a demand for a more thorough characterization of wall heat transfers to serve two main purposes: (i) determine wall temperature profiles in preheated conditions, and (ii) improve the description of wall heat transfers (for both) through a more sophisticated approach than the present wall functions. The former aspect can only be achieved numerically, since experimental temperature measurements are particularly difficult to perform in MICCA-Spray, at least at present. The foundation for these investigations is discussed in this chapter, notably multiphysics simulations and the development of a custom wall model.

5.1 Multiphysics simulations of heat transfer problems

Multiphysics simulations can be viewed as an extension of pure fluid flow simulations, aiming at a holistic approach to heat transfer problems, or any other field of research involving more than one physical process of a given system. In simulations of aeroengine combustors for example, heat conduction in solid parts, and even radiation may be considered, in addition to solving the governing equations of turbulent combustion. Thus, multiple mechanisms of heat transfer are covered in this manner, hence the name.

Although full multiphysics simulations of combustion chambers (including radiation) are not yet very common, coupled simulations have gained increasing attention that solve for turbulent combustion and heat conduction in solids simultaneously. This approach is referred to as Conjugate Heat Transfer (CHT) and constitutes a central part of the present work. Within the scope of determining wall temperature profiles in MICCA-Spray, we briefly present the relevant equations and solution strategies in the following sections.

5.1.1 Conjugate Heat Transfer

Heat transfer in pure fluid flow simulations is commonly determined by non-adiabatic wall boundary conditions, *e.g.,* imposed temperature profiles or heat transfer coefficients. If such

information is available *a priori* it simplifies the flow problem under consideration as it allows to replace the solid domain of a given geometry by appropriate boundary conditions at the interface between fluid and solid. Conversely, without *a priori* information, or if the computation of wall temperatures is of main interest, *e.g.,* to examine thermal material loads, a different approach must be employed: in solving the governing equations in both the fluid and solid domain simultaneously, we can obtain wall temperatures and heat fluxes at the interface between the domains. This approach is referred to as Conjugate Heat Transfer (CHT), which involves the coupling of fluid and solid domain simulations. In the context of LES of aeroengine combustion, CHT simulations have been successfully applied to compute wall temperature profiles in a section of a helicopter combustor (Duchaine et al., 2015; Berger et al., 2016). In lab-scale swirled combustion chambers it was also shown to be desirable for more accurate predictions of thermodynamic instabilities (Kraus et al., 2018) and flame dynamics (Agostinelli et al., 2021), or flame stabilization (Koren et al., 2017a). Insights from coupled DNS of bluff-body configurations have revealed a strong sensitivity of flame anchoring positions to the flame holder temperature (Miguel-Brebion et al., 2016) and its material properties (Berger et al., 2016). Other flow features such as mean velocity, temperature or CO mass fraction profiles were also found to be in better agreement with experimental data, as reported by Fureby (2021) for LES of the VOLVO case.

Fundamentally, Conjugate Heat Transfer simulations involve the solution of the energy equation. However, the governing mechanisms of heat transfer usually differ between the fluid and solid domain: in fluids, heat can be transported through convection and conduction, whereas in solids the only relevant transport mechanism is conduction (neglecting radiation for now). Compared to Eq. 2.4, the governing equation for the solid domain is therefore considerably simplified and expressed as

$$\rho_s C_s \frac{\partial T}{\partial t} = \frac{\partial}{\partial x_i}\left(\lambda_s \frac{\partial T}{\partial x_i}\right) \tag{5.1}$$

Equation 5.1 is also referred to as unsteady heat conduction equation and introduces the material properties of the solid domain (with a subscripted "*s*") such as the solid material's density ρ_s, its heat capacity C_s and its heat conductivity λ_s.

One aspect all references cited above have in common is the use of specialized solvers assigned to each domain. In theory, the fluid solver could be instructed to solve the governing equations of both domains together, but this approach is often undesired: not only is the number of equations to be solved very different in each domain (Eq. 5.1 in the solid versus Navier-Stokes Equations and additional models in the fluid), but also their respective time step. Consequently, the utilization of computational resources would be inefficient. Instead, employing specialized solvers for each domain brings modular code design, improved load balancing and resource utilization, although at the cost of increased code complexity due to the handling of the communication between the solvers.

In the present work, we rely on a separate solid domain solver and a coupling library which are both presented in the following sections.

5.1.2 Solid solver AVTP

The solver AVTP (Jaure et al., 2013; Duchaine et al., 2015) shares the general architecture of AVBP, but is developed as a separate code by CERFACS. It solves the unsteady energy equation (see Eq. 5.1) in solids and can account for variable local material properties (heat capacity C_s and heat conductivity λ_s) as a function of temperature, computed through polynomial fit

functions. In terms of the computational mesh, AVTP can handle unstructured and structured meshes as AVBP.

For spatial discretization, a second-order Galerkin diffusion scheme (Donea and Huerta, 2003) is employed, while an implicit first-order backward Euler scheme is employed for temporal integration, which is solved through a parallel matrix-free conjugate gradient algorithm (Frayssé et al., 2005). In all simulations of the solid domain, we intentionally impose a constant integration time step Δt specified later.

5.1.3 Radiative heat transfer

Heat transfer by radiation is caused by electromagnetic waves, which is fundamentally different from convection and conduction (Modest, 2013). All matter with a given temperature continuously emits and absorbs electromagnetic waves, or photons, to raise or lower their molecular energy levels. Most importantly however, radiation does not necessitate the presence of a medium for energy transfer, unlike convection and conduction. Photons can thus transverse far longer distances, constituting yet another distinguishing feature between radiation on one hand, and convection and conduction on the other hand.

The strength and wavelength of an emitted photon depends on the temperature of the emitting matter, and the resulting heat flux to its fourth power, *i.e.* $q \propto T^4 - T_\infty^4$. This implies that radiative heat transfer may become increasingly important at high temperature levels, and outweigh other mechanisms of heat transfer.

Of key interest for radiative heat transfer problems is the radiative heat flux q_{rad}, which in turn is obtained from the solution of the Radiative Transfer Equation (RTE). Consider an energy beam of a given frequency ν (or wavelength λ) with a corresponding frequency-dependent radiative intensity I_ν. Let s be the direction of its propagation and ds the distance traveled. Along its path, its radiative energy may lose or increase its intensity through absorption and scattering within the crossed medium, which is expressed mathematically as

$$\begin{aligned} \frac{d}{ds}\left(\frac{I_\nu}{n^2}\right) = &- \kappa_\nu \frac{I_\nu}{n^2} - \sigma_\nu \frac{I_\nu}{n^2} \\ &+ \kappa_\nu I_\nu^\circ \\ &+ \frac{\sigma_\nu}{4\pi n^2} \int_{4\pi} I_\nu\left(s_i\right) \Phi_\nu\left(s, s_i\right) d\Omega_i \end{aligned} \tag{5.2}$$

In the above equation, κ_ν and σ_ν denote the respective absorption and scattering coefficients, n the refractive index, $\Phi_\nu\left(s, s_i\right)$ a phase function yielding the probability of a photon to be scattered from direction s_i to direction s, and $d\Omega_i$ the solid angle. The blackbody intensity I_ν° is given by Planck's law written as

$$I_\nu^\circ = \frac{2\pi\hbar\nu^3}{c_0^2\left[\exp^{\frac{\hbar\nu}{k_b T}} - 1\right]} \tag{5.3}$$

where $\hbar$ is Planck's constant, k_b Boltzmann's constant, c_0 the speed of light in vacuum, and T the temperature. Integration of Eq. 5.2 over the entire frequency spectrum and all solid angles eventually yields the radiative heat flux at a given point in the medium

$$q_{rad} = \int_{\nu=0}^{\infty} \int_{4\pi} I_\nu s d\Omega d\nu \tag{5.4}$$

and the volumetric radiative power as the divergence of the radiative flux

$$P_{rad} = -\nabla \cdot q_{rad} \tag{5.5}$$

While these equations can be solved with numerical codes, which may also be included in a multiphysics approach, we use much simpler expressions to model (external) radiative heat transfer as specified in Sec. 5.2.1 (for quartz walls facing the ambient air). In turn, *internal* radiative heat transfer is neglected for the considered combustor configurations based on an *a priori* error estimation, which is briefly discussed in Appendix D.

5.1.4 Coupling approaches for Conjugate Heat Transfer

Coupled code execution of multiple solvers or programs commonly requires additional software tools to handle the communication and data exchange between individual codes, and provide other functionalities such as mesh interpolation or code synchronization. These functionalities are often encapsulated in code coupling libraries (*e.g.,* Model Coupling Toolkit (MCT) (Larson et al., 2005), Yet Another Coupler (YAC) (Hanke et al., 2016) or OpenPALM (Duchaine et al., 2015)), some of which have their origin in oceanographic data assimilation, but can readily be applied to other scientific problems. In this work, we employ the OpenPALM coupling library for CHT simulations and summarize its main features as well as the coupling strategy between AVBP and AVTP in the following sections. Preliminary coupled simulations were performed to assess the suitability of the coupling strategy (see Appendix E), however without success due to various uncertainties. Given the limited experimental data, we chose to retain the Conjugate Heat Transfer approach to determine internal wall temperatures.

5.1.5 Parallel code execution and mesh interfacing

OpenPALM (Duchaine et al., 2015) is a coupling library handling the coupled execution of an arbitrary number of codes, which were not necessarily developed with such use case in mind. It is part of a joint project between CERFACS and ONERA. The codes can be fairly heterogeneous (*e.g.,* written in different programming languages), executed sequentially or simultaneously, and may also have non-conforming domain interfaces. Data is exchanged through parallel communication via the MPI library and can be scheduled dynamically. A graphical user interface called PrePALM exists, allowing to design coupling scenarios, define coupling events, generate required service files or debug coupled runs and detect potential performance bottlenecks. For mesh interpolation, the external CWIPI library (Coupling With Interpolation Parallel Interface, Refloch et al. (2011)) developed by ONERA is used.

A typical Conjugate Heat Transfer simulation setup following the Dirichlet-Neumann approach is illustrated in Fig. 5.1. For stability reasons (see Giles (1997)), a wall temperature is specified as boundary condition for the fluid domain, while a heat flux is imposed as boundary condition for the solid domain. In a given interval n, all solvers are executed simultaneously (as opposed to a sequential code execution) and solve the governing equations of their respective domain. The Dirichlet boundary condition imposed in AVBP corresponds to the wall temperature T_w^{n-1} of the previous interval $n-1$ (or an appropriate initial boundary condition), whereas the Neumann boundary condition imposed in AVTP corresponds to the wall heat flux q_w^{n-1}. For the sake of simplicity we assume that AVBP and AVTP advance the solution (or physical) time by $n_F \Delta t_F$ in the fluid, and $n_S \Delta t_S$ in the solid respectively. Δt_F and Δt_S denote the time steps in each domain, with n_F and n_S representing arbitrary factors discussed later (along with the feasibility of such assumption). At the end of each interval, *i.e.* after n_F fluid time steps and n_S solid time steps, the boundary conditions of both domains are updated as visualized by orange arrows in Fig. 5.1: the instantaneous wall temperature of the solid T_w^n is imposed during the subsequent interval $n+1$ as a new boundary condition for the fluid domain, while the instantaneous wall heat flux q_w^n is imposed as a new boundary condition for

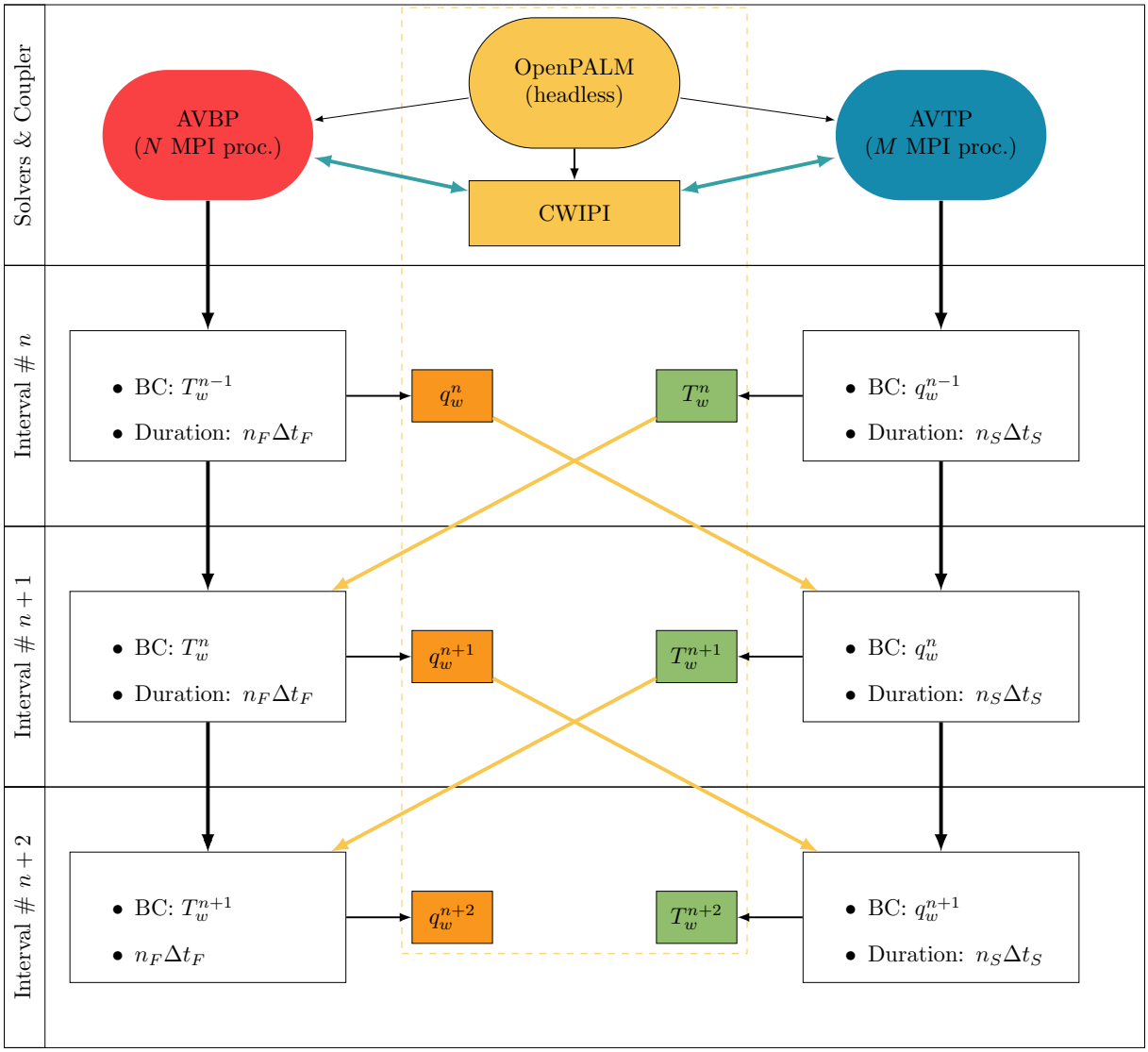

Figure 5.1: Parallel code execution of AVBP and AVTP (adapted from Duchaine et al. (2008)). Yellow arrows represent the information exchange between the solvers at the domain interfaces, which is handled by the OpenPALM/CWIPI libraries.

the solid domain. This process may repeat over multiple intervals as specified by the user. Data interpolation between the boundary meshes of each domain is handled by the CWIPI library during each coupling event.

An inherent problem of Conjugate Heat Transfer simulations is the strong discrepancy between the *characteristic* times of the fluid τ_F and solid domain τ_S. The former can be associated with a flow-through time for example, while the latter can be expressed as a conduction time scale given as

$$\tau_S = \frac{\delta^2}{\frac{\lambda_s}{\rho_s C_s}} \tag{5.6}$$

with δ denoting a characteristic length scale of the solid. In most practical combustor configurations, we find $\tau_S \gg \tau_F$, since the characteristic time of the solid is usually of the order of seconds or minutes, however τ_F is of the order of milliseconds. Such a large scale disparity also applies to other domains such as the flow over turbine blades, as highlighted by He and Oldfield (2011). Thus, the convergence of a CHT simulation towards a stationary state is essentially governed by the solid. The inherent problem is now fully unveiled recalling that

a discrepancy also exists between the *solver* time steps to satisfy numerical stability criteria, *i.e.* $\Delta t_S \gg \Delta t_F$: if both solvers are time-synchronized, simulating even multiple characteristic fluid times τ_F translates into a minuscule fraction of τ_S only. Most importantly, with Δt_F of the order of microseconds or even nanoseconds, and Δt_S of the order of milliseconds or seconds, it is generally unfeasible to perform such a large number of fluid time steps Δt_F to reach a single characteristic solid time τ_S. This problem can be partially alleviated by spawning a larger number of MPI processes reserved for the fluid solver and a lesser amount of processes for the solid solver. In most cases however, such kind of load balancing is limited by the mesh size and the scalability of the code. Instead, acceleration approaches have been devised such as the desynchronization method (Duchaine et al., 2009) or the Hybrid-cell Neumann-Dirichlet (HCND) method (Koren et al., 2017b), allowing for a faster convergence towards steady state conditions from a given initial state. We employ the desynchronization method in this work which we briefly outline in the following section.

5.1.6 Desynchronization method and coupling frequency

If stationary wall temperatures are of main interest as in Chap. 7, the desynchronization method (Duchaine et al., 2009) can provide useful means to attain steady-state conditions with acceptable computational costs. In intentionally breaking the time synchronization between the fluid and solid solver, the latter is allowed to advance at a larger time step between two coupling events, accelerating the comparably long transient phase and thus the convergence towards a steady state. A sufficiently high frequency of data exchange between both solvers ensures not only the stability of the Conjugate Heat Transfer simulation, but also reasonable load balancing and resource utilization. Common values range between 50 to 200 *fluid* time steps, after which a coupling event is performed. This method can be conceived as an artificial reduction of the solid material's heat capacity (Kraus et al., 2018), yielding a shorter characteristic solid time τ_S according to Eq. 5.6.

An undesired side effect of the desynchronization method consists in spurious temperature oscillations in the solid domain. These may result from turbulent temperature fluctuations in the fluid flow interacting with the solid at its boundaries (see *e.g.,* Jaure et al. (2013)). An attenuation strategy as in Duchaine et al. (2009) is used who replaced the Neumann boundary condition at the solid interface by a *mixed* boundary condition, also known as Dirichlet-Robin boundary condition (Errera and Chemin, 2013; Radenac et al., 2014). Unlike Fig. 5.1, the updated wall boundary condition of the solid also accounts for the interface temperatures in addition to the wall heat flux already received from the fluid solver and is expressed as

$$q_w^{\text{Solid}} = q_w^{\text{Fluid}} + h_F \left(T_w^{\text{Fluid}} - T_w^{\text{Solid}} \right) \tag{5.7}$$

h_F has the dimension of a heat transfer coefficient and can be thought of as a user-defined relaxation factor to ensure stability. An optimal value can be computed according to Errera and Chemin (2013) as

$$h_F^{opt} = \frac{K_F}{1 + \sqrt{1 + 2D_F}} \tag{5.8}$$

where D_F is the fluid's Fourier number (adopting the authors' notation)

$$D_F = \frac{a_F \Delta t_F}{\Delta x_F^2}, \quad \text{with } a_F = \frac{\lambda_F \rho_F}{C_{p,F}} \tag{5.9}$$

and K_F is defined as

$$K_F = \frac{\lambda_F}{\nu \Delta x_F} \tag{5.10}$$

Note that all quantities with a subscripted "F" are evaluated based on fluid properties. ν is a parameter which is $\nu = 1$ for cell-vertex schemes, or $\nu = 0.5$ for cell-centered schemes. Imposing h_F^{opt} in a Conjugate Heat Transfer simulation guarantees the fastest convergence for a given problem without any requirement for the time step of each domain.

5.2 Solid domain of the MICCA combustor and mesh

In order to carry out Conjugate Heat Transfer (CHT) simulations, all relevant solid parts of a given geometry must be modeled and meshed separately in addition to the fluid domain mesh (see Chap. 3). Although the solid domain consists of multiple individual components (*cf.* exploded view in Fig. 3.2), only one contiguous mesh is generated. Material indices are subsequently assigned to all mesh regions and are used during simulation to correctly select and compute the associated material properties. These are discussed in Sec. 5.2.1.

Taking advantage of its rotational symmetry, we perform Conjugate Heat Transfer simulations of MICCA-Spray in the bisector geometry (see Sec. 3.3.2.2) to limit the required computational costs. We reiterate that these simulations serve the main purpose of determining wall temperature profiles under stationary and fully ignited operating conditions, which are later applied as boundary condition in Chap. 7. It is thus reasonable to assume that the steady-state wall temperature is symmetric in azimuthal sense.

Figure 5.2(a) illustrates the solid domain considered for CHT simulations. Note that the injector in the foreground is shown in a cutaway view to reveal the swirler and atomizer. The material indices assigned to the individual component parts correspond to the following materials: (1) fused silica quartz tubes (CORNING® HPFS 7980, Corning Inc. (2015)); (2) stainless steel (atomizers, injector blocks, injector support); (3) brass (terminal plates, swirlers). We emphasize that the solid domain shown is Fig. 5.2 is simplified with respect to the real experimental geometry. Specifically, the 3D-model does not account for the internal water cooling, which must be considered as an additional source of modeling uncertainties. Since temperatures of the injector support are unknown and neither water flow rates nor water temperatures were monitored experimentally, we have no means to quantify these uncertainties either.

The swirlers and atomizers are meshed with a constant cell size of $0.5\,\mathrm{mm}$, and gradual coarsening is applied towards the bottom end of each injector block as well as in radial direction. In the lower outermost edges, the cell size is set to $1.6\,\mathrm{mm}$. Although larger cells could be justified in the injector assembly from a pure numerical point of view, mesh interpolation errors were observed in regions where the fluid and solid mesh sizing is very different. Therefore, similar cell sizes in both domains have been preferred in this region.

Axial coarsening is also applied to the quartz mesh, ranging between $0.6\,\mathrm{mm}$ in the vicinity of the flame, and $1.2\,\mathrm{mm}$ at the upper quartz edge (not visible in Fig. 5.2(b)). In total, the mesh consists of $688\,183$ nodes, equivalent to 3.5 million tetrahedral cells.

All internal surfaces exposed to the fluid flow are coupled (red surfaces in Fig. 5.2(c)) as visualized in Fig. 5.2(d), showing the coupling interface between the fluid and solid domain of the bisector. Conversely, both external quartz wall interfaces with the ambient air are uncoupled (green surfaces in Fig. 5.2(c)). At these surfaces, we impose a heat transfer coefficient instead which accounts for natural convection and radiation (see Sec. 5.2.2).

5.2.1 Solid material properties

The material properties of stainless steel (atomizer and injector block) and brass (swirlers and terminal plates) are taken from Valencia and Quested (2008): the heat capacities C_s and

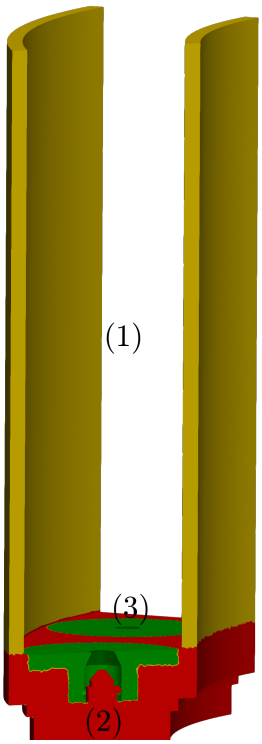

(a) Material indices used in the solid domain of the bisector. 1: quartz (fused silica "HPFS 7980", Corning Inc. (2015)); 2: stainless steel; 3: brass. The injector in the foreground is intentionally shown as cutaway view to reveal the swirler and atomizer.

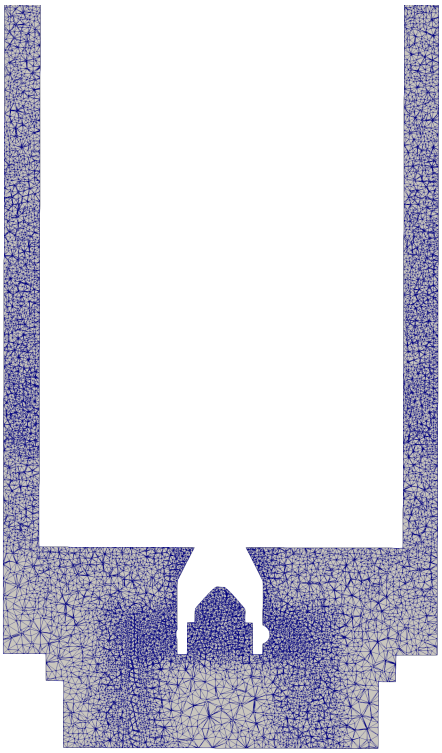

(b) Enlarged mesh view on the central cutplane through the solid domain.

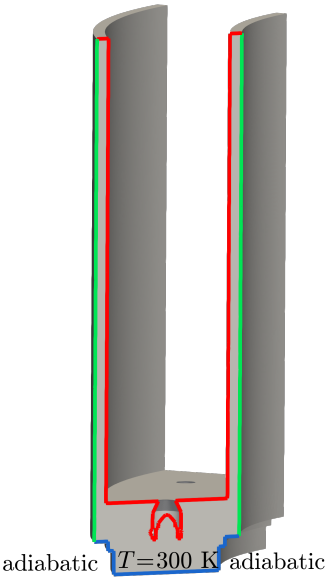

(c) Boundary conditions for CHT simulations: red surfaces: coupling interface; green surfaces: imposed heat transfer coefficient for convection and radiation; blue bottom edge: imposed temperature; left and right blue edges: adiabatic.

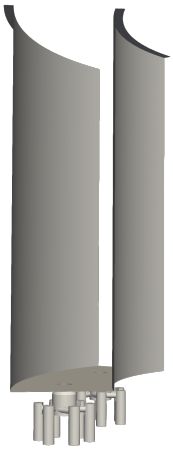

(d) Visualization of the coupling interface between the fluid and solid domain of the bisector geometry.

Figure 5.2: Solid domain visualization of the bisector, corresponding mesh, boundary conditions and coupling interface.

heat conductivities λ_s are expressed through polynomial functions of the local temperature (see Fig. 5.3(a) and (b)), while the material densities ρ_s are constant. In turn, manufacturer specifications are taken for the quartz characteristics (CORNING® HPFS 7980 fused silica, Corning Inc. (2015)), which are added in Fig. 5.3(a) and (b).

For the following (simplified) description of the radiative heat transfer at the quartz' interface with the ambient air, we assume that the quartz is semi-transparent. In general, the radiative properties of a generic quartz slab with a given thickness are characterized by a slab absorptance A_λ^{slab}, a slab reflectance R_λ^{slab} and a slab transmittance T_λ^{slab} (see for example Modest (2013)). These properties usually depend on the wavelength λ and can be computed from manufacturer specifications. For the present quartz for example, the internal transmittance of a $1\,\mathrm{cm}$ quartz slab (see Fig. 5.3(c)) and the wavelength-dependent refraction index are provided at ambient temperature. However, the radiative properties must be expressed as a function of temperature to be compatible with the AVTP solver. Thus, we derive Planck-mean radiative properties following the approach presented by Rodrigues et al. (2018) which is based on a simplified spectral band model.

In defining a threshold value for the slab transmittance $T_{threshold}^{slab}$, each spectral band is either set to be transparent if $T_\lambda^{slab} > T_{threshold}^{slab}$, or otherwise entirely opaque. This allows to simplify the mathematical expressions for A_λ^{slab}, R_λ^{slab} and T_λ^{slab}, which are plotted in Fig. 5.3(d) for a quartz slab of $5\,\mathrm{mm}$ thickness. Integrating and averaging the simplified expressions (superscript "model") over the entire wavelength spectrum yields Planck-mean radiative properties as a function of temperature (denoted with an overbar), which are plotted in Fig. 5.3(e). These results suggest that rays originating from a low temperature heat source are essentially absorbed by the quartz, whereas rays from a high temperature source are mostly transmitted.

The corresponding threshold value for the present configuration is $T_{threshold}^{slab} = 0.39$ for a slab of $5\,\mathrm{mm}$ thickness. It is determined such that it minimizes the error of the model transmittance $T_\lambda^{\mathrm{slab,\,model}}$ with respect to the detailed slab transmittance T_λ^{slab}. Within the relevant temperature range, the average error is 0.82%.

5.2.2 Modeling of the heat transfer at uncoupled walls

As we already mentioned in Sec. 5.2, all internal interfaces between the fluid and solid domain are coupled via a Dirichlet-Robin boundary condition, notably the internal combustor walls and the internal injector walls. In turn, the external quartz walls facing the ambient air are uncoupled and require a suitable description of heat transfer with the environment, which is assumed to be governed by natural convection and radiation.

Heat transfer by natural convection is expressed in terms of a heat transfer coefficient h_{conv}, which itself is evaluated according to a Nusselt-correlation proposed by Churchill and Chu (1975), valid in the laminar and turbulent regime

$$\mathrm{Nu}^{1/2} = 0.825 + \frac{0.387\mathrm{Ra}^{1/6}}{\left[1 + (0.492/\mathrm{Pr})^{9/16}\right]^{8/27}} \tag{5.11}$$

In the above expression, Ra denotes the Rayleigh number, and Pr the Prandtl number. The former is the product of the Grashof and the Prandtl number, *i.e.*

$$\mathrm{Ra} = \mathrm{Gr} \cdot \mathrm{Pr} \tag{5.12}$$

where

$$\mathrm{Gr} = \frac{g\beta(T_w - T_\infty)x^3}{\nu^2} \tag{5.13}$$

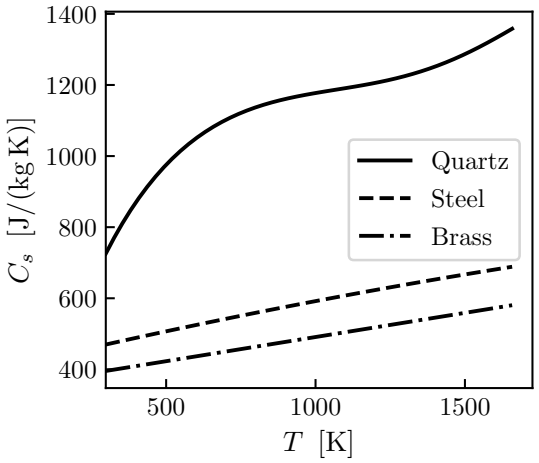

(a) Heat capacities

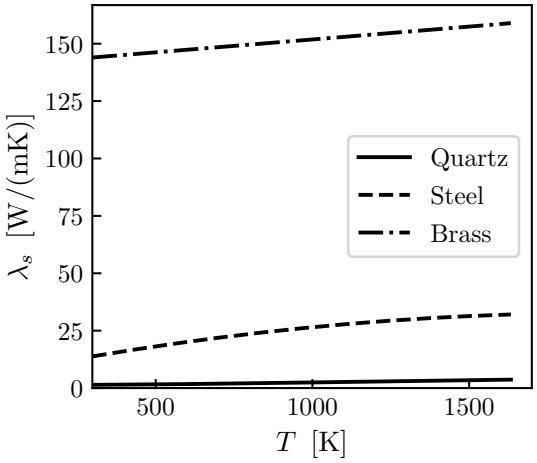

(b) Heat conductivities

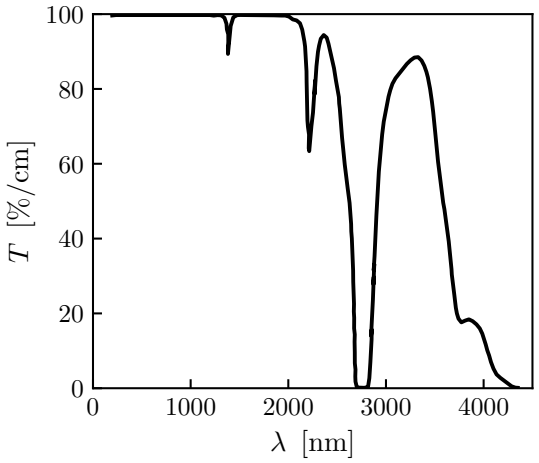

(c) Transmittance of a $1\,\mathrm{cm}$ CORNING® HPFS 7980 quartz slab (Corning Inc., 2015)

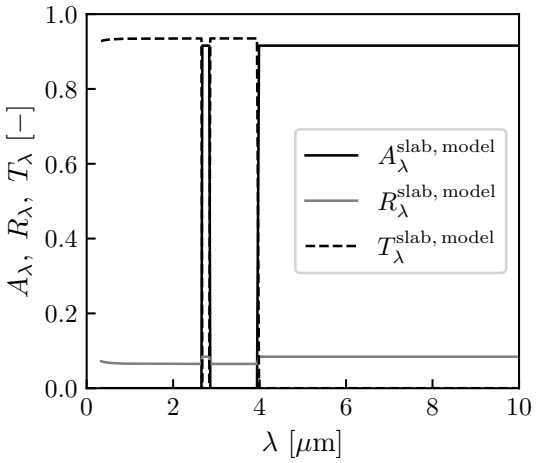

(d) Transparent and opaque spectral band model for a quartz slab of $5\,\mathrm{mm}$ thickness

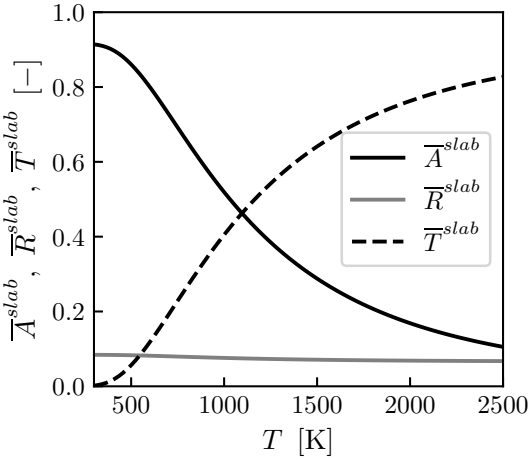

(e) Planck-mean radiative properties computed according to the simplified band model (quartz slab thickness $5\,\mathrm{mm}$)

Figure 5.3: Solid material properties as a function of temperature.

The Grashof number can be interpreted as the ratio between buoyant and viscous forces, where g is the gravitational acceleration, β the isobaric volume expansion coefficient, T_w the local wall temperature, T_∞ the far-field (or ambient) temperature, ν the kinematic viscosity, and x the streamwise coordinate.

With this correlation, we can compute the heat transfer coefficient for natural convection as

$$h_{conv}(x) = \frac{\mathrm{Nu} \cdot \lambda}{x} \tag{5.14}$$

The net radiative heat transfer between the external quartz surface and the ambient can be expressed as

$$q^{rad} = \sigma(\overline{A}^{slab}(T)T^4_{w,\,\mathrm{ext}} - \overline{A}^{slab}(T_{\mathrm{amb}})T^4_{\mathrm{amb}}) \tag{5.15}$$

where $\overline{A}^{slab}(T)$ is the Planck-mean absorptance of the quartz (see Sec. 5.2.1), $T_{w,\,\mathrm{ext}}$ the local wall temperature of the external quartz surface, and T_{amb} the ambient temperature. σ denotes the Stefan-Boltzmann constant. These equations have been implemented into AVTP to compute the net heat transfer between the external quartz walls and the environment.

5.3 Advanced wall modeling for heat transfer

As we pointed out in Sec. 2.7, detailed modeling of the near-wall flow constitutes a crucial part of light-round simulations, motivating the development of our custom wall model. The principal deficiencies observed with existing wall model implementations in AVBP originate from the fact that only density is allowed to vary in the boundary layer whereas C_p, μ and λ are assumed to be constant. This assumption is inappropriate for variable property flows in general (see Sec. 2.7.2), and for light-round ignition in particular, where hot burnt gases are exposed to combustor walls at ambient temperature. Puggelli et al. (2020) postulated in an *a priori* study that wall heat fluxes may be underestimated by up to 70% under such assumptions during light-round. The corresponding temperature ratio between burnt gases and the wall can reach $T_b/T_w \geq 6$, which exceeds ratios of $T_b/T_w = 3$ investigated by Cabrit and Nicoud (2009) with AVBP's wall functions. Even with combustor wall preheating, heat transfer cannot be neglected, as we shall see in Chap. 7. Hence, to improve the modeling of the near wall flow, a tabulated wall model approach is proposed here, abbreviated as "TABWM".

5.3.1 Table generation from 1D boundary layer simulations

A promising alternative to algebraic wall functions or full wall-resolved LES can be developed from the Thin Boundary Layer Equations (TBLE, Schlichting and Gersten (2017)). This equation set is flexible enough to handle more complex geometries and variable flow properties at lower computational costs than wall-resolved LES. Examples can be found in Cabot and Moin (2000) for a backward facing step with flow separation and attachment, Balaras et al. (1996) for a rotating channel flow (among other configurations) with a distinct absence of a logarithmic layer, Benarafa et al. (2007) for heated turbulent channel flows, Wang and Moin (2002) flows past an airfoil trailing edge, or Duprat et al. (2011) for channel flows with streamwise pressure gradients. The modeling approach proposed here is similar to the work of Maheu et al. (2012): an interpolation database is generated to compute local wall heat fluxes and wall shear stresses as a function of known quantities at the first off-wall node of the mesh, also referred to as matching point (MP). Essentially, the one-dimensional Thin

Boundary Layer Equations (TBLE, Schlichting and Gersten (2017), recalled below) are solved for a set of generic boundary layers with the EM2C in-house solver AGATH

$$\frac{\partial}{\partial y}\left[\left(\bar{\mu}+\mu_t\right)\frac{\partial \bar{u}}{\partial y}\right]=0 \qquad \text{(2.149 (revisited))}$$

$$\frac{\partial}{\partial y}\left[\left(\bar{\lambda}+\lambda_t\right)\frac{\partial \overline{T}}{\partial y}\right]=0 \qquad \text{(2.150 (revisited))}$$

Moreover, we assume the boundary layer to be stationary, which we justify in an *a posteriori* assessment in Sec. 6.5.5.3. The turbulent viscosity μ_t is evaluated according to the expression proposed by Cabot and Moin (2000)

$$\mu_t = \rho\kappa y u_\tau D \tag{5.16}$$

where κ is the von Kármán constant, y the wall distance and u_τ the friction velocity. D is a damping factor defined as

$$D = \left[1-\exp\left(-y^\star/A^+\right)\right]^2 \tag{5.17}$$

with $y^\star$ denoting the non-dimensional wall distance computed as in Eq. 2.169 (with semi-local scaling). The model parameter is set to $A^+ = 17$. The turbulent heat conductivity λ_t is computed according to the following expression

$$\lambda_t = \frac{\mu_t \overline{C}_p}{\mathrm{Pr}_t} \tag{5.18}$$

and the turbulent Prandtl number is evaluated from an expression proposed by Kays (1994)

$$\mathrm{Pr}_t = \frac{1}{\frac{1}{C_1\mathrm{Pr}_{t,\infty}} + C_2\mathrm{Pr}\frac{\mu_t}{\mu}\sqrt{\frac{1}{\mathrm{Pr}_{t,\infty}}} - \left(C_2\mathrm{Pr}\frac{\mu_t}{\mu}\right)^2\left[1-\exp\left(-\frac{1}{C_2\mathrm{Pr}\frac{\mu_t}{\mu}\sqrt{\mathrm{Pr}_{t,\infty}}}\right)\right]} \tag{5.19}$$

The model constants are set to $C_1 = 2$ and $C_2 = 0.3$, while $\mathrm{Pr}_{t,\infty} = 0.92$ designates the far-field Prandtl number in the limit of $y^\star$ approaching infinity.

The resulting wall shear stresses and wall heat fluxes obtained from Eqs. 2.149 and 2.150 are tabulated for each generic boundary layer as a function of three parameters: the temperature T_{MP}, the velocity u_{MP} and the distance δ_{MP} of the matching point, shown as red off-wall nodes in Fig. 5.6. If the wall temperature T_w is not constant, it is included in the table as an additional parameter. Since we intend to use the table as an interpolation database during later LES, we must ensure that the generic boundary layer conditions cover those encountered during LES. Hence, appropriate boundary conditions must be imposed for the solution of the Thin Boundary Layer Equations, specifically the fluid composition, the equivalence ratio, T_{MP}, u_{MP}, δ_{MP} and T_w, which is achieved as follows.

First, we make assumptions about the fluid composition and its equivalence ratio to limit the table's dimensionality. Three different scenarios are considered in this work, resulting in three individual tables:

1. **light-round ignition with combustor walls at $T_w = 300\,\mathrm{K}$:** in this case, hot burnt gases are exposed to cold combustor walls at *constant* wall temperature, requiring a table with three parameter dimensions T_{MP}, u_{MP} and δ_{MP}, and the corresponding values for $\overline{\tau}_w$ and $\overline{q}_w$. This table is referred to as "BURNT-3D" in Tab. 5.1.

	BURNT-3D	BURNT-4D	AIR-4D	Resolution
Composition	burnt gases	burnt gases	fresh gases	-
ϕ [-]	0.89	0.89	0.89	-
T_w [K]	300	300 - 1600	300 - 1550	- / $50\,\mathrm{K}$ / $50\,\mathrm{K}$
T_{MP} [K]	300 - 2300	300 - 2300	300 - 1000	$50\,\mathrm{K}$
u_{MP} [m/s]	0 - 50	0 - 50	0 - 50	$0.5\,\mathrm{m/s}$
δ_{MP} [mm]	0.2 - 1	0.2 - 1	0.2 - 1	$0.01\,\mathrm{mm}$
Data points	$324\,000$	$8\,966\,700$	$5\,686\,200$	-
File size	$5\,\mathrm{MB}$	$132\,\mathrm{MB}$	$87\,\mathrm{MB}$	-
Target c_{MP}	$0.5 \leq c_{\mathrm{MP}} \leq 1$	$0.5 \leq c_{\mathrm{MP}} \leq 1$	$0 \leq c_{\mathrm{MP}} < 0.5$	-

Table 5.1: Interpolation table characteristics. Table BURNT-3D contains only three parameter dimensions, with T_w being constant. The number of data points refers to each target variable ($\overline{\tau}_w$ and $\overline{q}_w$).

2. **light-round ignition with preheated combustor walls:** in this case, hot burnt gases may be exposed to a *range* of wall temperatures, thus requiring a fourth parameter dimension T_w. We refer to this table as "BURNT-4D" in Tab. 5.1.

3. **pre-fueling with preheated combustor walls:** in order to establish the initial conditions prior to light-round with preheated combustor walls, fuel and air are injected into the combustion chamber until stationary conditions are reached. Thus, the fluid composition exposed to preheated walls is necessarily a mixture of n-heptane and air. The corresponding table is referred to as "AIR-4D" in Tab. 5.1.

Consequently, the Thin Boundary Layer Equations are only solved for a constant fluid composition (either burnt gases or a n-heptane/air mixture) at a constant equivalence ratio of $\phi_{glob} = 0.89$, corresponding to the global equivalence ratio at which the combustor is operated. Due to n-heptane's high volatility and enhanced evaporation rates with preheated walls (see Sec. 7.3.2), it appears reasonable to assume a constant equivalence ratio.

Second, appropriate parameter ranges must be determined for the matching point properties T_{MP}, u_{MP} and δ_{MP}. The matching point distance is already known *a priori*, since it is dictated by the LES mesh sizing. In turn, we use a wider range for T_{MP} and u_{MP} as specified in Tab. 5.1 in order to safely cover the entire range of possible combinations which may be encountered during LES.

Third, for tables BURNT-4D and AIR-4D, we use the wall temperature profiles obtained from precursor Conjugate Heat Transfer (CHT) simulations to infer an appropriate range for T_w (see Tab. 5.1). Note that all wall temperature profiles are "frozen" during light-round simulations and pre-fueling, allowing for a narrow range of T_w to be considered for the solution of the Thin Boundary Layer Equations.

The resolution of each matching point quantity and T_w is given in the last column of Tab. 5.1, where appropriate. For example, table BURNT-3D is generated by solving the Thin Boundary Layer Equations for T_{MP} swept between $[300, 2300]\ \mathrm{K}$ in steps of $50\,\mathrm{K}$, u_{MP} between $[0, 50]\ \mathrm{m/s}$ in steps of $0.5\,\mathrm{m/s}$ and δ_{MP} between $[0.2, 1]\ \mathrm{mm}$ in steps of $0.01\,\mathrm{mm}$. For tables BURNT-4D and AIR-4D, the resolution of T_w is $50\,\mathrm{K}$, ensuring very low interpolation errors as discussed in Sec. 5.3.3.

The non-dimensional velocity and temperature profiles in the boundary layer are plotted in Fig. 5.4 (solid lines) for an arbitrary tuple of parameters within the limits defined above.

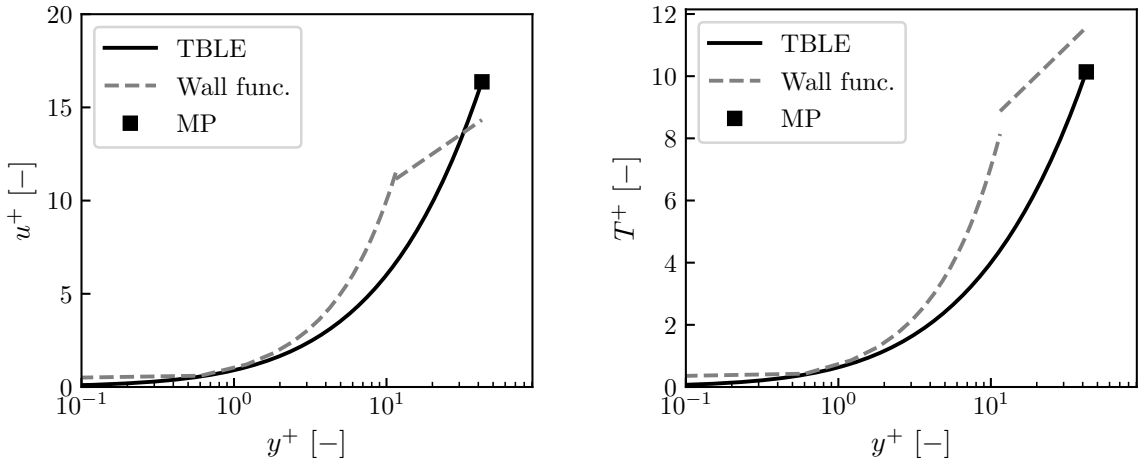

(a) Non-dimensional velocity profile

(b) Non-dimensional temperature profile

Figure 5.4: Non-dimensional velocity and temperature profiles of a turbulent and stationary boundary layer. Solid lines: general boundary layer equations (Eqs. 2.149 and 2.150) with variable properties; dashed lines: wall functions (Eqs. 2.164 - 2.167) with constant boundary layer properties. The following arbitrary parameter tuple is used: $T_{\mathrm{MP}} = 1700\,\mathrm{K}$, $u_{\mathrm{MP}} = 10\,\mathrm{m/s}$, $\delta_{\mathrm{MP}} = 1\,\mathrm{mm}$, $T_w = 300\,\mathrm{K}$.

These profiles are obtained from the solution of the Thin Boundary Layer Equations with variable thermophysical properties (ρ, λ, C_p and μ). Most importantly, they are distinctly different from theoretical profiles assuming *constant* boundary layer properties (dashed lines in Fig. 5.4): both TBLE profiles (velocity and temperature) do not exhibit a logarithmic region, but follow a linear evolution instead. Thus, while algebraic wall functions would predict the matching point (MP) to reside in the logarithmic region, it is actually found in the viscous sublayer in this example. Consequently, wall heat fluxes predicted through wall functions with constant thermophysical properties inevitably fail to predict the correct value that would have been obtained through the solution of the (steady) Thin Boundary Layer Equations. The root cause for such discrepancies has been emphasized by Patel et al. (2015): scaling laws for constant property boundary layers are not universally applicable if variable properties must be expected, since turbulent statistics are no longer a unique function of the wall distance and the friction Reynolds number. Under these conditions, a semi-local scaling (Huang et al., 1995; Patel et al., 2015) with local quantities (instead of quantities evaluated *at* the wall) is necessary. Hence, it is reasonable to pursue a modeling strategy incorporating variable thermophysical properties as expected during light-round.

Figure 5.5 visualizes arbitrarily selected two-dimensional cutplanes of table BURNT-4D at a fixed wall temperature of $T_w = 900\,\mathrm{K}$. The left column of Fig. 5.5 corresponds to the wall heat flux, the right column to the wall shear stress, which were both obtained from the solution of the Thin Boundary Layer Equations. By convention, q_w is positive if $T_{\mathrm{MP}} > T_w$ and negative vice versa. Since we deliberately chose a fixed $T_w = 900\,\mathrm{K}$, we can observe the change in sign of q_w at $T_{\mathrm{MP}} = 900\,\mathrm{K} = T_w$ in Fig. 5.5(c) and (e).

All tables are created only once and are conveniently stored in HDF5 files. They are subsequently supplied to AVBP as outlined in the following section.

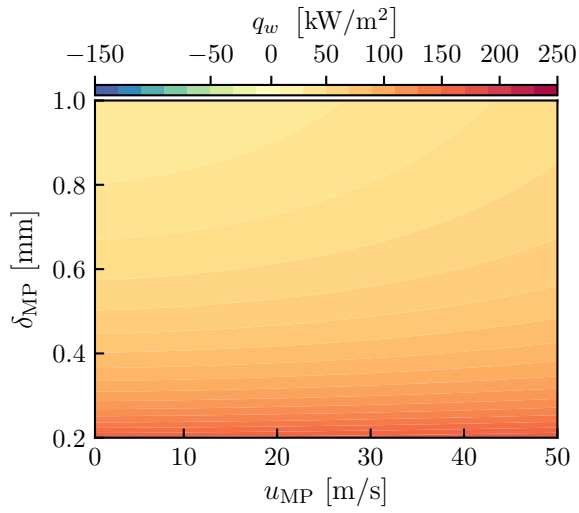

(a) $T_{MP} = 1300\,K$

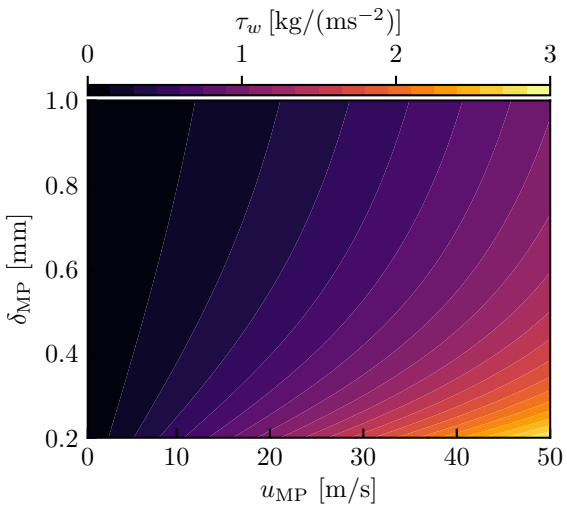

(b) $T_{MP} = 1300\,K$

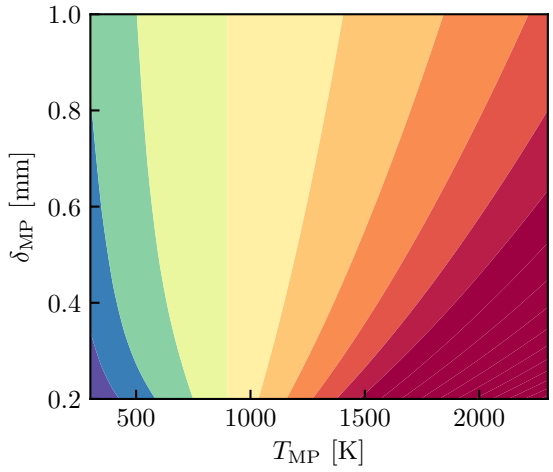

(c) $u_{MP} = 25.5\,m/s$

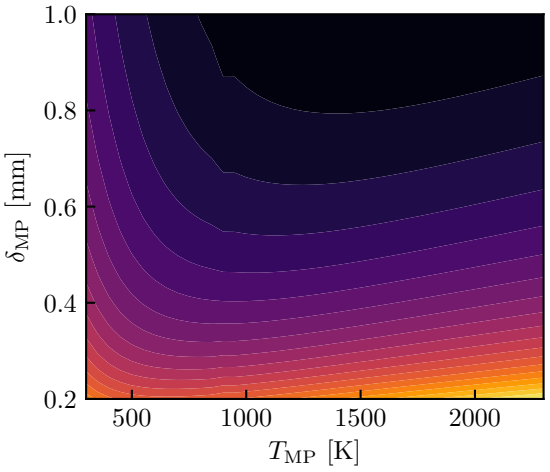

(d) $u_{MP} = 25.5\,m/s$

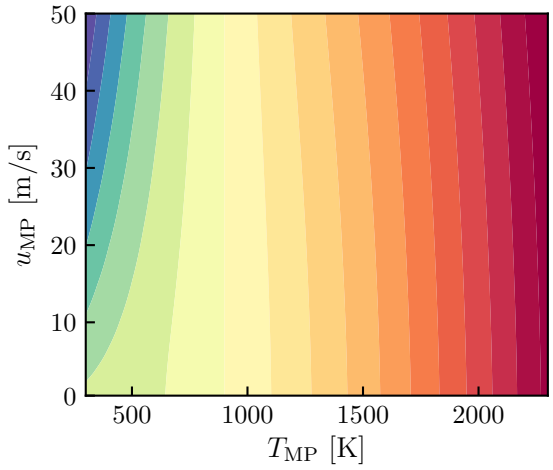

(e) $\delta_{MP} = 0.6\,mm$

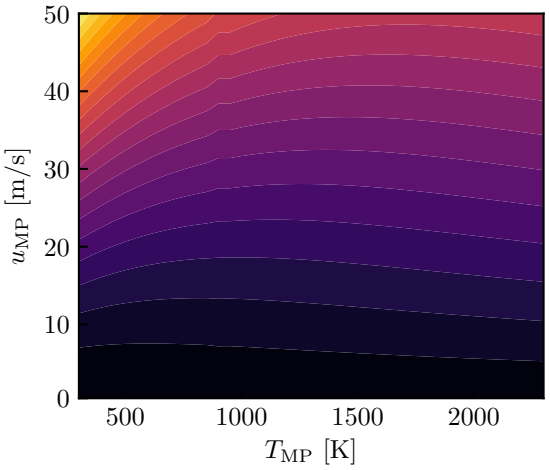

(f) $\delta_{MP} = 0.6\,mm$

Figure 5.5: Visualization of q_w ((a), (c), (e)) and τ_w ((b), (d), (f)) for table BURNT-4D. The wall temperature is fixed to an arbitrary value of $T_w = 900\,K$ in all images. A second parameter is set constant as indicated in each subcaption to obtain 2D table slices. These values are arbitrarily chosen to be the midpoints of each table dimension.

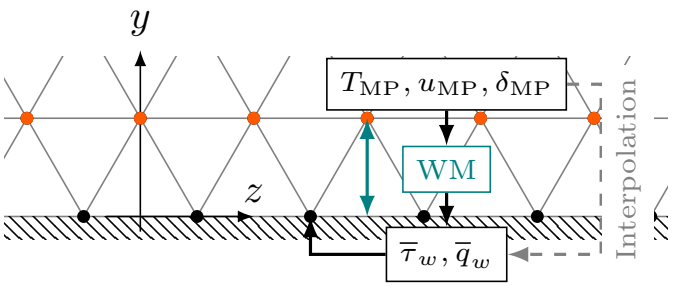

Figure 5.6: Simplified illustration of AVBP's wall modeling approach and the table interpolation approach proposed in this work. Instead of computing $\overline{\tau}_w$ and $\overline{q}_w$ from wall models (WM), we obtain those quantities from table interpolation based on the instantaneous properties at each matching point (red off-wall nodes). Wall nodes (black) may either have a constant or variable temperature.

5.3.2 Implementation into AVBP

Since the interpolation tables (see Tab. 5.1) are stored in AGATH's native table format, additional I/O routines have been developed for AVBP to correctly load the corresponding HDF5 files. Furthermore, AVBP is instructed to bypass the execution of its own wall model routines and instead interpolate $\overline{\tau}_w$ and $\overline{q}_w$ from the pre-generated tables based on T_{MP}, u_{MP}, δ_{MP} and optionally T_w (see Fig. 5.6).

In principle, multiple tables can be loaded into AVBP and assigned to separate wall "regions": for example, table BURNT-4D can be assigned to regions where burnt gases are in contact with a given combustor wall, whereas table AIR-4D can be assigned to fresh gas regions within the *same* simulation. This separation is achieved based on the matching point progress variable c_{MP} (or off-wall progress variable). It is defined as in Eq. 2.50, but evaluated at the matching point only

$$c_{\mathrm{MP}} = \frac{Y_{\mathrm{CO_2,MP}} + Y_{\mathrm{CO,MP}}}{(Y_{\mathrm{CO_2}} + Y_{\mathrm{CO}})|_{eq}} \tag{5.20}$$

In the above example, table interpolation is either performed in table BURNT-4D, if $c_{\mathrm{MP},c} \leq c_{\mathrm{MP}} \leq 1$, or in table AIR-4D, if $0 \leq c_{\mathrm{MP}} < c_{\mathrm{MP},c}$ (see last row in Tab. 5.1), owing to the fact that each table is constructed based on a constant fluid composition. Alternatively, table BURNT-3D (for burnt gases) can be used concurrently with AVBP's wall model (for fresh gases only), if the fresh gas temperature is the same as the wall temperature. Under such conditions, variations of fluid properties in the boundary layer (of the fresh gases) are supposed to be negligible, allowing to compute wall shear stresses and wall heat fluxes with good accuracy with standard wall functions. We employ this configuration in Chap. 6, since the table AIR-4D (not yet generated at the time when LES of Chap. 6 was carried out) would not have brought any improvement of the near-wall flow either.

$c_{\mathrm{MP},c}$ is an arbitrary cutoff value to toggle between interpolation tables. Its impact has been evaluated in a precursor sensitivity analysis, yielding $c_{\mathrm{MP},c} \equiv 0.5$ as the most suitable value.

For interpolation, we use the COMMCOMB-library, which encapsulates generic routines already used in AGATH. It is linked to AVBP upon building the main executable as any other external library. The interpolation routine itself proceeds in two steps: first, the interpolation weights are computed according to the input variables (T_{MP}, u_{MP}, δ_{MP} and optionally T_w), before batch-processing each target variable ($\overline{\tau}_w$ and $\overline{q}_w$) using the precomputed weights.

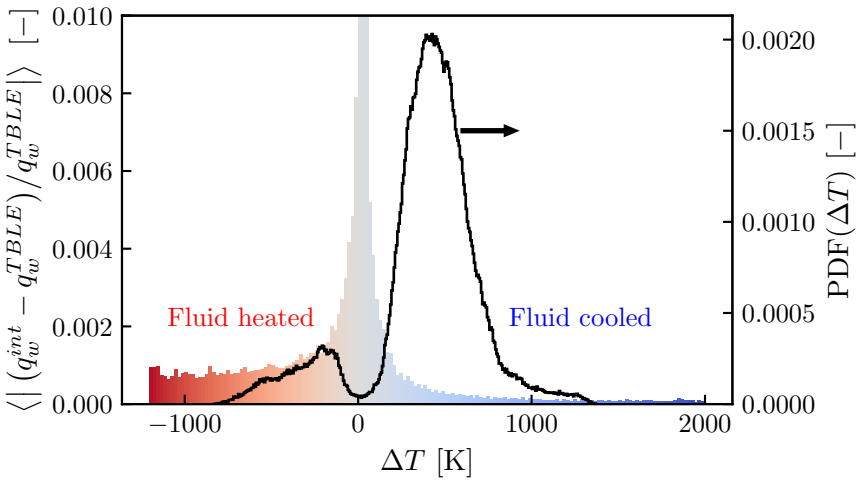

Figure 5.7: Filled histogram: bin-averaged relative error of the interpolated wall heat flux with respect to the predicted value from the Thin Boundary Layer Equations as a function of the temperature difference $\Delta T = T_{\mathrm{MP}} - T_w$. Error computed for random tuples of T_{MP}, u_{MP}, δ_{MP} and T_w (table: BURNT-4D). Black curve: probability density function (PDF) of ΔT sampled from the light-round simulation presented in Chap. 7, before flame front merging.

5.3.3 Interpolation error evaluation

In order to quantify the interpolation error for each table independently from LES, we employ the following strategy: first, random tuples of T_{MP}, u_{MP}, δ_{MP} and T_w (if required) are generated within the range limit of each parameter dimension. Second, we compute τ_w and q_w in two different manners using the *same* tuple for both: (i) by table interpolation and (ii) by solving the Thin Boundary Layer Equations in AGATH. Third, we compute the relative error ϵ_ϕ for each solution variable defined as

$$\epsilon_\phi = \frac{\phi^{int} - \phi^{TBLE}}{\phi^{TBLE}} \tag{5.21}$$

where ϕ can be either τ_w or q_w. A superscripted "int" denotes the result obtained through table interpolation, while a superscripted "TBLE" denotes the result obtained from solving Eqs. 2.149 and 2.150.

For table BURNT-3D, interpolation results are found to be very accurate, with relative errors below 1% for each solution variable based on a sample size of $20\,000$ random tuples. Interestingly though, larger relative errors may occur specifically in q_w if T_w is included as an additional table dimension. Therefore, it is worth examining if those larger errors are relevant for light-round simulations in Chap. 6 and 7. In the following, we focus on table BURNT-4D in the interest of brevity, but our conclusion also apply to table AIR-4D.

Figure. 5.7 shows the bin-averaged error ϵ_{q_w} as a function of the temperature difference $\Delta T = T_{\mathrm{MP}} - T_w$. The entire value range of ΔT is divided into bins of constant width, and the relative error is subsequently averaged over all samples that fall into a given bin. For $\Delta T > 0\,\mathrm{K}$, the fluid is cooled (heat flux from the fluid onto the combustor walls), and heated if $\Delta T < 0\,\mathrm{K}$ (heat flux in the opposite direction).

Plotting the relative error distribution in this manner reveals a distinct peak around $\Delta T = 0\,\mathrm{K}$, which steeply falls below 1% for increasing positive and negative temperature differences. This is because, in the limit of $\Delta T \to 0$, the heat flux q_w^{TBLE} approaches zero, and ϵ_{q_w} tends towards infinity in Eq. 5.21. Thus, even small numerical differences between q_w^{int} and q_w^{TBLE}

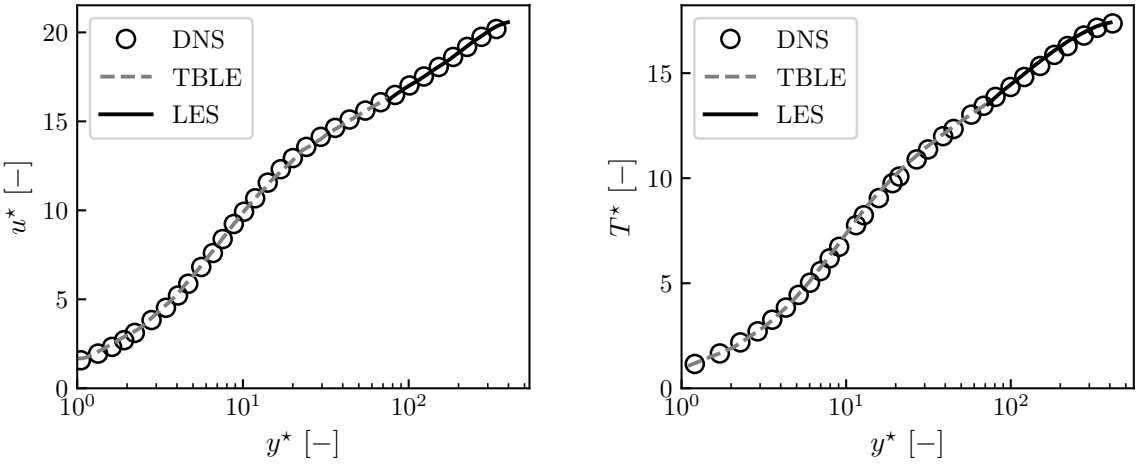

(a) Mean velocity profile

(b) Mean temperature profile

Figure 5.8: Validation of the equilibrium wall model: mean velocity and temperature profiles of a boundary layer in a generic channel flow. Circle markers: DNS results; dashed lines: profiles obtained from the solution of the TBLE equations up to the matching point; solid lines: LES profiles of the far-field flow. Images taken from Gelain (2021).

will cause large relative interpolation errors, although the absolute value of the wall heat flux remains negligible given the vanishing temperature differences.

Yet we have only been concerned with randomly sampled test data so far, from which we cannot infer if those large interpolation errors at $\Delta T = 0\,\mathrm{K}$ are also relevant during light-round simulations. More specifically, it seems unlikely to encounter vanishing temperature differences between the matching point and the combustor walls in either light-round case of Chap. 6 or 7: firstly, burnt gas temperatures are much higher than the imposed wall temperatures, even under preheated conditions, and the light-round durations too short for the matching point temperature to decrease fast enough to reach T_w. Secondly, the residence time of fresh gases in the preheated combustion chamber is too short to reach wall temperature levels from an initial temperature of $T = 300\,\mathrm{K}$.

To further substantiate this argument, it is instructive to compute the temperature differences obtained from preheated light-round simulations in Chap. 7. We have specifically chosen an instant before flame front merging in order to maximize the time burnt gases may be exposed to the combustor walls, thus maximizing the cooling effect. The probability density function (PDF) of ΔT (sampled from light-round LES) is given in Fig. 5.7 as black curve. It exhibits a larger peak at $\Delta T = +420\,\mathrm{K}$, corresponding to burnt gases cooled by the combustor walls, and a much smaller peak at $\Delta T = -180\,\mathrm{K}$, corresponding to heated fresh gases. For these temperature differences, the interpolation error is below 0.2% (see colored histogram). Most importantly however, the PDF is essentially zero around $\Delta T = 0\,\mathrm{K}$, proving that the interpolation error remains negligible over the relevant ΔT-range found in this work. Similarly, the interpolation error of table AIR-4D also remains below 1% for $\Delta T \neq 0$.

While the previous error assessment provides information about the *interpolation* accuracy, it does not evaluate the accuracy and appropriateness of the Thin Boundary Layer Equations as such. We recall that various assumptions (*e.g.,* boundary layer at equilibrium) and models (*e.g.,* for μ_t and λ_t) are used to derive the final expressions given in Eqs. 2.149 and 2.150, which deserve a separate model validation. This task has already been performed by Gelain (2021) using the same AGATH routines to evaluate the Thin Boundary Layer Equations. A comparison

of mean velocity and temperature profiles in a generic iso-thermal channel flow configuration has revealed a very good agreement between the TBLE approach and DNS results. The DNS profiles in Fig. 5.8 (taken from Gelain (2021)) are sampled from a fully developed turbulent boundary layer, while the TBLE profiles are obtained from solving Eqs. 2.149 and 2.150 up to the matching point. Beyond the matching point, velocity and temperature profiles are determined by the LES solver.

Although Gelain (2021) solves the Thin Boundary Layer Equations directly without table interpolation as in the present work, we consider both approaches to be essentially equivalent, given the negligible interpolation errors. Therefore, the previously cited channel flow validation also validates our tabulation setup.

5.4 Conclusions

Heat transfer problems are of central importance for combustor design and dynamic combustion processes relevant for aeroengine combustion chambers. Light-round ignition in particular was found to be sensitive to combustor wall temperatures, requiring accurate numerical models to describe the governing heat transfer processes. Therefore, we have addressed two major modeling limitations that were revealed in previous works: first, preheated combustor walls are likely to affect the fresh gas state prior to ignition, which had not been taken into account due to the lack of experimental wall temperature profiles in MICCA-Spray. Thus, we have presented computational approaches to determine temperatures at the interface between the fluid and solid domain by means of Conjugate Heat Transfer (CHT) simulations. Second, algebraic wall functions employed in previous works were shown to oversimplify the near-wall flow, specifically the thermophysical properties of the boundary later. As a consequence, we have developed and proposed a custom tabulated wall model based on pre-tabulated solutions of the Thin Boundary Layer Equations (TBLE).

With regard to the first aspect, we have introduced strategies for coupled code execution for CHT simulations, involving separate solvers for each domain (AVBP and AVTP), a code coupling library OpenPALM, and an interface mesh interpolation tool CWIPI. Owing to vastly different characteristic time scales in the solid and fluid domain, we have discussed the desynchronization method for convergence acceleration, whilst ensuring the stability of the simulation. We have subsequently presented the solid domain, material properties and coupling interfaces of the CHT simulations relevant for Chap. 7.

In the last part of this chapter, we have detailed the development and implementation of our custom tabulated wall model, termed TABWM. Essentially, a database of wall heat fluxes q_w and wall shear stresses τ_w was generated by solving the Thin Boundary Layer Equations for generic boundary layers and tabulating q_w and τ_w as functions of four parameters: (i) the matching point temperature, (ii) the matching point velocity, (iii) the matching point distance, and (iv) the wall temperature. This table can then be supplied to the LES solver, which uses the interpolated values of q_w and τ_w in the simulation, instead of solving expressions for algebraic wall models. The table interpolation error was evaluated for random parameter sets and showed an interpolation error below 1% compared to the exact solution of the TBLE within the relevant parameter range.

Chapter 6

Light-round simulation in an annular spray flame combustor with ambient temperature walls

Ignition in annular multi-burner combustors is marked by a succession of four phases, ending with a characteristic flame expansion from burner to burner, often referred to as light-round. During this last phase, flame propagation is prone to substantial change depending on the boundary and operating conditions. With realistic aero-engine conditions in mind, wall heat transfers can be enhanced during ignition in cold wall conditions, which aid an understanding of the main governing mechanisms of flame propagation. From a modeling perspective, several works have outlined the need for detailed descriptions of the liquid phase, turbulent combustion and wall heat transfer, which are all included in the present work for the first time. Large-Eddy Simulations of light-round are performed in the annular MICCA-Spray combustor with cold walls, Lagrangian particle tracking, a dynamic closure for the sub-grid scale flame surface wrinkling as well as a custom tabulated wall model. The predicted light-round duration from the simulation is found to be in good agreement with experimental data. It is shown that the volumetric expansion of burnt gases induces a flow acceleration in azimuthal direction which constitutes the main driving mechanism of flame propagation. Droplet accumulations in the wake of swirling jets are generated ahead of the propagating flame fronts, which in turn cause a characteristic sawtooth propagation mode of the leading point. A cooling effect of the combustor walls on burnt gases is particularly pronounced downstream, diminishing the resulting flame propagation speed.

Contents

6.1 Introduction

We have already established in the general introduction that LES is generally able to describe and qualitatively retrieve the light-round driving mechanisms observed experimentally. Yet, the results are quantitatively sensitive to the modeling choices. Detailed numerical models can improve the accuracy of the predicted light-round duration in LES, as separately highlighted and quantified by the following studies:

- The effect of dynamic combustion modeling has been investigated by Puggelli et al. (2021). The authors proved that a constant ("static") flame surface wrinkling parameter β cannot be justified from a physical standpoint given the heterogeneity of the β field revealed by a dynamic evaluation of said parameter. Despite worse results in terms of the observed light-round duration (increase by 20% over a constant β approach), the argument for a dynamic combustion model is still upheld. A cancellation of errors originating from *other* modeling choices is cited as principal reason for such discrepancy. This error cancellation was more unfavorable (and more pronounced) in the case of the dynamic approach, while hidden (by coincidence) in the constant β case.

- An appropriate description of the liquid phase appears to be essential, in particular the inherent polydispersion of the fuel droplets, resulting from the fuel injection characteristics, droplet evaporation and the flow field. A polydisperse Euler-Lagrange approach similar to Collin-Bastiani (2019b) should then be favored over previous monodisperse Euler-Euler computations of light-round with liquid fuel (Lancien et al., 2017, 2019; Puggelli et al., 2021).

- Puggelli et al. (2020) have demonstrated in an *a priori* study the intricate relation between variable thermodynamic properties of the boundary layer and the resulting wall heat fluxes. Their work postulated that detailed modeling of wall heat transfers would prove to be crucial in those cases in which hot burnt gases are in contact with cold combustor walls.

All these numerical works have anticipated or even proven an impact on the light-round duration and thus the flame propagation speed, intentionally limiting their modeling changes to one aspect per case. Despite this, no study has to date included *all* these findings in light-round simulations for a comprehensive *a posteriori* analysis of the governing mechanisms of flame propagation during light-round.

Thus, our objective within this chapter is first to characterize the main governing mechanisms during light-round with liquid fuels and cold (*i.e.* $T_w = 300\,\mathrm{K}$) combustor walls by means of LES. For the first time, detailed numerical models recently identified in the literature are combined establishing a new baseline case different from previous works: dynamic combustion modeling, polydisperse Euler-Lagrange formalism and advanced wall-modeling. The cold-wall case enhances the effect of wall heat transfer. It is therefore the subject of the present study. We recall that such conditions are not only relevant for engine start-up, but also for

high-altitude relight from windmilling, where inlet air temperatures can be as low as $238\,\mathrm{K}$ at $30\,000\,\mathrm{ft}$ $(9144\,\mathrm{m})$ of altitude and cool the engine substantially (see discussion in the general introduction). Our operating conditions (detailed later) admittedly represent an idealization of real engine conditions, but can still be considered as a first step towards characterizing heat transfer during light-round. We also note that only a few studies exist to date in the open literature which are concerned with emulating realistic high altitude relight scenarios in terms of low temperatures *and* low pressures (Read et al., 2008; Mosbach et al., 2010; Denton et al., 2018; Martinos et al., 2020; Klinger et al., 2011).

For an *a posteriori* quantification of heat loss effects, a complementary adiabatic case is included. A mathematical low-order model for turbulent flame propagation during light-round is the subject of Chap. 8.

Within the following sections, we will briefly recall the numerical setup, boundary and initial conditions, before presenting results in Sec. 6.5 focusing on the driving mechanisms of flame propagation.

6.2 Numerical setup

In light of recent numerical works on light-round ignition, the present work aims at including the previous individual findings in one *single* numerical setup. Since its key elements were already presented in Sec. 3.4, we will only recall the most important information here.

Large-Eddy Simulations are performed with the AVBP solver (Schönfeld and Rudgyard, 1999) developed by CERFACS. For the gas phase, we essentially employ

- the Two-step Taylor-Galerkin Centered scheme (TTGC) (Colin and Rudgyard, 2000) with third-order accuracy in space and time
- the SIGMA model (Nicoud et al., 2011) to evaluate the turbulent viscosity
- turbulent Schmidt (Sc_t) and Prandtl (Pr_t) numbers of 0.6 (for both) to determine the turbulent species diffusivity and the turbulent heat conduction coefficient.

The fundamental equations for droplet motion are solved in a Lagrangian framework using a two-step Runge-Kutta scheme and coupled at every iteration to the gas-phase solver. Droplets are assumed to be spherical and of constant density, and we limit the physics to those relevant for the dilute spray regime. The drag force exerted on droplets is modeled according to the Schiller-Naumann model (Schiller and Naumann, 1935). Heat and mass transfer is included via the polynomial evaporation model developed in Chap. 4, which itself is based on the Abramzon-Sirignano evaporation model (Abramzon and Sirignano, 1989).

A fully atomized, hollow-cone fuel spray is generated by the modified phenomenological FIM-UR model (fuel injection method by upstream reconstruction) (Sanjosé et al., 2011; Vignat et al., 2021) and injected at the tip of each of the sixteen atomizers. The corresponding model parameters were obtained from a precursor calibration discussed in Chap. 4 and are provided in Sec. 4.3.9. We note that at the beginning of the light-round simulation, over 30 million physical droplets are present in the entire domain.

Reaction kinetics (global two-step scheme Paulhiac et al. (2020)) and the dynamic combustion model (TFLES, Colin et al. (2000); Legier et al. (2000)) are employed according to Sec. 3.4.2. Local adaptive thickening is applied only to premixed zones through a superposition of a flame sensor (Legier et al., 2000) and the Takeno flame index (Yamashita et al., 1996). Most importantly, unresolved sub-grid scale wrinkling effects are corrected by a flame surface wrinkling factor (Charlette et al., 2002a) with a *dynamic* evaluation of the wrinkling

parameter β as in Volpiani et al. (2016) and Mouriaux et al. (2017). The model parameters are imposed as in Sec. 3.4.2.

Finally, we rely on the tabulated wall model developed in Chap. 5 to compute wall shear stresses and wall heat fluxes. For the light-round simulation in this chapter, we use the interpolation table BURNT-3D as specified in Tab. 5.1 to account for variable thermophysical properties in the boundary layer. Note that the tabulated wall model acts in the burnt gas region only (where $0.5 \leq c_{\mathrm{MP}} \leq 1$), whereas the standard linear/logarithmic wall model is employed for $c_{\mathrm{MP}} < 0.5$. This modeling choice is justified by the fact that wall heat fluxes in the fresh gas region are virtually negligible, since fresh gases and combustor walls are both at the same ambient temperature. Hence, variations in the thermophysical properties are arguably negligible as well.

6.3 Boundary conditions

Boundary conditions are essentially handled as detailed in Sec. 3.5. Mass flow rates are imposed at the air inlet ($\dot{m}_{air} = 30.21\,\mathrm{g/s}$) and at each of the fuel inlets ($\dot{m}_{fuel} = 0.11\,\mathrm{g/s}$/injector) yielding a global equivalence ratio of $\phi_{glob} = 0.89$. Flow variations in the experiment may cause a variation of the resulting laminar flame speed, but since the latter changes by less than $\pm 1\%$ of its nominal value, variations are not considered in the simulation, nor are they observed experimentally. All inlet temperatures are set to $T = 300\,\mathrm{K}$. A pressure boundary condition is imposed at the atmosphere outlet ($1\,\mathrm{bar}$). As mentioned in the previous section, the near-wall flow is modeled in the entire combustion chamber and injector, with wall temperatures set to $T_w = 300\,\mathrm{K}$ in this simulation. Liquid phase boundary conditions are set to allow elastic rebound in the combustion chamber. In the injectors, droplet–wall interactions are considered to be predominant, thus requiring a film-type boundary condition as developed in Chaussonnet et al. (2016).

6.4 Establishing stationary non-reacting initial conditions

Initial conditions are deliberately chosen to ensure a successful ignition and the initial flame kernel to survive the first stages of its development. We emphasize once more that these early stages are beyond the scope of this work. Instead, we focus specifically on the light-round phase (Lefebvre and Ballal, 2010; Mastorakos, 2017) as mentioned in the introduction. The combustion chamber is prefilled with a fuel/air mixture in the experiment for a few seconds before sparking. Since n-heptane is a volatile fuel, evaporation already occurs under ambient conditions. Stationary equivalence ratios are attained after around one second, but vary with chamber height due to a complex heterogeneous flow structure.

In an attempt to match these initial conditions of the experiment as best as possible, the simulation first starts with fuel injection and no combustion. Taking advantage of the rotational symmetry of the combustor, pre-fueling is performed on one eighth of the full geometry including the atmosphere (*i.e.* the bisector, see Sec. 3.3.2.2), greatly reducing computational costs. During this specific phase, periodic boundary conditions are applied to the tangential faces of the domain, and the total mass flow rates specified in Sec. 6.3 are both divided by 8, yielding $\dot{m}_{air} = 3.776\,\mathrm{g/s}$ and $\dot{m}_{fuel} = 0.2222\,\mathrm{g/s}$. The equivalence ratio is monitored over time until steady average values can be observed on several cut-planes at different heights. Figure 6.1 shows the temporal evolution at five select axial cutplanes. We clarify that this simulation was resumed from a converged solution obtained from Collin-Bastiani (2019b) in

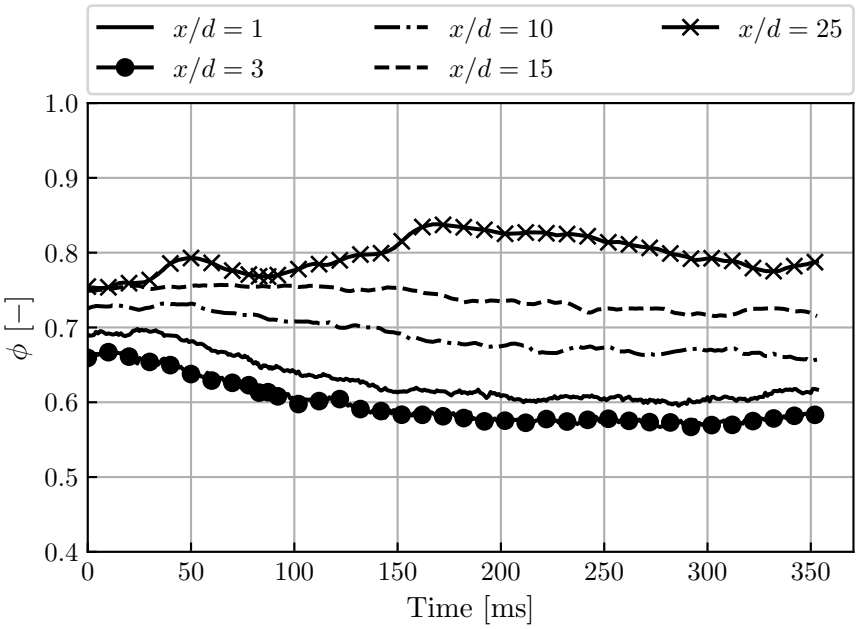

Figure 6.1: Evolution of the area-averaged gaseous equivalence ratio ϕ during pre-fueling at different flow-normal cutplanes across the bisector. d corresponds to the outlet diameter of the injector nozzle ($8\,\mathrm{mm}$), x to the streamwise coordinate. Simulation was resumed from a converged solution obtained from Collin-Bastiani (2019b) with different injection parameters. The total runtime is thus $t = 1.64\,\mathrm{s}$, of which only the last $350\,\mathrm{ms}$ are shown.

order to limit computational costs. Therefore, we only show the final $350\,\mathrm{ms}$ carried out with the setup relevant for this work, although the total runtime is $1.64\,\mathrm{s}$. A minor evolution in the area-averaged equivalence ratio can be observed for approximately $200\,\mathrm{ms}$ before the final steady state is reached. At $x/d = 25$, which corresponds to the chamber outlet, some fluctuations remain due to fresh air entrainment. Most importantly however, all cutplanes exhibit lower equivalence ratios than the global equivalence ratio ϕ_{glob} computed from the nominal air and fuel mass flow rates. This suggests that at least some residual droplets may reach the combustor outlet before full evaporation.

Figure 6.2 shows converged solution fields of the bisector after an averaging time of $t_{avg} = 20\,\mathrm{ms}$. The images represent a cylindrical cutplane at $R = 0.175\,\mathrm{m}$ transformed into a rectangular system. The mean gaseous axial velocity field resembles already observed in SICCA (see Sec. 3.7.2). The swirling jets of fresh gases are exiting each injector with axial velocities of $u = +50\,\mathrm{m/s}$, while exhibiting a distinct recirculation zone in their core, with axial velocities of $u = -20\,\mathrm{m/s}$ (see Fig. 6.2(a)). Conversely, the inter-injector recirculation zone features much lower axial velocities of approximately $u = -5\,\mathrm{m/s}$, causing a homogenization of the gaseous equivalence ratio ϕ (Fig. 6.2(b)). While the internal recirculation zones are extremely fuel-lean ($\phi \approx 0.4$), the equivalence ratio increases with increasing distance from the chamber backplane, consistently with a decreasing liquid volume fraction α_l (Fig. 6.2(c)) and liquid number density n_l (Fig. 6.2(d)).

In a next step, the converged solution is cloned eight times (including the geometry) to yield the full annular combustor assembly. Subsequently, the fuel injection phase is resumed in the actual full annular geometry for $24\,\mathrm{ms}$ to dissolve coherent flow structures resulting from the cloning procedure. The required simulation time of this step is derived from the autocorrelation rate of velocity fluctuations at $7.5\,\mathrm{mm}$ above the combustor backplane, yielding $\tau_{corr} = 6\,\mathrm{ms}$

(a) Mean gaseous axial velocity u

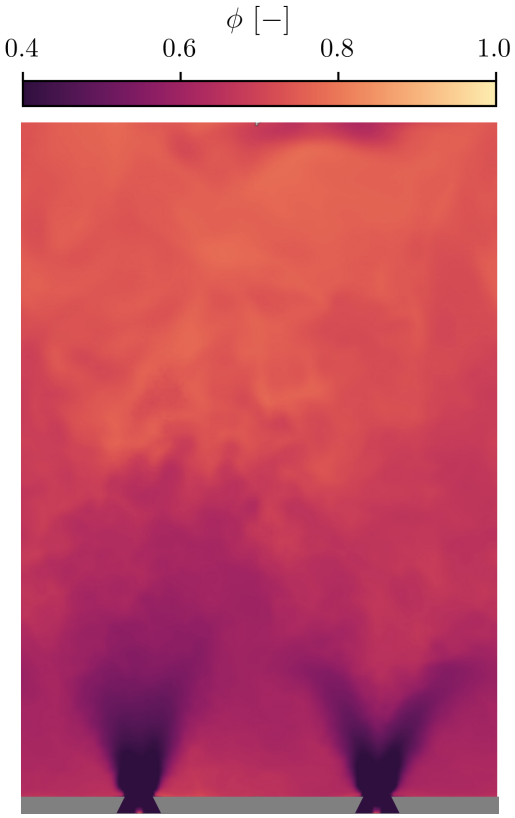

(b) Mean gaseous equivalence ratio ϕ

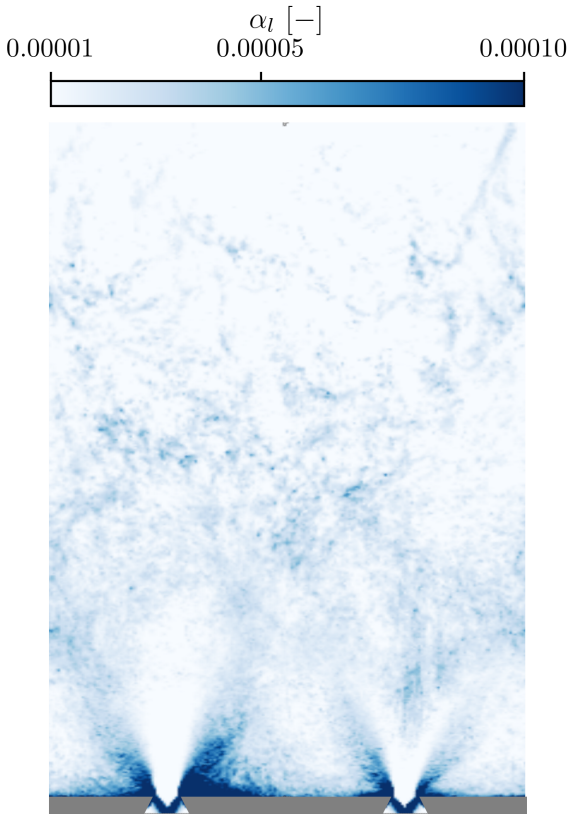

(c) Mean liquid volume fraction α_l

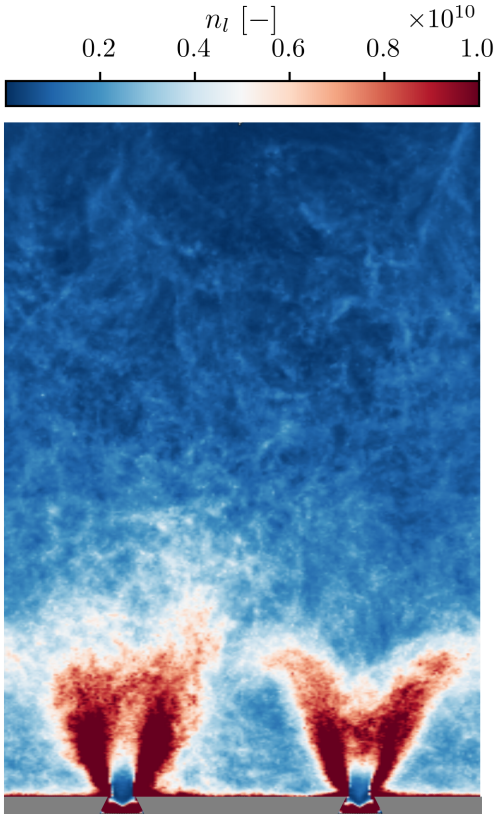

(d) Mean liquid number density n_l

Figure 6.2: Averaged gaseous and liquid solution fields on a cylindrical cutplane at $R = 0.175\,\mathrm{m}$ transformed into a rectangular system. The averaging duration is $t_{avg} = 20\,\mathrm{ms}$.

(Lancien, 2018). Alternatively, one could also estimate the required simulation time by relating it to the integral time scale (see *e.g.,* Eq. 6.4.12 in Tennekes and Lumley (1972)). Lastly, a $10 \times 24\,\mathrm{mm}$ ellipse of burnt gases is introduced at the experimental spark plug position to act as an initial flame kernel and ensure a successful and robust ignition procedure. *Smaller* spherical (Puggelli et al., 2021) or elliptical kernels (Lancien, 2018) did not result in successful ignition in the present configuration.

6.5 Results of light-round ignition with ambient combustor walls

We first draw the attention to the propagation mechanism during light-round with cold combustor walls. The effects of liquid fuels and heat losses are studied both from a global perspective as well as locally on particular points on each propagating flame front. The role of the dynamic combustion model is also briefly outlined.

6.5.1 Flame propagation during light-round

To approach the simulation results from a global perspective, it is useful to examine instantaneous snapshots of different stages during light-round shown in Fig. 6.3. Unless explicitly stated otherwise, the instant the simulation starts is used as time reference $t_0 = 0\,\mathrm{ms}$ (flame kernel delivered in the outer recirculation zone of the first burner). The images are obtained by transforming the full cylindrical chamber into a rectangular system and integrating the heat release rate in line-of-sight direction. In these transformed images, the flames propagate from the center (position of the initial flame kernel shown in Fig. 6.3(a)) to the sides. The nozzle outlets of the sixteen injectors are included at the bottom of each image for reference.

All characteristic phases of light-round ignition and their corresponding flame shapes are well retrieved in the simulation and are consistent with the experimental high-speed imaging performed by Prieur et al. (2017). Identical flame shapes are also observed in Lancien et al. (2017); Puggelli et al. (2021). Starting with **phase-I**, the evolution of the initial flame kernel is strongly influenced by the swirling flow motion: during its expansion its initial elliptical shape is increasingly wrinkled and stretched by the flow, resulting in a rapid increase of the heat release rate. At the same time, the kernel is successively entrained by the swirling flow exiting the injector in sector *S*0, where the first stable flame develops, along with a simultaneous ignition in sector *S*-1 (see Fig. 6.3(b)). We reiterate that the initial kernel size is selected such that it ensures a successful ignition in the first sector, since quenching effects are beyond the scope of this work. More importantly, we have addressed the limitations of the employed two-step reaction mechanism in Sec. 3.4.2, and noted that its inherent insensitivity to strain would certainly make it a poor modeling choice for simulations of flame quenching.

The bigger the flame grows, the more it transitions into an arch-like shape, marking the onset of **phase-II** of light-round ignition. This form can be observed in Fig. 6.3(c) and(d).

Once the upper part of the flame arch reaches the outlet of the combustion chamber, two separate flame fronts can be observed propagating through each half of the chamber, corresponding to **phase-III** (see Fig. 6.3(e) to (h)). Both flame fronts are moderately inclined in azimuthal direction, with a leading edge found close to the combustor backplane, and a trailing edge at the outlet. Moreover, they propagate at almost identical velocities up to sector *S8*, where they collide and merge. The onset of flame front merging can be observed in Fig. 6.3(i), which marks **phase-IV** of light-round ignition.

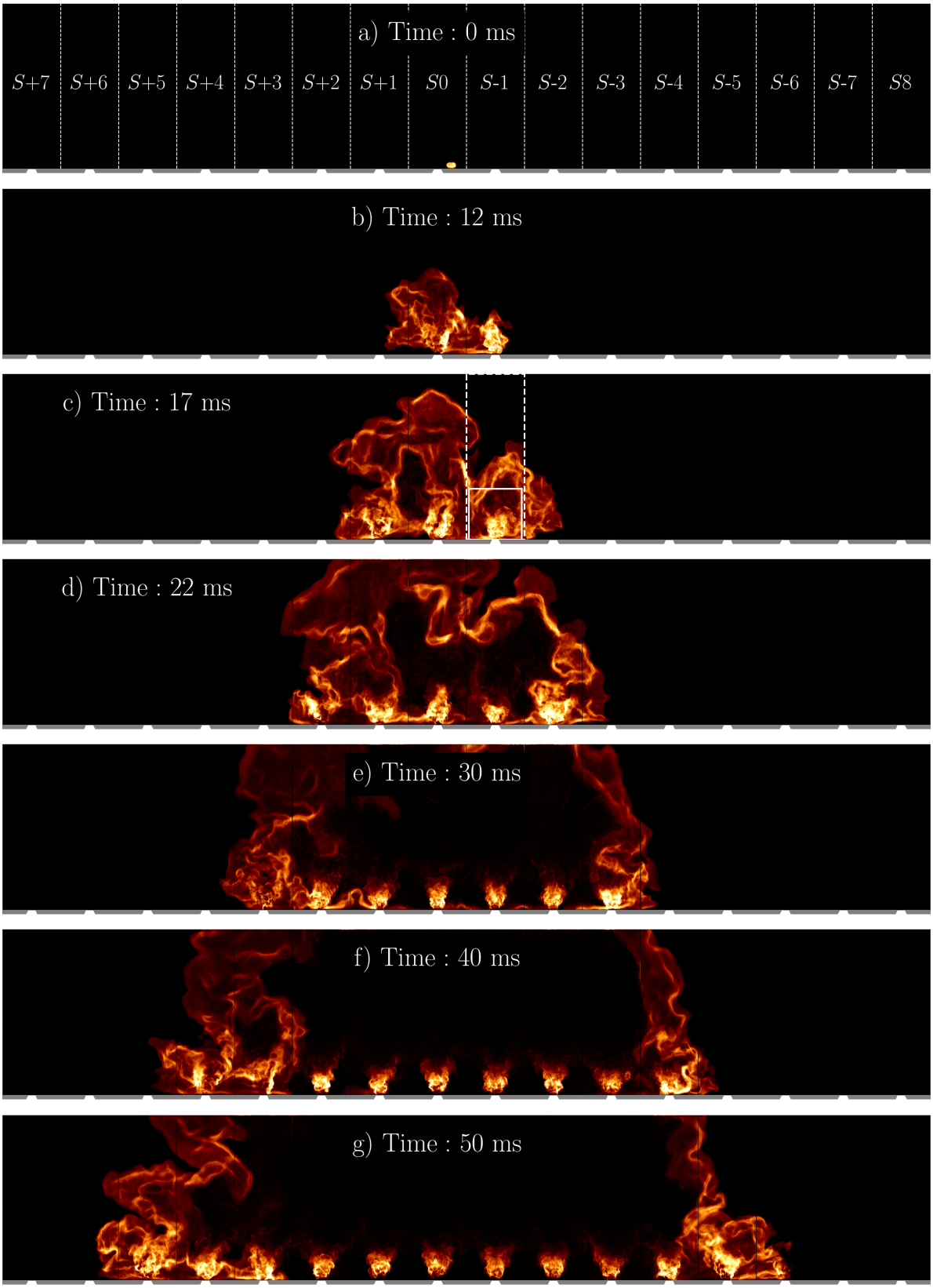

Figure 6.3: Visualization of flame propagation during light-round with cold combustor walls: line of sight integration of the heat release rate in LES for different instants after transforming the chamber from a cylindrical into a rectangular system. Sectors are labeled according to Fig. 3.2(c). Image c) (here) illustrates the sector volume considered for heat release rate integration as discussed in Sec. 6.5.2: solid line: chamber clipped at a height of $60\,\mathrm{mm}$; dashed line: full chamber height.

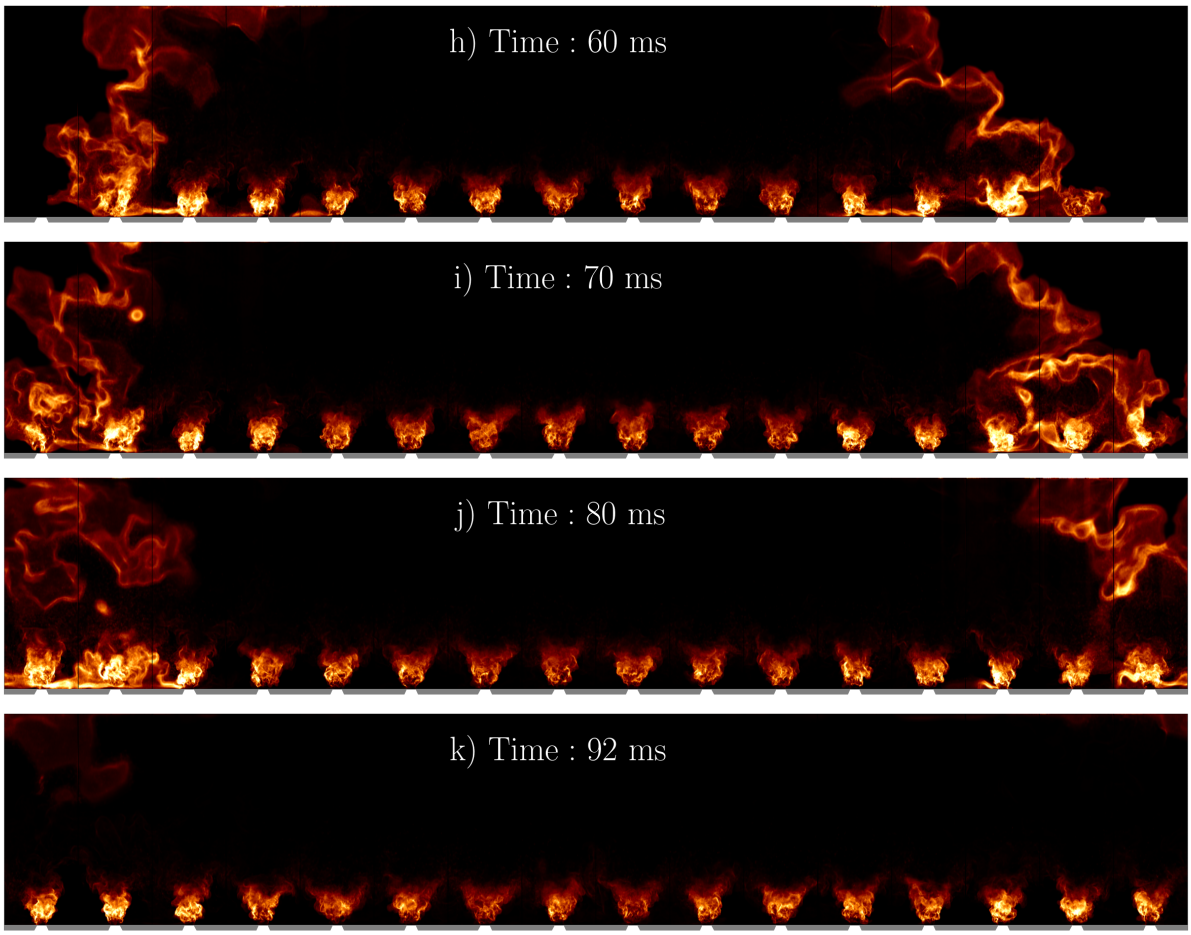

Figure 6.3: Line of sight integration of the heat release rate in LES for different instants after transforming the chamber from a cylindrical into a rectangular system (cont.).

Case	τ^{LR} [ms]	Case	τ^{LR} [ms]
EXP1	51.2	BASE	54.6
EXP2	52.7	ADIAB	43
EXP3	52.4		
EXP4	43.4		

Table 6.1: Light-round durations of four experimental runs (Puggelli et al., 2020) with combustor walls at ambient temperature ($T_w = 300\,\mathrm{K}$). The simulated light-round duration is given for the baseline case (BASE) for the same conditions as in the experiment. An additional simulation with adiabatic combustor walls (ADIAB) is also carried out for comparison. Numerical light-round durations are computed as visualized in Fig. 6.4.

Steady-state conditions are eventually reached, after a transition time shown in Fig. 6.3(j) during which the residual parts of the flame fronts exit the combustion chamber. In Fig. 6.3(k), all 16 burners are fully ignited, with flames anchoring close to each injector outlet. This phase is associated with **phase-V** of light-round ignition. However, flame shapes and light intensities appear to be different particularly between flames ignited at earlier phases (found in the center of Fig. 6.3(k)) and those at later phases (found towards the left and right edges of Fig. 6.3(k)): flames around sector *S*0 exhibit a lower light intensity and a more open form compared to flames in sectors $S\pm5$ to 8, which seem more compact. This is a distinct feature of flame dynamics during ignition which we examine separately in Chap. 9.

6.5.2 Light-round duration

To compare the simulation with experimental data, the light-round duration is commonly used as a global metric, defined here as the elapsed time between two specific events during ignition. Synchronization between LES and experiment is usually established once the initial flame (starting from the sector *S*0 marked with a bolt in Fig. 3.2(c)) has ignited the *adjacent* burner in sector *S*-1 (marked with a star in Fig. 3.2(c)). This common starting point eliminates at least those uncertainties associated with the stochastic behavior of the initial spark and the subsequent growth of the initial flame kernel. Hence the focus on phase IV of light-round (Lefebvre and Ballal, 2010; Mastorakos, 2017, "burner-to-burner flame propagation").

Conversely, the end of light-round can be determined more easily by taking the first recorded frame obtained from high-speed imaging (instantaneous solution in the case of LES) in which the two flame fronts start to overlap. The time difference between this instant and the synchronization point defined above yields the light-round duration τ^{LR}.

Following this definition, light-round durations for four experimental runs (EXP1 - EXP4, Puggelli et al. (2020)) and one simulation with cold combustor walls (referred to as baseline case, abbreviated as BASE) are compiled in Tab. 6.1. A complementary simulation (ADIAB) carried out using adiabatic wall boundary conditions only, is already listed here, but discussed later. Despite the lack of an unambiguous definition of τ^{LR}, the predicted duration (baseline case) agrees fairly well with the experimental data. Note that case EXP4 qualifies as an outlier, since experimental conditions were less well controlled for this specific run. Data obtained from other configurations and at different operating points suggests that there is only a very moderate variability of the experimental light-round duration between subsequent runs. We expect this to hold true for the present configuration as well and keep the entry EXP4 for the sake of completeness.

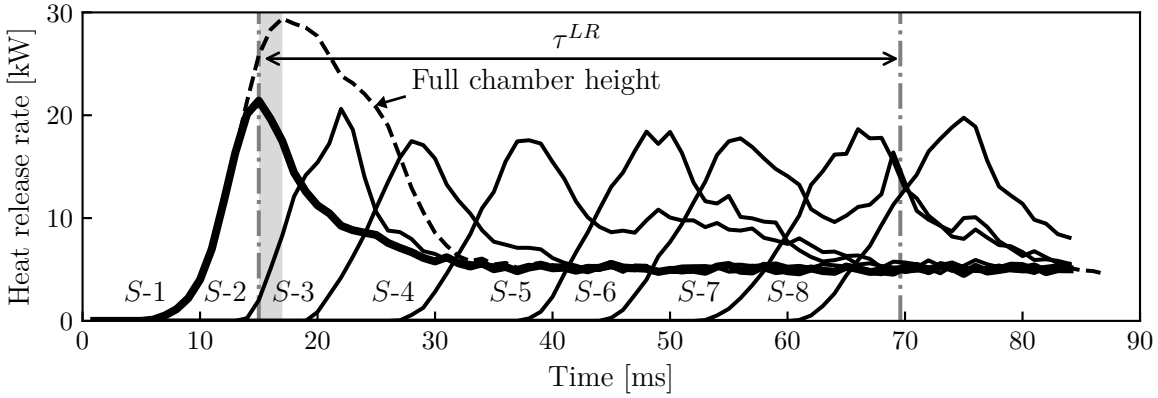

Figure 6.4: Volume integrated heat release rate (gray shaded area) per sector in the negative half without clipping (dashed line, first sector only) and clipped to a height of $60\,\mathrm{mm}$ (solid lines). The light-round duration τ^{LR} corresponds to the difference between the peak heat release in sector *S*-1 and flame front merging (vertical dash-dotted lines). The sensitivity associated with the definition of the synchronization point corresponds to the peak shift between the thick solid and the dashed line.

The inherent ambiguity for all definitions of a synchronization point between experiment and simulation clearly deserves further discussion. A metric (*i.e.* a "sensitivity") for the assessment of the numerical light-round duration is worth defining, rather than considering it as an exact measure. Reasonable definitions (numbered (i) to (iii)) can be based for example on a specific value of the heat release rate or the instant the propagating flame front in the negative chamber half H- has crossed a certain sector. In the former case, the heat release rate in sector *S*-1 is volume integrated and the instant of its peak value is used as synchronization point. The solid lines in Fig. 6.4 show the per-sector heat release rate for sectors *S*-1 to *S*-8 when performing the volume integral up to a height of $60\,\mathrm{mm}$. Thus, the light-round duration (i) $\tau^{LR} = 54.6\,\mathrm{ms}$ corresponds to the time difference between the two vertical dash-dotted lines in Fig. 6.4, *i.e.* the heat release peak in sector *S*-1 and the instant the propagating flame fronts start to overlap. Limiting the volume integration up to $60\,\mathrm{mm}$ aims at focusing on the attached flame at the burner while excluding heat release contributions from above and neighboring sectors (cf. solid line box in Fig. 6.3(c)). Performing the volume integral over the full chamber height instead results in a delayed peak in sector *S*-1 as visualized by the dashed line in Fig. 6.4, yielding a value of (ii) $\tau^{LR} = 52.6\,\mathrm{ms}$ (cf. dashed box in Fig. 6.3(c)). The peak shift between the dashed line and the thick solid line (in Fig. 6.4) may be interpreted as a sensitivity in terms of the employed definition (gray shaded area) and is less than 4% of the overall light-round duration τ^{LR}.

A third possible definition of the light-round duration can be derived from the instant at which the circumferentially outermost flame edge has entirely crossed sector *S*-1: (iii) $\tau^{LR} = 49\,\mathrm{ms}$, equivalent to sensitivity of 10% at worst, when using definition (i) as reference.

In summary, the light-round duration is deemed to be only moderately impacted by the choice of the definition for the synchronization point, yielding very acceptable results in either case, compared to the duration reported in experiments. The modeling setup then allows to describe the flame propagation quantitatively in the considered configuration that is characterized by cold walls. We reiterate that our critical assessment is meant to highlight a sensitivity with regard to the employed definition (due to the lack of a straightforward metric) and we do *not* intend to simply choose the definition which best fits our numerical results.

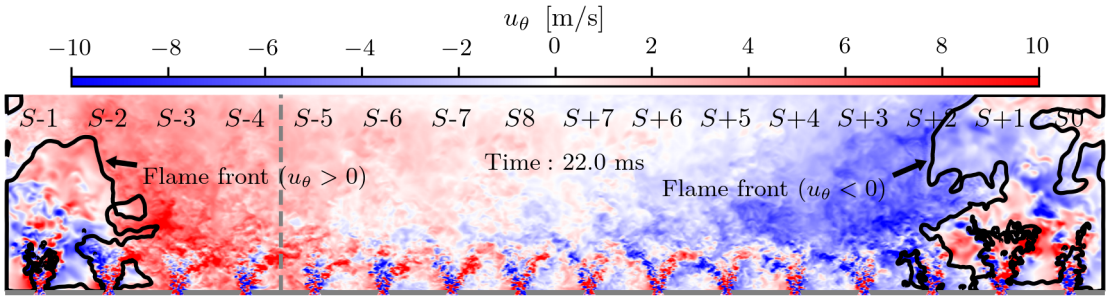

Figure 6.5: Azimuthal velocity u_θ on an unwrapped cylindrical cut-plane at $R = 0.175\,\mathrm{m}$. Dark shades correspond to high azimuthal velocities (from left to right and vice versa). Solid contour lines of iso-values of the progress variable ($c = 0.76$) indicate the instantaneous flame position. Axial velocity profiles are plotted along the dashed vertical line in Fig. 6.6.

6.5.3 Volumetric expansion of burnt gases

The most important driving mechanism of flame propagation consists in a flow acceleration in azimuthal direction during the volumetric expansion of burnt gases inside the chamber as illustrated in Fig. 6.5. Examining the azimuthal velocity u_θ on this unwrapped cylindrical cut-plane at $R = 0.175\,\mathrm{m}$ reveals dark shades upstream of each flame front representing high flow velocity values (red: from left to right, blue: vice versa). Lighter shades in turn indicate close to zero azimuthal velocity. The instantaneous flame position is visualized by black contour lines of the progress variable at $c = 0.76$ (peak of fuel species source term). The selected value is an arbitrary choice and used for visualization purposes in our figures. Results are insensitive to the chosen value. The sector layout in Fig. 6.5 still refers to the nomenclature of Fig. 3.2(c) and applies henceforth to all following unwrapped cutplanes.

It is worth noting that the effect of the volumetric burnt gas expansion can be observed several sectors ahead of each flame front, although not uniformly over the chamber height. Two instantaneous azimuthal velocity profiles are sampled along the dashed sampling line in Fig. 6.5 and plotted in Fig. 6.6. Initially ($t = 1\,\mathrm{ms}$), no mean azimuthal flow is observed except for the flow perturbations induced by the swirlers between the chamber bottom and up to $50\,\mathrm{mm}$ above (solid line in Fig. 6.6). The velocity profile exhibits at a later time $t = 22\,\mathrm{ms}$ positive values across the entire chamber height (dash-dotted line in Fig. 6.6), which is an indication of the flow acceleration induced by burnt gas expansion. It is most pronounced at $30\,\mathrm{mm}$ above the chamber bottom, where it reaches $u_\theta = 20\,\mathrm{m/s}$, around four times of its initial value at the same height. This strong velocity peak raises the question how fuel droplets react to this effect and interact with the flame on a local scale.

6.5.4 Flame interaction with droplets

In Fig. 6.7, the flame/droplet interaction induced by the flow acceleration through burnt gas expansion is visualized on the same unwrapped cylindrical cut-plane at $R = 0.175\,\mathrm{m}$ as before, with orange contour lines representing the progress variable ($c = 0.76$). A representative time frame at $t = 34.5\,\mathrm{ms}$ (propagation as two separate flame fronts) is chosen for an optimal visibility of the phenomenon on that plane. Dark shaded regions indicate an increased liquid volume fraction α_l and can be interpreted as droplet accumulations. Crucially, these accumulations prevail mostly in the wake of the swirling jets close to the chamber bottom (see squares in Fig. 6.7). Droplets entering the combustion chamber ahead of the propagating flame fronts deviate from their initial upward trajectory due to the burnt gas expansion and are trapped in the recirculating flow between adjacent injectors, similar to jet in crossflow

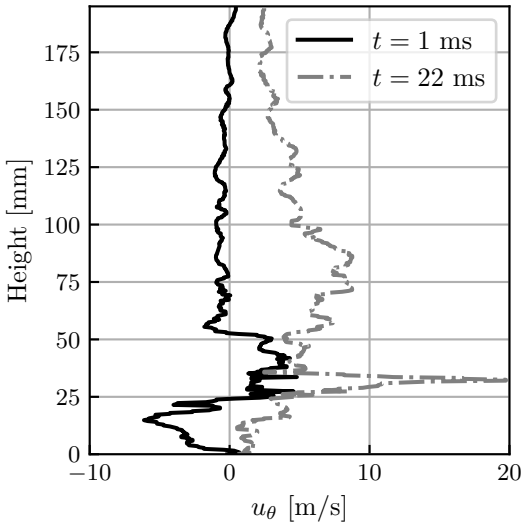

Figure 6.6: Axial velocity profile of the azimuthal velocity u_θ sampled along the dashed line in Fig. 6.5.

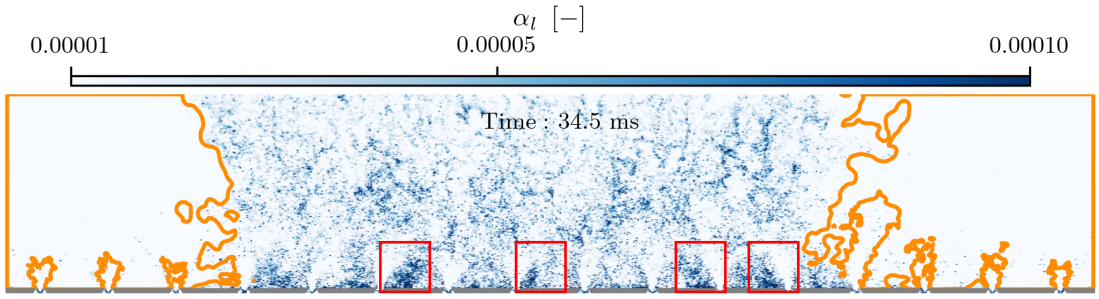

Figure 6.7: Liquid volume fraction α_l on an unwrapped cylindrical cut-plane at $R = 0.175\,\mathrm{m}$. Orange contour lines correspond to iso-values of the progress variable of $c = 0.76$. Droplet accumulations in the wake of the swirling jets are highlighted by red squares. Sector layout as in Fig. 6.5.

configurations (Lancien et al., 2019). As a consequence, the flame may locally burn in richer conditions than the overall global equivalence ratio, once it encounters such a droplet accumulation. These accumulations appear (more clearly than Fig. 6.7 may suggest) in Fig. 6.8 as rich pockets of increased equivalence ratio (light shades), specifically in the burnt gases, proving that droplets *remain* trapped in the recirculation zones between adjacent burners. The amount of accumulated droplets is certainly subject to temporal variations of the flame expansion in the combustion chamber. Note that the total equivalence ratio ϕ_{tot}, the sum of the gaseous and liquid equivalence ratio, plotted in Fig. 6.8 is essentially identical to the gaseous equivalence ratio in the burnt gas region, where contributions from liquid fuel is barely present. By contrast, the total equivalence ratio is more heterogeneous in the fresh gas region due to a spatially varying contribution from droplets.

The leading point (LP), *i.e.* the circumferentially outermost flame edge in each half of the combustor, appears to avoid regions with high droplet accumulations in favor of regions with a lower overall liquid volume fraction. The leading point trajectory tracked in Fig. 6.9 thus exhibits a characteristic sawtooth form as it is more favorable to pass *over* droplet accumulations instead of right through them. This leading point behavior is attributed to the fact that propagation along regions of lower liquid volume fraction is faster as it requires

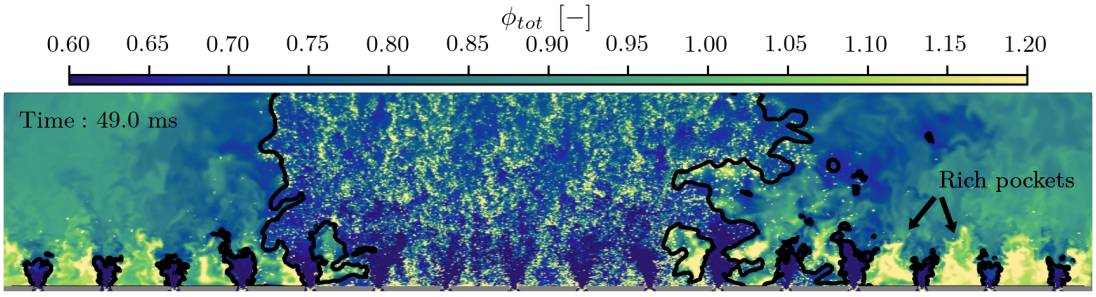

Figure 6.8: Total equivalence ratio ϕ_{tot} on an unwrapped cylindrical cut-plane at $R = 0.175\,\mathrm{m}$. Contour lines correspond to iso-values of the progress variable of $c = 0.76$.

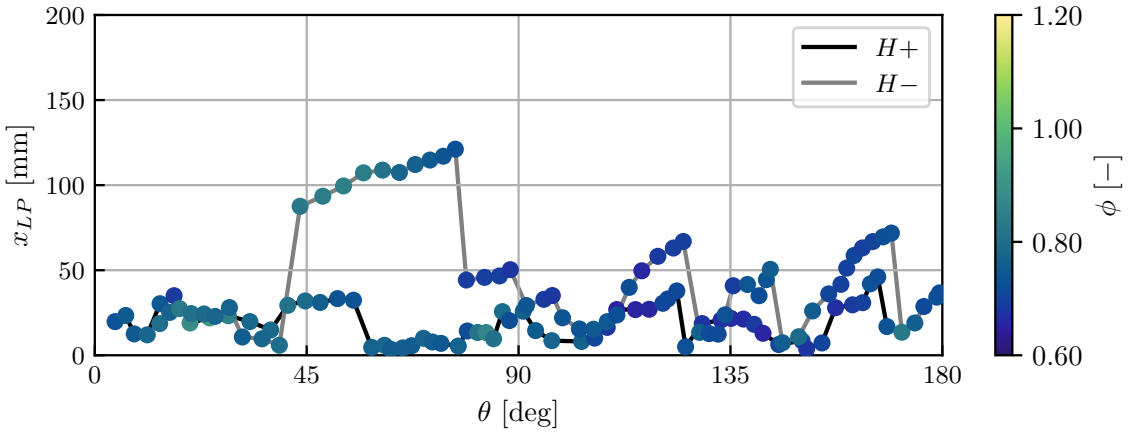

Figure 6.9: Leading point trajectory in each half of the chamber. Abscissa is given as arc length in degrees counting from sector *So* (see Fig. 3.2(c)). The ordinate corresponds to the leading point height above the chamber bottom. Colored markers indicate the local equivalence ratio ϕ.

fewer droplets to evaporate. We also note that the local equivalence ratio at the leading point (colored markers in Fig. 6.9) is lower than the global equivalence ratio $\phi_{glob} = 0.89$.

These findings support our stance that a polydisperse description of the liquid phase and a carefully adjusted injection model should be employed. The spray heterogeneity and flame/droplet interactions critically affect the flame trajectory and thus the light-round duration in the present configuration. The sawtooth-like leading point behavior in particular is even more striking when compared to previous works on flame propagation in multi-burner configurations: in Marrero-Santiago et al. (2017), an increased burner-to-burner spacing enforces a sawtooth propagation pattern along connecting "bridges" of neighboring spray branches, since the inter-injector region close to the combustor backplane is too lean to be ignitable. Insufficient fuel/air mixing due to high equivalence ratios and low bulk-flow velocities constitute another reason for sawtooth propagation (Gao et al., 2021). By contrast, the flame itself causes its characteristic sawtooth trajectory in the present work by generating upstream droplet accumulations during burnt gas expansion, and these accumulations are less favorable to cross. We postulate that combustor wall temperatures are likely to affect this pattern, since they control the fresh gas temperatures (prior to ignition), and thus the fuel evaporation rate. As the present case ($T_w = 300\,\mathrm{K}$) appears to be influenced by flame/droplet interactions, it is conceivable that enhanced evaporation rates caused by preheating may alleviate this influence. We will return to this discussion in Chap. 7.

6.5.5 Heat loss effects

Combustor wall temperatures not only affect the propagation pattern though. With the *a priori* study by Puggelli et al. (2020) in mind, a comprehensive *a posteriori* analysis of the effect of wall heat losses on flame propagation can now be provided in the present work. In particular, the relation between heat losses and burnt gas expansion is brought to the reader's attention. Differences are pointed out with regard to the complementary ignition simulation (ADIAB) which is based on the exact same setup except for the wall boundary condition set to be adiabatic instead. This second ignition case also starts from the very same initial solution as its isothermal counterpart. Most importantly, the altered thermal boundary condition preserves the (upstream) equivalence ratio field upon which the laminar flame speed chiefly depends. Differences observed in case ADIAB can therefore be related more clearly to the effect of heat losses.

6.5.5.1 Heat release rate and wall heat fluxes

Similar to previous works, the heat release rates (HRR) follow a characteristic evolution during each stage of light-round (Fig. 6.10). Each curve is obtained by integrating the local heat release rate over the combustor volume without the surrounding atmosphere. While the slope is initially more moderate, a steep increase of the heat release rate is observed up to almost twice the nominal thermal power ($\mathcal{P}_{th}$) of the combustor. Once the flame-arch reaches the outlet of the chamber, heat release rates slightly decrease before increasing again, and reach roughly 2.5 times of $\mathcal{P}_{th}$ at the instant both flame fronts start to merge (diamond marker in Fig. 6.10). Residual parts of the flame fronts leave the chamber during transition into steady-state operation, causing a steep decrease of the heat release rates until $\mathcal{P}_{th}$ will eventually be reached. Both cases were stopped prior to steady-state operation due to constraints in available computational hours. Nevertheless, it can be inferred from Fig. 6.4 that each burner operates at approximately $5\,\mathrm{kW}$ after full ignition (already visible for burners in sectors S-1 to S-7), which totals in $\mathcal{P}_{th}$ for all 16 burners.

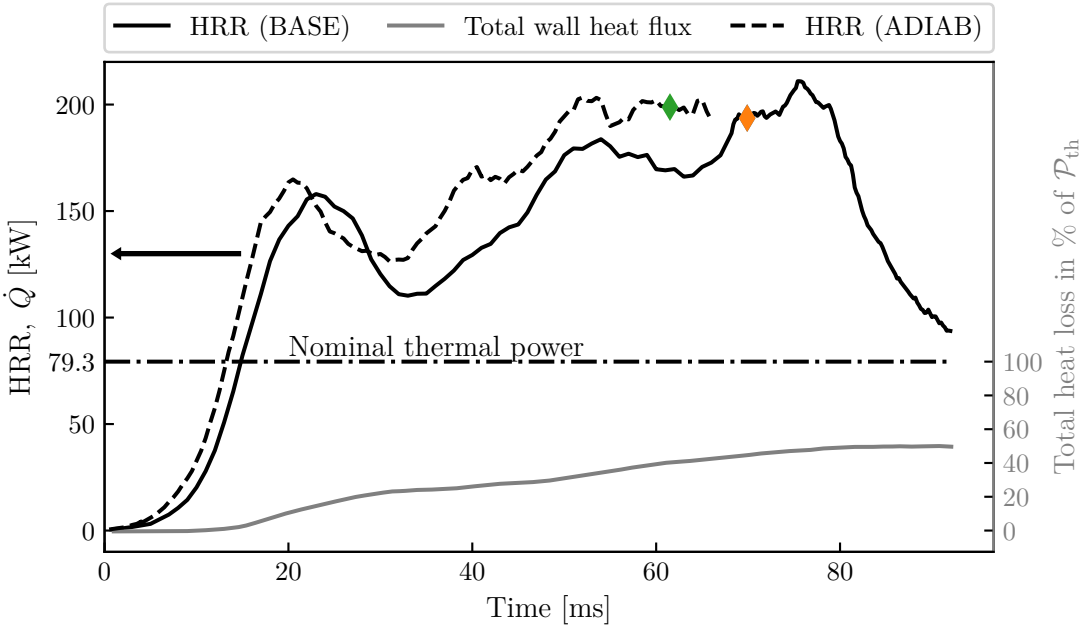

Figure 6.10: Evolution of the volume-integrated heat release rate (HRR) for the baseline case (solid line) and adiabatic case (dashed line). In the baseline case, total wall heat fluxes $\dot{Q}$ are plotted as gray line in absolute values (left axis) and in percent of the nominal thermal power $\mathcal{P}_{th}$ of combustor (right axis). Diamonds mark the instant at which the propagating flame fronts start to merge in each case.

For an overall quantification of the wall heat losses $\dot{Q}$, all heat fluxes (both lateral walls and chamber bottom) are summed up and related to the nominal thermal power output $\mathcal{P}_{th}$ of the combustor (when fully ignited) in Fig. 6.10. Note that these fluxes from the fluid onto the combustor walls are deliberately chosen to have a positive sign.

The sum of all wall heat fluxes across the chamber walls exhibits a steady increase up to 50% of $\mathcal{P}_{th}$ (grey line in Fig. 6.10) towards the end of light-round. Viewed from the perspective of the simulation case ADIAB where all walls are adiabatic, heat losses account for a 27% longer light-round duration ($\tau^{LR}_{\mathrm{ADIAB}} = 43\,\mathrm{ms}$ versus $\tau^{LR}_{\mathrm{BASE}} = 54.6\,\mathrm{ms}$).

To understand how heat losses act on the driving mechanism of flame propagation, local effects have to be taken into account; these effects are investigated in the following subsection.

6.5.5.2 Index of heat loss

The heat loss index I_{HL} may be considered as a useful metric to visually inspect the cooling of burnt gases (for case BASE), defined as:

$$I_{\mathrm{HL}} = \frac{h - h_{low}}{h_{adiab} - h_{low}} = \begin{cases} 1 & \text{adiabatic} \\ 0 & \text{max. local heat loss} \end{cases} \tag{6.1}$$

where h denotes the local enthalpy, h_{low} the enthalpy of the local mixture, if it had the temperature of the combustor walls (*i.e.* ambient temperature), and h_{adiab} the enthalpy of the local mixture in perfect adiabatic conditions. Since the values of h_{adiab} (adiabatic mixture) and h_{low} (mixture at ambient temperature) are chosen deliberately, I_{HL} reaches unity, if the local mixture is equivalent to an adiabatic mixture, and lower values, if it incurs heat losses.

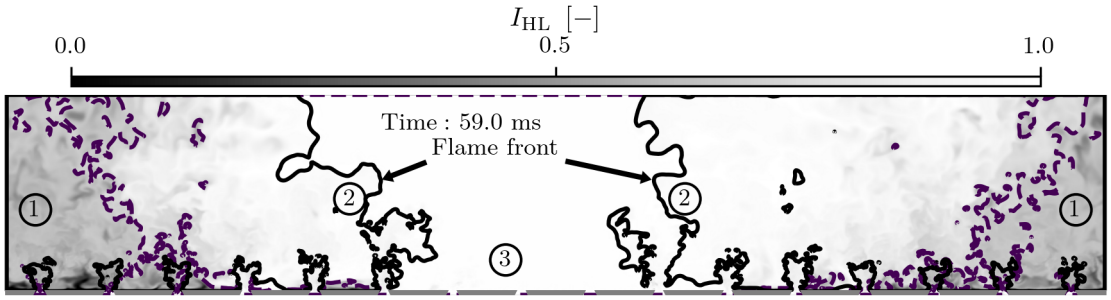

Figure 6.11: Heat loss index I_{HL} on an unwrapped cylindrical cut-plane at $R = 0.175\,\mathrm{m}$. Unity values mark fully adiabatic zones, zero marks the highest local heat loss possible. Solid contour lines correspond to iso-values of the progress variable of $c = 0.76$. Dashed contours limit zones where $I_{\mathrm{HL}} \leq 0.7$.

Upon examination of the unwrapped cutplane at $R = 0.175\,\mathrm{m}$, different regions with different levels of heat losses can be identified: burnt gases far downstream from each flame front (labeled as (1) in Fig. 6.11) take values of $I_{\mathrm{HL}} < 0.7$ as they have been exposed longer to the combustor walls than burnt gases immediately downstream of the flame fronts (labeled as (2)). In fact, large parts of the flame fronts propagate in almost adiabatic conditions ($I_{\mathrm{HL}} \approx 1$) across the full chamber height (on the presented cut-plane). Therefore, the longer the (downstream) burnt gases are in contact with the combustor walls, the more pronounced the heat loss effects, particularly towards the end of light-round. In turn, the fresh gas region labeled as (3) in Fig. 6.11 remains adiabatic, since fluid and walls are both at ambient temperature. The effect of evaporative cooling (particularly in the fresh gases) is comparably small and barely alters the fresh gas enthalpy.

As already discussed in Barré et al. (2014), the flow acceleration during burnt gas expansion, and thus the flame propagation speed, is proportional to the density ratio between fresh and burnt gases. Crucially, this density ratio may be altered due to heat transfer between hot burnt gases and combustor walls at ambient temperature. Volume-averaging the density in the burnt gas volume inside the chamber (denoted by angular brackets with subscripted "V") reveals a clear trend: since density and temperature are inversely proportional, the burnt gas density steadily increases with decreasing burnt gas temperature. In Fig. 6.12, this relation is conveniently plotted as density ratio $\langle \rho_u \rangle_V \,/\, \langle \rho_b \rangle_V$ to highlight the decaying driving effect of flame propagation (solid line). In turn, the density ratio in the adiabatic case (dashed line in Fig. 6.12) remains almost constant during the propagation of two separate flame fronts. A moderate decrease is observed at the end of this case when fresh air from the environment is entrained at the combustor outlet.

Therefore, an appropriate wall model in the baseline case is deemed essential to correctly predict wall heat transfers and thus the light-round duration under such conditions. This argument can be further substantiated by examining the instantaneous temperature on a horizontal cutplane at $x = 9\,\mathrm{cm}$ above the combustor backplane in Fig. 6.13(a). Consistently with the observations in Fig. 6.11, the burnt gas temperature decreases noticeably in the circumferential sense, downstream of the propagating flame fronts (visualized by solid black iso-contours of the progress variable $c = 0.76$). The temporal evolution of burnt gas cooling can also be observed in the image sequence of Fig. 6.13(c) to (g) on a radial cut-plane across the burner in sector $S0$.

More importantly however, the enlarged lower right quadrant in Fig. 6.13(b) shows a much steeper *radial* temperature gradient towards the combustor walls (at $T_w = 300\,\mathrm{K}$). Alongside these temperature variations, thermophysical properties (ρ, μ, c_p λ) in the boundary layer

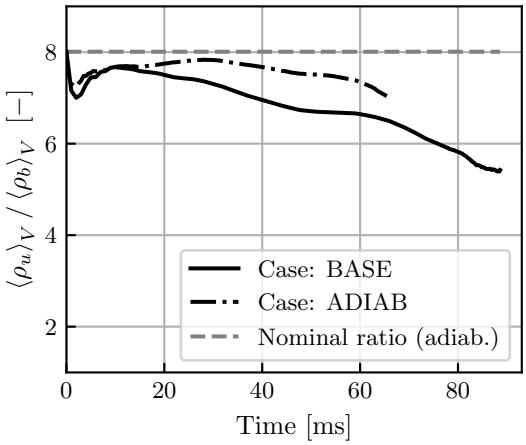

Figure 6.12: Density ratio (proportional to the volumetric burnt gas expansion) for the baseline case (solid line) and ADIAB (dash-dotted line). For reference, the nominal density ratio of adiabatic burnt gases at the global equivalence ratio $\phi_{glob} = 0.89$ and fresh gases is added as dashed line.

necessarily have to change as well and thus critically affect the resulting wall heat fluxes as already discussed in Puggelli et al. (2020).

To prove to what extent the amount of wall heat fluxes would change, if instead of variable thermophysical properties (as in our baseline case) only the boundary layer density was allowed to change, we compare the wall heat fluxes across the inner combustor wall with two different wall models in Fig. 6.14. In both images, negative values correspond to a (directional) heat flux from the fluid onto the combustor wall. Figure 6.14(a) represents the baseline case and exhibits substantial heat fluxes in the vicinity of stabilized flames where flow velocities are comparably high due to the swirling jets emerging from each injector. Heat fluxes are slightly less pronounced in the upper half of the combustor due to a lowered burnt gas velocity. In the fresh gas region at the center, heat fluxes are essentially zero, since fresh gases injected at $T = 300\,\mathrm{K}$ are at the same temperature as the combustor wall. In turn, the recomputed wall heat fluxes predicted by a classical logarithmic wall model are greatly diminished across the entire burnt gas region (Fig. 6.14(b)). This comparison clearly illustrates the importance of accounting for variable thermophysical boundary layer properties.

The intricate relation between heat losses, the density ratio and the turbulent flame propagation speed is further discussed in Chap. 8 based on a mathematical model.

6.5.5.3 Revisiting the equilibrium assumption in the tabulated wall model approach

Central to the development of the tabulated wall model has been the equilibrium assumption for the boundary layer. We recall that the stationary Thin Boundary Layer Equations have been solved for table generation (see Sec. 5.3.1) which we seek to justify from an *a posteriori* perspective. In comparing a characteristic boundary layer time τ^{BL} to the light-round duration of the baseline case τ^{LR}, we can infer the relative importance of unsteady boundary layer effects. These are presumably most pronounced when a propagating flame passes a given matching point, inducing a strong temporal variation of the thermophysical properties in the boundary layer. Adopting the assessment strategy of Puggelli et al. (2020), we construct the characteristic boundary layer time from the matching point distance δ_{MP} and the friction

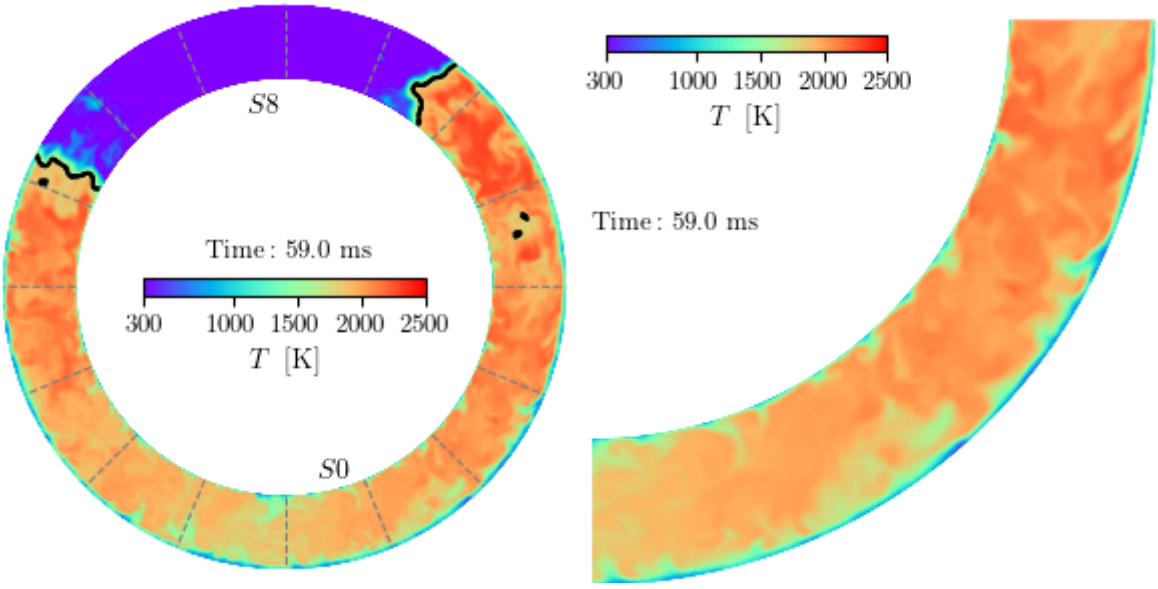

(a) (b)

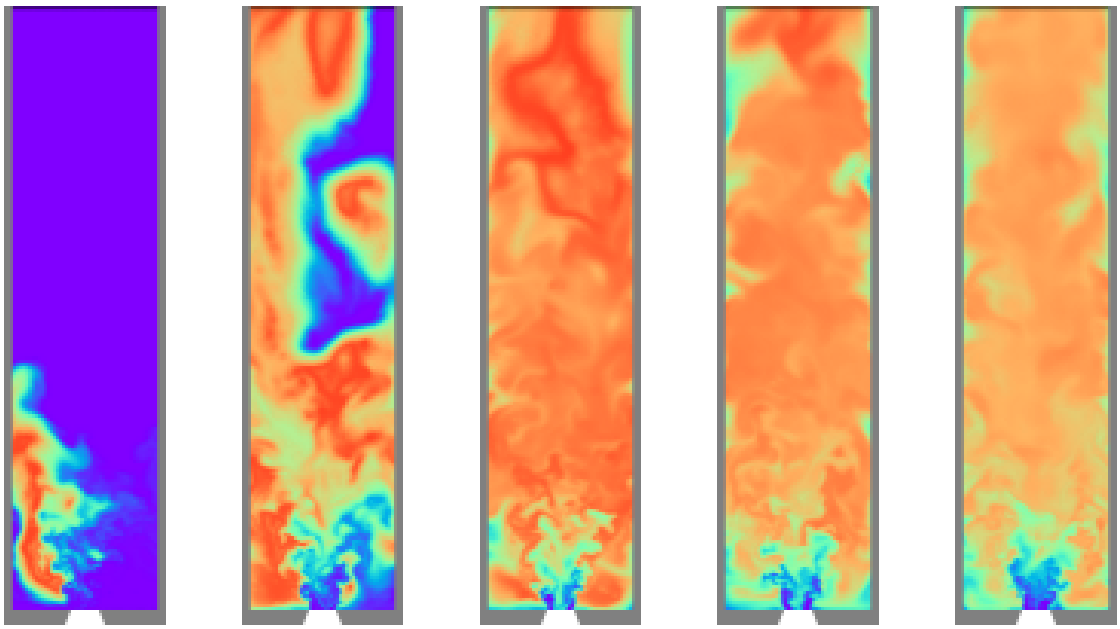

(c) $t = 10\,\mathrm{ms}$ (d) $t = 20\,\mathrm{ms}$ (e) $t = 30\,\mathrm{ms}$ (f) $t = 40\,\mathrm{ms}$ (g) $t = 50\,\mathrm{ms}$

Figure 6.13: Instantaneous temperature: a) horizontal cutplane at $x = 9\,\mathrm{cm}$ above the chamber backplane with a zoom on the lower right quadrant in b). Image sequence c) - g) shows the temperature of sector $S0$ at five time instants as radial cuts (constant azimuthal angle).

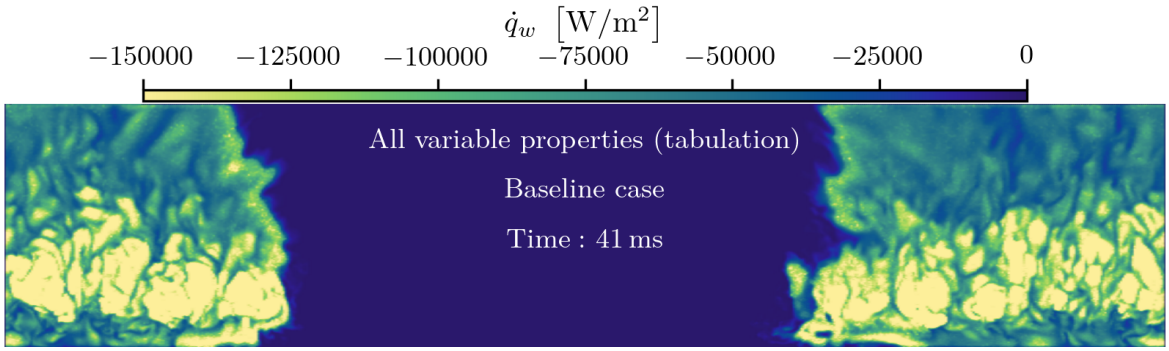

(a)

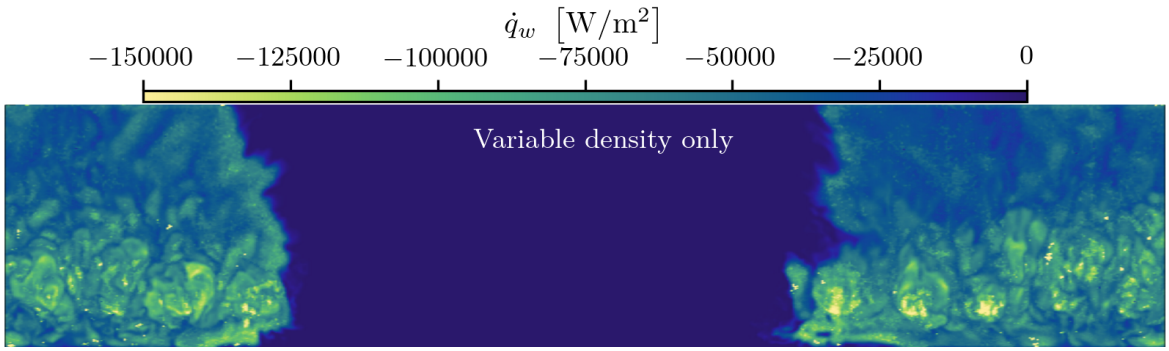

(b)

Figure 6.14: Comparison of wall heat fluxes across the inner combustor wall for two different wall models: a) corresponds to the baseline case where all thermophysical properties are variable (ρ, μ, c_p λ). In b) the wall heat flux is recomputed allowing only the boundary layer density to change.

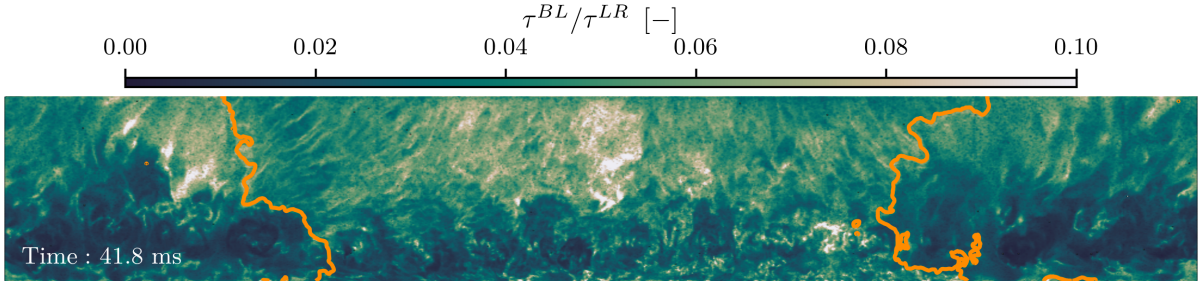

Figure 6.15: Characteristic boundary layer time normalized by the light-round duration on the external combustor wall at $R = 200\,\mathrm{mm}$. The contour lines correspond to an off-wall progress variable value of $c_{\mathrm{MP}} = 0.76$.

velocity u_τ

$$\tau^{BL} = \frac{\delta_{\mathrm{MP}}}{u_\tau} = \frac{\delta_{\mathrm{MP}}}{\sqrt{\tau_w/\rho_w}} \tag{6.2}$$

and plot the ratio τ^{BL}/τ^{LR} for the unwrapped outer combustor wall in Fig. 6.15. At the selected instant in time, approximately half of the burners are already ignited (or about to ignite). The flame front positions are visualized by iso-contours of the *off-wall* progress variable. Dark shades can be observed notably in the lower half of the combustor wall ($\tau^{BL}/\tau^{LR} \leq 3\%$), indicating that the impact of unsteady boundary layer effects is comparably small.

In turn, lower flow velocities in the upper half of the chamber lead to lower friction velocities, resulting in a longer characteristic boundary layer time particularly downstream of the flame front, which can reach up to 10% of the light-round duration (indicated by light shades in Fig. 6.15). Interestingly, we can also observe an increased ratio of characteristic times in the center of the image which coincides with the stagnation plane of the accelerated flow upstream of each flame front. Given these comparably low values for τ^{BL}/τ^{LR}, we assume unsteady boundary layer effects to have a rather moderate impact on the overall light-round duration.

6.5.6 Flame turbulence interactions

In light of the recent study published in Puggelli et al. (2021), the interaction of the flame with turbulence deserves further attention as well. This aspect is considered to be particularly relevant for the present case, since the flame surface wrinkling parameter β cannot be assumed constant over the entire flame. For a highly transient and inhomogeneous case such as light-round ignition, little physical argument can be made for a "universal" (*i.e.* constant) β. Therefore, it is more appropriate to employ a dynamic combustion model for light-round simulations, independently from the thermal boundary conditions (see also Puggelli et al. (2021)).

On a representative iso-surface of the progress variable $c = 0.76$ for a given instant $t = 44\,\mathrm{ms}$ (Fig. 6.16), both propagating flame fronts exhibit a comparably low wrinkling parameter ($\beta \approx 0.18$), while the stabilized flames downstream show higher values instead ($\beta \gtrsim 0.4$). Note that the color map is deliberately clipped to help distinguish β values on the flame fronts from ignited flames downstream.

The corresponding distribution of β on the flame surface is given for the same instant in Fig. 6.17 (solid line). The bin colors match the shading of the iso-surface in Fig. 6.16. Two major conclusions can be drawn from the PDF: first, the distribution of values of the wrinkling parameter is non-uniform. While the peak in the PDF at $\beta \approx 0.18$ originates from

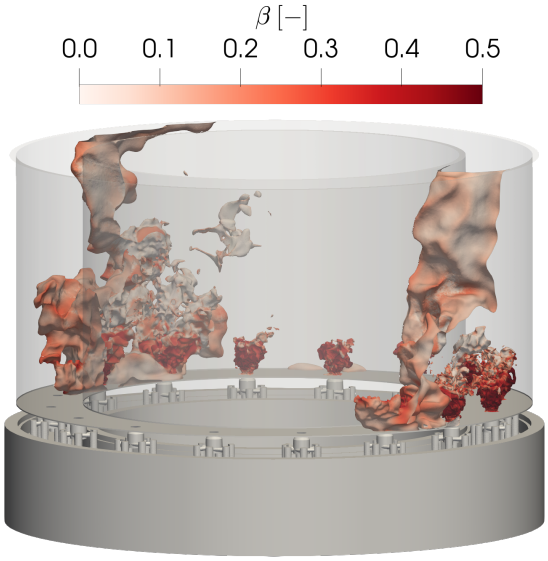

Figure 6.16: Flame surface wrinkling parameter β.

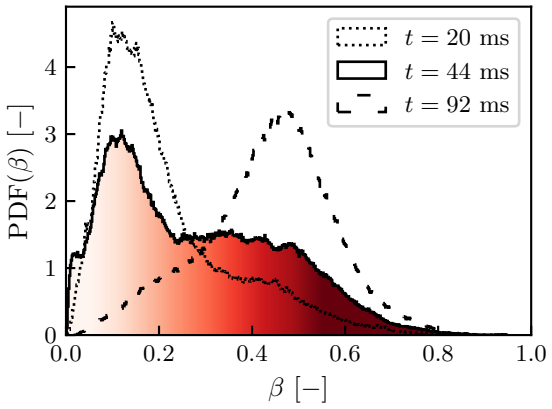

Figure 6.17: Distribution of flame surface wrinkling parameter β.

the propagating flame fronts, the ignited and stabilized flames take a wider range of values of $\beta \gtrsim 0.4$.

Second, the PDF considerably changes its shape over time. During the early stages of light-round, *i.e.* when the flame develops an arch-like form, only few burners are already ignited so that the peak in the PDF at $\beta \approx 0.18$ (cf. Fig. 6.17, dotted line) is initially more pronounced. The plateau at $\beta \gtrsim 0.4$ in turn is much less developed. However, the more burners are ignited during flame propagation, the more the plateau develops while the peak associated with the propagating flame fronts gradually diminishes. Once the entire combustor is fully ignited and reaches a steady state, the PDF transitions into a single-peak PDF at $\beta = 0.47$, since there is no contribution from the propagating flame fronts any more (dashed line in Fig. 6.17). This evolution of the wrinkling parameter β is consistent with the analysis in Puggelli et al. (2021) and occurs independently of the wall boundary conditions.

6.6 Conclusions

In the present chapter, we have explored the driving mechanisms of flame propagation during light-round and the role of physical modeling. Large-Eddy Simulations are performed in MICCA-Spray, an annular swirled spray-flame combustor with 16 fuel injectors fed by liquid n-heptane. Simulations are carried out with cold combustor walls at $T_w = 300\,\mathrm{K}$, allowing to assess the effect of wall heat transfer on flame propagation. Such conditions are highly relevant for flame propagation in confined multi-burner configurations, since a strong sensitivity to wall temperatures is observed in the available experimental data. Yet this relationship has not been thoroughly investigated in the literature. In a broader context, the role of physical models required to perform LES of light-rounds is analyzed. Specifically, the need for detailed models for the main governing mechanisms is highlighted.

The numerical setup follows previous works in terms of a dynamic closure for subgrid-scale flame surface wrinkling in the TFLES framework, polydisperse Lagrangian particle tracking, fuel injection and droplet evaporation. A tabulation approach is employed for the wall model (see Chap. 5) in order to overcome the limitations of standard logarithmic wall models and is capable of accounting for all variable properties in the boundary layer. Unlike previous related works that have concentrated on a single aspect at a time to isolate its effect on flame propagation (heat losses, two-phase flow and dynamic combustion modeling) without addressing the other aspects, the current simulation case attempts to incorporate the prior findings in a single numerical setup in order to draw general conclusions with respect to the impact of each model. Moreover, error cancellation can be avoided through this procedure as outlined by Puggelli et al. (2021).

The predicted light-round duration is found to be in fairly good agreement with available experimental data for cold-wall conditions, in particular when considering the uncertainties associated with the synchronization procedure. The volumetric expansion of burnt gases induces an azimuthal flow acceleration as primary driving mechanism of flame propagation. It also acts on the liquid phase by creating a heterogeneous droplet distribution upstream of the flame fronts: droplets accumulate in the wake of the swirled jets, which in turn affects the trajectory of the flame. A characteristic sawtooth trajectory is observed for the leading point. The presence of liquid fuel is also supposed to have an effect on the laminar flame speed S_l, which is studied in Chap. 8.

Furthermore, cold combustor walls also enhance the effect of heat losses on burnt gases, which are predominantly found further downstream in the burnt gas region, while the propagating flame fronts encounter almost adiabatic conditions. As a consequence, the burnt gas

density increases and leads to a lower flame propagation speed and longer light-round duration compared to light-round ignition with adiabatic walls. The lack of experimental data currently precludes further assessment of heat losses, in particular their impact on flame stabilization mechanisms at $T_w = 300\,\mathrm{K}$ and atmospheric conditions. Such investigations could be considered in the future.

The flame surface wrinkling parameter β is briefly examined and shows a heterogeneous distribution consistent with previous research (low values across the propagating flame fronts versus higher values at the stabilized flames). The use of a dynamic evolution of the wrinkling parameter must therefore be preferred as no universal value exists which would result in the same flame surface wrinkling and thus the same flame propagation speed.

The following chapter will be guided by the principal question, how combustor wall preheating affects and changes the observed governing mechanisms of flame propagation during light-round.

Chapter 7

Light-round simulation in an annular spray-flame combustor in preheated conditions

The second restart scenario of interest is quick relight. Unlike restart from windmilling (see Chap. 6), quick relight is likely to be performed with preheated combustor walls, since engine parts do not have sufficient time to cool within the short delay between engine shutdown and restart (typically within $5\,\mathrm{s}$). However, only few published studies exist which explicitly address wall temperature effects on ignition: for example, experiments in the annular spray-flame combustor MICCA with preheated walls have revealed that the ignition time — also referred to as light-round duration — decreases compared to cold combustor walls for otherwise same operating conditions. Numerical simulations of ignition have been carried out as well, but usually rely on approximations for the imposed wall temperature boundary condition (mostly adiabatic, iso-thermal at best) due to the lack of detailed experimental data. Therefore, the present chapter aims at studying the effect of preheated walls on light-round in more detail. Conjugate Heat Transfer simulations are first carried out to compute more realistic wall temperature profiles under steady reacting operating conditions in MICCA-Spray. These temperature profiles are then used in non-reacting Large-Eddy Simulations (LES) to establish preheated initial conditions. Finally, LES of light-round ignition with preheated walls are carried out. The predicted light-round duration is compared to experimental measurements, and effects on the governing flame propagation mechanisms as well as the liquid phase are examined. Differences with regard to light-round with ambient temperature walls are later discussed in Chap. 8.

Contents

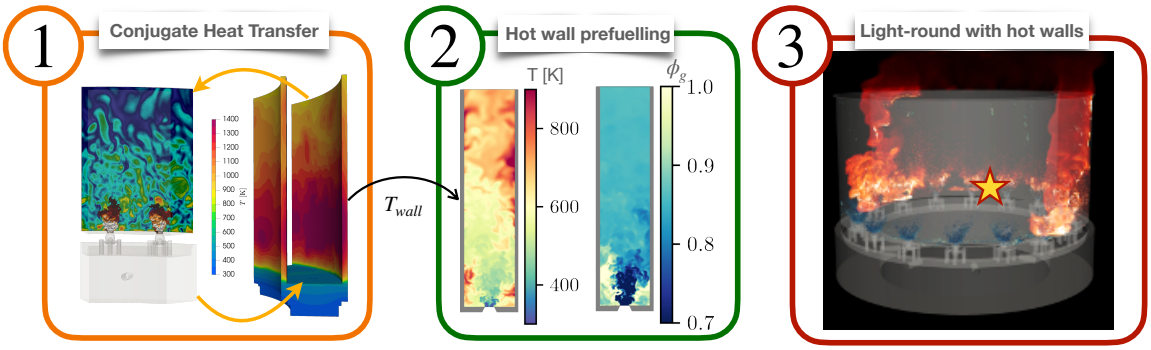

Figure 7.1: Illustration of the three-step procedure leading to the simulation of light-round ignition in preheated conditions. Step 1: coupled simulation to determine the combustor's steady-state wall temperature. Step 2: non-reactive flow simulation with preheated walls predicting the initial fields of fresh gases and liquid fuel (prefueling simulation). Step 3: light-round simulation.

7.1 Introduction

For the light-round analysis in the previous chapter, we have deliberately selected operating conditions with *cold* combustor walls to enhance the effect of wall heat losses on burnt gases, which in turn determine the state of the liquid phase. By contrast, we are chiefly concerned with the effect of combustor wall *preheating* on light-round within this chapter. We recall from previous findings (*e.g.*, Philip et al. (2015b); Prieur et al. (2019)) that increased wall temperatures cause faster flame propagation and shorter light-round durations. Despite this, detailed experimental temperature measurements remain extremely scarce.

Our principal goal is therefore to study and characterize the effects of preheated walls in more detail as would be encountered under quick relight in the lab-scale annular combustor MICCA-Spray. A three-step procedure is proposed as illustrated in Fig. 7.1. In step 1, we perform detailed Conjugate Heat Transfer (CHT) simulations to approximate wall temperature profiles under steady-state operation as outlined in Sec. 7.2. This constitutes a crucial enabling step for carrying out light-round simulations in preheated conditions without relying on *a priori* assumptions or iso-thermal walls. The obtained profiles are then imposed as temperature boundary condition in a prefueling simulation in step 2 as detailed in Sec. 7.3. Unlike adiabatic simulations in Philip et al. (2015b); Lancien et al. (2017, 2019), a thermal

equilibrium is established between the fresh gases and the preheated combustor walls *prior* to ignition, *i.e.* fresh gases are injected until stationary conditions are reached. This step is mandatory to correctly replicate the experimental relight procedure.

The modeling error induced by a reduced kinetic scheme is discussed in Sec. 7.4. Finally, Large-Eddy Simulations of preheated light-round are performed in MICCA-Spray in step 3, keeping the same wall temperature profiles as in the previous step. Results of this simulation are presented in Sec. 7.5. The predicted light-round duration is compared to available experimental data. We also analyze the effect of preheating on the governing mechanisms for flame propagation during light-round and highlight differences with regard to the same ignition case at ambient temperature walls presented in Chap. 6.

The results and observations of the present and previous chapter are later used in Chap. 8 as the foundation for the analysis and low-order modeling of flame propagation.

7.2 Conjugate Heat Transfer simulations of the bisector in stationary conditions

The first step towards running preheated light-round simulations consists in a coupled, fully ignited simulation of the established flow in MICCA-Spray. The setup and configuration is briefly recalled here, before discussing the obtained wall temperature profiles under steady-state operation. These profiles are used in non-reacting simulations detailed later in Sec. 7.3.

7.2.1 Numerical domains and setup

The numerical domain considered for CHT simulations is the bisector geometry already introduced in Sec. 3.3.2.2 for the fluid domain, and its solid domain counterpart in Sec. 5.2. The fluid domain's modeling approach is almost identical to the approach in Sec. 6.2, with the only exception of a constant flame surface wrinkling parameter. This simplification is justified by the fact that the β distribution exhibits a single peak at $\beta = 0.5$ (cf. dashed distribution in Fig. 6.17) under *stationary* operation. Therefore, it is reasonable to assume such value for the desired operating conditions, which is not only beneficial in terms of the required computational resources, but also in terms of the coupling procedure discussed later.

Wall heat fluxes and wall shear stresses are computed via the tabulated wall model as already done for light-round simulations in Chap. 6. However, burnt gases are expected to be exposed to *variable* wall temperatures, requiring the utilization of table BURNT-4D (as specified in Tab. 5.1) for an appropriate interpolation of q_w and τ_w as a function of the three matching point properties (T_{MP}, u_{MP} and δ_{MP}), and the local wall temperature T_w. This table operates in wall regions where $c_{\mathrm{MP}} \geq 0.5$, essentially covering the all internal combustor walls exposed to burnt gases (where $c_{\mathrm{MP}} \approx 1$).

The modeling approach for the Lagrangian phase is exactly identical to light-round simulations in Chap. 6, including the polynomial evaporation model and the modified fuel injection model FIM-UR.

In addition to the fluid domain, the three-dimensional and time-dependent energy equation is solved in the solid domain (as visualized in Sec. 5.2) with the AVTP code (cf. Sec. 5.1.2). We employ three different materials with variable conductivities and heat capacities depending on the local temperature: fused silica for the quartz tubes, stainless steel for the atomizers, injector blocks and the injector support, and brass for terminal plates and swirlers.

Code coupling between the AVBP and AVTP solver is handled by the OpenPALM library (cf. Sec. 5.1.5), retaining a temporal desynchronization procedure to handle the large difference of

	Δt	No. iterations	ΔT_{CPL}	No. MPI processes
AVBP	$59\,\mathrm{ns}$	200	$11.8\,\mu\mathrm{s}$	1536
AVTP	$0.1\,\mathrm{ms}$	1000	$1\,\mathrm{s}$	72

Table 7.1: Coupling setup for each solver during CHT simulations following a desynchronization approach: Δt: time step in each domain; number of iterations between coupling events; ΔT_{CPL}: elapsed time between two coupling events; total number of MPI processes. CPU resources: Intel® Xeon® E5-2690V3 @$2.6\,\mathrm{GHz}$.

time scales in both domains. Between two consecutive coupling events, AVBP is set to perform 200 iterations, AVTP however 1000 iterations (see Tab. 7.1). Due to the architecture of the HPC resources, we assign 1536 MPI processes to AVBP, and 72 to AVTP (multiples of 24). This setup ensures a reasonable load balancing and efficient resource utilization through an approximately equivalent solution wall-time, preventing CPUs from idling between two coupling events. Moreover, the static formulation of the combustion model (with $\beta = 0.5$) facilitates the optimization of load balancing, since a dynamic update of the wrinkling parameter is avoided, which would otherwise cause dynamic fluctuations of AVBP's solution time. We recall that the targeted configuration corresponds to fully ignited stationary conditions. Hence it is acceptable to employ a constant β parameter for the present CHT simulation, assuming comparable flame surface wrinkling of all flames anchoring at each burner. However, light-round simulations presented later in Sec. 7.5 still retain a dynamic evaluation of the β parameter as in the previous chapter.

7.2.2 Boundary and initial conditions

All fluid/solid interfaces exposed to the *internal* combustor flow (see Fig. 5.2(c), red surfaces, and coupling interface in Fig. 5.2(d)) are coupled using Robin-Dirichlet boundary conditions (Errera and Chemin, 2013). For stability reasons, we employ an optimal relaxation factor of $h_F^{opt} = 140\,\mathrm{W/K/m^2}$ for the evaluation of wall heat fluxes received by the solid domain solver (see Eq. 5.7). Conversely, heat transfer coefficients for free convection at the *external* quartz wall faces exposed to the atmosphere are computed from a Nusselt correlation (see Fig. 5.2(c), green surfaces). Radiative fluxes emitted from these semi-transparent quartz walls are modeled as detailed in Sec. 5.2.2. The reference ambient temperature is set to $T_{amb} = 300\,\mathrm{K}$. For symmetry planes, we employ axi-periodic boundary conditions for the fluid domain, and adiabatic boundary conditions for the solid domain, since AVTP does not offer axi-periodicity yet.

The effect of water cooling inside the injector support is approximated by a Dirichlet boundary condition at the bottom end of the injector support (see Fig. 5.2(c), blue bottom edge, $T_w = 300\,\mathrm{K}$). Such choice is certainly a source of modeling uncertainties which are difficult to quantify due to the lack of experimental data (*e.g.,* surface temperatures or even water temperatures). Despite this, we note that the total absolute wall heat flux through the chamber backplane is at least two times smaller than the heat flux through each of the uncooled quartz tubes. Therefore, we assume that the impact of the imposed temperature (at the injector support) on flame propagation is rather moderate.

Internal heat transfer between hot burnt gases and the internal quartz wall faces are computed through the tabulated wall model developed in Chap. 5. As we now expect variable wall temperatures, we employ table BURNT-4D (see Tab. 5.1), containing T_w as fourth dimension in addition to the matching point properties. Mass flow rates are identical to Sec. 6.4, as

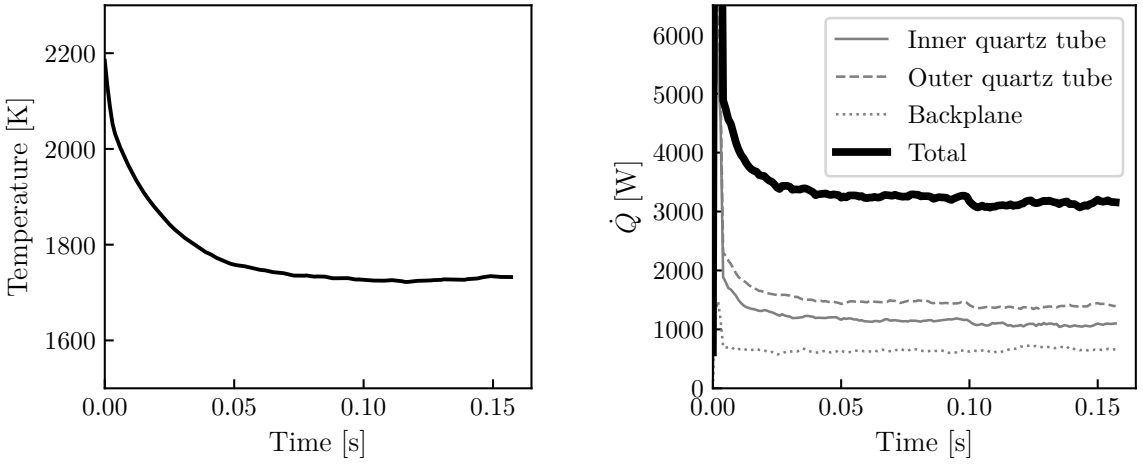

(a) Volume averaged fluid temperature inside the combustion chamber

(b) Wall heat fluxes from the fluid onto the combustor walls

Figure 7.2: Evolution of fluid quantities inside the bisector during CHT simulation in steady-state reacting conditions.

we are concerned with one-eighth of the full annular geometry, thus: $\dot{m}_{air} = 3.78\,\mathrm{g/s}$ and $\dot{m}_{fuel} = 0.22\,\mathrm{g/s}$.

For stability reasons, the quartz tubes are initialized at a constant temperature of $700\,\mathrm{K}$, and the entire injection unit at $300\,\mathrm{K}$. The initial solution of the fluid domain consists of a final converged solution obtained from separate reacting simulations of steady-state conditions with adiabatic walls. Furthermore, appropriate initial boundary conditions must be specified for the very first interval of the CHT simulations, which are only used until the first coupling event. For simplicity, we assume an initial quartz absorptance of $A_{\mathrm{init}}^{slab} = 0.8$ and an initial convective heat transfer coefficient of $h_{\mathrm{init}} = 10\,\mathrm{W/m^2K}$ at the quartz walls facing the atmosphere. After the first data exchange between the solvers, these initial values are discarded and replaced by the instantaneous (physical) values found from the simulation. Note, that the initial convective heat transfer coefficient at the atmosphere side of the quartz walls must not be confused with the relaxation factor h_F^{opt} (Eq. 5.8) used in the *fluid* domain to compute the wall heat fluxes sent to the solid solver according to Eq. 5.7.

7.2.3 Results obtained from reacting steady-state CHT simulations of the bisector

With the coupling setup specified above, CHT simulations of the fully ignited bisector are carried out over 1475 coupling intervals, corresponding to $24\,\mathrm{min}$ of physical time in the solid, and $157\,\mathrm{ms}$ of physical time in the fluid. The volume averaged fluid temperature inside the combustion chamber shows a steep decrease from adiabatic conditions during the first $80\,\mathrm{ms}$, before stabilizing at $T = 1720\,\mathrm{K}$ (see Fig. 7.2(a)). Such a substantial temperature change underscores the importance of accounting for realistic wall boundary conditions along with an appropriate wall model, which could not have been established with *adiabatic* boundary conditions as assumed in previous works. Interestingly, the wall heat fluxes from the fluid onto the combustor walls (see Fig. 7.2(b)) are found to be non-negligible as well, even after an initial transient (due to an initial solution obtained from adiabatic conditions).

Due to the time desynchronization between both domains, the convergence of the solid

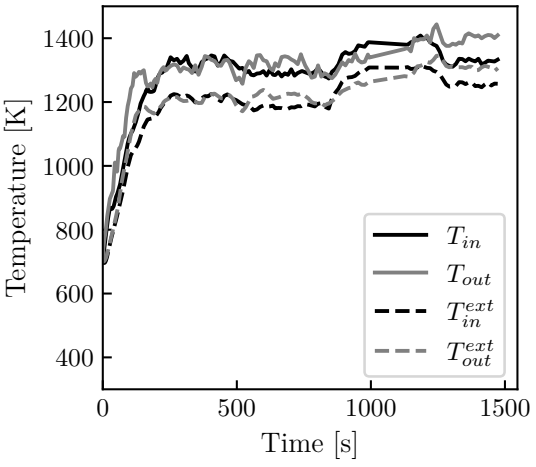

(a) Wall temperature evolutions during CHT

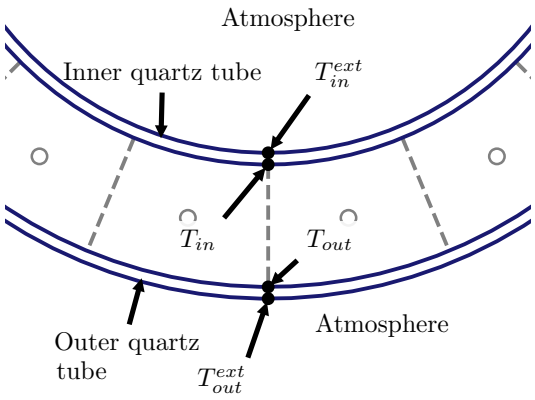

(b) Temperature monitoring locations

Figure 7.3: Temporal evolution of wall temperatures of both quartz tubes (a) sampled at the positions indicated in (b), at $x = 35\,\mathrm{mm}$ above the chamber backplane. T_{in}: internal quartz tube, burnt gas side; T_{out}: outer quartz tube, burnt gas side. T_{in}^{ext}: internal quartz tube, ambient side; T_{out}^{ext}: outer quartz tube, ambient side.

parts is accelerated, reaching stationary temperature levels after approximately $260\,\mathrm{s}$. The short transient heating period and subsequent steady-state can be examined for both quartz tubes in Fig. 7.3(a). These profiles are monitored at the locations indicated in Fig. 7.3(b). The burnt gas side of the quartz walls locally reaches temperatures between $T_{in} = 1350\,\mathrm{K}$ and $T_{out} = 1400\,\mathrm{K}$, whereas the atmosphere side exhibits a temperature range between $T_{in}^{ext} = 1200\,\mathrm{K}$ and $T_{out}^{ext} = 1350\,\mathrm{K}$. A three-dimensional view of the steady-state solution of the bisector's solid domain is given in Fig. 7.4, where the injector assembly in sector $S{+}1$ is shown in a cutaway view to reveal the temperature distribution of the internal injector parts. While the surface of the chamber backplane exposed to hot burnt gases reaches $T = 485\,\mathrm{K}$, we observe a steady temperature decrease towards $T = 300\,\mathrm{K}$ at the lower boundary of the solid domain, where iso-thermal boundary conditions are imposed to approximate the effect of water cooling (see also Fig. 5.2(c)). There is also a noticeable cooling effect at the bottom edges of the quartz tubes in contact with the injector support, where temperatures of $T = 500\,\mathrm{K}$ are found, more than $400\,\mathrm{K}$ lower than the top edges of the quartz walls.

A clearer representation of the surface temperatures is provided in Fig. 7.5, showing each side of both quartz tubes unwrapped into a rectangular system. The top row (Fig. 7.5(a) and (b)) corresponds to both sides of the inner quartz tube, the bottom row ((c) and (d)) to the outer quartz tube (see Fig.) 7.3(b) for reference). Peak temperatures prevail mostly in the lower half of the quartz tubes in the vicinity of flames. More importantly, the temperature difference in those regions does not exceed $T = 200\,\mathrm{K}$ between the inside and outside of each quartz tube. This raises the question how heat is dissipated at the atmosphere sides of the quartz tubes, where heat transfer is modeled through radiation and convection. We recall from the discussion of the quartz' radiative properties in Sec. 5.2.1 that its modeled absorptance decreases with increasing local temperature (see Fig. 5.3(e)). Comparably low values of $\overline{A}^{slab} = 0.4$ are therefore expected in the high-temperature regions of both quartz tubes in Fig. 7.6, only reaching $\overline{A}^{slab} = 0.55$ at the top edges. This suggests that heat transfer through radiation is less effective in the vicinity of the flames (*i.e.* at peak temperatures),

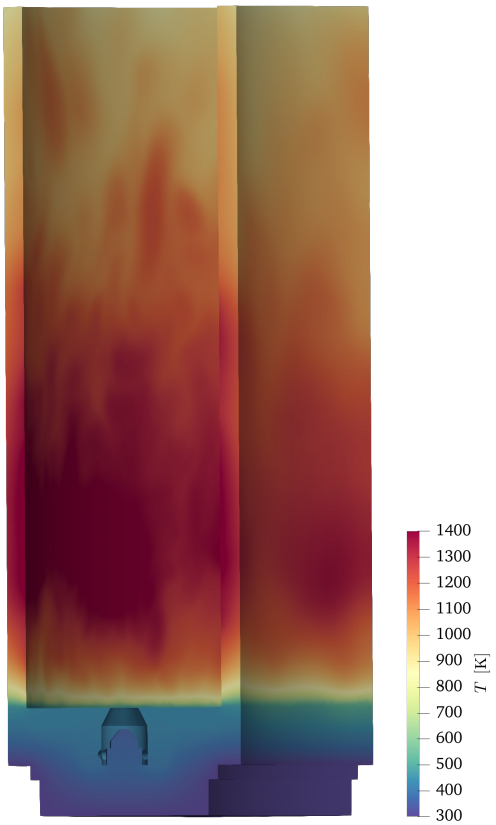

Figure 7.4: Three-dimensional view of the instantaneous temperature in the solid domain obtained from reacting CHT simulations of the bisector (final solution shown). The injector in sector $S{+}1$ is shown in a cutaway view to reveal the temperature distribution of the injector parts.

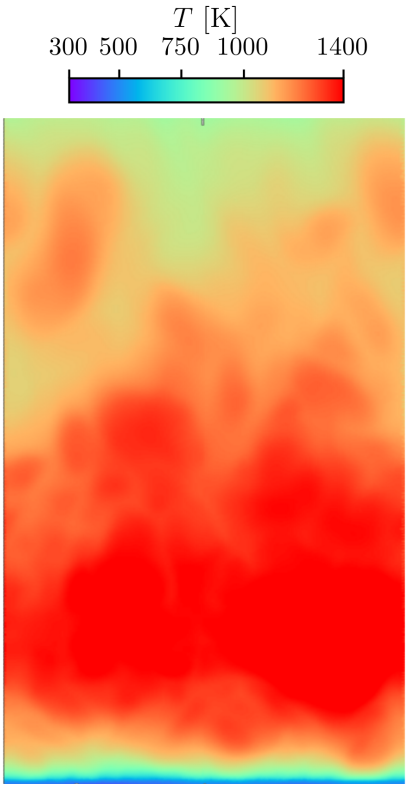

(a) Inner quartz tube, surface exposed to burnt gases

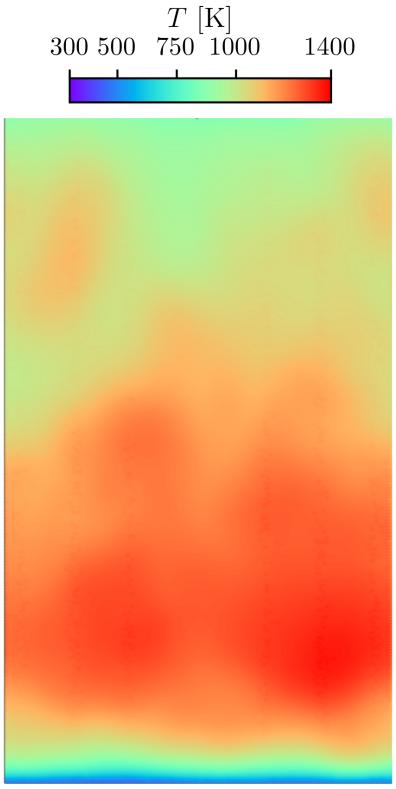

(b) Inner quartz tube, surface exposed to ambient air

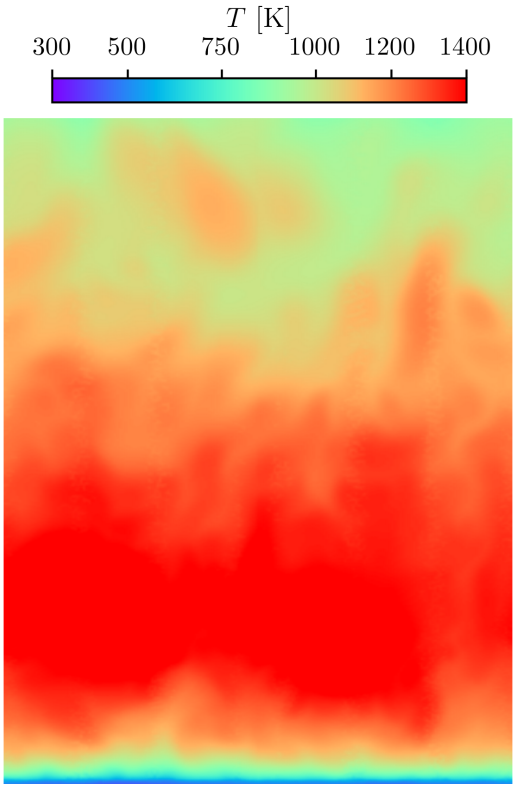

(c) Outer quartz tube, surface exposed to burnt gases

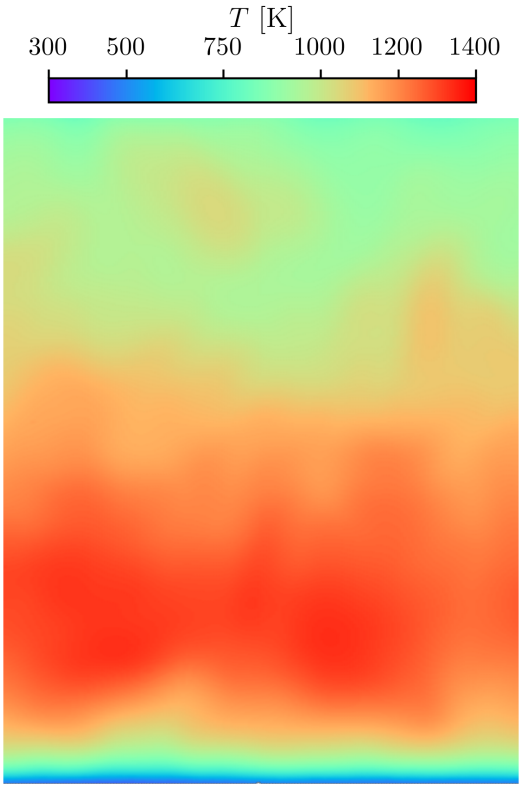

(d) Outer quartz tube, surface exposed to ambient air

Figure 7.5: Instantaneous wall temperatures obtained from CHT simulations at stationary operating conditions for both quartz tubes. Top row: inner quartz tube; bottom row: outer quartz tube.

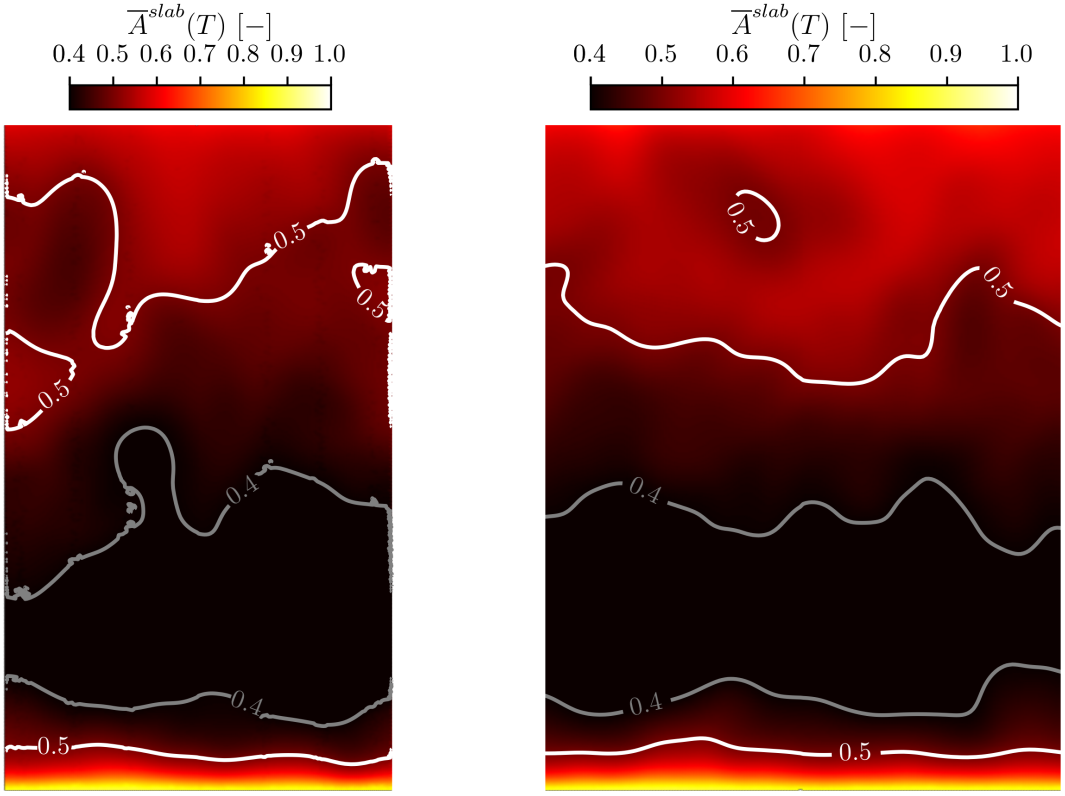

(a) Inner quartz tube (b) Outer quartz tube

Figure 7.6: Instantaneous Planck-mean absorptance obtained from CHT simulations of stationary operating conditions for both quartz tubes. (a) and (b) correspond to the respective surface facing the ambient air.

contributing to similar temperature levels at both sides of each quartz, as observed in Fig. 7.5.

Nevertheless, radiative heat transfer remains by large the dominating mechanism of (external) heat transfer as illustrated in Fig. 7.7: around 70% of the total wall heat flux received from the fluid domain is dissipated through radiation at the outside surfaces, followed by 20% through convection, and only 10% through heat conduction into the injector assembly. We thus conclude from the above analysis that beyond the importance of appropriate wall models in the fluid domain, radiative heat transfers of the *solid* domain (with the atmosphere) make up for a substantial amount of heat dissipation, justifying our present multiphysics approach. Even in light of major modeling uncertainties in terms of material properties or approximations of the water cooling circuit, this argument remains generally valid.

We acknowledge however that quantitative assessments of the accuracy of the predicted temperature profiles are limited due to the lack of detailed experimental data. In particular, external wall heat transfer through radiation is likely to be subject to some uncertainty in the present approach, since manufacturer data of the quartz' spectral emissivity is only specified at room temperature. Despite this, the present coupling approach should be considered as an attempt to base the later discussion of wall temperature effects on light-round timings on as much physical arguments as possible, rather than arbitrary assumptions of temperature profiles derived from macroscopic balance equations or single-point measurements. Therefore, temperature profiles obtained from CHT simulations are deemed to be more realistic to establish initial conditions for light-round.

For the next step, axial temperature profiles are required to be imposed as boundary

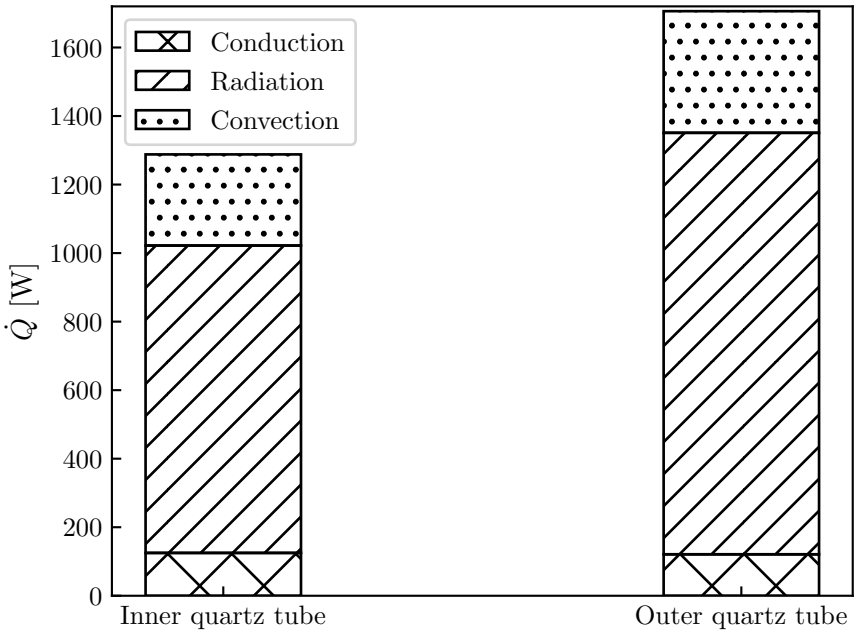

Figure 7.7: Energy balance for each quartz tube showing the percentage of the three main heat dissipation mechanisms of the total heat flux received from the fluid domain: (i) heat conduction from each quartz into the injector assembly, (ii) radiation and (iii) convection at the outside surfaces facing the atmosphere.

conditions in pure fluid flow simulations of prefueling. These profiles are obtained from azimuthal averaging of the surface temperatures of the final steady-state solution already shown in Fig. 7.5. The averaged axial profiles are plotted in Fig. 7.8 for the inside faces of each quartz tube. Signed wall-normal heat fluxes (fluid to solid with negative sign) are included for reference, but not imposed in the following step.

Finally, we emphasize that the characteristic time of the quartz estimated from Eq. 5.6, $\tau_S = 30.68\,\mathrm{s}$, is much larger than the light-round duration, $\tau^{LR} = 54.6\,\mathrm{ms}$ (see Tab. 6.1), found in Chap. 6. This is even more true for the presumably shorter light-round duration in preheated conditions as suggested by experimental measurements (shown later). Consequently, wall temperatures obtained from the previous CHT simulations can be viewed as "frozen" temperatures profiles which do not evolve during the relevant time scales of light-round. As we shall see in the following section, the same argument also applies to prefueling simulations.

7.3 Prefueling simulations

The previous Conjugate Heat Transfer simulations were motivated by the lack of experimental temperature profiles of MICCA-Spray required to establish initial conditions prior to relight. Specifically, prefueling into a preheated combustion chamber is supposed to raise the fresh gas temperature and fuel evaporation rates substantially, which cannot be achieved by imposing adiabatic wall boundary conditions in the simulation, as done in previous works. Instead, we rely on the results of CHT simulations, which we consider to be a more realistic representation of the walls' thermal state under quick relight.

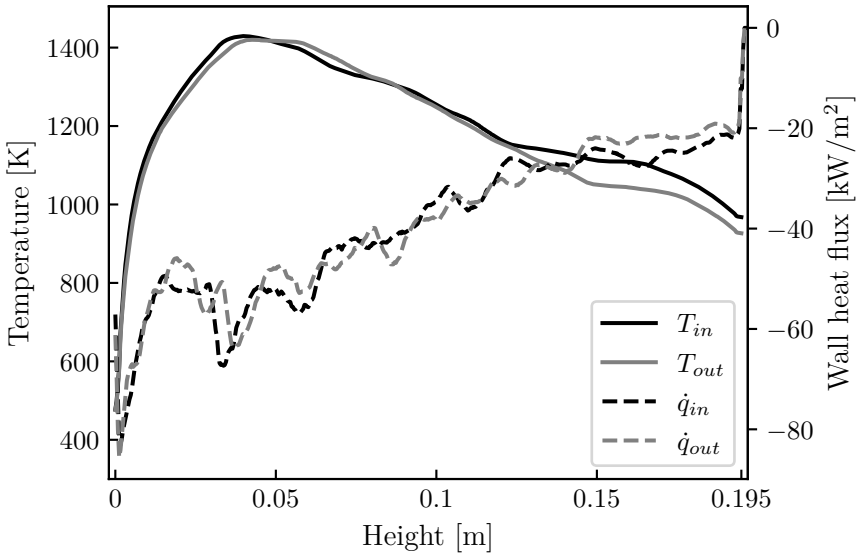

Figure 7.8: Azimuthally averaged wall temperature profiles for the inner (solid, black) and outer quartz wall (solid, gray) facing the inside of the combustor. Wall normal heat fluxes are given for the respective walls as dashed lines.

7.3.1 Boundary conditions

Stationary wall temperature profiles shown in Fig. 7.8 are imposed as new wall boundary conditions during the prefueling simulations as well as during the final relight simulation. We proceed in a similar manner with the wall temperatures of the injector assembly, though without azimuthal averaging due to spatially varying materials used inside the injector. The resulting wall boundary of the fluid domain is illustrated in Fig. 7.9 and colored by the local wall temperature. It corresponds to the interface between the internal combustor flow and the *inside* walls of the combustor that were previously coupled during CHT simulations. The *outside* combustor walls facing the atmosphere are intentionally omitted, since we are only concerned with the internal heat transfer between the fluid and solid domain. As Fig. 7.9 already suggests, prefueling simulations are performed in the bisector geometry, since we assume axi-periodic symmetry across all sectors of the combustor.

Heat transfer between the internal fluid flow and the internal combustor walls is computed by the tabulated wall model. Unlike CHT simulations, the fluid consists of pure fresh gases (n-heptane/air). Thus, we employ table AIR-4D (see Tab. 5.1) to interpolate the resulting wall heat fluxes and wall shear stresses. All other boundary conditions are identical to those presented in Sec. 7.2.2, notably the mass flow rates ($\dot{m}_{air} = 3.78\,\mathrm{g/s}$ and $\dot{m}_{fuel} = 0.22\,\mathrm{g/s}$) and the pressure condition imposed at the atmosphere outlet ($p = 1\,\mathrm{bar}$). Moreover, fresh air and fuel are still injected at $T = 300\,\mathrm{K}$ at their respective inlets. However, the airflow is subjected to moderate preheating up to $T = 320\,\mathrm{K}$ when passing through the injectors due to their elevated temperature levels: the injector blocks and swirlers reach peak temperatures of approximately $T = 430\,\mathrm{K}$, the terminal plates even $T = 460\,\mathrm{K}$ (see Fig. 7.9).

7.3.2 Results of prefueling simulations

In monitoring the temporal evolution of the fresh gas temperature and the gaseous equivalence ratio we can observe the convergence of the non-reacting prefueling simulation during its total runtime of $t = 500\,\mathrm{ms}$. From Fig. 7.10(a) we can infer that the volume averaged fresh gas

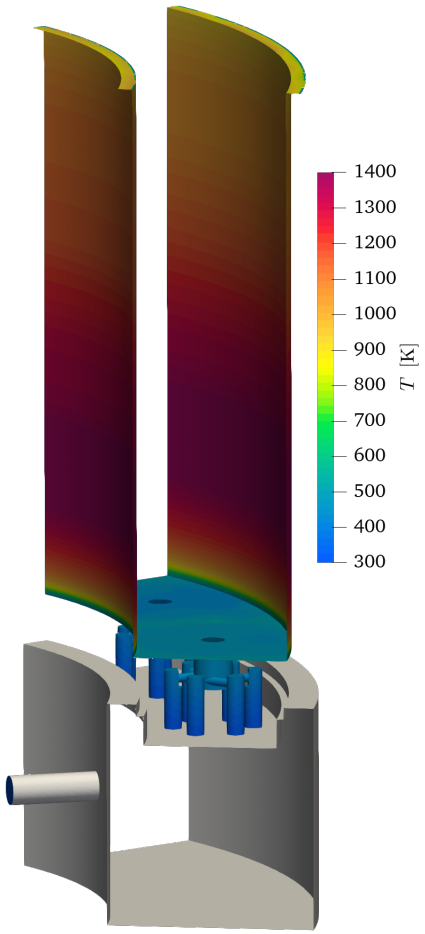

Figure 7.9: Wall temperature boundary conditions obtained from precursor CHT simulations imposed prefueling simulations in the bisector as well as later light-round simulations with preheated combustor walls. The air plenum (in gray) is assumed to be adiabatic.

temperature reaches stationary levels within $300\,\mathrm{ms}$, stabilizing at $T = 670\,\mathrm{K}$. Constant values of the volume averaged gaseous equivalence ratio are found already after $100\,\mathrm{ms}$, stabilizing at $\phi = 0.85$ (see Fig. 7.10(b)). The faster convergence of the equivalence ratio is certainly due to enhanced evaporation rates of fuel droplets in preheated air compared to the configuration with cold combustor walls in Chap. 6. Examining the area averaged gaseous equivalence ratio across different axial cutplanes inside the combustion chamber in Fig. 7.10(c) provides further proof for this argument: the variation of ϕ ranges in a very narrow band of $\phi = 0.85$ to 0.9, compared to a much larger spread observed during fuel injection into a combustion chamber with cold walls (see Fig. 6.1: $\phi = 0.6$ to 0.8). Thus, droplets can fully evaporate before reaching the outlet of the combustor.

Beyond spatially averaged quantities, it is also instructive to investigate the local flow field on the central azimuthal cutplane through the combustion chamber at $R = 0.175\,\mathrm{m}$, transformed from a cylindrical into a rectangular system. Figure 7.11 shows time averaged quantities during the final $10\,\mathrm{ms}$ of the prefueling simulation. While the mean axial velocity field in Fig. 7.11(a) resembles the flow field in cold wall conditions (see Fig. 6.2(a)), differences are visually much more striking when comparing the mean gaseous equivalence ratio between both configurations, *i.e.* Fig. 7.11(b) and Fig. 6.2(b). In preheated conditions, the inter-injector recirculation zone exhibits particularly high values of $\phi = 0.95$, where lower values were previously found with cold walls ($\phi = 0.75$). The same applies to the outer recirculation zone situated between the swirling jets and the inner and outer quartz tube, illustrated on a radial cutplane in Fig. 7.12(a). The entire upper half of the preheated combustion chamber is also more homogeneous ($\phi = 0.85 \approx \mathrm{const.}$) as a consequence of elevated fresh gas temperatures and virtually full droplet evaporation, which is also confirmed in Fig. 7.11(c) by a vanishing liquid volume fraction α_l. This is in stark contrast with the α_l field shown in Fig. 6.2(c).

The preheating effect is also apparent in the fresh gas temperature field in Fig. 7.11(d): the local temperature level clearly scales with the residence time of the fluid, exhibiting increasing temperatures with increasing height above the chamber backplane. It is worth noting however, that local temperatures can be even higher than this image may suggest: in fact, peak temperatures at $T = 1000\,\mathrm{K}$ prevail most noticeably in the near-wall flow, which can be examined on a radial cutplane in Fig. 7.12(b). From a modeling perspective, these regions are particularly concerning in light of the employed two-step reaction mechanism that was not developed with preheated fresh gas temperatures in mind. A correction is therefore proposed in the following section.

We wish to reiterate that the time to establish steady-state conditions during prefueling ($t = 300\,\mathrm{ms}$ as mentioned above) is substantially shorter than the characteristic time of the quartz walls ($\tau_S = 30.68\,\mathrm{s}$), justifying the "frozen" temperature profile imposed as boundary condition in the fluid flow simulations. Since the relight procedure is performed manually, a prefueling phase of *at least* $300\,\mathrm{ms}$ can reasonably be assumed. Consistent initial conditions for each experimental run are thus guaranteed, facilitating the comparison with numerical relight simulations.

Finally, we also ensure consistency with the light-round simulation presented in Chap. 6 in terms of the initialization procedure: after steady-state conditions are established in the bisector, we clone the final converged solution eight times to generate an initial solution for the full annular combustor geometry. The wall temperature conditions previously applied to the bisector are then imposed as boundary conditions of the annular combustor, and non-reacting simulations are resumed in this preheated annular geometry for $t = 24\,\mathrm{ms}$ to dissolve coherent flow structures resulting from the cloning procedure. For ignition, we use the same ellipse of burnt gases as in the previous chapter (dimensions: $10 \times 24\,\mathrm{mm}$) to maintain a comparable

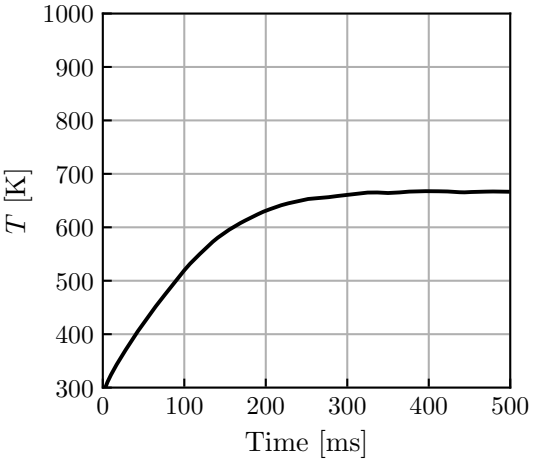

(a) Volume averaged fresh gas temperature

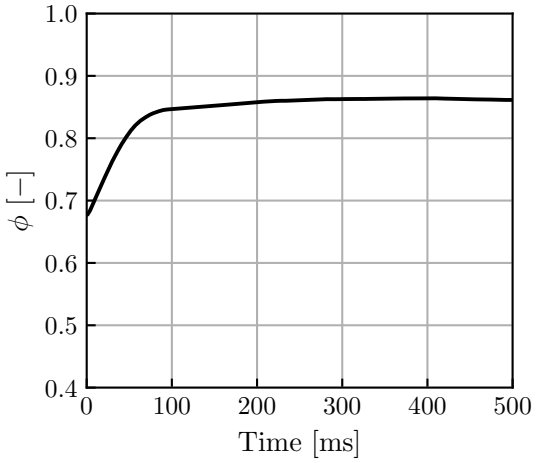

(b) Volume averaged gaseous equivalence ratio

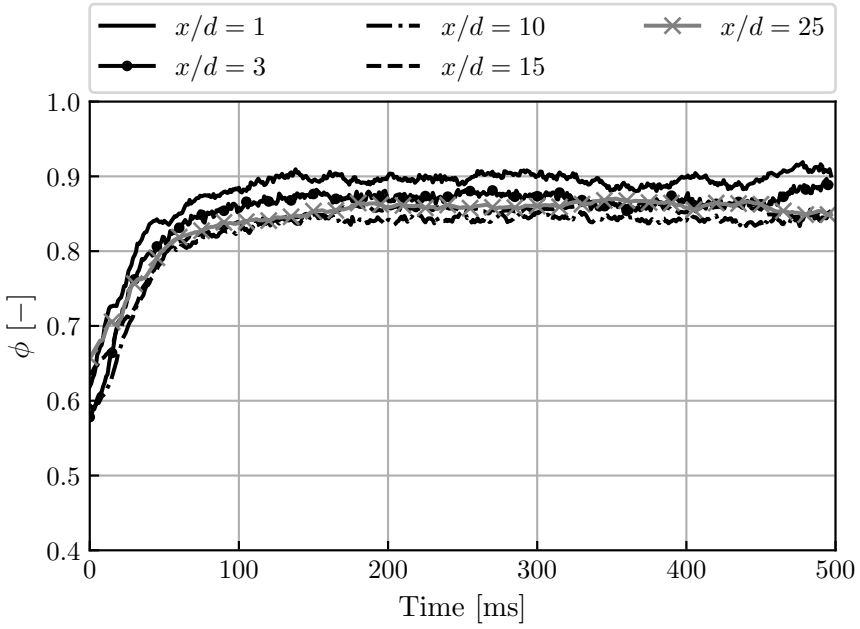

(c) Area averaged gaseous equivalence ratio

Figure 7.10: Temporal evolution of the fresh gas temperature (a) and gaseous equivalence ratio ((b), both volume averaged), and the area averaged gaseous equivalence ratio at different horizontal cutplanes through the combustion chamber. The axial distance x counted from the chamber backplane is normalized by the outlet diameter of the terminal plate $d = 8\,\mathrm{mm}$.

(a) Mean gaseous axial velocity u

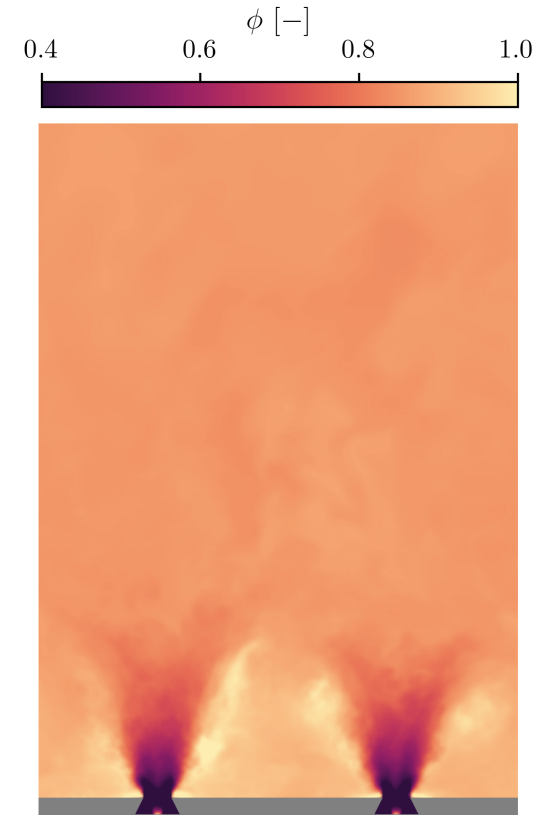

(b) Mean gaseous equivalence ratio ϕ

(c) Mean liquid volume fraction α_l

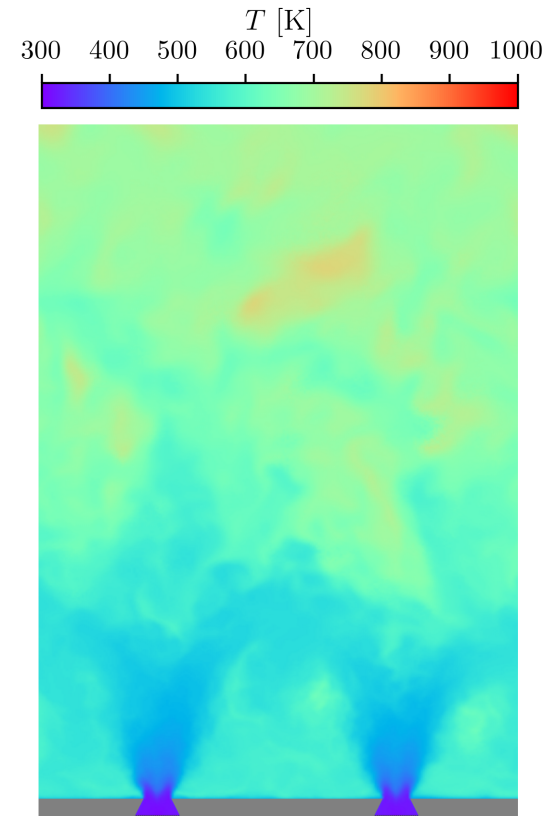

(d) Mean fresh gas temperature

Figure 7.11: Averaged gaseous and liquid solution fields of the preheated bisector on a cylindrical cutplane at $R = 0.175\,\mathrm{m}$ transformed into a rectangular system. The averaging duration is $t_{avg} = 10\,\mathrm{ms}$.

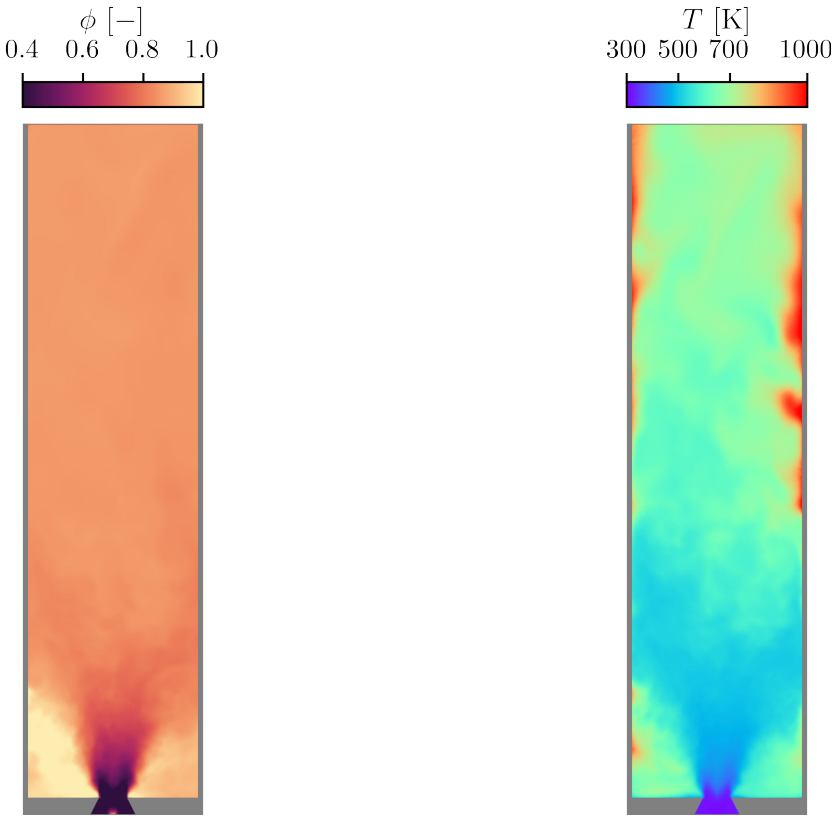

(a) Mean gaseous equivalence ratio ϕ (b) Mean fresh gas temperature

Figure 7.12: Averaged gaseous and liquid solution fields of the preheated bisector on a radial cutplane through injector *S*+1 at $\theta = 11.25°$. The averaging duration is $t_{avg} = 10\,\mathrm{ms}$.

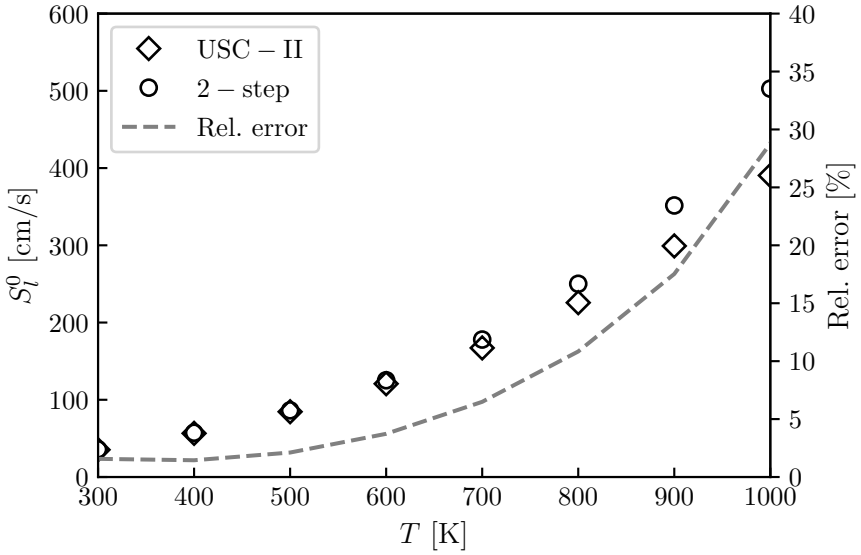

Figure 7.13: Comparison of the predicted values for the laminar flame speed S_l^0 obtained from a detailed kinetic scheme (USC-II, diamond markers, Smallbone et al. (2009)), and the two-step scheme (circle markers, Paulhiac et al. (2020)) as a function of the fresh gas temperature. For both schemes, a constant equivalence ratio $\phi = 0.9$ is used. The relative error is given as dashed gray curve (associated with the right axis).

ignition procedure between all light-round simulations. For heat transfer between the internal fluid flow and the internal combustor walls we use table AIR-4D in the fresh gas region, and table BURNT-4D in the burnt gas region. The appropriate table is locally selected based on the matching point (or off-wall) progress variable c_{MP} as defined in Tab. 5.1.

7.4 Correction of the two-step reaction mechanism

The main limitation of the employed two-step reaction mechanism by Paulhiac et al. (2020) consists in an overestimation of the laminar flame speed S_l^0, predominantly found beyond standard ambient conditions. With increasing fresh gas temperature, the discrepancy with respect to detailed reaction mechanisms gradually increases, as shown in Fig. 7.13 for a constant equivalence ratio of $\phi = 0.9$. The relative error compared to the USC-II mechanism (Smallbone et al., 2009) exceeds 5% at $T = 670\,\mathrm{K}$, *i.e.* the volume averaged fresh gas temperature in stationary conditions, and 28% at $T = 1000\,\mathrm{K}$, which is considered to be unacceptable.

To correct such erroneous behavior, an *ad hoc* correction factor is implemented in a similar fashion as the efficiency factor in the thickened flame model. By multiplying the species source terms as well as the species diffusion coefficients by a factor $\mathcal{C}$, the correct laminar flame speed can be retrieved. The ultimate goal is a tabulation of the correction factor based on the local fresh gas conditions. It can subsequently be used to interpolate the corresponding local value of $\mathcal{C}$ in simulations in AVBP. We define

$$\mathcal{C} = \frac{S_l^{\mathrm{USCII}}}{S_l^{\mathrm{2S}}} \tag{7.1}$$

as a ratio of laminar flame speeds, where S_l^{USCII} follows from the detailed kinetic scheme USC-II, and S_l^{2S} from the (unaltered) two-step reaction scheme by Paulhiac et al. (2020). $\mathcal{C}$ must necessarily be allowed to vary depending on the fresh gas state, thus it is a function of

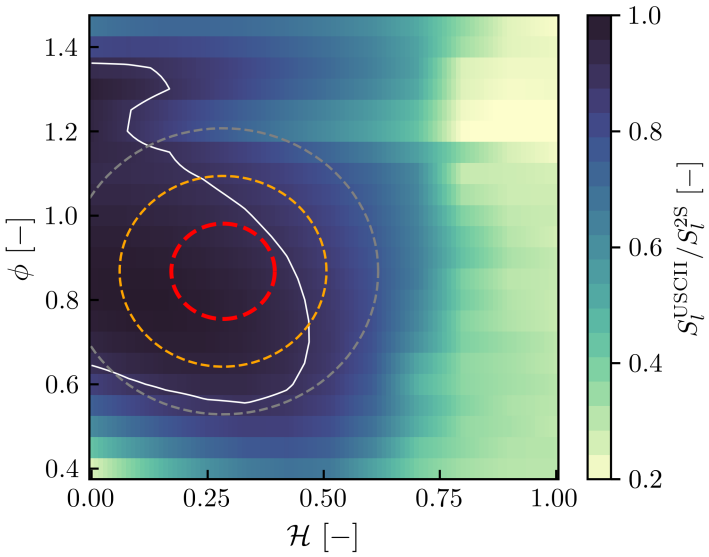

Figure 7.14: Visualization of the correction factor $\mathcal{C} \doteq S_l^{\mathrm{USCII}}/S_l^{\mathrm{2S}}$ as a function of $\mathcal{H}$ and ϕ. Dashed ellipses denote the standard deviation of the data points at the beginning of light-round (inner to outer: 1σ, 2σ, 3σ). The solid white contour line marks $S_l^{\mathrm{USCII}}/S_l^{\mathrm{2S}} = 0.9$.

e.g., the equivalence ratio ϕ and the fresh gas temperature T. It is obtained from precursor 1D laminar flame simulations in AGATH performed with both reaction mechanisms over a range of $\phi \in [0.4,\ 1.45]$ in steps of 0.5, and $T \in [300,\ 1400]\,\mathrm{K}$ in steps of $100\,\mathrm{K}$. These range limits are intentionally chosen to safely cover the expected fluid temperature range based on the wall temperature profiles obtained in Sec. 7.2.3. Similarly, the range of ϕ covers the value range inferred from Fig. 7.11(b). Although it is convenient to perform the table generation in terms of ϕ and T, it will prove more suitable to map the temperature to a normalized enthalpy $\mathcal{H} = f(T)$ instead. In this manner, $\mathcal{C}$ can be unambiguously determined in the entire numerical domain as $\mathcal{C} = f(\phi, \mathcal{H})$. Normalization of $\mathcal{H}$ is achieved by introducing an arbitrary lower and upper bound for the total enthalpy: $\mathcal{H} = 0$ is defined as the total enthalpy of fresh gases at $300\,\mathrm{K}$, while $\mathcal{H} = 1$ corresponds to fresh gases at $1400\,\mathrm{K}$. Different reference temperatures for species enthalpy databases (AVBP: $T_{ref} = 0\,\mathrm{K}$, AGATH: $T_{ref} = 298\,\mathrm{K}$) require a precursor enthalpy mapping from AGATH to AVBP to maintain consistency between both codes.

A visual representation of $\mathcal{C}$ is given in Fig. 7.14. The outer left edge at $\mathcal{H} = 0$ corresponds to a fresh gas temperature of $T = 300\,\mathrm{K}$ and shows reasonably high values of $\mathcal{C}$ (precisely $\mathcal{C} \geq 0.9$ within the white iso-contour) over a wide range of equivalence ratios. In those conditions, accurate laminar flame speed values are predicted by the two-step reaction mechanism as already shown in Fig. 2.2. Thus, the error of the (uncorrected) two-step reaction mechanism in terms of the predicted laminar flame speed is small. In turn, the higher the enthalpy (or the higher the temperatures), the lower the correction factor. Hence, a larger error in S_l^0.

To retrieve the correct laminar flame speed in AVBP, we write the species conservation

equation (cf. Eq. 2.44 for the Artificially Thickened Flame model) as

$$\begin{aligned}&\frac{\partial\overline{\rho}\tilde{Y}_k}{\partial t}+\frac{\partial\overline{\rho}\tilde{u}\tilde{Y}_k}{\partial x_i}=\\&\frac{\partial}{\partial x_i}\bar{\rho}\left[(\mathcal{C}E\mathcal{F}D_k+D_k^t(1-\theta_F))\frac{\partial\tilde{X}_k}{\partial x_i}-\tilde{Y}_k(\mathcal{C}E\mathcal{F}\tilde{V}_i^c+\tilde{V}_i^{c,t}(1-\theta_F))\right]\\&+\mathcal{C}\frac{E}{\mathcal{F}}\bar{\dot{\omega}}_k\end{aligned}\tag{7.2}$$

Note that we intentionally replaced the Hirschfelder-Curtiss diffusion law by a simple Fickian diffusion law (in AGATH as well as in AVBP)

$$V_{k,i}Y_k=-D\frac{\partial Y_k}{\partial x_i}\quad\text{with}\quad D=\frac{\lambda}{\rho C_p}\tag{7.3}$$

and strictly enforce unitary Lewis numbers for all species. In this manner, the total enthalpy remains constant across the flame front. With the tabulated correction factor loaded into AVBP we can then unambiguously interpolate its local value based on the local equivalence ratio ϕ and the normalized enthalpy $\mathcal{H}$ at each iteration.

Table interpolation is performed with the external COMMCOMB library already used for the tabulated wall model presented in Chap. 5. However, we have developed additional routines for the table handling and enthalpy normalization within AVBP, which does not support such correction natively.

Beyond the correction of the species transport equation, other submodels must be adapted as well in order to account for variable flame properties due to variable fresh gas temperatures. Specifically, appropriate values must be provided for (i) the local adaptive thickening approach depending on the laminar flame thickness δ_l (see Eq. 2.65), (ii) the flame sensor (Legier et al., 2000) depending on a reference reaction rate Ω_0 (Eq. 2.62), and (iii) the static formulation ($\beta=0.5$) of the flame surface wrinkling model (Charlette et al., 2002b) depending on the laminar flame speed S_l^0 (Eq. 2.47, only used during the initial instants after burnt gas deposition where the initial flame is still spherical). These quantities now depend on the fresh gas equivalence ratio *and* temperature (or enthalpy). Therefore, we employ the same tabulation strategy for δ_l, Ω_0 and S_l^0 as functions of ϕ and $\mathcal{H}$: the former two quantities are derived from the two-step reaction mechanism with enforced unitary Lewis numbers, whereas the latter is taken from the USC-II mechanism and can be conveniently interpolated in AVBP along with the interpolation of $\mathcal{C}$ at each iteration. Figure 7.15 illustrates the tabulated laminar flame properties used during light-round ignition with preheated combustor walls. Ω_0 (Fig. 7.15(a)) and S_l^0 (Fig. 7.15(c)) primarily increase with increasing total enthalpy, while δ_l^0 tends to increase with decreasing equivalence ratio. Most remarkably, the laminar flame speed is found to exceed $S_l^0=1\,\mathrm{m/s}$ for the volume averaged fresh gas temperature level reached in the combustion chamber, *i.e.* at $T=670\,\mathrm{K}$ or $\mathcal{H}=0.34$. Such value is one order of magnitude larger than the typical values found at standard ambient conditions. As we shall see, the laminar flame speed constitutes a crucial quantity in the modeling approach presented in Chap. 8, which demands for an accurate prediction depending on local fresh gas properties.

A final analysis is dedicated to the quantification of the impact of such correction. With the converged state of the prefueling simulation (see Sec. 7.3.2), we can infer the lowest possible value of $\mathcal{C}$ to be expected during the entire light-round simulation. We deliberately use the final prefueling solution as it has attained the highest possible fresh gas temperatures resulting from

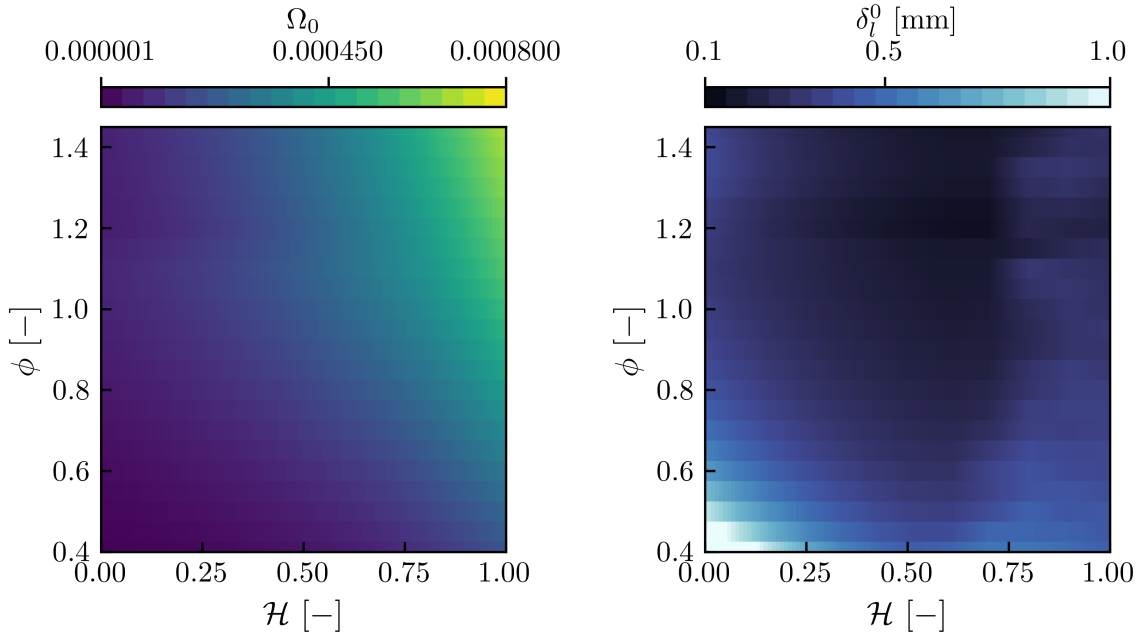

(a) Reference reaction rate Ω_0

(b) Laminar flame thickness δ_l^0

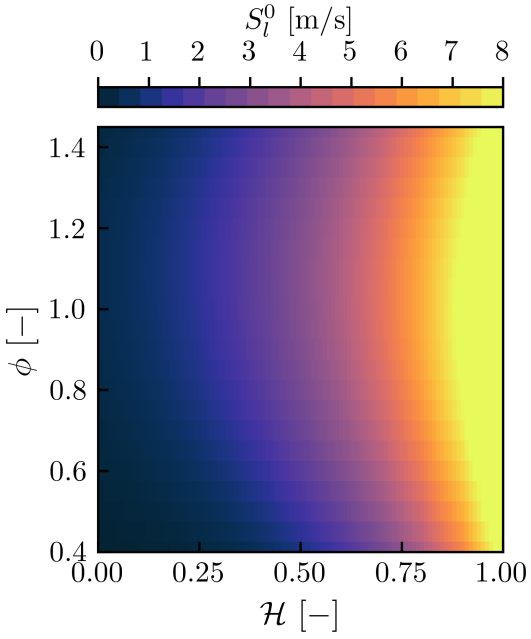

(c) Laminar flame speed S_l^0 obtained from the detailed reaction mechanism USC-II (Smallbone et al., 2009)

Figure 7.15: Visualization of the tabulated flame properties used within the thickened flame approach as functions of the fresh gas equivalence ratio ϕ and the normalized total enthalpy $\mathcal{H}$. The former properties (Ω_0 and δ_l^0, Figs. (a) and (b)) are based on the two-step reaction mechanism with unitary Lewis numbers. The laminar flame speed S_l^0 (Fig. (c)) in turn is computed from the USC-II reaction mechanism (Smallbone et al., 2009)).

the longest possible residence time in the combustion chamber. For newly injected fresh gases *during* light-round, the residence time is of the order of the light-round duration (τ^{LR}), which itself is much shorter than the characteristic time to reach thermal equilibrium ($\tau^{eq} = 300\,\mathrm{ms}$ as noted in Sec. 7.3.2). Hence, fresh gas temperatures cannot exceed the temperature level already established in stationary conditions during prefueling. Consequently, the lowest values of $\mathcal{C}$ are expected at the start of light-round.

Upon reexamining Fig. 7.14 however, the impact of $\mathcal{C}$ on the two-step reaction mechanism is generally smaller than 10% in most of the combustion chamber: the dashed ellipses (in Fig. 7.14) denote the standard deviations of the fresh gas properties ϕ and $\mathcal{H}$ encountered inside the combustion chamber volume. These are predominantly found in regions where $\mathcal{C} > 0.9$ (indicated by the white iso-contour). Given the moderate impact of the present approach, no further correction is performed for the laminar flame thickness δ_l^0, *i.e.* $\mathcal{C}$ only corrects the laminar flame speed S_l^0.

7.5 Results of light-round ignition with preheated combustor walls

Similar to Chap. 6, we approach the results of preheated light-round simulations from a macroscopic perspective first. In particular, we focus on flame shapes, the light-round duration and propagation mechanisms, and highlight the differences with regard to light-round ignition with cold combustor walls.

7.5.1 Flame propagation shapes

We start with an examination of instantaneous snapshots of flame propagation during light-round in Fig. 7.16. As in Sec. 6.5.1, the images are obtained by transforming the full cylindrical chamber into a rectangular system and integrating the heat release rate in line-of-sight direction. Note that the flames propagate from the center (position of the initial flame kernel) to the sides. The outlets of the sixteen injectors are included at the bottom of each image for reference.

Two major conclusions can be drawn from the comparison with the image sequence in Sec. 6.5.1: first, all characteristic phases of light-round ignition can be observed regardless of the thermal condition at the combustor walls. Consequently, flame shapes are comparable between both configurations. Second, and more importantly, flame front merging already occurs at $t = 35\,\mathrm{ms}$ (see Fig. 7.16(h), counting from the instant of burnt gas deposition at $t = 0\,\mathrm{ms}$), implying that the light-round duration τ^{LR} according to the definition in Sec. 6.5.2 is also substantially shorter with preheated combustor walls. Despite this, the flame front propagating through the positive half of the combustion chamber (sectors S+1 to S+7 in Fig. 7.16) appears to move faster than its counterpart in the negative half (sectors S-1 to S-7). Such discrepancy between both flame fronts is less pronounced in the image sequence in Fig. 6.3 with cold walls. Experimental high-speed imaging has confirmed this observation, pointing to an inherent stochastic phenomenon. A more detailed characterization however would clearly require more than two simulations, which is beyond the scope of the present work.

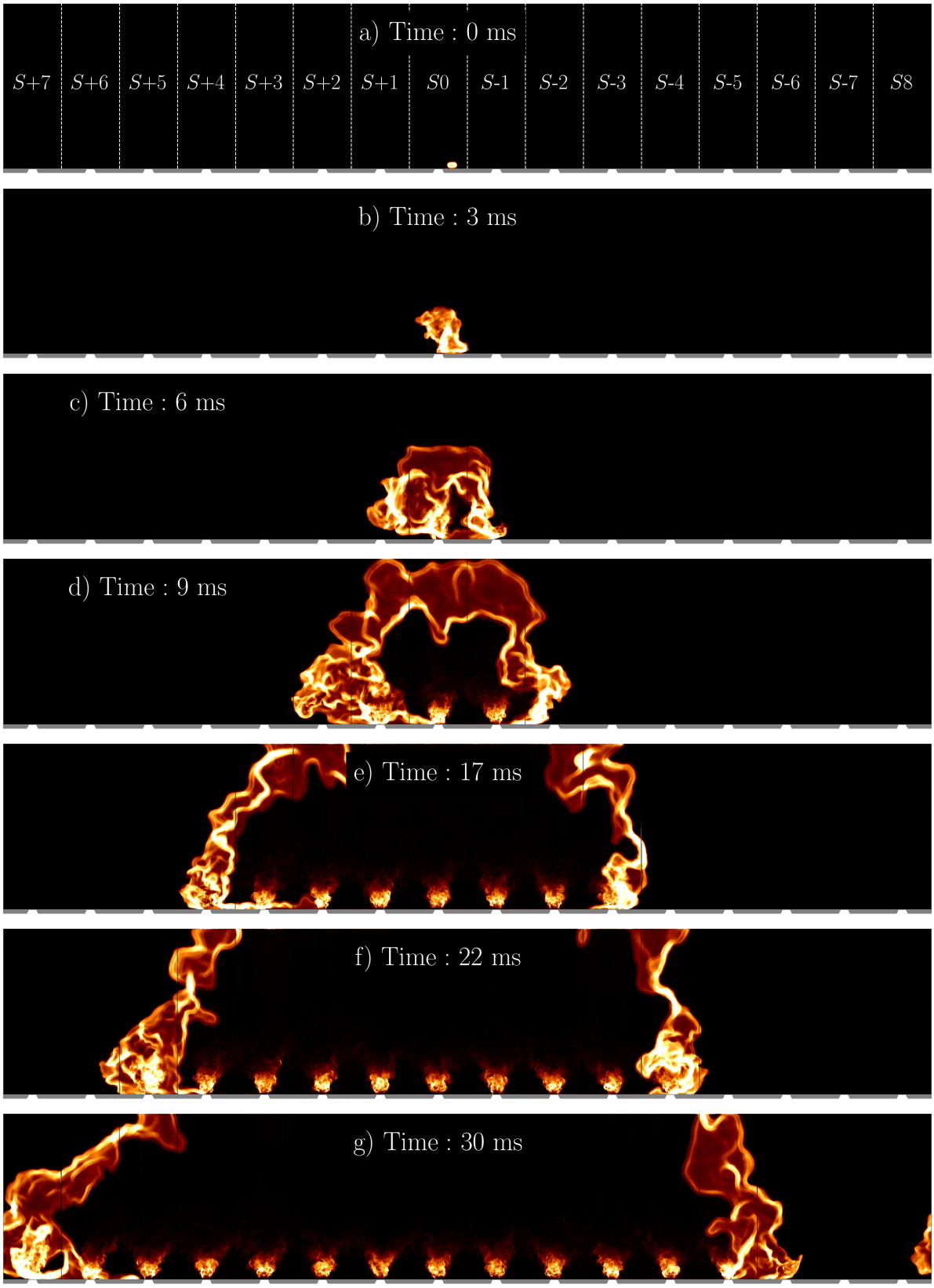

Figure 7.16: Visualization of flame propagation during preheated light-round. Line of sight integration of the heat release rate in LES for different instants after transforming the chamber from a cylindrical into a rectangular system. Sectors are labeled according to Fig. 3.2(c).

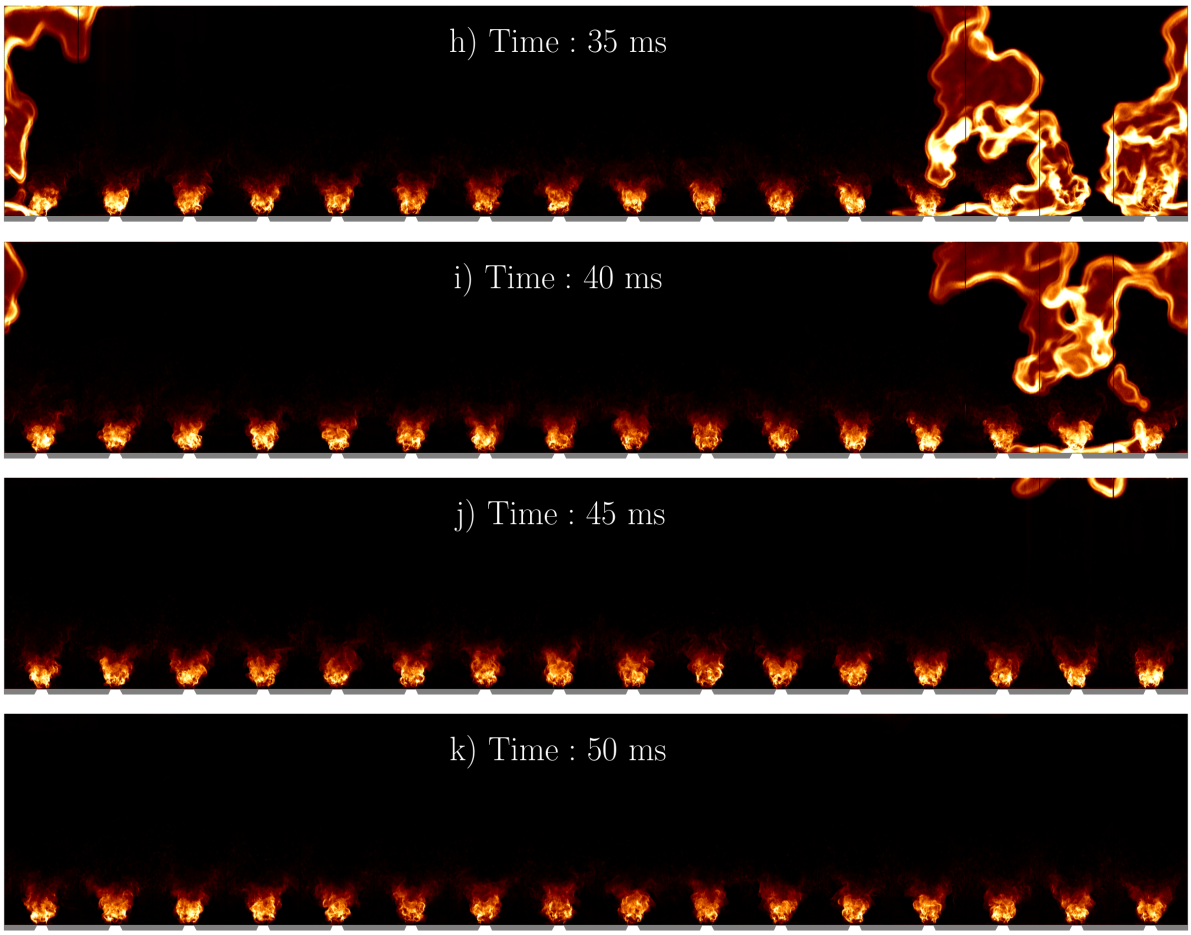

Figure 7.16: Visualization of flame propagation during preheated light-round. Line of sight integration of the heat release rate in LES for different instants after transforming the chamber from a cylindrical into a rectangular system (cont.).

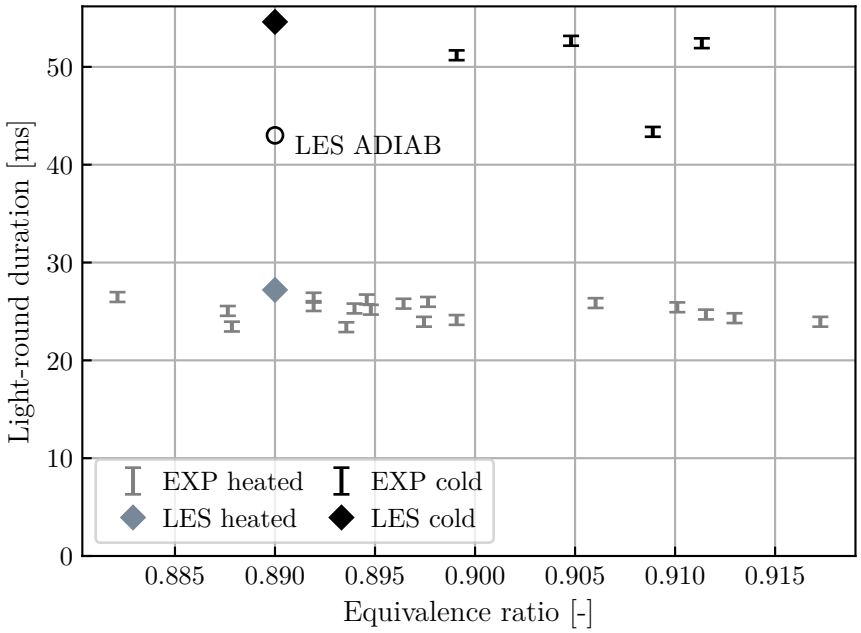

Figure 7.17: Light-round durations for preheated (gray symbols) and cold conditions (black symbols). Experimental markers (labeled "EXP", taken from Puggelli et al. (2020)) also indicate the uncertainty range determined by the camera frame rate. Gray diamond: LES with preheated combustor walls presented in this chapter; black diamond marker: LES with $T_w = 300\,\mathrm{K}$ presented in Chap. 6 (case BASE); circle marker: LES with adiabatic walls presented in Chap. 6 (case ADIAB).

7.5.2 Light-round duration

In comparing the predicted light-round duration to experimental measurements, a global assessment of the simulation can be performed. We recall that the duration τ^{LR} is defined as the elapsed time between the ignition of the burner *adjacent* to the sector of flame kernel deposition, and the flame front merging, consistent with Sec. 6.5.2 and previous works (Philip et al., 2015b; Lancien et al., 2019; Puggelli et al., 2021). Several experimental runs under preheated conditions are compiled in Fig. 7.17 (experimental markers taken from Puggelli et al. (2020)) for the nominal operating point with preheated combustor walls. These data points are matched by the preheated light-round LES (gray diamond in Fig. 7.17) with remarkable accuracy. Nevertheless, we do *not* imply that the agreement between the experiment and simulation validates our entire modeling setup as such. In fact, we can neither exclude uncertainties associated with the prescribed wall temperature profiles obtained from Conjugate Heat Transfer simulations, nor uncertainties related to the simplified ignition procedure through burnt gas deposition.

Despite this, LES results retrieve a two times shorter light-round duration under preheated conditions compared to light-round with ambient temperature walls (black diamond in Fig. 7.17, see Sec. 6.5.2) for otherwise same operating conditions. The same trend can also be observed in the experimental data in presented in Fig. 7.17. This implies that local conditions affecting the propagating flame fronts are substantially altered by preheated walls to allow for a faster flame propagation which becomes evident by comparing both detailed simulations. Note that adiabatic LES (circle marker in Fig. 7.17) matches neither experimental configuration with acceptable accuracy. It is therefore considered to be a poor approximation of the thermal conditions at the combustor walls. Hence, it is not included in the following analysis.

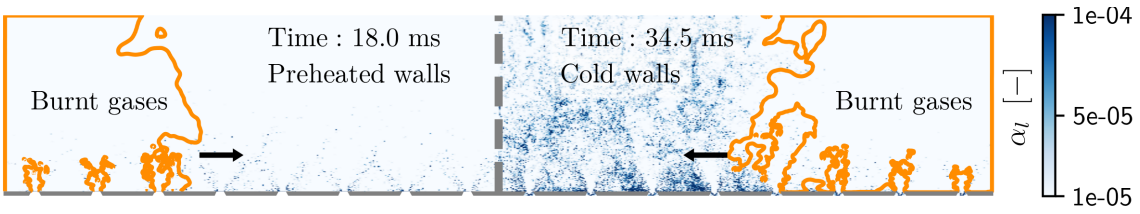

Figure 7.18: Comparison of liquid volume fractions α_l on an unwrapped cylindrical cutplane at $R = 0.195\,\mathrm{m}$ with preheated walls (left half), and cold walls (right half). Solid contour lines correspond to iso-values of the progress variable $c = 0.76$. Flame propagation from left and right edges to the center.

Instead, we investigate the impact of preheating on the liquid and gas phase separately in order to understand the differences in the observed flame propagation speeds.

7.5.3 Impact of preheating on the liquid phase and the leading point

Starting with the liquid phase, Fig. 7.18 shows an unwrapped cylindrical cutplane of the combustion chamber which contrasts the present (preheated) case on the left (labeled as "preheated walls") with the light-round case of Chap. 6 at ambient temperature walls on the right ("cold walls"). Flame fronts propagate from the sides of the image to the center and their instantaneous position is visualized by iso-contours of the progress variable $c = 0.76$. As already foreshadowed in Sec. 7.3.2, the difference in the liquid volume fraction α_l (blue shades) in the fresh gas region upstream of each flame front is visually striking. Preheated combustor walls cause higher fresh gas temperatures which in turn result in enhanced fuel evaporation (cf. Fig. 7.11(c) and (d)). Therefore, fuel droplets emerging from each injector are barely visible (light shades in Fig. 7.18) and vanish entirely in the upper half of the combustor, whereas higher liquid volume fractions are encountered across the full combustor height with ambient temperature walls. This observation has implications for the flame leading point trajectory which becomes less sensitive to the upstream α_l-field, contrary to the distinct sawtooth trajectory observed with cold combustor walls (see Sec. 6.5.4). Hence, its evolution tracked in Fig. 7.19 (gray line, showing the negative chamber half only) is much smoother over almost the entire duration of the simulation, compared to the trajectory found with cold combustor walls (thick black line). Moreover, it also encounters higher equivalence ratios due to enhanced evaporation.

7.5.4 Impact of preheating on the gas phase and flame expansion

Examining the gas phase, the attention is specifically drawn to the burnt gases first. Heat losses incurred by the burnt gases in contact with the combustor walls are plotted in Fig. 7.20 for preheated (solid gray lines) and cold (solid black lines) combustor walls. To facilitate the comparison between both cases with different light-round durations, we have normalized the time coordinate by the respective light-round duration. Although the absolute value of the wall heat flux from the burnt gases onto the combustor walls (Fig. 7.20(a)) is smaller with preheated combustor walls compared to cold combustor walls, it is not small enough to be entirely neglected as in *e.g.*, adiabatic simulations. Most importantly, the heat fluxes cause the volume averaged burnt gas temperatures (Fig. 7.20(b)) to decrease over the light-round duration by approximately $100\,\mathrm{K}$, which in turn cause the respective burnt gas densities to

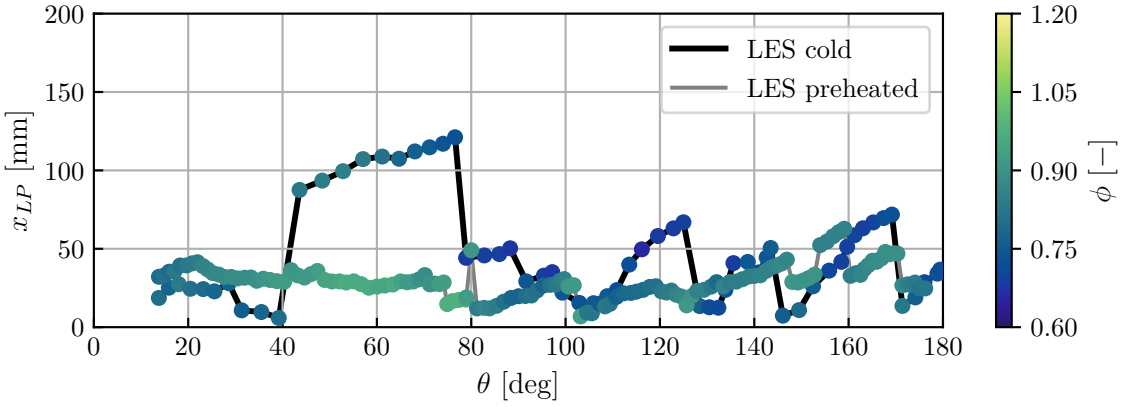

Figure 7.19: Comparison of the leading point trajectories of case LES preheated (gray curve) and LES cold (black curve) in the negative half of the combustion chamber. Abscissa is given as arc length in degrees counting from sector *So* (see Fig. 3.2(c)). The ordinate corresponds to the leading point height above the chamber backplane. Colored markers indicate the local equivalence ratio ϕ of each case.

slightly increase. At the same time, the fresh gas temperatures are subjected to more moderate variations, since they are either continuously preheated by the combustor walls or at the same temperature as the combustor in the cold wall case, and thus not shown here.

Previous studies have outlined that the large flame propagation velocities are promoted by a flow acceleration in azimuthal direction, resulting from the volumetric expansion of the burnt gases. Given the larger flame velocity in the preheated case, the azimuthal flow acceleration generated by the flame propagation is more pronounced, particularly in the upper half of the combustion chamber, reaching two times higher peak velocities ($u_\theta \approx 15\,\mathrm{m/s}$, see Fig. 7.21) compared to peak values of $u_\theta \approx 7\,\mathrm{m/s}$ for light-round ignition with cold walls (see Fig. 6.5). We recall that this flow acceleration is known to scale with the density ratio between fresh and burnt gases, written as respective averages (denoted by angular brackets) over the combustor volume V: $\langle\rho_u\rangle_V \,/\, \langle\rho_b\rangle_V$.

Upon examination of Fig. 7.22, however, the density ratio is initially twice as high in the cold wall case compared to the preheated counterpart, although the preheated case reaches a higher flame propagation speed, which translates into a shorter light-round duration. In spite of a distinct cooling effect with ambient temperature walls (compare the initial density ratio (dashed black line) with the evolution of the solid black curve in Fig. 7.22), the density ratio of the preheated case remains always lower and also appears to be less affected by heat losses. Therefore, it can neither explain the higher flow acceleration through burnt gas expansion, nor the higher flame propagation speed observed with preheated walls. Although these preliminary conclusions appear to be conflicting, we resolve the underlying physical problem in Chap. 8 and provide an appropriate low-order modeling approach.

7.5.5 Suitability of the artificially thickened flame approach in light of liquid fuel injection

With the results obtained from the present and the previous chapter, we wish to return to the hypothesis stated in Sec. 2.5.4 according to which the use of the artificially thickened flame model is justified in light of liquid fuel injection. An *a posteriori* verification of our assumptions is provided in Fig. 7.23, showing a map of the Takeno flame index (Yamashita et al., 1996)

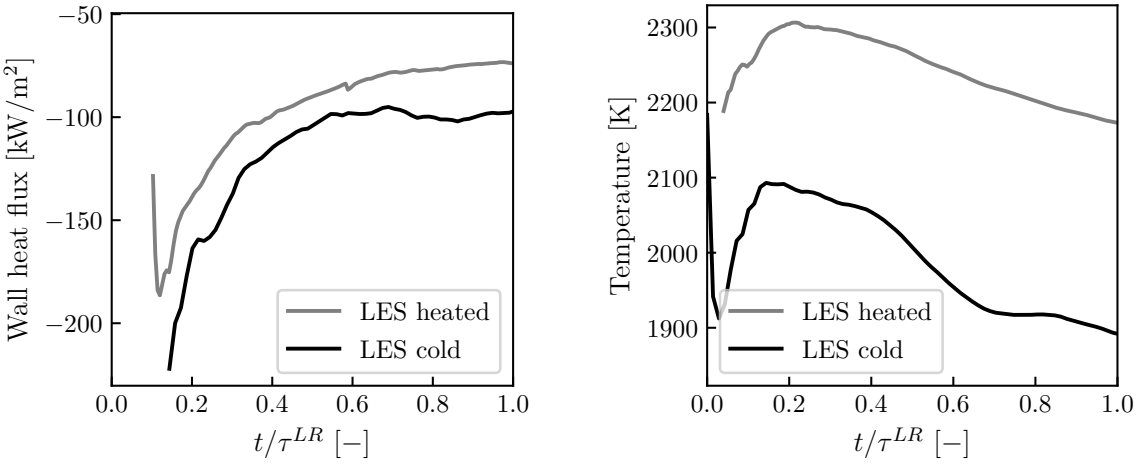

(a) Wall heat fluxes

(b) Volume averaged burnt gas temperature

Figure 7.20: Comparison of surface averaged wall heat fluxes from the burnt gases onto the inner combustor wall (Fig. (a)), and volume averaged burnt gas temperatures (Fig. (b)). The time coordinate is normalized by the respective light-round duration.

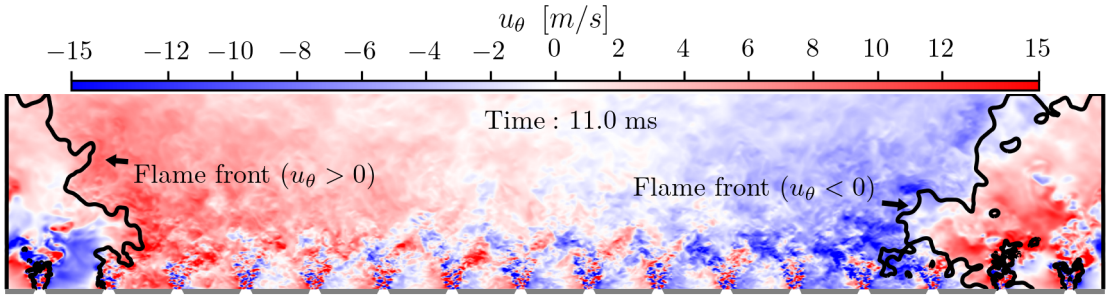

Figure 7.21: Azimuthal velocity u_θ during light-round ignition with preheated combustor walls on an unwrapped cylindrical cut-plane at $R = 0.175\,\mathrm{m}$. Dark shades correspond to high azimuthal velocities (from left to right and vice versa). Solid contour lines of iso-values of the progress variable ($c = 0.76$) indicate the instantaneous flame position.

on the central unwrapped cutplane at $R = 0.175\,\mathrm{m}$ for the baseline case of Chap. 6 with cold combustor walls (a), and the present case (b). By convention, the flame index takes values of $+1$ in the premixed combustion regime (shaded in red in Fig. 7.23) and -1 in the diffusion regime (shaded in blue). The shown time instants are arbitrarily chosen such that both flame fronts have approximately advanced by the same distance. Their relative position however is not relevant for the conclusion to be drawn here. The instantaneous position of the reaction zones are given by iso-contours of the heat release rate (HRR). These are found to be located in the premixed combustion zone *regardless* of the thermal state of the combustor walls. In the case of preheated walls, this result can certainly be expected given the strongly enhanced evaporation rates highlighted in Sec. 7.3.2 and reduced liquid volume fractions (see Fig. 7.11(c)). As far as cold combustor walls are concerned, we attribute the occurrence of premixed combustion to n-heptane's volatility.

The identification of premixed combustion zones then allows to artificially thicken the premixed reaction zone by applying a flame sensor (Legier et al., 2000). It allows the detection of the reaction zone where $\theta_F = 1$ (see Eq. 2.62), and $\theta_F = 0$ elsewhere in the domain, *i.e.* outside of the reaction zone. As we show in Fig. 7.24 for the case with cold combustor

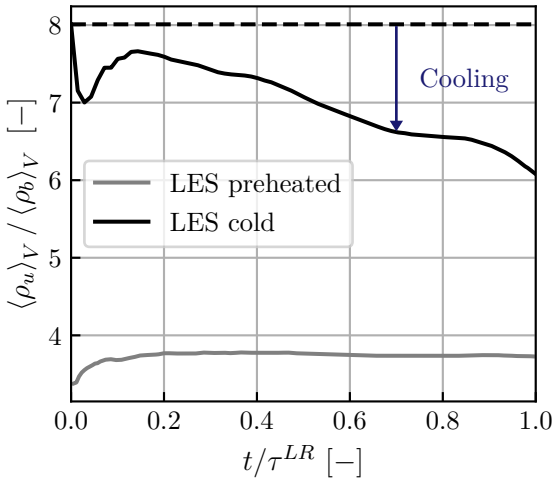

Figure 7.22: Comparison of the density ratios between fresh and burnt gases. The dashed horizontal line indicates the theoretical adiabatic density ratio of the case "LES cold". The more the *actual* density ratio of that case (solid black line) deviates from the dashed line, the stronger the burnt gas cooling effect.

walls, the white iso-contour of the progress variable $c = 0.76$ (corresponding to the peak of the fuel species source term) lies in-between the active region of the flame sensor marked by red contour lines, proving the correct functioning of the sensor. Blue contour lines are added to indicate the direction in which the sensor function θ_F decreases. With an imposed resolution of $n = 7$ grid points across the reaction zone the local amount of thickening can eventually be determined according to the equations outlined in Sec. 2.5.3. Typical values of F are comparably low closer to the chamber backplane ($F \lesssim 4$) and may be higher towards the combustor outlet ($F \approx 20$) as visualized in Fig. 7.25. We conclude from the above analysis that the use of the thickened flame model can be justified for both configurations.

7.6 Conclusions

In the present chapter we investigate flame propagation during light-round in an annular combustor with preheated walls and liquid fuel by means of Large-Eddy Simulations, mimicking a quick relight where the walls do not have time to cool down. The numerical setup follows the approach of the previous chapter, employing a Lagrangian description of the polydisperse droplet phase, dynamic combustion modeling, detailed modeling of the flow boundary layer, and additionally a correction factor for the laminar flame speed predicted by a reduced kinetic scheme. Most importantly, we seek to improve the description of the thermal state of the combustor walls by replacing adiabatic boundary conditions commonly used in previous works by more realistic temperature profiles at steady-state operation. These are obtained from Conjugate Heat Transfer simulations due to the lack of experimental data, involving coupled simulations with dedicated solvers for the fluid and solid domain alongside a coupling library. All combustor parts exposed to the internal fluid flow are coupled to the fluid domain via Dirichlet-Robin boundary conditions. The solid domain description includes multiple materials with varying properties depending on the local temperature. Heat transfer at the outside combustor walls (facing the atmosphere) simultaneously accounts for convection and radiation, based on a simplified band-averaged model of the quartz' absorptance. The internal water cooling circuit inside the injector support is approximated by an iso-thermal boundary condition

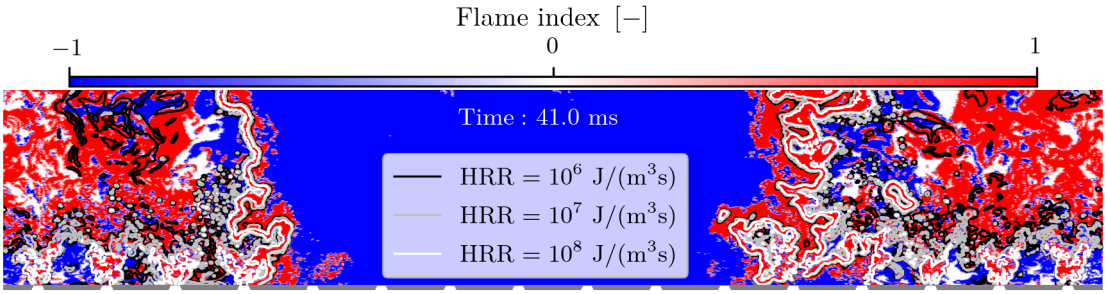

(a) Light-round ignition with cold combustor walls (see Chap. 6)

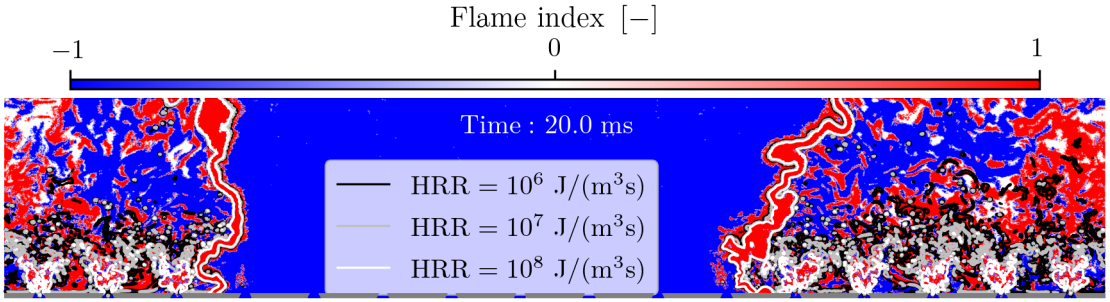

(b) Light-round ignition with preheated combustor walls

Figure 7.23: Takeno flame index (Yamashita et al., 1996) on an unwrapped cylindrical cut-plane at $R = 0.175\,\mathrm{m}$ for light-round ignition with cold (a) and preheated (b) combustor walls. Red zones indicate a premixed combustion regime, while blue zones indicate a diffusion regime. The instantaneous position of the reaction zone is given by iso-contours of the heat release rate (HRR).

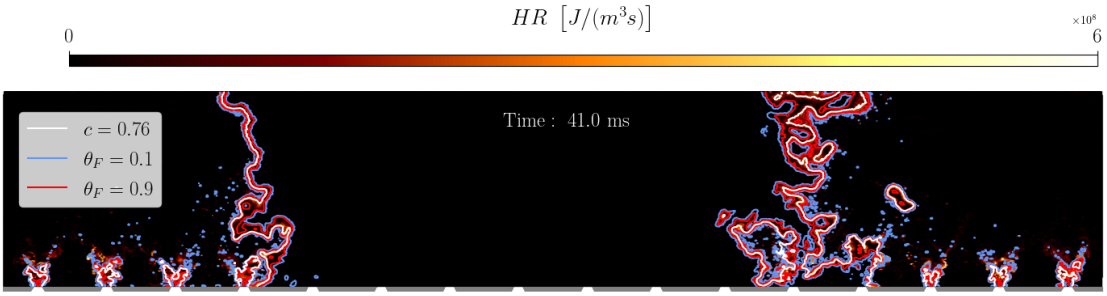

Figure 7.24: Instantaneous heat release rate on an unwrapped cylindrical cut-plane at $R = 0.175\,\mathrm{m}$. Iso-contours of the progress variable $c = 0.76$ (at peak heat release) are included as white lines which are surrounded by red contour lines marking the region where the flame sensor is active. Blue contour lines indicate the direction in which the sensor function θ_F decreases.

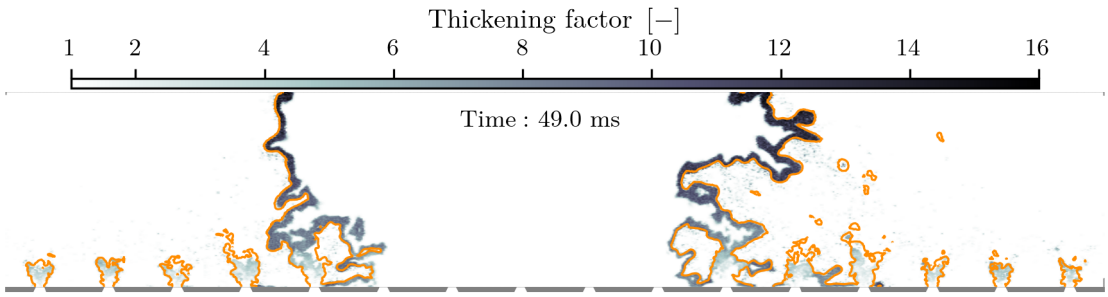

Figure 7.25: Local thickening factor F on an unwrapped cylindrical cut-plane at $R = 0.175\,\mathrm{m}$. Contour lines correspond to a progress variable value of $c = 0.76$.

at the bottom of the solid domain.

A quantitative assessment of modeling uncertainties is clearly needed and would deserve further research in that direction as well as detailed experimental measurements.

With temperature profiles obtained from CHT simulations and applied henceforth as boundary conditions, intermediate prefueling simulation are carried out to establish steady state conditions of the newly injected fresh gases. Finally, light-round simulations of the MICCA-Spray combustor with the same wall temperature profiles are performed starting from the aforementioned preheated initial conditions.

Comparing the numerical light-round duration with experimental measurements shows a remarkably good agreement, although uncertainties in the modeling approach could still be present. A detailed investigation of the liquid phase conditions upstream of the propagating flame fronts highlights the effect of preheating which greatly increases fuel evaporation rates. Consequently, the flame fronts are observed to be less sensitive to the upstream liquid volume fraction field compared to light-round with ambient temperature walls, which also translates into a smoother leading point trajectory.

The volumetric burnt gas expansion — also considered as the governing mechanism of flame propagation and expressed by the density ratio $\langle \rho_u \rangle_V \,/\, \langle \rho_b \rangle_V$ — exhibits lower values in preheated conditions than the previous case with cold walls. Yet, the azimuthal flow acceleration is still substantially higher. This observation is further analyzed in the following chapter.

The study demonstrates that regardless of the state of the wall temperature (cold or hot as considered here), attention must be paid to appropriate wall boundary conditions. In particular, the use of adiabatic wall boundary conditions to approximate light-rounds with preheated combustor walls *cannot* establish the same initial conditions, particularly when liquid fuels are involved. Predictions of light-round durations with previous adiabatic LES are most likely to be affected by hidden error cancellation as discussed in Puggelli et al. (2021), and further elaborated in Chap. 8.

Chapter 8

Low-order modeling of turbulent flame propagation during light-round

Light-round experiments and simulations have revealed a inherent sensitivity of flame propagation mechanisms to realistic thermal wall conditions. Depending on the restart scenario, combustor wall temperatures can substantially differ and enhance or diminish the effect of liquid fuels or wall heat transfer on propagating flames (among others). The most apparent consequence is a reduced light-round duration when walls are preheated. A more thorough examination of simulation results has exposed the preheating effect on fresh gases during the prefueling phase, enhancing fuel evaporation rates, but also diminishing the density ratio between fresh and burnt gases. This result is particularly intriguing, since the density ratio was previously identified as a driving mechanism for flame propagation with cold combustor walls. To better understand the impact of realistic thermal wall conditions on flame propagation, we thus propose a theoretical analysis. We derive a low-order model which is capable of making accurate predictions about average flame propagation speed, accounting for all relevant driving mechanisms. It is subsequently used to underscore the importance of detailed modeling through a priori predictions of average flame speeds with different modeling approaches. Finally, we employ the model to examine and quantify the impact of preheating on flame propagation.

Contents

8.1 Introduction

The previous two chapters provide insights into the governing mechanisms of flame propagation during light-round without quantifying their individual impact on the propagation speed yet. Moreover, the analysis of flame expansion with preheated combustor walls revealed an

intriguing result, since the azimuthal flow acceleration was found to be more pronounced compared to cold walls, despite a lower density ratio $\langle\rho_u\rangle_V / \langle\rho_b\rangle_V$. Therefore, a macroscopic flame speed model is derived here to serve two main purposes:

- with the regard to light-round simulations in general, we put forth the argument that *all* relevant phenomena previously discussed have to be taken into account in the simulation: a polydisperse description of the liquid phase, a detailed wall model accounting for variable thermophysical properties in the boundary layer, and a dynamic combustion model;
- with regard to the impact of the thermal boundary condition in particular, we demonstrate how and by which mechanism preheating affects the flame propagation speed during light-round.

First, the model is developed and benchmarked in terms of its prediction capabilities using the data obtained from the baseline case in Chap. 6 with cold walls. Second, the flame speed model is decomposed to identify the terms and variables which are affected by the main physical phenomena studied in this work. Third, *a priori* estimations for the flame propagation speed under *different* conditions are computed using the macroscopic model to underscore the fact that neither phenomenon can be neglected. Fourth, we apply the macroscopic flame speed model to the preheated light-round simulation of Chap. 7 to prove that it also captures the relevant governing mechanisms under preheated conditions. Finally, we address the reason for a faster flame propagation as observed in Chap. 7 by analyzing the changes in the model's leading terms.

We wish to clarify that we continue to use the case nomenclature we have previously introduced: the baseline case (or "BASE") still refers to the configuration with cold combustor walls ($T_w = 300\,\mathrm{K}$, see Chap. 6), the adiabatic case (or "ADIAB") refers to the configuration with adiabatic combustor walls (discussed in Chap. 6), and the preheated case refers to the configuration with imposed wall temperature profiles from precursor Conjugate Heat Transfer simulations (see Chap. 7).

8.2 Model for the absolute flame propagation speed during light-round

Deriving an expression for the turbulent absolute flame speed S_a^T (also referred to as flame propagation speed) requires several macroscopic balance equations for the burnt gas mass. The equations follow the notation already introduced in Philip (2016) and Puggelli et al. (2021). At this point, it should be clarified that the final expression for the flame speed is only valid when the flame propagation mode can be described as two separate, semi-confined flame fronts, limited by the chamber backplane, the lateral combustor walls and the combustor outlet. During this stage in the ignition process and with the approximation of the separate flame fronts as vertical planes, the rate change of the burnt gas volume V_b inside the combustion chamber is written as:

$$\frac{dV_b}{dt} = S_a^T A_0 \tag{8.1}$$

where the sectional surface area of the planes is $A_0 = 2h\Delta R$ (chamber height h and width ΔR computed as difference between outer and inner chamber radii). Next, the macroscopic balance equation of the progress variable within the combustor is given as:

$$\frac{dm_b}{dt} = \dot{m}_b^{in} - \dot{m}_b^{out} + \int_V \dot{\omega}_c dV \tag{8.2}$$

introducing the mass flow rates of burnt gases at the inlet (in case of any recirculation there) and outlet of the combustion chamber ($\dot{m}_b^{in}$ and $\dot{m}_b^{out}$), and the source term of the progress variable $\dot{\omega}_c$. The volume integral in Eq. 8.2 allows for introducing the LES flame consumption speed S_c^{Δ} through the following expression:

$$\langle \rho_u \rangle \, A_{res} S_c^{\Delta} = \int_V \dot{\omega}_c dV \tag{8.3}$$

where $\langle \rho_u \rangle$ denotes the averaged fresh gas density and A_{res} the resolved flame surface. In the context of LES, the consumption speed can be computed from the laminar flame speed S_l and the sub-grid scale flame surface wrinkling $\langle \Xi_{\Delta} \rangle_{res}$ averaged over the resolved flame surface

$$S_c^{\Delta} = \langle \Xi_{\Delta} \rangle_{res} \, S_l. \tag{8.4}$$

Eventually, the mass of burnt gases m_b can also be written as:

$$m_b = \langle \rho_b \rangle_V \, V_b \tag{8.5}$$

where $\langle \rho_b \rangle_V$ denotes the volume averaged burnt gas density. Differentiation of Eq. 8.5 with respect to time and substituting the corresponding terms with Eqs. 8.1 - 8.4 yields the final expression for the absolute turbulent flame speed:

$$S_a^T = \underbrace{\frac{\langle \rho_u \rangle_V}{\langle \rho_b \rangle_V} \Xi_{res} \langle \Xi_{\Delta} \rangle_{res} \, S_l}_{\text{Term I}} - \underbrace{\frac{\dot{m}_b^{out} - \dot{m}_b^{in}}{\langle \rho_b \rangle_V \, A_0}}_{\text{Term II}} - \underbrace{\left(\frac{V_b}{\langle \rho_b \rangle_V \, A_0} \frac{d\rho_b}{dt} \right)}_{\text{Term III}}. \tag{8.6}$$

The resolved flame surface wrinkling, $\Xi_{res} = A_{res}/A_0$, is defined as ratio between the resolved flame surface and the sectional surface area A_0 of the combustor.

For the following comparison, we first consider only the baseline and adiabatic case introduced in Chap. 6. The preheated case is addressed later in Sec. 8.3. Figure 8.1 shows the temporal evolution of S_a^T computed according to Eq. 8.6 for the baseline case (top) and case ADIAB (bottom) as thick solid lines. The masked time span at the beginning (in gray) indicates that Eq. 8.6 cannot be applied during the first instants of light-round by construction, as the initial flame has not yet developed two separately propagating flame fronts, *i.e.* during phase-I and II of light-round as defined in Sec. 6.5.1. Averaging S_a^T over the valid time span up to flame front merging yields $8.81\,\mathrm{m/s}$ for the baseline case and $10.03\,\mathrm{m/s}$ for the adiabatic case.

A meaningful reference velocity may be computed from one sector arc length (*i.e.* $s = 2\pi R/16$) and the averaged time between two consecutive sector heat release peaks (obtained from Fig. 6.4) in order to assess the accuracy of the modeled flame propagation speed S_a^T. These propagation speeds are subscripted with "HR" in the following. For the baseline case, a velocity of $\mathcal{S}_{a,\mathrm{HR}}^T = 7.6\,\mathrm{m/s}$ is obtained. This reference velocity is plotted as horizontal gray dashed line in Fig. 8.1 (for the flame branch in H-, see Fig. 3.2(c)) and is fairly well retrieved by the modeled velocity suggesting that the major physical phenomena involved in flame propagation during light-round are accurately captured by Eq. 8.6. The same holds true for case ADIAB, which yields $\mathcal{S}_{a,\mathrm{HR}}^T = 9.98\,\mathrm{m/s}$.

Equation 8.6 may be split into its three main parts (indicated by curly braces) to identify the leading terms. Such decomposition is an arbitrary choice to structure and simplify the following analysis. It is recalled that Term I resembles the classical expression for a turbulent spherically propagating flame or a developing flame in a closed duct, Term II arises due to the fact that the control volume (*i.e.* the combustion chamber) is semi-confined and Term III appears as a

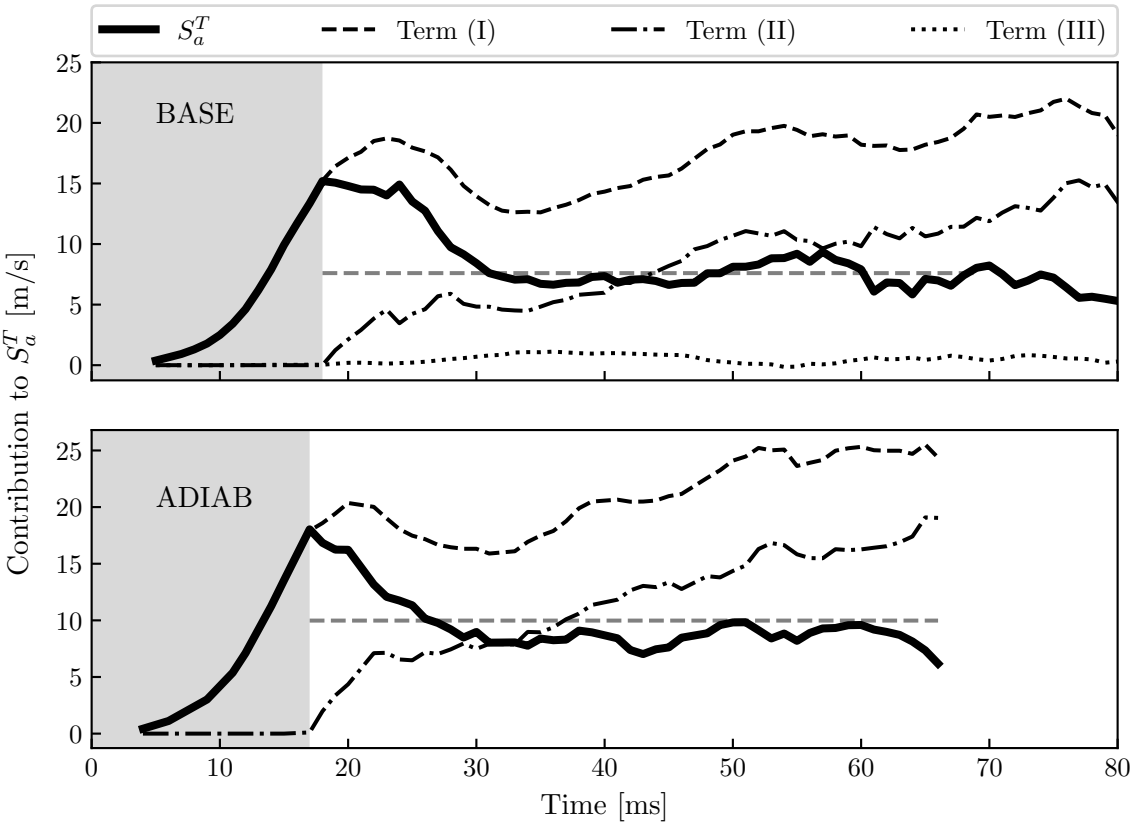

Figure 8.1: Decomposition of Eq. 8.6 into three main terms (thin lines) plotted as absolute values for both cases. The absolute turbulent flame speed S_a^T (thick line) is added for reference. The horizontal dashed grey lines correspond to the average velocity obtained from the sector arc length and the averaged elapsed time between two adjacent sector heat release peaks of the respective case (see Fig. 6.4 for the baseline case).

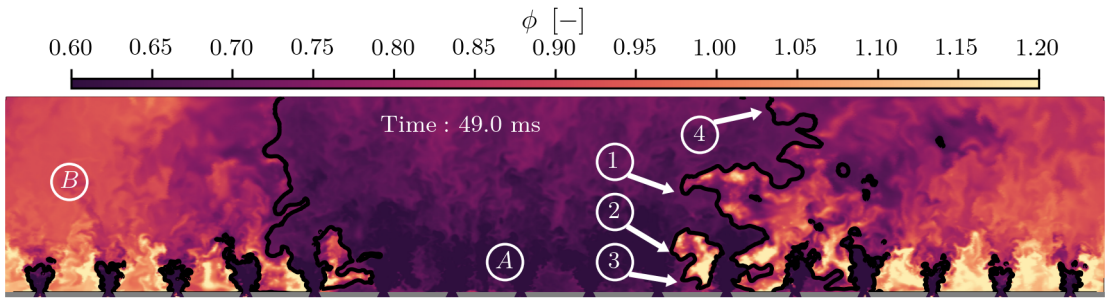

Figure 8.2: Gaseous equivalence ratio ϕ on an unwrapped cylindrical cut-plane at $R = 0.175\,\mathrm{m}$. The one-dimensional consumption speed S_c^{1D} is computed for Fig. 2.2 at the four labeled positions at the flame front. Contour lines correspond to iso-values of the progress variable of $c = 0.76$.

consequence of temporal density variations. Each of these terms is plotted in absolute values in Fig. 8.1 (black dashed lines) and reveals an interesting result. Essentially, Eq. 8.6 is governed by Terms I and II, while the effect of temporal density variations (Term III) appears to be almost negligible. The evolution of Term II is directly linked to $\dot{m}_b^{out}$: it is zero until the initial flame arch has reached the chamber outlet. At that point, the outflux of burnt gases starts to increase (as does Term II) with the propagation of the flame fronts. Furthermore, comparing the baseline case to ADIAB shows that in the absence of wall heat losses Terms I and II are shifted to higher velocities. This suggests that the main physical phenomena described in Secs. 6.5.3 - 6.5.6 are interdependent, *i.e.* react and adapt to deliberately introduced changes in the operating or boundary conditions, as is the case with deactivating wall heat transfers in Large-Eddy Simulations. These phenomena are therefore studied in detail in the following section.

8.2.1 Model decomposition

Apart from splitting Eq. 8.6 into its main terms, more insights into the main mechanisms of flame propagation can be gained when examining the governing physical phenomena individually and establishing links to the relevant variables in the model equation.

8.2.1.1 Laminar burning velocity and two-phase flow

The effects of the liquid phase on the absolute turbulent flame speed S_a^T enter through the laminar flame speed S_l appearing in Term I of Eq. 8.6 and are twofold. First, the equivalence ratio field ϕ is strongly heterogeneous due to complex interactions of droplets with the flow and different amounts of liquid and pre-vaporized fuel along the propagating flame fronts. For example, ϕ ranges from roughly $\phi = 0.7$ in the fresh gases (labeled as A in Fig. 8.2) up to $\phi = 0.95$ in the burnt gases in the upper half of the combustion chamber where all droplets are fully evaporated (labeled as B). In rich recirculation zones between adjacent burners, ϕ is larger than unity as a consequence of droplet accumulations. The mixture inhomogeneity then presumably prevents the identification of S_l with the theoretical laminar flame speed $S_l^0(\phi_{glob})$ determined trivially from the global equivalence ratio, at which the combustor is operated (*i.e.* computed from the global air and fuel mass flow rates).

Second, the gaseous equivalence ratio ϕ can also be seen to increase across the flame fronts in Fig. 8.2, underscoring the intrinsic two-phase flow structure of the flame front within which droplets are evaporating. This two-phase structure of the flame surely impacts the resulting

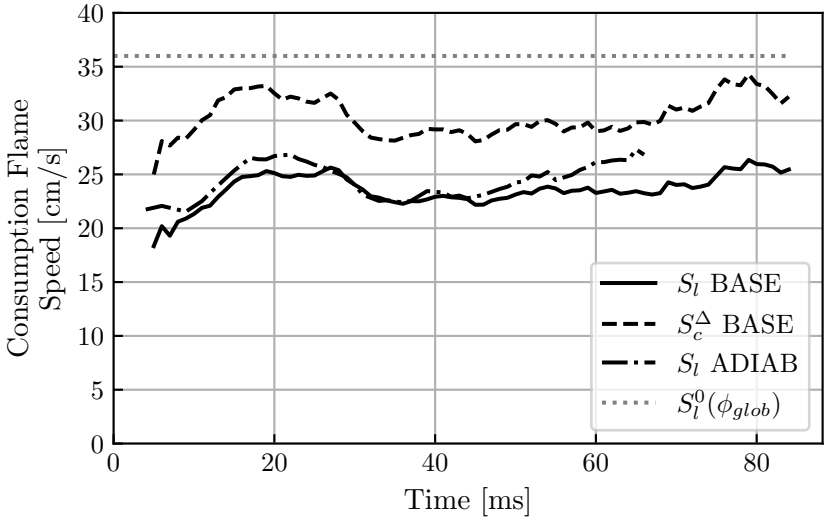

Figure 8.3: Flame consumption speeds (S_l) averaged over the total flame front surface for case BASE (solid line) and ADIAB (dash-dotted line). The dotted grey line corresponds to the theoretical laminar flame speed at global equivalence ratio $S_l^0(\phi_{glob})$. The consumption speed averaged over the resolved flame surface (S_c^Δ) is given as dashed line for case BASE.

laminar flame speed S_l.

Therefore, it is more appropriate from a global viewpoint to consider an averaged laminar flame speed over the total flame surface $A_{tot} = \langle \Xi_\Delta \rangle_{res} A_{res}$, computed as:

$$S_l = \frac{1}{\rho_u A_{tot} Y_c^{eq}} \int_V \widetilde{\dot{\omega}}_{Y_c} dV \tag{8.7}$$

where the integral is performed over the combustor volume V and normalized by the equilibrium value of the progress variable species Y_c^{eq}. The resolved flame surface A_{res} is given as $A_{res} = \int_V |\nabla \tilde{c}| dV$ (Veynante and Vervisch, 2002) which is also integrated over the combustor volume V, thus including the propagating flame fronts as well as the attached flames.

Plotting S_l according to Eq. 8.7 (or even according to Eq. 8.4 for S_c^Δ) yields $S_l \approx 24\,\mathrm{cm/s}$ (or $S_c^\Delta \approx 30\,\mathrm{cm/s}$), while the theoretical flame speed at global equivalence ratio is $S_l^0(\phi_{glob}) = 36\,\mathrm{cm/s}$ (see Fig. 8.3). It also reveals similar laminar flame speeds of case BASE and ADIAB. This confirms that the changed wall boundary condition preserves the (upstream) equivalence ratio as intended upon which S_l primarily depends.

Figure 8.3 shows that the actual laminar flame speed is, on average, much lower than $S_l^0(\phi_{glob})$. This is attributed to the leaner conditions encountered by the flame during its propagation and to its two-phase flow nature. Indeed, it has already been established in the literature (Ballal and Lefebvre, 1981; Neophytou and Mastorakos, 2009; Rochette et al., 2019) that the laminar flame speed of two-phase flames obeys the relation $S_l \leq S_l^0$ in overall lean mixtures. This implies that the effective (or averaged) equivalence ratio which corresponds to the averaged laminar flame speed plotted above must be smaller than the global equivalence ratio as well.

To provide further evidence for this argument, an average equivalence ratio of $\phi_{S_l=24\,\mathrm{cm/s}} = 0.70$ can be obtained from the flame speed diagram in Fig. 8.4 (gray arrows) assuming an average flame speed of $S_l = 24\,\mathrm{cm/s}$. This average equivalence ratio can then be compared to the probability density function of ϕ, PDF(ϕ), on a characteristic iso-surface of the progress

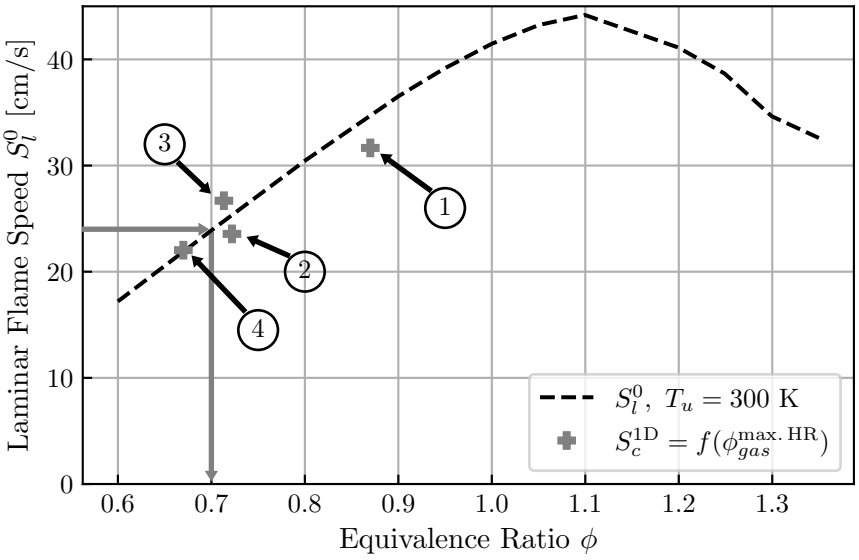

Figure 8.4: Laminar flame speed diagram for a gaseous n-heptane/air flame at varying equivalence ratios for $T_u = 300\,\mathrm{K}$ in fresh gases. The dashed line denotes reference data published in Paulhiac et al. (2020). Crosses refer to the one-dimensional laminar consumption speed S_c^{Δ} according to Eq. 8.8, which is computed for arbitrary locations along the flame front indicated in Fig. 8.2.

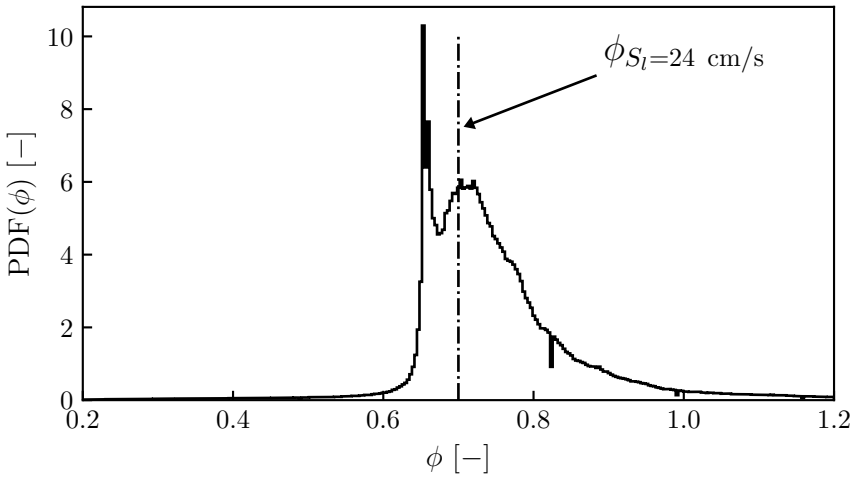

Figure 8.5: Probability density function of the gaseous equivalence ratio ϕ on a characteristic iso-surface of the progress variable $c = 0.76$.

variable $c = 0.76$, shown in Fig. 8.5. The distribution of the gaseous equivalence ratio on this iso-surface ranges from $\phi = 0.65$ to around $\phi = 1.2$ with a broader peak at $\phi = 0.7$ and matches the average equivalence ratio predicted by the flame speed diagram fairly well. As far as averaged quantities are concerned, the average (or effective) equivalence ratio for lean two-phase flames is proven to be lower than the overall equivalence ratio, leading to a lower laminar flame speed.

This does certainly not preclude the existence of *local* variations of the flame speed along the propagating flame fronts. In fact, it can be shown that the local laminar flame speed of a two-phase flame relates to an effective equivalence ratio at peak heat release rate (Neophytou and Mastorakos, 2009). These values scatter around the average laminar flame speed of $S_l = 24\,\mathrm{cm/s}$ in the present case. Assuming that each flame front element behaves like a one-dimensional flame, and that the consumption speed $S_c^{1\mathrm{D}}$ of such flame is equivalent to its laminar flame speed (after *unscaling* by the efficiency function), allows to apply Eq. 8.8 in direction of the three-dimensional flame front normal for arbitrary positions along the propagating flame fronts.

$$S_c^{1\mathrm{D}} = \frac{1}{\rho_u Y_c^{eq}} \int \dot{\omega}_{Y_c} dc \tag{8.8}$$

These positions correspond to the labels 1 - 4 in Fig. 8.2 and are plotted in Fig. 8.4 accordingly.

Given the assumptions made for the computation of such local flame speeds, all data points align remarkably well with reference S_l^0 values, although the local total equivalence ratio (gaseous and liquid) can be quite different from the local gaseous condition. Furthermore, the laminar flame speed tends to increase with increasing height above the chamber backplane, since droplets are more likely to fully evaporate the farther they penetrate the combustion chamber (data points 1 to 3). Although closest to the chamber outlet, data point 4 exhibits the lowest equivalence ratio due to dilution effects resulting from entrained air of the surrounding atmosphere. Regardless of the position on the flame front, all laminar flame speeds are found to be inferior to the theoretical laminar flame speed at global equivalence ratio (Neophytou and Mastorakos, 2009). Compared to a light-round case with a fully premixed gaseous mixture, liquid fuel affects the laminar flame speed as well as the resulting absolute turbulent flame speed through Eq. 8.6.

We emphasize that this observation holds true despite the two-step reaction mechanism's insensitivity to strain effects. On one hand, values for S_l are very close to the corresponding laminar unstrained flame speed for a given equivalence ratio as a consequence of the reduced mechanism with a unitary Lewis number. On the other hand, the flame fronts are found to be exposed to moderate strain rate values with alternating sign and a mean value close to zero, independently from the reaction mechanism (see Fig. 8.6(a)). Figure 8.7(a) (solid gray line) confirms that the strain rate a sampled on an iso-surface of $c = 0.76$ without contributions from the ignited burners exhibits a bell-shaped form centered at $a \approx 0\,\mathrm{s}^{-1}$. Sampling the strain rate over the entire flame surface (dashed line in Fig. 8.7(a)) necessarily results in a wider PDF as the contributions from the attached flames are also taken into account. Thus, averaging S_l over A_{res} results in flame speeds which are also close to the laminar unstrained flame speed, since local and unsteady strain effects vanish in the averaging procedure. This is classically assumed in flame surface density models such as the coherent flame model. We clarify that this argument is valid due to the detailed mechanism's response to strain that is fairly linear (see Fig. 2.3) in the range of resolved strain rates shown in Fig. 8.7(a). As for the reduced scheme used here, the corresponding average S_l is consequently even more bound to S_l^0, given its insensitivity to a. Under those conditions, a two-step reaction mechanism can be an acceptable choice, despite its limitations in predicting strained flame speeds. Detailed reaction mechanisms however can improve the predictions of Eq. 8.8. Note that the above

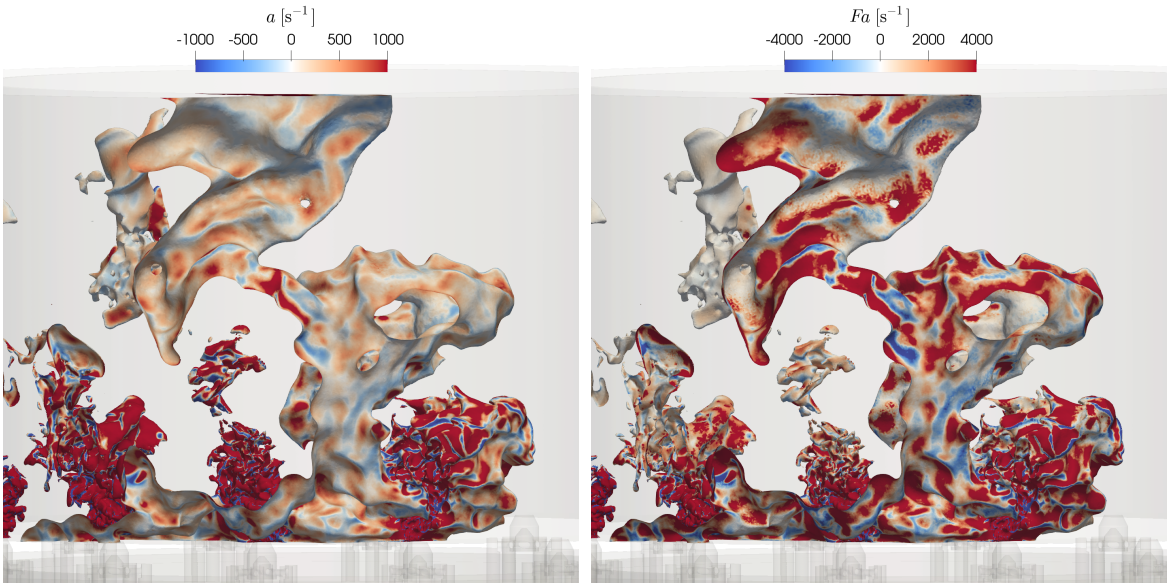

(a) (b)

Figure 8.6: Tangential strain rate (a) and effective tangential strain rate (b) on an iso-surface of the progress variable $c = 0.76$ at $t = 49\,\mathrm{ms}$.

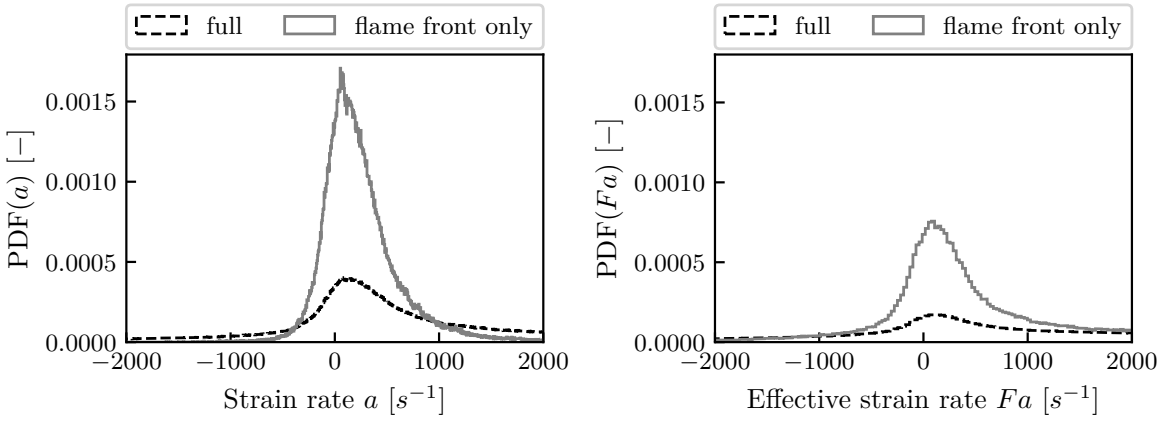

(a) (b)

Figure 8.7: Strain rate distribution (a) and effective strain rate distribution (b) of the full propagating flame fronts (black dashed curves, corresponding to the visualizations in Fig. 8.6 at $t = 49\,\mathrm{ms}$), and flame fronts without contributions from ignited burners (solid gray curves).

justification is valid for all wall boundary conditions (cold or adiabatic), since the flame's response to strain is governed by the Lewis number of the reaction mechanism.

Regarding the effect of thickening factors studied in *e.g.*, Popp et al. (2019) on laminar strained flames, also with a unitary Lewis number, we first wish to outline that the strain rate can only affect thin or thickened flames in this case ($\mathrm{Le} = 1$) when the time scale associated with the (effective) strain rate is getting closer the chemical time scale, eventually leading to flame quenching. This is a Damköhler effect, which is very different from the first one discussed above related to Lewis number effects. Popp et al. (2019) have then studied the effect of a modified Damköhler number of the thickened flame model in laminar flames. This impact on the Damköhler number is acknowledged at the very foundation of the model (Colin et al., 2000) and treated by introducing an efficiency function to correct the improper interaction with turbulence.

In our modeling approach, no particular treatment is considered to account for interactions between strain effects and the thickened flame model. Subgrid turbulence-flame interactions are handled by the wrinkling factor model. The question is then to know whether this reduced Damköhler effect affects our results or not. Figure 8.7(b) presents the distribution of the *effective* strain rate Fa (Popp et al., 2019). Most of the values are found in the range where the reduced scheme is insensitive to strain effects. The predicted local flame speed (although affected by the unity-Lewis number assumption) is then most likely not to be modified by the resolved strain in the present case. This could have turned out very differently with a non-unity Lewis number model that responds to small strain rates. Such a case was, however, not considered in the work of Popp et al. (2019) and would deserve a dedicated study.

Finally, even in the case of moderate effects resulting from the effective strain rate Fa, the average S_l on the total flame surface is not expected to be significantly affected by the flame's local and instantaneous exposure to strain given the present magnitude.

8.2.1.2 Burnt gas density and heat losses

As foreshadowed in Sec. 6.5.5, wall heat losses act on the burnt gas density $\langle \rho_b \rangle_V$, which appears in all terms of Eq. 8.6. In particular, the burnt gas expansion is affected as it scales with the density ratio $\langle \rho_u \rangle_V \,/\, \langle \rho_b \rangle_V$ (see also Fig. 6.12). Including wall heat losses translates into a lower density ratio, which in turn yields a lower flame propagation speed and also a lower azimuthal flow acceleration. This can be examined in Fig. 8.8 showing the outflux of *fresh* gases $\dot{m}_u^{out}$ at the combustor outlet as a consequence of the burnt gas expansion. The time coordinate is rescaled such that the flame front merging is attained at $t/\tau^{\mathrm{merging}} = 1$, where $\tau^{merging}$ corresponds to the diamond markers in Fig. 6.10. Two key differences can be observed between both cases: first, the initial peak value of fresh gas outflux is larger in the adiabatic case than in the baseline case. Second, and more importantly, the adiabatic case can also sustain a higher level of fresh gas outflux almost throughout the entire light-round duration. Thus, the higher the density ratio, the higher the fresh gas mass flow rate and the azimuthal flow acceleration. Recalling that the flame propagates approximately at the speed of the accelerated flow (Lancien et al., 2017), it can be inferred from the plot that flame propagation is generally faster when burnt gases are not subjected to wall heat losses.

Remarkably, S_a^T does not increase by the same amount as does the density ratio in Fig. 6.12 for example when passing from the baseline setup to an adiabatic setup. This behavior is attributed to the fact that the flame propagation speed is certainly not decoupled from Term II containing not only the burnt gas density $\langle \rho_b \rangle_V$, but also the *burnt* gas mass flow rate at the combustor outlet $\dot{m}_b^{out}$. When the flow acceleration through burnt gas expansion is more pronounced (*i.e.* when all walls are adiabatic), the outflux of burnt gases increases, which

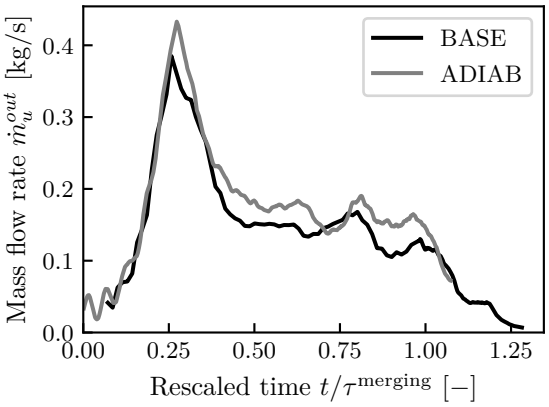

Figure 8.8: Mass flow rates of fresh gases $\dot{m}_u^{out}$ leaving the combustion chamber upstream of the propagating flame fronts. The time coordinate is rescaled by the respective flame front merging time τ^{merging} for each case.

counterbalances the increase of Term I through an increased Term II as already seen in Fig. 8.1 (comparing dash-dotted lines for both cases). Therefore, the change of the density ratio does not control the resulting flame propagation speed *alone*.

Beyond the density ratio and outflux of burnt gases, other phenomena have to be considered as well. While the laminar flame speed S_l is essentially the same for both cases (see Fig. 8.3), as it is controlled primarily by the liquid phase, turbulence levels may be enhanced by a higher azimuthal velocity and increase the flame surface wrinkling. Consequently, all effects on the flame propagation speed have to be taken into account at the same time, since changes in one phenomenon are prone to affecting another. To corroborate this argument, flame/turbulence interactions are covered in the next section, following a dedicated study on that subject published in Puggelli et al. (2021).

8.2.1.3 Flame/Turbulence interactions

The resolved flame surface wrinkling $\Xi_{res} = A_{res}/A_0$ can be examined in Fig. 8.9 (solid and dashed lines) to prove the interaction between the volumetric burnt gas expansion and turbulence. The grayed area masks the first phase of light-round, where Eq. 8.6 cannot be applied.

For both cases, the evolution of the resolved flame surface wrinkling Ξ_{res} is similar, but case ADIAB exhibits higher values almost throughout the entire light-round. Up to the first peak, Ξ_{res} is on average 25% larger in the adiabatic case at a given instant, and still 15% larger between $t = 30\,\text{ms}$ and $t = 45\,\text{ms}$ compared to the baseline case. This contributes entirely to a larger Term I in the model expression for S_a^T and thus to the higher absolute turbulent flame speed observed in the absence of wall heat losses.

Unlike the resolved flame surface wrinkling, the sub-grid scale flame surface wrinkling $\langle \Xi_\Delta \rangle_{res}$ averaged over the resolved flame surface is virtually the same for both cases (dash-dotted and dotted lines), and similar to the one examined in (Puggelli et al., 2021). Due to identical computational meshes for both cases, identical values for the laminar flame thickness ($\delta_l \propto \phi$), and ϕ unchanged, very similar values can be observed for $\langle \Xi_\Delta \rangle_{res}$ (see Eq. 2.48) as well. In spite of a moderately higher flow acceleration during burnt gas expansion in the adiabatic case, a potentially higher turbulence intensity does not affect the sub-grid scale flame surface wrinkling in its *saturated* formulation. Therefore, with a similar flame surface wrinkling

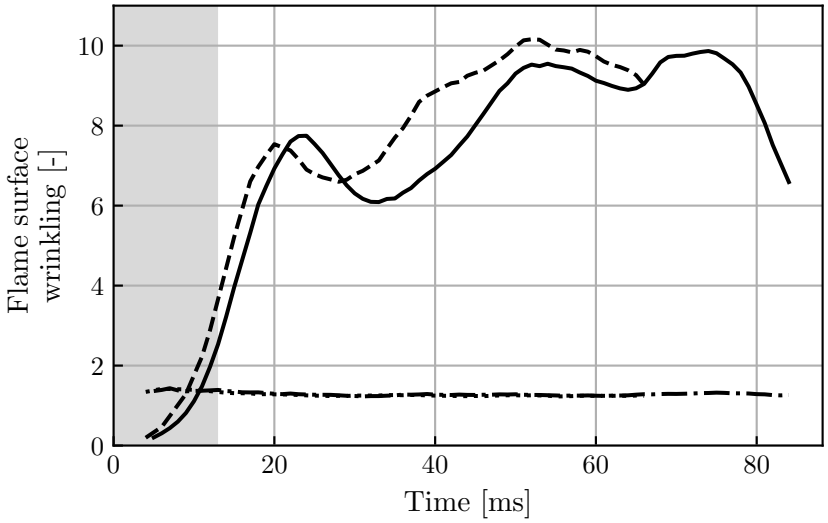

Figure 8.9: Resolved flame surface wrinkling Ξ_{res} for case BASE (solid line) and ADIAB (dashed line). The sub-grid scale flame surface wrinkling $\langle \Xi_\Delta \rangle_{res}$ averaged over the resolved surface is virtually the same for both cases (dash-dotted and dotted lines).

parameter β averaged over the resolved flame surface plotted in Fig. 8.10, a similar evolution of $\langle \Xi_\Delta \rangle_{res}$ can be expected.

8.2.2 Model sensitivities

With the insights of the previous model decomposition, the third goal listed in Sec. 8.1 can now be addressed. Changes are introduced separately to the model expression for S_a^T in Eq. 8.6 in the following way for otherwise unchanged variables:

- instead of a dynamic evaluation of the wrinkling parameter β, a constant value of $\beta \equiv 0.5$ is assumed and S_a^T is recomputed accordingly from the model expression showcasing a different modeling approach of flame/turbulence interactions;
- a constant laminar flame speed at the global equivalence ratio $S_l = S_l^0(\phi_{glob})$ is imposed instead of a flame surface averaged value addressing flame/droplet interactions and the role of the liquid phase in general;
- S_a^T is computed by setting Term III (temporal density variations) to zero to emulate a quasi-steady state;
- instead of variable values for the density ratio $\langle \rho_u \rangle_V \,/\, \langle \rho_b \rangle_V$, the corresponding values under nominal conditions are used to recompute the flame propagation speed targeting changes in the modeling of wall heat transfers.

While the analysis has outlined the relation between the different mechanisms, each of these changes is deliberately chosen to aim at one physical phenomenon at a time in order to estimate a new value for S_a^T from an *a priori* approach. Compared to the (unaltered) baseline simulation case, these new values for the flame propagation speed can then give an indication about the relative importance of each phenomenon. Such an *a priori* sensitivity study allows to establish a common methodology to compare the underlying mechanisms. Complementary studies with

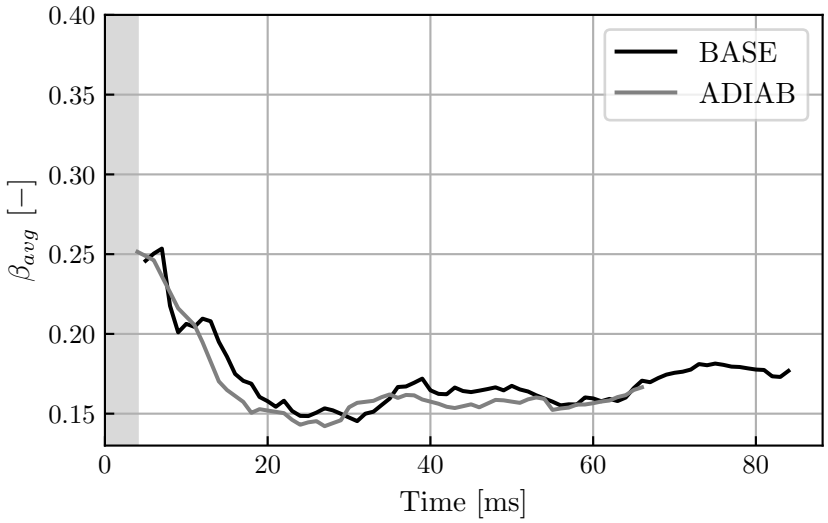

Figure 8.10: Temporal evolution of the flame surface wrinkling parameter β_{avg} averaged over the resolved flame surface for the baseline case (black line) and the adiabatic case (gray line). The initial period during the laminar flame kernel development are masked in gray as the dynamic evaluation of the flame surface wrinkling parameter cannot be applied.

a posteriori computations are further referenced, where available, to assess the bias of the *a priori* estimations.

The resulting flame propagation speed for all four cases listed above is plotted in Fig. 8.11 as grey lines. The baseline case is added for reference (solid black line). Starting with a constant β formulation, it shows the most substantial impact on S_a^T. With an approximately 50% higher flame surface averaged sub-grid scale wrinkling factor $\langle \Xi_\Delta \rangle_{res}$, the resulting flame propagation speed is around two times higher than in the baseline case. Compared to a 20% increase of the flame propagation speed as published in Puggelli et al. (2021) (*a posteriori*), this modification of Eq. 8.6 certainly overestimates the flame propagation speed, since the higher flow acceleration generated by a constant flame surface wrinkling parameter is not counterbalanced by an increased outflux of burnt gases in Term II. We have intentionally left $\Xi_{res} = A_{res}/A_0$ unmodified, even though a deliberate increase in β (from $\beta \approx 0.18$ to $\beta \equiv 0.5$, see *e.g.,* Sec. 6.5.6) would lead to a decreased resolved flame surface.

Next, imposing a constant flame speed $S_l = S_l^0(\phi_{glob})$ results still in an averaged 82% increase of the flame propagation speed. Such high values clearly neglect the effect on Term II, in addition to flame/droplet interactions (*e.g.,* droplet accumulations, lower gaseous equivalence ratio, see Sec. 6.5.4), which decelerate the propagating flame fronts. Similar to the previous case, we do not account for a decrease in Ξ_{res} as a result of an increased laminar flame speed S_l.

As expected with deactivating Term III, S_a^T increases marginally (6% on average), since temporal density variations are shown to be comparably small (see Sec. 8.2). It should be emphasized that neglecting the last term of Eq. 8.6 is not equivalent to case ADIAB, because Terms I and II are intentionally left unchanged for the sake of this *a priori* estimation.

Finally, recomputing the absolute turbulent flame propagation speed based on the nominal density ratio yields a 19% higher flame propagation speed. Interestingly, the predicted *a priori* value ($S^T_{a,\,a\,priori} = 10.44\,\mathrm{m/s}$) matches the averaged *a posteriori* value (given in Sec. 8.2) obtained from case ADIAB quite well.

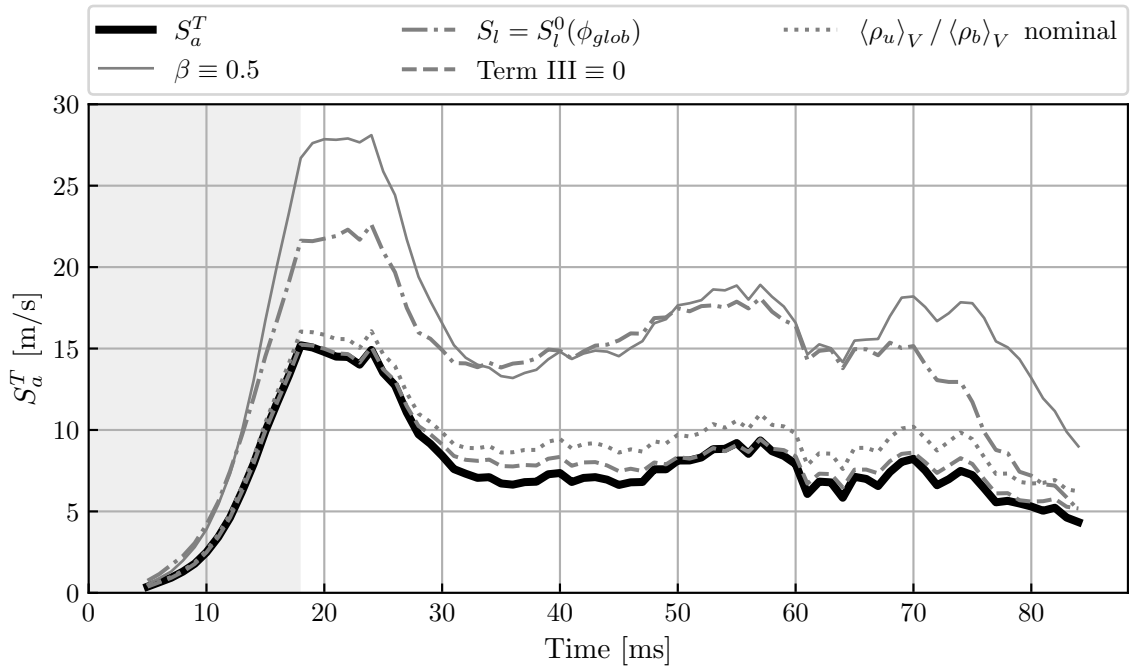

Figure 8.11: Impact of modeling choices: thick solid black line: S_a^T of baseline case; solid grey line: S_a^T for $\beta \equiv 0.5$; dash-dotted grey line: S_a^T for $S_l = S_l^0(\phi_{glob})$; dashed grey line: S_a^T with Term III set to zero; dotted grey line: S_a^T for nominal density ratio.

The main conclusion that can be drawn from these *a priori* estimations is the fact that all major governing mechanisms of flame propagation tend to substantially impact the resulting absolute turbulent flame speed. It also supports the argument that each of the underlying physical phenomena requires careful consideration in terms of the employed model approach in LES, since any unsubstantiated simplifications may yield incorrect values for S_a^T or cause hidden error cancellation at worst. Moreover, it justifies the modeling choices made for the baseline case in this work, which addresses all relevant phenomena at once, following the recommendations of previous studies. However, the *a priori* study has revealed a certain bias in terms of the predicted values, which has to be taken into consideration when estimating the impact of any phenomenon solely from an *a priori* perspective.

8.3 Analysis of the impact of the thermal boundary condition

Finally, we wish to address the question how the driving mechanisms of flame propagation are affected by the thermal boundary condition, specifically preheated versus cold combustor walls. We have noted that the density ratio between fresh and burnt gases associated with the flame expansion — a key driving mechanism of light-round — is substantially diminished by preheating. Yet, shorter light-round durations were observed compared to cold combustor walls, suggesting that other factors may have gained more importance over the density ratio. This hypothesis is the subject of the following discussion, which is backed by the analysis of the macroscopic flame speed model previously introduced.

The evolution of S_a^T according to Eq. 8.6 is plotted in Fig. 8.12 as thick black line for

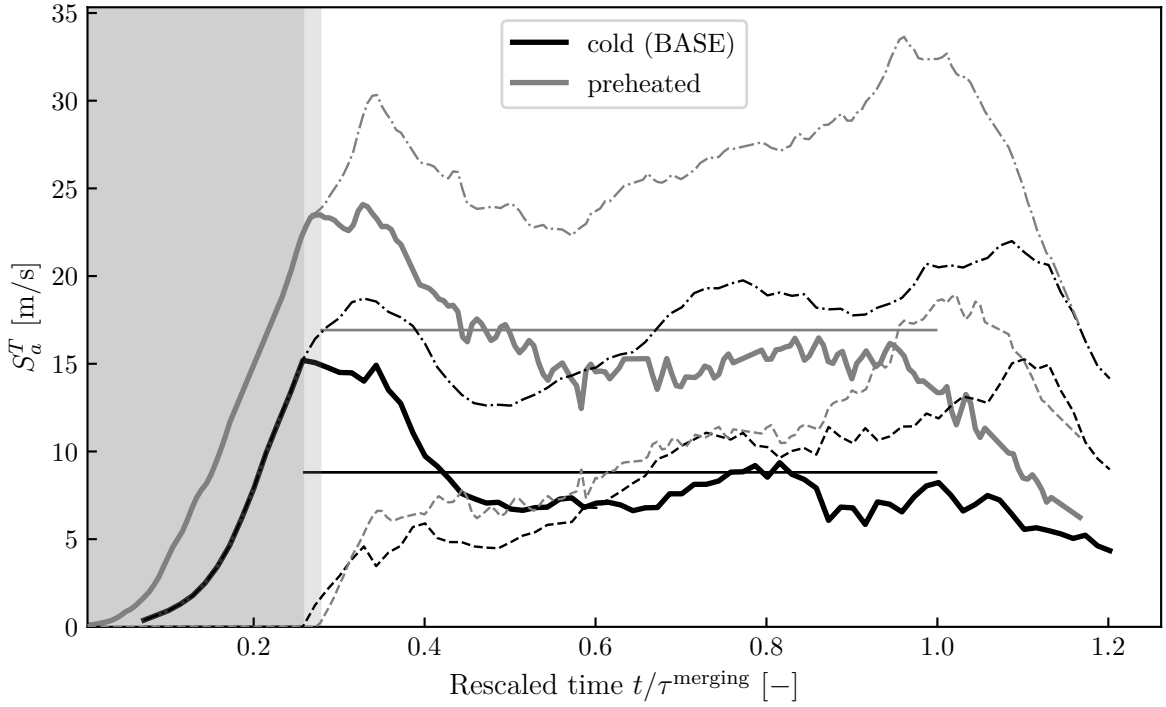

Figure 8.12: Absolute turbulent flame speed S_a^T (thick lines) for ambient temperature walls (black, baseline case of Chap. 6) and preheated walls (grey). Dash-dotted lines: Term I in Eq. 8.6. Dotted lines: Term II. Each term takes the line color of the corresponding S_a^T curve.

flame propagation with ambient temperature walls (baseline case of Chap. 6), and as thick gray line for preheated combustor walls. The initial instants are masked where Eq. 8.6 cannot be applied, (*i.e.* during phase-I and II of light-round ignition), since the initial flame has not yet developed two separate flame fronts (see Sec. 6.5.1). A non-dimensional time t/τ^{merging} is introduced to rescale each case by the respective time at which flame front merging is observed.

In agreement with experimental and numerical results (see also Fig. 7.17), the macroscopic flame speed model yields a two-times higher flame propagation speed during light-round with preheated compared to cold combustor walls, confirming a two times shorter light-round duration in the former case. This difference in flame speeds is most prominently apparent when comparing either the thick solid lines of S_a^T in Fig. 8.12 in black and gray, or the respective thin horizontal lines. The latter correspond to average flame propagation velocities evaluated from the sector arc length and the averaged time between consecutive sector heat release peaks as defined in Sec. 8.2. One finds $S_{a,\text{HR}}^T = 16.9\,\text{m/s}$ under preheated conditions (gray horizontal line), compared to $S_{a,\text{HR}}^T = 7.6\,\text{m/s}$ (black horizontal line) under cold wall conditions as mentioned earlier. The obtained average value for the preheated case approximates the *actual* evolution of the corresponding absolute turbulent flame propagation speed with good accuracy.

A closer examination of each term (broken line styles in Fig. 8.12) reveals a substantially increased Term I induced by preheating (compare gray and black dash-dotted lines), whereas the effect on Term II is more moderate (compare dashed lines). As already mentioned, *other* factors must necessarily compensate for the decrease of $\langle\rho_u\rangle_V \,/\, \langle\rho_b\rangle_V$ under preheated conditions to still yield an overall larger Term I. It appears from Fig. 8.13 that the effect of preheating causes a considerable decrease of the resolved wrinkling factor Ξ_{res} of almost 40%

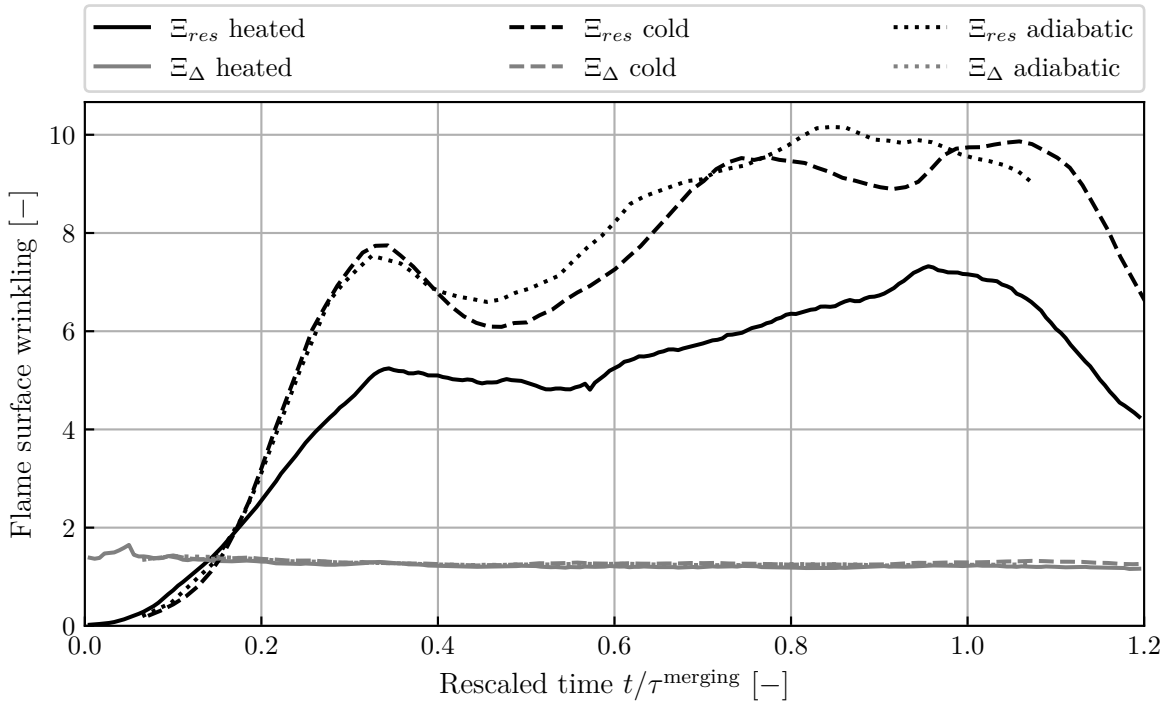

Figure 8.13: Resolved flame surface wrinkling $\Xi_{res} = A_{res}/A_0$ for heated, cold and adiabatic light-round simulations as function of the normalized time $t/\tau^{\mathrm{merging}}$. In addition, the sub-grid scale flame surface wrinkling Ξ_{Δ} is given for each case.

which results from an increase of the laminar flame speed value S_l. At this point, we also reiterate that preheating has virtually no effect on the sub-grid scale wrinkling factors (compare gray lines in Fig. 8.13).

This leaves the examination of the laminar flame speed S_l in Fig. 8.14 which indeed shows more than four times higher values in the preheated case ($S_l \approx 1.1\,\mathrm{m/s}$) compared to only $S_l \approx 0.24\,\mathrm{m/s}$ reached with cold combustor walls. Its evolution is computed from the expression in Eq. 8.7 where the total flame surface follows from $A_{tot} = \int_V \Xi_{\Delta} \left|\nabla \tilde{c}\right| \, dV$ and $\tilde{c}$ denotes the progress variable based on the mass fractions of CO_2 and CO.

Furthermore, the link between the laminar flame speed (solid line) and the average fresh gas temperature (dashed line) is visually striking, as the temporal evolution of T_u is followed by S_l. During the initial flame expansion ($t/\tau^{\mathrm{merging}} \lesssim 0.2$), fresh gases inside the combustion chamber are essentially at thermal equilibrium due to a sufficiently long exposure to preheated combustor walls throughout the prefueling stage. Hence, the fresh gas temperature remains constant. The farther the flame fronts advance, however, the more upstream preheated fresh gases are expelled towards the surrounding atmosphere as a consequence of the flow acceleration observed in Fig. 7.21. Newly injected fresh gases have therefore a shorter time period to heat up, precisely: $t < \tau^{LR}$. Since the light-round duration τ^{LR} (or even the flame front merging time τ^{merging}) is much smaller than the characteristic time to reach thermal equilibrium, $t = 300\,\mathrm{ms}$ (see Sec. 7.3.2), new fresh gases can no longer reach thermal equilibrium inside the combustion chamber. Hence the observed decrease in fresh gas temperature. The evolution of the fresh gas density ρ_u (dash-dotted line in Fig. 8.14) is also coupled to the evolution of T_u, although its increase is much less pronounced given the range of temperature variations. Most importantly however, the equivalence ratio (dotted line in Fig. 8.14) is strictly constant up to flame front merging due to enhanced evaporation rates through preheating.

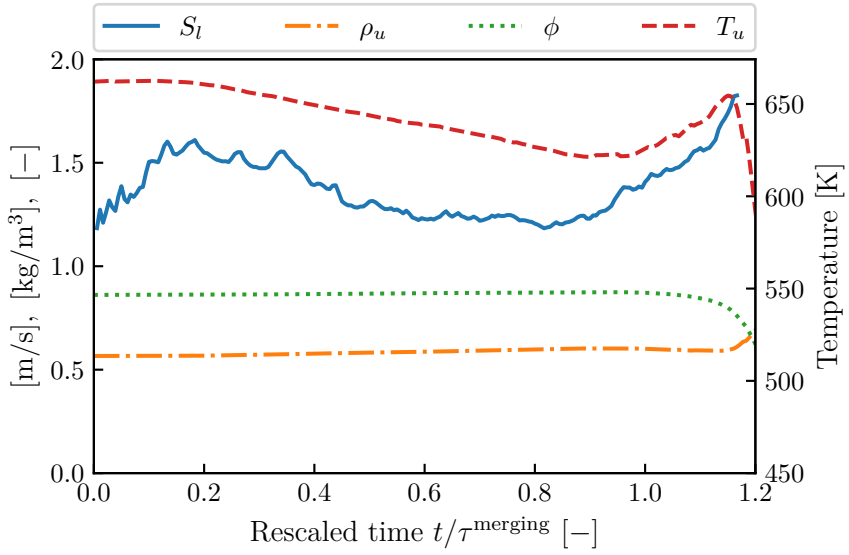

Figure 8.14: Laminar flame speed (S_l) averaged over the total flame front surface, volume averaged fresh gas density (ρ_u) and equivalence ratio associated to the left axis. Volume average fresh gas temperature (T_u) associated to the right axis.

Thus, instead of the upstream condition of the liquid phase governing S_l with cold combustor walls (see Fig. 8.4), it is the *residence time* of fresh gases inside the combustion chamber that governs the evolution of the laminar flame speed with preheated walls.

In summary, a two times higher absolute turbulent flame speed S_a^T in preheated conditions primarily follows from a substantially increased laminar flame speed which even outweighs the decrease of $\langle \rho_u \rangle_V \,/\, \langle \rho_b \rangle_V$ (see Fig. 7.22) *and* the more moderate decrease of Ξ_{res} (see Fig. 8.13). At a given equivalence ratio of a two-phase mixture, cold combustor walls tend to preserve the two-phase flow nature of the ignition process, if the fuel is not exceedingly volatile under ambient conditions. The laminar flame speed can then decrease depending on the upstream liquid volume fraction encountered by the propagating flame fronts as discussed in Sec. 8.2.1.1. This effect is visualized in the laminar flame speed map (Fig. 8.15) by the solid arrow between the diamond marker (fully premixed reference conditions) and the star denoting conditions of light-round ignition under ambient temperature walls with a distinct presence of the liquid phase. In turn, preheated combustor walls greatly increase the laminar flame speed (broken arrow in Fig. 8.15) not only due to higher fresh gas temperatures, but also due to enhanced evaporation, rendering flame propagation less sensitive to the upstream liquid volume fraction (see Sec. 7.5.3).

8.4 Conclusion

The present chapter is concerned with a mathematical expression to model the absolute turbulent flame propagation speed during light-round. It is shown to accurately predict averaged values for all cases under consideration (baseline, adiabatic and preheated). The main equation is decomposed to study the governing mechanisms in detail and relate them to the identified terms appearing in the model. Lastly, the expression for turbulent flame propagation is modified to estimate from an *a priori* perspective to what extent the absolute turbulent flame speed may change with different modeling choices.

The study, which assembles various models for dynamic flame wrinkling, polydisperse spray

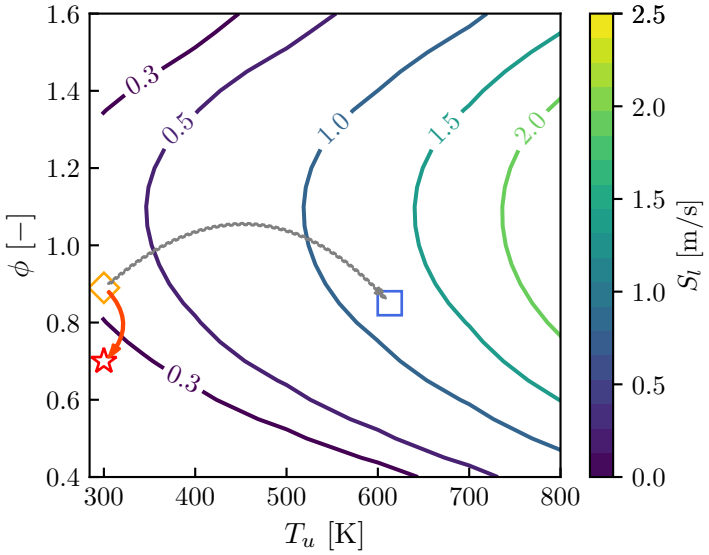

Figure 8.15: Laminar flame speed map. Diamond: fully premixed reference conditions with ambient temperature walls. Star: two-phase flow conditions without preheating. Square: preheated conditions.

description and wall heat losses, shows that neither corresponding physical mechanism outweighs the other ones and underscores the argument that each physical phenomenon must be accurately modeled. Variations in other modeling components have not been considered such as chemistry or subgrid-scale fluxes and could be investigated in future works. More specifically, local unsteady strain effects would certainly deserve a dedicated investigation in future works with better models to quantify their impact on the predicted flame speeds. Beyond light-round, we also expect strain corrections to better represent the very first instants of the initial stage of ignition which is only briefly covered on purpose.

Furthermore, we analyze reasons for the increased absolute turbulent flame propagation speed in preheated conditions. It is concluded that the decrease of the density ratio $\langle \rho_u \rangle_V / \langle \rho_b \rangle_V$ associated with the flame's volumetric expansion is outweighed by a more substantial increase in the laminar flame speed due to elevated fresh gas temperatures and a diminishing effect of the liquid phase.

The present analysis also demonstrates that regardless of the state of the wall temperature (cold or preheated), attention must be paid to appropriate wall boundary conditions. In particular, the use of adiabatic wall boundary conditions to approximate light-rounds with preheated combustor walls *cannot* establish the same initial conditions. Predictions of light-round durations with previous adiabatic LES are most likely affected by hidden error cancellation.

Chapter 9

Final dynamic flame stabilization after ignition in a single-injector combustor

During the ignition of a swirled single-injector combustor, two phases have been identified experimentally. In the first, the flame penetrates the injection unit, while in the second the flame lifts off after a substantial delay before stabilizing at a distance from the injector. This transient phenomenon is investigated using Large Eddy Simulations based on an Euler-Lagrange description of the liquid spray, an energy deposition model to mimic ignition and the thickened flame combustion model. It is shown that the initial penetration of the flame in the injector unit is linked with the positive pressure excursion induced by the rapid volumetric expansion of burnt gases. This sudden expansion is itself due to the fast increase in heat release rate that occurs during the initiation of the process. The corresponding positive and negative pressure disturbances induce a rapid reduction of the mass flow rate through the injector, followed by an acceleration of the flow and a return to the nominal value. It is also shown that the flame root disappears after another delay, which results in the flame edge lifting and stabilization at a distance from the injector exhaust corresponding to steady operation of the device. The relatively long delay time before this lift-off takes place is found to correspond to the residence time of the cooled burnt gases in the vicinity of the chamber walls, which are ultimately entrained by the internal recirculation zone and quench the lower flame foot.

Contents

9.1 Introduction

So far, we have been chiefly concerned with the final stage of forced ignition in annular combustion chambers which is characterized by burner-to-burner flame propagation (Lefebvre and Ballal, 2010; Mastorakos, 2017). In our analysis and macroscopic modeling approach, we have focused on characteristics and quantities that can either be associated with the propagating flame fronts, *e.g.,* flame surface averaged flame speeds or wrinkling factors (among others), the leading point, or global fresh and burnt gas conditions (*e.g.,* volume averaged densities, temperatures or equivalence ratios). Although flame *stabilization* mechanisms downstream of the propagating flame fronts were not yet addressed in particular, we have noted dynamic and transient changes of the flames anchoring at fully ignited burners in Sec. 6.5.1. These were visually most pronounced towards the end of light-round ignition (see Fig. 6.3) and deserve further analysis. As we shall see, their characteristic time is short enough to occur within the duration of full light-round ignition.

A recent work by Prieur et al. (2019) offers experimental insights into such dynamic behavior of spray flames during the ignition transient which are less well documented in the literature. Two consecutive phases were observed: first, flame was found to flashback and anchor with its lower flame brush inside the injection unit. This configuration persisted throughout a certain characteristic time until the lower flame brush quenched and the flame stabilized in a new position detached from the injector. These insights are of particular interest as a persistent flame flashback might damage the injection unit eventually.

Flame flashback has been known to occur, for example, due to thermo-acoustic instabilities (Keller et al., 1981; Lieuwen et al., 2006; Schulz et al., 2019) or transition between combustion regimes (Sommerer et al., 2004). However, experimental measurements reported in Prieur et al. (2019) and Yahou et al. (2022) suggest that flashback events are also possible during the combustor ignition sequence.

The present investigation relies on experimental observations made in a single-injector configuration, the SICCA chamber, operated at the EM2C laboratory. High-speed imaging revealed that the flame penetrates the injector and is initially present in this unit. After a delay, the lower flame brush is quenched, initiating a flame lift-off before stabilization at a distance from the injector. During the same period, the flame is also observed to change its shape.

The objective of the present chapter is to complement the experimental data and gain further insight into the mechanisms that drive the dynamic behavior which has not been covered in previous numerical studies and cannot be readily measured experimentally. This is achieved by making use of Large Eddy Simulations.

In the following sections, we first recall the setup of the SICCA combustor and briefly highlight those models, which are not identical to the simulation setup of Chapters 6 and 7. We reiterate that the present simulations were already carried out before some of our models and detailed experimental measurements of the liquid phase were developed or available. Second, results of the LES are analyzed, and flame stabilization mechanisms are outlined and compared to experimental data. Finally, we evaluate the impact of the employed kinetic mechanism on the prediction of quenching.

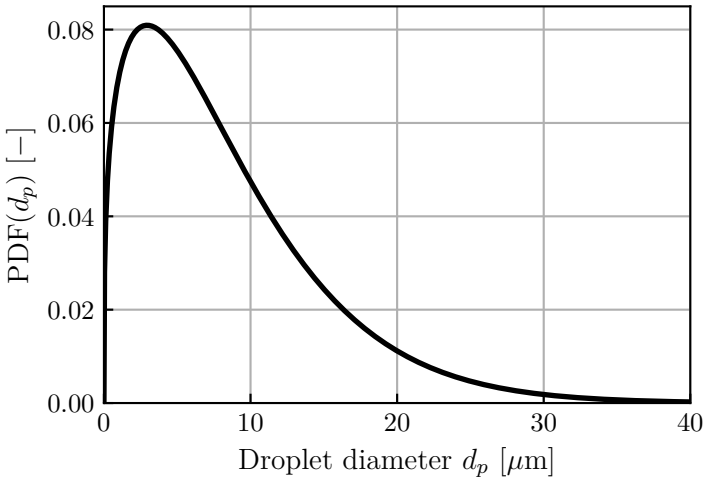

Figure 9.1: Probability density function (PDF) of the injected droplet size approximated by a Rosin-Rammler distribution with a shape parameter $q = 1.3$ and a diameter $d_{\mathrm{SMD}} = 18\,\mu\mathrm{m}$.

9.2 Numerical setup

The present Large-Eddy Simulations are carried out in the single-injector combustor SICCA already presented in Sec. 3.2.2. As for the previous simulations, we adopt an Euler-Lagrange approach with separate treatment for each phase using the flow solver AVBP (Schönfeld and Rudgyard, 1999). The treatment of the gas phase is identical to setup summarized in Sec. 6.2. In turn, the liquid phase modeling approach differs from the previous chapters only in terms of the handling of fuel injection: a fully atomized, hollow-cone fuel spray is generated by the *original* FIM-UR model (fuel injection method by upstream reconstruction, Sanjosé et al. (2011), see also Sec. 2.6.6). The injected droplet size is sampled from a Rosin-Rammler distribution expressed as

$$\mathrm{RR}(d_p) = q\frac{d_p^{q-1}}{X(d_{\mathrm{SMD}},q)^q}\exp\left[-\left(\frac{d_p^q}{X(d_{\mathrm{SMD}},q)^q}\right)\right] \tag{9.1}$$

with

$$X(d_{\mathrm{SMD}},q) = \frac{\Gamma(1+2/q)}{\Gamma(1+3/q)}d_{\mathrm{SMD}} \tag{9.2}$$

The shape parameter is set to $q = 1.3$, and $d_{SMD} = 18\,\mu\mathrm{m}$, yielding the distribution plotted in Fig. 9.1. The mean half-angle $\theta = 32°$ is chosen to best fit experimentally measured velocity profiles in non-reacting conditions at $2.5\,\mathrm{mm}$ above the chamber backplane. We emphasize that those profiles were obtained with a flush mounted atomizer (corresponding to $x_A = 0\,\mathrm{mm}$ in Fig. 3.3), which is substantially different from our later calibration strategy in Chap. 4. Despite this, all *other* models associated with the liquid phase are identical to the setup of Chap. 6 and Chap. 7, *i.e.* the Schiller-Naumann drag force model (Schiller and Naumann, 1935) and the polynomial evaporation model developed in Chap. 4.

The global two-step reaction scheme of Paulhiac et al. (2020) is employed alongside the thickened flame model (TFLES, Colin et al. (2000); Legier et al. (2000)). Local adaptive thickening is applied only to premixed zones through a superposition of a flame sensor (Legier et al., 2000) and the Takeno flame index (Yamashita et al., 1996). Unlike the previous light-round simulations however, unresolved sub-grid scale wrinkling effects are corrected by a flame surface wrinkling factor (Charlette et al., 2002b) with a *static* wrinkling parameter $\beta \equiv 0.5$.

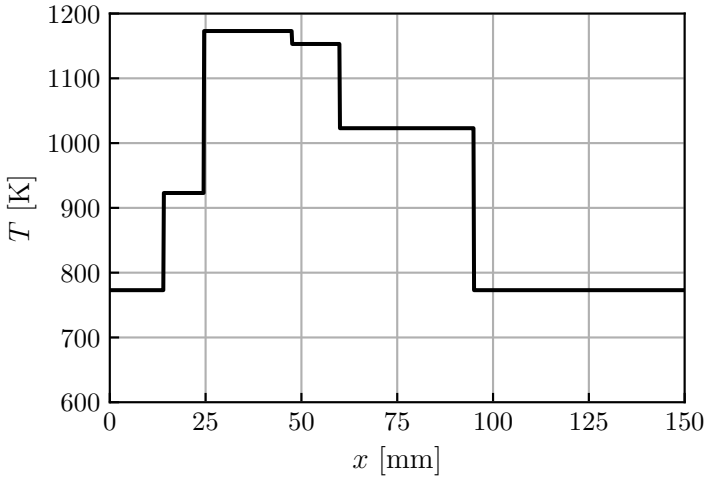

Figure 9.2: Experimental wall temperature profile of the inside surface of the quartz facing hot burnt gases. Profile obtained by using thermochromic paint.

Moreover, the near-wall flow inside the combustion chamber is considered to be sufficiently resolved and does not require additional wall models.

9.3 Boundary and initial conditions

For inlets and outlets, the Navier-Stokes Characteristic Boundary Conditions (NSCBC, Poinsot and Lele (1992)) are applied. Mass flow rates are imposed at the air inlet ($\dot{m}_{air} = 1.94\,\mathrm{g/s}$) and the fuel inlet ($\dot{m}_{fuel} = 0.111\,\mathrm{g/s}$) yielding a global equivalence ratio of $\phi_{glob} = 0.856$. All inlet temperatures are set to $T = 300\,\mathrm{K}$.

No-slip walls are assumed for the gas phase in the entire domain with the only exception being the swirler walls, for which a classic algebraic wall-law is used. Liquid phase boundary conditions are set to allow elastic rebound in the combustion chamber. In the injector, droplet-wall interactions are considered to be predominant and require a film-type boundary condition.

An experimentally measured wall temperature profile is imposed on the inner combustor walls (Fig. 9.2), while all other walls upstream of the fuel injector are adiabatic. The water-cooled combustor backplane is kept at a temperature of $T = 410\,\mathrm{K}$. We note that at the time of the simulation, a numerical characterization of wall heat transfers (*e.g.,* by means of Conjugate Heat Transfer simulations) were not yet carried out. Therefore, experimental measurements were imposed in spite of some measurement uncertainties to avoid imposing adiabatic wall boundary conditions instead.

The two-phase flow field has been converged prior to ignition by running a non-reacting simulation to reach the targeted global equivalence ratio in the ignition zone of the chamber. In contrast to Collin-Bastiani (2019b), the wall temperature profile is imposed *ab initio* to establish a thermal equilibrium between the fresh gases and the walls of the combustion chamber.

This initial solution is eventually ignited using a one-step energy deposition model (ED) as developed in Lacaze et al. (2009) to approximate the energy profile that a real spark would deliver, without simulating the initial plasma-phase. A volumetric source term is temporarily added to the energy equation featuring a Gaussian distribution in space and time. The center of the spherical energy source is positioned close to the combustor backplane in the outer

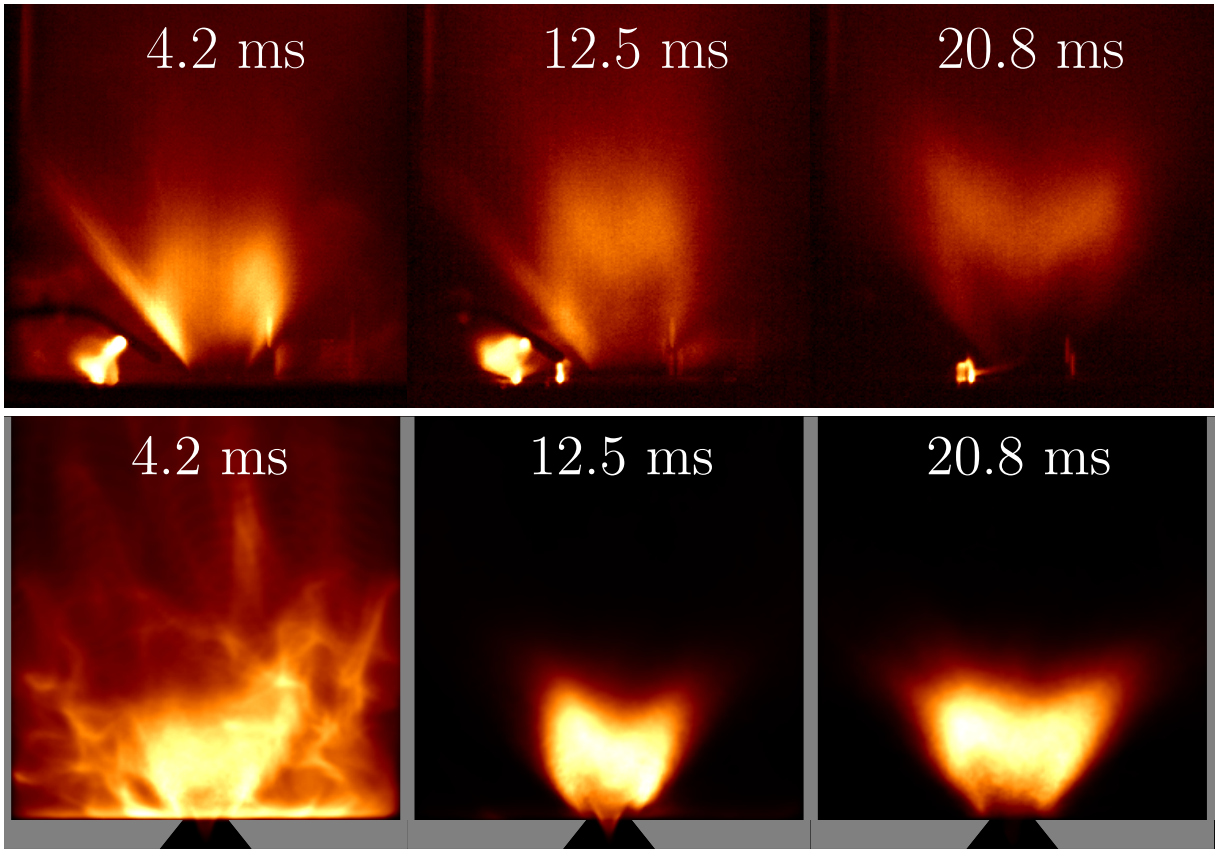

Figure 9.3: Top: Experimental ignition sequence recorded by high-speed imaging (reprinted from Prieur et al. (2019)). Bottom: Simulated ignition sequence: line-of-sight integrated heat release rate.

recirculation zone (total energy $E = 70$ mJ, diameter $d = 11$ mm).

9.4 Ignition in relight conditions

Three ignition sequences have been recorded with a high-speed camera (Prieur et al., 2019) at the same nominal conditions out of which one is used as a reference. Figure 9.3 (top) shows the experimental images which were averaged over 8.3 ms centered around the respective time instant. Two distinct flame configurations can be identified: during the first two instances, the flame is attached to the injector outlet which can be referred to as shape *A* (adopting the terminology in Prieur et al. (2019)). In the last instance, a flame detached from the swirler can be observed assuming shape *B*. Figure 9.3 (bottom) illustrates the simulated ignition sequence as a line-of-sight integration of the heat release rate inside the combustion chamber and the swirler nozzle. The same temporal averaging has been performed on the numerical data as in the experimental case. Similar flame configurations are found numerically supporting the argument of a dynamic flame behavior during ignition. The numerical images clearly reveal a flashback during the first two instances (shape *A*) as the lower flame brush is anchored inside the swirler nozzle which is particularly difficult to record experimentally without direct optical access. Conversely, in the following instance, the lower flame brush appears to be entirely extinguished. Therefore, complementary to the definition of the two flame shapes, the initial period will be defined as flashback phase (flame shape *A*) and the second period as lift-off

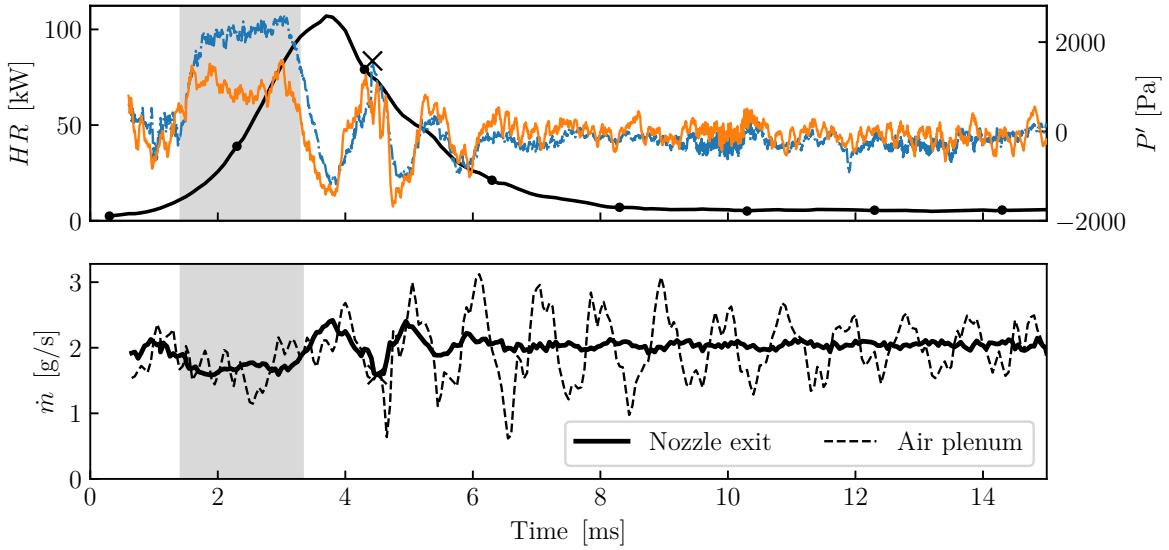

Figure 9.4: Top: volume integral of chamber heat release rate (solid line with bullet markers) and pressure signal sampled at the center of the combustor (dash dotted line) and at the injector outlet (solid line). Bottom: mass flow rates in the simulation at the injector outlet (thick line) and inside the air plenum (thin dashed line).

phase (flame shape *B*) in the remainder of this work. Note that flashback and liftoff phases are considered to appear within the flame propagation phase (2) of the general definition of forced ignition mentioned in the introduction (Lefebvre and Ballal, 2010). Each phase will be analyzed separately in the following sections.

9.4.1 Flashback phase

The volume integrated heat release rate inside the combustion chamber sampled during the ignition sequence is visualized in Fig. 9.4 (top, line with bullet markers). A short and intense peak of the heat release rate of $\dot{Q} \approx 100\,\mathrm{kW}$ can be observed during the consumption of the fresh gases inside the combustion chamber and a fast decay to the nominal thermal power of the combustor at $5\,\mathrm{kW}$. The rapid expansion of burnt gases induces a pressure perturbation that is propagating through the combustor and, more importantly, upstream through the swirler into the air plenum as well. In Fig. 9.4 (top) the pressure signal fluctuation P' is monitored at the swirler inlet and the center of the combustion chamber. As the peak duration of these two signals overlap almost perfectly during the increase of the heat release rate, the effect of the burnt gas expansion on the pressure field can be considered to be immediate inside the entire combustor.

This relation between pressure and heat release is important for the analysis of mass flow rates which are recorded at the injector outlet and upstream in the air plenum in Fig. 9.4 (bottom). In fact, the pressure perturbation during the burnt gas expansion modulates the mass flow rates upstream of the combustion chamber, that is, at the injector exit (fresh gas mass flow rate) and in the air plenum (pure air mass flow rate): during sustained high pressure fluctuation levels, mass flow rates decrease substantially (cf. light gray areas in Fig. 9.4). Due to the temporary decrease of the mass flow rates the lower flame brush is able to propagate in the upstream direction and penetrates into the injector which is shown in detail in Fig. 9.5

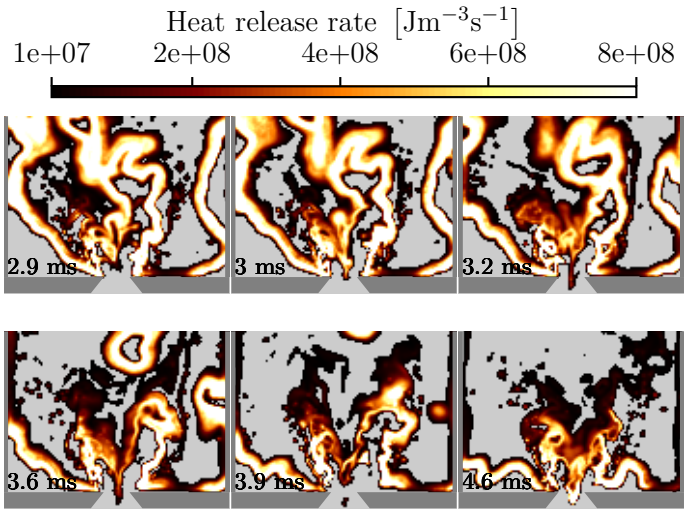

Figure 9.5: Instantaneous heat release rate on the central cut-plane of the combustor during the initial sustained high pressure levels (top) and during the second drop of the mass flow rates (bottom).

(top) in the central cut-plane of the combustor. However, the lower flame brush detaches from the injector immediately after that moment, since the mass flow rates overshoot their respective average values at $t = 3.9\,\mathrm{ms}$ (peak immediately after the gray area). Upon the subsequent drop of the mass flow rates due to another pressure peak at $t = 4.6\,\mathrm{ms}$ (marked by a cross in Fig. 9.4) the flame is able to re-enter the injector up to the atomizer and find a stable configuration inside this unit. This process is illustrated in Fig. 9.5 (bottom).

In order to understand why this flame configuration remains stable despite further fluctuations of pressure and mass flow rates, it is instructive to examine the flow field and temperature distribution in the Internal Recirculation Zone (IRZ) as shown in Fig. 9.6 corresponding to the central cut-plane of the combustor. The flame front is visualized as black contour lines of heat release and the IRZ is surrounded by gray contour lines of zero axial velocity emerging from the swirler exit. The left image corresponds to a snapshot at $t = 3.3\,\mathrm{ms}$ (sustained peak pressure), the right image to the reattached flame configuration at $t = 4.6\,\mathrm{ms}$ discussed earlier. In the second image, the IRZ entrains burnt gases at higher temperature compared to the preceding snapshot. This leads to high temperature combustion products being fed into the lower flame brush facilitating flame stabilization inside the injector.

With this result in mind, the question might be raised, whether the energy profile introduced in the simulation, the ignition method itself or even the presence of a liquid phase might intensify the pressure excursion in an inappropriate manner leading to a flame flashback which would not have appeared otherwise. While experimental data of a purely gaseous configuration prove that the flashback process also accompanies ignition independently of the presence of the liquid phase (see Appendix of Prieur et al. (2019)), additional data can also be provided to assess the impact of the ignition method. Instead of using the energy deposition model for ignition, a simplified approach can be used by locally replacing the fresh gas mixture at the position of the igniter by burnt gases. In order to compare this method to the energy deposition approach, a separate simulation has been carried out from the exact same initial conditions. Ignition is achieved by introducing a sphere of burnt gases with the same dimensions ($d = 11\,\mathrm{mm}$) at the same position as in the energy deposition case to preserve consistency. In this manner, a spherical heat release profile is initialized which corresponds to a laminar, adiabatic

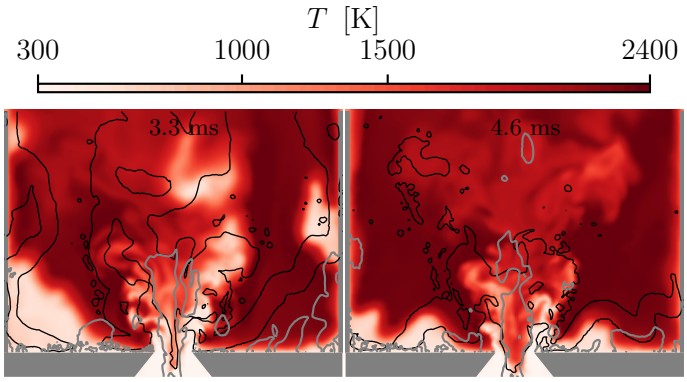

Figure 9.6: Instantaneous gas temperature in the central axial plane through the combustion chamber. Black contour lines correspond to a heat release rate of $10 \times 10^8\,\mathrm{Jm^{-3}s^{-1}}$, gray contours to zero axial velocity.

flame at the local composition. The resulting simulated evolution of the heat release rate profile as well as the corresponding pressure signal at the center of the combustion chamber is plotted in Fig. 9.7. The corresponding profiles of the energy deposition method (already shown in Fig. 9.4) are added to facilitate the comparison. As expected, the volume integrated heat release rate profiles are quite similar in both cases and induce similar pressure signals, although with a steeper initial transient in the case of the energy deposition model. Nevertheless, the same dynamical behavior (flashback and subsequent lift-off) can be observed (not shown here) even with a simplified ignition approach. Thus, the major conclusion that can be drawn from the previous discussion is that the flame flashback occurs independently from the kernel initialization method. In the context of this work, the main purpose of the initialization method is to deliver an appropriate flame kernel which does not require an explicit modeling of the very first flame initiation after the plasma-phase to reproduce the pressure evolution in the combustion chamber which eventually causes the flashback.

9.4.2 Lift-off phase

After the flame stabilization during the flashback phase, this configuration prevails for a total of $14\,\mathrm{ms}$ before transitioning into shape *B*. This transition is shown in the central cut-plane of the combustor in Fig. 9.8. Starting from the anchored position (Fig. 9.8 (left)), the flame splits into an upper and lower flame branch (Fig. 9.8 (center)). The lower branch shrinks and completely vanishes as the transition into shape *B* takes place. The flame is finally detached from the swirler (Fig. 9.8 (right)).

The characteristic delay time before the onset of this process is relatively long and may be linked to the cooling of the burnt gases that circulate in the vicinity of the combustor walls as will be shown in what follows. Between $t = 8.7\,\mathrm{ms}$ and $t = 15.4\,\mathrm{ms}$ (cf. light gray area in Fig. 9.9), the burnt gas temperature in the Outer Recirculation Zone (ORZ) is substantially reduced from $2400\,\mathrm{K}$ to around $1500\,\mathrm{K}$ due to cooling by the combustor walls. By contrast, the temperature in the IRZ remains nearly constant until the lower flame branch splits and quenches resulting in a steep temperature decrease in the IRZ (cf. dark gray area in Fig. 9.9).

However, a heat loss effect in the IRZ which is suggested here as the driving mechanism for the flame lift-off cannot be directly inferred from the temperature signals because no differentiation can be made locally between fresh and burnt gases. For this reason, we employ

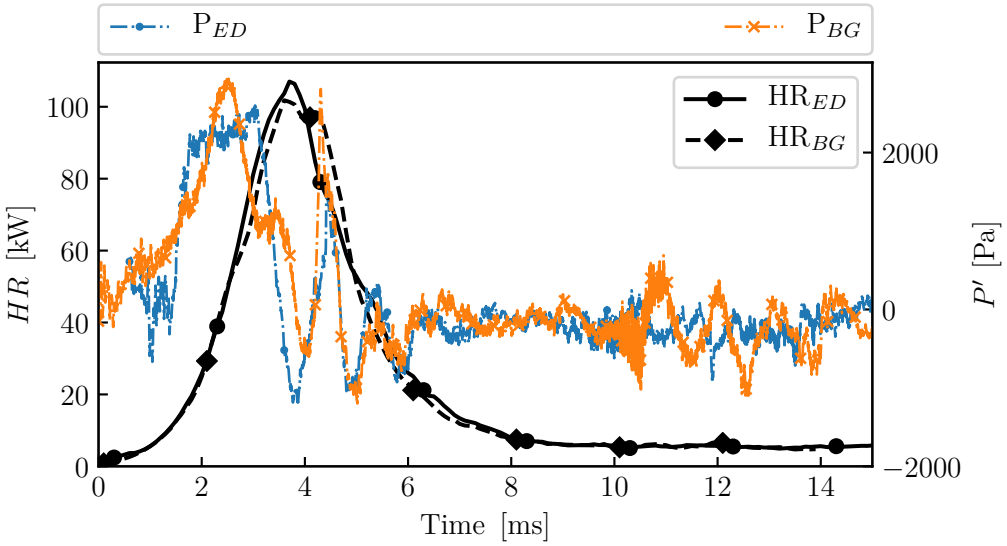

Figure 9.7: Volume integrated heat release rate using the energy deposition model (subscript ED, solid line, bullet markers) and a simplified burnt gases approach (subscript BG, dashed line, diamond markers). The corresponding pressure evolutions at the center of the combustion chamber are represented by dash-dotted lines.

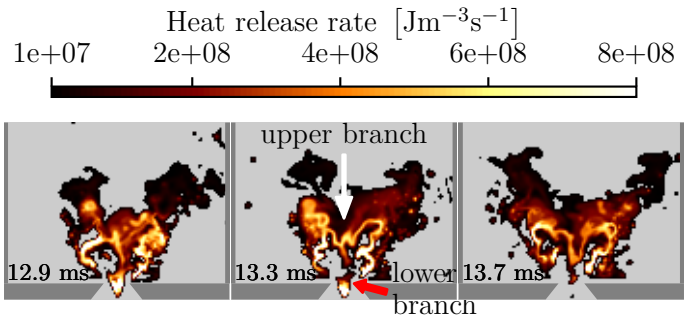

Figure 9.8: Instantaneous heat release rate on the central axial plane of the combustor during flame lift-off and transition from shape *A* to *B*.

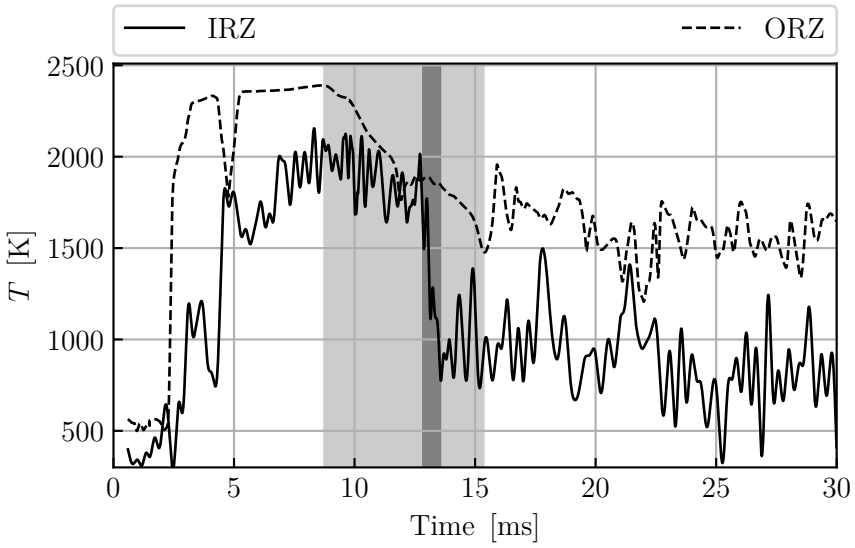

Figure 9.9: Temporal evolution of the temperature recorded in the IRZ and ORZ. The IRZ temperature signal is low-pass filtered (linear phase filter) for clearer identification of the curves.

the heat loss index I_{HL} already introduced in Sec. 6.5.5.2 to visualize the heat losses incurred by the burnt gases. We recall its definition written as

$$I_{\mathrm{HL}} = \frac{h - h_{low}}{h_{adiab} - h_{low}} = \begin{cases} 1 & \text{adiabatic} \\ 0 & \text{max. local heat loss} \end{cases} \qquad \text{(6.1 (revisited))}$$

where h is the local enthalpy value, h_{adiab} the adiabatic enthalpy at the local composition and h_{low} the enthalpy of the local composition at the lowest temperature in the chamber, which is deliberately set to the lowest wall temperature inside the combustion chamber $T = 410\,\mathrm{K}$. When I_{HL} is unity, adiabatic conditions prevail in the local composition, while $I_{\mathrm{HL}} = 0$ refers to the lowest enthalpy that a given composition may reach due to heat transfer onto the chamber walls (i.e. highest heat loss). The heat loss index I_{HL} distribution in the central cut-plane through the combustor is shown in Fig. 9.10 after stabilization of the flame inside the injector (a) and during the transition from shape *A* to *B* (b-d). The flame is represented by black contour lines of iso-heat release rate, whereas gray contour lines mark regions of zero axial velocity. Note that the value range of I_{HL} is intentionally clipped between 0 and 1, although the fresh gas mixture before ignition can take values of $I_{\mathrm{HL}} > 1$. This is only due to the fact that the fresh gases are heated by the combustor walls in the absence of combustion, resulting in higher enthalpy levels compared to a reference value which is (deliberately) set to the lowest temperature in the combustor. The same applies for burnt gases immediately after ignition and flame stabilization which is shown in Fig. 9.10(a). Contrary to the adiabatic flame and large parts of burnt gases that are in adiabatic conditions in the center of the combustion chamber which are not yet impacted by heat losses at this stage, near-wall fluid is constantly cooled by the combustor walls and I_{HL} is close to zero in this region. In the ORZ, flow velocities are comparably low (on the order of $15\,\mathrm{ms}^{-1}$) leading to a long exposure time of burnt gases to the walls. A substantial decrease of enthalpy starting in the ORZ and expanding downstream along the chamber walls can therefore be observed (Fig. 9.10(b-d)). The flame is affected in the same manner, since cooled burnt gases are transported back upstream to the flame zone by the ORZ. Mixing again with fresh gases then results in a lower enthalpy of the combustion products leading to $I_{\mathrm{HL}} < 1$ even in the flame zone.

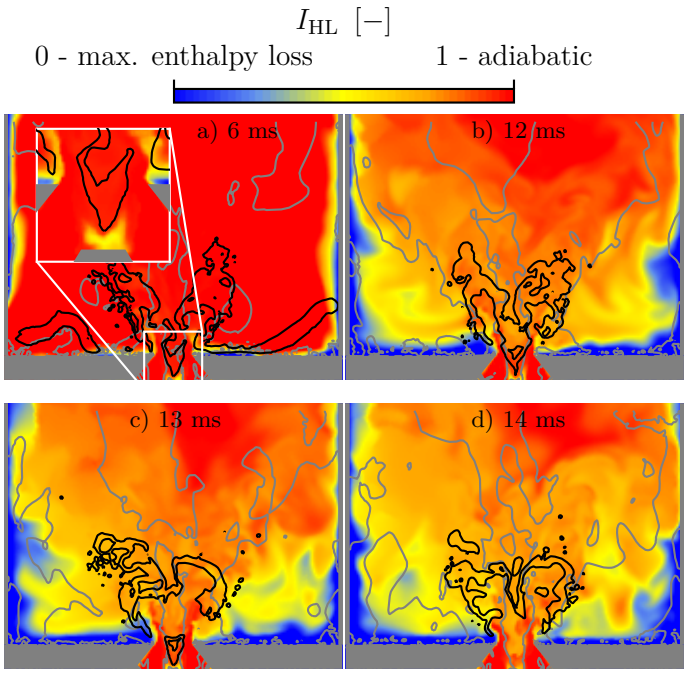

Figure 9.10: Heat-loss index I_{HL} in the central axial plane through the combustion chamber. Black contour lines correspond to a heat release rate of $4 \times 10^8\,\mathrm{Jm^{-3}s^{-1}}$, gray contours to zero axial velocity.

It may also be possible that the flame lift-off is locally enhanced by evaporative cooling of the gas phase close to the atomizer. The temporal evolution of the gaseous equivalence ratio ϕ_g inside the injection unit in Fig. 9.11 suggests that when the flame anchors inside the injector, evaporation is intensified causing a substantial increase of ϕ_g. Consequently, the gas phase locally incurs additional heat losses (cf. inset in Fig. 9.10(a)), which in turn may accelerate the extinction of the lower flame brush. However, evaporative cooling does not seem to have a first order impact on the flame lift-off as proven experimentally in a purely gaseous configuration (cf. Prieur et al. (2019)), but may alter the transition time from the flashback to the lift-off phase.

Therefore, the flame lift-off can be explained more effectively by considering wall heat-losses: the IRZ, which feeds the lower flame brush and sustains the initial flashback, is found to entrain burnt gases of decreasing enthalpy. As soon as the enthalpy is not sufficient to maintain a steady flame, the lower flame branch disintegrates and quenches entirely. The flame then stabilizes with a leading edge detached from the swirler.

9.4.3 Impact of the kinetic mechanism on the prediction of quenching

A final discussion is dedicated to the impact of the two-step reaction mechanism on the prediction of quenching of the lower flame brush quenching. It is known that reduced kinetic mechanisms are less sensitive to strain rate and that in turn may delay quenching and lift-off. This issue is assessed by comparing the different flame regimes for the employed two-step mechanism and for a detailed mechanism for n-heptane (65 species, 315 reaction, see Smallbone et al. (2009)).

Data is obtained by performing steady-state 1D simulations of stabilized counterflow flames

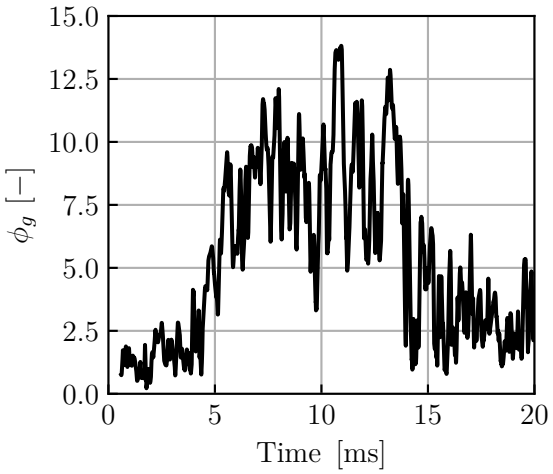

Figure 9.11: Gaseous equivalence ratio ϕ_g sampled inside the injector above the fuel atomizer at $x = -0.005\,\mathrm{mm}$ relative to the chamber backplane.

with the code AGATH. The flow configuration is chosen such that the fuel side represents the fresh gas composition at ϕ_{glob} while the opposing stream side is formed by the corresponding burnt gas composition. Each 1D simulation is performed for a different set of imposed strain rate a and burnt gas temperature T_{burnt}. In the resulting regime diagram plotted in Fig. 9.12, quenching occurs in the hatched region for the detailed reaction mechanism whereas the dotted region corresponds to quenching predicted by the two-step reaction mechanism. Conversely, a steady flame can be established in the region marked as *burning regime*.

This comparison may be used to assess the flame lift-off observed in the SICCA-combustor in terms of the employed combustion chemistry. While both schemes show similar trends for flame extinction at low burnt gas temperatures and high strain rates, the quenched regime of the detailed mechanism extends towards higher temperatures and lower strain rates than the two-step mechanism. Thus, as the temperature of the IRZ decreases over time (cf. Fig. 9.9) the lower flame brush might extinguish at an earlier stage with detailed chemistry compared to the two-step mechanism.

9.5 Conclusion

This final chapter is concerned with the transient stabilization process that occurs during the ignition of a swirling injector in a well-controlled laboratory-scale configuration. The injector offers an idealized version of practical systems used in aero-engines. The investigation is motivated by prior experimental observations in a multi-burner annular combustion chamber, indicating that flame flashback occurs during ignition followed by a final stabilization of the flame detached from the injection unit. This behavior is also retrieved in a single sector combustor equipped with one injector and characterized experimentally. This single-injector geometry SICCA is studied in this work using Large Eddy Simulations employing a polydisperse Euler-Lagrange formalism. The simulation suitably retrieves the two periods identified experimentally. During an initial period, the flame is attached to the chamber bottom with a lower flame brush anchoring inside the swirling injector. An analysis of pressure signals inside the combustion chamber and on the upstream side of the swirler indicates a strong transient perturbation of the pressure field which is related to the rapid expansion of the burnt gases

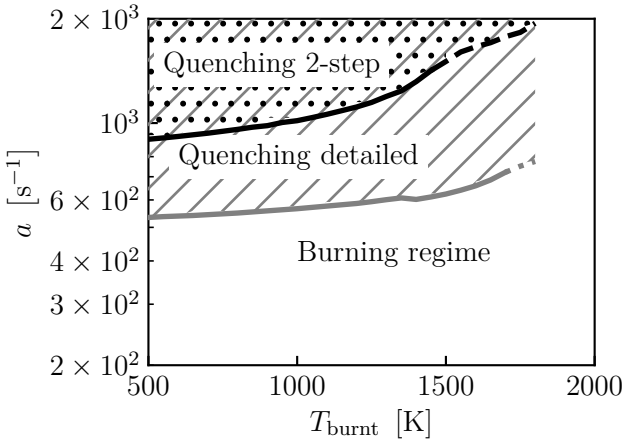

Figure 9.12: Regime diagram of a counterflow flame. Thick solid lines mark the critical point of extinction for a given temperature for each reaction mechanism. Dashed and dotted line continuations indicate conditions where the critical points of extinction and autoignition collapse.

inside the chamber. This pressure perturbation controls the mass flow rates of fresh gases at the injector outlet and even further upstream in the air plenum and leads to a temporary decrease of their respective levels. The flame is entrained by the internal recirculation zone which allows for an upstream propagation and eventually stabilizes inside the injector unit. This transient flashback during ignition highlights the potentially detrimental effect on the injector elements. The final stabilization in the form of a flame detached from swirler is found to be controlled by heat transfer taking place between recirculating burnt gases in the vicinity of the combustor walls. A heat-loss index defined as a normalized enthalpy calculated at different instants during the simulation reveals a continuous enthalpy decrease starting in the outer recirculation zone and gradually impacting the flame zone as the cooled burnt gases mix upstream with the fresh stream of reactants. Consequently, the internal recirculation zone progressively entrains colder combustion products and quenches the lower flame root that is initially located inside the injector. Finally, the flame detaches from the injection unit and takes its steady-state position with a leading edge separated from the swirler.

General conclusions

Our research addresses flame propagation during ignition, relevant for future aero-engine development. Given its paramount importance for safe and reliable operation, engine restart is subject to extremely strict regulations, requiring a successful ignition under a variety of very different conditions. With engine certification specifications in mind, the present work is a step forward in the direction of realistic representations of the combustor walls' thermal state, clarifies the impact of heat transfer on flame propagation, and improves physical and theoretical models describing the governing mechanisms of flame propagation. We further highlight how these models should be selected for numerical simulations to avoid compensation of errors resulting from invalid over-simplifications. These considerations have led to a numerical study of light-round ignition which simultaneously includes detailed models for *all* governing mechanisms of flame propagation previously investigated in isolated efforts. Interesting results have been found that are supported by a comprehensive theoretical analysis.

At the foundation of our work is the annular multi-burner combustor MICCA-Spray, designed and operated at the EM2C laboratory. It features sixteen swirled fuel injectors fed with liquid n-heptane and air. Two concentric transparent quartz tubes allow for direct optical access to the flames. A complementary single-injector combustor SICCA offers an additional setup with extended experimental diagnostics.

Although previous light-round studies (Prieur et al., 2019; Puggelli et al., 2020) have highlighted the first order effect of the combustor wall temperature on the light-round duration, the role of heat transfer was not comprehensively examined. Therefore, we have intentionally selected two distinct configurations which enhance the effect of wall heat transfer on light-round ignition. These can be considered as idealized representations of engine restart scenarios defined by aviation certification authorities, despite apparent simplifications (*e.g.,* atmospheric pressure levels): (i) light-round with cold combustor walls at $T_w = 300\,\mathrm{K}$ mimics high-altitude restart from windmilling after extended delay periods, whereas (ii) light-round with preheated combustor walls approximates a quick relight scenario during climb. Such conditions can safely and reliably be established in a laboratory setting.

Our numerical setup for light-round simulations has been carefully assembled, striking a reasonable balance between model accuracy and computational costs, without compromising the description of the governing mechanisms of flame propagation. Compressible Large-Eddy Simulations (LES) have thus been performed with CERFACS' AVBP solver, employing a two-step kinetic reaction mechanism comprising six species, the thickened flame model (TFLES), and a dynamic evaluation of the flame surface wrinkling factor. A pre-atomized polydisperse droplet spray was injected and tracked in a Lagrangian framework. Two major enhancements were proposed for the liquid phase: (i) an improved implementation of the Abramzon-Sirignano evaporation model accounting for variable properties of the droplet films, and (ii) a calibration

of the phenomenological fuel injection model FIM-UR based on experimental data. In addition, a tabulated wall model has been developed and implemented, improving the prediction of wall heat fluxes and wall shear stresses through detailed modeling of the boundary layer with variable thermophysical properties. The wall temperature profiles for quick relight were obtained from Conjugate Heat Transfer (CHT) simulations and based on physical arguments, constituting a substantial departure from previous adiabatic simulations. The novelty of our setup is the *simultaneous* incorporation of *all* aforementioned enhancements in our simulations: dynamic combustion modeling, improved evaporation and injection, and a detailed model for wall heat transfers. Such an endeavor was not achieved before.

Results of the first light-round case with cold combustor walls were found in good agreement with experimental data, both in terms of flame shapes and light-round duration. The volumetric burnt gas expansion scaling with the density ratio ρ_u/ρ_b was identified as the main driving mechanism of flame propagation in such conditions, inducing a distinct azimuthal flow acceleration. It was found to modulate the liquid phase upstream of the propagating flame fronts, generating droplet accumulations in the wake of each swirling jet, which in turn caused the flames' leading point to propagate along a characteristic sawtooth trajectory. With the gradually increasing influence of wall heat losses in the burnt gases, the flame expansion effect was observed to decrease. An important conclusion could then be drawn from the comparison with a complementary adiabatic simulation: wall heat losses critically affect flame propagation through a modulation of the main driving mechanism. Moreover, the adiabatic case clearly exemplifies the effect of compensating errors through poor modeling choices, which have impaired the predictions of previous works.

For the second light-round case with preheated walls, we have first computed stationary wall temperature profiles in fully ignited conditions by means of Conjugate Heat Transfer (CHT) simulations, given the lack of detailed experimental data. Although more simplified approaches could have been employed, which are common in the literature, we have instead opted to establish a more sound foundation for our later analysis and discussion. The obtained wall temperature profiles were imposed as "static" boundary conditions in the following prefueling simulations. At thermal equilibrium between the fresh gas mixture and the combustor walls, the presence of the liquid phase was substantially diminished due to enhanced evaporation. The subsequent light-round simulation was found to be in remarkably good agreement with experimental data in terms of the predicted light-round duration, despite uncertainties in the imposed wall temperature profile. The leading point trajectory was much smoother, given the more homogeneous upstream fresh gas mixture caused by elevated evaporation rates. In turn, a more pronounced azimuthal flow acceleration was found compared to the baseline case despite a diminished density ratio. Supported through later insights obtained from a macroscopic flame speed model, we have revealed that the decrease of the density ratio was outweighed by a more substantial increase of the laminar flame speed S_l in preheated conditions. We have thus reinforced our stance that the thermal state of combustor walls must be accurately represented in light-round simulations. Previous studies with *adiabatic* walls could not have had established *preheated* conditions, and are therefore considered to be impaired by hidden error cancellation.

To further substantiate our arguments from a theoretical perspective, we have derived a macroscopic flame propagation speed model already mentioned above. It was shown to predict average flame propagation speeds from LES data with good accuracy in all scenarios. Moreover, it has offered valuable insights into the relative importance of the main driving mechanisms,

and how these are altered through alternative modeling choices, or preheating.

Finally, we shifted the focus of our attention from propagating flames to a transient flame stabilization mechanism observed during light-round. Large-Eddy Simulations of the single-injector combustor SICCA have allowed a detailed study of said effect. An acoustic pressure excursion during burnt gas expansion was found to be the root cause of a transient flame flashback, resulting in a flame configuration with a lower flame brush anchoring inside the injection unit. After a characteristic delay time associated with the cooling of burnt gases in the vicinity of the combustor walls, the lower flame brush quenched and a final flame stabilization was observed detached from the injector.

In conclusion, the present work has allowed for a comprehensive numerical and theoretical analysis of flame propagation during light-round ignition in an annular multi-burner combustor with realistic thermal wall conditions. Detailed models were simultaneously assembled in a unique simulation setup, which was not achieved before. This has allowed for a final clarification of the role of heat transfer during light-round: heat losses incurred by the burnt gases decrease the resulting absolute turbulent flame propagation speed, while fresh gas preheating through hot combustor walls diminishes the impact of the liquid phase, largely increases the laminar flame speed, and thereby results in an increased absolute turbulent flame speed.

Perspectives

Throughout this work, we have emphasized the role of detailed modeling for simulations of dynamic combustion phenomena. Yet, certain simplifications were still unavoidable, given the large combustor size and available computational resources, opening a first avenue for research in the direction of incremental model improvement. In Chap. 4, we have critically reviewed the performance of our contribution to the evaporation model, noting a deterioration of the predicted evaporation time in pure burnt gases. As already mentioned, this could be remedied by implementing a tabulation approach instead of polynomials, along with a different choice of variables to parameterize the evolution of the droplet film's Prandtl and Schmidt numbers, *e.g.,* a normalized temperature Θ, the mixture fraction Z and the progress variable c. A possible alternative could be the more expensive but direct computation of detailed transport properties.

With regard to fuel injection modeling, phenomenological approaches will probably still be relevant for LES of industrial combustors in the next years. Although further development could be done to reach a higher level of sophistication, *e.g.,* imposing variable injection velocities per droplet class, or accounting for film evaporation, it cannot solve the more fundamental problem of the inherent ambiguity in terms of user-defined model parameters. Instead, a different development direction appears more attractive, as it would offer a more sound physics-motivated foundation: inspired by the work of Carlos Guillamon from the ANNULIGhT network, a coupled approach could be pursued in the following manner: a specialized solver is employed to perform resolved atomization simulations of a liquid jet. This solver is assigned to a sub-domain of the flow problem under consideration, while the larger part of the numerical domain, i.e. the bulk flow region, is handled by a multiphase LES solver. At the interface between both solvers, droplet size and velocity distributions are sampled from the resolved atomization simulation and subsequently injected as (pre-atomized) spray in the LES solver, which could still account for droplet interactions depending on the spray regime. Simultaneously, a momentum exchange must be ensured at the interface between both solvers to allow for the interaction between the bulk flow and the atomization process. This task can be achieved with coupling libraries such as OpenPALM, which is already used for Conjugate Heat Transfer simulations. Given the possibility of different characteristic times in each domain, the exchange (or update) frequency could be adjusted according to suitable criteria. Such a coupling approach could bring the following advantages over existing *ad hoc* solutions: (i) parameters such as injection angles or velocities are no longer user-defined, but follow from the simulation itself. (ii) The requirement for a precursor model calibration can be eliminated.

Beyond liquid phase modeling, the role of wall heat transfers in combustion devices must be more thoroughly investigated and quantified, which could guide the general direction for future research in that sense. As we have repeatedly mentioned throughout this manuscript, only limited quantitative data is available for the annular combustor MICCA-Spray studied here, since heat transfer was beyond the scope of initial experimental campaigns. Detailed exper-

imental temperature measurements would be welcome for a comprehensive validation of our light-round simulations. A comparison of experimental and numerical light-round durations does not validate the entire simulation setup as such, as it cannot reveal hidden error cancellation. Therefore, wall temperatures or heat fluxes are more suitable metrics and should be clearly characterized.

Future research should also explore the role of the chemical reaction mechanism on the early phases of flame kernel growth. Recalling the results of our comparisons between a two-step and detailed chemistry, we have highlighted the reduced mechanism's insensitivity to strain. Consequently, the initial flame kernel is more likely to survive high strain rates, when in reality quenching would occur. Since we only have considered successful ignition in this work, we have shown that reduced kinetic schemes can be an acceptable simplification. However, such modeling choice complicates a clear definition of a numerical light-round duration, rendering comparisons with experimental measurements less accurate (see also Chap. 6). Detailed schemes instead would not only improve the description of the early stages of the flame kernel, but also facilitate a comparison between experiment and simulation. The development of the initial flame kernel with *e.g.,* an Artificially Reduced Chemistry is certainly worth investigating, although this comes at substantially increased computational costs.

In the broader context of clean next-generation engine development, the present work could also be the starting point for research leading to new horizons. While we have considered realistic thermal wall conditions, a long-term research goal should certainly aim towards real *operating* conditions in terms of both low temperature *and* low pressure. The role of the employed fuel and its volatility were found to be intricately linked to wall temperatures and flame propagation modes. With less volatile fuels than n-heptane, real ignition procedures from windmilling could be more thoroughly investigated, as evaporation is strongly impaired.

Different equivalence ratios or mass flow rates could be envisioned to explore regimes where successful ignition is possible, and study the failure modes, where it is not.

With the upcoming transition towards clean combustion technology, safe and reliable ignition will remain an essential design constraint. Given the current trend towards sustainable aviation fuels, novel fuel blends or hydrogen-based or enriched fuels, we expect flame propagation to strongly depend on the fuel characteristics. Future research is therefore required to examine the suitability of these fuels in light of certification requirements.

In addition, architectural changes and improvements of combustor parts might have an impact on engine restart capabilities, which need to be assessed.

Beyond ignition, the thermal state of the combustor walls is likely to affect other engine characteristics such as pollutant formation, combustion instabilities or lean blow-off. These phenomena clearly deserve a comprehensive analysis with realistic thermal wall conditions and offer a plethora of future research opportunities as well.

Appendices

A Polynomial fit procedure for the evaporation model

A given dataset of Sc_{film} and Pr_{film} parameterized by the normalized film temperature Θ and fuel mass fraction $Y_{\mathrm{C_7H_{16}}}$ can be fitted to a bivariate polynomial in the following way: let A be a matrix of dimension $M \times K$ containing all products of $\Theta^i Y^j$ (with dropped $\mathrm{C_7H_{16}}$ subscripts)

$$\boldsymbol{A} = \begin{bmatrix} \Theta_0^0 \cdot Y_0^0 & \Theta_0^1 \cdot Y_0^0 & \Theta_0^0 \cdot Y_0^1 & \Theta_0^1 \cdot Y_0^1 & \cdots & \Theta_0^K \cdot Y_0^K \\ \Theta_1^0 \cdot Y_1^0 & \Theta_1^1 \cdot Y_1^0 & \Theta_1^0 \cdot Y_1^1 & \Theta_1^1 \cdot Y_1^1 & \cdots & \Theta_1^K \cdot Y_1^K \\ \vdots & \vdots & \vdots & \vdots & \ddots & \vdots \\ \Theta_M^0 \cdot Y_M^0 & \Theta_M^1 \cdot Y_M^0 & \Theta_M^0 \cdot Y_M^1 & \Theta_M^1 \cdot Y_M^1 & \cdots & \Theta_M^K \cdot Y_M^K \end{bmatrix} \tag{3}$$

The number of columns depends on the monomial order N and is given as $K = (N+1)^2$ for a bivariate polynomial. For example, a monomial order of $N = 1$ results in $K = 4$ columns due to interaction terms ($\Theta^0 Y^0$, $\Theta^1 Y^0$, $\Theta^0 Y^1$ and $\Theta^1 Y^1$). Consequently, K fit coefficients have to be computed for Sc_{film} and Pr_{film} each, thus the coefficient vector x must contain K rows

$$x = \begin{bmatrix} c_{0,0}^{\mathrm{Sc}} & c_{0,0}^{\mathrm{Pr}} \\ c_{1,0}^{\mathrm{Sc}} & c_{1,0}^{\mathrm{Pr}} \\ c_{0,1}^{\mathrm{Sc}} & c_{0,1}^{\mathrm{Pr}} \\ c_{1,1}^{\mathrm{Sc}} & c_{1,1}^{\mathrm{Pr}} \\ \vdots & \vdots \\ c_{K,K}^{\mathrm{Sc}} & c_{K,K}^{\mathrm{Pr}} \end{bmatrix} \tag{4}$$

Each column in x represents the set of coefficients for Sc_{film} and Pr_{film}, respectively.

b is a column vector of dimension $M \times 2$ and contains the Schmidt and Prandtl numbers for a given tuple of $(\Theta,\ Y_{\mathrm{C_7H_{16}}})$

$$b = \begin{bmatrix} \mathrm{Sc}_0 & \mathrm{Pr}_0 \\ \mathrm{Sc}_1 & \mathrm{Pr}_1 \\ \mathrm{Sc}_2 & \mathrm{Pr}_2 \\ \vdots & \vdots \\ \mathrm{Sc}_M & \mathrm{Pr}_M \end{bmatrix} \tag{5}$$

Eventually, we can solve the equation system $\|b - Ax\|$ to obtain the coefficient vector x, for example by invoking NumPy's `numpy.linalg.lstsq`.

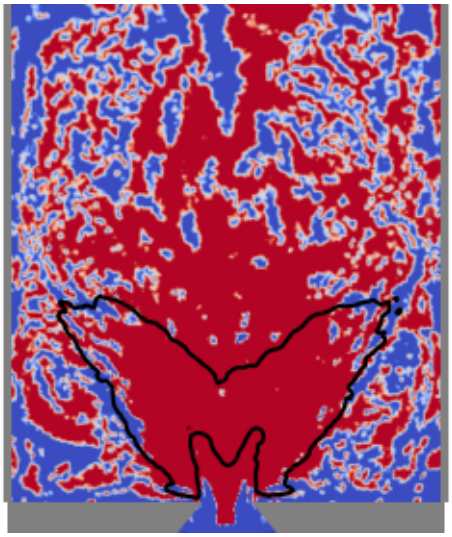

Figure 13: Time-averaged Takeno flame index on the central cutplane through the SICCA combustion chamber. Red corresponds to purely premixed combustion, blue to purely non-premixed combustion. The black contour line represents a heat release rate of $5 \times 10^7\,\mathrm{W/m^3}$. The injection parameters correspond to those in Tab. 4.3.

B Combustion regime identification for the reacting calibration simulations

Computing the Takeno flame index according to Eq. 2.66 allows to identify the local combustion regime, which is $+1$ in premixed conditions, and -1 in non-premixed conditions. Figure 13 shows such a regime map for the injection parameters defined in Tab. 4.3. The reaction zone, which is limited by the black iso-contour of the heat release rate, is dominantly found to reside in the premixed combustion regime, associated with red colors. This plot confirms not only that the droplets' impact on the flame is very weak, but also that the TFLES combustion model remains a reasonable modeling choice in the present setup.

C A priori quantification of fuel pyrolysis effects in preheated fresh gases

In order to quantify the relevance of fuel pyrolysis effects in preheated conditions, we ran separate 1D laminar flame simulations with a detailed chemical reaction mechanism (USC-II, 65 species, 315 reactions Smallbone et al. (2009)). Results suggest that those effects would occur *beyond* a fresh gas temperature of $T_u = 1000\,\mathrm{K}$ which is far from the fresh gas temperature in the present light-round simulation. Fuel mass fractions obtained from these detailed 1D flame simulations are plotted in Fig. 14 for two equivalence ratios and three fresh gas temperatures each. Thin lines correspond to a fresh gas temperature of $T_u = 1000\,\mathrm{K}$ exhibiting constant values of the fuel mass fraction Y_{C7H16} in the fresh gas region. In turn, a decrease of the fuel mass fraction in the fresh gas region can be observed at $T_u = 1100\,\mathrm{K}$ (dash-dotted lines) indicating the onset of pyrolysis effects.

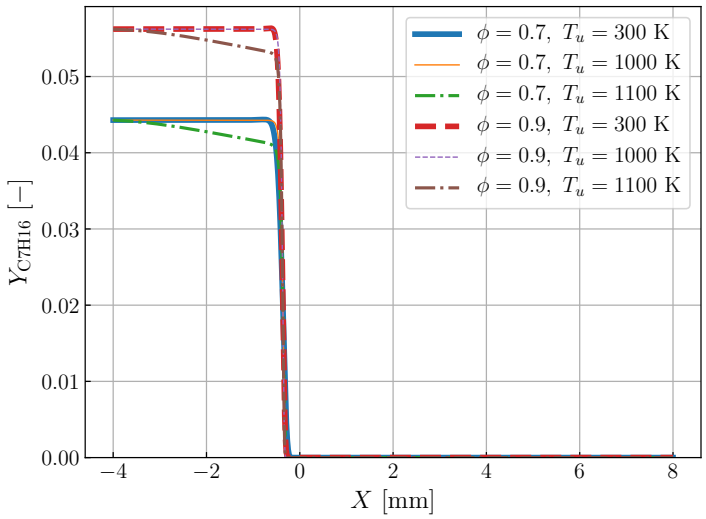

Figure 14: Profile of fuel mass fractions obtained from 1D laminar flame simulations using a detailed chemical reaction mechanism (USC-II, Smallbone et al. (2009). Fuel pyrolysis effects appear at fresh gas temperatures $T_u = 1100\,\mathrm{K}$ (dash-dotted lines).

D Estimation of internal radiative heat transfer from a frozen flame solution

Additional "frozen flame" simulations have been performed in the bisector to assess the contribution of internal radiative heat transfer under stationary operating conditions. Essentially, we have solved the radiative transfer equation using a Quasi Monte-Carlo solver (RAINIER, Zhang (2011); Refahi (2013); Zhang (2013); Koren (2016)) for a converged solution obtained from Conjugate Heat Transfer (CHT) simulations of the bisector (see Sec. 7.2). Gas radiative properties are accounted for through a ck-model, while spectral radiative properties of the quartz walls are modeled according to a simplified band model discussed in Sec. 5.2.2, similar to the work of Palluotto (2019). Wall temperatures are imposed in the entire domain and correspond to the temperature profiles from CHT simulations. In this manner, we can estimate the instantaneous radiative heat transfer for a single ("frozen") snapshot of the fluid and solid domain, which are not advanced in time. The local radiative power obtained from the Monte-Carlo solver RAINIER is plotted in Fig. 15 on a cylindrical cutplane through the bisector. The integrated radiative power inside the combustion chamber is thus found to be $P_{rad} = 291\,\mathrm{W}$, which is 9.2% of the total convective heat transfer between the fluid and solid domain (shown in Sec. 7.2.3). Given the substantially increased computational cost of including the Monte-Carlo solver in the CHT setup, we have chosen to neglect *internal* radiative heat transfer, accepting the incurred error as specified above. For the sake of clarity we reiterate that we *do* account for radiative heat transfer at the *external* quartz wall surfaces exposed to the ambient air.

E Conjugate Heat Transfer simulations of reacting steady state conditions in SICCA

Prior to Conjugate Heat Transfer (CHT) simulations of the bisector, attempts have been made to validate the coupling setup against experimental wall temperature measurements

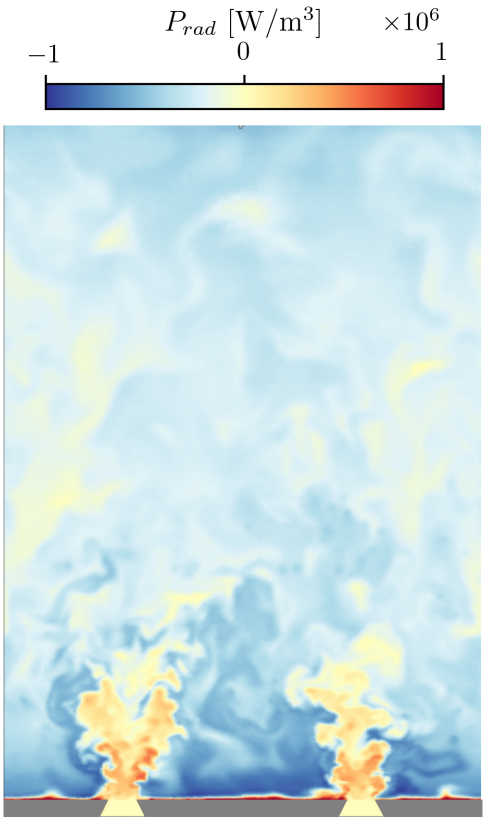

Figure 15: Radiative power on a cylindrical cutplane through the bisector at $R = 0.175\,\mathrm{m}$ transformed into a rectangular system.

of the single-injector combustor SICCA. Two techniques were applied to obtain temperature data experimentally: (i) the internal quartz face exposed to burnt gases was measured with thermochromic paint, whereas (ii) the external quartz face exposed to the ambient air was measured with a thermocouple of type K. Note that the thermocouple measurements were performed with a *longer* quartz tube ($h = 200\,\mathrm{mm}$), which does *not* correspond to the image shown in Fig. 3.5 (where $h = 150\,\mathrm{mm}$). All *other* combustor components remain the same, particularly the injector assembly. The nominal inner quartz diameter is unmodified ($d = 70\,\mathrm{mm}$) as well as the nominal quartz thickness ($\delta = 5\,\mathrm{mm}$). The changed quartz dimensions have thus required to adjust and remesh the computational domains of the fluid and solid.

In terms of the numerical setup for CHT simulations, we have however employed the approach detailed in Sec. 5.1 including material properties as in Sec. 5.2.1, but with one notable exception: the internal fluid flow inside the combustion chamber was wall-resolved, since the tabulated wall model (see Sec. 5.3) was still in development.

E.1 Results

An instantaneous CHT solution snapshot of both fluid and solid domains is shown in Fig. 16. In addition, we show surface temperatures for both quartz sides in Fig. 17. Comparing the azimuthally averaged wall temperatures from CHT simulations with experimental data in Fig. 18 reveals a substantial overestimation of the internal quartz wall temperature at $x = 30\,\mathrm{mm}$ of approximately $200\,\mathrm{K}$ (black lines). However, in the upper half of the quartz tube (*i.e.* for $x \geq 100\,\mathrm{mm}$), the discrepancy between experimental and numerical profiles is much less pro-

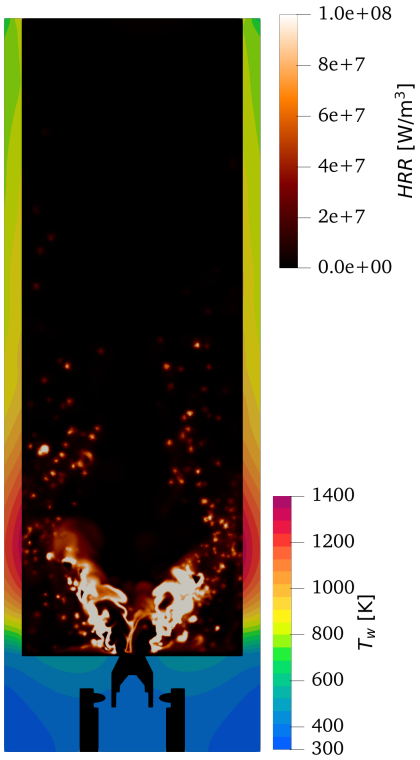

Figure 16: Instantaneous solution obtained from CHT simulations of the SICCA combustor in steady state operating conditions. The solid domain is colored by its local temperature, whereas the fluid domain shows the heat release rate.

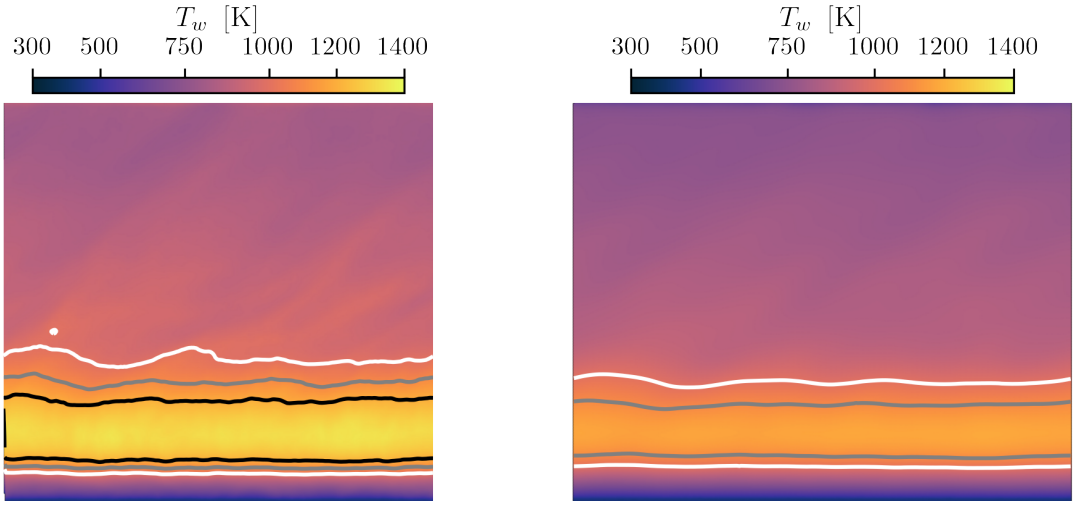

(a) Internal quartz wall (coupled with fluid)

(b) External quartz wall (imposed radiative/convective boundary condition)

Figure 17: Quartz wall temperatures in SICCA obtained from CHT simulations. Images are transformed from a cylindrical into a rectangular system. Iso-contours correspond to $T_w = 1000\,\mathrm{K}$ (white), $T_w = 1100\,\mathrm{K}$ (gray), and $T_w = 1200\,\mathrm{K}$ (black).

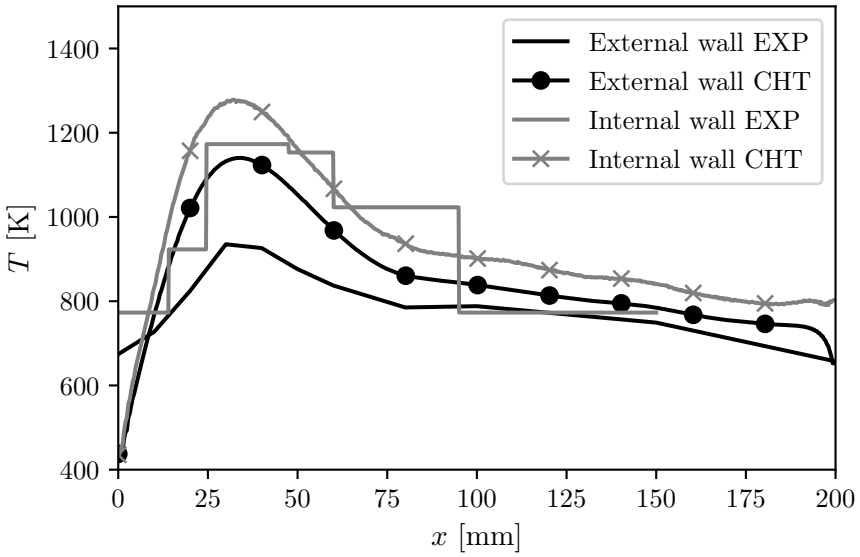

Figure 18: Comparison of experimental wall temperature measurements with data from Conjugate Heat Transfer simulations in SICCA. Both sides of the *same* quartz tube are plotted: the external quartz wall faces the atmosphere, while the internal wall is exposed to burnt gases. CHT profiles are azimuthally averaged.

nounced (overestimation by less than $50\,\mathrm{K}$). Interestingly, the temperature difference between the external and internal quartz wall face is much lower in the simulation compared to experimental measurements. It should be noted though that larger uncertainties exist for the thermochromic measurements, implying that a comparison of the internal quartz wall temperature is rather qualitative.

As can be observed in Fig. 19(a), the convective wall heat flux between the burnt gases and the internal quartz wall face is highest around $x = 30\,\mathrm{mm}$, where highest temperatures prevail. In turn, the modeled absorptance at the *external* wall face, given in Fig. 19(b), takes the lowest values at $x = 30\,\mathrm{mm}$, suggesting that external radiative heat transfer with the atmosphere is less effective in the high temperature region.

The high-temperature mismatch observed between numerical and experimental data clearly deserves further discussion. In Fig. 20, we compare the numerical heat flux at the external quartz wall (facing the atmosphere) with the theoretical experimental profile computed from the temperature profile in Fig. 18 $T(x)$ and $T_{amb} = 300\,\mathrm{K}$ the ambient temperature. The corresponding convective heat flux is computed using the correlation given in Eq. 5.14. The maximum allowed radiative flux is depicted by the idealized black body formula *i.e.*

$$q_{rad}(x) = \sigma(T(x)^4 - T_{amb}^4) \tag{6}$$

where σ denotes the Stefan-Boltzmann constant, and the quartz absorptance is deliberately set to unity to obtain the highest possible radiative heat flux. Upon examination of Fig. 20 it appears that neither the theoretical radiative heat flux (labeled as "Rad only"), nor the convective heat flux (labeled as "Conv only"), both evaluated from the experimental profile $T(x)$, can match the result obtained from CHT simulations, even if the quartz was assumed to be a black body, which certainly overestimates the actual radiative heat flux. The following reasons could thus explain the temperature (and heat flux) discrepancy:

- a possible inaccuracy in the experimental wall temperature profile,

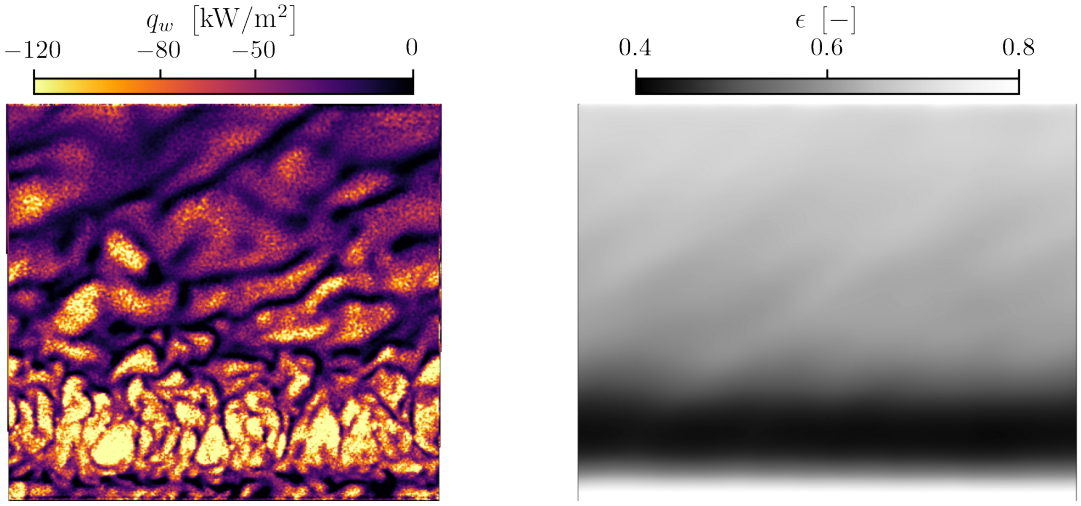

(a) Wall heat flux

(b) Modeled absorptance $\bar{A}^{slab}(T)$ of the external quartz face

Figure 19: Internal wall heat flux from the fluid onto the solid domain (at the internal quartz face), and modeled absorptance ($\epsilon = \bar{A}^{slab}(T)$) at the external quartz wall face exposed to the atmosphere. Images are transformed from a cylindrical into a rectangular system.

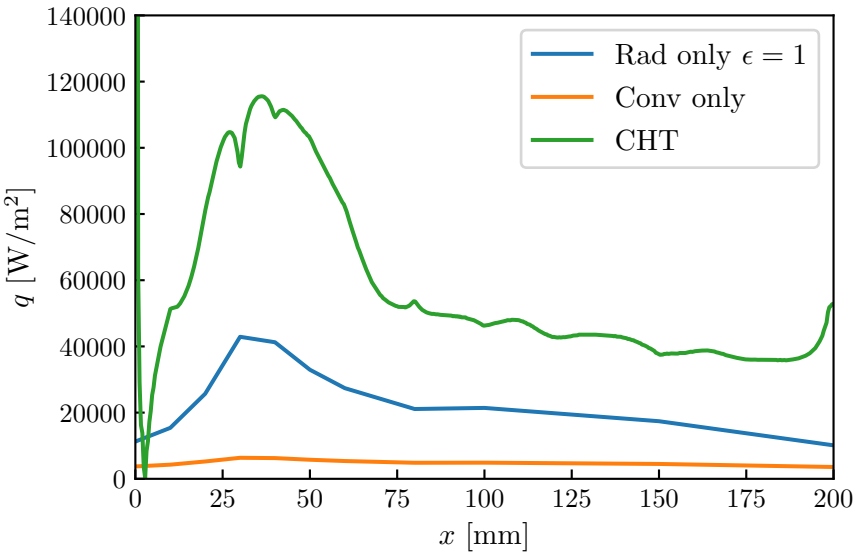

Figure 20: Comparison of the simulated heat flux at the external quartz wall with theoretical heat flux profiles based on experimental temperature measurements. The quartz absorptance is deliberately set to $\epsilon \equiv 1$ to estimate the highest possible radiative heat flux that can be obtained based on the experimental temperature measurements.

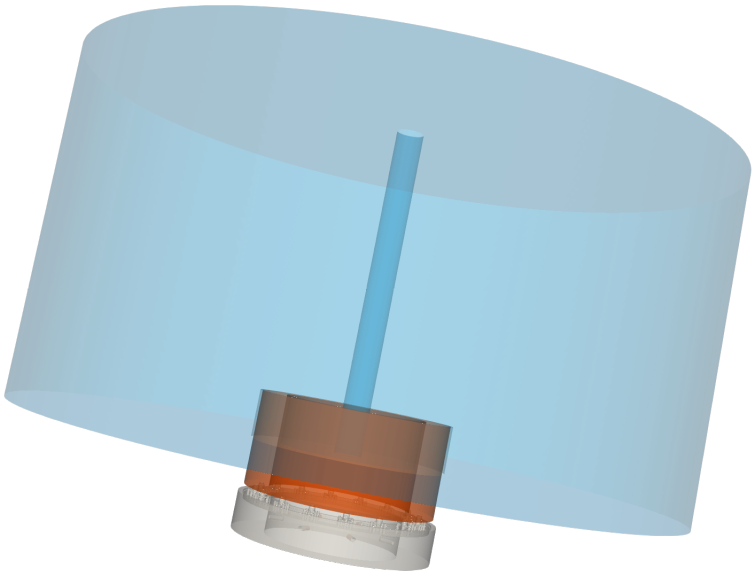

Figure 21: Full numerical domain of the MICCA combustor including the atmosphere (light blue cylinder). The combustion chamber is shown in red, the injector and air plenum in gray. The atmosphere is intentionally designed as a hollow cylinder to avoid the treatment of wedge-shaped cells at the axis of rotation when cloning the bisector to obtain the full MICCA combustor.

- the material properties of the quartz tube, which are specified at ambient temperature only (particularly the transmissivity and the heat conductivity). However, it is conceivable that these properties are substantially different at *elevated* temperatures observed in steady-state operating conditions.
- The water cooling system of the injector support modeled in a simplified manner and constituting an additional source of modeling uncertainties,
- the amount of entrained fresh air at the chamber outlet as a consequence of the protruding internal recirculation zone.

F Full numerical domain views

Figures 21 and 22 show the full numerical domains of MICCA-Spray and SICCA. The domain extension (referred to as "atmosphere", in light blue) is introduced with the purpose of imposing the numerical outlet boundary condition as far away from the *chamber* outlet as possible, where atmospheric pressure levels can be assumed safely. Moreover, we can avoid imposing "ill-posed" (or artificial) boundary conditions *at* the chamber outlet which can potentially influence the solution. Since our computational mesh is unstructured and tetrahedral, we can use gradually larger cell sizes towards the end of the numerical domain (*i.e.* the "atmosphere outlet") without incurring unreasonable penalties in terms of the computational cost. Even at the end of the simulation, burnt gases barely emerge half-way into the atmosphere as shown on an unwrapped cut-plane through the combustion chamber and the upper part of the atmosphere in Fig. 23. Thus, we assume that our results are not sensitive to this specific height of the atmosphere, since interactions of the flame with the domain outlet can be avoided.

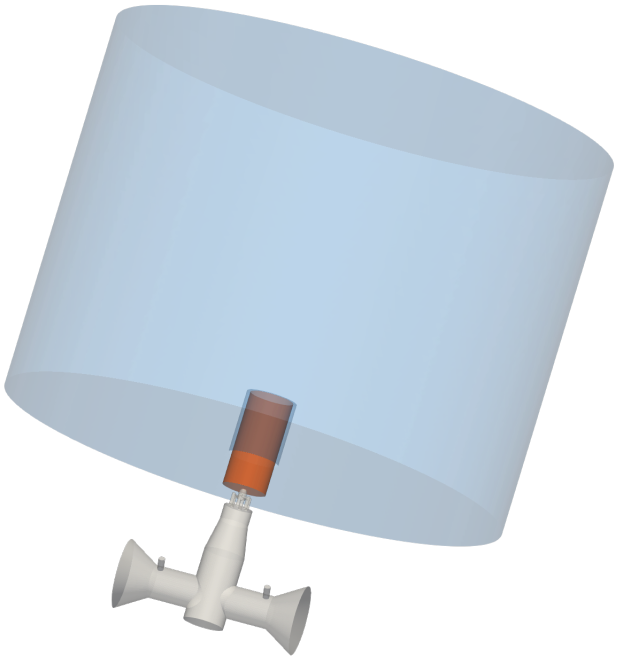

Figure 22: Full numerical domain of the SICCA combustor including the atmosphere (light blue cylinder). The combustion chamber is shown in red, the injector and air plenum in gray.

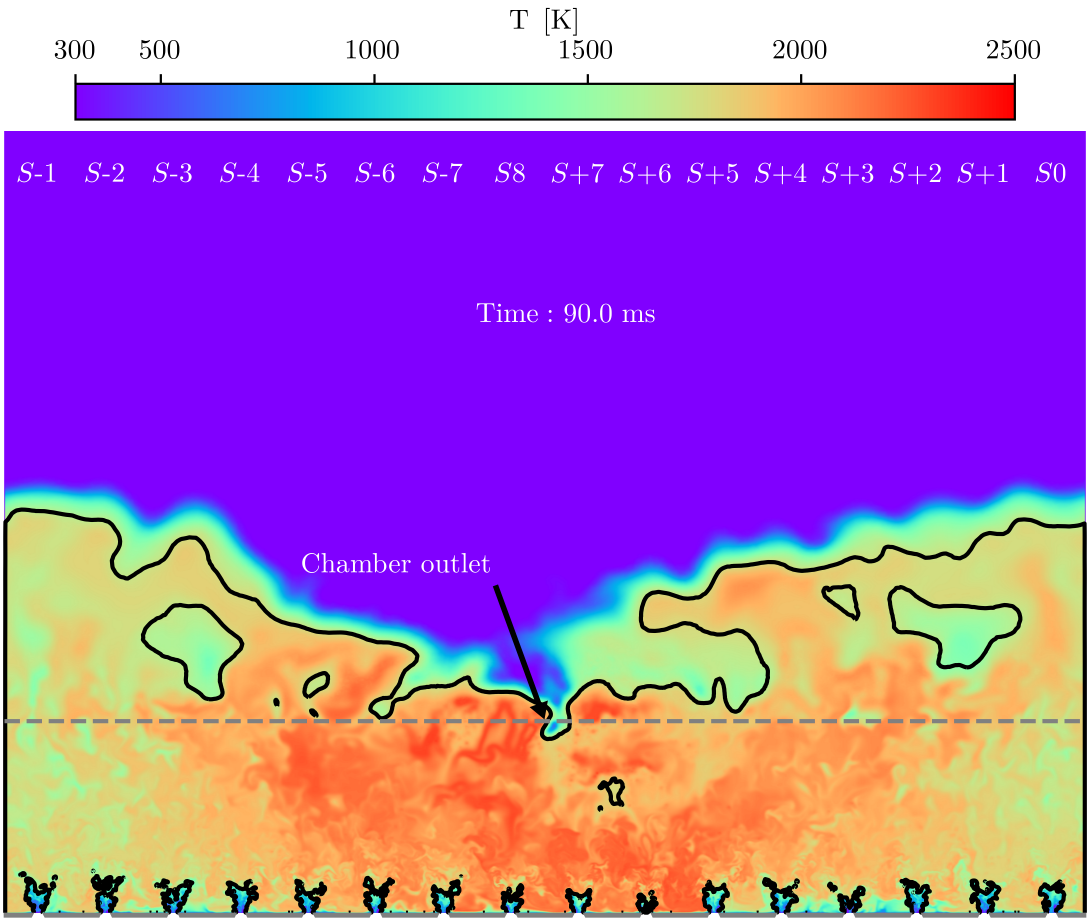

Figure 23: Temperature on an unwrapped cylindrical cut-plane at $R = 0.175\,\mathrm{m}$. Solid black lines correspond to iso-contours of the progress variable $c = 0.76$. The dashed horizontal line marks the outlet of the combustion chamber. The atmosphere outlet (domain outlet) corresponds to the upper edge of the image.

Bibliography

Certification Memorandum Turbine Engine Relighting In Flight (EASA CM No.: CM-PIFS-010 Issue 01). Technical report, European Aviation Safety Agency (EASA), 2015. URL https://www.easa.europa.eu/sites/default/files/dfu/'final'CM-PIFS-010Issue_01_TurbineEngineRelightingInFlight_PUBL.pdf.

Certification Specifications and Acceptable Means of Compliance for Engines (CS-E), Amendment 6. Technical report, European Union Aviation Safety Agency (EASA), 2020. URL https://www.easa.europa.eu/downloads/116287/en.

B. Abramzon and W. A. Sirignano. Droplet vaporisation model for spray combustion calculations. *International Journal of Heat and Mass Transfer*, 32(9):1605–1618, 1989. *(pp. 52, 79, 92, 96, 119, and 147)*

P. W. Agostinelli, D. Laera, I. Boxx, L. Gicquel, and T. Poinsot. Impact of wall heat transfer in Large Eddy Simulation of flame dynamics in a swirled combustion chamber. *Combustion and Flame*, 234:111728, 2021. *(p. 125)*

P. W. Agostinelli, Y. H. Kwah, S. Richard, G. Exilard, J. R. Dawson, L. Gicquel, and T. Poinsot. Numerical and experimental flame stabilization analysis in the new spinning combustion technology framework. *Proceedings of the ASME Turbo Expo*, 4A-2020(June), 2020. *(p. 16)*

E. Bach, J. Kariuki, J. R. Dawson, E. Mastorakos, and H. J. Bauer. Spark ignition of single bluff-body premixed flames and annular combustors. *51st AIAA Aerospace Sciences Meeting including the New Horizons Forum and Aerospace Exposition 2013*, (January), 2013. *(p. 9)*

E. Balaras, C. Benocci, and U. Piomelli. Two-layer approximate boundary conditions for large-eddy simulations. *AIAA Journal*, 34(6):1111–1119, 1996. *(p. 134)*

D. Ballal and A. Lefebvre. Flame propagation in heterogeneous mixtures of fuel droplets, fuel vapor and air. *Symposium (International) on Combustion*, 18(1):321–328, 1981. *(pp. 11 and 208)*

J. Bardina, J. H. Ferziger, and W. C. Reynolds. Improved Subgrid-Scale Models for Large-Eddy Simulation. *AIAA Paper*, 1980. *(p. 30)*

D. Barré, L. Esclapez, M. Cordier, E. Riber, B. Cuenot, G. Staffelbach, B. Renou, A. Vandel, L. Y. Gicquel, and G. Cabot. Flame propagation in aeronautical swirled multi-burners: Experimental and numerical investigation. *Combustion and Flame*, 161(9):2387–2405, 2014. *(pp. 4, 5, and 161)*

Y. Benarafa, O. Cioni, F. Ducros, and P. Sagaut. Temperature wall modelling for large-eddy simulation in a heated turbulent plane channel flow. *International Journal of Heat and Mass Transfer*, 50(21-22):4360–4370, 2007. *(p. 134)*

S. Berger, S. Richard, F. Duchaine, G. Staffelbach, and L. Y. Gicquel. On the sensitivity of a helicopter combustor wall temperature to convective and radiative thermal loads. *Applied Thermal Engineering*, 103:1450–1459, 2016. *(p. 125)*

R. Bird, W. Stewart, and E. Lightfoot. *Transport Phenomena*. John Wiley & Sons, 2 edition, 2002. *(pp. 52 and 93)*

M. Boger, D. Veynante, H. Boughanem, and A. Trouvé. Direct numerical simulation analysis of flame surface density concept for large eddy simulation of turbulent premixed combustion. *Symposium (International) on Combustion*, 27(1):917–925, 1998. *(p. 35)*

M. Boileau, G. Staffelbach, B. Cuenot, T. Poinsot, and C. Bérat. LES of an ignition sequence in a gas turbine engine. *Combustion and Flame*, 154(1-2):2–22, 2008. *(p. 13)*

M. Boivin, O. Simonin, and K. D. Squires. Direct numerical simulation of turbulence modulation by particles in isotropic turbulence. *Journal of Fluid Mechanics*, 375:235–263, nov 1998. *(p. 47)*

J. F. Bourgouin, D. Durox, T. Schuller, J. Beaunier, and S. Candel. Ignition dynamics of an annular combustor equipped with multiple swirling injectors. *Combustion and Flame*, 160 (8), 2013. *(pp. 7, 8, 9, and 71)*

J. Boussinesq. Essai sur la theorie des eaux courantes. *Memoires à l'académie des Sciences*, 23(1), 1872. *(p. 60)*

G. E. P. Box and M. E. Muller. A Note on the Generation of Random Normal Deviates. *The Annals of Mathematical Statistics*, 29(2):610–611, jun 1958. *(p. 57)*

K. P. Burnham and D. R. Anderson. *Model Selection and Multimodel Inference*. Springer New York, New York, NY, 2 edition, 2002. *(p. 95)*

T. D. Butler and P. J. O'Rourke. A numerical method for two dimensional unsteady reacting flows. *Symposium (International) on Combustion*, 16(1):1503–1515, 1977. *(pp. 35, 36, and 37)*

W. Cabot and P. Moin. Approximate wall boundary conditions in the large-eddy simulation of high Reynolds number flow. *Flow, Turbulence and Combustion*, 63(1):269–291, 2000. *(pp. 134 and 135)*

O. Cabrit and F. Nicoud. Direct simulations for wall modeling of multicomponent reacting compressible turbulent flows. *Physics of Fluids*, 21(5):0–29, 2009. *(p. 134)*

D. R. Chapman. Computational aerodynamics development and outlook. *AIAA Journal*, 17 (12):1293–1313, 1979. *(p. 27)*

F. Charlette, C. Meneveau, and D. Veynante. A power-law flame wrinkling model for LES of premixed turbulent combustion Part II: Dynamic formulation. *Combustion and Flame*, 131 (1-2):181–197, 2002a. *(pp. 38, 39, 40, and 147)*

F. Charlette, D. Veynante, and C. Meneveau. A power-law wrinkling model for LES of premixed turbulent combustion: Part I - non-dynamic formulation and initial tests. *Combustion and Flame*, 131:159–180, 2002b. *(pp. 38, 79, 189, and 225)*

G. Chaussonnet, E. Riber, O. Vermorel, B. Cuenot, S. Gepperth, and R. Koch. Large Eddy Simulation of a prefilming airblast atomizer. *ILASS – Europe 2013, 25th European Conference on Liquid Atomization and Spray Systems, Chania, Greece, 1-4 September 2013*, (September):1–4, 2013. *(pp. 58 and 81)*

G. Chaussonnet, O. Vermorel, E. Riber, and B. Cuenot. A new phenomenological model to predict drop size distribution in Large-Eddy Simulations of airblast atomizers. *International Journal of Multiphase Flow*, 80:29–42, 2016. *(pp. 119 and 148)*

C. Chauveau, M. Birouk, F. Halter, and I. Gökalp. An analysis of the droplet support fiber effect on the evaporation process. *International Journal of Heat and Mass Transfer*, 128: 885–891, 2019. *(pp. 96, 97, 98, and 104)*

H. Choi and P. Moin. Grid-point requirements for large eddy simulation: Chapman's estimates revisited. *Physics of Fluids*, 24(1):1–6, 2012. *(pp. 27 and 28)*

S. W. Churchill and H. H. Chu. Correlating equations for laminar and turbulent free convection from a vertical plate. *International Journal of Heat and Mass Transfer*, 18(11):1323–1329, 1975. *(p. 132)*

R. Ciardiello, P. M. de Oliveira, A. W. Skiba, E. Mastorakos, and P. M. Allison. Effect of spark location and laminar flame speed on the ignition transient of a premixed annular combustor. *Combustion and Flame*, 221:296–310, 2020. *(pp. 9, 11, and 12)*

P. Clavin. Dynamic behavior of premixed flame fronts in laminar and turbulent flows. *Progress in Energy and Combustion Science*, 11(1):1–59, 1985. *(p. 33)*

O. Colin, F. Ducros, D. Veynante, and T. Poinsot. A thickened flame model for large eddy simulations of turbulent premixed combustion. *Physics of Fluids*, 12(7):1843–1863, 2000. *(pp. 13, 36, 37, 38, 41, 42, 43, 44, 78, 147, 212, and 225)*

O. Colin and M. Rudgyard. Development of High-Order Taylor-Galerkin Schemes for LES. *Journal of Computational Physics*, 162(2):338–371, 2000. *(pp. 26, 63, 77, and 147)*

F. Collin-Bastiani. *Modeling and Large Eddy Simulation of Two-Phase Ignition in Gas Turbines*. Phd thesis, Université de Toulouse, 2019a. *(p. 102)*

F. Collin-Bastiani. *Modeling and Large Eddy Simulation of Two-Phase Ignition in Gas Turbines*. Phd thesis, Institut National Polytechnique de Toulouse, France, 2019b. *(pp. xviii, 13, 76, 81, 92, 100, 101, 124, 146, 148, 149, and 226)*

M. Cordier, A. Vandel, B. Renou, G. Cabot, M. A. Boukhalfa, L. Esclapez, D. Barré, E. Riber, B. Cuenot, and L. Gicquel. Experimental and Numerical Analysis of an Ignition Sequence in a Multiple-Injectors Burner. In *Volume 1A: Combustion, Fuels and Emissions*, San Antonio, Texas, USA, jun 2013. American Society of Mechanical Engineers. *(p. 4)*

Corning Inc. Corning HPFS 7979, 7980, 8652, 8655 Fused Silica Optical Materials Product Information. Technical report, Corning Inc., 2015. *(pp. 130, 131, 132, and 133)*

C. T. Crowe, J. N. Chung, and T. R. Troutt. Particle mixing in free shear flows. *Progress in Energy and Combustion Science*, 14(3):171–194, 1988. *(p. 47)*

C. T. Crowe, J. D. Schwarzkopf, M. Sommerfeld, and Y. Tsuji. *Multiphase Flows with Droplets and Particles*. CRC Press, Boca Raton, 2 edition, aug 2011. *(p. 46)*

B. Cuenot, F. Shum-Kivan, and S. Blanchard. The thickened flame approach for non-premixed combustion: Principles and implications for turbulent combustion modeling. *Combustion and Flame*, page 111702, 2021. *(pp. 36 and 44)*

G. Damköhler. Der Einfluss der Turbulenz auf die Flammengeschwindigkeit in Gasgemischen. *Zeitschrift für Elektrochemie und angewandte physikalische Chemie*, 46(11):601–652, 1940. *(p. 37)*

G. De Luca. *Development of a dynamic LES model for turbulent diffusion flames*. Theses, Université Paris-Saclay, June 2021. *(p. 44)*

P. M. de Oliveira and E. Mastorakos. Mechanisms of flame propagation in jet fuel sprays as revealed by OH/fuel planar laser-induced fluorescence and OH* chemiluminescence. *Combustion and Flame*, 206:308–321, 2019. *(p. 11)*

J. W. Deardorff. A numerical study of three-dimensional turbulent channel flow at large Reynolds numbers. *Journal of Fluid Mechanics*, 41(2):453–480, 1970. *(pp. 29 and 58)*

M. J. Denton, S. B. Tambe, and S. M. Jeng. Experimental investigation into the high altitude relight of a three-cup combustor sector. *Proceedings of the ASME Turbo Expo*, 4B:1–12, 2018. *(pp. 11 and 147)*

J. Donea and A. Huerta. *Finite Element Methods for Flow Problems*. John Wiley & Sons, Ltd, Chippenham, Great Britain, 2003. *(p. 126)*

L. Dressler, F. L. Sacomano Filho, A. Sadiki, and J. Janicka. *Influence of Thickening Factor Treatment on Predictions of Spray Flame Properties Using the ATF Model and Tabulated Chemistry*, volume 106. Springer Netherlands, 2021. *(p. 56)*

F. Duchaine, S. Mendez, F. Nicoud, A. Corpron, V. Moureau, and T. Poinsot. Conjugate Heat Transfer with Large Eddy Simulation . Application to Gas Turbine Components . *2nd Colloque INCA*, 2008. *(p. 128)*

F. Duchaine, A. Corpron, L. Pons, V. Moureau, F. Nicoud, and T. Poinsot. Development and assessment of a coupled strategy for conjugate heat transfer with Large Eddy Simulation : Application to a cooled turbine blade. *Int. J. Heat Fluid Fl.*, 30(33):1129–1141, 2009. *(p. 129)*

F. Duchaine, S. Jauré, D. Poitou, E. Quémerais, G. Staffelbach, T. Morel, and L. Gicquel. Analysis of high performance conjugate heat transfer with the OpenPALM coupler. *Computational Science and Discovery*, 8(1), 2015. *(pp. 125 and 127)*

F. Ducros, F. Nicoud, and T. Poinsot. Wall-adapting local eddy-viscosity models for simulations in complex geometries. *Conference on Numerical Methods in Fluid Dynamics*, pages 1–7, 1998. *(p. 31)*

C. Duprat, G. Balarac, O. Métais, P. M. Congedo, and O. Brugière. A wall-layer model for large-eddy simulations of turbulent flows with/out pressure gradient. *Physics of Fluids*, 23 (1), 2011. *(p. 134)*

L. Durand and W. Polifke. Implementation of the thickened flame model for large Eddy simulation of turbulent premixed combustion in a commercial solver. *Proceedings of the ASME Turbo Expo*, 2:869–878, 2007. *(p. 43)*

C. Duwig. Study of a filtered flamelet formulation for large eddy simulation of premixed turbulent flames. *Flow, Turbulence and Combustion*, 79(4):433–454, 2007. *(p. 41)*

M. P. Errera and S. Chemin. Optimal solutions of numerical interface conditions in fluid-structure thermal analysis. *Journal of Computational Physics*, 245:431–455, 2013. *(pp. 129 and 174)*

G. M. Faeth. Current Status of Droplet and Liquid Combustion. In N. CHIGIER, editor, *Energy and Combustion Science*, pages 149–182. Pergamon Press Ltd, 1979. *(pp. 52, 56, and 71)*

G. M. Faeth. Evaporation and combustion of sprays. *Progress in Energy and Combustion Science*, 9(1-2):1–76, 1983. *(pp. 45, 48, 49, 51, 52, 54, and 55)*

G. M. Faeth. Mixing, transport and combustion in sprays. *Progress in Energy and Combustion Science*, 13(4):293–345, 1987. *(pp. 45, 46, and 55)*

C. Fefferman. Existence and Smoothness of the Navier-Stokes Equations, 2000. *(p. 26)*

A. Felden, P. Pepiot, L. Esclapez, E. Riber, and B. Cuenot. Including analytically reduced chemistry (ARC) in CFD applications. *Acta Astronautica*, 158(March):444–459, 2019. *(p. 32)*

B. Fiorina, R. Baron, O. Gicquel, D. Thevenin, S. Carpentier, and N. Darabiha. Modelling non-adiabatic partially premixed flames using flame-prolongation of ILDM. *Combustion Theory and Modelling*, 7(3):449–470, 2003. *(p. 39)*

B. Fiorina, O. Gicquel, L. Vervisch, S. Carpentier, and N. Darabiha. Premixed turbulent combustion modeling using tabulated detailed chemistry and PDF. *Proceedings of the Combustion Institute*, 30(1):867–874, 2005. *(p. 39)*

B. Fiorina, R. Vicquelin, P. Auzillon, N. Darabiha, O. Gicquel, and D. Veynante. A filtered tabulated chemistry model for LES of premixed combustion. *Combustion and Flame*, 157 (3):465–475, 2010. *(pp. 13 and 35)*

B. Fiorina, D. Veynante, and S. Candel. Modeling combustion chemistry in large eddy simulation of turbulent flames. *Flow, Turbulence and Combustion*, 94(1):3–42, 2015. *(pp. 32, 35, and 39)*

R. O. Fox. Large-eddy-simulation tools for multiphase flows. *Annual Review of Fluid Mechanics*, 44:47–76, 2011. *(p. 45)*

B. Franzelli, E. Riber, M. Sanjosé, and T. Poinsot. A two-step chemical scheme for kerosene-air premixed flames. *Combustion and Flame*, 157(7):1364–1373, 2010. *(pp. 33 and 77)*

V. Frayssé, L. Giraud, S. Gratton, and J. Langou. Algorithm 842: A set of GMRES routines for real and complex arithmetics on high performance computers. *ACM Transactions on Mathematical Software*, 31(2):228–238, 2005. *(p. 126)*

N. Frössling. Über die Verdunstung fallender Tropfen (On the evaporation of falling drops). *Gerlands Beiträge zur Geophysik*, 52:170–216, 1938. *(p. 52)*

C. Fureby. Large Eddy Simulation of turbulent reacting flows with conjugate heat transfer and radiative heat transfer. *Proceedings of the Combustion Institute*, 38(2):3021–3029, 2021. *(p. 125)*

W. Gao, J. Yang, F. Liu, Y. Mu, C. Liu, and G. Xu. Experimental investigation on the flame propagation pattern of a staged partially premixed annular combustor. *Combustion and Flame*, 230:111445, 2021. *(pp. 7 and 159)*

E. Garnier, N. Adams, and P. Sagaut. *Large Eddy Simulation for Compressible Flows*. Scientific Computation. Springer Netherlands, Dordrecht, 2009. *(p. 29)*

M. Gelain. *Aerothermal characterisation of a surface heat exchanger implemented in a turbofan by-pass duct*. Theses, Université Paris-Saclay, November 2021. *(pp. 141 and 142)*

M. Germano, U. Piomelli, P. Moin, and W. H. Cabot. A dynamic subgrid-scale eddy viscosity model. *Physics of Fluids A*, 3(7):1760–1765, 1991. *(pp. 30 and 39)*

O. Gicquel, N. Darabiha, and D. Thévenin. Laminar premixed hydrogen/air counterflow flame simulations using flame prolongation of ILDM with differential diffusion. *Proceedings of the Combustion Institute*, 28(2):1901–1908, 2000. *(p. 32)*

M. B. Giles. Stability analysis of numerical interface conditions in fluid-structure thermal analysis. *International Journal for Numerical Methods in Fluids*, 25(4):421–436, 1997. *(p. 127)*

D. G. Goodwin, H. K. Moffat, I. Schoegl, R. L. Speth, and B. W. Weber. Cantera: An object-oriented software toolkit for chemical kinetics, thermodynamics, and transport processes. https://www.cantera.org, 2022. Version 2.6.0. *(p. 64)*

F. C. Gouldin. An application of fractals to modeling premixed turbulent flames. *Combustion and Flame*, 68(3):249–266, 1987. *(pp. 38 and 40)*

F. C. Gouldin, K. N. Bray, and J. Y. Chen. Chemical closure model for fractal flamelets. *Combustion and Flame*, 77(3-4):241–259, 1989. *(pp. 38 and 40)*

Ö. L. Gülder. Turbulent premixed combustion modelling using fractal geometry. *Symposium (International) on Combustion*, 23(1):835–842, 1991. *(p. 38)*

W. Han, H. Wang, G. Kuenne, E. R. Hawkes, J. H. Chen, J. Janicka, and C. Hasse. Large eddy simulation/dynamic thickened flame modeling of a high Karlovitz number turbulent premixed jet flame. *Proceedings of the Combustion Institute*, 37(2):2555–2563, 2019. *(p. 36)*

M. Hanke, R. Redler, T. Holfeld, and M. Yastremsky. YAC 1.2.0: new aspects for coupling software in Earth system modelling. *Geoscientific Model Development*, 9(8):2755–2769, aug 2016. *(p. 127)*

G. Hannebique, P. Sierra, E. Riber, and B. Cuenot. Large eddy simulation of reactive two-phase flow in an aeronautical multipoint burner. *Flow, Turbulence and Combustion*, 90(2): 449–469, 2013. *(pp. 54, 93, 99, and 100)*

A. Haselbacher, F. M. Najjar, and J. P. Ferry. An efficient and robust particle-localization algorithm for unstructured grids. *Journal of Computational Physics*, 225(2):2198–2213, 2007. *(p. 63)*

D. C. Haworth and T. J. Poinsot. Numerical simulations of Lewis number effects in turbulent premixed flames. *Journal of Fluid Mechanics*, 244:405–436, nov 1992. *(pp. 33 and 37)*

L. He and M. L. Oldfield. Unsteady conjugate heat transfer modeling. *Journal of Turbomachinery*, 133(3):1–12, 2011. *(p. 128)*

R. Hilbert, F. Tap, H. El-Rabii, and D. Thévenin. Impact of detailed chemistry and transport models on turbulent combustion simulations. *Progress in Energy and Combustion Science*, 30(1):61–117, 2004. *(p. 31)*

C. Hirsch. Finite Volume Method and Conservative Discretization with an Introduction to Finite Element Method. In *Numerical Computation of Internal and External Flows*, chapter 5, pages 203–248. Elsevier, 2 edition, 2007. *(p. 63)*

J. O. Hirschfelder, C. F. Curtiss, and R. B. Bird. *Molecular Theory of Gases and Liquids*. John Wiley & Sons, New York, 2 edition, 1964. *(pp. 25 and 54)*

W. G. Horner. A New Method of Solving Numerical Equations of All Orders by Continuous Approximation. *Philosophical Transactions of the Royal Society of London*, 109:308–335, 1819. *(p. 95)*

J. A. Horwitz and A. Mani. Accurate calculation of Stokes drag for point-particle tracking in two-way coupled flows. *Journal of Computational Physics*, 318:85–109, 2016. *(p. 47)*

P. G. Huang, G. N. Coleman, and P. Bradshaw. Compressible turbulent channel flows: DNS results and modelling. *Journal of Fluid Mechanics*, 305:185–218, dec 1995. *(pp. 63 and 137)*

Y. Huang and V. Yang. Dynamics and stability of lean-premixed swirl-stabilized combustion. *Progress in Energy and Combustion Science*, 35(4):293–364, 2009. *(p. 35)*

G. L. Hubbard, V. E. Denny, and A. F. Mills. Droplet Evaporation: Effects of Transients and Variable Properties. *International Journal of Heat and Mass Transfer*, 18:1003–1008, 1975. *(p. 53)*

M. Ihme, L. Shunn, and J. Zhang. Regularization of reaction progress variable for application to flamelet-based combustion models. *Journal of Computational Physics*, 231(23):7715–7721, 2012. *(p. 39)*

S. Jaure, F. Duchaine, G. Staffelbach, and L. Y. M. Gicquel. Massively parallel conjugate heat transfer methods relying on large eddy simulation applied to an aeronautical combustor. *Computational Science & Discovery*, 6(1):015008, 2013. *(pp. 125 and 129)*

P. Jenny, D. Roekaerts, and N. Beishuizen. Modeling of turbulent dilute spray combustion. *Progress in Energy and Combustion Science*, 38(6):846–887, 2012. *(pp. 44 and 79)*

W. P. Jones and R. P. Lindstedt. Global reaction schemes for hydrocarbon combustion. *Combustion and Flame*, 73(3):233–249, 1988. *(p. 32)*

B. A. Kader. Temperature and concentration profiles in fully turbulent boundary layers. *International Journal of Heat and Mass Transfer*, 24(9):1541–1544, 1981. *(p. 62)*

Y.-h. Kao, M. Denton, X. Wang, S.-m. Jeng, and M.-c. Lai. Experimental Spray Structure and Combustion of a Linearly-Arranged 5-Swirler Array. In *Volume 4A: Combustion, Fuels and Emissions*, pages 1–17. American Society of Mechanical Engineers, jun 2015. *(pp. 5 and 9)*

J. Kariuki and E. Mastorakos. Experimental investigation of turbulent flames in uniform dispersions of ethanol droplets. *Combustion and Flame*, 179:95–116, 2017. *(p. 45)*

W. M. Kays. Turbulent Prandtl Number—Where Are We? *Journal of Heat Transfer*, 116(2): 284–295, may 1994. *(p. 135)*

S. J. Kazmouz, D. C. Haworth, P. Lillo, and V. Sick. Extension of a thickened flame model to highly stratified combustion—Application to a spark-ignition engine. *Combustion and Flame*, 236:111798, 2022. *(p. 43)*

R. J. Kee, F. M. Rupley, E. Meeks, and J. A. Miller. Chemkin-iii: A fortran chemical kinetics package for the analysis of gas-phase chemical and plasma kinetics. Technical report, Sandia National Lab.(SNL-CA), Livermore, CA (United States), 1996. *(p. 64)*

J. O. Keller, L. Vaneveld, a. F. Ghoniem, J. W. Daily, a. K. Oppenheim, D. Korschelt, and G. L. Hubbard. Mechanism of instabilities in turbulent combustion leading to flashback. *AIAA Journal*, 20(2):254–262, 1981. *(p. 224)*

A. R. Kerstein, W. T. Ashurst, and F. A. Williams. Field equation for interface propagation in an unsteady homogeneous flow field. *Physical Review A*, 37(7):2728–2731, apr 1988. *(p. 35)*

A. Klimenko and R. Bilger. Conditional moment closure for turbulent combustion. *Progress in Energy and Combustion Science*, 25(6):595–687, dec 1999. *(p. 34)*

H. Klinger, S. Bake, H. F. Vogt, D. Knieschke, and P. Schober. Altitude testing of the E3E core engine. *Proceedings of the ASME Turbo Expo*, 1:223–232, 2011. *(pp. xvii, 3, 13, and 147)*

E. Knudsen and H. Pitsch. Large-Eddy Simulation for Combustion Systems: Modeling Approaches for Partially Premixed Flows. *The Open Thermodynamics Journal*, 4(3):76–85, 2010. *(p. 43)*

A. Kolmogorov. The Local Structure of Turbulence in Incompressible Viscous Fluid for Very Large Reynolds Numbers. *Doklady Akademiia Nauk SSSR*, 30:301–305, 1941. *(p. 27)*

C. Koren, R. Vicquelin, and O. Gicquel. High-fidelity multiphysics simulation of a confined premixed swirling flame combining large-eddy simulation, wall heat conduction and radiative energy transfer. *Proceedings of the ASME Turbo Expo*, 5C-2017, 2017a. *(p. 125)*

C. Koren. *Modélisation des transferts de chaleur couplés pour la simulation multi-physique des chambres de combustion*. Theses, Université Paris-Saclay, April 2016. *(p. 249)*

C. Koren, R. Vicquelin, and O. Gicquel. Self-adaptive coupling frequency for unsteady coupled conjugate heat transfer simulations. *International Journal of Thermal Sciences*, 118:340–354, 2017b. *(p. 129)*

C. Kraus, L. Selle, and T. Poinsot. Coupling heat transfer and large eddy simulation for combustion instability prediction in a swirl burner. *Combustion and Flame*, 191:239–251, 2018. *(pp. 125 and 129)*

K. K.-y. Kuo. *Principles of Combustion*. John Wiley & Sons, Hoboken, New Jersey, 2 edition, 2005. *(pp. 25, 51, and 52)*

Y. Kwah, P. Agostinelli, S. Richard, G. Exilard, S. Pascaud, L. Gicquel, and J. Dawson. Effect of strong azimuthal swirl on ignition and light-around in an annular combustor. In *Proceedings of ASME Turbo Expo 2022 Turbomachinery Technical Conference and Exposition*, pages 1–12, Rotterdam, Netherlands, 2022. *(p. 13)*

G. Lacaze, E. Richardson, and T. Poinsot. Large eddy simulation of spark ignition in a turbulent methane jet. *Combustion and Flame*, 156(10):1993–2009, 2009. *(pp. 81 and 226)*

C. E. Lacey, A. G. Novoselov, and M. E. Mueller. In-Situ Adaptive Manifolds: Enabling computationally efficient simulations of complex turbulent reacting flows. *Proceedings of the Combustion Institute*, 38(2):2673–2680, 2021. *(p. 32)*

T. Lancien. *Etude numérique de l'allumage diphasique de foyers annulaires multi-brûleurs*. PhD thesis, Université Paris-Saclay, France, 2018. *(pp. 14, 43, 102, 124, and 151)*

T. Lancien, K. Prieur, D. Durox, S. Candel, and R. Vicquelin. Large Eddy Simulation of Light-Round in an Annular Combustor With Liquid Spray Injection and Comparison With Experiments. *Journal of Engineering for Gas Turbines and Power*, 140(2), 2017. *(pp. 13, 71, 146, 151, 172, and 212)*

T. Lancien, K. Prieur, D. Durox, S. Candel, and R. Vicquelin. Leading point behavior during the ignition of an annular combustor with liquid n-heptane injectors. *Proceedings of the Combustion Institute*, 37(4), 2019. *(pp. 13, 71, 146, 157, 172, and 194)*

J. Larson, R. Jacob, and E. Ong. The Model Coupling Toolkit: A New Fortran90 Toolkit for Building Multiphysics Parallel Coupled Models. *The International Journal of High Performance Computing Applications*, 19(3):277–292, aug 2005. *(p. 127)*

C. K. Law. Dynamics of stretched flames. *Symposium (International) on Combustion*, 22(1): 1381–1402, 1989. *(p. 33)*

C. K. Law. Combustion at a crossroads: Status and prospects. *Proceedings of the Combustion Institute*, 31(1):1–29, 2007. *(p. 31)*

A. Lefebvre and V. Mcdonell. *Atomization and Sprays, Second Edition.* CRC Press, Boca Raton, 2 edition, 2017. *(pp. 44, 46, 47, 51, 52, 56, 57, and 71)*

A. H. Lefebvre and D. R. Ballal. *Gas turbine combustion: alternative fuels and emissions*. CRC Press, 2010. *(pp. 4, 71, 81, 148, 154, 224, and 228)*

J. P. Legier, T. Poinsot, and D. Veynante. Dynamically thickened flame LES model for premixed and non-premixed turbulent combustion. *Proceedings of the Summer Program, Centre for Turbulence Research*, pages 157–168, 2000. *(pp. 13, 42, 43, 44, 78, 147, 189, 197, and 225)*

T. Lieuwen, V. McDonell, E. Petersen, and D. Santavicca. Fuel Flexibility Influences on Premixed Combustor Blowout, Flashback, Autoignition and Instability. In *Volume 1: Combustion and Fuels, Education*, volume 2006, pages 601–615. ASME, 2006. *(p. 224)*

A. N. Lipatnikov. Stratified turbulent flames: Recent advances in understanding the influence of mixture inhomogeneities on premixed combustion and modeling challenges. *Progress in Energy and Combustion Science*, 62:87–132, 2017. *(p. 32)*

U. Maas and S. B. Pope. Simplifying chemical kinetics: Intrinsic low-dimensional manifolds in composition space. *Combustion and Flame*, 88(3-4):239–264, 1992. *(p. 32)*

E. Machover and E. Mastorakos. Spark ignition of annular non-premixed combustors. *Experimental Thermal and Fluid Science*, 73, 2016. *(p. 9)*

E. Machover and E. Mastorakos. Experimental investigation on spark ignition of annular premixed combustors. *Combustion and Flame*, 178:148–157, 2017a. *(pp. 7, 9, and 10)*

E. Machover and E. Mastorakos. Experimental and numerical investigation on spark ignition of linearly arranged non-premixed swirling burners. *Combustion Science and Technology*, 189(8):1326–1353, 2017b. *(p. 5)*

N. Maheu, V. Moureau, P. Domingo, F. Duchaine, and G. Balarac. Large-Eddy Simulations and of flow and heat transfer and around a low-Mach number turbine blade. *Center for Turbulence Research Proceedings of the Summer Program*, 2012. *(p. 134)*

B. B. Mandelbrot. On the geometry of homogeneous turbulence, with stress on the fractal dimension of the iso-surfaces of scalars. *Journal of Fluid Mechanics*, 72(3):401–416, dec 1975. *(pp. 38 and 40)*

J. Marrero-Santiago, A. Verdier, C. Brunet, A. Vandel, G. Godard, G. Cabot, M. Boukhalfa, and B. Renou. Experimental Study of Aeronautical Ignition in a Swirled Confined Jet-Spray Burner. *Journal of Engineering for Gas Turbines and Power*, 140(2), 2017. *(pp. 5 and 159)*

J. Marrero-Santiago, A. Verdier, A. Vandel, G. Cabot, A. M. Boukhalfa, and B. Renou. Effect of injector spacing in the light-around ignition efficiency and mechanisms in a linear swirled spray burner. *Heat and Mass Transfer/Waerme- und Stoffuebertragung*, 55(7):1871–1885, 2019. *(pp. 5 and 6)*

J. Marrero-Santiago, F. Collin-Bastiani, E. Riber, G. Cabot, B. Cuenot, and B. Renou. On the mechanisms of flame kernel extinction or survival during aeronautical ignition sequences: Experimental and numerical analysis. *Combust. Flame*, 222:70–84, 2020. *(p. 13)*

A. D. Martinos, N. Zarzalis, and S. R. Harth. Analysis of ignition processes at combustors for aero engines at high altitude conditions with and without effusion cooling. *Proceedings of the ASME Turbo Expo*, 1:1–10, 2020. *(pp. 11 and 147)*

A. R. Masri. Partial premixing and stratification in turbulent flames. *Proceedings of the Combustion Institute*, 35(2):1115–1136, 2015. *(p. 43)*

A. R. Masri. Turbulent Combustion of Sprays: From Dilute to Dense. *Combustion Science and Technology*, 188(10):1619–1639, 2016. *(pp. 44, 45, 79, 102, and 110)*

A. R. Masri. Challenges for turbulent combustion. *Proceedings of the Combustion Institute*, 38(1):121–155, 2021. *(pp. 1 and 43)*

E. Mastorakos. Forced ignition of turbulent spray flames. *Proceedings of the Combustion Institute*, 36(2):2367–2383, 2017. *(pp. 4, 81, 148, 154, and 224)*

M. Matalon and B. J. Matkowsky. Flames in Fluids: Their Interaction and Stability. *Combustion Science and Technology*, 34(1-6):295–316, 1983. *(p. 33)*

M. R. Maxey and J. J. Riley. Equation of motion for a small rigid sphere in a nonuniform flow. *Physics of Fluids*, 26(4):883–889, 1983. *(pp. 45 and 47)*

P. A. McMurthy, S. Menon, and A. R. Kerstein. A linear eddy sub-grid model for turbulent reacting flows: Application to hydrogen-AIR combustion. *Symposium (International) on Combustion*, 24(1):271–278, jan 1992. *(p. 34)*

C. Meneveau and J. Katz. Scale-Invariance and Turbulence Models for Large-Eddy Simulation. *Annual Review of Fluid Mechanics*, 32(1):1–32, jan 2000. *(p. 28)*

S. Menon and N. Patel. Subgrid modeling for simulation of spray combustion in large-scale combustors. *AIAA Journal*, 44(4):709–723, 2006. *(p. 45)*

F. Menter, A. Hüppe, A. Matyushenko, and D. Kolmogorov. An overview of hybrid RANS-LES models developed for industrial CFD. *Applied Sciences (Switzerland)*, 11(6), 2021. *(p. 58)*

H. Meuert, E. Strohmaier, J. Dongarra, H. Simon, and M. Meuer. TOP500 list, 2021. *(p. 29)*

M. Miguel-Brebion, D. Mejia, P. Xavier, F. Duchaine, B. Bedat, L. Selle, and T. Poinsot. Joint experimental and numerical study of the influence of flame holder temperature on the stabilization of a laminar methane flame on a cylinder. *Combustion and Flame*, 172: 153–161, 2016. *(p. 125)*

M. F. Modest. *Radiative Heat Transfer*. Academic Press, New York, 3 edition, 2013. *(pp. 126 and 132)*

T. Mosbach, R. Sadanandan, W. Meier, and R. Eggels. Experimental analysis of altitude relight under realistic conditions using laser and high-speed video techniques. *Proceedings of the ASME Turbo Expo*, 2(Parts A and B):523–532, 2010. *(pp. 11, 13, and 147)*

V. Moureau, P. Domingo, and L. Vervisch. From Large-Eddy Simulation to Direct Numerical Simulation of a lean premixed swirl flame: Filtered laminar flame-PDF modeling. *Combustion and Flame*, 158(7):1340–1357, 2011. *(p. 42)*

S. Mouriaux, O. Colin, and D. Veynante. Adaptation of a dynamic wrinkling model to an engine configuration. *Proceedings of the Combustion Institute*, 36(3):3415–3422, 2017. *(pp. 41, 79, and 148)*

A. Neophytou and E. Mastorakos. Simulations of laminar flame propagation in droplet mists. *Combustion and Flame*, 156(8):1627–1640, 2009. *(pp. 11, 208, and 210)*

A. Neophytou, E. Mastorakos, and R. S. Cant. The internal structure of igniting turbulent sprays as revealed by complex chemistry DNS. *Combustion and Flame*, 159(2):641–664, 2012. *(p. 45)*

F. Nicoud, H. B. Toda, O. Cabrit, S. Bose, and J. Lee. Using singular values to build a subgrid-scale model for large eddy simulations. *Physics of Fluids*, 23(8), 2011. *(pp. 31, 77, and 147)*

H. Nomura, Y. Ujiie, H. J. Rath, J. Sato, and M. Kono. Experimental study on high-pressure droplet evaporation using microgravity conditions. *Symposium (International) on Combustion*, 26(1):1267–1273, 1996. *(pp. 97 and 98)*

P. O'Rourke and F. Bracco. Two scaling transformations for the numerical computation of multidimensional unsteady laminar flames. *Journal of Computational Physics*, 33(2):185–203, nov 1979. *(p. 36)*

L. Palluotto. *Quasi-Monte Carlo computation of radiative heat transfer in coupled Large Eddy Simulation of a swirled premixed flame*. Theses, Université Paris-Saclay ; Université libre de Bruxelles (1970-....), July 2019. *(p. 249)*

A. Patel, J. W. Peeters, B. J. Boersma, and R. Pecnik. Semi-local scaling and turbulence modulation in variable property turbulent channel flows. *Physics of Fluids*, 27(9), 2015. *(pp. 62, 63, and 137)*

D. Paulhiac. Modelisation de la combustion d'un spray dans un bruleur aeronautique, 2015. *(p. 56)*

D. Paulhiac, B. Cuenot, E. Riber, L. Esclapez, and S. Richard. Analysis of the spray flame structure in a lab-scale burner using Large Eddy Simulation and Discrete Particle Simulation. *Combustion and Flame*, 212:25–38, 2020. *(pp. xvii, xviii, 32, 33, 34, 37, 43, 77, 78, 102, 147, 187, 209, and 225)*

P. Pepiot-Desjardins and H. Pitsch. An efficient error-propagation-based reduction method for large chemical kinetic mechanisms. *Combustion and Flame*, 154(1-2):67–81, 2008. *(p. 32)*

C. Pérez Arroyo, J. Dombard, F. Duchaine, L. Gicquel, N. Odier, G. Exilard, S. Richard, N. Buffaz, and J. Démolis. Large-Eddy Simulation of an Integrated High-Pressure Compressor and Combustion Chamber of a Typical Turbine Engine Architecture. In *Volume 2C: Turbomachinery*, London, UK, sep 2020. American Society of Mechanical Engineers. *(p. 13)*

N. Peters. Laminar diffusion flamelet models in non-premixed turbulent combustion. *Progress in Energy and Combustion Science*, 10(3):319–339, 1984. *(p. 34)*

N. Peters. Laminar flamelet concepts in turbulent combustion. *Symposium (International) on Combustion*, 21(1):1231–1250, jan 1986. *(p. 34)*

N. Peters. Multiscale combustion and turbulence. *Proceedings of the Combustion Institute*, 32(1):1–25, 2009. *(pp. 35 and 36)*

N. Peters. *Turbulent Combustion*, volume 21. Cambridge University Press, aug 2000. *(pp. 34, 35, and 37)*

N. Peters and B. Rogg, editors. *Reduced Kinetic Mechanisms for Applications in Combustion Systems*, volume 15 of *Lecture Notes in Physics Monographs*. Springer Berlin Heidelberg, Berlin, Heidelberg, 1993. *(p. 32)*

A. Petitet, R. C. Whaley, J. Dongarra, and A. Cleary. HPL - A Portable Implementation of the High-Performance Linpack Benchmark for Distributed-Memory Computers, 2018. *(p. 29)*

M. Philip. *Dynamics of light-round in multi-injector annular combustors*. PhD thesis, Université Paris-Saclay, France, apr 2016. *(p. 204)*

M. Philip, M. Boileau, R. Vicquelin, E. Riber, T. Schmitt, B. Cuenot, D. Durox, and S. Candel. Large Eddy Simulations of the ignition sequence of an annular multiple-injector combustor. *Proceedings of the Combustion Institute*, 35(3):3159–3166, 2015a. *(pp. 13 and 71)*

M. Philip, M. Boileau, R. Vicquelin, T. Schmitt, D. Durox, J. F. Bourgouin, and S. Candel. Simulation of the ignition process in an annular multiple-injector combustor and comparison with experiments. *Journal of Engineering for Gas Turbines and Power*, 137(3), 2015b. *(pp. 9, 11, 12, 13, 71, 172, and 194)*

C. D. Pierce and P. Moin. Progress-variable approach for large-eddy simulation of non-premixed turbulent combustion. *Journal of Fluid Mechanics*, 504(March 2002):73–97, 2004. *(p. 32)*

U. Piomelli and E. Balaras. Wall-Layer Models for Large-Eddy Simulations. *Annual Review of Fluid Mechanics*, 34(1):349–374, jan 2002. *(p. 58)*

T. Poinsot and S. Lele. Boundary conditions for direct simulations of compressible viscous flows. *Journal of Computational Physics*, 101(1):104–129, 1992. *(pp. 81 and 226)*

T. Poinsot, D. Veynante, and S. Candel. Quenching processes and premixed turbulent combustion diagrams. *Journal of Fluid Mechanics*, 228:561–606, 1991. *(pp. 33, 36, and 37)*

T. Poinsot and D. Veynante. *Theoretical and Numerical Combustion*. R. T. Edwards Inc., Philadelphia, USA, 2 edition, 2005. *(pp. 25, 31, and 32)*

S. B. Pope. PDF methods for turbulent reactive flows. *Progress in Energy and Combustion Science*, 11(2):119–192, 1985. *(p. 34)*

S. B. Pope. Computationally efficient implementation of combustion chemistry using in situ adaptive tabulation. *Combustion Theory and Modelling*, 1(1):41–63, 1997. *(p. 32)*

S. B. Pope. *Turbulent Flows*. Cambridge University Press, New York, aug 2000. *(pp. 35, 46, and 60)*

S. B. Pope. Ten questions concerning the large-eddy simulation of turbulent flows. *New Journal of Physics*, 6, 2004. *(p. 28)*

S. B. Pope. Small scales, many species and the manifold challenges of turbulent combustion. *Proceedings of the Combustion Institute*, 34(1):1–31, 2013. *(pp. 28, 31, and 32)*

S. Popp, G. Kuenne, J. Janicka, and C. Hasse. An extended artificial thickening approach for strained premixed flames. *Combustion and Flame*, 206:252–265, 2019. *(pp. 36, 37, 78, and 212)*

K. Prieur, D. Durox, J. Beaunier, T. Schuller, and S. Candel. Ignition dynamics in an annular combustor for liquid spray and premixed gaseous injection. *Proceedings of the Combustion Institute*, 36(3):3717–3724, 2017. *(pp. 11, 70, 71, and 151)*

K. Prieur, G. Vignat, D. Durox, T. Schuller, and S. Candel. Flame and spray dynamics during the light-round process in an annular system equipped with multiple swirl spray injectors. *Journal of Engineering for Gas Turbines and Power*, 141(6), 2019. *(pp. xxii, 16, 70, 71, 73, 74, 124, 172, 224, 227, 229, 233, and 239)*

S. Puggelli, T. Lancien, K. Prieur, D. Durox, S. Candel, and R. Vicquelin. Impact of Wall Temperature in Large Eddy Simulation of Light-Round in an Annular Liquid Fueled Combustor and Assessment of Wall Models. *Journal of Engineering for Gas Turbines and Power*, 142(1):1–11, jan 2020. *(pp. 11, 12, 14, 15, 59, 63, 124, 134, 146, 154, 159, 162, 194, and 239)*

S. Puggelli, D. Veynante, and R. Vicquelin. Impact of dynamic modelling of the flame subgrid scale wrinkling in large-Eddy simulation of light-round in an annular combustor. *Combustion and Flame*, 230, 2021. *(pp. 14, 15, 38, 41, 71, 146, 151, 165, 167, 194, 200, 204, 213, and 215)*

E. Radenac, J. Gressier, and P. Millan. Methodology of numerical coupling for transient conjugate heat transfer. *Computers and Fluids*, 100:95–107, 2014. *(p. 129)*

P. Rajendram Soundararajan, G. Vignat, D. Durox, A. Renaud, and S. Candel. Effect of Different Fuels on Combustion Instabilities in an Annular Combustor. *Journal of Engineering for Gas Turbines and Power*, 143(3):1–13, mar 2021. *(p. 71)*

W. E. Ranz and W. R. Marshall. Evaporation from drops. Part 1. *Chemical Engineering Progress*, 48:141–146, 1952. *(p. 52)*

R. W. Read, J. W. Rogerson, and S. Hochgreb. Relight imaging at low temperature, Low pressure conditions. *46th AIAA Aerospace Sciences Meeting and Exhibit*, (January):1–13, 2008. *(pp. 11 and 147)*

S. Refahi. *Développement d'un code de transfert radiatif et de son couplage avec un code LES*. Theses, Ecole Centrale Paris, February 2013. *(p. 249)*

A. Refloch, B. Courbet, A. Murrone, C. Laurent, J. Troyes, G. Chaineray, J. B. Dargaud, and F. Vuillot. CEDRE Software. *Journal AerospaceLab*, (2):1–10, 2011. *(p. 127)*

J. Reveillon and L. Vervisch. Analysis of weakly turbulent dilute-spray flames and spray combustion regimes. *Journal of Fluid Mechanics*, 537:317–347, 2005. *(p. 45)*

L. F. Richardson. *Wheather Prediction by Numerical Process*. Cambridge University Press, London, 1922. *(p. 27)*

W. L. Roberts, J. F. Driscoll, M. C. Drake, and L. P. Goss. Images of the quenching of a flame by a vortex-To quantify regimes of turbulent combustion. *Combustion and Flame*, 94 (1-2), 1993. *(p. 38)*

B. Rochette, E. Riber, and B. Cuenot. Effect of non-zero relative velocity on the flame speed of two-phase laminar flames. *Proceedings of the Combustion Institute*, 37(3):3393–3400, 2019. *(p. 208)*

B. Rochette, E. Riber, B. Cuenot, and O. Vermorel. A generic and self-adapting method for flame detection and thickening in the thickened flame model. *Combustion and Flame*, 212: 448–458, 2020. *(p. 43)*

P. Rodrigues, O. Gicquel, N. Darabiha, K. P. Geigle, and R. Vicquelin. Assessment of External Heat Transfer Modeling of a Laboratory-Scale Combustor: Effects of Pressure-Housing Environment and Semi-Transparent Viewing Windows. *Journal of Engineering for Gas Turbines and Power*, 141(3), jun 2018. *(p. 132)*

M. A. Rudgyard. Cell vertex methods for steady inviscid flow. In *Lectures Series 1993-04 (Von Karman Institute for Fluid Dynamics)*, Rhode-Saint-Genèse, Belgium, 1993. Von Karman Institute for Fluid Dynamics. *(p. 63)*

F. L. Sacomano Filho, G. C. Krieger Filho, J. A. van Oijen, A. Sadiki, and J. Janicka. A novel strategy to accurately represent the carrier gas properties of droplets evaporating in a combustion environment. *International Journal of Heat and Mass Transfer*, 137:1141–1153, 2019. *(pp. 54 and 92)*

F. L. Sacomano Filho, A. Hosseinzadeh, A. Sadiki, and J. Janicka. On the interaction between turbulence and ethanol spray combustion using a dynamic wrinkling model coupled with tabulated chemistry. *Combustion and Flame*, 215:203–220, 2020. *(p. 45)*

M. Sanjosé. *Evaluation de la méthode Euler-Euler pour la simulation aux grandes échelles des chambres à carburant liquide*. Phd thesis, Institut National Polytechnique de Toulouse, France, 2009. *(p. 54)*

M. Sanjosé, J. M. Senoner, F. Jaegle, B. Cuenot, S. Moreau, and T. Poinsot. Fuel injection model for Euler-Euler and Euler-Lagrange large-eddy simulations of an evaporating spray inside an aeronautical combustor. *International Journal of Multiphase Flow*, 37(5):514–529, 2011. *(pp. xviii, 56, 57, 81, 102, 147, and 225)*

S. S. Sazhin. Advanced models of fuel droplet heating and evaporation. *Progress in Energy and Combustion Science*, 32(2):162–214, 2006. *(p. 47)*

S. S. Sazhin. Modelling of fuel droplet heating and evaporation: Recent results and unsolved problems. *Fuel*, 196:69–101, 2017. *(p. 52)*

L. Schiller and A. Naumann. A drag coefficient correlation. *Zeitschrift des Vereins Deutscher Ingenieure*, 77:318–320, 1935. *(pp. 46, 79, 147, and 225)*

H. Schlichting and K. Gersten. *Boundary-Layer Theory*. Springer Berlin Heidelberg, Berlin, Heidelberg, 2017. *(pp. 58, 61, 62, 134, and 135)*

T. Schönfeld and M. Rudgyard. Steady and Unsteady Flow Simulations Using the Hybrid Flow Solver AVBP. *AIAA Journal*, 37(11):1378–1385, 1999. *(pp. 26, 63, 147, and 225)*

O. Schulz, U. Doll, D. Ebi, J. Droujko, C. Bourquard, and N. Noiray. Thermoacoustic instability in a sequential combustor: Large eddy simulation and experiments. *Proceedings of the Combustion Institute*, 37(4):5325–5332, 2019. *(p. 224)*

P. Sierra Sanchez. *Modeling the dispersion and evaporation of sprays in aeronautical combustion chambers*. Phd thesis, Institut National Polytechnique de Toulouse, France, 2012. *(p. 54)*

W. A. Sirignano. *Fluid Dynamics and Transport of Droplets and Sprays*. Cambridge University Press, New York, 2 edition, jul 2010. *(pp. 47 and 52)*

J. Smagorinsky. General Circulation Experiments With The Primitive Equations. *Monthly Weather Review*, 91(3):99–164, mar 1963. *(p. 31)*

A. J. Smallbone, W. Liu, C. K. Law, X. Q. You, and H. Wang. Experimental and modeling study of laminar flame speed and non-premixed counterflow ignition of n-heptane. *Proceedings of the Combustion Institute*, 32(1):1245–1252, 2009. *(pp. xvii, xxii, 33, 34, 77, 187, 190, 233, 248, and 249)*

M. D. Smooke, editor. *Reduced Kinetic Mechanisms and Asymptotic Approximations for Methane-Air Flames*, volume 384 of *Lecture Notes in Physics*. Springer Berlin Heidelberg, Berlin, Heidelberg, 1991. *(p. 32)*

Y. Sommerer, D. Galley, T. Poinsot, S. Ducruix, F. Lacas, and D. Veynante. Large eddy simulation and experimental study of flashback and blow-off in a lean partially premixed swirled burner. *Journal of Turbulence*, 5, 2004. *(p. 224)*

P. R. Spalart. Detached-eddy simulation. *Annual Review of Fluid Mechanics*, 41:181–202, 2009. *(p. 58)*

D. B. Spalding. The combustion of liquid fuels. *Symposium (International) on Combustion*, 4 (1):847–864, 1953. *(p. 47)*

G. Stokes. On the Effect of the Internal Friction of Fluids on the Motion of Pendulums. *Transactions of the Cambridge Philosophical Society*, 9(8), 1851. *(p. 46)*

H. Tennekes and J. L. Lumley. *A first course in turbulence*. MIT Press, 1972. *(p. 151)*

J. J. Valencia and P. N. Quested. *Thermophysical Properties*, volume 15. ASM International, 2008. *(p. 130)*

J. A. van Oijen and L. P. de Goey. Modelling of premixed laminar flames using flamelet-generated manifolds. *Combustion Science and Technology*, 161(1):113–137, 2000. *(p. 32)*

J. A. van Oijen, A. Donini, R. J. Bastiaans, J. H. ten Thije Boonkkamp, and L. P. de Goey. State-of-the-art in premixed combustion modeling using flamelet generated manifolds. *Progress in Energy and Combustion Science*, 57:30–74, 2016. *(p. 34)*

D. Veynante and T. Poinsot. Large eddy simulation of combustion instabilities in turbulent premixed burners. *Center for Turbulence Research Annual Research Briefs*, pages 253–275, 1997. *(p. 36)*

D. Veynante and V. Moureau. Analysis of dynamic models for large eddy simulations of turbulent premixed combustion. *Combustion and Flame*, 162(12):4622–4642, 2015. *(pp. 38 and 41)*

D. Veynante and L. Vervisch. Turbulent combustion modeling. *Progress in Energy and Combustion Science*, 28(3):193–266, 2002. *(pp. 31, 39, and 208)*

R. Vicquelin, B. Fiorina, N. Darabiha, O. Gicquel, and D. Veynante. Coupling tabulated chemistry with Large Eddy Simulation of turbulent reactive flows. *Comptes Rendus - Mecanique*, 337(6-7):329–339, 2009. Combustion for aerospace propulsion. *(p. 35)*

G. Vignat, D. Durox, T. Schuller, and S. Candel. Combustion Dynamics of Annular Systems. *Combustion Science and Technology*, 192(7):1358–1388, 2020a. *(p. 71)*

G. Vignat. *Injection and combustion dynamics in swirled spray flames and azimuthal coupling in annular combustors*. Phd thesis, University Paris-Saclay, 2020. *(pp. 73 and 74)*

G. Vignat, D. Durox, A. Renaud, and S. Candel. High amplitude combustion instabilities in an annular combustor inducing pressure field deformation and flame blow off. *Journal of Engineering for Gas Turbines and Power*, 142(1):1–11, 2020b. *(p. 71)*

G. Vignat, P. Rajendram Soundararajan, D. Durox, A. Vié, A. Renaud, and S. Candel. A Joint Experimental and LES Characterization of the Liquid Fuel Spray in a Swirl Injector. *Journal of Engineering for Gas Turbines and Power*, jan 2021. *(pp. 56, 57, 81, 102, 105, and 147)*

P. S. Volpiani, T. Schmitt, and D. Veynante. A posteriori tests of a dynamic thickened flame model for large eddy simulations of turbulent premixed combustion. *Combustion and Flame*, 174:166–178, 2016. *(pp. 41, 79, and 148)*

D. H. Wacks and N. Chakraborty. Flame Structure and Propagation in Turbulent Flame-Droplet Interaction: A Direct Numerical Simulation Analysis. *Flow, Turbulence and Combustion*, 96(4):1053–1081, 2016. *(p. 11)*

D. H. Wacks, N. Chakraborty, and E. Mastorakos. Statistical Analysis of Turbulent Flame-Droplet Interaction: A Direct Numerical Simulation Study. *Flow, Turbulence and Combustion*, 96(2):573–607, 2016. *(p. 11)*

G. Wang, M. Boileau, and D. Veynante. Implementation of a dynamic thickened flame model for large eddy simulations of turbulent premixed combustion. *Combustion and Flame*, 158 (11):2199–2213, 2011. *(pp. 38, 42, and 43)*

G. Wang, M. Boileau, D. Veynante, and K. Truffin. Large eddy simulation of a growing turbulent premixed flame kernel using a dynamic flame surface density model. *Combustion and Flame*, 159(8):2742–2754, 2012. *(p. 38)*

G. Wang, L. Zhong, Y. Yang, Y. Zheng, Y. Fang, Y. Xia, and C. Ye. Experimental investigation of the ignition dynamics in an annular premixed combustor with oblique-injecting swirling burners. *Fuel*, 287:119494, 2021. *(p. 13)*

M. Wang and P. Moin. Dynamic wall modeling for large-eddy simulation of complex turbulent flows. *Physics of Fluids*, 14(7):2043–2051, 2002. *(p. 134)*

J. Warnatz, U. Maas, and R. W. Dibble. *Combustion: Physical and Chemical Fundamentals, Modeling and Simulation, Experiments, Pollutant Formation*. Springer Berlin Heidelberg, Berlin, Heidelberg, 3 edition, 2001. *(p. 32)*

C. R. Wilke. A viscosity equation for gas mixtures. *The Journal of Chemical Physics*, 18(4): 517–519, 1950. *(p. 54)*

F. A. Williams. Theory of Combustion in Laminar Flows. *Annual Review of Fluid Mechanics*, 3(1):171–188, jan 1971. *(p. 34)*

F. A. Williams. *Combustion theory: The fundamental theory of chemically reacting flow systems*. Benjamin/Cummings Publishing Company, Menlo Park, CA, 2 edition, 1985. *(pp. 33 and 36)*

N. A. Worth and J. R. Dawson. Modal dynamics of self-excited azimuthal instabilities in an annular combustion chamber. *Combustion and Flame*, 160(11):2476–2489, 2013. *(pp. 7 and 13)*

H. Wu, Y. C. See, Q. Wang, and M. Ihme. A pareto-efficient combustion framework with submodel assignment for predicting complex flame configurations. *Combustion and Flame*, 162(11):4208 – 4230, 2015. *(p. 34)*

Y. Xia, C. Linghu, Y. Zheng, C. Ye, C. Ma, H. Ge, and G. Wang. Experimental Investigation of the Flame Front Propagation Characteristic During Light-round Ignition in an Annular Combustor. *Flow, Turbulence and Combustion*, pages 247–269, 2019. *(pp. 7 and 13)*

T. Yahou, J. R. Dawson, and T. Schuller. Impact of ignition strategy and back pressure on bluff body flame stabilization for hydrogen enriched mixtures. In *Low-Carbon Combustion*, Cambridge, UK, 2022. *(p. 224)*

H. Yamashita, M. Shimada, and T. Takeno. A numerical study on flame stability at the transition point of jet diffusion flames. *Symposium (International) on Combustion*, 26(1): 27–34, 1996. *(pp. xxi, 44, 78, 147, 196, 199, and 225)*

C. Ye, G. Wang, Y. Fang, C. Ma, L. Zhong, and S. Moreau. Ignition dynamics in an annular combustor with gyratory flow motion. *Proceedings of the ASME Turbo Expo*, 4B-2018(1), 2018. *(pp. 9, 13, and 82)*

J. Zhang. *Radiation Monte Carlo approcah dedicated to the coupling with LES reactive simulation.* Theses, Ecole Centrale Paris, January 2011. *(p. 249)*

Y. Zhang. *Coupled convective heat transfer and radiative energy transfer in turbulent boundary layers*. Theses, Ecole Centrale Paris, September 2013. *(p. 249)*

W. Zhao, L. Zhou, W. Qin, and H. Wei. Large Eddy Simulation of Multiple-Stage Ignition Process of n-Heptane Spray Flame. *Journal of Engineering for Gas Turbines and Power*, 141 (8):1–12, aug 2019. *(p. 13)*

université PARIS-SACLAY

ÉCOLE DOCTORALE
Sciences mécaniques et énergétiques, matériaux et géosciences (SMEMAG)

Titre: Analyse numérique de l'allumage circulaire dans les foyers annulaires diphasiques avec conditions thermiques de paroi réalistes

Mots clés: allumage; chambres de combustion annulaires; simulation aux grandes échelles; flammes diphasiques; transferts thermiques

Résumé : La transition vers des technologies à faibles émissions nécessite que les chambres de combustion des moteurs aéronautiques fonctionnent avec des carburants de plus en plus propres. Le redémarrage du moteur doit se produire de manière fiable et sûr et doit être assuré pour différentes points de fonctionnement. Les scénarios de redémarrage impliquent (entre autres) un rallumage rapide en montée, ou un redémarrage à haute altitude en auto-rotation, ce qui entraine une large gamme de températures d'air, de délais de redémarrage et de températures pariétales de chambre de combustion. L'étude des effets de la température pariétale sur l'allumage dans des foyers annulaires simplifiés à l'échelle du laboratoire a récemment reçu plus d'attention. En particulier, l'impact sur la propagation de la flamme pendant l'allumage circulaire (*light-round* en anglais) a été révélé expérimentalement, indiquant une propagation plus rapide de la flamme et des durées d'allumage plus courtes à des températures de paroi élevées par rapport aux parois à température ambiante. Malgré son impact de premier ordre, le rôle des transferts de chaleur n'a pas été entièrement clarifié. Par conséquent, l'allumage circulaire est étudié numériquement et théoriquement dans la chambre de combustion annulaire diphasique MICCA-Spray en deux configurations : (i) parois à température ambiante, représentant un cas de redémarrage à haute altitude, et (ii) parois de la chambre de combustion préchauffées, ce qui correspond à un rallumage rapide. Des simulations aux grandes échelles (*LES* en anglais) sont effectuées dans une configuration unique comprenant une description lagrangienne polydispersé des gouttes du spray de combustible, un modèle de combustion dynamique et un nouveau modèle de paroi tabulé avec une description détaillée des propriétés thermophysiques dans la couche limite. Les durées prédites d'allumage retrouvent remarquablement bien les données expérimentales. Il est démontré que l'expansion volumétrique des gaz brûlés induit une accélération azimutale de l'écoulement qui constitue un mécanisme clé de la propagation de flamme. Un effet de refroidissement des parois de la chambre de combustion sur les gaz brûlés est particulièrement prononcé en aval, diminuant la vitesse de propagation résultante. Pour le deuxième cas, des simulations de transfert conjugué de chaleur sont effectuées pour obtenir des profils de température de paroi réalistes dans des conditions de fonctionnement stationnaires, faute de données expérimentales. Ces profils de température sont ensuite imposés comme conditions aux limites pour les simulations de carburation ainsi que d'allumage. Les résultats montrent que le préchauffage des gaz frais dans le second cas provoque une augmentation importante de la vitesse de la flamme laminaire, qui compense la diminution observée du rapport de densité. Ces observations sont ensuite analysées théoriquement à l'aide d'un modèle d'ordre réduit, capable de prédire les vitesses moyennes de propagation de la flamme à partir des données LES. Ce modèle souligne également l'importance d'une modélisation détaillée de tous les mécanismes pilotant la propagation de flamme, afin d'éviter de possibles compensations d'erreur. L'analyse complète clarifie également le rôle des transferts de chaleur pendant l'allumage circulaire. Enfin, un processus dynamique de stabilisation de la flamme est examiné, initialement observé pendant la phase d'allumage et étudié en détail dans une chambre de combustion mono-brûleur. Deux phases distinctes sont observées, commençant par une flamme attachée à l'intérieur de l'injecteur pendant un temps caractéristique, avant la transition vers la position finale détachée de l'injecteur.

Title: Numerical analysis of light-round ignition in annular spray-flame combustors with realistic thermal wall conditions

Keywords: ignition; annular combustors; large-eddy simulation; spray flames; heat transfer

Abstract: The forthcoming transition in aviation burner technology towards renewable energy sources and reduced emissions requires aero-engine combustors to operate on increasingly cleaner fuels and new designs without compromising on safety. Engine restart in particular is of paramount importance, as its success must be ensured under a variety of operating conditions. Restart scenarios involve (among others) quick relight in climb, or restart from windmilling at high altitude, equivalent to a large range of inflow temperatures, restart delay periods, and combustor wall temperatures. In quick relight, engine parts will remain at an elevated temperature as there is not enough time for the air flow to cause a noticeable cooling effect. Conversely, restart from windmilling at high altitude after extended delay periods is likely to be performed with substantially cooled combustor walls, impeding fuel evaporation and successful ignition. Academic test facilities which can emulate real engine conditions in terms of both temperature and pressure are extremely scarce due to their complexity and cost. However, the study of wall temperature effects on ignition in simplified lab-scale annular combustors has recently received more attention. In particular, the impact on flame propagation during light-round has been revealed experimentally, indicating faster flame propagation and shorter light-round durations at increased wall temperatures over ambient temperature walls. Despite its first order impact, the role of heat transfer was not fully clarified. Therefore, we study light-round ignition numerically and theoretically in the annular spray-flame combustor MICCA-Spray in a lab-scale setting in two configurations to enhance the effect of heat transfer: (i) ambient temperature walls, approximating restart from windmilling, and (ii) preheated combustor walls, approximating quick relight. Large-Eddy Simulations are performed in a unique setup including Lagrangian particle tracking for the polydisperse liquid fuel spray, a dynamic combustion model, and a novel tabulated wall model with a detailed description of thermophysical properties in the boundary layer. Predicted light-round durations agree remarkably well with experimental data. It is shown that the volumetric expansion of burnt gases induces a flow acceleration in azimuthal direction which constitutes the main driving mechanism of flame propagation in the first case. A cooling effect of the combustor walls on burnt gases is particularly pronounced downstream, diminishing the resulting flame propagation speed. For the second case, precursor Conjugate Heat Transfer simulations are carried out to obtain realistic wall temperature profiles in stationary operating conditions, which are not readily available from the experiment. These temperature profiles are subsequently imposed as boundary conditions for prefueling and final light-round simulations in preheated conditions. Results suggest that preheating diminishes the effect of the liquid phase, and enhances the azimuthal flow acceleration. Fresh gas preheating in the second case causes a substantial increase of the laminar flame speed over the first case, outweighing the observed decrease of the density ratio. These observations are supported by a theoretical analysis using a low-order model, capable of predicting average flame propagation speeds from LES data. It is also used to emphasize the importance of detailed modeling of all governing mechanisms in LES, which would otherwise be impaired by compensating errors. The comprehensive analysis also clarifies the role of heat transfers during light-round. Finally, a dynamic flame stabilization process is examined, initially observed during light-round and studied in detail in a single-injector combustor. Two distinct phases are observed, starting with a flame anchoring inside the injector unit during a characteristic time, before transitioning into the final position detached from the injector.